

Modeling Strategies for Electro–Mechanical Microsystems with Uncertainty Quantification

PROEFSCHRIFT

ter verkrijging van de graad van doctor
aan de Technische Universiteit Delft,
op gezag van de Rector Magnificus Prof. ir. K.C.A.M. Luyben,
voorzitter van het College voor Promoties,
in het openbaar te verdedigen
op maandag 25 oktober 2010 om 14.00 uur
door

Stephan David Arjan HANNOT

werktuigkundig ingenieur
geboren te Rotterdam.

Dit proefschrift is goedgekeurd door de promotor:

Prof. dr. ir. D.J. Rixen

Samenstelling promotiecommissie:

Rector Magnificus	voorzitter
Prof. dr. ir. D.J. Rixen	Technische Universiteit Delft, promotor
Prof. ing. A. Corigliano	Politecnico di Milano
Prof. dr. ir. E.H. van Brummelen	Technische Universiteit Eindhoven
Prof. dr. ir. A. de Boer	Universiteit Twente
Prof. dr. Z. Gurdal	Technische Universiteit Delft
Prof. dr. ir. F. van Keulen	Technische Universiteit Delft
Dr. ir. V. Rochus	Université de Liège

Copyright © 2010 by S.D.A Hannot

All rights reserved. No part of the material protected by this copyright notice may be reproduced or utilized in any form or by any means, electronic or mechanical, including photocopying, recording or by any information storage and retrieval system, without the prior permission of the author.

ISBN 978-90-9025680-1

Author email: stephanhannot@gmail.com

Contents

Preface	ix
Abstract	xi
Samenvatting	xv
1 Introduction	1
1.1 Microsystems or MEMS	1
1.2 Multiphysical and electro-mechanical coupling	2
1.3 Modeling electromechanical coupling	4
1.4 Layout of this thesis	6
1.5 Notation and units	6
I Electro-mechanical modeling	9
2 Modeling electrostatics and electrostatic forces	11
2.1 Introduction	11
2.2 Basic electrostatics	11
2.3 Analytical modeling	16
2.4 Finite Element Method in 2D	28
2.5 Finite Element Method in 3D	46
2.6 Conclusions	49
3 Electro-mechanical modeling	51
3.1 Introduction	51
3.2 Continuum formulation of electro-mechanical coupling	51
3.3 A 1 dimensional example	53
3.4 General numerical modeling	62
3.5 Staggered and monolithic solution approaches	65
3.6 FEM formulation of the electro-mechanical coupling	67
3.7 Summary	73
4 Detailed implementation of a test problem	75
4.1 Introduction	75
4.2 A two dimensional model	75
4.3 A three dimensional model	81

II	Quasi-static simulation	87
5	Computing the Load-Displacement curve	89
5.1	Introduction	89
5.2	Incremental–iterative algorithms	89
5.3	Staggered solution strategies	90
5.4	Monolithic solution strategies	101
5.5	General Remarks	107
5.6	2D linear FEM test case	110
5.7	2D non-linear FEM test case	113
5.8	Experimental validation	117
5.9	Branching	117
5.10	2D FEM with branching	120
5.11	Conclusions	123
6	Sensitivity of the pull-in voltage	125
6.1	Introduction	125
6.2	Sensitivity of the pull-in voltage	125
6.3	Second order sensitivity of the pull-in voltage	129
6.4	2D FEM test case	133
6.5	Conclusions	138
7	Stochastic analysis of pull-in	139
7.1	Introduction	139
7.2	Random numbers and Stochastic FEM	139
7.3	Uniform microbridge	144
7.4	Random field discretization	149
7.5	A uniform beam with realistic numbers	152
7.6	Conclusions	156
III	Dynamic simulation	157
8	Undamped modeling	159
8.1	Introduction	159
8.2	Undamped eigenfrequency modeling	159
8.3	Transient modeling and dynamic pull-in	161
8.4	The two dimensional model	164
8.5	Experimental validation of the frequency computations	166
8.6	Conclusions	167
9	Sensitivity based stochastic analysis of dynamic pull-in	171
9.1	Introduction	171
9.2	Sensitivity of dynamic pull-in	171
9.3	Uncertainty analysis	181
9.4	Reliability analysis	182
9.5	A uniform beam with realistic numbers	183
9.6	Conclusions and recommendations	184

10 Damped modeling	187
10.1 Introduction	187
10.2 Damping model	188
10.3 Time integration	198
10.4 Eigenfrequencies with damping	204
10.5 Numerical results	205
10.6 Experimental validation	209
10.7 Conclusions	213
11 Sensitivity and stochastic analysis of damped frequencies	215
11.1 Introduction	215
11.2 Undamped frequency sensitivity	215
11.3 Damped eigenvalue sensitivities	216
11.4 Q-factor sensitivities	219
11.5 Matrix sensitivities	220
11.6 Stochastic FEM	222
11.7 Example	222
11.8 Conclusions	226
12 Model reduction for electro mechanically actuated systems	229
12.1 Introduction	229
12.2 Modal truncation and the remaining challenges	230
12.3 Step response reduction	232
12.4 Time varying applied potential	239
12.5 Which modes to use?	246
12.6 Including squeeze film damping	248
12.7 Conclusions	258
IV Combining and concluding	261
13 A general modeling framework	263
13.1 The basic framework	263
13.2 Selecting a simulation approach	265
13.3 Selecting a solution strategy	265
13.4 Statics and dynamics	266
13.5 Where to find the methods?	267
14 Conclusions and recommendations	269
14.1 Conclusions	269
14.2 Recommendations	271
A Summary of the classical Finite Element equations	273
A.1 Finite Element formulation of electrostatics	273
A.2 Finite Element formulation of structural mechanics	276
A.3 Shape functions and natural coordinates	282

B Rounding corners	285
B.1 Introduction	285
B.2 Finite Element Modeling	285
B.3 Analytical modeling	286
B.4 Conclusions	291
C A stiffness and mass sensing cantilever	293
C.1 Introduction	293
C.2 Model	295
C.3 Simple stiffness and mass measurement	299
C.4 Multiple frequency mass sensing	300
C.5 Measuring surrounding fluid and gas properties	307
Bibliography	313
Illustration credits	325
Curriculum vitae	327

Preface

Alle geleerden zijn min of meer
kinderen die spelen

De tranen der accacia's
Willem Frederik Hermans

Modeling electro-mechanical systems is what this thesis is about, which in essence became the derivation and solution of differential equations. It turned out to be a fascinating tour through science and engineering. I saw old and new papers, visited dull and interesting presentations and wrote frustrating computer code. And at the end of the day there is this thesis, which I hope that the reader will enjoy reading.

However I could not have written this thesis if there was no help or support. Therefore I would like to thank those people. Firstly the Dutch tax payers, which I would like to thank through my gratitude for the financial support of the MicroNed program of the Dutch Ministry of Economic Affairs.

Thereafter I would like to thank first of all my daily supervisor prof. Daniel Rixen, who spent a lot of his time and sharp wit on improving my work. Also my predecessor as MEMS modeler within the Engineering Dynamics group should be thanked: Véronique Rochus, who helped me start up quickly and has always been a helpful collaborator.

However they were not the only persons helping me, many within the Engineering Dynamics group and the larger PME department were very helpful either for the necessary distraction or the content, but mainly for both. Therefore I would like to thank you all for a wonderful time here at TU Delft. I cannot name you all, but I would like to name some of you specially: Alexander, Bert, Caspar, Chris, Clemens, Corinne, Daniel, Edwin, Hamed, Hans, Laura, Matt, Matthijs, Nico, Paul, Paul, Paulo, Saputra, Sven and Wijnand.

Finally, I would like to especially thank Golar, who made life pleasant, even during those stages where I had to actually write this thesis.

Stephan Hannot

Abstract

The ever increasing miniaturization trend sparked the development of very small mechanisms, used as sensors or actuators. These devices are created using the same fabrication technologies as integrated circuits and are called microsystems or Micro-Electro-Mechanical-Systems (MEMS). Because the characteristic dimension of these microsystems is in the order of micrometers the physical forces behave differently for microsystems than for traditional *macro* systems. One of the most important effects of this different behavior is the electro-mechanical coupling: electrostatic forces are able to move and deform parts at those scales.

The simplest version of an electro-mechanically coupled device is a parallel plate capacitor of which one of the plates can move. The value of the potential difference between the plates determines the electrostatic force on the moving plate. This force depends non-linearly on the value of the applied potential difference and the displacement of the moving plate. This electro-mechanical coupling is used for several applications, such as accelerometers and micro-switches.

However proper designing requires proper modeling. There are essentially two types of models: *system level models* and *physical level models*. System level models use simplified relations to build small models, for instance the behavior of a complex design is assumed to be equal to a parallel plate model, for which only some global parameter such as a spring stiffness have to be determined. Physical level models use partial differential equation on complicated domains to describe the physics of the device. Therefore they can be much more accurate, but the solution of the equations is much more difficult than those of a system level model and often requires the discretization of the partial differential equations. This discretization can be performed using the finite element method, but other methods are feasible as well.

The goal of this work is to build a framework for accurately modeling an electro-mechanical problem, which includes an estimate of the uncertainty of the computed values due to material uncertainties. Therefore this work focuses on improving the physical level models and their solution procedures instead of system level models.

When a physical level model is build this can be done in two ways. The first option is to use two different codes for the mechanical and the electrostatic models and couple them on an ad hoc basis. This limits flexibility, but the usage of optimal models for the separate problems is enabled. In this work that strategy is called *co-simulation*. The second option is to build both models in the same code using matching meshes. This allows for the computation of tangent and sensitivity information, which greatly increases flexibility. This option is called *coupled simulation* within this work.

Once a model is created the result is a set of non-linear equations that have to be solved. If the model has been obtained using co-simulation each problem, mechanically or electric, can only be solved separately and iteration between the different codes is necessary, which results in a *staggered* solution procedure. However if a coupled

simulation model is used there is also another solution strategy available: solving all equations together in a *monolithic* manner.

One of the main characteristics of an electro-mechanically coupled microsystem is the *pull-in voltage*. The pull-in voltage is the highest voltage that can be applied to microsystem, for which the response of the system will be a stable and bounded displacement. If a higher voltage is applied the response will be unstable and unbounded, which will result in contact between the moving and fixed parts of such a device. This contact can be desirable or highly undesirable, in both cases the prediction of this value is very important.

This pull-in value can be defined statically or dynamically. In the static case the pull-in value is the highest voltage for which the static equilibrium is stable and bounded. In the dynamic case it is the highest voltage, applied as a step, for which the transient step response is bounded.

In the static case the equilibrium curve has to be computed to be able to determine pull-in. The optimal approach to find the curve for both structurally linear elastic as well as non-linear elastic problems is determined in this work. The optimal method uses an arc-length constraint on the displacement and the applied charge instead of the voltage to pass the pull-in singularity. Monolithic approaches are better for mechanically non-linear problems and staggered approaches for mechanically linear problems. Also the first and second order sensitivities of the pull-in voltage to material parameter variations are determined, which allows for the stochastic analysis of this pull-in voltage. Both uncertainty and reliability analyses are performed.

Dynamically the pull-in voltage is determined using a trial and error approach. For the dynamic pull-in value a first order sensitivity analysis is derived as well, which is used for a stochastic analysis.

Other often used properties of electro-mechanical microsystems are their eigenfrequencies which depend on the equilibrium displacement and applied potential. This has for instance been used for the development of tunable resonators. This voltage dependency of the frequency can be simulated as well. A staggered approach is compared with a monolithic approach for computing the coupled eigenfrequencies.

Squeeze film damping is that damping that occurs when two parallel plates are moving towards each other or away from each other. In that case air is squeezed out of or sucked into the gap between the plates, which removes energy from the system. A finite element model for this squeeze film damping is derived which is coupled with either transient or eigenfrequency simulations of coupled electro-mechanical devices. Also the uncertainty analysis due to material property variations is developed for damped frequencies.

The squeeze film model is based on Reynolds equation which neglects inertia terms within the fluid, an assumption which is investigated. It is found that inertia effects are not really relevant for MEMS applications. The solution of such a squeeze film model can be simplified by assuming that the gas behaves incompressible. The validity of this assumption is investigated as well, where it is concluded that only for very low pressures compressibility becomes important.

Because of gas *rarefaction*, gas molecules do not behave as a continuum at very small scales or pressures, the equations have to be adapted, this adaptation was obtained from literature. A measure for rarefaction is the Knudsen number, which is high for rarefied gases. Using the adaptation from literature the squeeze film equation is shown to be useful for Knudsen number up to 600.

When a dynamic model is big, transient analyses become computationally very expensive. Therefore an approach to reduce the coupled equations is developed. The mechanical part is reduced with a classical modal truncation approach, but the electric force cannot be reduced with such ease. Therefore several approaches are developed to reduce this part. For most applications an approach where the electric force depends quadratically on the generalized displacement is advised. The quadratic dependency was obtained by using a Taylor expansion of the electric force. Only when dynamic pull-in has to be computed another approach is advised: the piecewise quadratic Taylor approach. The reduction approaches are enhanced by deriving a reduction of the squeeze film damping model as well.

All solution approaches mentioned above are cast into a framework that a designer can use to select the optimal modeling approach for a certain electro-mechanically coupled problem.

Samenvatting

De almaar toenemende miniaturisatie trend heeft er ook voor gezorgd dat er hele kleine mechanismen zijn ontwikkeld die als sensoren en actuatoren worden gebruikt. Deze machientjes worden gemaakt met de zelfde technieken als geïntegreerde circuits en worden microsystemen (Engels: Microsystems of MEMS) genoemd. Omdat de karakteristieke dimensie van deze apparaten zich in de orde van grote van een micrometer bevindt gedragen de krachten op een dergelijk apparaat zich anders dan voor grotere systemen. Een van de belangrijker gevolgen van dit andere gedrag is de elektromechanische koppeling: elektrostatische krachten kunnen op deze schalen onderdelen vervormen of verplaatsen.

De simpelste versie van een elektromechanisch gekoppeld apparaat is een parallelle plaat condensator waarvan een van de platen kan bewegen. De waarde van de aangebrachte spanning over de condensator bepaalt de elektrostatische kracht op de bewegende plaat. Deze kracht hangt niet lineair af van die spanning en de verplaatsing van de bewegende plaat. Deze elektromechanische koppeling wordt voor verscheidene toepassingen gebruikt, bijvoorbeeld voor versnellingsensoren en microschakelaars.

Echter goed ontwerpen vraagt om goed modelleren. Er bestaan twee soorten modellen: *systeemlaag modellen* en *fysicalaag modellen*. Systeemlaag modellen gebruiken versimpelde vergelijkingen om kleine modellen te maken, er wordt bijvoorbeeld verondersteld dat het gedrag van een complex ontwerp gelijk is aan dat van een parallelle plaat condensator. Daarentegen gebruiken fysicalaag modellen partiële differentiaal vergelijkingen over het gehele domein van het ontwerp om het gedrag te beschrijven. Hierdoor kunnen zij met een grotere nauwkeurigheid het gedrag beschrijven, maar de oplossing van die vergelijkingen kost meer moeite. Zo moeten de differentiaal vergelijkingen discreet gemaakt worden met bijvoorbeeld de eindige elementen methoden om de oplosbare niet lineaire vergelijkingen te verkrijgen.

Het maken van een raamwerk voor het accuraat modelleren van een elektromechanisch probleem, waarbij de kwantificatie van de onzekerheden door materiaal variaties hoort is het doel van dit proefschrift. Daarvoor richt dit werk zich op het verbeteren van fysicalaag modellen in plaats van systeemlaag modellen.

Een fysicalaag model kan op twee manieren worden gemaakt. De eerste mogelijkheid is om twee modellen in twee verschillende codes te ontwikkelen en deze op een ad hoc wijze te koppelen. Dit beperkt de flexibiliteit, maar hierbij is het wel mogelijk om de optimale modellen voor de verschillende deelproblemen te gebruiken. Deze methode wordt hier *co-simulatie* genoemd. De andere optie is om twee modellen in dezelfde code te maken, waarbij ook gebruik wordt gemaakt van dezelfde rekengrid. Hierbij is het mogelijk afgeleide informatie en gevoeligheden te bepalen. Deze methode wordt hier *gekoppelde simulatie* genoemd.

Als er een model is gemaakt levert dit een set niet lineaire vergelijkingen op die opgelost moeten worden. Als het model met de co-simulatie methode gemaakt is

kunnen de mechanische en elektrische sets vergelijkingen alleen apart opgelost worden, waardoor een iteratie tussen de modellen nodig is, wat een *getrapte* methode wordt genoemd. Echter als een gekoppelde methode wordt gebruikt kunnen de vergelijkingen ook tegelijk opgelost worden op een *monolithische* manier.

Een van de belangrijkste eigenschappen van een elektromechanisch gekoppeld microsysteem is het *intrek voltage* (Engels: pull-in voltage). Het intrek voltage is het hoogste voltage dat op het systeem gezet kan worden waarvoor de responsie nog steeds stabiel en begrensd is. Als een hoger voltage wordt toegepast zal de responsie onstabiel en onbegrensd zijn wat tot een contact tussen de twee elektroden van het systeem kan leiden. Dit kan gewenst of zeer ongewenst zijn, in beide gevallen is de voorspelling van deze waarde zeer belangrijk.

Dit intrek voltage kan zowel statisch als dynamisch gedefinieerd worden. In het statische geval is het intrek voltage het hoogste voltage waarvoor het statische evenwicht stabiel en begrensd is. In het dynamische geval is het het hoogste voltage dat met een stap aangebracht wordt en een stabiele en onbegrensde tijdsafhankelijke responsie oplevert.

Statisch zal eerst de kracht-verplaatsingscurve moeten worden berekend om het intrek voltage te kunnen berekenen. De optimale manier om deze curve te berekenen is bepaald voor zowel lineair elastische als niet lineair elastische problemen. De optimale methode maakt gebruik van een hoek-lengte beperking op de aangebrachte lading en de verplaatsing om de intrek singulariteit te passeren. Monolithische methoden zijn beter geschikt voor niet lineair elastische problemen en getrapte methoden voor lineair elastische problemen. Ook de eerste en tweede orde gevoeligheden van dit intrek voltage voor veranderingen van materiaal eigenschappen is bepaald. Met deze gevoeligheden wordt een onzekerheids- en betrouwbaarheidsanalyse uitgevoerd.

Dynamisch moet het intrek voltage met een proefondervindelijk proces worden bepaald. Voor het dynamisch intrek voltage is de eerste orde gevoeligheid ook bepaald, waarmee een stochastische analyse is uitgevoerd.

Een andere eigenschap van elektromechanische apparaten die vaak gebruikt wordt is hun eigenfrequentie die afhankelijk is van de evenwichtspositie en het voltage. Deze afhankelijkheid wordt bijvoorbeeld gebruikt door afstembare resonatoren en kan ook gesimuleerd worden. Een getrapte en een monolithische methode om deze frequenties te berekenen wordt vergeleken.

Samengeperste laag demping (Engels: squeeze film damping) is die demping die plaatsvindt als twee parallelle platen naar elkaar of van elkaar bewegen. Dan wordt lucht tussen de platen uit geperst of juist ertussen gezogen, wat energie uit het systeem haalt. Een eindige elementen model voor deze demping is ontwikkeld, dat gekoppeld wordt met het elektromechanische model. Hiermee kunnen zowel tijdsafhankelijk gedrag evenals gedempte frequenties worden bepaald. Ook de gevoeligheden van deze gedempte frequenties zijn bepaald.

Het samengeperste laag model is gebaseerd op de Reynolds vergelijking, welke de traagheids termen verwaarloost. Deze aanname is onderzocht en het is geconcludeerd dat deze aanname voor microsystemen meestal gedaan mag worden. De oplossing van een dergelijk model kan versimpeld worden door aan te nemen dat het gas zich niet comprimeerbaar gedraagt. Ook de geldigheid van deze aanname is onderzocht, hieruit bleek dat alleen voor lage drukken deze aanname problemen oplevert.

Door gasverdunning gedraagt een gas zich op hele kleine schalen of drukken niet meer als een continuüm. Daardoor moeten de vergelijkingen op deze schalen worden

aangepast, dat gedaan wordt met een methode uit de literatuur. Het is aangetoond dat deze methode geldig is tot aan Knudsen getallen van ongeveer 600. Een hoog Knudsen getal vertelt dat een gas erg verdund is.

Als een dynamisch model erg groot is duurt de tijdsafhankelijke analyse erg lang. Daarom wordt een methode ontwikkeld om de modellen te reduceren. Voor het mechanisch gedeelte wordt de klassieke modale afknotting methode gebruikt (Engels: modal truncation). Deze kan echter niet voor het elektrostatische gedeelte gebruikt worden, daarom zijn verschillende methoden ontwikkeld. Voor de meeste toepassingen is een methode waarbij de elektrische kracht kwadratisch van de verplaatsing afhangt aanbevolen. Deze kwadratische afhankelijkheid is gebaseerd op een Taylor benadering. Alleen als het dynamisch intrek getal moet worden berekend zal een andere methode moeten worden gebruikt: de stuksgewijs kwadratische Taylor benadering. De reductiemethode is ook uitgebreid met een gereduceerd model voor de demping.

Alle methoden zijn samengevoegd in een raamwerk. Dit raamwerk moet een ontwerper de mogelijkheid geven om een optimale modelleermethode te vinden voor een bepaald elektromechanisch model.

Chapter 1

Introduction

Humans, or at least a certain kind of them, have always been striving to make the most beautiful things. Often the most beautiful meant the biggest: the biggest pyramid, church or skyscraper. The Dutch national pride *de nachtwacht* is a very large tableau as well. However there has always been a reverse current of artists that favored the small. They liked the restriction of size that required them to use a different artistic expression. Consider for instance the small paintings called miniatures that formed the first letter of a chapter in ancient and medieval ‘illuminated’ manuscripts. See for such a decorated letter *A* figure 1.1.

Engineers have the same preoccupations. Spanning big gorges with big bridges or building the largest plane has fascinated countless engineers. However, often it was clear that smaller devices are more elegant and energy efficient. The smallest became the goal. One of the first fields to benefit from miniaturization was the electronics field, yielding the microchip. Design followed suit: elegant small laptops could be built with the small electronic devices. And they became popular and similarly the small modern mobile phones became popular.

In the last quarter of the 20th century it was discovered that the production techniques used to build smaller and smaller electronics, could be efficiently used to build mechanical, or in other words moving, structures as well. These small mechanical systems became known quickly known as microsystems in Europe and as MEMS in the USA.

1.1 Microsystems or MEMS

Microsystems or Micro–Electro–Mechanical Systems (MEMS) are small (micrometer size) machines usually built by lithographic technologies originally developed for microchips. MEMS are designed to integrate sensing and actuation (and even data processing) on a single chip, therefore they often include moving and deforming parts. Currently microsystem technologies are used for a wide variety of purposes such as: read/write heads in hard-disk drives, ink-jet print heads, Digital Light Processing (DLP) chips in video projection systems and several types of sensors for pressure, flow, acceleration or biological elements [64, 120, 115, 128, 35].

Especially the use of acceleration sensors is rapidly increasing. In the beginning they were only used for sensing whether a car was decelerating too fast, which is useful information for airbags. At the moment one of the most imaginative applications is in the controller for Nintendo’s Wii game computer [37]. In this controller several



Figure 1.1: A late 14th century miniature showing the *birth of John the Baptist* painted by *Niccolò da Bologna*.

MEMS accelerometers are used to detect how the controller is positioned and in which direction it is moving. When a gamer is playing computerized tennis the controller can detect if the gamer is moving his hand like a real tennis player would do when hitting a ball.

Another modern application of MEMS accelerometers is Apple's iPhone [39]. The accelerometers are used to detect how the iPhone is held by the user. This determines which of the four edges of the screen is directed upwards, thus how the image on the screen should be rotated for optimal viewing.

1.2 Multiphysical and electro-mechanical coupling

Due to their very small size, the dominant driving forces for microsystems differ from the ones in the macro-world. For instance gravitational forces are negligible with respect to the elastic, adhesive and electrostatic forces at these scales [139]. These scaling effects may cause a strong coupling between different physical domains. For instance small silicon devices can be heated by an electric current relatively fast and they will cool down rapidly by conduction to the surrounding parts. Devices can be heated and cooled several times per second. Due to the thermal expansion of the material this effect can be used to actuate a device at frequencies that are high compared to macroscopic systems [59, 60, 70].

Another coupling that becomes useful at small scales is the coupling between structural displacement and electrostatic forces. At small scales electrostatic forces are big enough to actuate devices. These forces cause the type of coupling on which this thesis focuses: electro-mechanical coupling.

The basic physical principle of electromechanically actuated microsystems is illustrated in fig. 1.2. Once a potential difference between a moving (or deformable) elec-

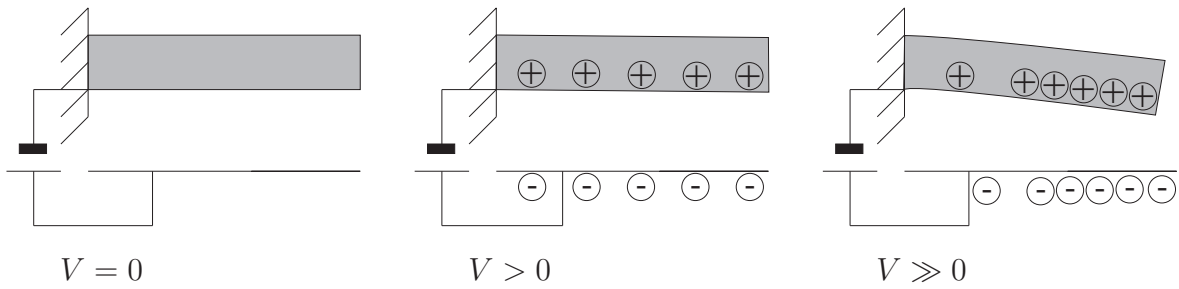


Figure 1.2: Electromechanical coupling

trode and a fixed electrode is applied a charge difference is created. Coulomb forces between the charges will make the flexible electrode deform. This effect depends non-linearly on the shape of the electrode and the deformation itself, because the charge will concentrate near the point where the gap between the electrodes is smallest, which causes even higher Coulomb forces at this point [4].

Two examples of MEMS that utilize the electromechanical coupling are micro switches and comb drives. Micro switches are the oldest type of microsystems. They are similar to magnetic relay switches, but the magnetic actuation is replaced by electrostatic actuation, which is made possible by the very small dimensions [142, 84]. The first ones to build a microswitch was Nathanson *et.al.* in 1967 [89]. Closely related to these devices is the micro mirror used in optics, which is basically a large switch with a reflecting surface. A picture of a small micro bridge that can be used as micro switch is given in fig. 1.3.

The comb drive is an array of small fingers which can be used to maximize the electrostatic force or capacitance between a moving and a fixed set of fingers while still allowing a large displacement of the moving set. The first one was introduced by [125]. Their main use at the moment is in the accelerometers mentioned above. A picture is shown in fig. 1.4.

Because there are already some good reviews on the history and design of electromechanical MEMS such a review is not presented here. Rather, a very short survey of those reviews is given in this paragraph. One is referred to chapter 2 of [85] for an overview of MEMS resonators and sensors. The first chapters of [106] present a general introduction to electromechanical MEMS and the range in which the electrostatic assumption is valid. An introduction to switches can be found in [103]. A general review on the structural dynamics of MEMS, including the modeling of electromechanical microsystems, can be found in [80].

Modeling this electro-mechanic coupling is particularly challenging because the resulting equations are non-linear and the physics are strongly coupled. Therefore proper models are essential for a designer of microsystems. Improving those models is the goal of this thesis. Which should increase the capability of a designer to predict the behavior of MEMS, therefore his or hers effective usage of the capabilities of the electromechanical interaction.

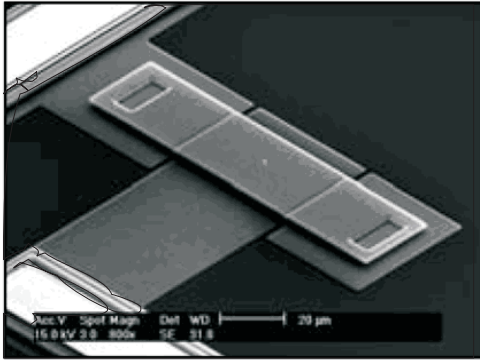


Figure 1.3: Micro bridge, reproduced from [106]

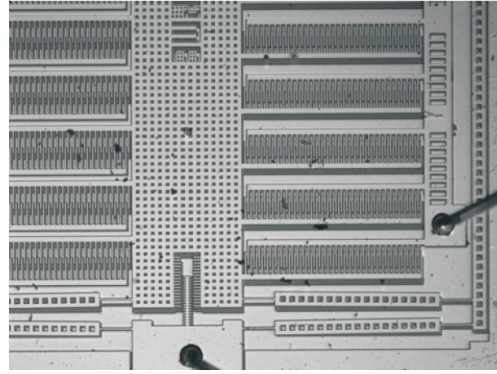


Figure 1.4: Comb drive (Delft University design used for teaching)

1.3 Modeling electromechanical coupling

1.3.1 Types of modeling

Because the designer needs to globally understand the physical effects that are occurring during MEMS operation he needs to model. Also if a designer wants to know how a design will behave before he makes an expensive prototype he needs to model. There are many different approaches to model electro-mechanical coupling. But following [118] two different modeling types are distinguished: *system level models* and *physical level models*.

System level models are small models often yielding a small number of ordinary differential equations (ODE) that can be solved within milliseconds. There often is the possibility to use closed form solutions or cheap numerical simulations. Frequently they utilize a simplified geometry of the microsystem. A common approach is to use some parallel plate type capacitor assumption for the electric field coupled with very simple beam models for the mechanics [83, 42]. The advantage of these type models is that they are computationally very cheap and capture a lot of the typical behavior, however they are not very accurate for prediction of precise values. Hence these types of models are useful for the first goal of the designer: understanding the physical effects that are happening. This enables him to make a conceptual design.

However if a designer is really close to designing the actual prototype, he needs accurate values, as well as detailed models of physical phenomena and proper estimates of the accuracy of his models. In other words he needs physical level models that utilize the full 2D/3D partial differential equations (PDE) that describe the physics. These approaches often use the Finite Element Method (FEM) to discretize and solve the PDE's, but other approaches to solve PDE's are used as well [87].

Physical models can also be used to generate system level models [15]. This requires that computations with physical level models are used to make a reduced order model, hence this type of modeling is often called *reduced order modeling*, however also the term *macro modeling* is used [118].

This thesis focuses on physical level modeling. These models can be used for an accurate quantitative prediction of MEMS motions, because they use the complete geometry of a device. Of course this comes at a price: they are computationally expensive.

The purpose of this work is to select and develop these physical level models and their solution procedures to such an extent that a more or less complete modeling framework can be distilled from them. With this framework a designer should be able to choose the proper physical level modeling and solution procedure given the problem that the designer wants to solve.

1.3.2 Challenges in the physical level modeling

One of the aspects of electro-mechanical coupling is that there are two physical fields involved, an electric field and a mechanic field. Therefore a model has to be able to model both fields and their interaction. For the formulation of the interaction the model of the surface that defines interface between mechanical and electrical domain is crucial. In line with Pauli's quote 'God created bulk but the Devil created surface', this interface relation can make or break a model. Therefore the formulation of the interaction is one of the focus points of this thesis.

This also means that the efficient solution of the electromechanical problem becomes difficult [119]. This thesis tries to find strategies for the solution of the highly non-linear electromechanical equations. This non-linearity also causes that statically there is a maximum allowable actuation voltage. The computation of this point requires advanced solution strategies and this thesis tries to determine which are best and how to improve them. The main novelty in this thesis is the combination of charge loading with efficient arc length methods as well as deriving the arc length method for staggered formulations.

The fact that this limit point is very crucial in operation also means that the characterization of the uncertainty of this value is very important. To perform a perturbation based stochastic Finite Element Method design sensitivities are required [49], which are discussed in this thesis. The main challenge here is to derive second order sensitivities of pull-in which have not been reported in MEMS literature before, in contrast with first order sensitivities [78].

The efficient modeling of coupled dynamics and time integration is always challenging. This thesis treats the efficient modeling of transient electromechanical behavior as well as squeeze film damping, including all non-linear effects. Of course vibration frequencies are very relevant since these microsystems are used for resonating accelerometers as well. This thesis therefore has an extra interest in linearizing the equations and computing the frequencies, Q-factors and their uncertainties. Damping is based on squeeze film modeling which has been used before (e.g. [11]). However especially the full nonlinear Reynolds equation that is used here has not been used in literature before nor the combination of a fully deformable structure with electric and squeeze film finite element models. Also the derivations of dynamic pull-in sensitivities and stochastic properties have not been reported before as well as the computation of frequency sensitivities while remaining on the pull-in curve.

Another important usage of FEM models is the reliable creation of macro models or reduced order models [119, 133]. Therefore a novel method to extract reduced order models that captures the non-linearity in displacement as well as applied potential is developed based on the principle of modal truncation.

1.4 Layout of this thesis

The purpose of the research is to develop reliable modeling tools for electro-mechanical coupling, that are based on modeling the full displacement and electric fields. So no special attention is given to lumped models.

This document is separated in four parts.

- Part I focuses on general electro-mechanical modeling. One of the first challenges is the reliable computation of electrostatic forces from the solution of an electrostatic field. This is the main focus of the chapter on electrostatic modeling: chapter 2. Chapter 3 discusses the continuum equations describing the electromechanical coupling and some issues about the formulation, discretization and solution of these equations. A short example concludes part I.
- Often a lot of the behavior of the device can be estimated from the static equilibrium behavior. Therefore part II focuses on quasi-static simulations. An interesting quasi-static aspect of electrostatic MEMS is the pull-in phenomenon and the load-displacement curve. It is not trivial to exactly find the pull-in point or the load-displacement curve beyond the pull-in point with coupled FEM models. Numerical procedures to find these curves are developed and evaluated in chapter 5. In chapter 6 a numerical approach to obtain the design sensitivity of this pull-in voltage is presented, which is used to perform a stochastic analysis to estimate the uncertainty of the pull-in voltage in chapter 7.
- The extension to dynamic simulation is made in part III. First undamped modeling is treated in chapter 8: transient as well as eigenfrequency modeling. Also the dynamic version of the pull-in limit is defined in this chapter. In the ninth chapter the stochastic properties of dynamic pull-in are derived. In chapter 10 a plate model of a micro switch is used to discuss the modeling of dynamics including damping. A FEM model of the Reynolds equation is derived and used to describe squeeze film damping due to a gas. The stochastic properties of the damped frequencies are investigated a chapter later. The last chapter of this part is filled with the goal of developing reduced order dynamic models from the very big damped electromechanical models.
- The fourth part combines the static and dynamic analyses with the general views presented in part I. In chapter 13 the components are cast into a general physical level modeling framework, which is the main goal of this thesis. Chapter 14 finishes part IV with the conclusions and recommendations.

Parts of this thesis have in been published in the following publications: [57, 52, 55, 54, 53, 56, 58].

1.5 Notation and units

Finally some remarks about the notations used in this thesis. Bold symbols represent vectors or matrices depending on the context, normal symbols represent scalars. With a differentiation of a vector by a vector:

$$\mathbf{a} = \frac{\partial \mathbf{f}}{\partial \mathbf{b}},$$

the Jacobian derivative is indicated:

$$a_{ij} = \frac{\partial f_i}{\partial b_j}.$$

If a scalar is differentiated by vector

$$\mathbf{a} = \frac{\partial f}{\partial \mathbf{b}},$$

that indicates:

$$a_j = \frac{\partial f}{\partial b_j}.$$

If index notation is used in general also Einstein's summation convention is used, meaning that if an index occurs twice this indicates a sum:

$$c_{ik} = a_{ij}b_{jk},$$

means:

$$c_{ik} = \sum_{j=1}^n a_{ij}b_{jk}.$$

The exception on this is with the manipulation of eigenvalues and eigenvectors. In that case the context should make clear if sums are used or not.

A dot above a symbol, bold or not, indicates a total time derivative of that property:

$$\dot{u} = \frac{du}{dt}, \tag{1.1}$$

so if u is a displacement \dot{u} is an absolute velocity. Similarly:

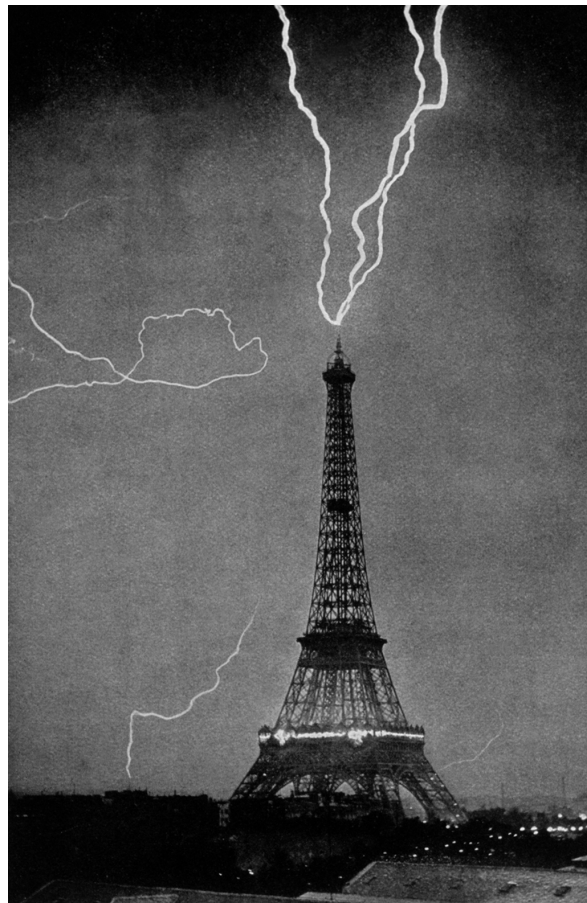
$$\ddot{u} = \frac{d^2u}{dt^2}, \tag{1.2}$$

giving an absolute acceleration if u is a displacement.

If no specific statement about the units is made in the text SI-units are used.

Part I

Electro-mechanical modeling



Chapter 2

Modeling electrostatics and electrostatic forces

2.1 Introduction

The electrostatic forces that deform the microsystems depend on the electric field. Therefore it is important to model this electric field accurately. This thesis is mainly written from and for the mechanical engineering point of view, not the electric engineering one. Therefore a thorough treatment of this electrostatic modeling is considered a requirement. But also the computation of the force resulting from this electric field needed to couple electrics with mechanics is not trivial, hence this chapter might also be useful for the interested electrical engineer.

The basic equations of electrostatics are introduced in the first section. To be able to evaluate the numerical modeling techniques an analytical benchmark solution can be very useful. Therefore an analytical modeling technique that can only be applied on a limited range of geometries is discussed and applied on a benchmark geometry in section 2.3. After those two sections the finite element discretizations of the electrostatic equations is discussed for 2D as well as 3D problems, including the precautions that should be taken when electrostatic forces are computed.

2.2 Basic electrostatics

The starting point for any Electromagnetic analysis is given by Maxwell's equations, a set of time dependant differential equations describing the electric and magnetic fields and their interaction¹. However when the geometry of the electric domain is small enough and the speed by which it changes is low enough, the electromagnetic problem can be assumed to be electrostatic. In that case the electric problem is solved as if it has reached a steady state configuration that is only a function of the geometry of the domain.

¹The main source for the complete section is [48].

2.2.1 The electrostatic equation

The fundamental electrostatic law is Coulomb's law, which describes the experimental relation for the force between charges Q_1 and Q_2 :

$$\mathbf{F} = \frac{Q_1 Q_2}{4\pi\epsilon r^2} \hat{\mathbf{r}}, \quad (2.1)$$

where ϵ is the permittivity, r is the distance between the charges and $\hat{\mathbf{r}}$ is the unit vector pointing from charge Q_1 to charge Q_2 . Coulomb's law is used to define the electric field \mathbf{E} generated by a point charge at a distance r as:

$$\mathbf{E} = \frac{Q}{4\pi\epsilon r^2} \hat{\mathbf{r}}. \quad (2.2)$$

This equation can be generalized to Gauss's law, which states that the electric flux through any surface is proportional to the charge enclosed by that surface:

$$\oint \epsilon \mathbf{E} \cdot d\mathbf{A} = \int \rho dV, \quad (2.3)$$

where ρ is the charge density within the enclosed volume. In differential form Gauss's law can be written as:

$$\nabla \cdot \epsilon \mathbf{E} = \rho. \quad (2.4)$$

When an electrostatic potential ϕ caused by a point charge is defined as:

$$\phi = \frac{Q}{4\pi\epsilon r}, \quad (2.5)$$

the electric field can be defined as:

$$\mathbf{E} = -\nabla\phi, \quad (2.6)$$

which can be used to simplify the vector differential equation (2.4) to a scalar differential equation, sometimes known as the electrostatic equation:

$$-\nabla \cdot (\epsilon \nabla\phi) = \rho \quad (2.7)$$

If it is assumed that ϵ is not a function of location but constant, this equation simplifies even further to:

$$-\epsilon \nabla^2 \phi = \rho, \quad (2.8)$$

which is a form of Poisson's equation. When there is no unpaired charge in the electrostatic domain, as in a vacuum or in air, ρ equals zero, therefore the electrostatic equation reduces to Laplace's equation:

$$\epsilon \nabla^2 \phi = 0, \quad (2.9)$$

All these equations are valid when the electric domain consists of so-called dielectrics which have finite values of electric permittivity, making it nearly impossible for charges to move through the dielectric. In air or vacuum, when equation (2.9) can be used, there are no charges at all within the domain, the only charges are at the boundaries.

In MEMS-simulation, normally there are only two kinds of boundaries: ideal conductors and ideal insulators. Ideal conductors are materials in which charges can freely

move without doing work, in other words they have an infinite permittivity, therefore the electric field within a conductor is zero and all charge is at the surface. At the surface the tangential component of the electric field will always be zero because the freely moving charges will level any potential differences. The field in perpendicular direction can have a value due to the charges at interface. Hence ideally conducting interfaces with dielectrics are commonly modeled as equipotential surfaces, where the problem is only solved on the dielectric domain. These boundary conditions are also known as Dirichlet boundary conditions.

Ideal insulators are materials which do not have charges at the boundary, therefore their contact with the electrostatic domain is normally modeled as a zero charge boundary condition, which means according to Gauss' law that the electric field normal to the surface must be zero ($\partial\phi/\partial n = 0$, a Neumann boundary condition).

2.2.2 Electrostatic forces

The electrostatic or Coulomb forces generated by an electric field are of vital importance for MEMS. Microsystems are often made from conducting materials, therefore the computation of electrostatic forces on conductor surfaces is elaborated below.

If there are several different charges in a space the force on a single charge is the vector sum of the forces resultant from the other charges, thus for charge Q_1 ²:

$$\mathbf{F}_{es} = \frac{1}{4\pi\epsilon} \frac{Q_1 Q_n}{r_n^2} \hat{\mathbf{r}}_n \quad n \neq 1. \quad (2.10)$$

By Coulomb's law the electric field at the location of a point charge is given by the following equation:

$$\mathbf{F}_{es} = Q_1 \mathbf{E}. \quad (2.11)$$

Thus the electric field at that point is:

$$\mathbf{E} = \frac{1}{4\pi\epsilon} \frac{Q_n}{r_n^2} \hat{\mathbf{r}}_n \quad n \neq 1. \quad (2.12)$$

In general a MEMS structure consists of several conductors and dielectrics surrounded by air or a vacuum. There are no charges within the dielectrics, but a lot of free charges within the conductor. However when a potential is applied on a conductor, all the charges within the conductor will move infinitely fast to the surface of the conductor. There they pile up because the charges can not 'jump' into the air, but remain at the surface. Thus the only charges are at the boundary of conductors, hence the only forces are at those boundaries.

As a consequence of the assumption that the charges can move infinitely fast through the conductor, it is assumed that when there is a tangential electric field between two points at the surface, the charges will move infinitely fast to a state where this tangential electric field at the boundary of the conductor is zero everywhere. However the electric field outside the conductor and normal to the surface is not zero per definition, since the surface charge allows for a jump of the electric field in the normal direction.

²Einstein's summation convention is used throughout this document

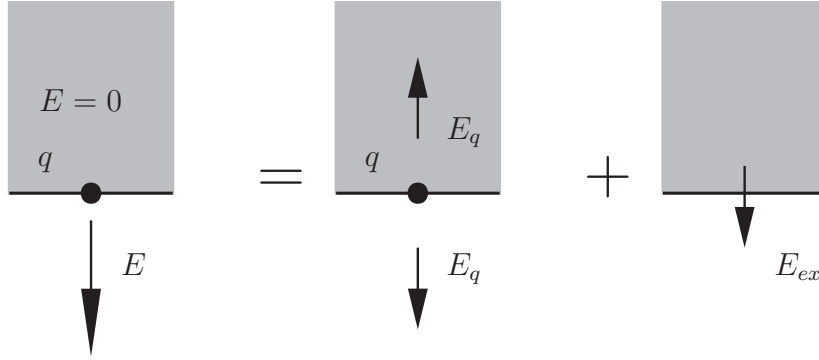


Figure 2.1: A charge q on the interface between conductor (top) and dielectric (bottom).

The electric field jump can be calculated using Gauss's law on the surface of the boundary. The charge in the equation is replaced by the surface charge, thus Coulomb per square meters:

$$\oint_{surface} \mathbf{E} \cdot d\mathbf{A} = \int \frac{1}{\epsilon} q dA_s, \quad (2.13)$$

with q the surface charge density and A_s the Area. Thus for an infinitesimal surface the jump in electric field becomes:

$$\mathbf{E}_{outside} - \mathbf{E}_{within} = \frac{1}{\epsilon} q \hat{\mathbf{n}}, \quad (2.14)$$

with $\hat{\mathbf{n}}$ the unit normal vector. Thus, when applying (2.13) to the boundary of an infinite conductor a zero electric field remains within the conductor domain:

$$\mathbf{E} = \mathbf{E}_{outside} - \mathbf{E}_{inside} = \mathbf{E}_{outside}, \quad (2.15)$$

yielding:

$$\mathbf{E} = \frac{1}{\epsilon} q \hat{\mathbf{n}}. \quad (2.16)$$

This defined the charge at the interface, now this charge has to be used to compute the force. A charge on such an interface between conductor and dielectric is shown in figure 2.1. The first configuration on the left-hand side shows the electric field, which is zero inside the conductor and non-zero outside the conductor. This electric field E is a superposition of the symmetric field induced by the charge itself (E_q in the middle configuration) and the external electric field (E_{ex} on the right-hand side). This gives the following equations for the different fields:

$$E = E_{ex} + E_q, \quad (2.17)$$

$$0 = E_{ex} - E_q. \quad (2.18)$$

from which it follows that $E_{ex} = \frac{1}{2}E$.

The electric force on force Q_1 computed with equation (2.11) required the electric field induced by all other charges, but not the field induced by charge Q_1 itself. Hence when equation (2.11) is used to compute the force on an interface charge one has to use the definition:

$$\mathbf{F}_{es} = \int q \mathbf{E}_{ex} dA_s = \int \frac{1}{2} q \mathbf{E} dA_s. \quad (2.19)$$

The charge computed by equation (2.16) is substituted into equation (2.11):

$$\mathbf{F}_{es} = \int \frac{1}{2} q \mathbf{E} dA_s = \int \frac{\varepsilon |\mathbf{E}|^2}{2} dA_s \hat{\mathbf{n}}. \quad (2.20)$$

Thus the electrostatic pressure is:

$$f_{es} = \frac{\varepsilon |\mathbf{E}|^2}{2} \hat{\mathbf{n}}, \quad (2.21)$$

which can be used in numerical and analytical models.

2.2.3 Maxwell stress tensor

An alternative method to derive the electric forces is by starting with the Maxwell stress tensor as is often done in literature. The Maxwell stress tensor gives the interaction between electric and magnetic fields and mechanical momentum. In essence the Maxwell tensor is derived in a very similar method as the force above, thus it will be logical that when applying the Maxwell tensor, this provides the same force.

Disregarding the magnetic aspects, the Maxwell stress tensor \mathbf{T} for a purely electrostatic problem is defined as:

$$\mathbf{T} = \varepsilon \nabla \phi \nabla \phi^T - \frac{1}{2} \varepsilon \nabla \phi^T \nabla \phi \mathbf{I}. \quad (2.22)$$

which in 2D can be written as:

$$\mathbf{T} = \begin{bmatrix} T_{xx} & T_{xy} \\ T_{yx} & T_{yy} \end{bmatrix} = \varepsilon \begin{bmatrix} \frac{1}{2} E_x^2 - \frac{1}{2} E_y^2 & E_x E_y \\ E_x E_y & \frac{1}{2} E_y^2 - \frac{1}{2} E_x^2 \end{bmatrix}, \quad (2.23)$$

where $E_i = -\frac{\partial \phi}{\partial x_i}$ is the electric field in the x_i -direction, ε is the electric permittivity and T_{ij} are the components of the stress tensor.

Similar to mechanical stresses, the electrostatic force density in the electrostatic area Ω is then $\nabla \cdot \mathbf{T}$ [48] so that the force exerted by that area on its surroundings is:

$$\mathbf{f}_e = - \int_{\Omega} \nabla \cdot \mathbf{T} dV \quad (2.24)$$

However this volume integral is rarely used directly because it requires the second spatial derivatives of the electric potential ϕ . Therefore traditionally Gauss' theorem is used to find the electric force as an integral over the contour Γ of Ω :

$$\mathbf{f}_e = - \int_{\Omega} \nabla \cdot \mathbf{T} dV = \int_{\Gamma} \mathbf{T} \cdot \mathbf{n} dS, \quad (2.25)$$

where \mathbf{n} is the inner normal to the boundaries of the electric domain Ω , thus the outer normal of the surrounding structure.

On the boundary of a conductor the electric potential is constant. Thus the electric field on a conductor will always be perpendicular to the surface and equation (2.25) reduces to [48]:

$$\mathbf{f}_e = \int_{\Gamma} \frac{1}{2} \varepsilon |\nabla \phi|^2 \mathbf{n} dS = \int_{\Gamma} \frac{1}{2} \varepsilon |\mathbf{E}|^2 \mathbf{n} dS, \quad (2.26)$$

which is exactly the same definition of electrostatic forces as before (2.21).

2.3 Analytical modeling

In this section the analytical solution for electrostatic problems is discussed. Specific attention is given to an electrostatic corner problem. The main analytical solution strategy that will be used is the conformal transformation approach. The used reference for these conformal transformations is [16], in which there is a lengthy discussion about conjugate functions and conformal mappings. One of those mappings was used to model the corner. Other references that use conformal transformations to calculate electrostatic forces are [129, 20], where the conformal transformations are used to build simple low DOF combdrive models. The conformal transformations are in those cases not used to model the exact geometry but to approximate the geometry better than parallel plate assumptions.

2.3.1 A simple 1D problem

However another benchmark is investigated first: a very simple 1D problem. In figure 2.2 such a model of micro resonator in 1D is given. In the air gap the electrostatic problem is described by Laplace's equation, which reduces to the following equation in 1D:

$$\varepsilon \frac{\partial^2 \phi}{\partial \xi^2} = 0, \quad (2.27)$$

where ϕ is the electrostatic potential, ξ is the spatial coordinate and ε the electric permittivity. The domain on which this differential equation has to be solved is $\xi = [0, x]$, with boundary conditions: $\phi = V$ at $\xi = x$ and $\phi = 0$ at $\xi = 0$. The solution to this boundary value problem is:

$$\phi = \frac{V}{x} \xi, \quad (2.28)$$

and the electric field is per definition:

$$E = -\frac{\partial \phi}{\partial \xi} = -\frac{V}{x}. \quad (2.29)$$

Thus the electrostatic force on the plates is:

$$F_{es} = \frac{1}{2} \varepsilon E^2 = \frac{1}{2} \varepsilon \frac{V^2}{x^2}. \quad (2.30)$$

This basic derivation of the electrostatic force between a parallel plate capacitor can be found in many sources, e.g. [108].

2.3.2 Conjugate functions

For more complex (2D) problems closed form solutions are very difficult to obtain. One method that is still able to find closed form solutions is the conformal mapping approach, however it can only be applied for a limited number of geometries. To understand conformal transformations one needs to understand conjugate or complex functions, which will be introduced in this section first. Thereafter it is shown that regular complex functions form a set of solution to Laplace's equation in 2D. Finally is shown that the real and imaginary parts of a regular complex function satisfy the Cauchy-Riemann equations.

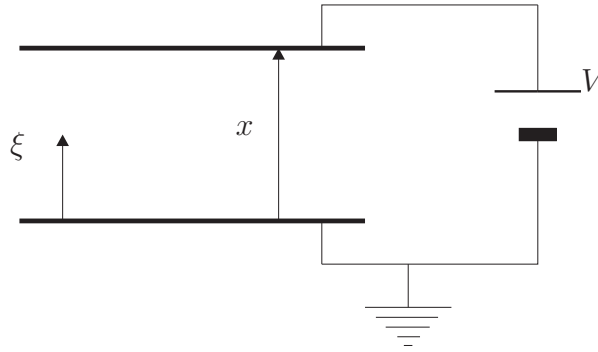


Figure 2.2: 1D parallel plate capacitor

Conjugate functions and Laplace's equation

Let there be the complex variables z and t .

$$z = x + iy, \quad (2.31)$$

$$t = u + iv. \quad (2.32)$$

Assume that t is a continuous regular function (a function of which both its first and second derivative are unique) of z :

$$t = F(z). \quad (2.33)$$

Thus the derivative of t with x is:

$$\frac{\partial t}{\partial x} = \frac{\partial F(z)}{\partial z} \frac{\partial z}{\partial x}, \quad (2.34)$$

since $\frac{\partial z}{\partial x} = 1$, the derivative of t with x must be:

$$\frac{\partial t}{\partial x} = \frac{\partial F(z)}{\partial z}. \quad (2.35)$$

Differentiating again with respect to x :

$$\frac{\partial^2 t}{\partial x^2} = \frac{\partial^2 F(z)}{\partial z^2}. \quad (2.36)$$

Similar with respect to y :

$$\frac{\partial t}{\partial y} = \frac{\partial F(z)}{\partial z} \frac{\partial z}{\partial y}, \quad (2.37)$$

except here $\frac{\partial z}{\partial y} = i$, hence the derivative of t with respect to y is:

$$\frac{\partial t}{\partial y} = i \frac{\partial F(z)}{\partial z}, \quad (2.38)$$

since $i^2 = -1$ the second derivative is:

$$\frac{\partial^2 t}{\partial y^2} = -\frac{\partial^2 F(z)}{\partial z^2}. \quad (2.39)$$

Combining equations (2.36) and (2.39) yields:

$$\frac{\partial^2 t}{\partial x^2} + \frac{\partial^2 t}{\partial y^2} = 0, \quad (2.40)$$

which is Laplace's equation, therefore any regular function of a complex variable obeys Laplace's equation.

Equation (2.40) can also be split in two parts, by using the real and imaginary parts of t . First:

$$\begin{aligned} \frac{\partial^2 t}{\partial x^2} &= \frac{\partial^2 u}{\partial x^2} + i \frac{\partial^2 v}{\partial x^2}, \\ \frac{\partial^2 t}{\partial y^2} &= \frac{\partial^2 u}{\partial y^2} + i \frac{\partial^2 v}{\partial y^2}. \end{aligned} \quad (2.41)$$

Since both the real and imaginary part of (2.40) must be zero:

$$\begin{aligned} \frac{\partial^2 u}{\partial x^2} + \frac{\partial^2 u}{\partial y^2} &= 0, \\ \frac{\partial^2 v}{\partial x^2} + \frac{\partial^2 v}{\partial y^2} &= 0. \end{aligned} \quad (2.42)$$

Hence also the real and imaginary parts of any regular complex function satisfy Laplace's equation.

Cauchy-Riemann equations

To show that the real and imaginary parts of t satisfy the Cauchy-Riemann equations, equation (2.32) is differentiated with respect to x , yielding:

$$\frac{\partial t}{\partial x} = \frac{\partial u}{\partial x} + i \frac{\partial v}{\partial x}, \quad (2.43)$$

therefore, using equation (2.35):

$$\frac{\partial F(z)}{\partial z} = \frac{\partial u}{\partial x} + i \frac{\partial v}{\partial x}, \quad (2.44)$$

and similarly using (2.38):

$$i \frac{\partial F(z)}{\partial z} = \frac{\partial u}{\partial y} + i \frac{\partial v}{\partial y}. \quad (2.45)$$

Combining equations (2.44) and (2.45) to eliminate $\frac{\partial F(z)}{\partial z}$ results in:

$$i \frac{\partial u}{\partial x} - \frac{\partial v}{\partial x} = \frac{\partial u}{\partial y} + i \frac{\partial v}{\partial y}. \quad (2.46)$$

Using the fact that on both sides of the equation the real and the imaginary parts must be equal:

$$\frac{\partial u}{\partial x} = \frac{\partial v}{\partial y}, \quad (2.47)$$

$$\frac{\partial v}{\partial x} = -\frac{\partial u}{\partial y}. \quad (2.48)$$

These are the Cauchy-Riemann equations, which are satisfied by the real and imaginary parts of any regular function of a complex variable.

The potential function as a complex function

Because a constant real or imaginary part of t indicates a constant value of u and v that situation corresponds to two families of curves in the z plane: $u(x, y) = \text{constant}$ and $v(x, y) = \text{constant}$. Assume that $u = u_0$ and $v = v_0$ define one curve each, which intersect at point $z = z_0$. Since u is constant along the curve $u = u_0$ the slope is zero in the t -plane:

$$\frac{\partial u}{\partial x} \partial x + \frac{\partial u}{\partial y} \partial y = 0, \quad (2.49)$$

thus at the intersection point z_0 , to calculate the slope of the curve $u = u_0$ in the z -plane:

$$\left(\frac{\partial y}{\partial x} \right)_{z_0} = \left(- \frac{\frac{\partial u}{\partial x}}{\frac{\partial u}{\partial y}} \right)_{z_0}. \quad (2.50)$$

The same for $v = v_0$:

$$\left(\frac{\partial y}{\partial x} \right)_{z_0} = \left(- \frac{\frac{\partial v}{\partial x}}{\frac{\partial v}{\partial y}} \right)_{z_0}, \quad (2.51)$$

hence the product of the slopes is, in combination with the Cauchy-Riemann equation:

$$\left(\frac{\frac{\partial u}{\partial x}}{\frac{\partial u}{\partial y}} \right)_{z_0} \cdot \left(\frac{\frac{\partial v}{\partial x}}{\frac{\partial v}{\partial y}} \right)_{z_0} = -1. \quad (2.52)$$

Since the product equals -1 the two curves must intersect at right angles in the z plane³. Because functions of constant u intersect functions of constant v at right angles in the t -plane conjugate functions define orthogonal families.

Potential and stream functions (electric stream lines or electric flux lines are lines defined by a constant value of the stream function and point in the direction of the electric field) have to satisfy Laplace's equation and have to be orthogonal. Since conjugate functions are both, they can be used to describe potential and stream functions.

Therefore let the potential ϕ and the stream value ψ describe a field in the (x, y) plane:

$$\begin{aligned} \psi &= f_1(x, y) = f_1(z), \\ \phi &= f_2(x, y) = f_2(z), \end{aligned} \quad (2.53)$$

if they are represented as a conjugate function:

$$\begin{aligned} w(z) &= f_1(z) + i f_2(z), \\ w &= \psi + i \phi. \end{aligned} \quad (2.54)$$

This function is called the complex potential function.

To see a possible usage for this equation assume a potential field on the t plane:

$$\begin{aligned} w &= kt, \\ \psi + i \phi &= ku + kiv. \end{aligned} \quad (2.55)$$

This field corresponds to the uniform potential field $\phi = kv$. Thus for instance the field between a grounded conductor at the line $v = 0$ and a conductor kept at $\phi = k\pi$ at the line $v = \pi$. Both conductors have an infinite length.

³Consider two perpendicular curves: one at an angle of 45° and one at 135° . The first one has a slope of 1, the second one of -1, the product is -1. This argument can be extended to a general angle α , yielding $\tan(\alpha) \cdot \tan(90^\circ - \alpha) = -\tan(\alpha) \cdot \cot(\alpha) = -1$.

2.3.3 Conformal transformations

Above it was shown that conjugate functions describe solutions of the Laplace equation. Also it was shown that the uniform field can be described by such a function. A uniform field describes the parallel plate capacitor, for which the electric forces are easily computed. Therefore it would be nice if one could map a more difficult two conductor system back onto such a parallel plate field.

The conformal transformation is such a mapping and a well known method to find the analytical solution to Laplacian fields. It is used in many applications as in magnetic fields, heat conduction and fluid flow or off course electrostatics. The method is able to easily yield expressions for the potential gradient and capacitance. The limiting factors are the boundary shapes that have to be followed cannot be too complex of shape and the boundary conditions have to be equipotential (ideal conductors) or have to coincide with the stream lines (zero charge boundaries)

In general conformal transformations can be described by the regular function (2.56).

$$z = f(t) = x(u, v) + iy(u, v). \quad (2.56)$$

This equation defines a variable $z = x + iy$ as a function of another variable $t = u + iv$. A particular value of t can be seen as a point in the Argand diagram, which has on the horizontal axis the real units and the vertical axis the imaginary units. With equation (2.56) a corresponding point in the Argand diagram of z can be found. Also curves from point t_1 to point t_2 can be mapped into curves for corresponding z_1 into z_2 .

The Transformations are known as conformal because the angle at which two curves intersect in the t plane remains the same when both curves are mapped onto the z plane, with the exception of singular points.

Example: Logarithmic transformation

The logarithmic transformation is a common transformation used to build more complex transformations. Furthermore it is used to describe the potential field in the next section.

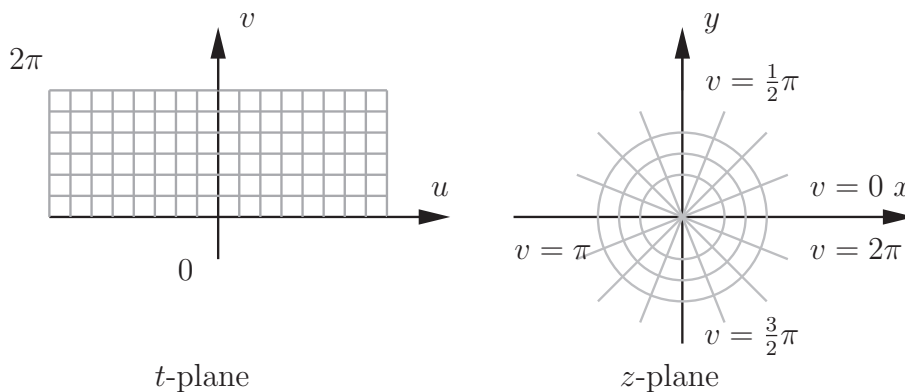


Figure 2.3: Logarithmic transformation.

Consider the transformation in figure 2.3. This transformation can be described by the field:

$$t = \log(z). \quad (2.57)$$

To see that this equation describes the shown transformation, the transformation is inverted:

$$e^t = z, \quad (2.58)$$

or when real and imaginary parts are considered separately:

$$\begin{aligned} e^u \cos(v) &= x, \\ e^u \sin(v) &= y. \end{aligned} \quad (2.59)$$

Hence, combining the equations above gives:

$$\sqrt{x^2 + y^2} = e^u, \quad (2.60)$$

which states that the line in the z plane corresponding to a constant u is a circle with radius e^u . Another combination of equations (2.59) provides:

$$\arctan\left(\frac{y}{x}\right) = v. \quad (2.61)$$

Which states that when v is constant the lines through the origin have slope $\tan(v)$ in the z plane.

Let's remember the uniform field:

$$w = kt. \quad (2.62)$$

When the z plane is defined by equation (2.57), this field can be written as:

$$w = k \log(z). \quad (2.63)$$

This field corresponds to the conductor with boundary condition $\phi = k\pi$ on the x -axis for $x = \langle -\infty, 0 \rangle$ and $\phi = 0$ on the x -axis for $x = \langle 0, \infty \rangle$. This seems like a very strange field, but will be useful when two opposite conductors in a relatively complicated geometry are mapped onto the same axis of a reference problem. This will be used in section 2.3.4.

2.3.4 Corners and corner singularities

In this section conformal transformations are used to calculate the electric field and force in the neighborhood of a sharp corner. First the general transformation of the corner problem will be discussed, which will be used for a specific corner that can also be simulated with numerical methods will be treated.

During these discussions it will become clear that corners cause geometric singularities in the electrostatic problem. Therefore in the final two parts of this section some remarks are made on the general order of singularity caused by a corner. These orders can later be used to enhance numerical modeling.

General problem

Sometimes conformal transformations can be derived easily by hand as for instance the transformation described in figure 2.3. However when complexity increases these derivations can become rather tedious, therefore most text books that promote conformal transformations contain libraries with conformal transformations. The parallel

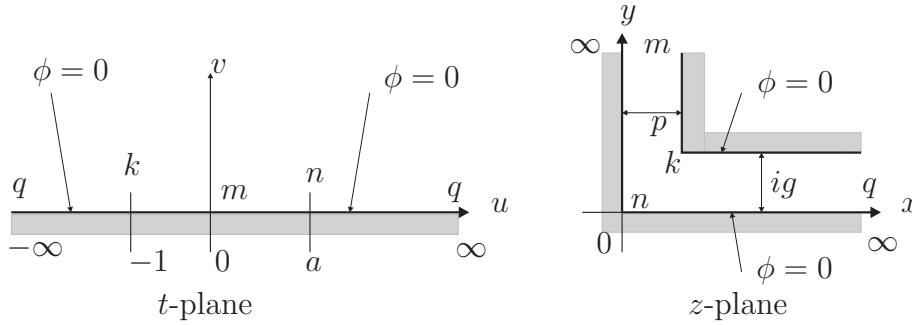


Figure 2.4: Corner transformation.

corner transformation shown in figure 2.4 was originally developed to examine the magnetic field of a rectangular salient pole in an electric motor as early as 1900.

Basically the geometry in the z plane is a polygon with three angles: an angle of $3\pi/2$ at point k , an angle of π at point m and another of $\pi/2$ at point n . This long polygon can be mapped onto the u axis of the t plane. One boundary will be mapped onto the positive x -axis and the other onto the negative x -axis. The origin of the t plane will then correspond to point m . The objectives of the transformation are summarized in table 2.1.

point	z plane	t plane
l	$z = p + ig$	$t = -1$
m	$z = i\infty$	$t = 0$
n	$z = 0$	$t = a$

Table 2.1: Objections for the transformation.

When looking in the transformation library of [16] for transformations that satisfy these demands, the following transformation is found:

$$z = \frac{2g}{\pi} \left[\frac{p}{g} \arctan \frac{ps}{g} + \frac{1}{2} \log \left(\frac{1+s}{1-s} \right) \right], \quad (2.64)$$

where:

$$s^2 = \frac{t - \left(\frac{g}{p}\right)^2}{t + 1}. \quad (2.65)$$

The Jacobian of this transformation is:

$$\frac{\partial z}{\partial t} = \frac{g}{\pi t} \sqrt{\frac{t+1}{t-a}}, \quad (2.66)$$

where:

$$a = \left(\frac{g}{p}\right)^2. \quad (2.67)$$

Example: Reference problem

The reference problem corresponds to the situation where $p = 1$ and $g = 1$, thus $a = 1$. Here the gap is equal on both sides of the corner. Hence the transformation (2.64)

reduces to:

$$z(t) = \frac{2}{\pi} \arctan \left(\sqrt{\frac{t-1}{t+1}} \right) + \frac{1}{\pi} \log \left(\frac{1 + \sqrt{\frac{t-1}{t+1}}}{1 - \sqrt{\frac{t-1}{t+1}}} \right). \quad (2.68)$$

The Jacobian for this transformation is:

$$\frac{\partial z}{\partial t} = \frac{1}{\pi t} \sqrt{\frac{t+1}{t-1}}. \quad (2.69)$$

It is not possible to calculate t as a function of z , but it is possible for a specific value of z to calculate the corresponding value of t .

In the problem a unit potential is applied on the boundary of the inner corner, thus on boundary $m - k - q$. On the other boundary $m - n - q$ a zero potential is applied.

It has been mentioned that this transformation maps boundary $m - n - q$ on the positive x-axis and boundary $m - k - q$ on the negative x-axis of the t plane. This means that in the t plane on the positive part of the x-axis has a zero potential and on the negative part a unit potential. In section 2.3.3 it was shown that the field in the t plane corresponding to this situation can be written as:

$$w = \frac{1}{\pi} \log(t), \quad (2.70)$$

which has the following first derivative with respect to t :

$$\frac{\partial w}{\partial t} = \frac{1}{\pi t}. \quad (2.71)$$

As just has been said it is not possible to derive an analytical function $t = f(z)$, but by using t as a parameter in a parametric plot, it is possible to create a contour plot of the potential w on the z plane. Contour plots give constant potential lines, thus constant v lines. From section 2.3.3 it is known that in the t plane these are straight lines through the origin. For each point on such a line the complete $u - v$ coordinate can be calculated and for a certain t both the corresponding z coordinate and the potential w can be calculated and used to build the contour plot of w in figure 2.5.

Using equations (2.35) and (2.38) in combination with the definition of w : $w = \psi + i\phi$, with ϕ the electrostatic potential and ψ the stream function, it can be said that:

$$\frac{\partial w}{\partial z} = \frac{\partial w}{\partial x} = \frac{\partial \psi}{\partial x} + i \frac{\partial \phi}{\partial x}, \quad (2.72)$$

and:

$$i \frac{\partial w}{\partial z} = \frac{\partial w}{\partial y} = \frac{\partial \psi}{\partial y} + i \frac{\partial \phi}{\partial y}. \quad (2.73)$$

The Cauchy-Riemann equations tell that:

$$\frac{\partial \phi}{\partial y} = \frac{\partial \psi}{\partial x}. \quad (2.74)$$

The electric field $E = iE_x + E_y$ on the z plane is:

$$E = -i \frac{\partial \phi}{\partial x} - \frac{\partial \phi}{\partial y} = -i \frac{\partial \phi}{\partial x} - \frac{\partial \psi}{\partial x} = -\frac{\partial w}{\partial z}. \quad (2.75)$$

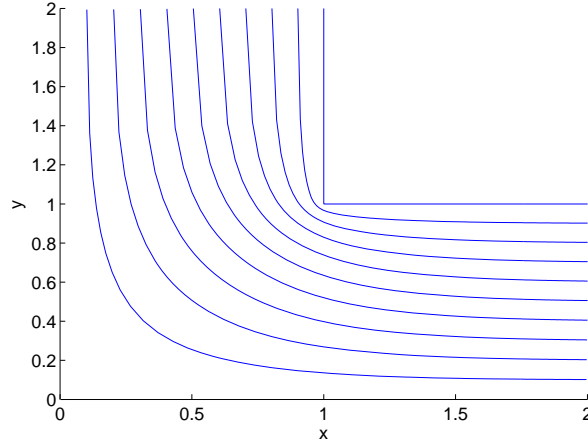


Figure 2.5: Contour plot of the electrostatic potential near the corner.

The transformation has to be compensated for:

$$E = -\frac{\partial w}{\partial z} = -\frac{\partial w}{\partial t} \frac{\partial t}{\partial z}, \quad (2.76)$$

thus, when combining with equations (2.71) and (2.69) this yields the following electric field in the z plane:

$$E = -\sqrt{\frac{t-1}{t+1}}. \quad (2.77)$$

Equation (2.70) shows that at the singular point k , thus at $t = -1$ the potential is a bounded function, however the electric field in equation (2.77) is infinite at $t = -1$.

To compute the electrostatic pressure $f_{es} = if_x + f_y$ the relation (2.21) is used:

$$f_{es} = \frac{1}{2}\varepsilon_0(iE_x^2 + E_y^2), \quad (2.78)$$

where ε_0 is the electric permittivity in the gap. This results in a very long equation when calculated completely. But when using symmetry it is easy to see that the force on the horizontal boundary in vertical direction should be equal in value to the force in horizontal direction on the vertical boundary of the corner. On the horizontal boundary the electric field has only a component in y direction, thus $E = E_y$. Therefore only for this boundary the pressure can be written as:

$$f_{es} = \frac{1}{2}\varepsilon_0 E^2. \quad (2.79)$$

Substituting of equation (2.77) into the equation above gives:

$$f_{es} = \frac{1}{2}\varepsilon_0 \frac{t-1}{t+1}. \quad (2.80)$$

From this equation can be seen that the pressure has a singular point near the corner at the point k where $t = -1$. At this point the pressure will reach an infinite value. The force distribution shown in figure 2.6 was derived using this equation.

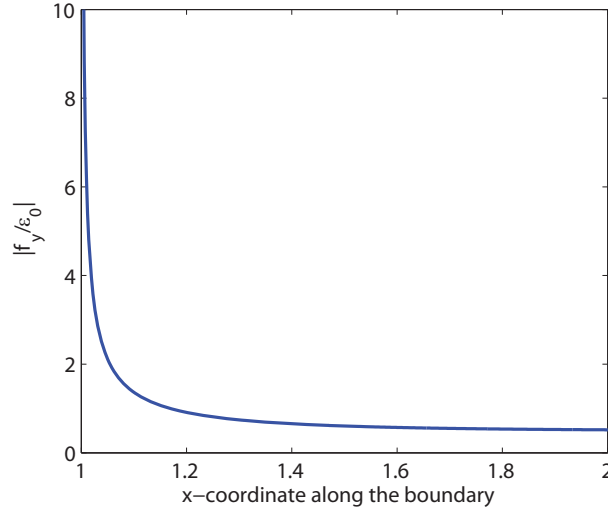


Figure 2.6: Electric force distribution on horizontal corner boundary.

However the value of interest is the pressure integrated over part of the boundary near the corner to be able to compare this analytical solution of the force with finite element computations. It is chosen to integrate the force over a unit length of the boundary near the corner, thus from $z = 1 + i$ to $z = 1 + 2i$:

$$F_{es} = \frac{1}{2}\varepsilon_0 \int_{1+i}^{1+2i} E^2 dz, \quad (2.81)$$

which after transforming the variable of integration and the range of integration gives:

$$F_{es} = \frac{1}{2}\varepsilon_0 \int_{t=-54.66}^{-1} E^2 \frac{\partial z}{\partial t} dt, \quad (2.82)$$

$$F_{es} = \frac{1}{2}\varepsilon_0 \int_{t=-54.66}^{-1} \frac{1}{\pi} \frac{(t-1)\sqrt{\frac{t+1}{t-1}}}{(t+1)t} dt.$$

It is clear that the integrand still reaches a singular point, but of the order $1/\sqrt{t+1}$ near $t = -1$. This should yield a finite value after integration. And so it did:

$$F_{es} = iF_x + F_y = 0i - 0.9942\varepsilon_0, \quad (2.83)$$

which is a downward directed force on the horizontal boundary of the corner.

Order of singularity for a conducting corner

Above, it was shown that an exterior corner in an electric domain creates a singularity. It would be interesting to have a measure of the order of this singularity for general corners.

An appropriate conformal transformation has to be chosen. It can be shown [16] that a straight electrode is mapped to an electrode with a single corner of an angle θ by the transformation:

$$z = t^{\theta/\pi}, \quad (2.84)$$

which gives a corner surrounded by the infinitely expanding field as shown in figure 2.7. It is assumed that locally, all sharp corners cause a potential distribution that looks like this distribution. The inverse relation of (2.84) $t = z^{\pi/\theta}$, substituted in the

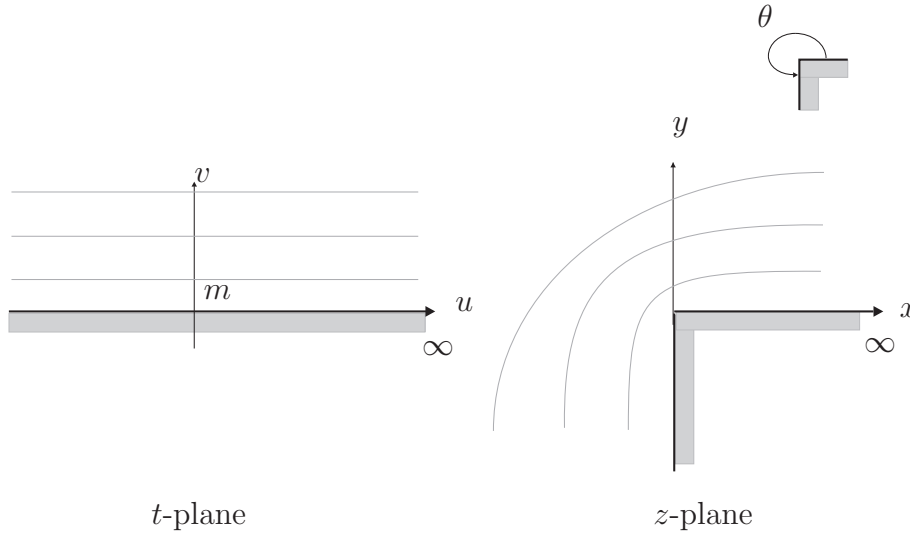


Figure 2.7: Exterior corner transformation for $\theta = 3\pi/2$.

complex potential $w = \phi_b t$, yields:

$$w = \phi_b z^{\pi/\theta}. \quad (2.85)$$

This means that in the t -plane ϕ is zero at the conductor and equal to ϕ_b at a distance of 1 from that conductor in the v -direction. When this equation is rewritten in polar form ($z = r e^{i\varphi}$), the following complex potential distribution is found:

$$w = \phi_b r^{\pi/\theta} e^{i\varphi\pi/\theta}. \quad (2.86)$$

Since it was seen that the electric potential is the imaginary part of the complex potential function, the potential is equal to (using the Euler formula):

$$\phi = \phi_b r^{\pi/\theta} \sin(\varphi\pi/\theta), \quad (2.87)$$

and the electric field with this potential distribution will be:

$$E_r = -\frac{\partial\phi}{\partial r} = -\frac{\pi}{\theta} \phi_b r^{(\pi/\theta-1)} \sin(\varphi\pi/\theta) = -\frac{\pi}{\theta} \phi_b r^k \sin(\varphi\pi/\theta). \quad (2.88)$$

The order of singularity $k = (\pi/\theta - 1)$ will always be bigger than -0.5, because θ must be smaller than 2π . Thus the singularity cannot become worse than a $1/\sqrt{r}$ singularity. If θ is smaller than π , $(\pi/\theta - 1)$ is bigger than 0, therefore such a corner will not show a singularity, the opposite is true. The electric field will be zero at such a corner. However when θ becomes bigger than π , thus the conductor starts *pointing* into the dielectric, $k = (\pi/\theta - 1)$ becomes smaller than zero, therefore the electric field will become unbounded at $r = 0$. For a right angle ($\theta = \frac{3}{2}\pi$) the order k will be $-\frac{1}{3}$.

This distribution can also be obtained by solving Laplace's equation in polar coordinates using separation of variables [66], but for the sake of continuity and simplicity in this document, the conformal transformation approach was chosen.

Order of singularity for a dielectric corner

A geometric singularity occurs not only when the sharp corner is part of a conductor, but also when the corner is part of the interface between two dielectrics. That case is sketched in figure 2.8, where θ is the interior angle of the corner. It is assumed that ε_1 is the higher dielectric constant. The derivation in this section is based on [5].

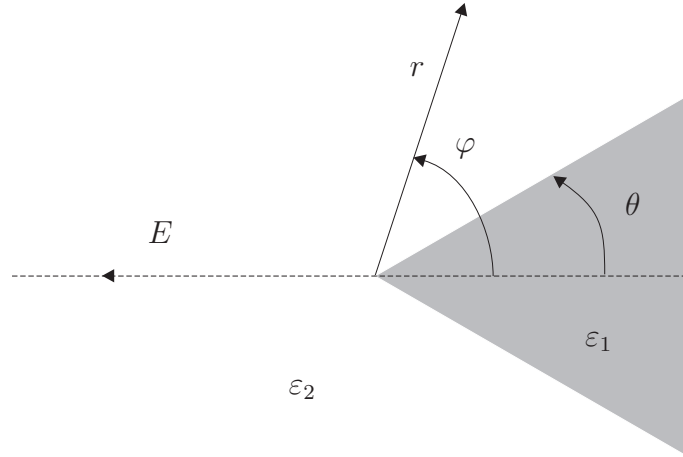


Figure 2.8: Dielectric corner.

To be able to solve the problem it is assumed that the overall electric field is directed parallel to the line of symmetry. When $\varphi = 0$ or $\varphi = \pi$, then $\partial\phi/\partial\varphi = 0$ due to this symmetry. Furthermore across the interface the potential ϕ must be continuous. Because the electric equation (2.8) must hold across the interface, the electric displacement in the direction normal to the interface $D_n = \varepsilon(\partial\phi/\partial\varphi)$ must be continuous across the interface as well.

The solution in both regions have to satisfy the 2D Laplace equation in polar coordinates (r, ψ) :

$$\frac{1}{r} \frac{\partial}{\partial r} \left(r \frac{\partial \phi}{\partial r} \right) + \frac{1}{r^2} \frac{\partial^2 \phi}{\partial \varphi^2} = 0. \quad (2.89)$$

Therefore it is assumed that the solution in each dielectric region is similar to the solution found in the previous section (2.87). However, that solution assumed that it was potentials that were applied on the boundary of the corner, where in this problem it is as if there are two corners for which the fluxes are defined on the boundaries, also the flux must locally be perpendicular to the horizontal axis. Therefore the horizontal axis must be a stream line, thus the stream function must be constant on that axis.

In the previous discussions the complex potential was defined as $w = \psi + i\phi$ with ψ the stream function and ϕ the electric potential. If only for this problem it is defined as $w = \phi + i\psi$, the complex potential (eq. (2.86) for the corner with imposed fluxes can be written as:

$$w = \psi_b r^{\pi/\theta} e^{i\varphi\pi/\theta}. \quad (2.90)$$

The figure of interest is however still the electric potential, in this case the real part of the complex potential, which using Euler's formula is equal to:

$$\phi = \phi_b r^{\pi/\theta} \cos(\varphi\pi/\theta). \quad (2.91)$$

Hence on the domain $0 \leq \psi \leq \pi$ it is assumed that the electric potential can be written as:

$$\begin{cases} \phi = A r^p \cos(p\varphi), & 0 \leq \varphi \leq \theta, \\ \phi = B r^p \cos(p(\pi - \theta)), & \theta \leq \varphi \leq \pi, \end{cases} \quad (2.92)$$

where A and B constants. When the interface conditions are applied this gives (first continuous potential, then continuous electric displacement):

$$\begin{cases} A r^p \cos(p\theta) = B r^p \cos(p(\pi - \theta)), \\ -\varepsilon_1 A r^p p \cos(p\theta) = \varepsilon_2 B r^p p \cos(p(\pi - \theta)). \end{cases} \quad (2.93)$$

Eliminating A and B from the equations gives:

$$\varepsilon_1 \cos(p(\pi - \theta)) \sin(p\theta) = -\varepsilon_2 \sin(p(\pi - \theta)) \cos(p\theta). \quad (2.94)$$

After rearrangement (2.94) can be written as:

$$\sin(p\pi) + \left(\frac{\varepsilon_1 - \varepsilon_2}{\varepsilon_1 + \varepsilon_2} \right) \sin(p(2\theta - \pi)) = 0, \quad (2.95)$$

which can be used to find p . There will be infinitely many solutions to this equation, but negative solutions are not of interest, since infinite potentials do not represent a physical solution. The smallest positive solution for p represents the physical solution. When θ is bigger than $\pi/2$, the smallest p is bigger than 1, thus the order of singularity of the electric field $k = p - 1$ will be bigger than 0, thus as with the conductor corner there will be no singularity⁴. However when θ is smaller than $\pi/2$ the solutions of p will be smaller than 1, showing a singularity.

To see how this singularity compares to the conductor singularity, the order was determined for the specific corner angle of $\theta = \pi/4$ for different values of ε_1 . It is assumed that the lower dielectric value equals the vacuum permittivity ($\varepsilon_2 = \varepsilon_0$). The results are shown in figure 2.9. It clear that when $\varepsilon_1 = \varepsilon_2 = \varepsilon_0 \rightarrow \varepsilon_1/\varepsilon_0 = 1$, the order of singularity equals 1, hence the singularity does not exist. Furthermore when $\varepsilon_1 \rightarrow \infty$ then $p \rightarrow \frac{2}{3}$, thus k approaches $k = -\frac{1}{3}$ and therefore the solution for the ideal conductor singularity.

2.4 Finite Element Method in 2D

In the previous section the singularity was investigated that enters Laplace's equation when there are polygonal boundaries with Dirichlet boundary conditions. In other words: that singularity that appears when the boundary of the domain has sharp corners. The direct motive for this investigation was the electrostatic field and the forces that this electrostatic field exerts on conducting bodies. Within microsystem applications these forces are of vital importance and the geometry of such a microsystem normally has a lot of corners.

In the past a lot of research has been done on the influence of such a singularity on the convergence of the FEM solution of Laplace's equation [141, 9]. However, the main

⁴When comparing the results, note that the angle θ was defined differently with the conducting corner. Also remember that $E_r = -\frac{\partial\phi}{\partial r} = -\frac{\partial}{\partial r}(A r^p \cos(\varphi p))$, which can be written as: $E_r = p A r^{p-1} \cos(p\varphi)$ or: $E_r = p A r^k \cos(p\varphi)$.

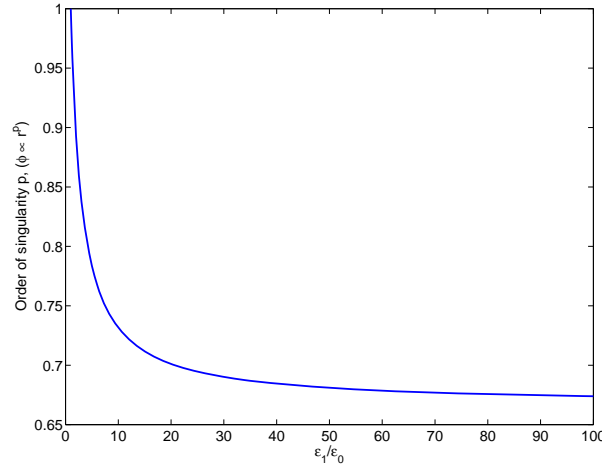


Figure 2.9: Order of singularity for a straight corner ($\theta = \pi/4, \epsilon_2 = \epsilon_0$).

concern of those investigations was to limit the error of the singularity to the region close to the singular point and to estimate the value of the error.

Though, when the electrostatic force is the main interest, a converged potential field is not sufficient. It was shown before and in literature that the electric force on a conductor is a simple function of the electric field at the exterior boundary of that conductor [48]. To get correct force values with that force function also the electric field must have converged, also at the singular point, where at an infinitesimal region an infinite pressure will appear.

One method to overcome this problem is to use the principle of virtual work to derive the nodal forces instead of the standard force function [108]. In this document the derivation of forces based on the principle of virtual work is called *the variational approach*. Another option to solve the problem of singularity is to use specific elements and shape functions as proposed in [81, 82]. In this text these elements are investigated and compared to the standard approach and the variational approach. But first the FEM discretization of the electrostatic problem is recapitulated.

2.4.1 Finite element equations

When the finite element method is used to discretize the electrostatic differential equation on the domain in figure 2.10, this domain is separated into regions called elements as in figure 2.11. Within each element it is assumed that the potential is a linear function of x and y (or at least the relation $\phi(x, y)$ is a simple relationship). If the potential is such a linear function within the element, a piecewise linear relationship describes the total field, if all those elements are connected. Such a piecewise linear potential distribution is shown in figure 2.12. Furthermore it is assumed that there is a linear relationship between the potential and the discrete values of the potential at the corners of the element. The locations of those corners are called nodes. In that case the continuous potential is discretized as (summation over index i):

$$\phi(x, y) = N_i(x, y)\phi_i, \quad (2.96)$$

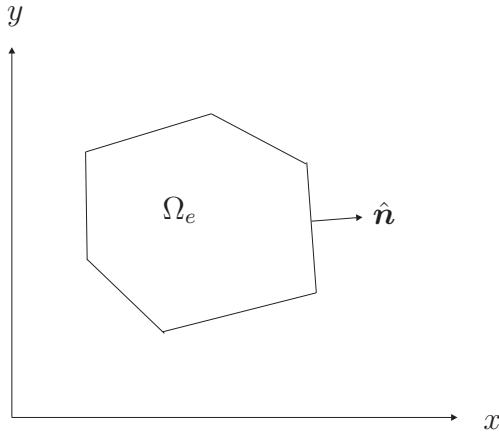


Figure 2.10: Electrostatic domain

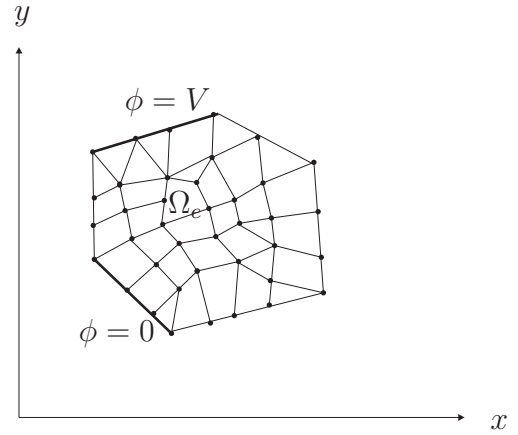


Figure 2.11: Mesh consisting of triangles and quadrilaterals.

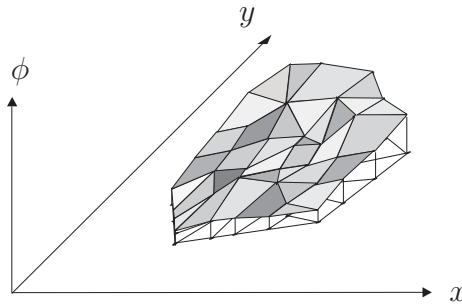


Figure 2.12: A piecewise linear potential distribution.

where the ϕ_i are the discretized potential values at the corners of the element and the N_i are the linear (or simple) relations that describes how the a unit potential at node i propagates through an element. More information on these shape functions can be found in appendix A.3. Equation (2.96) can be written in matrix vector notation as:

$$\phi = \mathbf{N}\phi. \quad (2.97)$$

Appendix A.1.1 shows how this assumption applied on the electrostatic equation (2.9) can end up in a linear matrix vector equation, that describes the relation between the nodal potentials ϕ and the charges present at the location of the nodes \mathbf{Q} :

$$\mathbf{K}\phi = \mathbf{Q}, \quad (2.98)$$

where:

$$\mathbf{K} = \int_{\Omega_e} \nabla \mathbf{N}^T \varepsilon \nabla \mathbf{N} d\Omega. \quad (2.99)$$

Because there are no space charges these are zero inside the domain. On the boundary they are zero on those places were there is a symmetry boundary condition, but not on the nodes where there is an imposed potential.

Appendix A.1.1 also shows that after application of the boundary conditions the remaining equation that has to be solved can be written as.

$$\mathbf{K}_{\phi\bar{\phi}}\phi_\phi = -\mathbf{K}_{\phi,\bar{\phi}}\bar{\phi}. \quad (2.100)$$

or:

$$\mathbf{K}_{\phi\bar{\phi}}\phi = \mathbf{q}_{ext}. \quad (2.101)$$

Where $\mathbf{K}_{\phi\bar{\phi}}$ and $\mathbf{K}_{\bar{\phi}\phi}$ are sub matrices of \mathbf{K} associated with free (ϕ) degrees of freedom and prescribed ($\bar{\phi}$) DOFs and \mathbf{q}_{ext} is the apparent charge on the free DOFs due to the Dirichlet boundary condition.

2.4.2 Methods using Lagrangian finite elements

Lagrange type elements are the standard elements with only one potential DOF per node. A typical Lagrange type element is shown in figure 2.13. This element has 4 nodes, therefore $\phi = N_i\phi_i$ will be a bi-linear function of the spatial coordinates ξ and η . These elements are the simplest elements to use, because only constraints on the potentials have to be identified, because no other DOFs are present in the model.

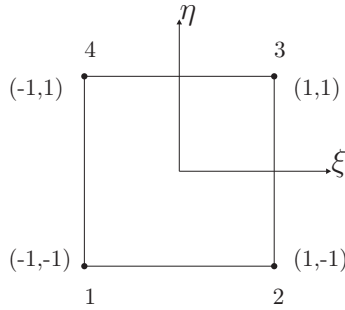


Figure 2.13: Bilinear square element.

Traditional Maxwell stress tensor surface integral

As derived before in section 2.2.3, when the Maxwell tensor is used this yields the following electrostatic force relation (2.26):

$$\mathbf{f}_e = \int_{\Gamma} \frac{1}{2} \varepsilon |\mathbf{E}|^2 \mathbf{n} dS = \int_{\Gamma} \frac{1}{2} \varepsilon |\mathbf{E}|^2 \mathbf{n} dS. \quad (2.102)$$

The electrostatic force is thus obtained by integrating the local Maxwell surface stress over the edge of the conductor, therefore this last form will be called the *local force approach* in this document. When the structural displacements are discretized by finite elements with shape functions \mathbf{N} , the nodal forces originating from the Maxwell stress on the surface are computed as

$$\mathbf{f}_{e,nodes} = \int_{\Gamma} \frac{1}{2} \varepsilon \mathbf{N}^T \left| \frac{\partial \phi}{\partial n} \right|^2 \mathbf{n} dS. \quad (2.103)$$

this approach is used in most commercial codes, where one normally has the possibility to use higher order elements as well, such as the element in figure 2.14. In that case the shape functions are bi-quadratic functions of ξ and η . Still each node has only a potential DOF, hence the element is still Lagrangian.

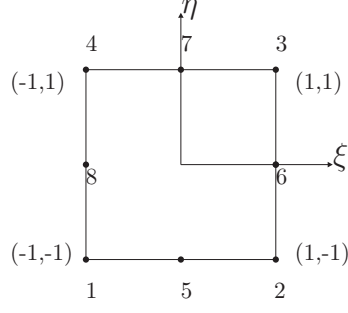


Figure 2.14: Quadratic square element.

Variational force calculation

Another way of computing the electrostatic force is not to resort to the Maxwell stress tensor but rather to start from the total electric energy:

$$W_e = \frac{1}{2} \int_{\Omega} \varepsilon \nabla \phi \cdot \nabla \phi dV. \quad (2.104)$$

In that case the electrostatic forces can be obtained by computing the virtual work related to a variation of the displacement field $\delta \mathbf{u}$ of the structure on which the forces are acting (see for instance [108]):

$$\mathbf{f}_e \cdot \delta \mathbf{u} = \frac{\partial W_e}{\partial \mathbf{u}} \delta \mathbf{u} = W'_e - W_e. \quad (2.105)$$

Here the perturbed energy W'_e relates to the perturbed Ω' , namely Ω deformed by the virtual displacement $\delta \mathbf{u}$:

$$W'_e = \frac{1}{2} \int_{\Omega'} \nabla' \phi^T \varepsilon \nabla' \phi dV' = \frac{1}{2} \int_{\Omega} \nabla' \phi^T \varepsilon \nabla' \phi \frac{dV'}{dV} dV. \quad (2.106)$$

After defining the deformation gradient tensor as

$$\mathbf{F} = \frac{\partial(\mathbf{x} + \delta \mathbf{u})}{\partial \mathbf{x}}, \quad (2.107)$$

the determinant in the integral of equation (2.106) can be written as

$$J = \frac{dV'}{dV} = \det(\mathbf{F}) \approx 1 + \nabla \cdot \delta \mathbf{u}. \quad (2.108)$$

Because by definition:

$$\nabla' \phi = \mathbf{F}^{-T} \nabla \phi \approx (\mathbf{I} - \nabla \delta \mathbf{u}^T) \nabla \phi, \quad (2.109)$$

where $\nabla \delta \mathbf{u}$ is a tensor with components $\frac{\partial \delta u_j}{\partial x_i}$, the following approximation can be made:

$$\nabla' \phi^T \approx \nabla \phi^T (\mathbf{I} - \nabla \delta \mathbf{u}), \quad (2.110)$$

Subsequently, substitution of all relevant terms into equations (2.106) and (2.105) yields:

$$\mathbf{f}_e \cdot \delta \mathbf{u} = \frac{1}{2} \int_{\Omega} \nabla \phi^T (\mathbf{I} - \nabla \delta \mathbf{u}) \varepsilon (\mathbf{I} - \nabla \delta \mathbf{u}^T) \nabla \phi (1 + \nabla \cdot \delta \mathbf{u}) dV - W_e, \quad (2.111)$$

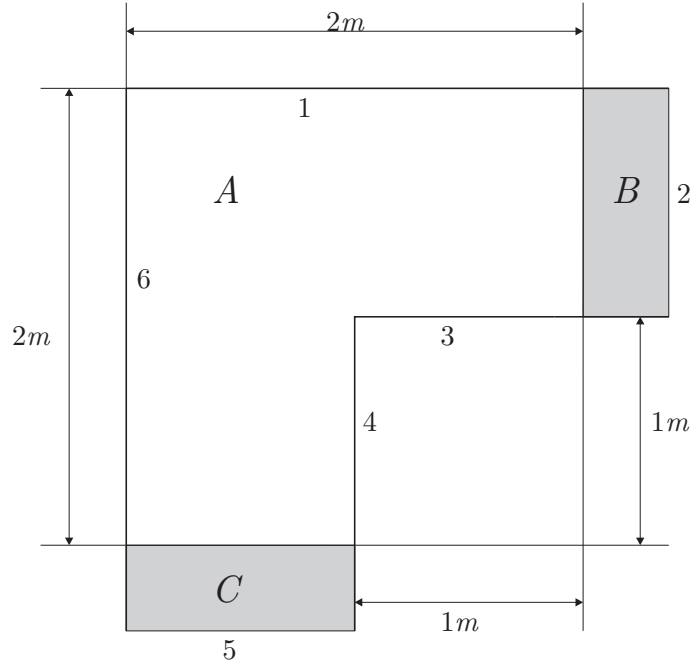


Figure 2.15: FEM model of the corner.

If the higher order terms in $\delta \mathbf{u}$ are neglected this gives

$$\mathbf{f}_e \cdot \delta \mathbf{u} = \frac{1}{2} \int_{\Omega} \varepsilon \nabla \phi^T \nabla \phi (\nabla \cdot \delta \mathbf{u}) dV - \frac{1}{2} \int_{\Omega} \varepsilon \nabla \phi^T (\nabla \delta \mathbf{u} + \nabla \delta \mathbf{u}^T) \nabla \phi dV. \quad (2.112)$$

This approach was first presented in [108], where it was shown that equation (2.112) can be written as:

$$\mathbf{f}_e \cdot \delta \mathbf{u} = \frac{1}{2} \int_{\Omega} \varepsilon \mathbf{E}^T \begin{bmatrix} \frac{\partial \phi}{\partial x} & 0 & 2 \frac{\partial \phi}{\partial y} & -\frac{\partial \phi}{\partial x} \\ -\frac{\partial \phi}{\partial y} & 2 \frac{\partial \phi}{\partial x} & 0 & \frac{\partial \phi}{\partial y} \end{bmatrix} \begin{bmatrix} \nabla \delta u_x \\ \nabla \delta u_y \end{bmatrix} dV, \quad (2.113)$$

where $\nabla \delta u_j$ is a vector with components $\frac{\partial \delta u_j}{\partial x_i}$.

After finite element discretization the equation above becomes:

$$\mathbf{f}_{e,nodes}^T = \frac{1}{2} \int_{\Omega} \varepsilon \mathbf{E}^T \begin{bmatrix} \frac{\partial \phi}{\partial x} & 0 & 2 \frac{\partial \phi}{\partial y} & -\frac{\partial \phi}{\partial x} \\ -\frac{\partial \phi}{\partial y} & 2 \frac{\partial \phi}{\partial x} & 0 & \frac{\partial \phi}{\partial y} \end{bmatrix} \mathbf{B} dV, \quad (2.114)$$

where \mathbf{B} is the matrix containing the derivatives of the shape functions \mathbf{N} for the structural displacement field:

$$\mathbf{B} = \begin{bmatrix} \frac{\partial \mathbf{N}}{\partial x} & 0 \\ 0 & \frac{\partial \mathbf{N}}{\partial x} \end{bmatrix}. \quad (2.115)$$

First comparison of the approaches

The *variational* and *local force* approaches will be compared with each other by computing the forces for a reference problem. The FEM geometry of this reference problem is shown in figure 2.15. It models the same problem as the analytical model. Boundaries 1 and 6 have a zero potential, boundaries 3 and 4 have a unit potential. The

right-hand and bottom boundaries 2 and 5 are assumed to represent symmetry conditions: Neumann conditions ($\partial\phi/\partial n = 0$) are applied on them. The air gap is formed by regions A , B and C . Region A is meshed with standard linear Lagrange elements. Region B has infinite elements in the horizontal direction and region C has infinite elements in the vertical direction [145]. These infinite elements map the decay of the field as if the length of B and C would be infinitely long, as was the case for the analytical problem.

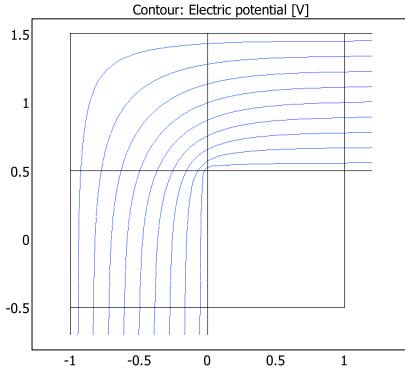


Figure 2.16: Electric potential around a corner.

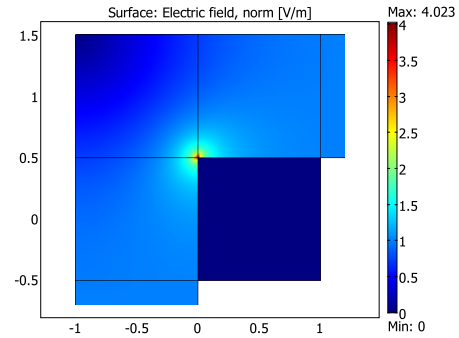


Figure 2.17: Electric field around a corner.

In figure 2.16 a contour plot of the electrostatic potential is given. This plot was determined using FEM. The electric field is given in figure 2.17. It can be seen that near the singularity the field has a maximum value.

The convergence of the electrostatic force has to be determined for both FEM approaches. Therefore the corner is meshed with a number of square elements with linear shape functions. This number is increased, or equivalently the element size h is decreased. The results of this convergence analysis are given in figure 2.18. In the figure the x-axis denotes $1/h$, with h the size of an element, the y-axis denotes the absolute value for the force in x-direction integrated over side 4 and subsequently divided by the vacuum permittivity ε_0 .

It is clear from the left-hand side of picture 2.18 that at an element size of approximately 0.025 the variational solution (2.113) with a force of $0.99\varepsilon_0$ has almost converged to the analytical solution of $0.9942\varepsilon_0$, whereas the local force function (2.26) has not yet converged. The final value it has reached before computations times become too large is $0.85\varepsilon_0$. The right-hand side of figure 2.18 shows that the rate of convergence is equal for both approaches but the variational approach starts from a better value. The next section will investigate why the variational approach starts from a better value.

2.4.3 Maxwell stress tensor vs. variational forces

In the example of the previous section it has become clear that the local approach using the Maxwell stress tensor does not accurately approximate the electrostatic forces in the vicinity of a corner. To better understand this, the corner problem considered above (figure 2.15) will be reduced to its simplest discretization: a three element mesh. Thereafter the theoretical relation between the Maxwell stress tensor and the electrostatic force obtained from the variational approach will be uncovered. At the end it

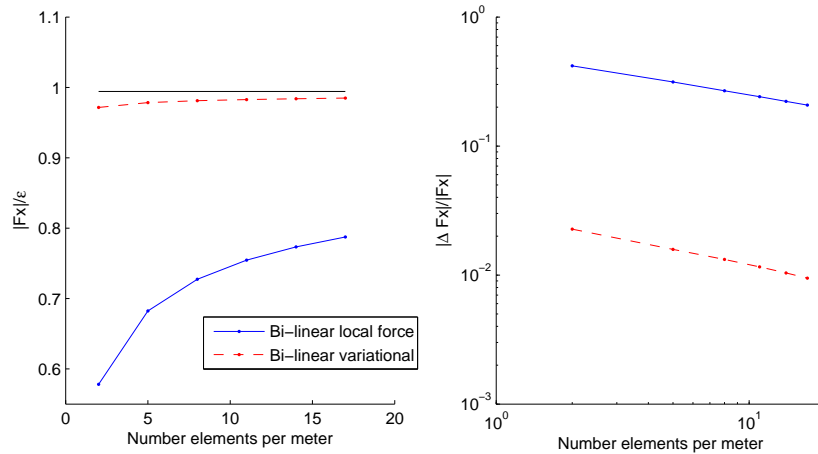


Figure 2.18: Convergence for both the variational and local force approaches using bilinear elements.

is shown that for the simplest discretization of the corner indeed both methods can provide the same results when properly applied.

Comparison with only three elements

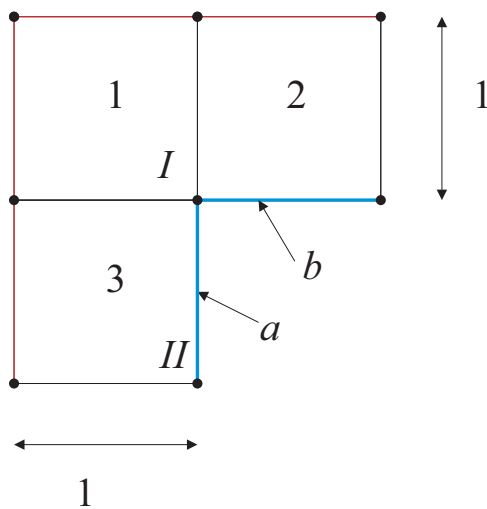


Figure 2.19: Corner meshed with three elements.

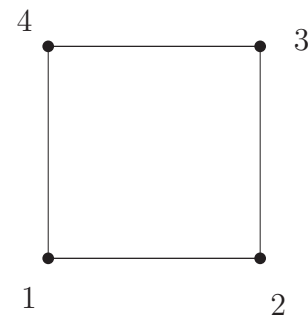


Figure 2.20: An element.

The corner problem is meshed with only 3 square elements of 1 by 1 each (figure 2.19). Each of the elements has its nodes numbered as in figure 2.20. Nodes on the red boundary have a potential of 1 and those on the blue boundary have a potential of 0. Using linear elements the electric field in elements 2 and 3 is directly obtained from the boundary conditions: $E_x^2 = 0$, $E_y^2 = -1$ and $E_x^3 = 1$, $E_y^3 = 0$ respectively. The electric field in element 1 is found by writing the potential as

$$\phi = N_1\phi_1 + N_2\phi_2 + N_3\phi_3 + N_4\phi_4 = N_1 + N_3 + N_4, \quad (2.116)$$

where the N_i are the linear shape functions. Choosing the origin of the local reference in the middle of the element the electric field is found to be:

$$E_x^1 = -\frac{\partial\phi}{\partial x} = \frac{1}{2}(1-2y), \quad E_y^1 = -\frac{\partial\phi}{\partial y} = -\frac{1}{2}(1+2x). \quad (2.117)$$

As in the previous section the electrostatic force is computed on the corner in one direction only, therefore the computed force originates from only one of the edges. Here the force is evaluated horizontal direction, therefore this force is being generated on the vertical side a (figure 2.19). Hence the required electrostatic forces are those on nodes I and II (figure 2.19), as obtained after assembly of the element contributions.

Surface integral of Maxwell stress tensor

The electric field obtained from the discretization is orthogonal to the edges of the corner, as it should be according to the equipotential condition on those boundaries. Hence the Maxwell stress tensor (2.23) and the surface normal vectors are

$$\begin{aligned} \mathbf{T} &= \varepsilon \begin{bmatrix} \frac{1}{2}(E_x^3)^2 & 0 \\ 0 & -\frac{1}{2}(E_x^3)^2 \end{bmatrix} = \begin{bmatrix} \frac{1}{2}\varepsilon & 0 \\ 0 & -\frac{1}{2}\varepsilon \end{bmatrix} & \mathbf{n} &= \begin{bmatrix} -1 \\ 0 \end{bmatrix} & \text{on } a \\ \mathbf{T} &= \varepsilon \begin{bmatrix} -\frac{1}{2}(E_y^2)^2 & 0 \\ 0 & \frac{1}{2}(E_y^2)^2 \end{bmatrix} = \begin{bmatrix} -\frac{1}{2}\varepsilon & 0 \\ 0 & \frac{1}{2}\varepsilon \end{bmatrix} & \mathbf{n} &= \begin{bmatrix} 0 \\ 1 \end{bmatrix} & \text{on } b \end{aligned}$$

The forces in direction x obtained from the local force equation (2.103) for elements 2 and 3 on nodes I and II are:

$$\mathbf{f}_{e,I}^{2,x} = [0], \quad \mathbf{f}_{e,I,II}^{3,x} = [-\frac{1}{4}\varepsilon \quad -\frac{1}{4}\varepsilon] \quad (2.118)$$

Clearly edge b does not contribute to the horizontal force, and a summation the nodal forces in the horizontal direction gives:

$$f_e^x = -\frac{1}{2}\varepsilon. \quad (2.119)$$

The analytical solution for this problem being $f_e^x = -0.9942\varepsilon$, it is clear that the electrostatic forces are badly estimated.

Variational approach

When the variation force equation (2.114) is used to compute the nodal electrostatic forces, one needs to perform a volume integral which yields the following contribution of elements 1, 2 and 3 on nodes I and II :

$$\mathbf{f}_{e,I}^{1,x} = [-0.2083\varepsilon] \quad \mathbf{f}_{e,I}^{2,x} = [-\frac{1}{4}\varepsilon] \quad \mathbf{f}_{e,I,II}^{3,x} = [-\frac{1}{4}\varepsilon \quad -\frac{1}{4}\varepsilon] \quad (2.120)$$

It is noteworthy that the electrostatic force associated to element 3 is identical to the force obtained with the local approach, but in this approach elements 1 and 2 also contribute to the horizontal force on the corner node. The total horizontal force is:

$$f_e^x = -0.9583\varepsilon, \quad (2.121)$$

which is very close to the analytical solution of -0.9942ε .

The Maxwell stress tensor and the variational method

Form the simple example above it is clear that the Maxwell stress tensor and the variational approach yield the same nodal forces except on corners. This seems paradoxical since on one hand the Maxwell stress vector on the edge seems to properly represent the physics, namely the Coulomb forces on the surface charges, whereas the variational approach yields a significantly more accurate corner force. Obviously: when the element size decreases, both methods converge to the same solution and are thus consistent. However one would expect a true equivalence between the Maxwell stress tensor and the forces derived from the variational approach.

Let's therefore consider again the forces (2.112) derived from the variational approach, namely

$$\mathbf{f}_e \cdot \delta \mathbf{u} = \frac{1}{2} \int_{\Omega} \varepsilon \nabla \phi^T (\nabla \cdot \delta \mathbf{u}) \nabla \phi dV - \frac{1}{2} \int_{\Omega} \varepsilon \nabla \phi^T (\nabla \delta \mathbf{u} + \nabla \delta \mathbf{u}^T) \nabla \phi dV \quad (2.112)$$

and transform both terms in this expression using Gauss' theorem, giving for the first term:

$$\begin{aligned} \frac{1}{2} \int_{\Omega} \varepsilon \nabla \phi^T \nabla \phi (\nabla \cdot \delta \mathbf{u}) dV &= \frac{1}{2} \int_{\Omega} \nabla \cdot (\varepsilon \nabla \phi^T \nabla \phi \delta \mathbf{u}) dV - \int_{\Omega} \varepsilon \nabla^2 \phi \nabla \phi^T \delta \mathbf{u} dV \\ &= \frac{1}{2} \int_{\Gamma} (-\mathbf{n})^T (\nabla \phi^T \varepsilon \nabla \phi) \delta \mathbf{u} dS - \int_{\Omega} \varepsilon \nabla^2 \phi (\nabla \phi)^T \delta \mathbf{u} dV \end{aligned} \quad (2.122)$$

where as before \mathbf{n} is the inner normal pointing into to the electric domain. The second term in (2.112) can be transformed into:

$$\begin{aligned} \frac{1}{2} \int_{\Omega} \varepsilon \nabla \phi^T (\nabla \delta \mathbf{u} + \nabla \delta \mathbf{u}^T) \nabla \phi dV &= \frac{1}{2} \int_{\Omega} \varepsilon \nabla \phi \nabla \phi^T : (\nabla \delta \mathbf{u} + \nabla \delta \mathbf{u}^T) dV \\ &= \int_{\Gamma} \varepsilon (-\mathbf{n})^T \nabla \phi \nabla \phi^T \delta \mathbf{u} dS - \int_{\Omega} \varepsilon \delta \mathbf{u}^T \nabla \phi \nabla^2 \phi dV. \end{aligned} \quad (2.123)$$

Now substitution of the two equations above into (2.112) gives:

$$\begin{aligned} \mathbf{f}_e \cdot \delta \mathbf{u} &= -\frac{1}{2} \int_{\Gamma} \mathbf{n}^T (\nabla \phi^T \varepsilon \nabla \phi) \delta \mathbf{u} dS + \int_{\Gamma} \varepsilon \mathbf{n}^T \nabla \phi \nabla \phi^T \delta \mathbf{u} dS \\ &= \int_{\Gamma} \mathbf{n}^T \mathbf{T} \delta \mathbf{u} dS, \end{aligned} \quad (2.124)$$

where:

$$\mathbf{T} = \varepsilon \nabla \phi \nabla \phi^T - \frac{1}{2} \varepsilon \nabla \phi^T \nabla \phi \mathbf{I}. \quad (2.125)$$

is the Maxwell stress tensor which was given by (2.2.3). The final result (2.124) proves that computing the electrostatic forces with the Maxwell stress tensor as in (2.25) is exactly equivalent to computing those forces with the variational principle.

So the discrepancy observed in the numerical examples between the electrostatic forces obtained from both approaches must come from the fact that when using the Maxwell stress tensor, one uses in practice (2.26) a surface integration over the edges describing the physical interface between the structural and electric domain only. Implicitly one thereby assumes that the edges that are fully embedded within the electric

domain and thus not bordering a structure due not contribute to the force on that interface, which seems to be consistent with the fact that physically speaking the Coulomb forces are originating from that interface only.

Considering the exact electromechanical problem in a continuum, it is indeed correct to state that on edges that are not electro-mechanical interfaces and thus fully in the electric domain, no electric forces will appear. This remains true after a finite discretization for edges inside the electric domain and connected to a non-corner mechanical interface only: the contribution of all the elements connected to that edge in the electric domain balances out. But when the edge inside the electric domain is connected to a structural corner, those edges also contribute to the electric force on the mechanical interface as illustrated in the previous simple example by equation (2.120).

Summarizing the discussion above, it can be concluded that it is fine to use the Maxwell stress tensor in a Finite Element model but it has either to be used as a volume force (equation (2.24)), or equivalently as surface stresses but then integrated over all edges of the electric elements bordering the mechanical interface as in (2.25). Integrating the contribution of the Maxwell stress tensor only over the mechanical interface edges can lead to a significant loss of accuracy in the vicinity of corners.

Note that this observation is in fact a more general issue discussed by several authors, for instance in the field of fluid structure interaction [46] or when computing stress intensity factors in solid mechanics [7, 8]. From those earlier works it is clear that evaluating interface forces by local integrals instead of considering the dual field associated to the weak formulation can lead to a loss of accuracy. In the discussion above the origin of this loss of accuracy for electrostatic coupling is pinpointed.

Three element model with full edge integrals

Below the equivalence between the two approaches for computing electrostatic forces by computing the forces using the full surface integral of the Maxwell tensor on the simple corner problem treated in section 2.4.3 is shown. In that section a discrepancy between the forces computed by the variational approach and the Maxwell stress tensor was found. But the Maxwell stress tensor was then only considered on the mechanical interface, namely on the conductor edges of element 2 and 3 (figure 2.20). Here also the contribution of elements 1, 2 and 3 to the horizontal forces through the edges in the electric field is computed.

The contribution of element 1 to the horizontal force on the corner node is obtained by computing the nodal forces originating from the Maxwell stress tensor on its right and bottom edge, namely

$$\begin{aligned}
 f_I^{1,x} &= \left[\int_{\text{edges on } I} \mathbf{T}^1 \mathbf{n} d\Gamma \right]_x \\
 &= \begin{bmatrix} 1 & 0 \end{bmatrix} \left[\int_{-0.5}^{0.5} \mathbf{T}^1 \begin{bmatrix} -1 \\ 0 \end{bmatrix} N_2(x=0.5) dy + \int_{-0.5}^{0.5} \mathbf{T}^1 \begin{bmatrix} 0 \\ 1 \end{bmatrix} N_2(y=-0.5) dx \right] \\
 &= \frac{\varepsilon}{8} + \frac{-\varepsilon}{3}, \tag{2.126}
 \end{aligned}$$

where x, y are the local element coordinates and the element field (2.117) was used to compute \mathbf{T} .

Similarly the complete contribution of elements 2 and 3 can be computed by adding to the forces already computed on the conductor surface in section 2.4.3 the contribu-

tions from the edges connected to the corner node:

$$\begin{aligned} f_I^{2,x} &= \begin{bmatrix} 1 & 0 \end{bmatrix} \left[\int_{-0.5}^{0.5} \mathbf{T}^2 \begin{bmatrix} 1 \\ 0 \end{bmatrix} N_1(x = -0.5) dy + \int_{-0.5}^{0.5} \mathbf{T}^2 \begin{bmatrix} 0 \\ 1 \end{bmatrix} N_1(y = -0.5) dx \right] \\ &= \frac{-\varepsilon}{4} + 0, \end{aligned} \quad (2.127)$$

$$\begin{aligned} f_I^{3,x} &= \begin{bmatrix} 1 & 0 \end{bmatrix} \left[\int_{-0.5}^{0.5} \mathbf{T}^3 \begin{bmatrix} -1 \\ 0 \end{bmatrix} N_3(x = 0.5) dy + \int_{-0.5}^{0.5} \mathbf{T}^3 \begin{bmatrix} 0 \\ -1 \end{bmatrix} N_3(y = 0.5) dx \right] \\ &= 0 + \frac{-\varepsilon}{4}. \end{aligned} \quad (2.128)$$

Clearly elements 1 and 2 contribute to the horizontal force. Summing up all the horizontal forces on the corner node I and the horizontal force (2.118) on the lower node of edge a provides the total force:

$$f_x = -0.9583\varepsilon, \quad (2.129)$$

which is equal to the value computed with the variational approach and very close to the analytical solution even for this coarse mesh.

Therefore it can be concluded that when corners form a significant part of the geometry, it is equivalent to use the variational form (2.113), the volume integral of the divergence of the Maxwell tensor (2.24) or the surface (edge) integral over all boundaries attached to a corner. But the commonly used approach (2.26), where the force is computed by considering the Maxwell stress tensor only on the electro-mechanical interface, can significantly underestimate the electrostatic forces at the corner.

2.4.4 Methods using special elements

In section 2.4.2 the principle of virtual work was used to overcome the inaccuracy of force computations using Lagrange type elements without extra consideration. Another approach could be to use different types of elements. Elements with derivative DOFS might prove more accurate, because they directly discretize the derivative of the potential, the electric field, as well. If those elements work the simple local force function (2.26) could be used to calculate the electric forces on the boundary. In [81] several of such elements were proposed to model singularities in electrostatic FEM.

Adini elements

One of the elements that could be used is the Adini element shown in figure 2.21. This element was originally developed to model plate bending, in which the spatial derivatives of the deformation characterize the solution. The element has at each node

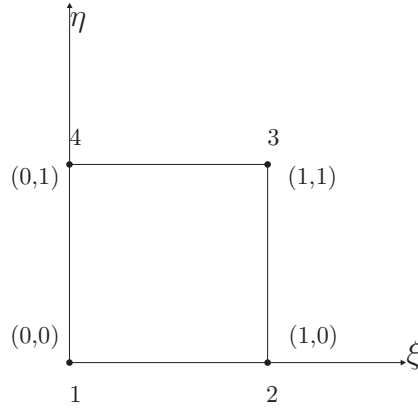


Figure 2.21: Adini square element.

3 DOFs: $\phi, \frac{\partial\phi}{\partial x}, \frac{\partial\phi}{\partial y}$. The shape functions for this elements are:

$$\begin{aligned}
 N_1 &= (1 - \xi)(1 - \eta)(1 + \xi + \eta - 2\xi^2 - 2\eta^2), \\
 N_2 &= (\xi)(1 - \eta)(3\xi + \eta - 2\xi^2 - 2\eta^2), \\
 N_3 &= (\xi)(\eta)(-1 + 3\xi + 3\eta - 2\xi^2 - 2\eta^2), \\
 N_4 &= (1 - \xi)(\eta)(\xi + 3\eta - 2\xi^2 - 2\eta^2), \\
 N_5 &= (1 - \eta)(\xi^3 - 2\xi^2 + \xi), \\
 N_6 &= (1 - \eta)(\xi^3 - \xi^2), \\
 N_7 &= \eta(\xi^3 - \xi^2), \\
 N_8 &= \eta(\xi^3 - 2\xi^2 + \xi), \\
 N_9 &= (1 - \xi)(\eta^3 - 2\eta^2 + \eta), \\
 N_{10} &= \xi(\eta^3 - 2\eta^2 + \eta), \\
 N_{11} &= \xi(\eta^3 - \eta^2), \\
 N_{12} &= (1 - \xi)(\eta^3 - \eta^2),
 \end{aligned} \tag{2.130}$$

here N_1 to N_4 are the shape functions for the ϕ values, N_5 to N_8 for the $\frac{\partial\phi}{\partial x}$ values and N_9 to N_{12} for the $\frac{\partial\phi}{\partial y}$ values. To illustrate the behavior of these shape functions, they are shown in figure 2.22. Note the similarity with beam elements.

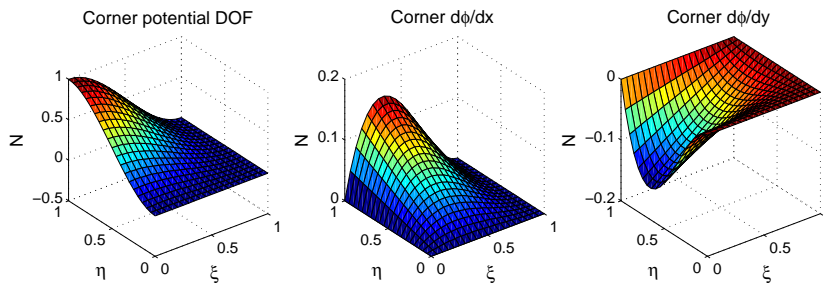


Figure 2.22: Adini shape functions for node 4.

When these elements are used it is not only important to define the appropriate constraints for the potential, but also for the derivatives. For instance the tangent derivatives at the $Q = 0$ boundaries have to be zero.

Uncoupled Adini

Analytically the electric field near a singular point behaves somewhat like Green's function. This can be explained by the charge concentration at the corner, which behaves like a point charge. And e.g. in [48] it is shown that the electric field near a point charge can be described by a Green's function. Furthermore one can say that the potential field at a point charge can be described by a continuous function and the electric field by a discontinuous function.

In [81] it is shown that near a singular point Adini elements smoothen the solution too much and prove to perform even worse than Lagrangian elements. Therefore the uncoupling of the derivatives near the singular point was proposed. Basically this uncoupling of the DOFS means that two extra DOFS are created as shown in figure 2.23. The derivative DOF E_x at node P is split into E_{+x} and E_{-x} and the same is done to DOF E_y . Next DOF E_{-x} is only assembled into elements 1 and 3 and E_{+x} is only assembled into element 2. Similarly E_{+y} is assembled into elements 1 and 2 and E_{-y} into element 3. However, the potential DOF at node P is assembled into all three elements. Effectively this creates a continuous potential, but a discontinuous electric field at point P .

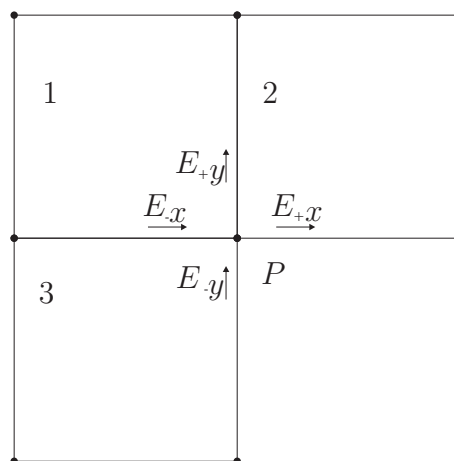


Figure 2.23: Uncoupled Adini elements.

Incomplete biquadratic element

Although the uncoupled Adini element is the best performing element treated by [81], it is rather complicated to use, because at specific points these DOFs have to be uncoupled. For a simple model such as the reference problem, this is still doable, but when more realistic models have to be solved, this can become a very time consuming task. Therefore an element was considered that has the same number of DOFs as the Adini element, but has only derivative DOFs at its midpoint nodes. This element, known as the incomplete biquadratic element (IBQ), is shown in figure 2.24.

At nodes 1,2,3 and 4 it has only potential a DOF and at nodes 5,6,7 and 8 it has a potential DOF and a derivative DOF, which is equal to the derivative in the direction normal to the edge. Since there is no constraint on the derivative value at the corner node, the solution should not be smoothed too much.

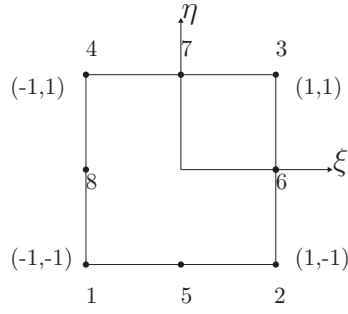


Figure 2.24: Incomplete biquadratic element.

The shape functions for this element are listed below:

$$\begin{aligned}
 N_1 &= \frac{1}{4}(1-\xi)(1-\eta)(-1-1\xi-1\eta) + \frac{1}{4}(1-\xi^2)(1-\eta^2)(\xi^2+\eta^2), \\
 N_2 &= \frac{1}{4}(1+\xi)(1-\eta)(-1+1\xi-1\eta) + \frac{1}{4}(1-\xi^2)(1-\eta^2)(\xi^2+\eta^2), \\
 N_3 &= \frac{1}{4}(1+\xi)(1+\eta)(-1+1\xi+1\eta) + \frac{1}{4}(1-\xi^2)(1-\eta^2)(\xi^2+\eta^2), \\
 N_4 &= \frac{1}{4}(1-\xi)(1+\eta)(-1-1\xi+1\eta) + \frac{1}{4}(1-\xi^2)(1-\eta^2)(\xi^2+\eta^2), \\
 N_5 &= \frac{1}{2}(1-\xi^2)(1-\eta) - \frac{1}{4}(1-\xi^2)(1-\eta^2)(2\xi^2+\eta), \\
 N_6 &= \frac{1}{2}(1-\eta^2)(1+\xi) - \frac{1}{4}(1-\xi^2)(1-\eta^2)(2\eta^2-\xi), \\
 N_7 &= \frac{1}{2}(1-\xi^2)(1+\eta) - \frac{1}{4}(1-\xi^2)(1-\eta^2)(2\xi^2-\eta), \\
 N_8 &= \frac{1}{2}(1-\eta^2)(1-\xi) - \frac{1}{4}(1-\xi^2)(1-\eta^2)(2\eta^2+\xi), \\
 N_9 &= -\frac{1}{4}(1-\xi^2)(1-\eta^2)(\eta^2-\eta), \\
 N_{10} &= -\frac{1}{4}(1-\xi^2)(1-\eta^2)(\xi^2+\xi), \\
 N_{11} &= -\frac{1}{4}(1-\xi^2)(1-\eta^2)(\eta^2+\eta), \\
 N_{12} &= -\frac{1}{4}(1-\xi^2)(1-\eta^2)(\xi^2-\xi).
 \end{aligned} \tag{2.131}$$

To illustrate the behavior of these shape functions, they are shown in figure 2.25. Just as with the Adini elements, one should take care when applying imposed boundary constraints.

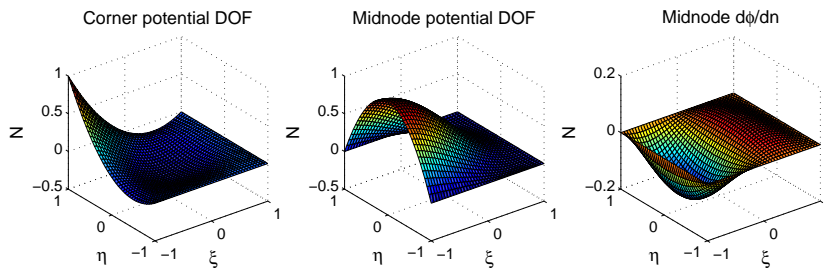


Figure 2.25: IBQ shape functions.

Singular elements compatible with bilinear elements

Another type of elements for singularities was proposed by Akin [3]. They were developed for simulating crack tips and were applied on electrostatics by [121]. The basic assumption for the element is that the potential varies radially according to the relation

$$\phi \approx cr^{(\pi/\theta)}, \tag{2.132}$$

if the radius r is small enough. Here $\theta > \pi$ is the angle of the corner, where that angle is measured through the dielectric part of the problem. The constant c is a proportionality constant. The derivation of this potential distribution can be found in section 2.3.4. The electric field corresponding with this potential field is:

$$E_r = -\frac{\partial\phi}{\partial r} = -\frac{\pi}{\theta}cr^{(\pi/\theta-1)}. \quad (2.133)$$

The shape functions P derived for this behavior are (k denotes the singular node) :

$$\begin{aligned} P_i &= \frac{N_i}{(1 - N_k)^p}, \quad i \neq k, \\ P_k &= 1 - (1 - N_k)^{1-p}, \end{aligned} \quad (2.134)$$

where N_i is an usual bilinear shape function. The parameter p defines the asymptotic behavior of the singularity and has to equal $p = 1 - \pi/\theta$ for all the elements connected to a singular node.

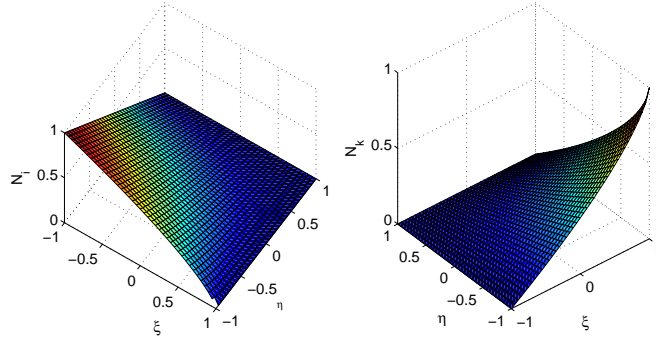


Figure 2.26: 'Akin' shape functions.

This value for p can be derived by assuming polar coordinates ρ and φ departing from an origin at point k . The normal shape function N_k can then be polynomially expanded in these coordinates (neglecting higher order terms and variation with respect to φ):

$$N_k = 1 + a_1\rho + \dots, \quad (2.135)$$

therefore:

$$P_k = 1 - (1 - 1 - a_1\rho + \dots)^{1-p} = 1 - (-a_1)^{1-p}\rho^{1-p} + \dots, \quad (2.136)$$

which can be differentiated with respect to ρ :

$$\frac{\partial P_k}{\partial \rho} = -(-a_1)^{1-p}\rho^{-p}, \quad (2.137)$$

which will only have the same asymptotic behavior as equation (2.133) if $p = 1 - \pi/\theta$.

The shape functions for an element connected to a $\theta = 3\pi/2$ corner are shown in figure 2.26. On the left a non-corner node is shown, the function looks much like a traditional bilinear shape function. On the right a singular node is shown, which clearly has an infinite derivative at the singular point.

One disadvantage of this method is that the elements and singular nodes have to be defined for each individual corner, which probably is the reason that the method has not yet been implemented in commercial codes.

A restriction on the element is that the correct asymptotic behavior can only be guaranteed if the non-corner shape function can be expanded as in equation (2.135), therefore the element only works with geometric mappings characterized by a constant Jacobian, thus (bi)linear mappings.

Comparison

In the report and article [82, 81] it is concluded that the uncoupled Adini element and the IBQ element perform optimal, but the IBQ-element is easier to use. However the selection criteria have all been potential values or undefined⁵ electric field values. Furthermore the results are not compared with standard Lagrange type elements or the ‘Akin’ elements. Hence it is not known how well they work.

It is difficult to combine the special elements with infinite elements. Therefore the reference problem is changed to the configuration in figure 2.27. However the analytical solution shown in figure 2.5 suggest that the Neumann conditions ($\partial\phi/\partial n = 0$) at the $Q = 0$ boundaries are correct enough to compare the numerical results with the analytical solution. Moreover when solutions obtained with standard Lagrange elements are compared, one can conclude that electrostatic forces change only at the fourth digit when infinite elements are added.

The problem was modeled with several meshes and the results were compared with the results from section 2.4.2 and shown in figure 2.28.

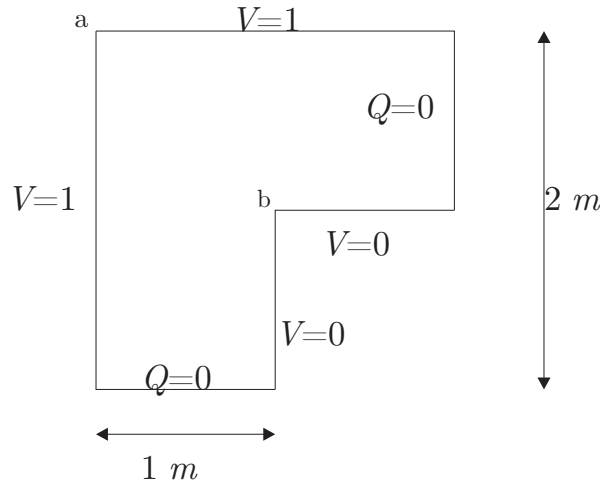


Figure 2.27: Reference problem.

To explain the different convergence curve of the solution obtained with the ‘Akin’ or singular bilinear elements, the potential on the cross section $a - b$ as defined in figure 2.27 has been plotted in figure 2.29. Here the parameter r is the distance from the singularity at point b . The number of elements used for this cross section is 2 per meter. It is clear that solution is closer to the real one than the solution of normal bilinear elements, but the derivative is larger near the singularity than the analytical one. The

⁵It is not clear from the report or the article how and where these electric field values were defined.

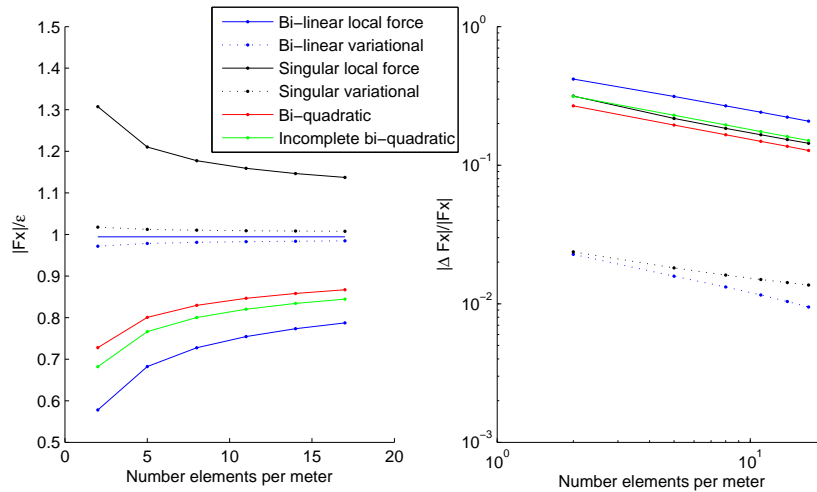


Figure 2.28: Force convergence ratios for different types of elements.

standard linear element underestimates this derivative. This can be explained by the fact that the element assumes a certain behavior of the field within the element. That assumption that is only valid in the neighborhood of the singularity. Therefore, if the element is large, this assumption overestimates the effect of the singularity on the field far from the corner.

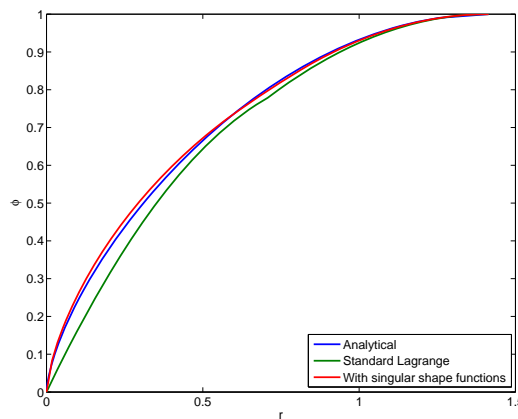


Figure 2.29: Potential through section $a - b$, computed with 2 elements per meter.

To explain why the IBQ element provides worse results than ordinary quadratic ones for the reference problem, the electric field through cross section $a-b$ has been calculated with IBQ and quadratic Lagrange elements. In figure 2.30 it can be seen that with quadratic shape functions the element next to a singularity shows a wiggle in the derivative. The bad thing about IBQ elements is that the bubble function, which is needed in the element to incorporate the derivatives, enhances this wiggle.

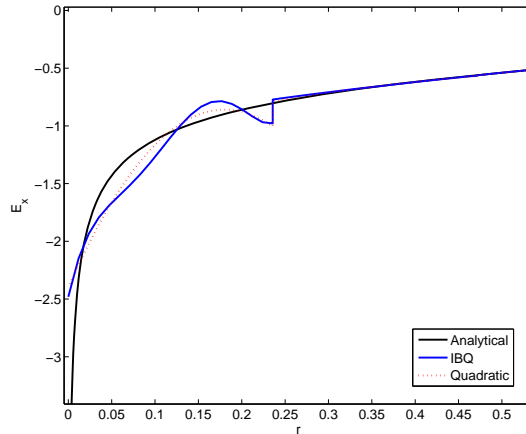


Figure 2.30: Electric field through section $a-b$, computed with 6 elements per meter.

2.5 Finite Element Method in 3D

Until now all modeling has been in two dimensions only. However it would be interesting to see how the numerical approaches hold in three dimensions, because in that case there are more types of singularities. Not only the 2D corner, which is in 3D an edge, yields a singularity, but also the 3D corner, where 2 or more edges join. In this report the chosen 3D corner is the type of 3D corner that can be found on a cube.

The mesh is build up from hexahedral elements, which can be mapped onto cubes with an isoparametric mapping. In the end the same type of matrix vector equation as in 2D is found (see appendix A.1.2).

2.5.1 Reference problem

The reference problem is shown in figure 2.31. Only the air part of the problem is shown from two different viewpoints. The corner of a conductor causes a bite out of the cubic air region. Surfaces A , B and C define the surface of the conductor and are during modeling assumed to be grounded. The surfaces on the opposite of the gap, D , E and F are fixed at 1 volt. In this problem the three edges between surfaces A , B and C will show an edge singularity and the corner k will create a corner singularity.

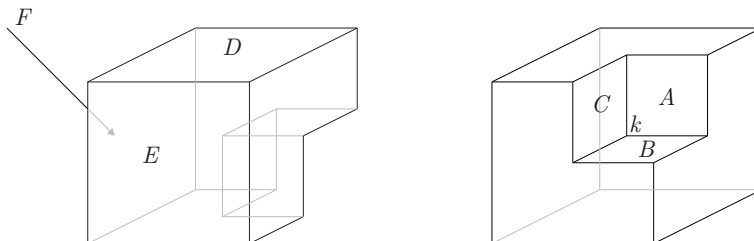


Figure 2.31: The 3D reference problem seen from two different angles.

2.5.2 Reference solution

An analytical solution for this 3D problem does not exist. However a very good approximation can be made by applying the principle of virtual work on a very dense mesh. In stead of a regular mesh of cubes, a locally refined very dense mesh of tetrahedral elements was used to compute the reference solution. A picture of the converged mesh is shown in figure 2.32. For comparison a typical mesh of cubes that will be used below to compare different approaches is shown in figure 2.33. The fully converged solution for the reference problem is $|F/\varepsilon_0| = 1.76$.

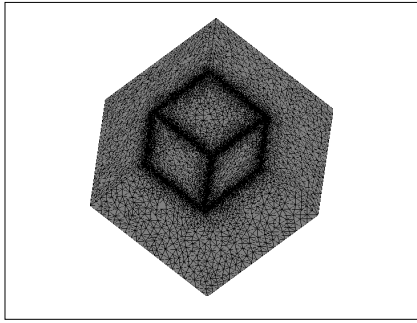


Figure 2.32: The tetrahedral mesh used to compute the reference solution.

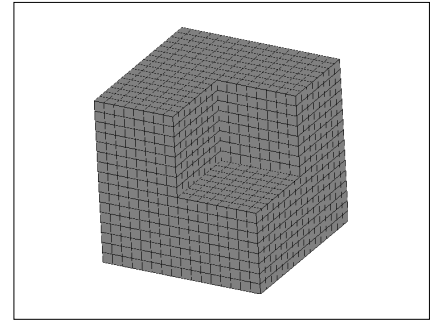


Figure 2.33: A typical cubical mesh used to compare the approaches (8 elements per meter).

2.5.3 Force discretization

In section 2.4.2 two different approaches to discretize the force in 2D were discussed: the variational approach and the local force approach. Both approaches can also be used in 3D. The resulting forces on surface A , in the direction perpendicular to that surface, are shown in figure 2.34. It can be seen that the variational approach converges quite fast towards the reference solution, but the local force approach seems to have the same difficulty as in 2D.

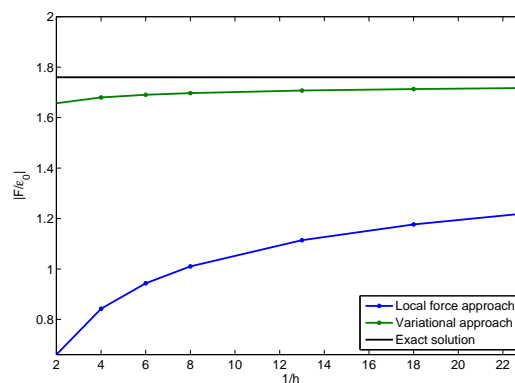


Figure 2.34: Convergence curves for the 3D model.

2.5.4 Extension of the *Akin* element to 3D

In the section on 2D FEM modeling it was concluded that the only type of shape function modifications that really improved the solution were the *Akin* or singular bilinear elements. Therefore these elements will be expanded to the 3D case. However, this is not a trivial problem, because as mentioned before in 3D there exist two types of singularity: edges and corners.

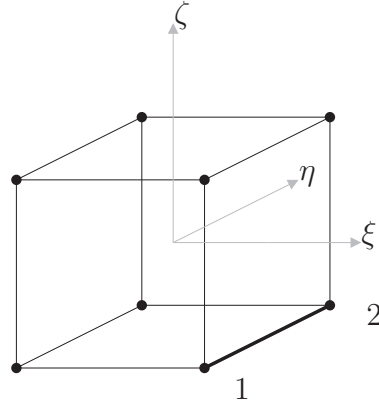


Figure 2.35: A 3D hexahedral element with singular edge in natural coordinates.

The edge singularity can be tackled with relative ease. All elements connected to a simple edge look like the element in figure 2.35, where the thick edge, connected to nodes 1 and 2, indicates the singular edge. This problem is very similar to the 2D corner, because the singularity only acts in the ξ and ζ direction and not in the η direction. Therefore the same order of singularity can be applied, using the following procedure:

$$N_i(\xi, \eta, \zeta) = L_i(\xi)L_i(\eta)L_i(\zeta), \quad (2.138)$$

where the $L_i(x) = \frac{1}{2}(\pm x + x_i)$ indicate the classic 1 dimensional shape functions. Since there is no singularity in the η direction, it can be left unmodified, but the other two will have to be modified. Because nodes 1 and 2 are on the same edge that is parallel to to the η -axis, there dependency on ξ and ζ is equivalent. Therefore the following relation holds:

$$L_1(\xi)L_1(\zeta) = L_2(\xi)L_2(\zeta), \quad (2.139)$$

which can be used to define the augmented basis functions D_i as follows:

$$D_i = \frac{L_i(\xi)L_i(\zeta)}{(1-L_1(\xi)L_1(\zeta))^p}, \quad i \neq 1, 2 \quad (2.140)$$

$$D_k = 1 - (1 - L_k(\xi)L_k(\zeta))^{(1-p)}, \quad k = 1, 2,$$

where just as in the 2D case $p = 1/3$ for an edge with a $(3/2)\pi$ angle. The total set of modified shape functions for the edge singular element becomes:

$$P_i(\xi, \eta, \zeta) = L_i(\eta)D_i(\xi, \zeta). \quad (2.141)$$

Results on very simple 3D geometries without corners, but with edges, show that these elements provide the desired improved convergence.

For elements with not only an edge but also a corner singularity, the following approach is used. The field within the element is modified as if the edge only node creates a corner singularity:

$$\begin{aligned} P_i &= \frac{N_i}{(1-N_k)^p}, & i \neq k, \\ P_k &= 1 - (1 - N_k)^p, \end{aligned} \quad (2.142)$$

with $p = 1/3$. This approach is repeated for all the 'edge only' nodes, to insure continuity between this element and edge elements to which it is connected.

Next the same procedure is done for the corner node with $p = 0.5475$. The order of the 3D corner singularity is extracted from [96], where the order of singularity for a 3D corner is used to improve solutions obtained with the boundary element method. Hence essentially for the element the field is assumed to be a superposition of the singular effects of the real 3D corner and the edge only node that is seen as a corner.

The results for the reference problem obtained using this approach are shown in figure 2.36, where it can be seen that results improve a lot compared to the local force only solution. The solution does not converge directly from above as in the 2D case, but diverges from the reference solution before it converges again. This can be explained by the fact that the used order of singularity is relatively low, simulations with arbitrarily chosen higher orders of singularity do show a direct convergence from above.

Another problem with the singular elements is the numerical integration of the element matrices and forces. With these high orders of singularity the integrals become difficult, explaining some of the poor performance.

It is clear though that all approaches do have problems. Because both the variational solution (standard and Akin type) have not yet fully converged and are still slightly increasing before the limits of the 2GB RAM are encountered⁶. The local force solution, without singular elements is not even near convergence and the singular bilinear enhanced local force approach is not yet completely converged either. For low mesh densities the bilinear enhanced variational approach performs poorer than the standard variational approach, however for denser meshes the bilinear enhanced ones starts to outperform the variational one.

2.6 Conclusions

This chapter introduced electrostatic modeling. Thereafter analytical solutions were derived for several geometries, that would later be used in the FEM discussion. Next the FEM modeling of electrostatics was introduced, including the difficulties that singularities provide for FEM computations of electrostatic forces.

There are some approaches available to tackle the corner singularities. The first one based on the method of force discretization, where a variational force formulation is used in stead of the local interface force based on the Maxwell stress tensor. The second approach is to use special singular elements. In 2D three such special elements were tested:

- Uncoupled Adini elements,

⁶The memory limit is only reached when exact solvers are used. For the reference solution with many more degrees of freedom an iterative solver was used.

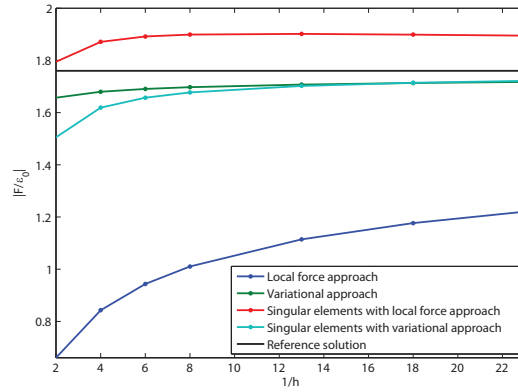


Figure 2.36: Convergence curves for the 3D model.

- Incomplete Bi-Quadratic elements,
- Akin elements.

Of these methods was the only viable one: the ‘Akin’ approach. However the variational approach was better than all singularity tailored approaches. Of course the two methods, variational forces and special elements, can be combined. A combination of this variational approach with the Akin shape functions proved to be the optimal strategy, however the difference with the variational only approach is limited. Furthermore the application of special elements requires a sophisticated corner detection algorithm. Therefore their usage is difficult for industrial problems.

The difference between the local force approach as used by many commercial codes and the variational force formulation was investigated more thoroughly. It was found that, although the local force approach might be based on the Maxwell stress tensor, it is not a proper discretization of that stress tensor. Some crucial information is omitted by neglecting the integrals over element edges that are not part of the solid–dielectric interface. When this information is re-inserted into the local force approach, the Maxwell stress tensor is properly discretized. As expected, in that case the Maxwell stress tensor approach is equivalent to the variational approach and the computed forces are equal.

This chapter also developed a novel 3D version of the 2D Akin element tailored for electrostatic singularities. This element was better than classical FEM, however was outperformed by the variational formulation. Therefore in general, due to the simplicity of the implementation and high accuracy of the results, the variational formulation is the best approach and should be used.

Chapter 3

Electro-mechanical modeling

3.1 Introduction

The basic physical principle of electromechanically actuated microsystems is illustrated in fig. 3.1. Once a potential difference between a moving (or deformable) electrode and a fixed electrode is applied a charge difference is created. Coulomb forces between the charges will make the flexible electrode deform. This effect depends non-linearly on the shape of the electrode and the deformation itself, because the charge will concentrate near the point where the gap between the electrodes is smallest, which causes even higher Coulomb forces at that point [4].

Because the focus of this thesis is on physical level models, continuum equations are required. This chapter first presents those continuum equations, which describe the coupling. Next the numerical form of the equations will be presented in section 3.4, including a discussion on the approaches available to derive them. Section 3.5 continues with solution techniques that can be used to solve the discretized equations. Finally in section 3.6 the implementation of the problem into a specific discretization procedure, the finite element code, is presented.

3.2 Continuum formulation of electro-mechanical coupling

A coupled electro-mechanical model normally consists of two domains: a structural domain and an electrical domain. The structural domain contains all moving electrodes. The electric domain in principle contains the whole model, but if it is assumed

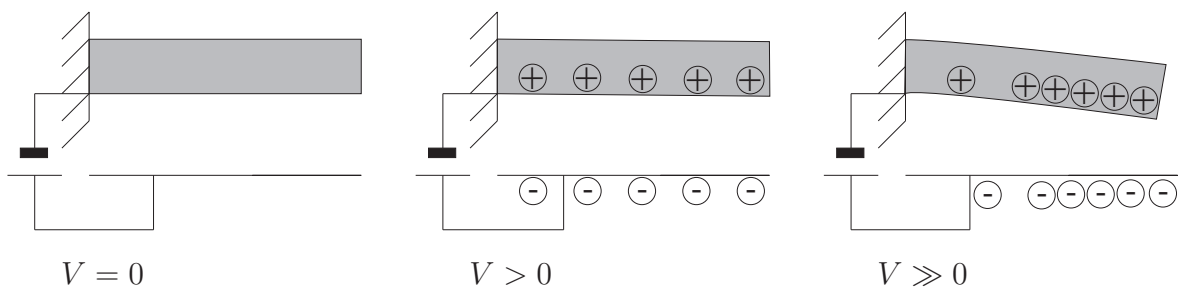


Figure 3.1: Electromechanical coupling

that the electrodes are ideal conductors the electrostatic equation has to be solved only in the domain between the conductors. In that case the applied potentials on the electrodes can be modeled as fixed potential boundary conditions (Dirichlet boundary conditions).

Once the ideal conductor assumption has been made and it is also assumed that there are no free charges in the electric domain the equation that describes the electrostatics in the air gap is the electrostatic equation as seen in chapter 2 [48, 66]:

$$\frac{\partial}{\partial x_i} \left(\varepsilon \frac{\partial \phi}{\partial x_i} \right) = 0, \quad (3.1)$$

where ε is the electric permittivity in the gap and $\phi = \phi(x, y, z)$ is the electric potential. Einstein's summation convention was used for $i = x, y, z$.

The static mechanical equilibrium equations, when assuming small deformations, can be written as [44]:

$$\frac{\partial}{\partial x_i} \sigma_{ji} + F_j = 0, \quad (3.2)$$

where $\boldsymbol{\sigma}$ is the mechanical stress tensor and \mathbf{F} is the external force field which incorporates all applied forces. For simplicity it is assumed that the only applied forces are the Coulomb forces due to the electrostatic field. When there are no moments proportional to a volume, which is the case for most solid materials the stress tensor is symmetric:

$$\sigma_{ij} = \sigma_{ji}. \quad (3.3)$$

Equation (3.2) is the quasi-static mechanical equilibrium equation. If the purpose of the modeling requires the inclusion of dynamics the inertia terms can be added [45]:

$$-\rho \ddot{u}_j + \frac{\partial}{\partial x_i} \sigma_{ji} + F_j = 0, \quad (3.4)$$

where ρ is the density of the solid part.

To compute the displacement caused by an applied load a relation between stress $\boldsymbol{\sigma}$ and displacement \mathbf{u} is required. This is done in two steps. First the strain tensor $\boldsymbol{\epsilon}$ is determined as a function of \mathbf{u} and then the stress as a function of the strain. These relations are in principle non-linear but once it is assumed that the stresses and strains remain relatively small the relations can be assumed to be linear¹, which yields the linear relations:

$$\sigma_{ij} = C_{ijkl} \epsilon_{kl}, \quad (3.5)$$

$$\epsilon_{ij} = \frac{1}{2} \left(\frac{\partial u_j}{\partial x_i} + \frac{\partial u_i}{\partial x_j} \right), \quad (3.6)$$

where \mathbf{C} is Hooke's tensor which has constant coefficients.

Thus the electric problem is linear and the mechanical problem is assumed to be linear, however the coupled problem is non-linear. The non-linearity stems on one hand from the fact that the electrostatic domain is defined by the deformed position of the electrodes, and on the other hand from the fact that the electrostatic forces depend on

¹Note that when modeling thin MEMS the non-linear mechanical equations need to be considered. For simplicity linear mechanics is assumed but all the concepts discussed in this text can be extended to non-linear mechanics.

the accumulated charges on the surfaces of the electrodes. There the distributed force follows from coulombs law (see section 2.2.2):

$$F_j = qE_j , \quad (3.7)$$

where q is the distributed charge on the surface and \mathbf{E} is the electric field generated by the other electrode. In the vicinity of charges on the surface of a conductor one has to note that half of the electric field is generated by those charges themselves and does therefore not contribute to the force. Hence, if \mathbf{E} is the total electric field in the domain one must use $F_j = q(E_j/2)$ (see section 2.2.2).

According to Gauss' law the surface charge q on a conductor can be written as a function of the electric field at the boundary and the unit normal vector \mathbf{n} pointing towards the electric domain:

$$q = \varepsilon E_i n_i . \quad (3.8)$$

The electric potential is defined such that the electric field is (minus) the gradient of an electric potential ϕ , therefore the force can be defined as a function of this potential (see section 2.2.2):

$$F_j = \frac{1}{2}\varepsilon \left(\frac{\partial \phi}{\partial x_i} \frac{\partial \phi}{\partial x_i} \right) n_j \quad (3.9)$$

where it has to be noted that this force is always pointing into the electric domain. It is stressed that the non-linear coupling is caused by the non-linear dependency of \mathbf{F} on ϕ and by the dependency of the shape of the electric domain on the structural displacements. Thus even with a linear mechanical model, electro-mechanical modeling requires a non-linear model.

3.3 A 1 dimensional example

The consequences of this non-linear relation between structural displacements and electrostatic forces can be explained best by a simple one-dimensional model. Such a 1D model shows already some of the complicated non-linear behavior of the FEM models that are addressed in the later parts of this thesis.

Figure 3.2 gives such a very simple model of a micro actuator. In an air gap, the electrostatic problem is described by Laplace's equation, which reduces to the following equation in 1D:

$$\varepsilon \frac{\partial^2 \phi}{\partial \xi^2} = 0 , \quad (3.10)$$

where ϕ is the electrostatic potential, ξ is the spatial coordinate and ε the electric permittivity. The domain on which this differential equation has to be solved is $\xi = [0, x]$, x describing the position of the moving electrode. The boundary conditions are: $\phi = V$ at $\xi = x$ and $\phi = 0$ at $\xi = 0$. The simple solution to this boundary value problem is:

$$\phi = \frac{V}{x} \xi . \quad (3.11)$$

The electric field is then by definition:

$$E = -\frac{\partial \phi}{\partial \xi} = -\frac{V}{x} , \quad (3.12)$$

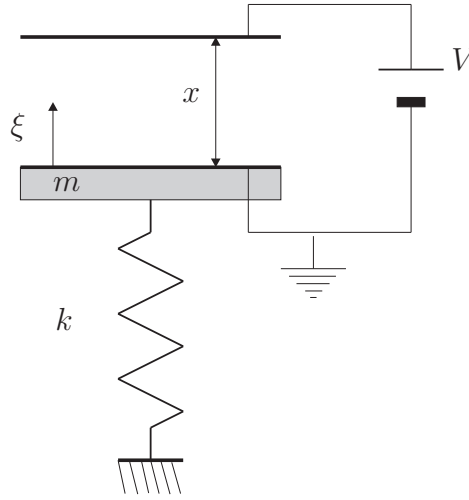


Figure 3.2: 1D micro resonator

and the electrostatic force on the mass is:

$$F_{es} = \frac{1}{2} \varepsilon E^2 = \frac{1}{2} \varepsilon \frac{V^2}{x^2} . \quad (3.13)$$

The mechanical force applied on the electrode by the spring is

$$F_{mech} = k(x - x_0) , \quad (3.14)$$

with k the linear stiffness of the spring and x_0 the position of the spring when it is at its natural length.

3.3.1 Static equilibrium and pull-in

The static equilibrium equation is found by summing all applied forces:

$$k(x - x_0) + \frac{1}{2} \varepsilon \frac{V^2}{x^2} = 0 . \quad (3.15)$$

Clearly to a given applied potential V corresponds an equilibrium position x and vice-versa, hence this equation defines a relation $V(x)$. Furthermore it can be shown that there exists a voltage and corresponding displacement for which $\frac{\partial V}{\partial x} = 0$, thus for which the voltage as function of displacement reaches a maximum. This maximum voltage equals: $V_{PI} = \sqrt{\frac{8kx_0^3}{27\varepsilon}}$ and the corresponding gap size is: $x_{PI} = \frac{2}{3}x_0$. Using this maximum voltage to normalize equation (3.15) it can be written as:

$$\left(\frac{V}{V_{PI}} \right)^2 = \frac{27}{4} \left(\frac{x_0 - x}{x_0} \right) \left[\left(\frac{x_0 - x}{x_0} \right) - 1 \right]^2 . \quad (3.16)$$

The curve $V(x)$ defined by this equation is shown in figure 3.3.

Due to the non-linearity of this equation, there are two solutions for each applied voltage V . For the two solutions it can be shown that the solution closest to the bottom conductor is unstable: at this position a small perturbation of the moving electrode will make it either return to the equilibrium position close to the undeformed position

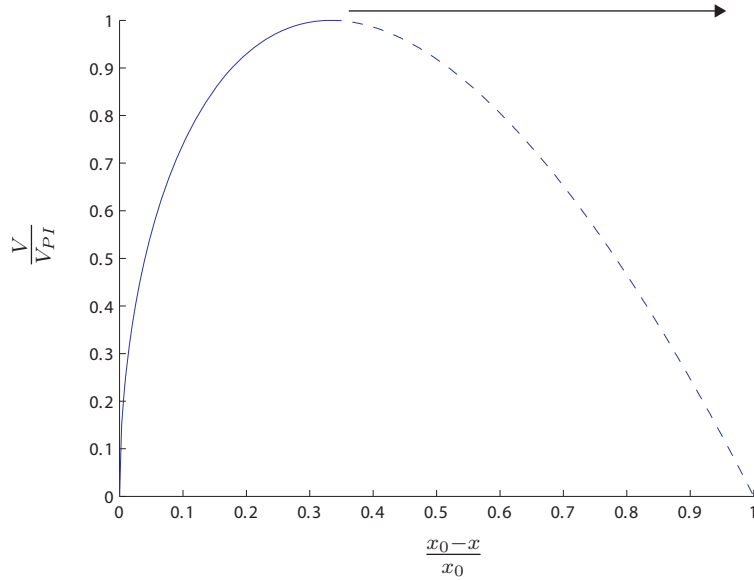


Figure 3.3: 1D voltage-displacement curve

or smash against the fixed electrode (the electrodes are pulled together). The other solution is stable and can be used to perform a linearized vibration analysis. There exists a voltage above which there exist no more static solutions, this voltage (equal to the maximum V_{PI} mentioned above) is called the *pull-in voltage* and is located at the maximum of the curve. The solid part of the curve in figure 3.3 gives the stable solutions, the dashed part the unstable solutions. The pull-in voltage depends on stiffness as well as on the initial gap, however the pull-in gap only depends on the initial gap. Of course this is only valid for a 1D model, but it is interesting to see that for linear mechanical MEMS with very complex shapes the pull-in gap is often very close to two thirds of the original gap.

The result in figure 3.3 also provides an indication of the real behavior of electrostatic microsystems. As mentioned the pull-in voltage is the maximum of the curve. This means that when a voltage above this pull-in voltage is applied to the system, the moving electrode will snap to the fixed electrode and they will stick together, possibly short-circuiting the device. This is indicated by the arrow in figure 3.3. Since this pull-in phenomenon is a very critical mode of operation, an important goal of MEMS modeling is the prediction of reliable pull-in voltages and displacements [24, 33].

An important characteristic of pull-in is its similarity to limit point buckling. Limit point buckling is defined by a maximum point of the applied force in the force-displacement relationship for a non-linear mechanical problem [21, 127]. A simple version of limit point buckling is presented in figure 3.4. At this buckling point the derivative of the applied load with the generalized coordinate is zero:

$$\frac{\partial P}{\partial \alpha} = 0, \quad (3.17)$$

which is very similar to the definition of the pull-in point:

$$\frac{\partial V}{\partial x} = 0. \quad (3.18)$$

There exist many numerical techniques designed to handle the specific problems of limit

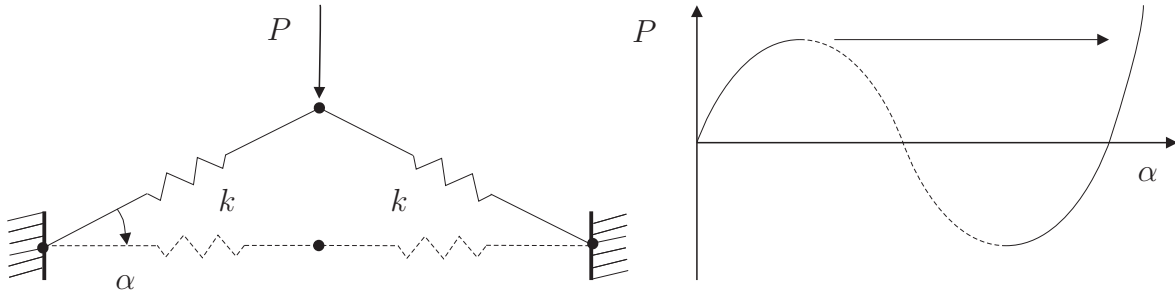


Figure 3.4: Limit point buckling of a two spring model actuated by force P [127]

point buckling. Several of those techniques can be adapted for pull-in computations as explained in the following chapters.

3.3.2 Dynamic response

If dynamics is included, equation (3.15) is extended to:

$$m\ddot{x} + k(x - x_0) + \frac{1}{2}\varepsilon\frac{V^2}{x^2} = 0, \quad (3.19)$$

where m is the mass of the moving part. This equation can be used to see a lot of the typical features of MEMS-motion. A relatively complete analysis of the equation, including dynamic pull-in and the proof that the dashed part of figure 3.3 is unstable can be found in chapter three of [106] and a part of that work is used as an inspiration for this section.

Eigenfrequencies

Equation (3.19) is highly non-linear, therefore no closed form solutions exist. However, it is possible to use numerical time integration algorithms to find the motion when the initial conditions are known. Another approach is keep V constant and to linearize the equation around a constant equilibrium solution $x = x_{eq} + \Delta x$, where x_{eq} is a solution to the static equation (3.15):

$$m\ddot{x}_{eq} + m\Delta\ddot{x} + k(x_{eq} + \Delta x - x_0) + \frac{1}{2}\varepsilon\frac{V^2}{(x_{eq} + \Delta x)^2} = 0, \quad (3.20)$$

where $m\ddot{x}_{eq} = 0$, because x_{eq} is constant. If the electrostatic term is approximated by a Taylor series expansion the equation becomes:

$$m\Delta\ddot{x} + k\Delta x + k(x_{eq} - x_0) + \frac{1}{2}\varepsilon\frac{V^2}{x_{eq}^2} - \varepsilon\frac{V^2}{x_{eq}^3}\Delta x + \text{h.o.t.} = 0. \quad (3.21)$$

Using the fact that x_{eq} is a solution of (3.15) and neglecting the higher order terms gives:

$$m\Delta\ddot{x} + \left(k - \varepsilon\frac{V^2}{x_{eq}^3}\right)\Delta x = 0, \quad (3.22)$$

which is an ordinary second order differential equation, that is common in structural mechanics [45]. From this equation follows that the eigenfrequency of the system is:

$$\omega = \sqrt{\frac{k}{m} - \varepsilon\frac{V^2}{m x_{eq}^3}}. \quad (3.23)$$

From that definition can be deduced that the eigenfrequency depends on the applied potential V . It becomes lower with increasing potential, giving rise to the creation of tunable MEMS resonators [74, 2, 30]. One of the earliest applications of electromechanical MEMS is such a microresonator [125]. Its advantage over classical quartz resonators is that the eigenfrequency can be changed by a bias potential.

Furthermore it should be noted that if $V = V_{PI}$ and $x_{eq} = x_{PI}$ the eigenfrequency is zero. If $V < V_{PI}$ and x_{eq} is on the stable part of the curve of figure 3.3, ω is real, but if x_{eq} is on the unstable part of the curve ω is imaginary, indicating instability.

This can be shown graphically by normalizing equation (3.23) by dividing it with the purely mechanical eigenfrequency $\omega_0 = \sqrt{k/m}$ and using equation (3.15) to remove the potential V from the equation:

$$\frac{\omega}{\omega_0} = \sqrt{3 - 2 \left[1 - \left(\frac{x_0 - x}{x_0} \right) \right]^{-1}}, \quad (3.24)$$

which gives the normalized frequency as a function of the normalized displacement. This relation is plotted in figure 3.5. The normalized displacement is a function of the normalized potential trough (3.15), providing the curve in figure (3.6). These two curves show perfectly that the eigenfrequency is tunable and becomes zero at pull-in.

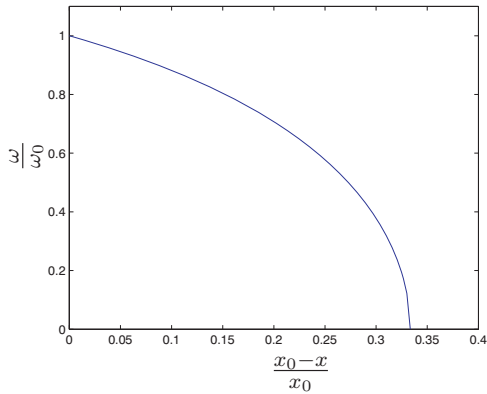


Figure 3.5: Frequency vs. normalized displacement.

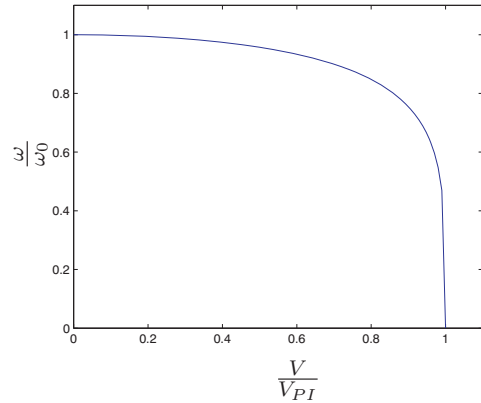


Figure 3.6: Frequency vs. normalized potential.

Transient response and dynamic pull-in

Another interesting response of the model is the transient response to a voltage step. This is one of the most critical methods of applying a certain voltage to the device, because steps can generate a large overshoots. For a voltage step from 0 to V_D the equations required to solve are:

$$\begin{cases} m\ddot{x} = -k(x - x_0) - \frac{1}{2}\varepsilon\frac{V_D^2}{x^2}, & t > 0, \\ x = 0, & t = 0, \\ \dot{x} = 0, & t = 0, \\ \ddot{x} = 0, & t = 0. \end{cases} \quad (3.25)$$

These equations do not have a closed form solution, but a typical time integration algorithm such as the fourth order Runge–Kutta algorithm can be used to solve the equations.

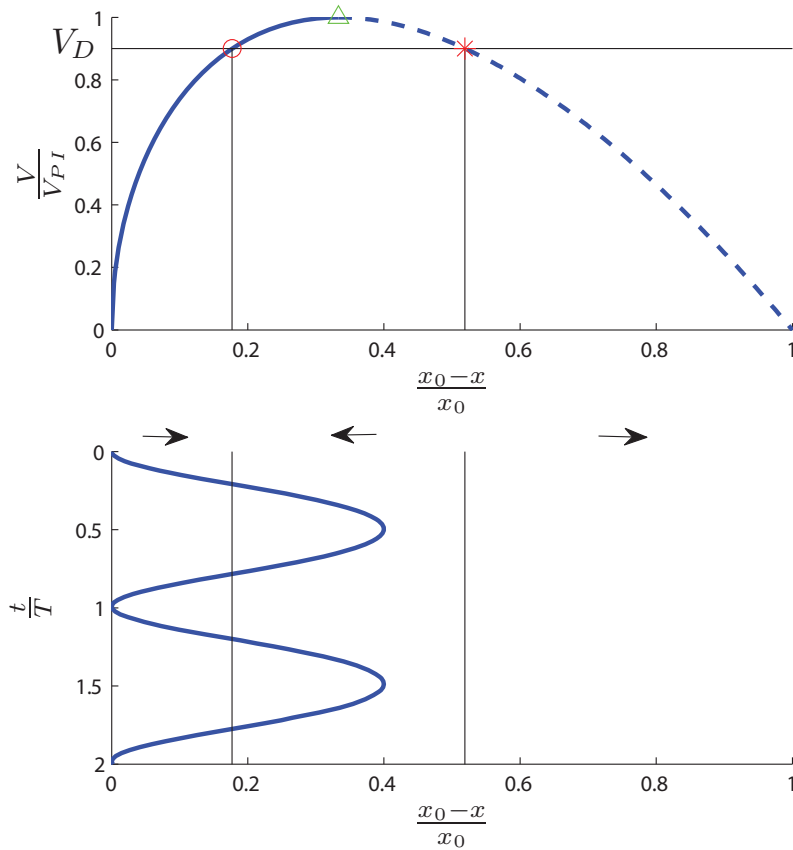


Figure 3.7: A voltage step: on the top the static pull-in curve, on the bottom the transient for a load step of V_D .

If V_D is relatively low, such a voltage step will give a periodic solution, because there is no damping in the model. The amplitude of this periodic solution depends on the applied voltage, mechanical stiffness, electric permittivity and initial gap, but not on the mass of the movable electrode. Contrary to amplitude the period T of the oscillation does depend on the mass.

The bottom half of figure 3.7 shows such a transient response for a voltage step $V_d = 0.9 \cdot V_{PI}$. Note that the time axis is scaled with the period. The top half of figure 3.7 shows the static load displacement curve. The stable static equilibrium for this voltage is indicated with a red circle. The arrows in the middle indicate the direction of the electro-mechanic force for this specific value of V_D (the right-hand side of eq. (3.25)). The forces change direction at the static equilibrium positions. Therefore the transient response oscillates asymmetrically around the stable equilibrium. If there would be damping, the position would converge to this stable equilibrium. Note that dynamically, a stable response can have a displacement larger than the static pull-in displacement. The static pull-in displacement is indicated by a green triangle.

But, if during the transient the displacement is larger than the unstable equilibrium: the resulting electro-mechanical force is directed to the right and the electrode is pulled in. For the voltage of $V_D = 0.9 \cdot V_{PI}$ this does not happen, nor for any voltage lower than that. However the voltage for which the displacement just touches the unstable equilibrium is not much higher: $V_D = 0.92 \cdot V_{PI}$. The transient for this voltage is

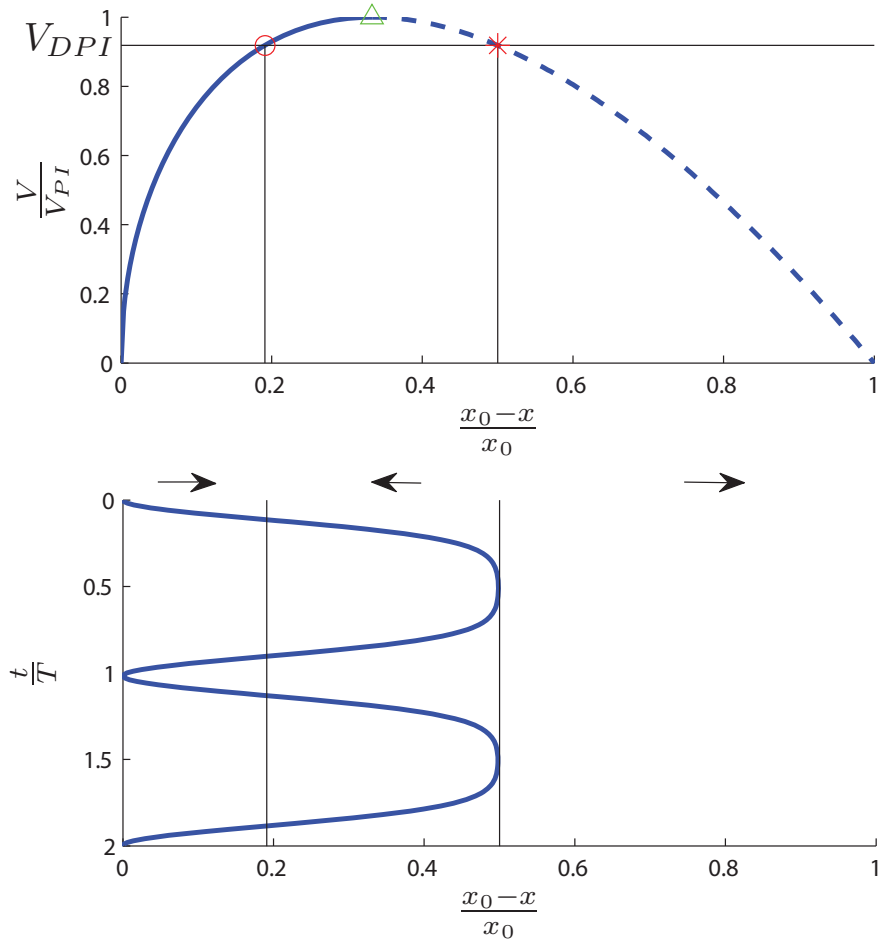


Figure 3.8: Dynamic pull-in for a 1D model: on the top the static pull-in curve, on the bottom the transient for a load step equal to the dynamic pull-in value V_{DPI} .

plotted in figure 3.8. Again the red circle shows the stable equilibrium and the red star the unstable one. If the voltage is only a minute fraction larger than this one the mass would move with a positive velocity into the domain on the right where the force is directed towards the fixed electrode and the device pulls in. Therefore this voltage can be called the *dynamic pull-in* voltage V_{DPI} , which for this problem is equal to $0.92 \cdot V_{PI}$. The dynamic pull-in displacement is equal to 0.5 times the initial gap x_0 .

As is written above, there exist no closed form solutions for the transient step response, however it is possible to find an exact solution for V_{DPI} . The derivation of this parameter starts with the knowledge that at dynamic pull-in displacement x_{DPI} the acceleration is zero because it is an equilibrium point:

$$k(x - x_0) + \frac{1}{2}\varepsilon \frac{V_{DPI}^2}{x_{DPI}^2} = 0, \quad (3.26)$$

Due to the conservation of energy principle, the energy during the transient must remain constant. Thus the energy at $V = V_{DPI}$, $x = x_0$ must be equal to the energy at $V = V_{DPI}$, $x = x_{DPI}$:

$$\frac{1}{2}k(x_{DPI} - x_0)^2 - \frac{1}{2}\varepsilon \frac{V_{DPI}^2}{x_{DPI}} = -\frac{1}{2}\varepsilon \frac{V_{DPI}^2}{x_0}. \quad (3.27)$$

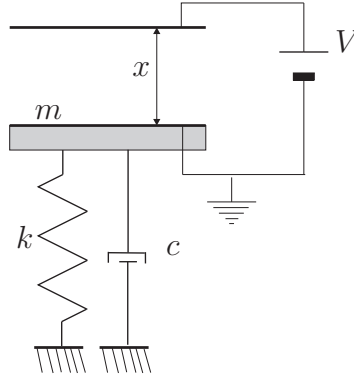


Figure 3.9: 1D resonator with damping.

Therefore two equations with two unknowns have been defined. Simultaneously solving (3.26) and (3.27) yields the following closed form solution for the dynamic pull-in voltage and displacement:

$$V_{DPI} = \sqrt{\frac{kx_0^3}{4\epsilon}} = \frac{3}{8}\sqrt{6}V_{PI} \approx 0.92V_{PI}, \quad (3.28)$$

$$x_{DPI} = \frac{1}{2}x_0. \quad (3.29)$$

Thus as with static pull-in the pull-in displacement is only depending on the gap size.

3.3.3 Damping

It is very easy to include damping into this traditional 1D model. A simple viscous damper is added to the model as shown in figure 3.9. Mathematically this damping can be written as:

$$F_{damp} = c \cdot \dot{x}. \quad (3.30)$$

Added to the total equation this gives:

$$m\ddot{x} + c\dot{x} + k(x - x_0) + \frac{1}{2}\epsilon\frac{V^2}{x^2} = 0. \quad (3.31)$$

But how to find the value of c ? One of the most common sources of microsystem damping is air damping in the form of squeeze film damping [11]. At small scales air is relatively viscous, hence the squeeze film damping can be pretty big. Squeeze film damping is the damping caused by air being trapped and squeezed between the moving mass and the fixed electrode. This effect is illustrated in figure 3.10. The left shows the mass moving up and down, therefore sucking in and pushing out air at the edges. This causes a relative pressure build up as shown on the right-hand side of the figure.

At relatively low moving mass velocities or frequencies the air has time to be sucked in and out during the motion. This means that the compressibility of the gas is not important. Therefore the pressure has time to build up making the damping force is mainly proportional to the velocity of the mass. Thus compared with the undamped case only the c value has to be added. On the other hand, when the frequency of the oscillation is relatively high the air does not have the time to move in and out of the gap, does not have time to flow in and out. Therefore the gas cannot be assumed to behave incompressible and there is also a very big term that is proportional to the

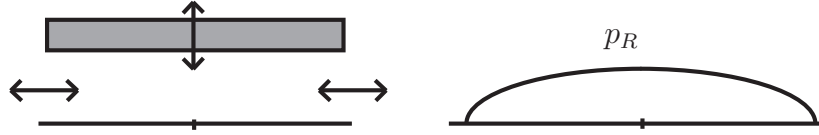


Figure 3.10: Squeeze film air damping: on the left the principle of damping, on the right the pressure build up.

displacement of the moving mass, thus also the k value has to be changed. When the acceleration of the gas is high as well, also the inertia of the fluid starts to count and the m value has to be changed. However this effect is for MEMS often negligible [11].

How to compute the c value due to squeeze film damping can be found, amongst others, in [11]. To give an indication on what kind of parameters influence the damping an example from that paper will be presented: the top view of the moving mass is a rectangular plate with length and width L . When the gas can be assumed incompressible is, hence the force is assumed to be proportional to the velocity, this would give the following approximation for the damping:

$$c = \frac{0.42\mu L^4}{x_0^3}, \quad (3.32)$$

and for the additional stiffness $k_f = 0$. Here μ is the viscosity of the air. Note that the pressure is not present in this term.

When the incompressibility assumption is not valid, c becomes dependent on pressure and on frequency. When the gas is very compressible c becomes almost 0 and the addition stiffness relatively big:

$$k_f = \frac{p_A L^2}{x_0}. \quad (3.33)$$

To investigate the effects of damping, the equation is written in state-space form:

$$\begin{bmatrix} \dot{x} \\ \ddot{x} \end{bmatrix} = \begin{bmatrix} \dot{x} \\ -\frac{k(x-x_0)}{m} - \frac{c\dot{x}}{m} - \frac{1}{2m}\varepsilon\frac{V^2}{x^2} \end{bmatrix}, \quad (3.34)$$

which can be written as:

$$\dot{\mathbf{y}} = \mathbf{f}(\mathbf{y}), \quad (3.35)$$

where:

$$\mathbf{y} = \begin{bmatrix} x \\ \dot{x} \end{bmatrix}. \quad (3.36)$$

The state space formulation can be used to find a linearized Jacobian matrix:

$$\mathbf{A} = \frac{\partial \mathbf{f}}{\partial \mathbf{y}} = \begin{bmatrix} 0 & 1 \\ -\frac{k}{m} + \frac{1}{m}\varepsilon\frac{V^2}{x^3} & -\frac{c}{m} \end{bmatrix}. \quad (3.37)$$

The eigenvalues of this Jacobian matrix evaluated at a certain V and d say something about the free vibration around an equilibrium position. When it is assumed that the free vibration can be described by:

$$\mathbf{y} = \boldsymbol{\mu}e^{\lambda t}, \quad (3.38)$$

where $\boldsymbol{\mu}$ is independent of time. This can be combined with (3.37) to give:

$$\lambda \boldsymbol{\mu} e^{\lambda t} = \mathbf{A} \boldsymbol{\mu} e^{\lambda t}. \quad (3.39)$$

This defines the eigenvalue problem:

$$\lambda \boldsymbol{\mu} = \mathbf{A} \boldsymbol{\mu}. \quad (3.40)$$

In general the eigenvalues λ that will form a complex conjugated pair, thus the values have a real part and an imaginary part: $\lambda = \zeta + i\omega$. In the beginning it was assumed that the motion could be described by:

$$\mathbf{y} = \boldsymbol{\mu} e^{(\zeta + i\omega)t}, \quad (3.41)$$

which can be written as:

$$\mathbf{y} = \boldsymbol{\mu} e^{\zeta t} e^{i\omega t}. \quad (3.42)$$

The term $e^{i\omega t}$ describes a sinusoidal motion with frequency ω . The part $e^{\zeta t}$ describes how the sinusoidal motion damps out ($\zeta < 0$) or increases ($\zeta > 0$) and $\boldsymbol{\mu}$ gives the relation between displacement and velocity. Of course the amplitude of the mode does not have a physical meaning, because when s is a constant scalar, $\boldsymbol{\mu} \cdot s$ will also be a solution to equation (3.40).

When the static equilibrium path is traced, it is possible to track the evolution of the eigenfrequency as a function of equilibrium displacement. First it is known that the equilibrium path is described by:

$$V = \sqrt{-k(x - x_0) \frac{2x^2}{\varepsilon}}, \quad (3.43)$$

and was already plotted in figure 3.3. These equilibrium solutions can be substituted into A , after which the eigenvalue λ can be determined.

Eigenvalues were computed with the following values: $k = 1$, $m = 1$ and $c = 0.5$. The results are shown in figure 3.11. It is clear that damping slows the motion down, decreasing the frequency. A result of this effect is that the natural frequency reaches a zero value before pull-in. From that point to the original pull-in point the device behaves as a critically damped system. At the pull-in point the real part of the eigenvalue becomes positive, therefore the damped system becomes unstable at the same point as the original undamped system.

3.4 General numerical modeling

The coupled equilibrium equations (3.1) and (3.2) are partial differential equations. To solve these equations numerically they have to be discretized. Different discretization techniques can be applied, but the mechanical equations (3.2) are almost always discretized with the Finite Element Method (FEM) for which an abundant body of literature exists (e.g. [12, 28]). The electrostatic problem (3.1) is a Laplace equation. This equation also describes other physical fields such as thermics, potential fluid flow or membrane displacements. Therefore scientists from several application fields have investigated the Laplace equation. Structural engineers prefer to use the Finite Element Method for solving this equation, whereas engineers from the fluid mechanics

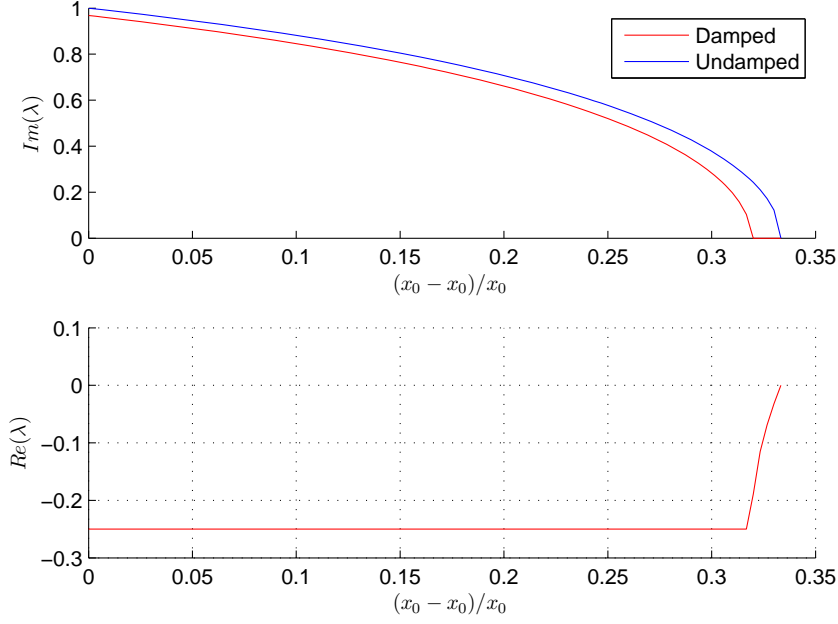


Figure 3.11: Eigenvalue as function of equilibrium displacement.

field typically apply the Finite Volume Method (FVM) [138, 43] or Finite Difference schemes. The Boundary Element Method (BEM) is also quite popular because it handles infinitely extending domains in a natural manner [68].

Once such a discretization procedure has been chosen the discretized equations can be written in the following form:

$$\mathbf{K}_{uu}^m \mathbf{u} = \mathbf{f}^{elec}(\mathbf{u}, \phi, V), \quad (3.44)$$

$$\mathbf{K}_{\phi\phi}(\mathbf{u}) \phi = \mathbf{q}(\mathbf{u}, V), \quad (3.45)$$

where $\mathbf{K}_{\phi\phi}$ is the electric stiffness matrix, \mathbf{K}_{uu}^m the mechanical stiffness matrix, ϕ the set of discretized potentials (nodal potentials for a FEM model), \mathbf{u} the set of discretized displacements, \mathbf{q} are applied charges (on the boundaries or in the electric domain) and V the imposed potentials on Dirichlet boundaries. \mathbf{f}^{elec} are the applied electrostatic forces obtained with eq. (3.9) or, alternatively, by formulations based on variational calculus and total energy approaches. The latter methods to construct the electrostatic forces are more efficient when the structure exhibits sharp corners, as was discussed in chapter 2. From the discretized equations (3.44) it can be seen clearly that the non-linear electrostatic coupling originates on one hand from the fact that the electrostatic forces applied on the structure are non-linear functions of the potential field, and on the other by the fact that the electrostatic domain (hence the operator $\mathbf{K}_{\phi\phi}$) depends on the structural response \mathbf{u} .

After defining the internal forces and internal charges as

$$\mathbf{f}^{int} = \mathbf{K}_{uu}^m \mathbf{u}, \quad (3.46)$$

$$\mathbf{q}^{int} = \mathbf{K}_{\phi\phi}(\mathbf{u}) \phi, \quad (3.47)$$

the coupled equilibrium equations can be written in the following monolithic form [108]:

$$\mathbf{F}^{elec}(\mathbf{U}, V) - \mathbf{F}^{int}(\mathbf{U}) = 0, \quad (3.48)$$

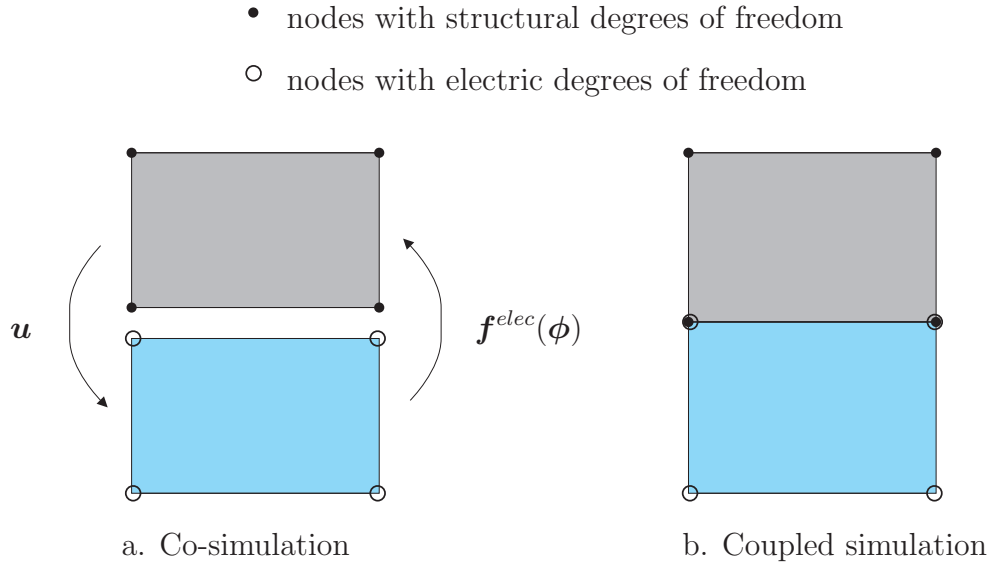


Figure 3.12: Modeling strategies

where

$$\mathbf{U} = \begin{bmatrix} \mathbf{u} \\ \phi \end{bmatrix}, \quad (3.49)$$

$$\mathbf{F} = \begin{bmatrix} \mathbf{f} \\ \mathbf{q} \end{bmatrix}, \quad (3.50)$$

There are two ways to obtain these sets of equilibrium equations: *co-simulation* or *fully coupled simulation*.

In a *co-simulation* method separate structural and electric models are handled by separate codes to solve the different physical domains and the results are communicated between the codes at some synchronization moments during the solution procedure: mechanical displacements are sent to the electric model to update its geometry and electric potentials or fields are sent to the structural model to generate electrostatic forces. This is schematically depicted in figure 3.12.a. An advantage of co-simulation is that different discretization procedures can be used for the different domains and established specialized software can be used for each physical domain. For instance a structural FEM model and a separate electrostatic FEM model can be co-simulated [63, 144], but it is also common in the literature to combine a structural FEM model with electrostatic BEM approach [4, 87, 47]. Structural FEM models coupled to electrostatic FVM models are rare, which is surprising because structural FEM models coupled with fluid FVM models are very common [41], even structural FVM with fluid FVM does exist [122]. Since FVM handles singularities at corners better than FEM, coupling FEM and FVM in electrostatics is probably an interesting aspect for future research. One problem is that data has to be transferred between different meshes, which has generated a body of literature in itself [40, 67, 6].

In *fully coupled simulation* the entire problem is handled in a single code: only one mesh is used to model both domains as schematically explained in figure 3.12.b. In that case all the properties of the multiphysical problem are known in a single code, which greatly simplifies analyzing global properties such as eigenfrequencies. An advantage of the coupled simulation is that it is much easier to obtain a linearization of the coupled equations, which enables the creation of very efficient coupled solvers [108].

3.5 Staggered and monolithic solution approaches

Traditionally non-linear solvers rely on successive linear iterations to find a solution to (3.48). In this chapter the distinction will be made between solvers that solve the coupled problem in a *staggered* manner and solvers that handle the different physics in a *monolithic* way.

A staggered solver basically solves one physical domain at a time. Figure 3.13 presents a simple diagram for a staggered solver: at iteration k first the electrostatic force is computed using the electric potential solution from step $k - 1$, next the new displacements are computed by the mechanic solver and sent to the electric solver, which can subsequently compute the new electrostatic potential solution. This can be repeated until convergence. This scheme can be interpreted from a mathematical point of view as a block Gauss-Seidel iteration and can be written as [10, 22]:

$$\phi_k = \mathbf{K}_{\phi\phi}^{-1}(\mathbf{u}_{k-1})\mathbf{q}(\mathbf{u}_{k-1}, V), \quad (3.51)$$

$$\mathbf{u}_k = \mathbf{K}_{uu}^{m-1}\mathbf{f}^{elec}(\mathbf{u}_{k-1}, \phi_k, V). \quad (3.52)$$

The algorithm is converged when the update for the displacements is smaller than a specified tolerance ($\|\mathbf{u}_k - \mathbf{u}_{k-1}\| < \text{tol}$).

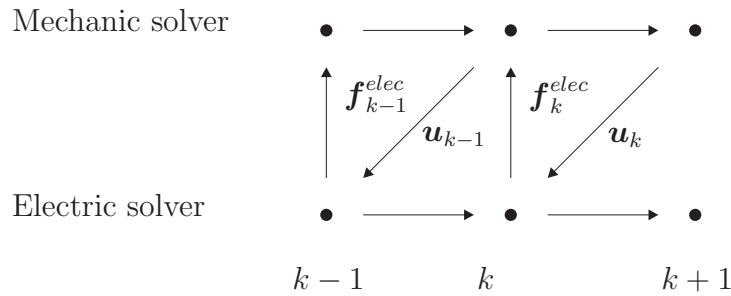


Figure 3.13: Staggered solution procedure

It is clear that this algorithm can be implemented when the problem when the structural and electrostatic equations are solved in separate codes, that is in co-simulation. But obviously the staggered approach can also be used when the discretization is done in a fully coupled simulation. An advantage of a staggered solver is that the structural and electrostatic problems taken separately are, for many applications, linear. Also, for each subproblem efficient specialized solvers can be used.

Monolithic solvers attempt to solve the fully coupled equations as a whole and lead to specific solution procedures [22] (see figure 3.14). Clearly monolithic solvers need to have access to the fully coupled model and are not appropriate for co-simulation strategies. So far mainly FEM-FEM coupling can be found in the literature [50, 108]. The advantage of monolithic solvers is that the convergence rate tends to be faster but, the full equilibrium equation being non-linear, the monolithic approaches are typically using successive linearized problems and thus often require computing the global tangent stiffness matrix $\mathbf{K} = \frac{\partial \mathbf{F}}{\partial \mathbf{U}}$.

Using equations (3.44) and (3.45) the monolithic linearized problem can be written as

$$\begin{bmatrix} \mathbf{K}_{uu}(\mathbf{u}, \phi) & \mathbf{K}_{u\phi}(\mathbf{u}, \phi) \\ \mathbf{K}_{u\phi}^T(\mathbf{u}, \phi) & \mathbf{K}_{\phi\phi}(\mathbf{u}) \end{bmatrix} \begin{bmatrix} \Delta \mathbf{u} \\ \Delta \phi \end{bmatrix} = \begin{bmatrix} \Delta \mathbf{f}(\mathbf{u}, \phi, V) \\ \Delta \mathbf{q}(\mathbf{u}, V) \end{bmatrix}, \quad (3.53)$$

3.6 FEM formulation of the electro-mechanical coupling

3.6.1 Discretization of the electric domain

The discretization of the electric domain was discussed extensively in chapter 2, hence only the 2D results are recalled here. If the electric potential field is approximated by:

$$\phi = N_i(x, y)\phi_i, \quad (3.59)$$

where N_i are the linear shape functions and ϕ_i the nodal potentials. The electrostatic equilibrium equation is

$$\mathbf{K}\phi = \mathbf{Q}. \quad (3.60)$$

Electrostatic forces can be computed once ϕ is known with:

$$\mathbf{F}_{es}^T = \frac{1}{2} \int_{\Omega} \mathbf{D}^T \begin{bmatrix} \frac{\partial \phi}{\partial X} & 0 & 2\frac{\partial \phi}{\partial Y} & -\frac{\partial \phi}{\partial X} \\ -\frac{\partial \phi}{\partial Y} & 2\frac{\partial \phi}{\partial X} & 0 & \frac{\partial \phi}{\partial Y} \end{bmatrix} \mathbf{B} d\Omega, \quad (3.61)$$

where \mathbf{D} is computed using the shape functions and the nodal voltages:

$$\mathbf{D} = \varepsilon \mathbf{E} = \varepsilon \begin{bmatrix} \frac{\partial N_i}{\partial x} \phi_i \\ \frac{\partial N_i}{\partial y} \phi_i \end{bmatrix}. \quad (3.62)$$

3.6.2 Discretization of the structural domain

Also the mechanical equilibrium equations as discussed in section 3.2 can be discretized with finite elements. This procedure can be found in appendix A.2. The result is the following equation in its classical form:

$$\mathbf{M}_{uu}\ddot{\mathbf{u}} + \mathbf{K}_{uu}^m \mathbf{u} = \mathbf{f}, \quad (3.63)$$

where $\ddot{\mathbf{u}}$ are the nodal accelerations, \mathbf{u} the nodal displacements and \mathbf{f} is the external force vector. The matrix \mathbf{M}_{uu} is the mechanical mass matrix and \mathbf{K}_{uu}^m is the mechanical stiffness matrix.

In a staggered scheme the forces computed with an electrostatic FEM model are substituted into the force vector \mathbf{f} .

3.6.3 Electric mesh deformation

So far the implementation of an electrical model coupled with a mechanical model was discussed. Here it became clear that the electric domain depends on the mechanical displacements. To be able to implement this domain dependency, the electrical mesh has to be changed when the displacement changes.

Basically two options exist to implement this mesh change: *re-meshing* and *mesh deformation*. Re-meshing means that a complete new mesh is generated, while mesh deformation implies that the existing mesh is deformed to cope with the changing geometry. The advantage of mesh deformation is that this procedure can be defined by a single equation, which allows an easy implementation of tangent matrices.

When such a mesh deformation algorithm is implemented two displacement fields can be defined as in figure 3.15. The mechanical displacement u_m is simply the displacement field used before. Furthermore a mesh displacement field u_e is defined, which describes the relocation of electric nodes, due to mechanic displacements. It is easy to state that the deformation of the electric mesh only depends on those mechanical displacements that are located on the interface $u_i = \bar{u}_e$. In that case the mesh deformation can be written mathematically as (after discretization):

$$\mathbf{g}(\mathbf{u}_e, \mathbf{u}_i) = 0. \quad (3.64)$$

The interface displacements form a subset of the mechanical displacements as well $u_i \subseteq u_m$.



Figure 3.15: Definition of mechanical and mesh displacements.

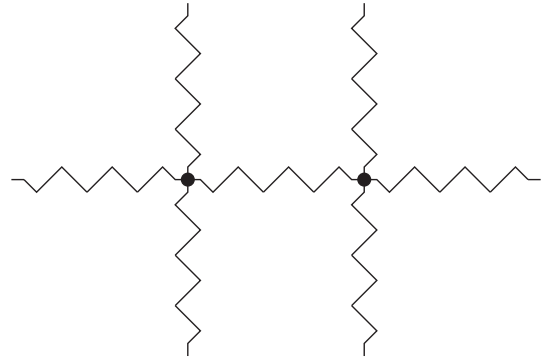


Figure 3.16: A network of springs.

There exist many options for selecting a function \mathbf{g} . The easiest option is to use a network of linear springs to define the relationship between the mesh node displacements. However many more advanced options exist, see for instance the overview in [31]. A simple method slightly more advanced than a network of linear springs is to use a pseudo structure, where linear elastic solid equations are solved within the electric domain. Instead of the linear elastic equations simpler equations, such as the Laplace equation, can be used to describe such a pseudo structure. In the end the result is that equation (3.64) can be cast into the form:

$$\mathbf{K}_{u_e u_e} \mathbf{u}_e = -\mathbf{K}_{u_e \bar{u}_e} \mathbf{u}_i. \quad (3.65)$$

Because \mathbf{u}_i is only a subset of \mathbf{u}_m this will be written as:

$$\mathbf{K}_{u_e u_e} \mathbf{u}_e = -\mathbf{K}_{u_e \bar{u}_e} \mathbf{u}_m, \quad (3.66)$$

where the notation is slightly abused because the matrix $\mathbf{K}_{u_e \bar{u}_e}$ changes its definition between the two equations above, however the information contained by this matrix does not change, therefore the same symbol is used for simplicity. This gives:

$$\mathbf{u}_e = -\mathbf{K}_{u_e u_e}^{-1} \mathbf{K}_{u_e \bar{u}_e} \mathbf{u}_m, \quad (3.67)$$

or $\mathbf{u}_e = \mathbf{u}_e(\mathbf{u}_m)$.

Equation (3.66) combined with the mechanical and electrical equations, yields the system:

$$\begin{cases} \mathbf{K}_{uu}^m \mathbf{u}_m = \mathbf{f}^{elec}(\mathbf{u}_e, \phi, V) \\ \mathbf{K}_{u_e u_e} \mathbf{u}_e = -\mathbf{K}_{u_e \bar{u}_e} \mathbf{u}_m \\ \mathbf{K}_{\phi\phi}(\mathbf{u}_e) \phi = \mathbf{q}^{elec}(\mathbf{u}_e, V) \end{cases}. \quad (3.68)$$

However the equation describing the mesh deformation can be condensed out of the set to give:

$$\begin{cases} \mathbf{K}_{uu}^m \mathbf{u}_m = \mathbf{f}^{elec}(\mathbf{u}_e(\mathbf{u}_m), \phi, V) \\ \mathbf{K}_{\phi\phi}(\mathbf{u}_e(\mathbf{u}_m))\phi = \mathbf{q}^{elec}(\mathbf{u}_e(\mathbf{u}_m), V) \end{cases}, \quad (3.69)$$

where the notation is abused again because the precise definition of the function \mathbf{f}^{elec} changes, however it still is the *electrostatic force*. The equation can be concisely written as:

$$\begin{cases} \mathbf{K}_{uu}^m \mathbf{u}_m = \mathbf{f}^{elec}(\mathbf{u}_m, \phi, V) \\ \mathbf{K}_{\phi\phi}(\mathbf{u}_m)\phi = \mathbf{q}^{elec}(\mathbf{u}_m, V) \end{cases}, \quad (3.70)$$

which from the next section on will be written simply as:

$$\begin{cases} \mathbf{K}_{uu}^m \mathbf{u} = \mathbf{f}^{elec}(\mathbf{u}, \phi, V) \\ \mathbf{K}_{\phi\phi}(\mathbf{u})\phi = \mathbf{q}^{elec}(\mathbf{u}, V) \end{cases}. \quad (3.71)$$

For simplicity, in all derivations presented in this thesis the system under consideration is the last one. Hence the chosen mesh deformation is not explicitly considered. Therefore once a derivative is presented, such as:

$$\frac{\partial \mathbf{f}^{elec}}{\partial \mathbf{u}},$$

this actually means:

$$\frac{\partial \mathbf{f}^{elec}}{\partial \mathbf{u}} = \frac{\partial \mathbf{f}^{elec}}{\partial \mathbf{u}_e} \frac{\partial \mathbf{u}_e}{\partial \mathbf{u}_m} = -\frac{\partial \mathbf{f}^{elec}}{\partial \mathbf{u}_e} \mathbf{K}_{u_e u_e}^{-1} \mathbf{K}_{u_e \bar{u}_e}. \quad (3.72)$$

Note that if in the text the implementation or computation of a derivative with respect to \mathbf{u} is discussed, only the derivative with respect to \mathbf{u}_e is discussed in detail. The extra term $\frac{\partial \mathbf{u}_e}{\partial \mathbf{u}_m}$ is not explicitly discussed, but implicitly assumed to be trivial.

It is important to include that term $\frac{\partial \mathbf{u}_e}{\partial \mathbf{u}_m}$ in the derivations because the actual nodal potentials depend on the exact location of the nodes. Thus the tangent terms depend on the displacement of mesh nodes due to structural displacements. Therefore in a monolithic solution scheme the terms are very important for defining the coupling between the fields.

It is interesting to see what happens when now also the electric is condensed on the mechanical equations:

$$\mathbf{K}_{u_m u_m}^m \mathbf{u}_m = \mathbf{f}^{elec}(\mathbf{u}_e(\mathbf{u}_m), \phi(\mathbf{u}_e(\mathbf{u}_m), V), V), \quad (3.73)$$

which of course should not depend on the specific mesh deformation algorithm (if the mesh is dense enough). The force \mathbf{f}^{elec} should not depend on the mesh of the electric domain, in contrast to \mathbf{q}^{elec} . Therefore the derivative:

$$\frac{\hat{\partial} \mathbf{f}^{elec}}{\partial \mathbf{u}_m} \triangleq \frac{\partial \mathbf{f}^{elec}}{\partial \mathbf{u}_e} \frac{\partial \mathbf{u}_e}{\partial \mathbf{u}_m} + \frac{\partial \mathbf{f}^{elec}}{\partial \phi} \frac{\partial \phi}{\partial \mathbf{u}_e} \frac{\partial \mathbf{u}_e}{\partial \mathbf{u}_m}, \quad (3.74)$$

should be independent of the chosen mesh deformation algorithm. Here the hat-derivative was defined because the partial it is not a true partial derivative and not a true total derivative. Within this derivative the direct effects of the mesh displacement choice on \mathbf{f}^{elec} within the first term should cancel the indirect effects through the second

term. This is a property that can be abused: a hybrid method can use a staggered algorithm to compute equilibrium solutions, after which a very simple mesh deformation algorithm, where only boundary DOFs are displaced, can be used to compute tangent information. This reduces the complexity of this tangent computation. This tangent information is required for certain analysis such as frequencies or sensitivities.

This differentiation required the definition of the hat-derivative $\frac{\hat{\partial}}{\partial \mathbf{u}_m}$, because after condensation the force can be written as $\mathbf{f}^{elec}(\mathbf{u}_m, V)$ and one is interested in the partial derivative of this force: $\frac{\partial \mathbf{f}^{elec}(\mathbf{u}_m, V)}{\partial \mathbf{u}_m}$. However if the notation of (3.73) is used, this notation means something else, therefore one has to use a different notation. Within this thesis that need is fulfilled by the hat notation.

3.6.4 A monolithically coupled FEM formulation

As seen above a coupled electromechanical FEM model has two types of degrees of freedom (DOFs): mechanical nodal displacements (\mathbf{u}) and nodal electric potentials (ϕ)². The dual quantity of the displacement is the mechanical force (\mathbf{f}) on the node and the dual of the electric potential is the electric charge on the node (\mathbf{q}):

$$\mathbf{U} = \begin{bmatrix} \mathbf{u} \\ \phi \end{bmatrix}, \quad (3.75)$$

$$\mathbf{F} = \begin{bmatrix} \mathbf{f} \\ \mathbf{q} \end{bmatrix}, \quad (3.76)$$

where so called shape functions are used to approximate the real (2D) displacement field (u, v) and potential field ϕ :

$$\begin{aligned} u_x &= N_i u_{xi}, \\ u_y &= N_i u_{yi}, \\ \phi &= N_i \phi_i, \end{aligned} \quad (3.77)$$

or in matrix vector notation:

$$\begin{bmatrix} u_x \\ u_y \\ \phi \end{bmatrix} = \mathbf{N}_u \mathbf{u}, \quad (3.78)$$

$$\phi = \mathbf{N}_\phi \phi.$$

The tangent stiffness matrix \mathbf{K} gives the relation between an increment of the DOFs and an increment of their dual quantities:

$$\mathbf{K} \Delta \mathbf{U} = \Delta \mathbf{F}, \quad (3.79)$$

where \mathbf{K} can be computed with:

$$\mathbf{K} = \frac{\partial \mathbf{F}}{\partial \mathbf{U}}. \quad (3.80)$$

However to determine the values in the tangent stiffness matrix for an electromechanical coupled FEM model it is easier to start with the total coupled electromechanical energy:

$$W = W_{mech} + W_{elec} = \int_{V_{mech}} \frac{1}{2} \boldsymbol{\epsilon}^T \boldsymbol{\sigma} dV + \int_{V_{elec}} -\frac{1}{2} \mathbf{D}^T \mathbf{E} dV, \quad (3.81)$$

²This section is based on the modeling approach developed by V. Rochus and presented in [108].

where $\boldsymbol{\epsilon}$ is the mechanical strain, $\boldsymbol{\sigma}$ is the mechanical stress, \mathbf{D} the electric displacement and \mathbf{E} the electric field. The domain of integration for both energies is the complete domain, but often the mechanical domain is limited to the deformable conductors. Only when the dielectric is a solid material, deformations are of interest within the electric domain. In that case this domain should be included in the domain of integration for the mechanical energy. Similarly the electric energy is zero within (ideal) conductors, hence the electric domain of integration is limited to the dielectric domain.

With this coupled energy the equilibrium equations can be written as (external minus internal loads):

$$\begin{bmatrix} \mathbf{f}^{elec} - \mathbf{f}^{int} \\ \mathbf{q}^{elec} - \mathbf{q}^{int} \end{bmatrix} = - \begin{bmatrix} \frac{\partial W}{\partial \mathbf{u}} \\ \frac{\partial W}{\partial \phi} \end{bmatrix} = 0, \quad (3.82)$$

which can be used to define the *symmetric* tangent stiffness matrix:

$$\frac{\partial^2 W}{\partial \mathbf{U}^2} \Delta \mathbf{U} = \mathbf{K} \Delta \mathbf{U} = \Delta \mathbf{F}, \quad (3.83)$$

therefore the stiffness matrix can be written as:

$$\mathbf{K} = \begin{bmatrix} \mathbf{K}_{uu} & \mathbf{K}_{u\phi} \\ \mathbf{K}_{\phi u} & \mathbf{K}_{\phi\phi} \end{bmatrix} = \begin{bmatrix} \frac{\partial^2 W}{\partial \mathbf{u}^2} & \frac{\partial^2 W}{\partial \mathbf{u} \partial \phi} \\ \frac{\partial^2 W}{\partial \phi \partial \mathbf{u}} & \frac{\partial^2 W}{\partial \phi^2} \end{bmatrix}. \quad (3.84)$$

The mechanical energy does not depend on the electric potential however the electric domain is deformed by mechanical displacements therefore the electric energy does depend on the mechanical displacements, hence:

$$\begin{bmatrix} \mathbf{K}_{uu}^m + \mathbf{K}_{uu}^e & \mathbf{K}_{u\phi} \\ \mathbf{K}_{\phi u} & \mathbf{K}_{\phi\phi} \end{bmatrix} = \begin{bmatrix} \frac{\partial^2 W_{mech}}{\partial \mathbf{u}^2} + \frac{\partial^2 W_{elec}}{\partial \mathbf{u}^2} & \frac{\partial^2 W_{elec}}{\partial \mathbf{u} \partial \phi} \\ \frac{\partial^2 W_{elec}}{\partial \phi \partial \mathbf{u}} & \frac{\partial^2 W_{elec}}{\partial \phi^2} \end{bmatrix}. \quad (3.85)$$

Normally electric constitutive relationships establish a linear relation between the electric displacement \mathbf{D} and \mathbf{E} the electric field: $\mathbf{D} = \varepsilon \mathbf{E}$, where ε is the electric permittivity. The electric field is simply defined as the gradient of the electric potential: $\mathbf{E} = -\nabla \phi$. Therefore the electric stiffness $\mathbf{K}_{\phi\phi}$ is constant with respect to the nodal potentials ϕ . However, due to the dependency of the electric domain on the displacement field, the electric stiffness does depend on \mathbf{u} . If the displacements are assumed to be small enough to have linear mechanics, this can be summarized as:

$$\begin{bmatrix} \mathbf{K}_{uu}^m + \mathbf{K}_{uu}^e(\mathbf{u}, \phi) & \mathbf{K}_{u\phi}(\mathbf{u}, \phi) \\ \mathbf{K}_{\phi u}(\mathbf{u}, \phi) & \mathbf{K}_{\phi\phi}(\mathbf{u}) \end{bmatrix}. \quad (3.86)$$

In appendix A.2 it was shown than for linear 2D mechanics the strain within a body can be described by:

$$\begin{bmatrix} \epsilon_{xx} \\ \epsilon_{yy} \\ \gamma_{xy} \end{bmatrix} = \begin{bmatrix} \frac{\partial}{\partial x} & 0 \\ 0 & \frac{\partial}{\partial y} \\ \frac{\partial}{\partial y} & \frac{\partial}{\partial x} \end{bmatrix} \begin{bmatrix} u \\ v \end{bmatrix} = \mathbf{L}_u \begin{bmatrix} u \\ v \end{bmatrix}, \quad (3.87)$$

thus the approximated strain is:

$$\boldsymbol{\epsilon} = \mathbf{L}_u \mathbf{N}_u \mathbf{u} = \mathbf{B}_u \mathbf{u}. \quad (3.88)$$

Similarly the electric field is discretized by:

$$\begin{bmatrix} E_x \\ E_y \end{bmatrix} = \begin{bmatrix} \frac{\partial}{\partial x} \\ \frac{\partial}{\partial y} \end{bmatrix} \phi = \mathbf{L}_\phi \phi, \quad (3.89)$$

and:

$$\mathbf{E} = \mathbf{L}_\phi \mathbf{N}_\phi \phi = \mathbf{B}_\phi \phi. \quad (3.90)$$

To define the coupling also the simple gradient of the displacement is required:

$$\begin{bmatrix} \frac{\partial u}{\partial x} \\ \frac{\partial u}{\partial y} \\ \frac{\partial \phi}{\partial x} \\ \frac{\partial \phi}{\partial y} \end{bmatrix} = \begin{bmatrix} \frac{\partial}{\partial x} & 0 \\ 0 & \frac{\partial}{\partial y} \\ \frac{\partial}{\partial x} & 0 \\ 0 & \frac{\partial}{\partial y} \end{bmatrix} \begin{bmatrix} u \\ v \end{bmatrix} = \mathbf{L}_{u2} \begin{bmatrix} u \\ v \end{bmatrix}, \quad (3.91)$$

$$\nabla \begin{bmatrix} u \\ v \end{bmatrix} = \mathbf{L}_{u2} \mathbf{N}_u \mathbf{u} = \mathbf{B}_{u2} \mathbf{u}. \quad (3.92)$$

With these assumptions the following relations can be established:

$$\mathbf{K}_{uu}^m = \int_{V_{mech}} \mathbf{B}_u^T \mathbf{C} \mathbf{B}_u dV, \quad (3.93)$$

$$\mathbf{K}_{uu}^e(\mathbf{u}, \phi) = \int_{V_{elec}} \mathbf{B}_{u2}^T \mathbf{F}_2 \mathbf{B}_{u2} dV, \quad (3.94)$$

$$\mathbf{K}_{u\phi}(\mathbf{u}, \phi) = \int_{V_{elec}} \mathbf{B}_{u2}^T \mathbf{F}_1 \mathbf{B}_\phi dV, \quad (3.95)$$

$$\mathbf{K}_{\phi u}(\mathbf{u}, \phi) = \int_{V_{elec}} \mathbf{B}_\phi^T \mathbf{F}_1^T \mathbf{B}_{u2} dV, \quad (3.96)$$

$$\mathbf{K}_{\phi\phi}(\mathbf{u}) = \int_{V_{elec}} \mathbf{B}_\phi^T \varepsilon \mathbf{B}_\phi dV, \quad (3.97)$$

with:

$$\mathbf{F}_1 = \begin{pmatrix} E_x & E_y & E_y & -E_x \\ -E_y & E_x & E_x & E_y \end{pmatrix}^T, \quad (3.98)$$

and:

$$\mathbf{F}_2 = -\frac{1}{2} \begin{pmatrix} 2D_x E_x & 0 & 2D_x E_y & -(D_x E_x + D_y E_y) \\ 0 & 2D_x E_x & (D_x E_x + D_y E_y) & 2D_y E_x \\ 2D_x E_y & (D_x E_x + D_y E_y) & 2D_y E_y & 0 \\ -(D_x E_x + D_y E_y) & 2D_y E_x & 0 & 2D_y E_y \end{pmatrix}. \quad (3.99)$$

Another thing that is important to mention here is that the applied electrostatic force:

$$\mathbf{F}_{elec} = \mathbf{F}^{elec} = \frac{\partial W_{elec}}{\partial \mathbf{u}}, \quad (3.100)$$

can be shown to be:

$$\mathbf{F} = \frac{1}{2} \int_V \mathbf{B}_{u2} \mathbf{F}_3 dV, \quad (3.101)$$

where:

$$\mathbf{F}_3 = \begin{bmatrix} -E_x^2 + E_y^2 & -2E_xE_y & -2E_xE_y & E_x^2 - Ey^2 \end{bmatrix}^T. \quad (3.102)$$

Once such a fully coupled stiffness matrix has been computed, the discretized dynamic equations are:

$$\mathbf{M}_{uu}\ddot{\mathbf{u}} + \mathbf{K}_{uu}^m \mathbf{u} = \mathbf{f}^{elec}(\mathbf{u}, V) \quad (3.103)$$

$$, \mathbf{K}_{\phi\phi}(\mathbf{u})\phi = \mathbf{q}(\mathbf{u}, V). \quad (3.104)$$

With the coupled stiffness matrix the linearized dynamic equations can be written as:

$$\mathbf{M}\Delta\ddot{\mathbf{U}} + \mathbf{K}\Delta\mathbf{U} = \Delta\mathbf{F}. \quad (3.105)$$

where:

$$\mathbf{M} = \begin{bmatrix} \mathbf{M}_{uu} & 0 \\ 0 & 0 \end{bmatrix}. \quad (3.106)$$

This can be used to define the coupled eigenfrequency problem.

$$[\mathbf{K} - \omega_i \mathbf{M}] \mathbf{X}_i = 0, \quad (3.107)$$

which defines the eigenfrequencies of the coupled problem.

3.7 Summary

This chapter presented the equations required for modeling electro-mechanical coupling.

A one dimensional example was used to illustrate the phenomena of electro-mechanical modeling. For instance static and dynamic pull-in were introduced, as well as the voltage dependency of the eigenfrequency around static equilibriums. The computation and characterization of those quantities is an important goal of numerical modeling of MEMS, therefore these phenomena will be discussed in later chapters for FEM models.

After the introduction of the equations, two different approaches for obtaining them were treated: *co-simulation* or *fully coupled simulation*. The first one being characterized by the combinations of two models built in two different modeling environments and the second one by one coupled model built in one environment capable of modeling both domains.

Thereafter, two approaches to actually solve those equations were presented: *staggered* and *monolithic*. Staggered solving being the reiteration between mechanical and electric equations, whereas monolithic methods try to solve both sets of equations in one attempt. In practice monolithic methods can only be used when the model was derived in using a fully coupled modeling approach, because monolithic methods require fully coupled tangent matrices.

Finally the implementation of a fully coupled model into the finite element method was recapitulated.

Chapter 4

Detailed implementation of a test problem

4.1 Introduction

The preliminaries of electromechanical modeling have been discussed. However, for a general understanding and to present the notations used in the next chapters it is very useful to look in detail to the modeling of a micro switch.

Important applications of electro-mechanically actuated microsystems are RF-MEMS switches. An RF switch is a switch in a Radio Frequency circuit that depending on the actuation voltage cuts off an RF line [110]. This is illustrated in figure 4.1, where the open state of an RF-MEMS switch shown. Because the capacitance between the top and bottom electrode is relatively small the RF wave can easily travel from RF-in to RF-out. If the switch is closed, the moving conductor is pulled against the small solid dielectric layer. In that case the capacitance between top and bottom electrode becomes very high¹, therefore the wave traveling from RF-in to RF-out is blocked. A very simple model is just a beam with a dielectric gap as in figure 4.2.

It is a 2D model, therefore 3D fringe effects are neglected. First the electric part is described, after that the mechanical part finally the implementation including the moving mesh is discussed. This model can be extended to a very simple 3D model as discussed in the final section of this chapter. These models will be the benchmarks used throughout this document.

4.2 A two dimensional model

4.2.1 The electric domain

Since fringe effects are neglected the initial domain shown in figure 4.2 is very simple. The electric domain is the blue part of the model. Only the actuated electrode at the top can deform. The permittivity of the structure is equal to the vacuum permittivity of: $\epsilon_0 = 8.8542 \cdot 10^{-12}$. On the sides, where there are no electrodes, the symmetry boundary condition or *zero charge* condition is applied, which is a Neumann boundary condition ($\frac{\partial \phi}{\partial n} = 0$).

¹Remember that for a parallel plate actuator the capacitance is: $C = \frac{\epsilon A}{d}$, where C is the capacitance, A is the surface of the plates and d is the gap.

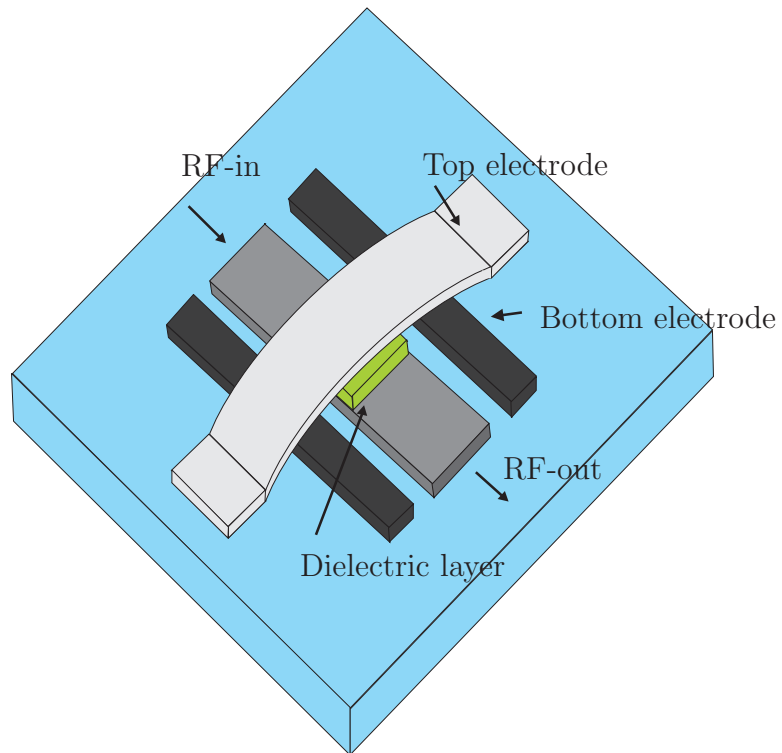


Figure 4.1: Schematic representation of an RF-MEMS switch.

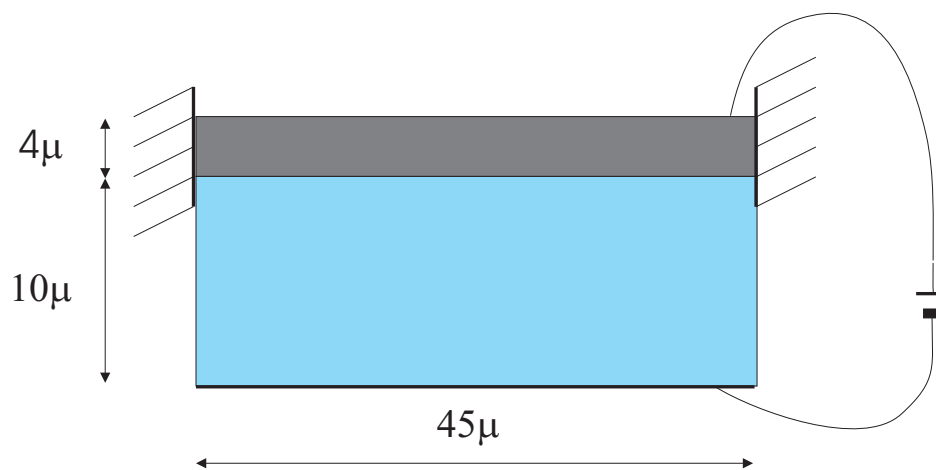


Figure 4.2: Simple beam.

4.2.2 The mechanical domain

The mechanical domain is the gray beam in figure 4.2. It is almost as simple as the electric domain: a beam clamped on both sides. The electrostatic pressure acts on the bottom side of the beam, which corresponds to the top electrode of the electric domain.

Table 4.1: Summary of the material properties.

Air gap			
Property	Symbol	Value	Units
<i>Electric permittivity</i>	ε	$8.8542 \cdot 10^{-12}$	<i>F/m</i>
Structure			
Property	Symbol	Value	Units
<i>Elasticity modulus</i>	E	$1 \cdot 10^5$	<i>Pa</i>
<i>Poisson's ratio</i>	ν	0.33	-

4.2.3 Implementation

The FEM model has been implemented in *Matlab*. First the implementation of the electrostatic part is discussed, next the mechanical part using volume elements, thereafter the mechanical part using beam elements and finally the mesh deformation algorithm.

4.2.4 Electrostatics

For the electrostatic part simple bilinear quadrilateral elements were used. The electric stiffness matrix has to be reassembled and integrated (4 Gauss-points per element) each moment that an electric solution is required. This is because the electric part is solved using an Eulerian formulation, which means that the moving coordinates of the mesh change the values of the stiffness matrix. The shape functions and formulations for the stiffness matrix can be found in section 2.4.

The used force discretization is the variational implementation (eq. 2.113).

Linear elasticity using volume elements

In 2D, the mechanical equations can be modeled in two distinct ways: by using volume elements or by beam elements. If volume elements are used, the full geometry is meshed by triangular or quadrilateral elements which discretize the continuum equations. In this work bilinear quadrilateral elements were used.

The beam is assumed to be structurally linear, therefore when 2D solid elements such as quadrilaterals are used to mesh the complete domain, there is the choice between two constitutive relations: plane strain or plane stress. The plane strain assumption implies that the *strain* in out-of-plane direction is zero, plane stress implies that the *stress* in out-of-plane direction is zero. Coarsely speaking the plane strain assumption can be better used if the out-of-plane dimensions are relatively large compared to the characteristic in-plane dimensions, the in-plane assumption should be used when the ratio between the dimensions is the other way around. The specific formulation of the constitutive relations can be found in appendix A.2.

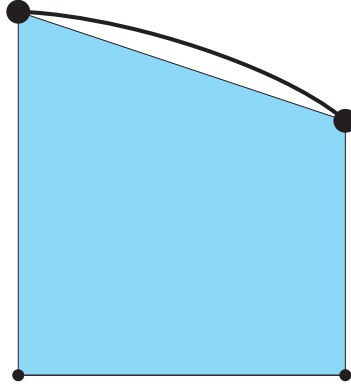


Figure 4.3: One beam element and one electrostatic element.

In the end a matrix vector equation is obtained:

$$\mathbf{K}\mathbf{u} = \mathbf{F}, \quad (4.1)$$

The electrostatic force discretization (eq. 2.113) yields nodal forces, which can be entered directly in the force vector.

Linear elasticity using beam elements

Classical beam elements are also an option when modeling the beam mechanics. If beam elements are used it is assumed that the displacement profile (not amplitude) in the direction perpendicular to the beam is known *a priori*. Therefore only elements in the other direction are required. In that case the finite element method is used to discretize the Euler-Bernoulli beam equation and not the already mentioned volume equations. The precise implementation and derivation of those elements is discussed in appendix A.2. Per node such an element has a displacement and a rotational degree of freedom.

Statically the solution obtained with this method is the exact solution to Euler-Bernoulli beam equation (see in the appendix equation (A.51)). Therefore theoretically only 2 elements are required for modeling the beam in this chapter. However the applied electrostatic force f_{elec} cannot be described exactly with only 2 elements, therefore more beam elements are required.

If dynamic contributions are added to the beam equation (A.51) it is not possible anymore to find an exact solution anymore with only two elements.

It has to be noted that beam elements have four DOFs each on the interface with the electric domain: two displacements and two rotations, one displacement and one rotation per node. Therefore the shape of the beam is not a straight line. This causes the meshes to not exactly match as is shown in figure 4.3. Because the rotations are very small it is assumed that this is not really a problem and the electric forces are computed using a mesh that assumes a straight line between two nodes. Thereafter the electric forces are simply applied on the displacement DOFs only.

Moving mesh

To compute the electrostatic solution for deformed configurations, the electrostatic stiffness matrix has to be reassembled over the deformed electrical domain. Therefore

it is crucial for any electromechanical model to deform the mesh of the electrostatic problem to be able to follow the displacements of the structure.

This means that a mesh deformation algorithm has to be implemented. In this work the following procedure is followed. At the initial configuration the electrostatic mesh is not only used to obtain the electric stiffness matrix, but also to obtain an elastic stiffness matrix. This stiffness matrix is obtained using a pseudo structure based on an uncoupled Laplace equation: if \mathbf{u}_x are the displacements of the nodes within the electrostatic mesh in x -direction and \mathbf{u}_y the displacements in y -direction, the following equations are used:

$$\nabla^2 \mathbf{u}_x = 0, \quad (4.2)$$

$$\nabla^2 \mathbf{u}_y = 0, \quad (4.3)$$

where the boundary conditions depend on the structural displacement.

4.2.5 Some Results

The deformed shape obtained with volume elements at the unstable equilibrium point of $V = 40$ and with a center node displacement of $u = 6 \cdot 10^{-6}$ is shown in figure 4.4. The deformed shape computed with beam elements is shown in figure 4.5. The shapes are very similar. Also it is clear that moving mesh routine deforms the electrostatic mesh nicely.

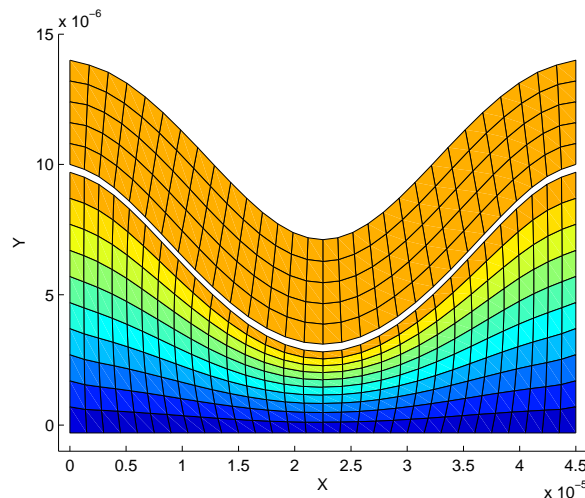


Figure 4.4: Deformed shape computed with volume elements (pot. ≈ 40 volts, disp. $\approx 6\mu$).

The load-displacement curves computed with three different types of elements are presented in figures 4.6 and 4.7. How to compute these curves will be presented in chapter 5. It is clear that the difference is very small. The plane strain elements are somewhat different from the other two, which is logical because the beam elements were derived for slender beams, which naturally undergo plane stress situation. The plane stress and beam element results are almost equal therefore it is acceptable to use beam elements combined with non-matching meshes.

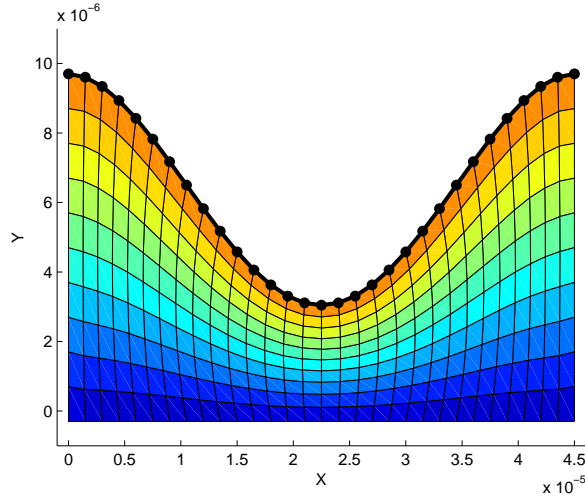


Figure 4.5: Deformed shape computed with beam elements (pot. ≈ 40 volts, disp. $\approx 6.5\mu$).

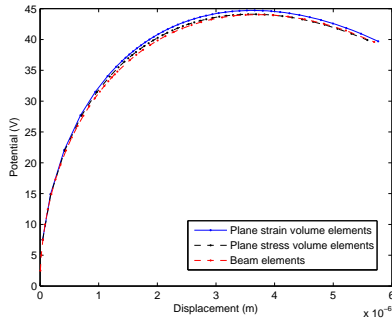


Figure 4.6: Load-displacement relation using several element types.

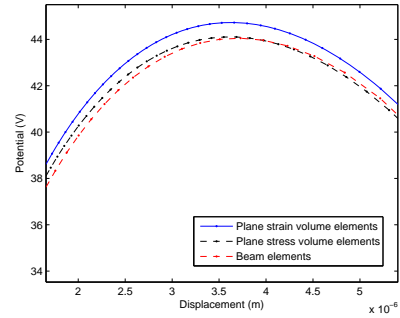


Figure 4.7: Close up of the load-displacement relation.

Another interesting test result is the convergence of the pull-in voltage with element size. There is no exact solution for this problem, but it is possible to compute the pull-in voltage with a very dense mesh (90 beam elements, $90 \cdot 30$ electrostatic elements) and look at the convergence of the voltage when discretized with a lower number of elements. The pull-in voltage computed with this dense mesh will be denoted by: V_{ref} and is equal to:

$$V_{ref} = 43.78. \quad (4.4)$$

The pull-in voltage was also computed with 4 other meshes that have each time n beam elements and $n \cdot \frac{1}{3}n$ electrostatic elements, where $n = 12, 24, 36, 48$. The error is defined as:

$$\text{Error}_n = \frac{|V_{PI}^n - V_{ref}|}{|V_{ref}|}. \quad (4.5)$$

The resulting voltage convergence is shown in figure 4.8. The black line in this figure gives the reference solution. The logarithmic relation between error and mesh density is plotted in figure 4.9. From this figure it is clear that there is approximately an order 2 convergence of the pull-in voltage.

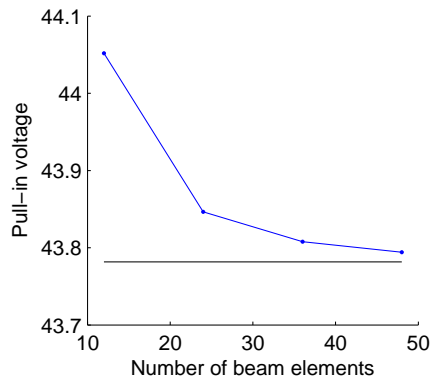


Figure 4.8: Pull-in voltage as function of the number of elements.

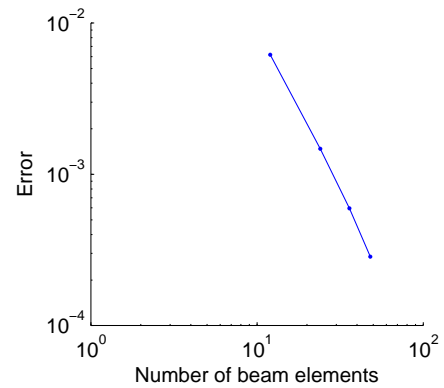


Figure 4.9: Error as function of the number of elements.

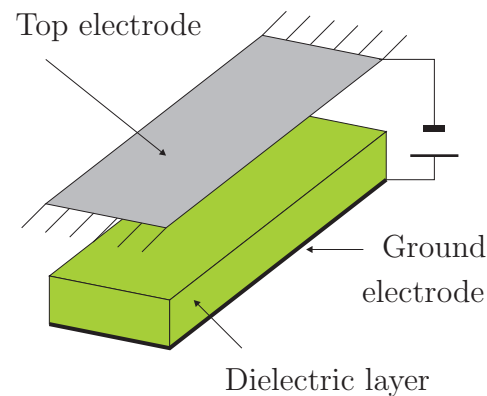
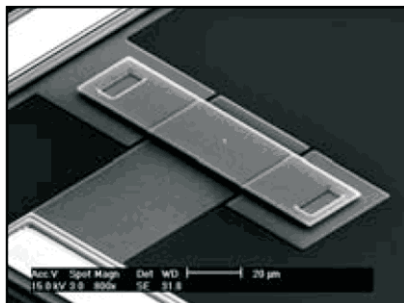


Figure 4.10: A microswitch and a model of a microswitch.

4.3 A three dimensional model

The next step is to introduce a 3D model. This model is the carrier model that will be used in the chapters dealing with squeeze film damping. The model is shown in figure 4.10 and is a model of a microswitch as shown in chapter 4. Since a microswitch can have contact with a dielectric layer a contact model is included with a very simple penalty method. Basically this just means that non-linear springs are added.

4.3.1 Mechanical domain

For the 2D simulations discussed until now 2D volume elements or beam elements were used. The 2D volume elements assumed piecewise linear shape functions in both directions, which requires a mesh of several elements in the direction perpendicular to the beam to capture the correct behavior. Beam elements use the fact that a stress-profile in the direction perpendicular to the beam can be assumed before simulation, therefore requiring only elements in longitudinal direction. The 3D equivalents of beam elements are plate elements. Because the assumptions of the stress field in the third direction are less straightforward than for beam elements there is wide variety of plate elements available in literature [135, 13, 146]. In this document a so called Reissner-Mindlin plate element based on mixed interpolation of the out-of-plane displacement,

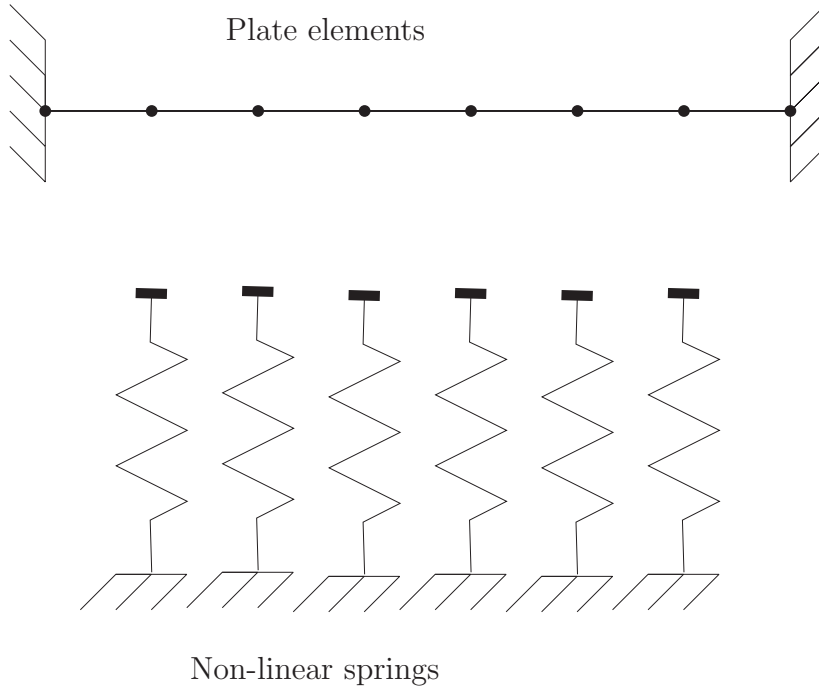


Figure 4.11: 2D projection of the mechanical domain.

rotations and out-of-plane shear strain components is used [12]. In the reference the used plate element is called the *MITC4* element.

The element has 4 nodes with at each node 3 DOFs: one displacement and two rotations. All three fields have their own independent piecewise linear interpolation field, for which coupling is obtained through the formulation of the element strain. An advantage of this element is its robustness with respect to shear locking [12]. Another advantage of this element is that the out-of-plane displacements are approximated by linear shape functions, ensuring that the electric mesh will match perfectly with the mechanical mesh.

The length of the plate is 45μ and the thickness of the plate is 4μ , both are the same as for the 2D models. The width of the beam is chosen to be 30μ . Both short edges are clamped, thus all DOFs are fixed.

In the dynamic simulations rotational inertia is neglected. Therefore the mass matrix can be written as:

$$\mathbf{M}_{uu} = \begin{bmatrix} \mathbf{M}_w & 0 & 0 \\ 0 & \mathbf{M}_{\theta_x} & 0 \\ 0 & 0 & \mathbf{M}_{\theta_y} \end{bmatrix} = \begin{bmatrix} \mathbf{M}_w & 0 & 0 \\ 0 & 0 & 0 \\ 0 & 0 & 0 \end{bmatrix}, \quad (4.6)$$

where \mathbf{M}_w is the mass working on the out-of-plane displacement and \mathbf{M}_{θ_x} is the inertia working on the rotation around the x -axis. For the mass matrix \mathbf{M}_w the consistent mass matrix:

$$\mathbf{M}_w = \int \rho \mathbf{N}_w \mathbf{N}_w^T dV, \quad (4.7)$$

is used, where \mathbf{N}_w are the shape functions used to discretize the displacement.

Contact is modeled with a penalty method [12], which basically means that non-linear springs are used to model the contact as shown in figure 4.11. They are only active if the displacement of the corresponding node is larger than the size of the air

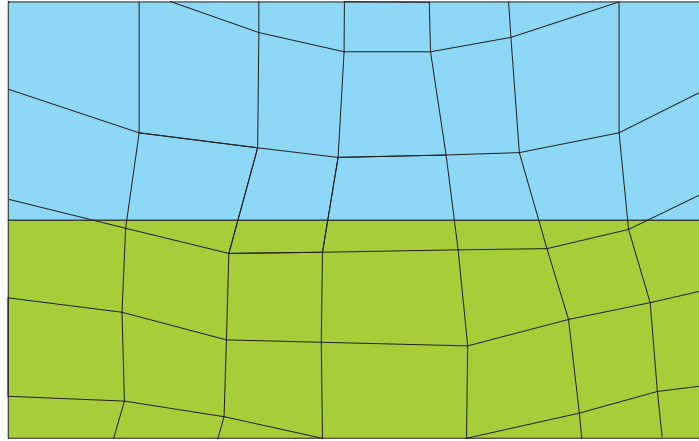


Figure 4.12: 2D projection of the mesh of a part of the deformed electrostatic domain.

gap. In that case the force is given by:

$$f_i = k_2(|u_i| - d)^2, \quad (4.8)$$

where d is the initial air gap and k_2 (N/m^2) is a constant that can be determined experimentally. For this chapter $k_2 = 5 \cdot 10^{11}$ was used.

The influence on the mechanical stiffness matrix is implemented as:

$$k_{ii} = 2 k_2(|u_i| - d). \quad (4.9)$$

If the maximum displacement reaches the gap size the increment size of the incremental-iterative procedure has to be reduced sharply.

4.3.2 Electrostatic domain

The electrostatic domain is meshed with linear 8 node hexahedral elements. The only important consideration is that the mesh is deformed into the dielectric for modeling the solid dielectric layer. If that would not have been done, the electric elements within the air gap would have been squeezed to a zero area, which would give conditioning problems.

Because the mesh is deformed into the dielectric layer some elements are initially part of the air gap, but will become part of the solid dielectric material during the simulation. This does not have to be a problem, because the electric matrices are re-computed at each solution step, therefore the dielectric properties can be changed at any time. The only problem is that the interface between air and dielectric can cut through an element as is shown in figure 4.12. If the dielectric constant of the layer is different from air this causes a discontinuity within the element. This discontinuity has to be accounted for and the eXtented-FEM (X-FEM) methods as presented in [109] and [6] would be ideal candidates for modeling that discontinuity. However for simplicity in this work the dielectric constant of the layer was chosen to be equal to that of air.

4.3.3 Results

The load displacement curve in figure 4.13 was obtained with this model. Also the deformed shape of the plate just before contact and when fully pulled against the

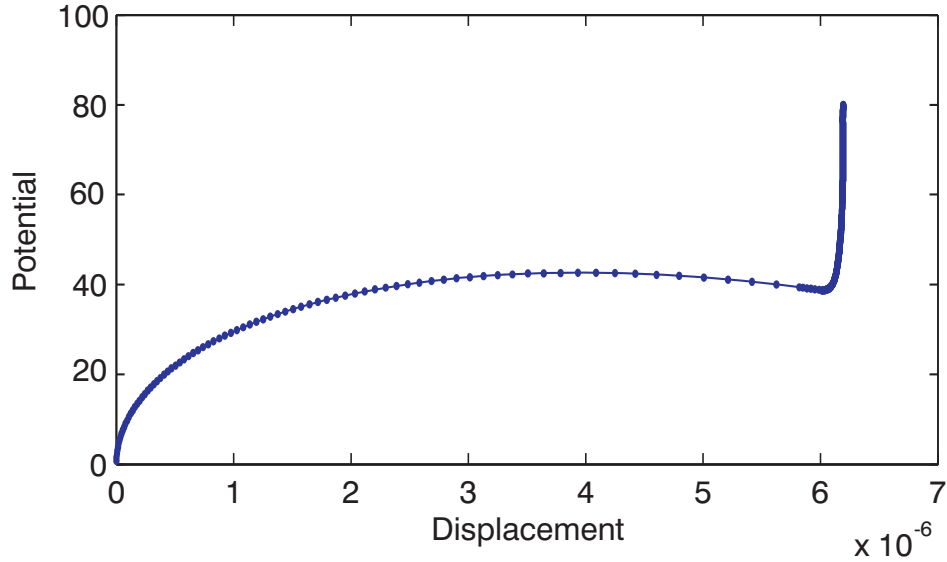


Figure 4.13: Quasi static load displacement curve of the plate model.

dielectric were computed and are shown in figures 4.14 and 4.15. The color in these figures indicates the magnitude of the out-of-plane displacement.

For MEMS modeling traditionally a lot of effort is put into the characterization of the eigenfrequency as function of applied potential or displacement [89, 108]. In chapter 5 it will be mentioned that it is easy to compute the eigenfrequencies of a coupled electro-mechanical system near the equilibrium positions. To compute the eigenfrequencies one has to find solutions to the eigenvalue problem:

$$\omega_i^2 \begin{bmatrix} \mathbf{M}_{uu} & 0 \\ 0 & 0 \end{bmatrix} \begin{bmatrix} \boldsymbol{\mu}_i^u \\ \boldsymbol{\mu}_i^\phi \end{bmatrix} - \begin{bmatrix} \mathbf{K}_{uu} & \mathbf{K}_{u\phi} \\ \mathbf{K}_{u\phi}^T & \mathbf{K}_{\phi\phi} \end{bmatrix} \begin{bmatrix} \boldsymbol{\mu}_i^u \\ \boldsymbol{\mu}_i^\phi \end{bmatrix} = 0, \quad (4.10)$$

where the matrices are evaluated at the equilibrium position. All matrices are symmetric, thus simple inverse power iteration suffices to compute the eigenfrequencies. The first eigenfrequency is only relevant up to the pull in point. It is plotted as a function of the applied potential in figure 4.16 and as a function of the displacement in figure 4.17. As was said in chapter 3 the eigenfrequency decreases when the potential is increased. The frequency finally becomes zero at the pull in voltage and displacement (43V, 3.7 μ). The curves are very similar to the analytically computed curves for a 1D model in section 3.3.

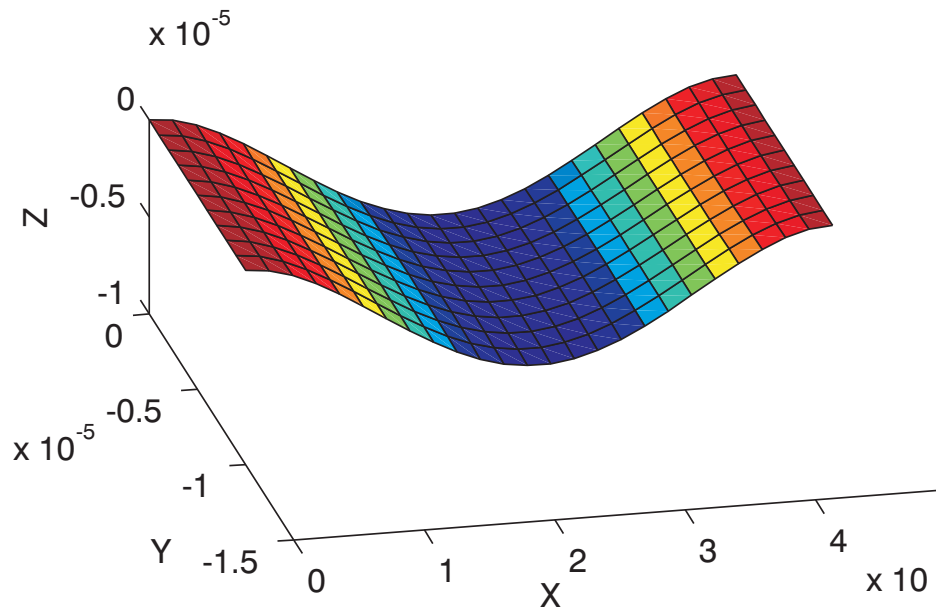


Figure 4.14: Deformation of the plate just before contact.

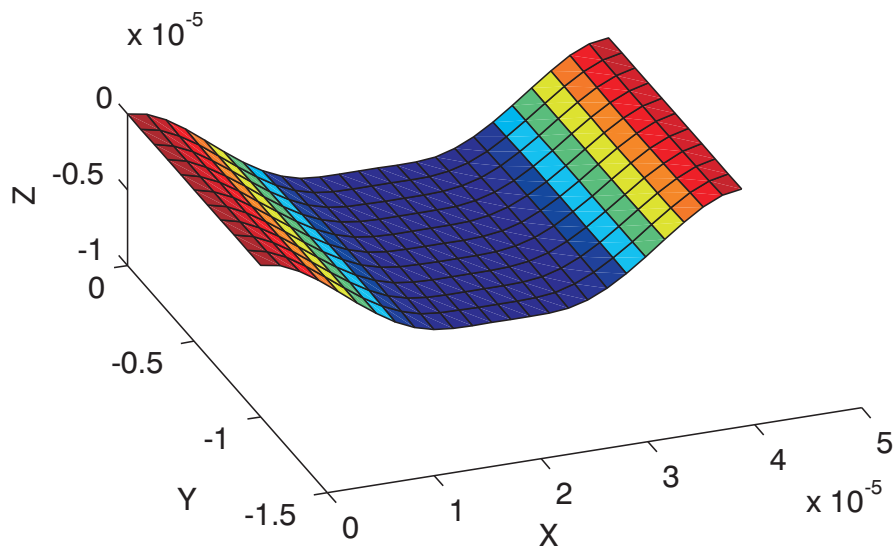


Figure 4.15: Final shape of the beam when fully pulled against the dielectric.

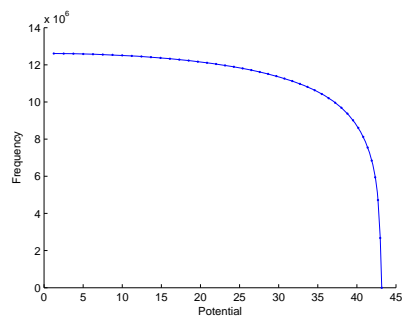


Figure 4.16: Frequency (rad/s) vs. applied potential (V).

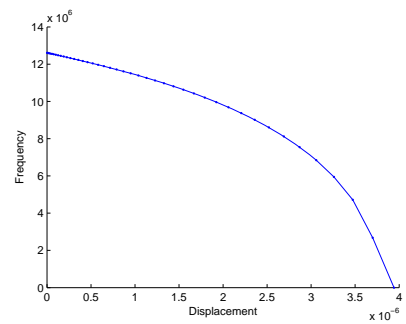
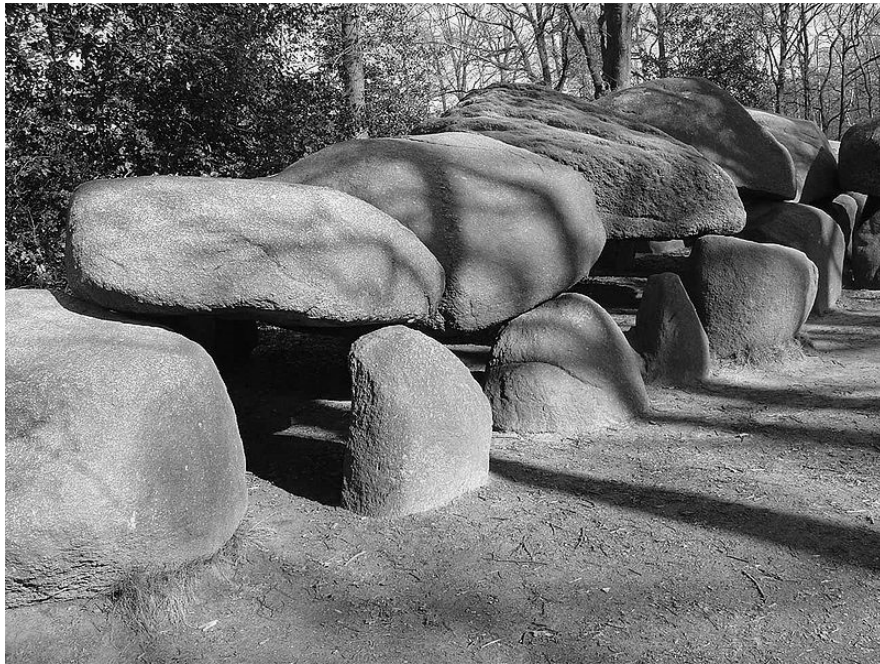


Figure 4.17: Frequency (rad/s) vs. equilibrium displacement (m).

Part II

Quasi-static simulation



Chapter 5

Computing the Load-Displacement curve

5.1 Introduction

The relation between the displacement and the electrical voltage displayed by MEMS is highly non linear. A feature of that nonlinear behavior is the pull-in phenomenon, which was introduced in the previous chapters (for a reference from literature see: [89]¹). To determine this pull-in voltage the load-displacement curve has to be known. This chapter discusses the algorithms that can be used for computing the load-displacement curve once a numerical model is available.

Therefore this chapter starts with an introduction to the incremental–iterative procedures that can be used to trace curves. After that section 5.3 discusses staggered procedures and section 5.4 discusses monolithic strategies. A short overview of some general implementation issues is presented section 5.5. Sections 5.6, 5.7 present some finite element test cases used to evaluate the methods. Once the optimal methods have been determined an experimental paper is used to verify if the methods can predict actual pull-in voltages accurately in section 5.8, after which branching is presented in sections 5.9 and 5.10. Section 5.11 completes the chapter by giving the conclusions.

5.2 Incremental–iterative algorithms

The discretized coupled equilibrium equations (3.44) and (3.48) were written in the form:

$$\mathbf{K}_{\phi\phi}(\mathbf{u})\phi = \mathbf{q}(\mathbf{u}, V), \quad (5.1)$$

$$\mathbf{K}_{uu}^m \mathbf{u} = \mathbf{f}^{elec}(\mathbf{u}, \phi, V), \quad (5.2)$$

where for the sake of simplicity, it was assumed that the mechanical and electrostatic problems are linear when taken separately. But the discussions in this chapter are also applicable if the mechanical problem is non-linear. The electrostatic equation is per definition linear with respect to the electric potentials. The computation of the external forces on the structure (\mathbf{f}^{elec}) from the potential distribution (ϕ) can be found in section 2.4.

¹This 1967 paper by Nathanson *et.al.* describes the first real MEMS and already discussed most aspects now used to characterize electro-mechanical microsystems

Essentially the coupled equations define a total set of equations of three (vectors of) unknowns: ϕ , \mathbf{u} and V . When the static state is defined as $\mathbf{U} = [\mathbf{u} \ \phi]^T$ the total set of equations can be written as:

$$\mathbf{F}(\mathbf{U}, V) = \mathbf{0}. \quad (5.3)$$

Let's call the number of electrical DOFs: n_e and the number of mechanical DOFs: n_m . In that case the total number of equations is as: $n_e + n_m$ and the total number of unknowns is: $n_e + n_m + 1$. Hence, there is one unknown more than there are equations.

This means there is not a single solution, but the equations define a curve, which was expected and seen before. The equations are non linear to such a degree that there does not exist a closed form solution $\mathbf{U}(V)$, which would define the load displacement curve required to characterize pull-in. Therefore iterative numerical solvers have to be used to solve the set of non-linear equations. However these solvers can only handle systems where the number of equations and the number of unknowns are equal. Hence an extra equation has to be defined to create $n_e + n_m + 1$ equations. An easy extra equation would be:

$$V = 1, \quad (5.4)$$

or equal to any other constant value. However many other constraints are imaginable.

With such a constraint the total system of equations can be solved, however this provides only one result for \mathbf{U} , not a curve. Therefore, the constraint has to be changed such that a new value for \mathbf{U} can be found. If this is done many times, many points on the curve are found. Those dots can be connected to form an approximation to the curve.

For instance, if the constraint is chosen to be a fixed potential, one could for instance start with $V = 0$ and solve for $\mathbf{U}(0)$. Then increase to $V = 1$ and solve for $\mathbf{U}(1)$. Then increase the constraint to $V = 2$ and so on. One such step from a point (e. g. $\mathbf{U}(1)$) to the next (e. g. $\mathbf{U}(2)$) is called an increment, which gives this type of stepping strategies their name: incremental-iterative procedures.

The type of constraint that is chosen determines for a large part the efficiency and applicability of the incremental-iterative algorithm. Therefore the text below will focus on the different options that are available or can be developed and compares them. A distinction will be made between staggered solution algorithms and monolithic algorithms.

5.3 Staggered solution strategies

5.3.1 Block Gauss-Seidel

The basic block Gauss-Seidel algorithm assumes a simple fixed applied voltage constraint in combination with a staggered solution procedure. The block Gauss-Seidel process at voltage increment V and at iteration step k can then be written as [10, 22]:

$$\phi_k = \mathbf{K}_{\phi\phi}^{-1}(\mathbf{u}_{k-1})\mathbf{q}(\mathbf{u}_{k-1}, V), \quad (5.5)$$

$$\mathbf{u}_k = \mathbf{K}_{uu}^{m-1}\mathbf{f}^{elec}(\mathbf{u}_{k-1}, \phi_k, V), \quad (5.6)$$

which were reported before: (3.51) and (3.52). This provides the estimate of the equilibrium position at k , based on the static state at $k-1$. Making a new estimate with

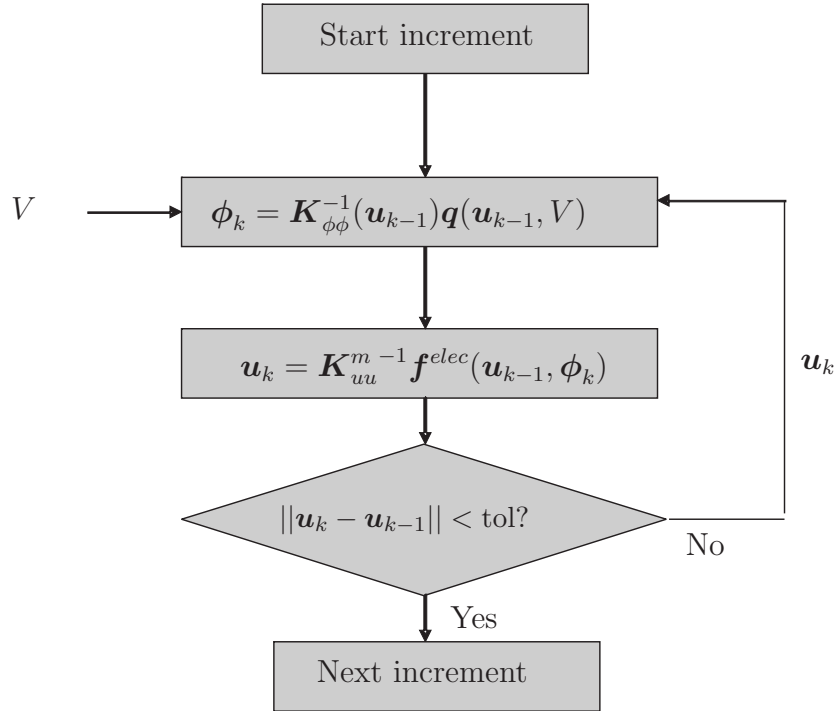


Figure 5.1: The block Gauss-Seidel algorithm.

this procedure can be repeated until convergence. The algorithm is converged when the update for the displacements is smaller than a specified tolerance ($\|\mathbf{u}_k - \mathbf{u}_{k-1}\| < \text{tol}$). The block diagram for the procedure can be found in figure 5.1. The actuation charge $\mathbf{q}(\mathbf{u}_{k-1}, V)$ can be computed with equation (A.16).

This algorithm has problems with converging near the pull-in point. This can best be shown graphically as in figure 5.2. Here it can be seen that the algorithm converges well from A to B and from B to C , but it diverges when the total applied load above the pull-in as shown for the step to D .

5.3.2 Block Gauss-Seidel with path following

The traditional method to overcome similar problems in limit point buckling simulation is by using path-following techniques also known as arc-length methods [71]. These methods go back to the early papers by E. Riks [105] and M.A. Crisfield [27]. The basic idea is the addition of an extra constraint to the set of equations that is a function of both \mathbf{U} and V . The circular version of such a constraint is shown in figure 5.3. The algorithm with this circular constraint is known as the Riks-Crisfield algorithm. However other options are possible as well, such as the Riks-Wempner and normal flow constraints [101].

Since these algorithms are originally developed for monolithic models, first a short discussion about the monolithic Riks Crisfield algorithms is required. Of course the extra constraint could be applied by simply adding one equation to the matrix equations and solve the augmented system, but that destroys the symmetric, banded and sparse structure of the original system of equations, therefore the original paper of Crisfield advised a more elegant implementation. The discussion of this implementation start

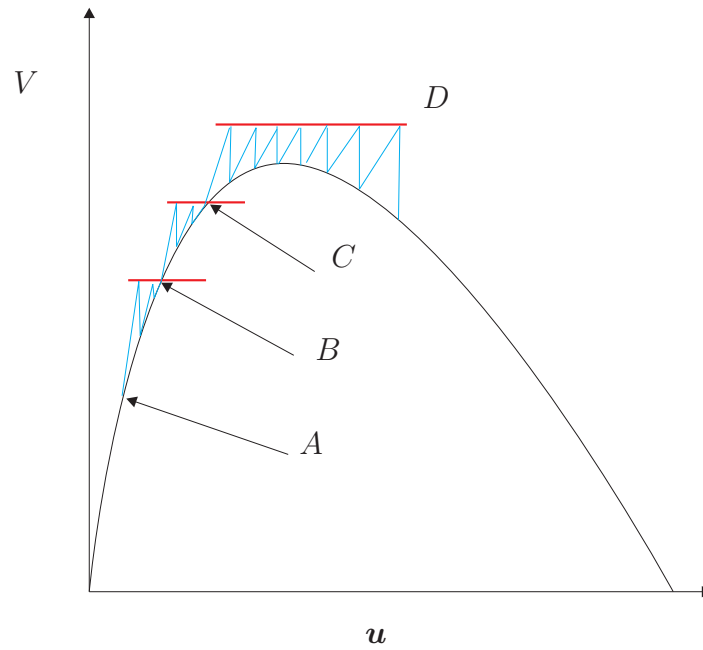


Figure 5.2: Several block Gauss-Seidel increments (schematic representation).

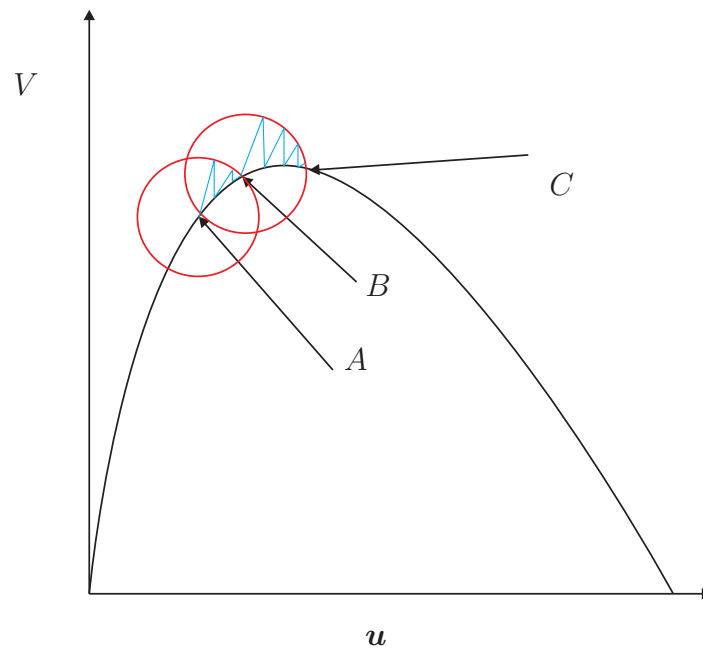


Figure 5.3: Several block iterative arc-length iterations (schematic representation).

with the definition of the derivative of the load vector \mathbf{F} with the load factor V :

$$\hat{\mathbf{F}} = \frac{\partial \mathbf{F}}{\partial V}, \quad (5.7)$$

and the derivative of \mathbf{U} with V :

$$\hat{\mathbf{U}} = \mathbf{K}^{-1} \hat{\mathbf{F}}. \quad (5.8)$$

Subsequently it is assumed that the system is not yet in equilibrium. In that case the total applied load on the system at iteration k can be approximated by:

$$\mathbf{F}_{k+1}^{elec} = \mathbf{F}_k^{elec} + dV_{k+1} \hat{\mathbf{F}}, \quad (5.9)$$

therefore through equation (3.53) the linear update required to approach equilibrium is:

$$d\mathbf{U}_{k+1} = \mathbf{K}^{-1} (dV_{k+1} \hat{\mathbf{F}} + \mathbf{F}_k^{elec} - \mathbf{F}_k^{int}). \quad (5.10)$$

which can be separated in:

$$d\mathbf{U}_{k+1} = d\mathbf{U}_s + dV_{k+1} \hat{\mathbf{U}}, \quad (5.11)$$

where:

$$d\mathbf{U}_s = \mathbf{K}^{-1} (\mathbf{F}_k^{elec} - \mathbf{F}_k^{int}). \quad (5.12)$$

During an increment the norm of the allowed displacement increment (of all DOFs, thus structural DOFs and potential DOFs) augmented with the load increment is kept constant:

$$\Delta \mathbf{U}_{k+1}^T \Delta \mathbf{U}_{k+1} + \Delta V_{k+1}^2 \hat{\mathbf{F}}^T \hat{\mathbf{F}} = S^2, \quad (5.13)$$

where S is the constraint on the increment. Because S remains constant from iteration k to $k+1$ this equation can also be written as:

$$\Delta \mathbf{U}_{k+1}^T \Delta \mathbf{U}_{k+1} + \Delta V_{k+1}^2 \hat{\mathbf{F}}^T \hat{\mathbf{F}} = \Delta \mathbf{U}_k^T \Delta \mathbf{U}_k + \Delta V_k^2 \hat{\mathbf{F}}^T \hat{\mathbf{F}}. \quad (5.14)$$

The total increments are defined as:

$$\Delta \mathbf{U}_{k+1} = \Delta \mathbf{U}_k + d\mathbf{U}_{k+1}, \quad (5.15)$$

$$\Delta V_{k+1} = \Delta V_k + dV_{k+1}. \quad (5.16)$$

Substitution of these increments and equation (5.11) into equation (5.14) yields:

$$a dV_{k+1}^2 + b dV_{k+1} + c = 0, \quad (5.17)$$

where:

$$a = \hat{\mathbf{F}} \cdot \hat{\mathbf{F}} + \hat{\mathbf{U}} \cdot \hat{\mathbf{U}}, \quad (5.18)$$

$$b = 2 \left(\Delta V_k \hat{\mathbf{F}} \cdot \hat{\mathbf{F}} + \Delta \mathbf{U}_k \cdot \hat{\mathbf{U}} + \hat{\mathbf{U}} \cdot d\mathbf{U}_s \right), \quad (5.19)$$

$$c = 2\Delta \mathbf{U}_k \cdot d\mathbf{U}_s + d\mathbf{U}_s \cdot d\mathbf{U}_s, \quad (5.20)$$

which can be used to compute dV_{k+1} once $d\mathbf{U}_s$ has been computed with equation (5.12). All other terms have been computed during the previous iteration step or at the beginning of the increment. When dV_{k+1} is known, $d\mathbf{U}_{k+1}$ can be computed with equation (5.11). It is obvious that equation (5.17) has two solutions, therefore the

correct one has to be selected. Because for electro-mechanical problems the desired solution always has a larger displacement than the previous converged solution, it is not difficult to select the correct solution to (5.17).

Problems arise at $k = 1$ since in that case ΔV_1 and $\Delta \mathbf{U}_1$ have not yet been defined, thus ΔV_2 and $\Delta \mathbf{U}_2$ cannot be computed. An easy approach to solve that problem is to define ΔV_1 as the control parameter for the algorithm and to use $\Delta \mathbf{U}_1 = \Delta V_1 \hat{\mathbf{U}}$ as initial displacement step. This effectively defines S .

In a block iterative procedure it proves to be very difficult to use the full circular constraint on all DOFs because the full tangent stiffness is not known. But it is possible to assume that the problem is purely mechanical with a very complicated external force, that depends on the potential V and displacements \mathbf{u} . Or in other words the electrostatic is condensed onto the mechanics:

$$\mathbf{f}^{elec} = \mathbf{f}^{elec}(\mathbf{u}, V), \quad (5.21)$$

with the extra assumption:

$$\hat{\mathbf{f}} = \frac{\partial \mathbf{f}^{elec}(\mathbf{u}, V)}{\partial V} \approx \frac{1}{\Delta V_1} (\mathbf{f}^{elec}(\mathbf{u}, V + \Delta V_1) - \mathbf{f}^{elec}(\mathbf{u}, V)). \quad (5.22)$$

Theoretically it is possible to use a full circular constraint on the mechanical DOFs only. This would mean that one only has to replace \mathbf{U} with \mathbf{u} in equation (5.13) to get the staggered algorithm. However simulations showed that a linearized version of the circular constraint condition works better in the staggered case. The linearized constraint can be written as [28]:

$$\Delta \mathbf{u}_k^T \Delta \mathbf{u}_{k+1} + \Delta V_k \Delta V_{k+1} \hat{\mathbf{f}}^T \hat{\mathbf{f}} = S^2, \quad (5.23)$$

which is a linear function of $\Delta \mathbf{u}_{k+1}$. After the relevant substitutions this yields the following relation to determine dV_{k+1} :

$$dV_{k+1} = -\frac{\Delta \mathbf{u}_k \cdot d\mathbf{u}_s}{\Delta \mathbf{u}_k \cdot \Delta \hat{\mathbf{u}}}, \quad (5.24)$$

where:

$$d\mathbf{u}_s = \mathbf{K}_{uu}^{-1} \Delta \mathbf{f}_k. \quad (5.25)$$

The complete algorithm is summarized by the diagram in figure 5.4.

5.3.3 Fixed point iterations with displacement control

Another strategy to tackle the convergence problem of the Gauss-Seidel iterations is to use displacement control: a displacement DOF is given a prescribed displacement. Thus instead of an constraint on V , or on both \mathbf{u} and V simultaneously, an constraint on one entry of \mathbf{u} is used. Once an element of \mathbf{u} has been constrained a block Gauss-Seidel iteration loop is started to compute the corresponding voltage as is illustrated in figure 5.5.

However for problems with more than one DOF this is not a trivial problem, therefore a relaxation scheme called DIPIE has been proposed in literature [18]. The algorithm uses the quadratic dependency of \mathbf{f}^{elec} on the applied potential V :

$$\mathbf{f}_{elec}(V) = (\mathbf{f}^{elec}(V = 1)) V^2, \quad (5.26)$$

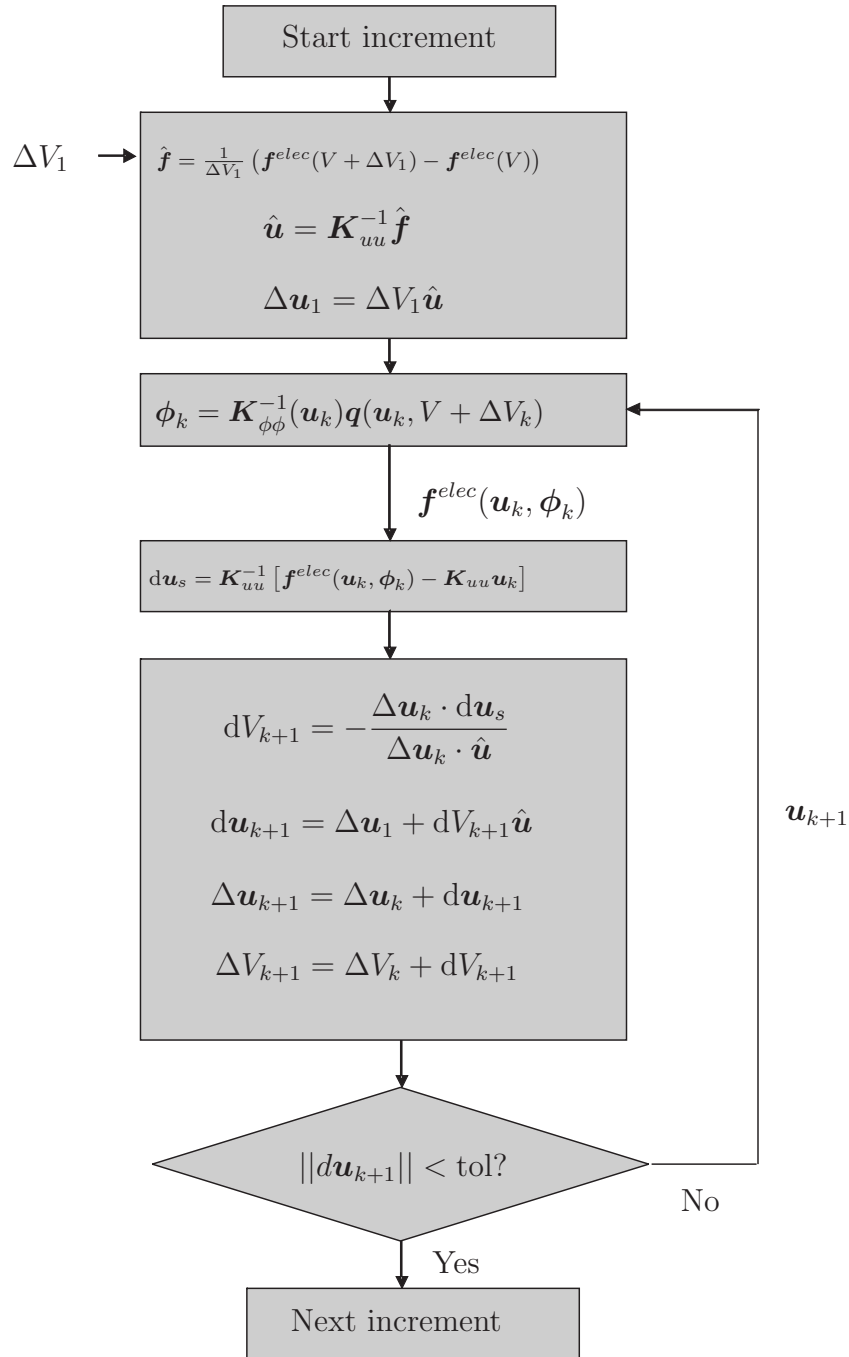


Figure 5.4: The block Gauss-Seidel with path-following algorithm.

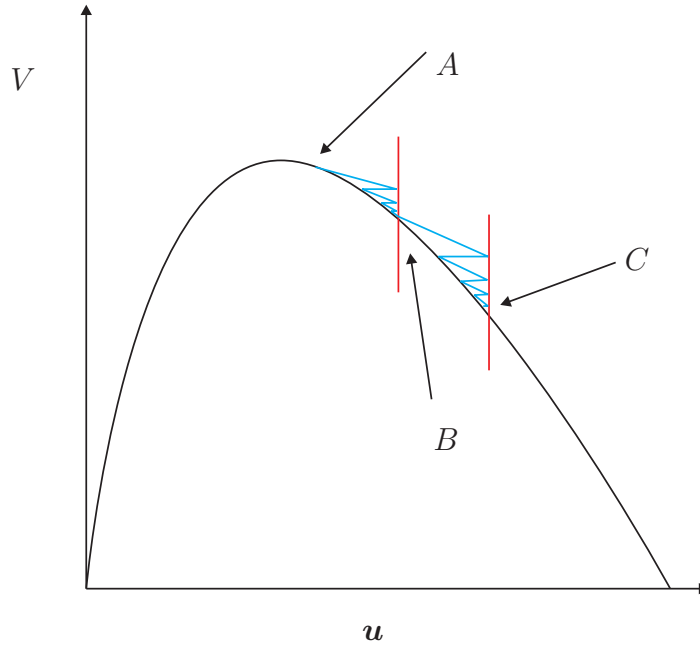


Figure 5.5: Several displacement iterations.

combined with the fact that at equilibrium:

$$\mathbf{f}^{elec} = \mathbf{f}^{int}, \quad (5.27)$$

where:

$$\mathbf{f}^{int} = \mathbf{K}_{uu}^m \mathbf{u}. \quad (5.28)$$

If the system has an imposed displacement \mathbf{u}_k , a guess of the corresponding voltage would be:

$$V^2 = \frac{1}{n} \sum_{i=1}^n \frac{f_i^{int}(\mathbf{u}_k)}{f_i^{elec}(\mathbf{u}_k, V=1)}, \quad (5.29)$$

where i indicates those n DOFs that have a non zero entry in the electric force vector \mathbf{f}^{elec} . Once this initial guess is made an update of the mechanical force can be done:

$$\mathbf{f}^{int}(\mathbf{u}_{k+1}) = V^2 \mathbf{f}^{elec}(\mathbf{u}_k, V=1), \quad (5.30)$$

which can be used to update the displacement. This can be repeated until convergence.

The convergence of the algorithm depends to a large extent on the chosen initial deformation. The authors of the original paper suggest prescribing the displacement \bar{u}^j of the node j for which the largest displacement is expected. The initial deflection \mathbf{u}_1 of the structure follows from a simple Dirichlet problem:

$$\mathbf{K}_{uu}^m \mathbf{u}_1 = \begin{bmatrix} \mathbf{K}_{uu} & \mathbf{K}_{u\bar{u}} \\ \mathbf{K}_{u\bar{u}}^T & \mathbf{K}_{\bar{u}\bar{u}} \end{bmatrix} \begin{bmatrix} \mathbf{u} \\ \bar{u}^j \end{bmatrix} = \begin{bmatrix} 0 \\ F_j^{int} \end{bmatrix} = \mathbf{F}^{int}, \quad (5.31)$$

$$\mathbf{u} = -\mathbf{K}_{uu}^{-1} \mathbf{K}_{u\bar{u}} \bar{u}^j. \quad (5.32)$$

For a proper convergence it is essential to keep the prescribed DOF at the same displacement while updating the displacement with equation (5.30). This can be assured by including the structural Dirichlet problem in the formulation.

A block diagram summary of the complete algorithm can be found in figure 5.6. Effectively this algorithm uses a fixed point iteration procedure around the equilibrium solution.

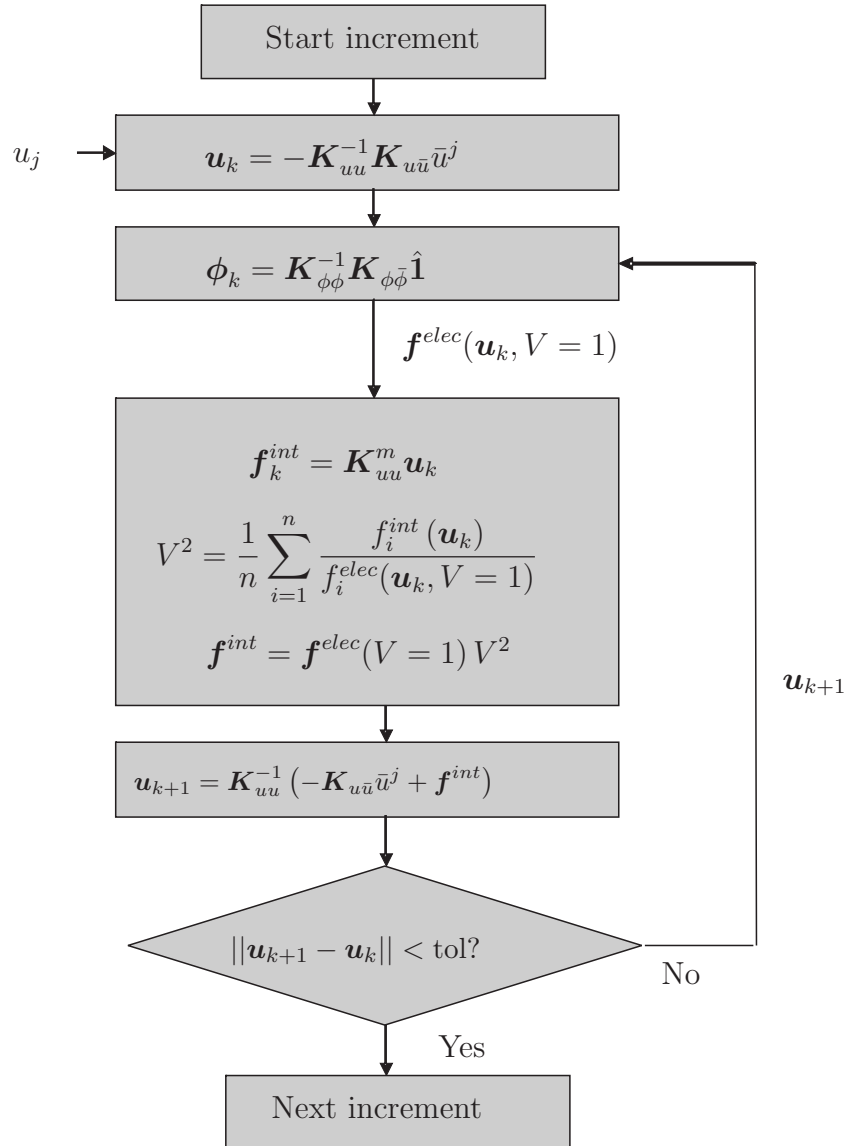


Figure 5.6: The DIPIE algorithm.

5.3.4 Block Gauss-Seidel with charge control

A new approach to solve these types of problems is inspired by some motion control strategies used for actual MEMS [88, 117]. The idea is to prescribe the total electric charge instead of the voltage on the moving conductor. Thereafter the voltage can be determined by a post processing step. The advantage of this method is explained with the 1D example problem originally presented in section 3.3 and shown in figure 3.2. Thereafter the implications of charge control for multiple DOF systems will be discussed.

In chapter 2 it was shown that Coulomb's law implicated that the force on a 1D charged conductor is:

$$F_{es} = \frac{1}{2}QE, \quad (5.33)$$

with E the field outside the conductor, that can be written as:

$$E = \frac{1}{\varepsilon}Q. \quad (5.34)$$

Thus the force becomes equal to:

$$F_{es} = \frac{1}{2\varepsilon}Q^2, \quad (5.35)$$

resulting in the equation of motion:

$$m\ddot{x} + k(x - x_0) + \frac{1}{2\varepsilon}Q^2 = 0. \quad (5.36)$$

Hence the static equilibrium equation is:

$$Q = \sqrt{2\varepsilon k(x_0 - x)}. \quad (5.37)$$

which is a monotonously increasing function as can be seen in figure 5.7. Hence unlike the voltage-displacement curve it does not have an extremum and moreover it shows less non-linear behavior. It will be easier to follow the charge-displacement curve and extract from it the voltage-displacement curve and pull-in characteristics by post-processing.

For more complicated structures it is not possible to simply apply the charge on the moving structure, because the charge distribution over the structure depends on the shape of the electric domain. However due to the assumption that electrodes are perfect conductors it is known that the potential over the conductor is constant, which effectively defines an equipotential constraint. Thus the charge can be applied on one DOF of the conductor boundary only in combination with an equipotential constraint, as will be explained below.

The electric problem can be separated in a free (ϕ) and a constrained ($\bar{\phi}$) part:

$$\begin{bmatrix} \mathbf{K}_{\phi\phi} & \mathbf{K}_{\phi\bar{\phi}} \\ \mathbf{K}_{\phi\bar{\phi}}^T & \mathbf{K}_{\bar{\phi}\bar{\phi}} \end{bmatrix} \begin{bmatrix} \phi \\ \bar{\phi} \end{bmatrix} = \begin{bmatrix} \mathbf{q} \\ \bar{\mathbf{q}} \end{bmatrix}. \quad (5.38)$$

For this problem there are three ways to implement the equipotential constraint on a surface: using Lagrange multipliers, using a transformation matrix or using an infinite electric permittivity. When Lagrange multipliers are used the constraint is written as:

$$\mathbf{B}\bar{\phi} = \mathbf{0}, \quad (5.39)$$

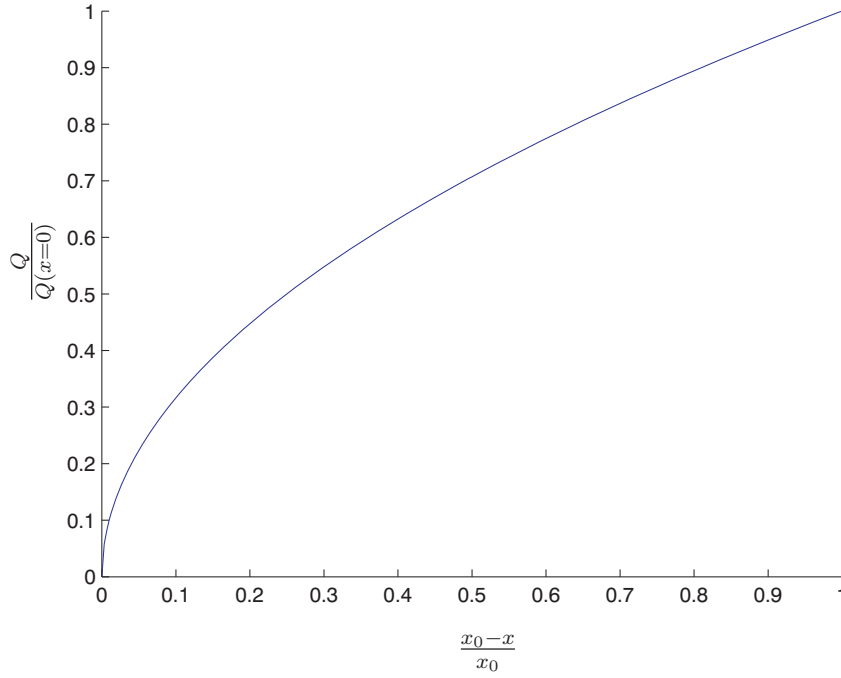


Figure 5.7: 1D charge-displacement curve

where \mathbf{B} is a $n_c - 1$ by n_c matrix, with n_c the number of constrained DOFs:

$$\mathbf{B} = \begin{bmatrix} 1 & -1 & 0 & \cdots & 0 \\ 0 & 1 & -1 & & \vdots \\ \vdots & & \ddots & \ddots & 0 \\ 0 & \cdots & 0 & 1 & -1 \end{bmatrix}. \quad (5.40)$$

In that case the total electric problem can be written as:

$$\begin{bmatrix} \mathbf{K}_{\phi\phi} & \mathbf{K}_{\phi\bar{\phi}} & 0 \\ \mathbf{K}_{\phi\bar{\phi}}^T & \mathbf{K}_{\bar{\phi}\bar{\phi}} & \mathbf{B}^T \\ 0 & \mathbf{B} & 0 \end{bmatrix} \begin{bmatrix} \phi \\ \bar{\phi} \\ \lambda \end{bmatrix} = \begin{bmatrix} \mathbf{q} \\ \bar{\mathbf{q}} \\ \mathbf{0} \end{bmatrix}, \quad (5.41)$$

where the block-iterative procedure can be controlled with the partial charge on one of the constrained DOFs $\bar{\mathbf{q}}$.

When the constraint is implemented using a transformation matrix the starting point is the following relation:

$$\hat{\phi} = \hat{\mathbf{1}}V, \quad (5.42)$$

where:

$$\hat{\mathbf{1}} = \begin{bmatrix} 1 \\ \vdots \\ 1 \end{bmatrix}. \quad (5.43)$$

Thus the electric problem can be written as:

$$\begin{bmatrix} \mathbf{K}_{\phi\phi} & \mathbf{K}_{\phi\bar{\phi}}\hat{\mathbf{1}} \\ \hat{\mathbf{1}}^T \mathbf{K}_{\phi\bar{\phi}}^T & \hat{\mathbf{1}}^T \mathbf{K}_{\bar{\phi}\bar{\phi}} \hat{\mathbf{1}} \end{bmatrix} \begin{bmatrix} \bar{\phi} \\ V \end{bmatrix} = \begin{bmatrix} \mathbf{q} \\ \bar{q}_{total} \end{bmatrix}, \quad (5.44)$$

which can be written as:

$$\mathbf{K}_{\phi} \tilde{\phi} = \tilde{\mathbf{q}}, \quad (5.45)$$

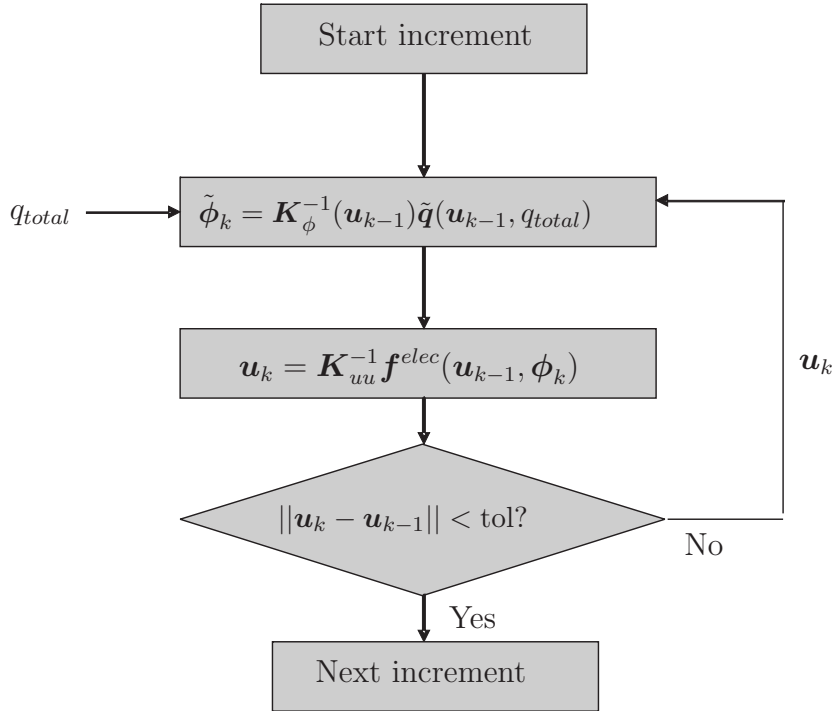


Figure 5.8: The charge block Gauss-Seidel algorithm.

where $\bar{q}_{total} = \hat{\mathbf{1}}^T \bar{\mathbf{q}}$ is the total charge on the equipotential surface. This value can be used as loading parameter in the block-iterative procedure.

The third way to model the constraint is by meshing the conductor with elements that are given a permittivity that is much higher than the permittivity in the gap. In that case the control charge can be applied on one of the conductor nodes. This will not exactly constrain the potentials on the conductor, but when the used permittivity is high enough the effect will be nearly the same.

For the computations in this document the constraint was implemented using the transformation approach, because that results in the smallest set of equations. The summary of this algorithm can be found in figure 5.8, which is very similar to the voltage loaded scheme. The true difference is in the computation of $\phi_k(\mathbf{u}_{k-1}, \bar{q}_{total})$. The original voltage loaded algorithm used equation (A.16) while the charge loaded algorithm uses equation (5.44).

There are two pitfalls when using the charge loading approach; the first one is the so-called charge pull-in. When systems with more than one DOF are investigated, fringe effects cause instability in the charge displacement relation as well. However, the charge pull-in point is generally located well beyond the voltage pull-in point [117].

The second pitfall is caused by structurally non-linear problems, especially those that show snap-trough behavior. This can simply be seen in the 1D model: if a non-linear stiffness $k = k(x)$ is substituted to equation (5.37), the resulting charge-displacement relation is:

$$Q = \sqrt{2\varepsilon k(x)(x_0 - x)}, \quad (5.46)$$

which for some functions $k(x)$ can show a (local) decrease in the relation between Q and x .

When it is needed to compute the curve beyond the charge pull-in or if non-linear snapping is expected, the charge loading method can be combined easily with arc-length

control.

5.4 Monolithic solution strategies

5.4.1 Newton-Raphson

As has been mentioned in section 5.3 the general equilibrium equations are:

$$\mathbf{K}_{uu}^m \mathbf{u} = \mathbf{f}^{elec}(\mathbf{u}, \phi, V), \quad (5.47)$$

$$\mathbf{K}_{\phi\phi}(\mathbf{u})\phi = \mathbf{q}(\mathbf{u}, V). \quad (5.48)$$

Furthermore the static state and force vectors were defined as:

$$\mathbf{U} = \begin{bmatrix} \mathbf{u} \\ \phi \end{bmatrix}, \quad (5.49)$$

$$\mathbf{F} = \begin{bmatrix} \mathbf{f} \\ \mathbf{q} \end{bmatrix}, \quad (5.50)$$

and the coupled tangent stiffness matrix was defined by (see chapter 3):

$$\mathbf{K}(\mathbf{U}) = \frac{\partial \mathbf{F}}{\partial \mathbf{U}}, \quad (5.51)$$

which can be used to define the linearization of the equilibrium equations:

$$\mathbf{K}\Delta\mathbf{U} = \Delta\mathbf{F} = \mathbf{F}^{elec} - \mathbf{F}^{int}. \quad (5.52)$$

The matrix \mathbf{K} depends on the static state vector \mathbf{U} , therefore computation of \mathbf{K} is a costly procedure, which is a disadvantage of all monolithic methods.

The basic monolithic solution algorithm for non-linear problems is the Newton-Raphson algorithm. For an electro-mechanical problem it can be used as follows. For a certain applied voltage the unbalance in the right hand-side of the equation at iteration step k is:

$$\Delta\mathbf{F}_k = \mathbf{F}^{elec}(\mathbf{U}_{k-1}, V) - \mathbf{F}^{int}(\mathbf{U}_{k-1}), \quad (5.53)$$

therefore, through the linearized equilibrium equations, the update for the displacements is:

$$\Delta\mathbf{U}_k = \mathbf{K}^{-1}\Delta\mathbf{F}_k, \quad (5.54)$$

which can be used to find the displacement at iteration k :

$$\mathbf{U}_k = \mathbf{U}_{k-1} + \Delta\mathbf{U}_k. \quad (5.55)$$

The algorithm is summarized by the diagram in figure 5.9.

The advantage of the Newton-Raphson (and other monolithic methods) can be explained graphically. Figure 5.10 shows two type of iterations: on the left are several block Gauss-Seidel iterations and on the right are several Newton-Raphson iterations². For the Gauss-Seidel iterations the mechanical tangent stiffness is not updated, only the external force is updated, therefore convergence is relatively slow. For the

²It should be noted that although these drawings give a simplified view, which is not completely correct. However the drawings do give a view that is accurate enough for illustrative purposes.

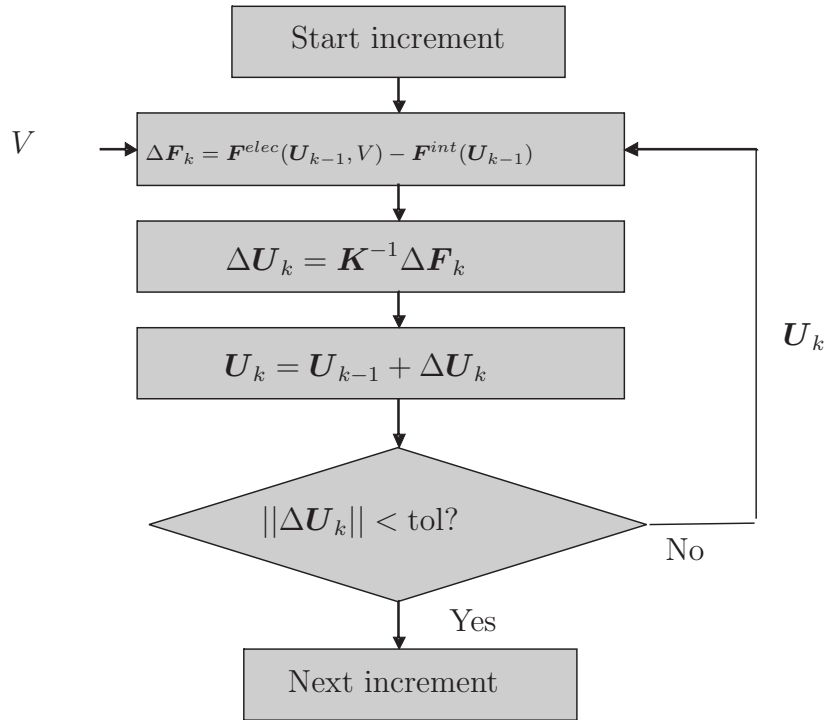


Figure 5.9: The coupled Newton-Raphson algorithm.

Newton-Raphson iterations the full tangent is updated at each iteration step, therefore convergence is relatively fast.

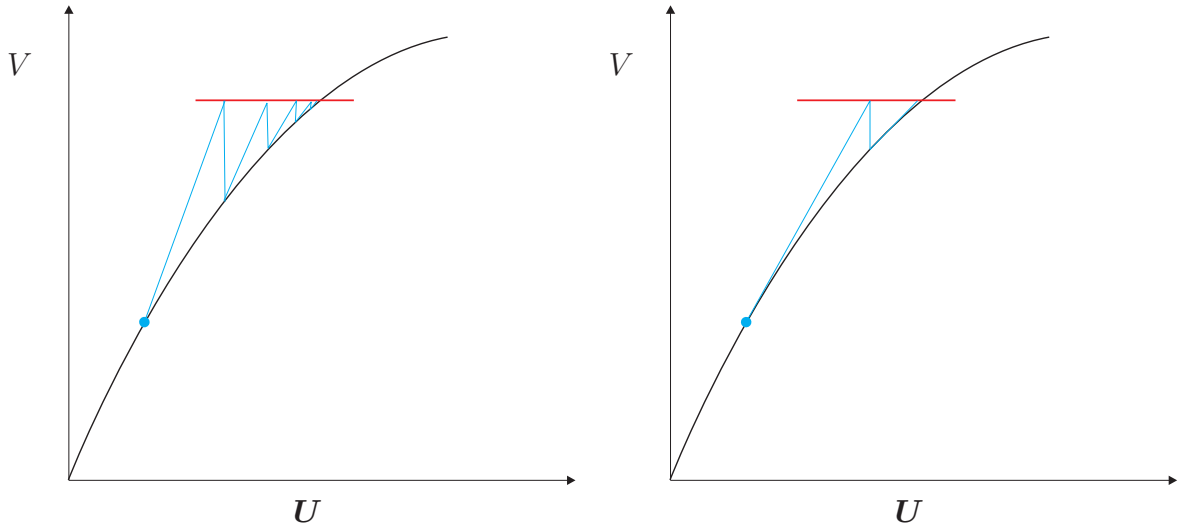
As mentioned this faster convergence comes at the price of updating the stiffness, therefore alternative procedures have been proposed. One often used method is derived from the Newton-Raphson. The difference is that the stiffness matrix is updated only at the beginning of an increment and not at every iteration step. This method is known as the the modified Newton-Raphson method [28], and is faster for some type of problems. A different class of methods is that of the quasi-Newton methods. These methods use the previously computed equilibriums to approximate the tangent. One such method is the well known BFGS algorithm [94].

5.4.2 Monolithic path-following

The monolithic Riks-Crisfield method of path-following was derived in section 5.3.2 as a starting point for the staggered path-following method. Riks-Crisfield adds a circular constraint to the set of equations, which makes sure that not only the state vector \mathbf{U} is updated, but also the applied load V . The visual interpretation of monolithic Riks-Crisfield is given in figure 5.11, which slightly differs from the monolithic arc-length method in figure 5.3.

This resulted in the following equation for the load parameter update dV :

$$a dV_{k+1}^2 + b dV_{k+1} + c = 0, \quad (5.56)$$



a: Gauss-Seidel iterations.

b: Newton Raphson iterations.

Figure 5.10: The advantage of Newton-Raphson iterations.

where:

$$a = \hat{\mathbf{F}} \cdot \hat{\mathbf{F}} + \hat{\mathbf{U}} \cdot \hat{\mathbf{U}}, \quad (5.57)$$

$$b = 2 \left(\Delta V_k \hat{\mathbf{F}} \cdot \hat{\mathbf{F}} + \Delta \mathbf{U}_k \cdot \hat{\mathbf{U}} + \hat{\mathbf{U}} \cdot d\mathbf{U}_s \right), \quad (5.58)$$

$$c = 2\Delta \mathbf{U}_k \cdot d\mathbf{U}_s + d\mathbf{U}_s \cdot d\mathbf{U}_s, \quad (5.59)$$

where:

$$\hat{\mathbf{U}} = \mathbf{K}^{-1} \hat{\mathbf{F}}, \quad (5.60)$$

and:

$$d\mathbf{U}_s = \mathbf{K}^{-1} (\mathbf{F}_k^{elec} - \mathbf{F}_k^{int}). \quad (5.61)$$

The displacement update is than:

$$d\mathbf{U}_{k+1} = d\mathbf{U}_s + dV_{k+1} \hat{\mathbf{U}}. \quad (5.62)$$

This method seems to be a bit over complicated to impose a constraint, because the constraint can also be added to the original equilibrium equations (3.53). That was actually the approach proposed by Riks in 1979 when he proposed the linearized version of Riks-Crisfield [105]. However in that case the problem becomes asymmetric, therefore when Crisfield proposed to use the full circular version in 1981 he also rewrote the formulation to remove the asymmetry [27]. This required solving one extra equation (5.60) at the beginning of each increment. But solving symmetric systems is much faster than solving asymmetric systems and \mathbf{K} is already factorized at that moment, therefore the Crisfield formulation is normally used.

The remaining issue is the computation of $\hat{\mathbf{F}}$. To compute the term $\frac{\partial \mathbf{F}}{\partial V}$ can be started with differentiating equation (3.82):

$$\frac{\partial}{\partial V} (\mathbf{F}) = \frac{\partial}{\partial V} (\mathbf{F}^{elec} - \mathbf{F}^{int}). \quad (5.63)$$

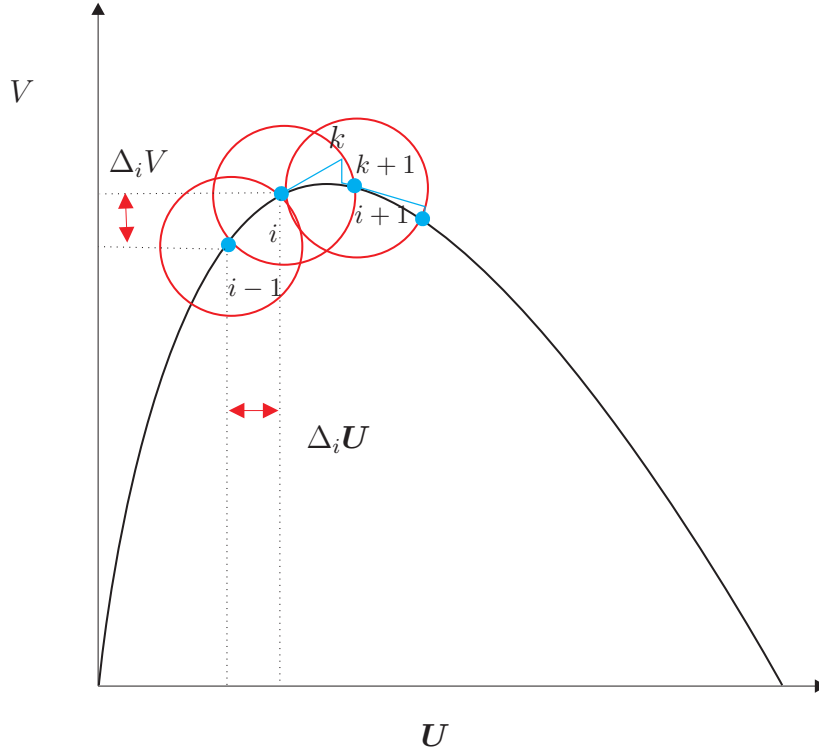


Figure 5.11: Several path following iterations

Since

$$\mathbf{F}^{int} = \begin{bmatrix} \mathbf{K}_{uu}^m \mathbf{u} \\ \mathbf{K}_{\phi\phi} \phi \end{bmatrix} \quad (5.64)$$

does not depend directly on V , the following holds:

$$\frac{\partial \mathbf{F}}{\partial V} = \frac{\partial \mathbf{F}^{elec}}{\partial V}. \quad (5.65)$$

In the formulation above only the DOFs that are not constrained were considered. On the other hand it is possible to include those DOFs that have an applied potential:

$$\mathbf{U}_{tot} = \begin{bmatrix} \mathbf{U} \\ \bar{\phi} \end{bmatrix} = \begin{bmatrix} \mathbf{U} \\ \hat{\mathbf{1}} V \end{bmatrix}, \quad (5.66)$$

where:

$$\hat{\mathbf{1}} = \begin{bmatrix} 1 \\ \vdots \\ 1 \end{bmatrix}, \quad (5.67)$$

which will result in the following tangent stiffness:

$$\mathbf{K}_{tot} = \begin{bmatrix} \mathbf{K}_{UU} & \mathbf{K}_{U\bar{\phi}} \\ \mathbf{K}_{U\bar{\phi}}^T & \mathbf{K}_{\bar{\phi}\bar{\phi}} \end{bmatrix}. \quad (5.68)$$

Therefore the total right hand-side can be seen as:

$$\mathbf{F} = \mathbf{F}(\mathbf{U}, \bar{\phi}(V)), \quad (5.69)$$

and its derivative as:

$$\frac{\partial \mathbf{F}}{\partial V} = \frac{\partial \mathbf{F}}{\partial \bar{\phi}} \frac{\partial \bar{\phi}}{\partial V} = \frac{\partial \mathbf{F}}{\partial \bar{\phi}} \hat{\mathbf{1}}, \quad (5.70)$$

therefore the following must hold:

$$\hat{\mathbf{F}} = \frac{\partial \mathbf{F}}{\partial V} = -\mathbf{K}_{U\bar{\phi}} \hat{\mathbf{1}}. \quad (5.71)$$

This procedure results in the full algorithm as shown in figure 5.12.

5.4.3 Monolithic charge control

These monolithic methods can be combined with charge loading as well. To show how this can be done the problem will be split into three parts: the mechanical part \mathbf{u} , the unconstrained or free electric part ϕ and the actuated conductor part $\bar{\phi}$:

$$\begin{bmatrix} \mathbf{K}_{uu} & \mathbf{K}_{u\phi} & \mathbf{K}_{u\bar{\phi}} \\ \mathbf{K}_{\phi u} & \mathbf{K}_{\phi\phi} & \mathbf{K}_{\phi\bar{\phi}} \\ \mathbf{K}_{\bar{\phi}u} & \mathbf{K}_{\bar{\phi}\phi} & \mathbf{K}_{\bar{\phi}\bar{\phi}} \end{bmatrix} \begin{bmatrix} \Delta \mathbf{u} \\ \Delta \phi \\ \Delta \bar{\phi} \end{bmatrix} = \begin{bmatrix} \Delta \mathbf{f} \\ \Delta \mathbf{q} \\ \Delta \bar{\mathbf{q}} \end{bmatrix}, \quad (5.72)$$

where the grounded conductor part has been removed from the equation. As with the staggered version the floating conductor can be removed from the equations. First it is assumed that the update for the potentials can be written as:

$$\Delta \bar{\phi} = \begin{bmatrix} 1 \\ \vdots \\ 1 \end{bmatrix} \Delta V = \hat{\mathbf{1}} \Delta V. \quad (5.73)$$

Hence the tangent stiffness matrix is defined as:

$$\begin{bmatrix} \mathbf{K}_{uu} & \mathbf{K}_{u\phi} & \mathbf{K}_{u\bar{\phi}} \hat{\mathbf{1}} \\ \mathbf{K}_{\phi u} & \mathbf{K}_{\phi\phi} & \mathbf{K}_{\phi\bar{\phi}} \hat{\mathbf{1}} \\ \hat{\mathbf{1}}^T \mathbf{K}_{\bar{\phi}u} & \hat{\mathbf{1}}^T \mathbf{K}_{\bar{\phi}\phi} & \hat{\mathbf{1}}^T \mathbf{K}_{\bar{\phi}\bar{\phi}} \hat{\mathbf{1}} \end{bmatrix} \begin{bmatrix} \Delta \mathbf{u} \\ \Delta \phi \\ \Delta V \end{bmatrix} = \begin{bmatrix} \Delta \mathbf{f} \\ \Delta \mathbf{q} \\ \Delta \bar{\mathbf{q}} \end{bmatrix}. \quad (5.74)$$

The right hand-side can be computed by:

$$\Delta \mathbf{f} = \mathbf{f}^{elec} - \mathbf{K}_{uu}^m \mathbf{u}, \quad (5.75)$$

and:

$$\Delta \mathbf{q} = \mathbf{q}^{apl} - \mathbf{K}_{\phi} \phi, \quad (5.76)$$

where:

$$\mathbf{K}_{\phi} = \begin{bmatrix} \mathbf{K}_{\phi\phi} & \mathbf{K}_{\phi\bar{\phi}} \hat{\mathbf{1}} \\ \hat{\mathbf{1}}^T \mathbf{K}_{\bar{\phi}\phi} & \hat{\mathbf{1}}^T \mathbf{K}_{\bar{\phi}\bar{\phi}} \hat{\mathbf{1}} \end{bmatrix}, \quad (5.77)$$

$$\mathbf{q}^{apl} = \begin{bmatrix} 0 \\ \vdots \\ 0 \\ \bar{\mathbf{q}}^{total} \end{bmatrix}, \quad (5.78)$$

$$\phi = \begin{bmatrix} \phi \\ V \end{bmatrix}. \quad (5.79)$$

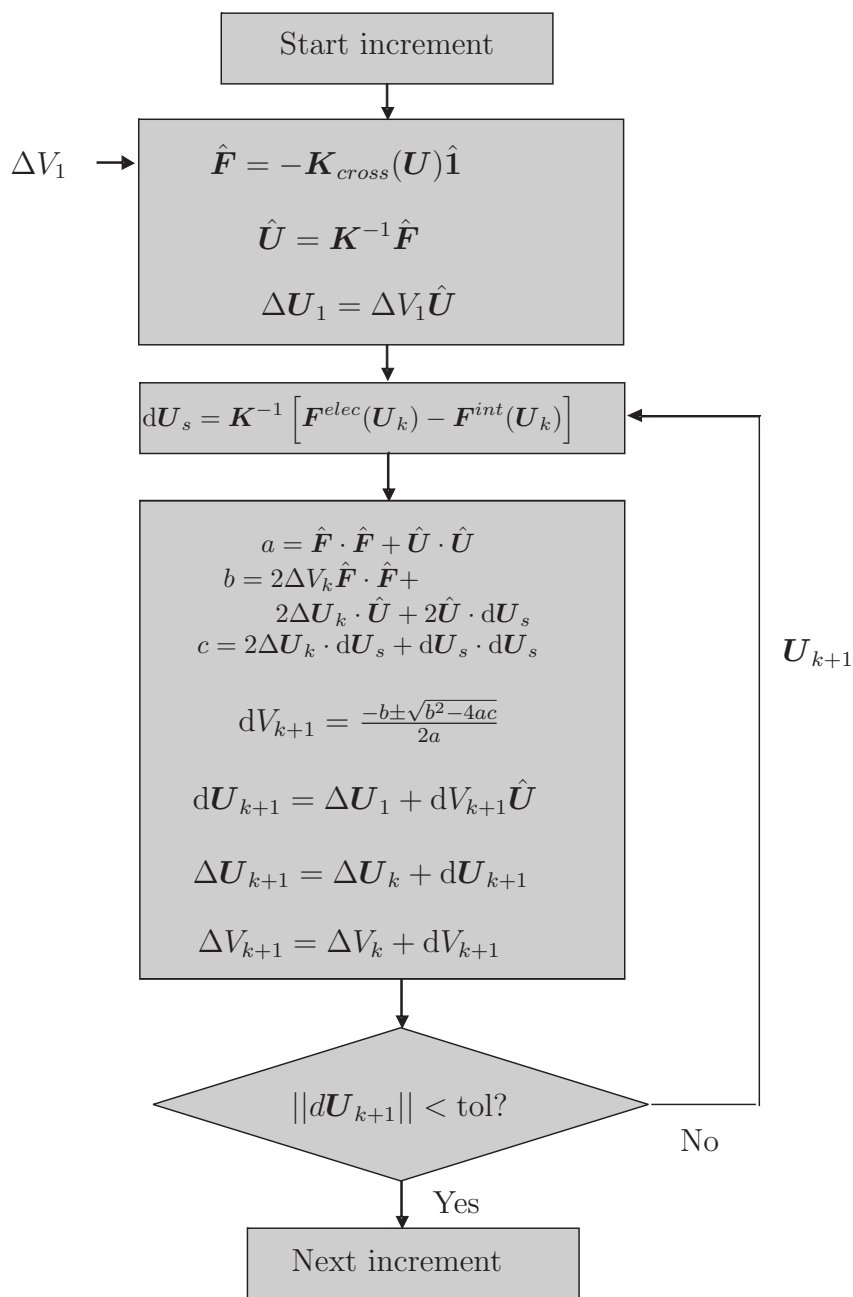


Figure 5.12: The monolithic Riks-Crisfield algorithm.

The driving parameter in both the Newton-Raphson and the Riks-Crisfield scheme is \bar{q}^{total} . Hence the definition of the derivative $\hat{\mathbf{F}}$ is a very simple one for this scheme:

$$\hat{\mathbf{F}} = \frac{\partial \mathbf{F}^{elec}}{\partial \bar{q}^{total}} = \begin{bmatrix} 0 \\ \vdots \\ 0 \\ 1 \end{bmatrix}. \quad (5.80)$$

5.5 General Remarks

5.5.1 Overview of the methods

An overview of the all the different methods to compute the pull-in curves that have been presented in literature and/or discussed here is shown in figure 5.13. Green squares indicate methods realized in literature so far, the green and white square indicates a method which is explained in literature but never truly implemented in literature. The yellow squares indicate methods which were implemented for the first time in this thesis.

The figure indicates on the top how the model can be made: *co-simulation* or *coupled simulation* and the impact that this has on the choice between *staggered* and *monolithic* solution schemes. The terms *Voltage control*, *Charge control* and *Displacement control* indicate if the voltage, the charge or the displacement is included in the constraint used to enhance the system (5.3) to create $n_m + n_e + 1$ equations. If the method is in the *without path-following* region the control parameter is the only item in the constraint. If it is in the *with path-following* region, the constraint defines a relation between the control parameter and the displacement. It does not make sense to combine displacement as control parameter with more displacements in a constraint, hence that part of the figure does not have a method square.

5.5.2 Controlling the convergence and continuation

Increment size control

An aspect of path-following that is common to all the algorithms is the continuation once a converged solution for an increment has been found. At that moment the size of the new increment has to be determined. A popular approach is Ramm's method [71], which defines the new step size ΔV_{i+1} as:

$$\Delta V_{i+1} = \Delta V_i \sqrt{\frac{k_{desired}}{k_{realized}}}, \quad (5.81)$$

where $k_{desired}$ is the desired number of steps per iteration loop and $k_{realized}$ is the number of steps that were needed for the last converged iteration loop i . Of course this method can also be used for the displacement in the DIPIE algorithm.

An important part of the path following methods discussed here is the step size reduction in case of convergence failure. The path-following methods should be able to converge at any position of the curve. However if the initial increment ΔV_1 is relatively large, these methods have convergence problems even if equation (5.81) is used to control the increment size. Therefore these algorithms are not very robust:

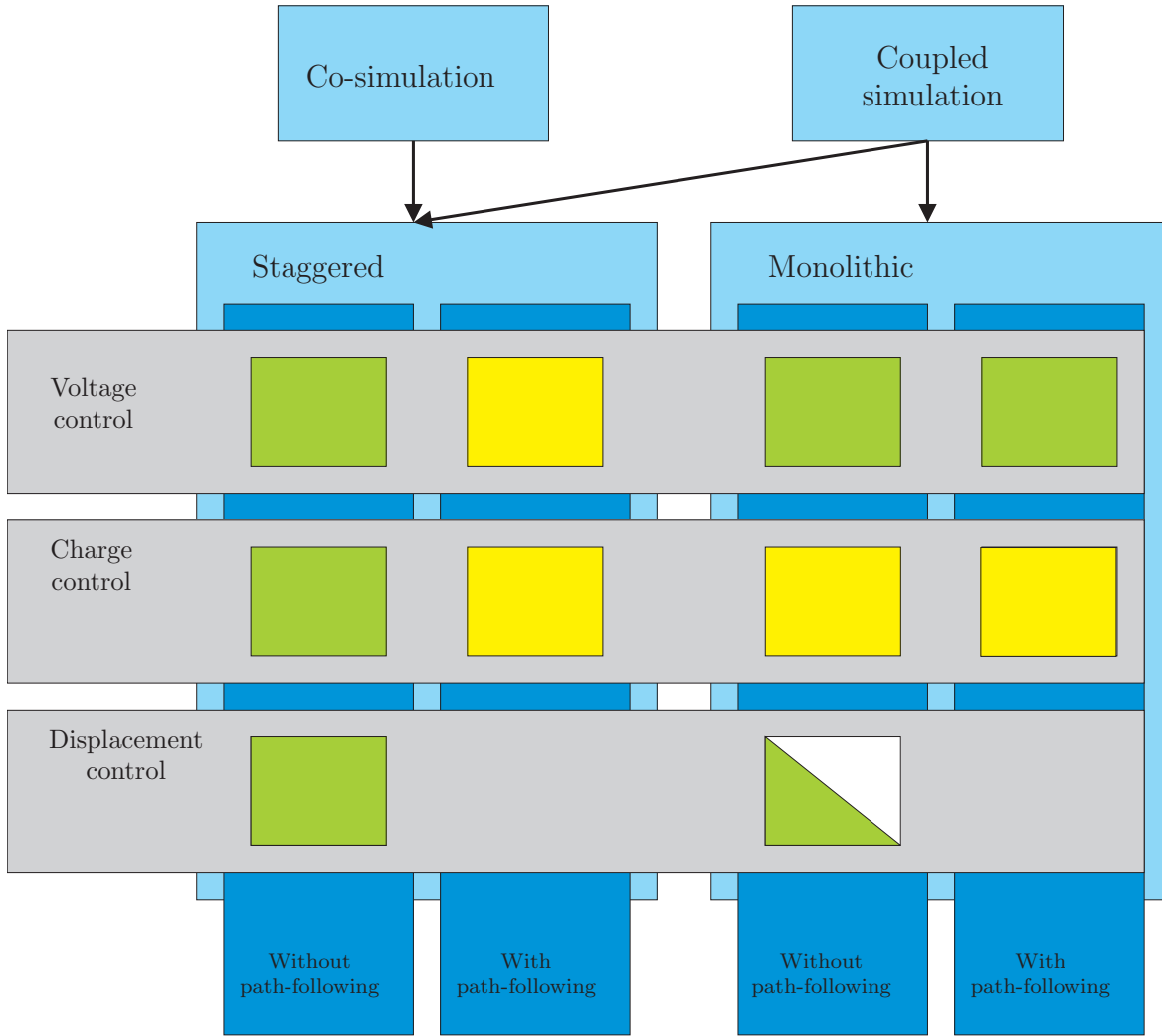


Figure 5.13: Overview of the different procedures to compute the pull-in point (Green indicates methods from literature, yellow indicates newly developed methods and the mixed green/white square provides a non-implemented method from literature).

near pull-in they sometimes do not converge. If that happens the increment is divided by 2: $\Delta V_1^{restart} = \frac{1}{2} \Delta V_1^{original}$ and the iteration procedure is restarted.

Matrix conditioning problems

Monolithic methods suffer from a specific problem: the tangential stiffness matrix is ill-conditioned. The mechanical contributions to the stiffness matrix is composed of elements that are in the order of $\|\mathbf{B}\|^2 \cdot |E|$, where E is the Elasticity modulus. The electric contributions are in the order of $\|\mathbf{B}\|^2 \cdot |\varepsilon|$, where ε is the electric permittivity and \mathbf{B} is the matrix with shape function derivatives. The Young's modulus for a typical MEMS material as polysilicon is in the order of 10^8 while the permittivity of air is in the order of 10^{-11} . It is not hard to imagine that the conditioning will be horrible.

The basic method to overcome this problem is to transform the complete matrix equation to an equation that is better conditioned:

$$\mathbf{K}\mathbf{U} = \mathbf{F} \rightarrow \tilde{\mathbf{K}}\tilde{\mathbf{U}} = \tilde{\mathbf{F}}. \quad (5.82)$$

The simplest method that is effective is by pre- and post-multiplying with a diagonal scaling matrix \mathbf{P} :

$$P_{ij} = \frac{1}{\sqrt{|K_{ij}|}} \delta_{ij}, \quad (5.83)$$

where δ_{ij} is the Kronecker delta which is 1 if i equals j and 0 if i is unequal to j . The transformed stiffness matrix and force vector are than:

$$\tilde{\mathbf{K}} = \mathbf{P}\mathbf{K}\mathbf{P}, \quad (5.84)$$

$$\tilde{\mathbf{F}} = \mathbf{P}\mathbf{F}. \quad (5.85)$$

Once $\tilde{\mathbf{U}}$ has been computed with the transformed equation (5.82), \mathbf{U} can simply be computed with:

$$\mathbf{U} = \mathbf{P}\tilde{\mathbf{U}}. \quad (5.86)$$

When the definition of \mathbf{P} (5.83) is substituted into (5.84) this gives:

$$\tilde{K}_{ij} = \frac{1}{\sqrt{|K_{ii}|}} K_{ij} \frac{1}{\sqrt{|K_{jj}|}}, \quad (5.87)$$

thus every element of \mathbf{K} is scaled by the diagonal element of its row position and the diagonal element of its column position. Therefore the coupling terms between mechanics and electrostatics are scaled properly as well.

Convergence criteria

There are different ways to measure the error that determines whether the solution has converged. In the previous sections 5.3 and 5.4 the used error measure was the norm of the update of the state vector:

$$e_k = \|\mathbf{U}_k - \mathbf{U}_{k-1}\|, \quad (5.88)$$

which is one of the simplest possible error measures and was therefore used to explain the algorithms. There are two problems with this error measure though. Firstly it is an absolute error measure, therefore the strictness of the error depends on the geometry of the problem. Normally it is better to use a relative measure. In this document a relative measure on the force unbalance was used:

$$e_k = \frac{\|\mathbf{F}_k^{elec} - \mathbf{F}_k^{int}\|}{\|\mathbf{F}_k^{elec}\|}. \quad (5.89)$$

Secondly it does not really compare well, because in the staggered methods the state vector only contains the mechanical displacements where the monolithic state vector contains all DOFs. For convergence in a monolithic method it is important to apply the error measure on all DOFs, but for comparison only the error on the mechanical DOFs will be stored:

$$e_k = \frac{\|\mathbf{f}_k^{elec} - \mathbf{f}_k^{int}\|}{\|\mathbf{f}_k^{elec}\|}. \quad (5.90)$$

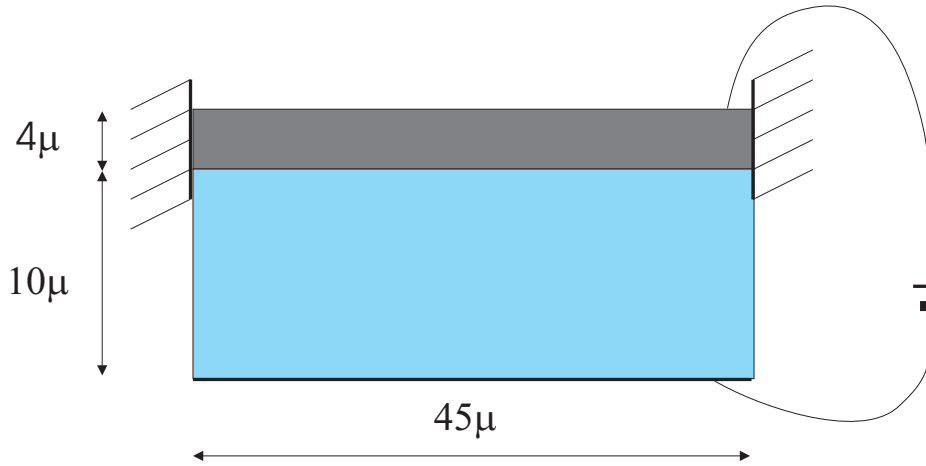


Figure 5.14: Linear beam.

5.5.3 Pull-in detection

A final remark on pull-in detection: pull-in is characterized by a singular stiffness matrix \mathbf{K} . This can be detected by checking if $\det(\mathbf{K}) = 0^3$. Detection is easy because before pull-in $\det(\mathbf{K}) > 0$ but beyond pull-in, within the unstable region, $\det(\mathbf{K}) < 0$. Checking whether the pivots of the matrix \mathbf{K} are all positive during the factorization of the matrix should be enough to determine if the determinant of \mathbf{K} is still positive, hence it does not have to be an expensive check.

If one includes such a test after each converged iteration, the methods can easily be enhanced with a zero finding algorithm that precisely computes the pull-in point. In principle this is only possible if the full coupled stiffness matrix is available, therefore only for the monolithic methods. Although hybrid methods are conceivable where a staggered method is used to compute the equilibrium position, after which the coupling terms are evaluated at the converged solution, than the complete tangent stiffness can be computed for evaluation of $\det(\mathbf{K})$.

Of course this is also true for the computation of a linearized eigenfrequency ω_i and eigenmode $\boldsymbol{\mu}_i$ around an equilibrium position, as defined by the eigenvalue problem:

$$\mathbf{M}\boldsymbol{\mu}_i\omega_i^2 = \mathbf{K}(\mathbf{U}_{eq})\boldsymbol{\mu}_i. \quad (5.91)$$

5.6 2D linear FEM test case

The first comparison between the approaches is done with the finite element model of a simple beam. The geometry of the beam and the air gap below is depicted in figure 5.14⁴. Both domains are meshed with quadrilaterals.

The structural beam is modeled with 2D solid elements under plane strain assumption and with linear shape functions to approximate the displacement field [12]. The Young's modulus is $1 \cdot 10^5 \text{ GPa}$ and the Poisson's ratio is 0.3.

The air gap is modeled with standard electrostatic elements with linear shape functions. The vacuum electric permittivity of $8.85 \cdot 10^{-12} \text{ F/m}$ is used to characterize the electric domain.

³Again this phenomena is very similar to limit point buckling.

⁴For more detail on the FEM implementation of this test case see chapter 4.

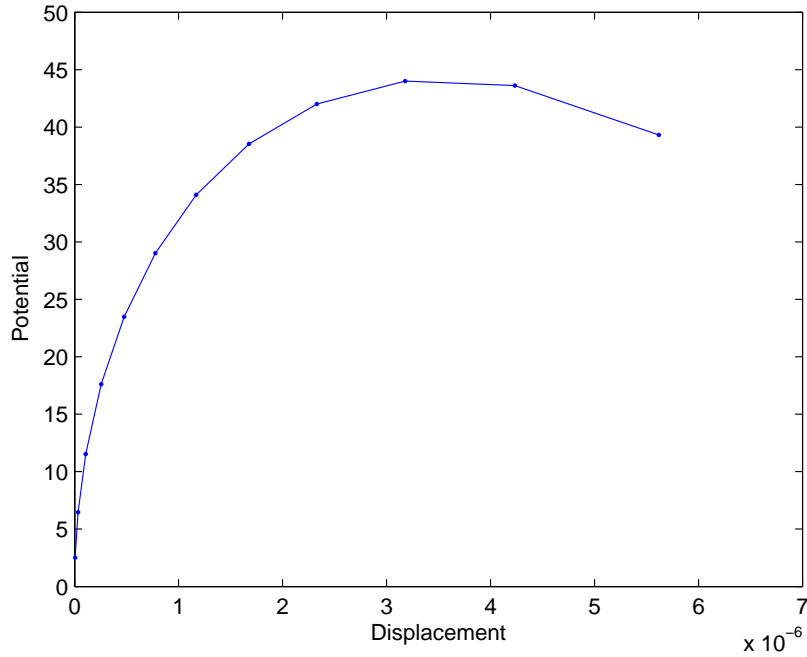


Figure 5.15: Voltage displacement curve.

Figure 5.15 presents the voltage displacement curve for this beam up to a displacement of $5.5\mu\text{m}$, which is 55% of the initial air gap. The absolute displacement of the middle node is shown.

The deformed geometry of the beam and air gap at this displacement is shown in figure 5.16. In this figure the beam is the part above the white division line and the gap is the part below that line. The beam has a uniform color and the color in the gap indicates the potential distribution (red is high potential, blue is low potential).

The voltage-displacement curve in figure 5.15 was computed with the charge loaded block Gauss-Seidel procedure, but the same results were also computed with the other approaches. Computation times are listed in table 5.1. The computations were performed in Matlab on a simple desktop computer (3 GHz, 2 GB RAM). The first thing that should be noted is that the relative error tolerance on the residual of the structural force for the DIPIE method is less strict than that for the other methods, this is because it was not possible to make it converge to a relative error below $5 \cdot 10^{-2}$. The second thing to note is that the computation took the least of time with the full Newton-Raphson algorithm, but this one and the voltage block Gauss-Seidel do not compute the complete curve, they only compute the stable part, therefore they only approximate the pull-in point. The fastest of the methods that actually make a reliable estimate of pull-in is the charge loaded block Gauss-Seidel. Also noteworthy is the fact that monolithic path-following with voltage control is faster than the block-iterative version, but not faster than using charge control.

The second comparison between of the approaches is presented in figure 5.17, which shows the decrease of the relative error during an iteration procedure. For clarity the two approaches that do not compute the complete curve were left out of the figure. These error curves were determined at an increment near the pull-in point. The reason of the fast computation time for the charge algorithm in table 5.1 can easily be ex-

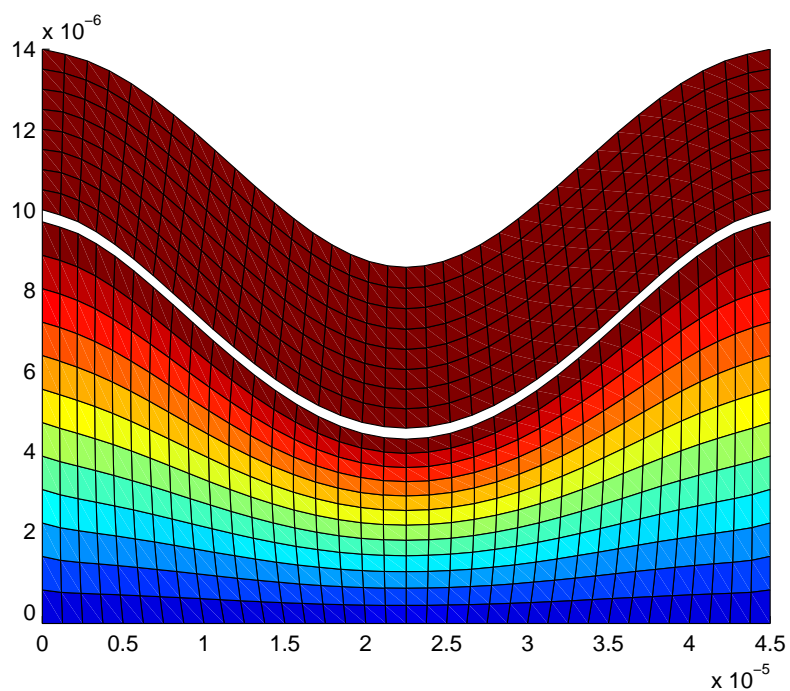


Figure 5.16: Deformed shape of the simple beam.

Table 5.1: Computation times required to trace the path.

Method	Computation time (s)	Error tolerance (relative)
Voltage block Gauss-Seidel	86	10^{-3}
Voltage block GS with path following	277	10^{-3}
DIPIE	296	$5 \cdot 10^{-2}$
Charge block Gauss-Seidel	76	10^{-3}
Voltage Newton Raphson	54	10^{-3}
Voltage monolithic path following	181	10^{-3}
Charge Newton Raphson	82	10^{-3}

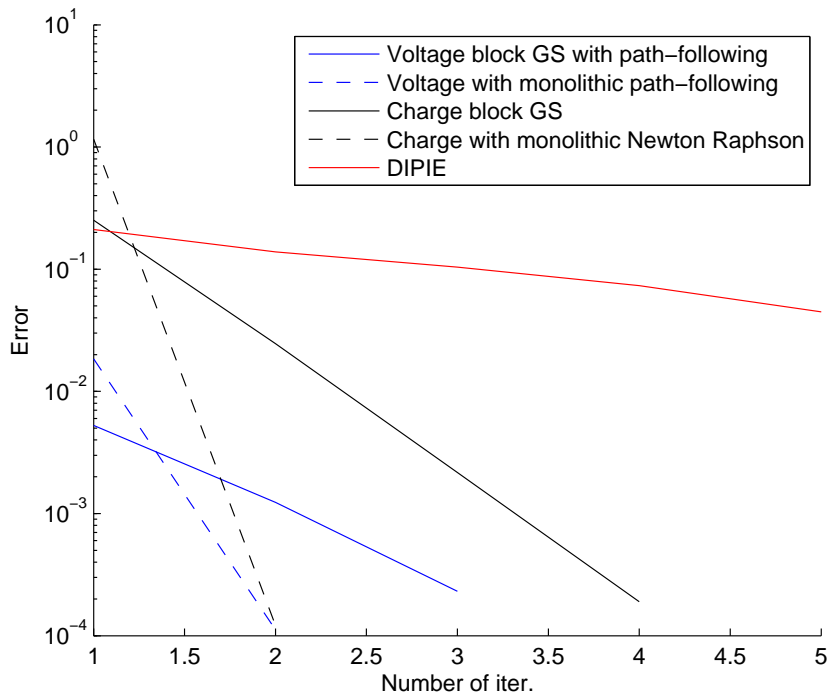


Figure 5.17: Error curves for the simple beam.

plained because its error curve has the steepest descent of the staggered methods. Only the monolithic methods converge faster, but they require much more computation time per iteration step. Therefore the overall computation time of the monolithic methods is lower than that of the staggered charge loaded method. The computation time of the monolithic charge Newton Raphson method does come very close to the staggered charge method though.

The curve in figure 5.15 is good enough to characterize the voltage pull-in point in both displacement and potential, however in section 4 there was a warning: there exists a charge pull-in point. To show that the charge pull-in is far enough from the voltage pull-in point the charge path-following algorithm was used to compute the curve up to 80% of the gap. Figure 5.18 shows the total charge and applied potential, which shows that charge pull-in is located at about 70% of the gap, while the voltage pull-in is located at 35% of the gap. Therefore it is possible to characterize voltage pull-in with the charge block iterative algorithm without path-following,

5.7 2D non-linear FEM test case

So far the problems could effectively be solved with staggered algorithms. However if the mechanics becomes non-linear as well, havoc is created. Phenomena such as mechanical snap-through might be seen. This type of behavior is not uncommon in MEMS due to the high levels of residual stress that can occur [38, 86]. In that case one might really need a monolithic algorithm. One very simple structure that will experience this type of behavior is shown in figure 5.19. It is initially curved, so no pre-stress is included.

To be able to model the snap through for this structure the structural FEM model

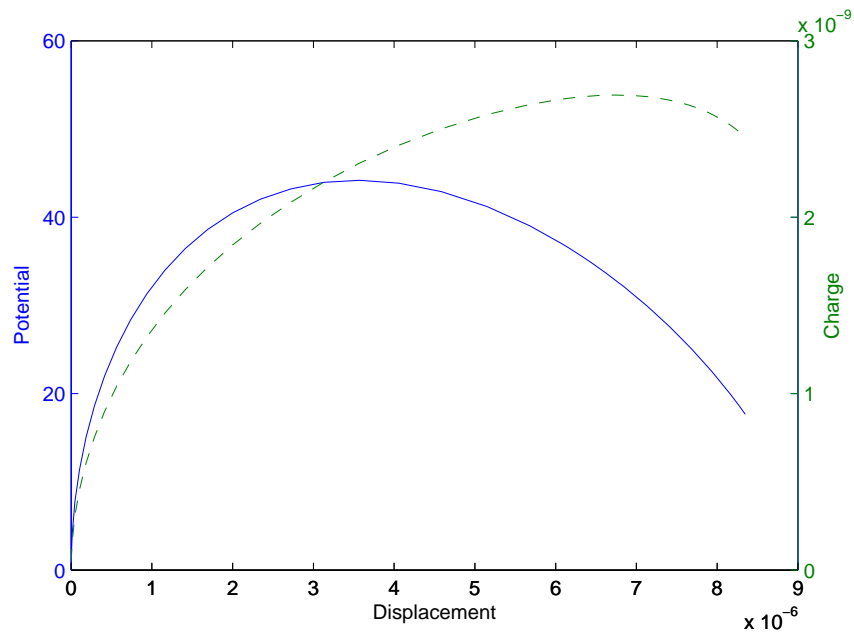


Figure 5.18: Charge and voltage pull-in.

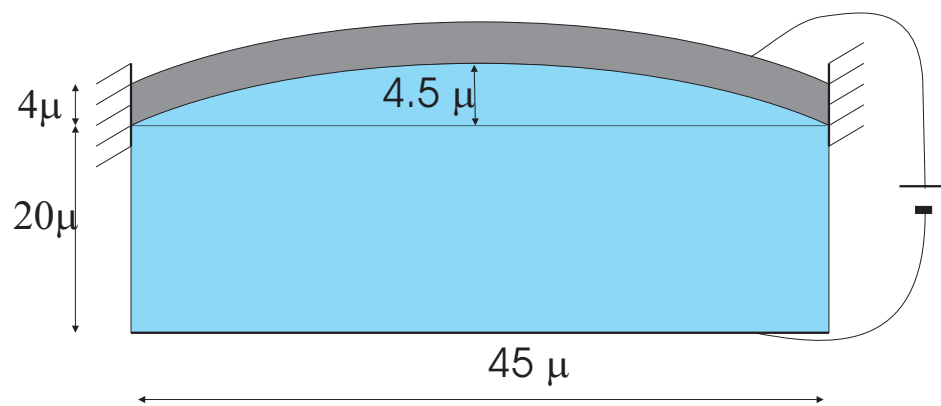


Figure 5.19: Curved non-linear beam.

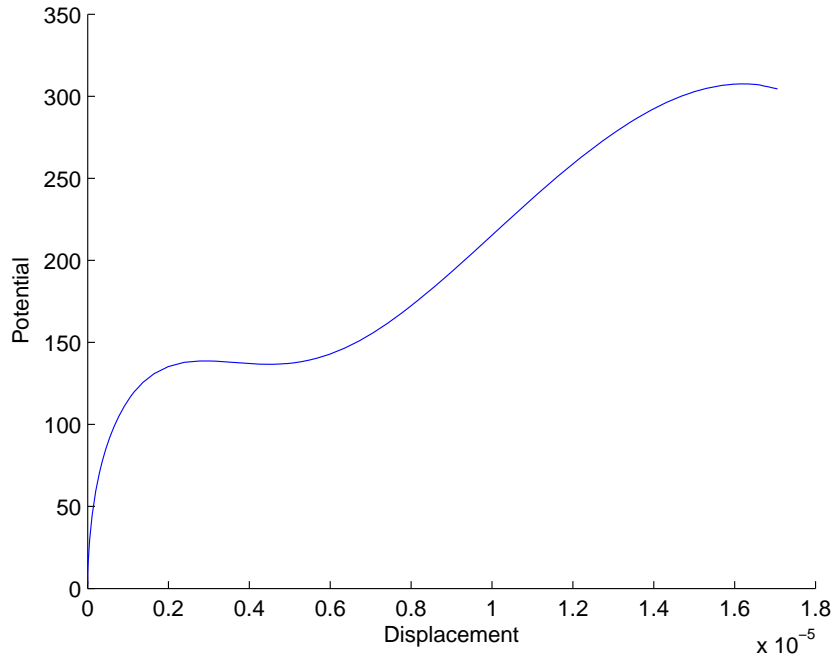


Figure 5.20: Load-displacement curve for the non-linear beam.

is a geometrically non-linear one, based on the Green-Lagrange strain and the 2nd Piola-Kirchhoff stress [12]. The voltage displacement curve computed with the charge loaded path-following algorithm is shown in figure 5.20. The deformed shape plotted in figure 5.21 is that shape for which the middle node displacement is about 10μ .

This curve was also computed by the two voltage path-following schemes. Theoretically it is also possible to compute it with the DIPIE method, but the slow convergence for the simple linear beam in section 5.6 showed that this is not a good alternative. Therefore this problem was only computed with the path-following methods. Computation times are summarized in table 5.2. These are measurements of the time taken to compute the curve up to a displacement of 10μ .

Table 5.2: Computation times required to trace the curve.

Method	Computation time (s)	Error tolerance (relative)
Voltage block GS with path following	4486	10^{-4}
Charge block GS with path following	837	10^{-4}
Voltage monolithic path following	1352	10^{-4}
Charge monolithic path following	652	10^{-4}

Again, these times can be explained by error curves. The curves in figure 5.22 are computed at a displacement of about 4μ . They show that after the snapping point the staggered charge algorithm converges a bit faster than the staggered voltage algorithm. The monolithic voltage scheme converges even faster, but has the disadvantage of larger matrix. Therefore the total computation time of the monolithic voltage method is better than the staggered voltage scheme, but slower than the both the charge loaded methods. The monolithic charge loaded method is the fastest of them all.

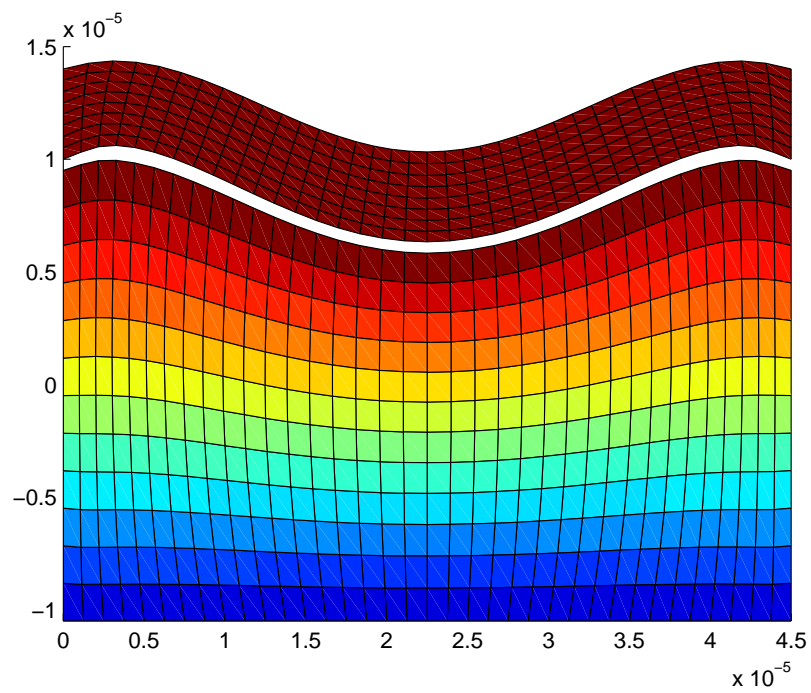


Figure 5.21: Deformed shape of the curved non-linear beam.

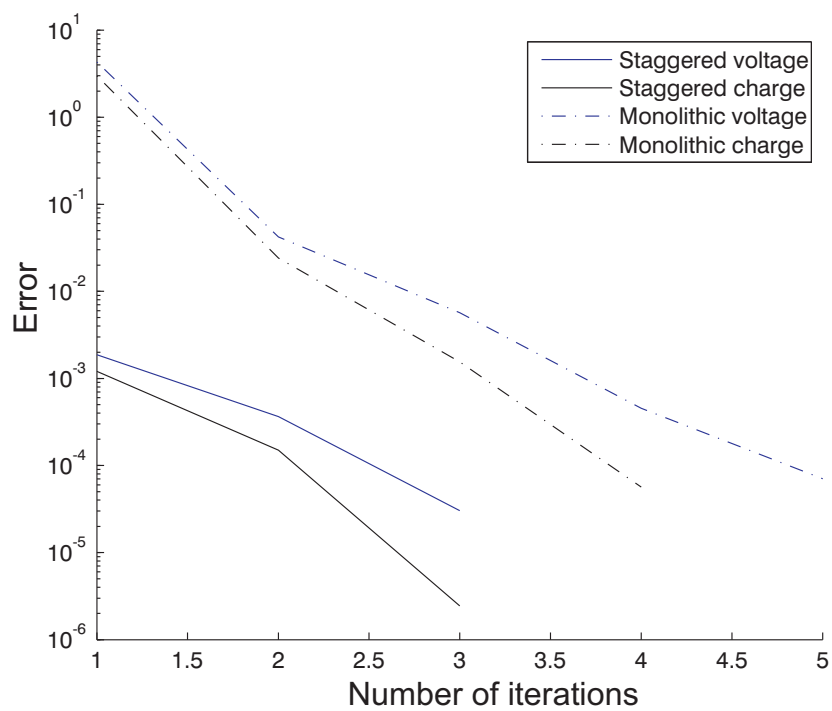


Figure 5.22: Error curves for the curved beam.

5.8 Experimental validation

A paper from Tilmans and Legtenberg from 1994 presents pull-in measurements for a very simple microbridge [130]. Because of its simplicity it is ideal for modeling with the plate type model that was introduced in chapter 4, hence an ideal case for validating the methods presented above. Above it was shown that all methods give the same result. However they are developed to compute pull-in accurately, hence this section tests whether the methods actually compute the correct pull-in values.

A picture of such a bridge was presented in figure 4.10. The thickness of the bridge from the paper is 1.5μ and the gap between plate and ground plane is 1.2μ . The length of the bridge was varied. A value of $E_p = 166 \text{ GPa}$ for the plate modulus was reported in the paper. This plate modulus is defined as $E_p = E/(1 - \nu^2)$, which can be used to compute the elasticity modulus E required for the FEM model. With a Poisson's ratio of 0.22, this gives a Young's modulus of 160 GPa .

Initial stresses due to fabrication have to be accounted for, therefore the tensile initial strain of $\epsilon_0 = 36.8 \cdot 10^{-6}$ in the direction along the beam that was reported in the paper is included in the model using the geometric stiffness matrix⁵.

For the modeling of the mechanics of the plate a mesh of 22 elements in the length and 14 elements in width of the plate were used. The electric mesh in the air gap contained 4 elements in the direction perpendicular to the plate. In the other 2 directions the number of elements was equal to the number of elements in the mechanical mesh. For this mesh the pull-in results have converged below a relative error of 10^{-3} .

Bridges of four different lengths were measured: 210μ , 310μ , 410μ and 510μ . The results of the measurement and the simulation are listed in table 5.3. The results show that the simulations are pretty accurate, hence the approach is validated. However it should be noted that the quality of the pull-in simulation depends for a large part on the FEM implementation as discussed in the previous part of this report.

It should also be noted that the initial stress was very important. Without initial stress the pull-in voltage was consistently lower, but also the relation between the length and pull-in voltage was different. For longer lengths the relative error is bigger without initial stress. Therefore just increasing the Young's modulus to match one pull-in voltage does not give the correct pull-in voltage for other lengths.

5.9 Branching

Until now only the computation of load displacement curves that follow a single path have been discussed, however it is possible that the curve at some point has a bifurcation and several branches can be found.

⁵When a tensile stress is pulling on a plate in the direction tangential to the plate the response in the direction perpendicular to the plate is stiffened. This is similar to tuning a guitar string by stretching it. The *geometric* stiffness matrix that describes this behavior is amongst others discussed [100]. Crudely speaking it shows the following: Define the initial force pulling on the wire in the tangential direction caused by the initial stress as N . The angle which the plate makes with the horizontal is $\varphi = \frac{\partial w}{\partial x}$, where w is the out of plane displacement. Hence the force in out of plane direction is $F = N \cdot \sin(\varphi) \approx N \cdot \varphi$. Subsequently it is assumed that $\frac{\partial w}{\partial x} \approx \delta w/L$ where $\Delta w = w_i - w_j$ is the increase of displacement within an element and L is the length of the element. Hence the stiffness matrix contains terms $\frac{\partial F_i}{\partial w_j} = \pm \frac{N}{L}$.

Table 5.3: Pull-in voltages for different beam lengths.

Length (μm)	Measured pull-in (V)	Simulated pull-in (V)
210	28.0	28.2
310	13.8	14.2
410	9.1	9.0
510	6.6	6.5

To illustrate this branching consider the 1D problem in figure 5.23. The total force on this mass in upward direction is:

$$F = kx + \frac{1}{2}\varepsilon\frac{V^2}{(d+x)^2} - \frac{1}{2}\varepsilon\frac{V^2}{(d-x)^2}, \quad (5.92)$$

where d is the initial gap between mass and electrodes. The linearized stiffness for the mass is:

$$k_{lin}(V, x) = \frac{\partial F}{\partial x} = k - \varepsilon\frac{V^2}{(d+x)^3} - \varepsilon\frac{V^2}{(d-x)^3}. \quad (5.93)$$

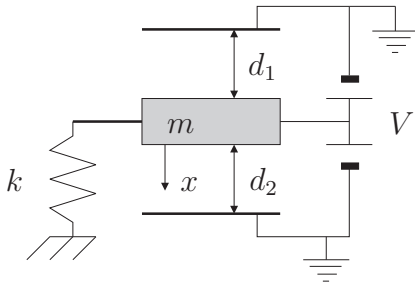


Figure 5.23: Movable electrode that is actuated on two sides.

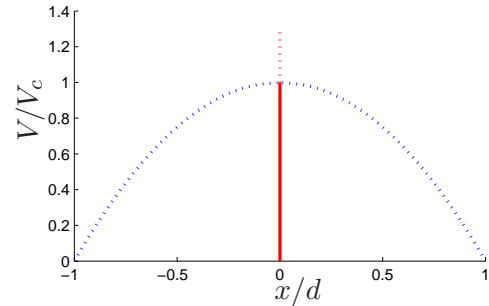


Figure 5.24: Load displacement for the movable electrode.

Obviously the trivial equilibrium solution for $F = 0$ is $x = 0$. The stability of this solution can be tested by checking if $k_{lin}(V, 0)$ is positive. From this test follows that k_{lin} changes sign at:

$$V_c = \frac{\sqrt{2}}{2} \sqrt{\frac{kd^3}{\varepsilon}}. \quad (5.94)$$

When the applied voltage is lower than this critical voltage the solution $x = 0$ is stable, when it is higher it is unstable. Moreover when it is lower, there exist two other solutions that do not exist when the applied voltage is higher than V_c :

$$x = \pm \sqrt{\frac{kd^2 - \sqrt{2\varepsilon kdV}}{k}}, \quad (5.95)$$

which are always unstable, except for $V = V_c$, because at that point also the displacement x for these two solutions is zero and $k_{lin} = 0$, making it impossible to determine stability without higher order analysis. This complicated load-displacement behavior is summarized in figure 5.24, where dotted lines indicate unstable curves and the continuous line the stable path. It is clear that at the critical load a bifurcation occurs from which three other paths emerge.

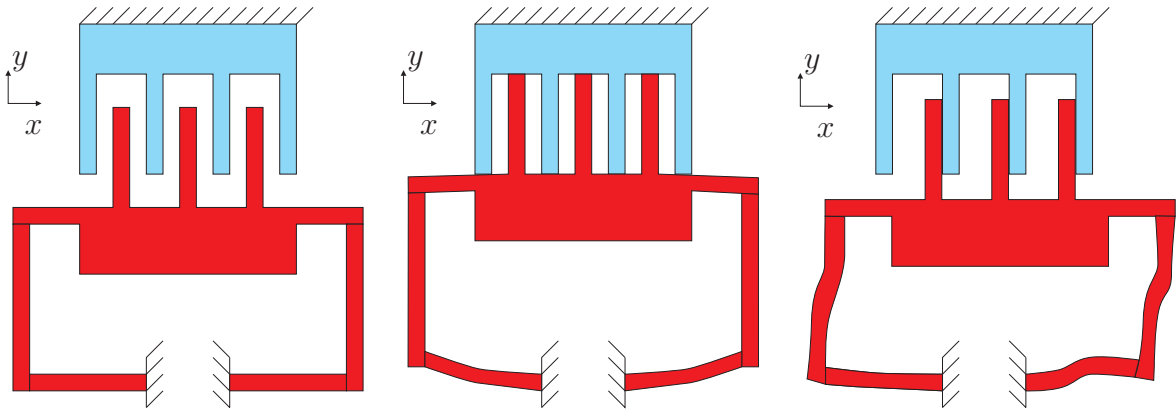


Figure 5.25: Normal and side pull-in of a simple comb drive actuator.

A typical MEMS operation case where such a bifurcation can happen is side pull-in of comb drives. Figure 5.25 shows a very simple comb drive. The red color in the figure indicates the moving part which is actuated with a potential and the blue color indicates the fixed and grounded part. Normally such a comb drive is actuated in the direction of the fingers, thus the comb drive on the left hand-side of the figure is actuated in y -direction. Therefore the comb drive will show the same type of behavior as the classical 1D parallel plate actuator and the final position after pull-in will be the position shown in the middle of figure 5.25. However, if the comb drive is not designed properly, the side pull-in mode can become active and the final displacement can become the one on the right hand-side of figure 5.25. Due to symmetry the final deformation can also be in the negative x -direction. This bifurcation can appear if the critical voltage of side pull-in is lower than the pull-in voltage is lower than the normal pull-in voltage. Therefore during electromechanical modeling of MEMS, the proper computation of branching curves can be very important.

However this is not the first time such problems occur. As normal pull-in was very similar to limit point buckling, this side pull-in phenomenon is very similar to a classical mechanical problem: the symmetric bifurcation that can be seen for the inverted pendulum of figure 5.26. In that figure M_s indicates the restoring torque due to the torsion spring. The typical bifurcation is shown in figure 5.27.

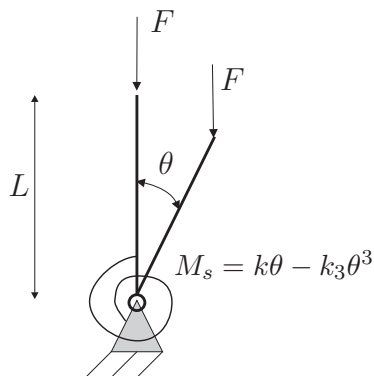


Figure 5.26: Inverted pendulum loaded by force F .

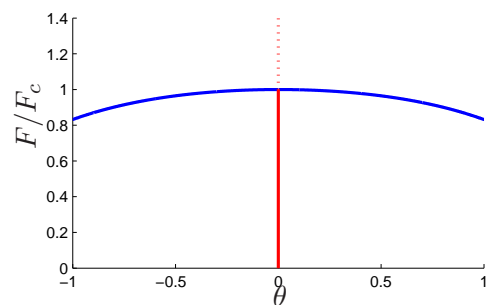


Figure 5.27: Load displacement relation for the inverted pendulum ($k_3/k = 0.3$).

This similarity suggests that it might be possible to use one of the classical strategies to tackle branching for non-linear mechanical problems. Therefore a slightly adapted version of an algorithm from chapter 21 of [29] will be used.

First a curve is computed with a standard path-following algorithm. This will normally find the easiest solution to compute, therefore in the example above it would find the $x = 0$ solution.

Next, the bifurcation point or singular point has to be computed, this can often be done by starting with the solution from the standard path following approach. A method to detect this point has been discussed in the previous section (find $\det(\mathbf{K}) = 0$), which is equivalent to determining whether the lowest eigenvalue of the coupled electromechanical stiffness matrix λ is still positive:

$$\mathbf{K}\boldsymbol{\mu} = \lambda\boldsymbol{\mu}. \quad (5.96)$$

If λ equals zero, the bifurcation point is detected. Linear interpolation or some bisection steps can be included to determine the point more accurately. The corresponding applied charge (or voltage) and state at this critical point will be defined as Q_c and \mathbf{U}_c .

Once the eigenvalue is detected it is known that one of the equilibrium paths will depart in the positive direction of the eigenmode $\boldsymbol{\mu}$ and another one in the negative direction. Thus a logical predictor for an arc-length method that has to follow these equilibrium paths is:

$$\Delta\mathbf{U}_1 = \Delta l\boldsymbol{\mu}. \quad (5.97)$$

If a monolithic charge loading algorithm is used to trace the curve, the standard linearized arc-length constraint can be used to find the corresponding charge update required to find equilibrium at this curve.

$$dQ_{k+1} = -\frac{\Delta\mathbf{U}_k d\mathbf{U}_s}{\Delta\mathbf{U}_k \hat{\mathbf{U}}} \quad (5.98)$$

This Δl is a crucial parameter that determines the size of the first step and therefore the capability of the algorithm to converge. An initial guess for Δl that works in practice is:

$$\Delta l_1 = \pm \frac{|\mathbf{U}_c|}{|\boldsymbol{\mu}|}, \quad (5.99)$$

where \mathbf{U}_c is the displacement at the critical point. Once the initial step has converged, the size can be determined with the same formula as the voltage step in equation (5.81).

Because one predicts the first step of the solution with the eigenmode, it is unlikely that the solution converges back to the unwanted part of the curve that was already computed by the traditional path following algorithm (the $x = 0$ solution in the 1D example). Once far enough away from the bifurcation point, one could switch back to the original solution method that was used to find the first part of the curve.

The monolithic charge control algorithm for branching can be found in the scheme of figure 5.28.

5.10 2D FEM with branching

The next example is not used to compare approaches, but to show that these methods can handle branching as well. The FEM model under investigation is shown in figure

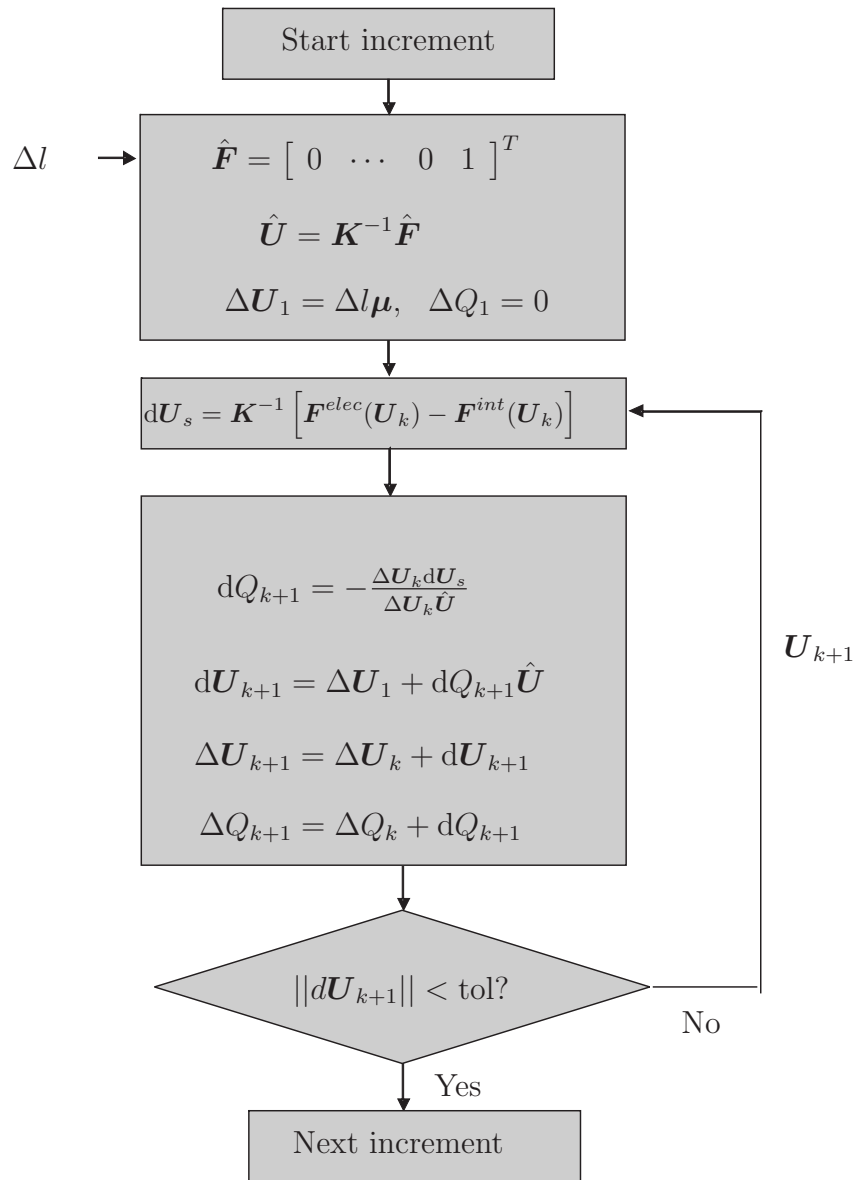


Figure 5.28: The simple branch switching algorithm.

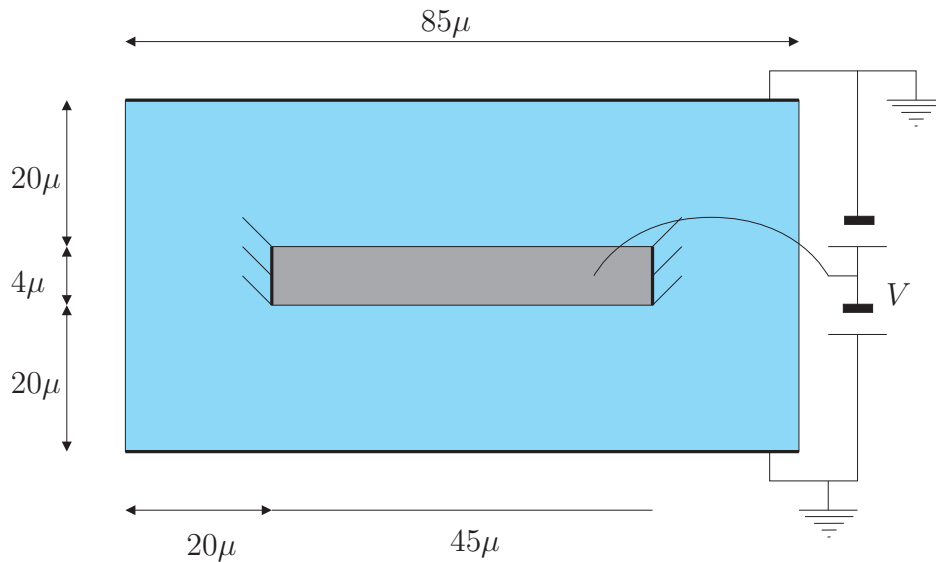


Figure 5.29: Beam actuated on two sides.

5.29. The beam is clamped on two sides and actuated with a constant potential V . The two long sides of the air domain are grounded, the short sides are assumed to have a zero charge boundary condition.

The beam was assumed to have an elasticity modulus of $1 \cdot 10^9 Pa$ and a Poisson's ratio of 0.33. The permittivity of the electric air is assumed to be equal to the vacuum permittivity.

The curve was computed with a hybrid method: staggered charge loading for the incremental iterations combined with monolithic stiffness matrix evaluation for eigenvalue/eigenmode computation. The resulting curves are shown in figures 5.30 and 5.31.

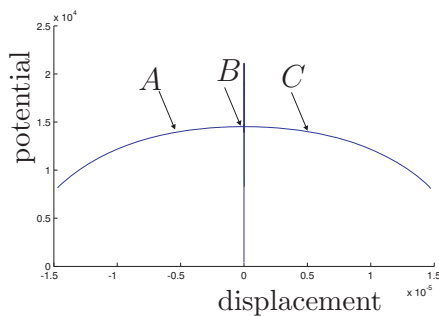


Figure 5.30: Potential-displacement curve for beam.

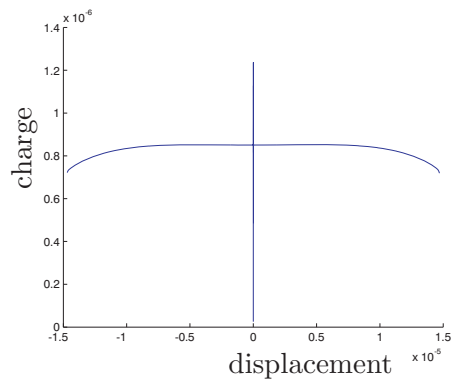


Figure 5.31: Charge-displacement curve for beam.

The 'displacement= 0' solution was computed by just following the solution with the staggered charge loaded algorithm. After that the singular point and eigenmode were determined, which could be used to start the two loops ($\Delta l_1 = \pm |U_c|/|\mu|$) to compute the two paths that diverge from the 'displacement= 0' solution.

Figures 5.32 until 5.34 show deformed shapes and meshes at points A, B and C as defined in figure 5.30. The color indicates the potential, where the maximum potential is mentioned in the caption of the figures.

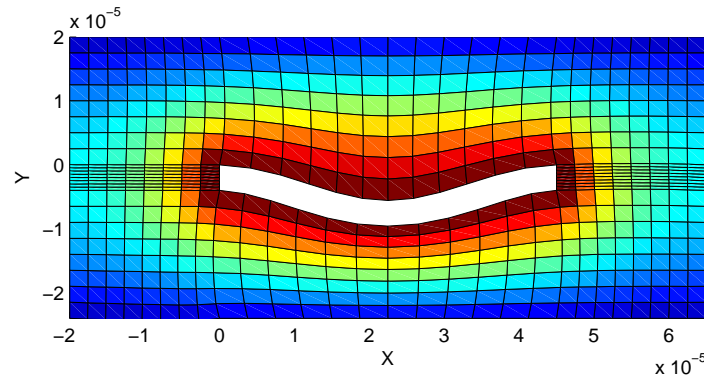


Figure 5.32: Deformed shape at A , where $V = 1.4 \cdot 10^4$.

5.11 Conclusions

A short review of approaches to compute the pull-in curves for electrostatically actuated microsystems was presented. The methods could be characterized by two characteristics: the extra constraint on the system needed to make the system solvable and whether the algorithm was a staggered one or a monolithic one.

There are basically five choices for the constraint:

- Prescribe the applied voltage,
- Prescribe a relation between applied voltage and displacement,
- Prescribe the applied charge,
- Prescribe a relation between applied charge and displacement,
- Prescribe an applied displacement.

The option to prescribe charge had not been reported in literature for numerical simulations, but has been used for control purposes. Of the possible choices the best option is to prescribe a relation between applied charge and displacement by using the charge loaded Riks-Crisfield algorithm.

To be able to make a comparison between staggered and monolithic approaches, the arc-length (Riks-Crisfield) constraint, needed to prescribe a relation between either voltage or charge and displacement, had to be adapted for staggered usage. Once this had been implemented the conclusion could be drawn is that for problems that are mechanically linear the staggered approach is faster, but that for mechanically non-linear problems, where a dip in the charge displacement curve occurs, the monolithic method is faster.

It was shown that the approach with a constraint on charge and displacement was best. However it was not shown which type of constraint work best: the Riks constraint, the Crisfield constraint or even the normal flow algorithm. A study in that direction is recommended for future work.

Finally it was shown that branching can be added to these solution algorithms easily.

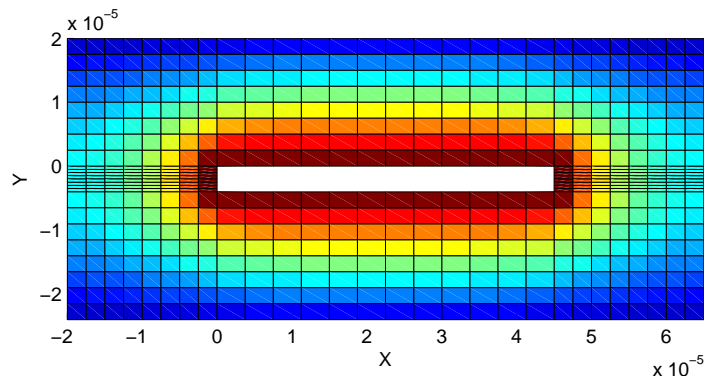


Figure 5.33: Deformed shape at B , where $V = 1.45 \cdot 10^4$.

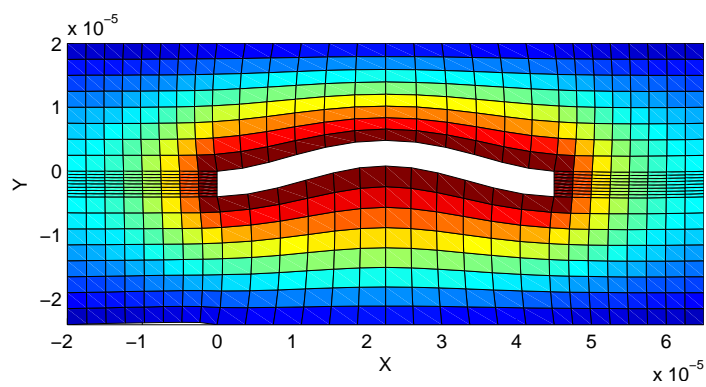


Figure 5.34: Deformed shape at C , where $V = 1.4 \cdot 10^4 V$.

Chapter 6

Sensitivity of the pull-in voltage

6.1 Introduction

So far the static responses of structures were computed. However during the design period of a microsystem the parameters of the design are not yet chosen. This means that it is interesting to know how the result varies with parameter variations.

Of course it is possible to approximate the sensitivities of global parameters by finite differences, but that is expensive and not robust, therefore this chapter will discuss analytic sensitivities. Therefore the derivation is more difficult, but the result more robust.

This chapter attempts to explain how the sensitivity of the pull-in voltage to a perturbation of structural parameters for a coupled electromechanical FEM model can be computed. For that reason it is really necessary to have read section 3.6.4 where the creation of a fully coupled FEM model was discussed. This coupled FEM formulation will be used in section 6.2 to derive the sensitivity of the pull-in voltage to a perturbation of a structural mechanic parameter. Section 6.3 shows a new semi-analytical method to compute the second order sensitivity of the pull-in voltage. Second order sensitivities are required for second order stochastic analyses, but are also useful to estimate the accuracy of the first order sensitivities. Finally in section 6.4 a FEM example is used to test the method.

6.2 Sensitivity of the pull-in voltage

In this section the sensitivity of the pull in voltage to parameter variations will be derived.¹ The derivation is limited to structural parameters such as: the Young's modulus, Poisson's ratio or beam/plate element thicknesses.

It is known that at pull-in the tangent stiffness matrix is singular, therefore the tangent to the load displacement curve is zero at pull-in, as is illustrated graphically in figure 6.1. This causes the lowest eigenvalue of the stiffness matrix (λ_1) to be zero at pull-in:

$$\mathbf{K}(U_{PI}, V_{PI})\boldsymbol{\mu}_1 = \lambda_1\boldsymbol{\mu}_1 = 0. \quad (6.1)$$

The starting point for the derivation of the sensitivity of the pull-in voltage to a perturbation of a structural parameter p is the definition of the electro mechanic

¹This section is inspired by the derivation of the sensitivity of the structural buckling load to parameter variations presented amongst others in [32, 95].

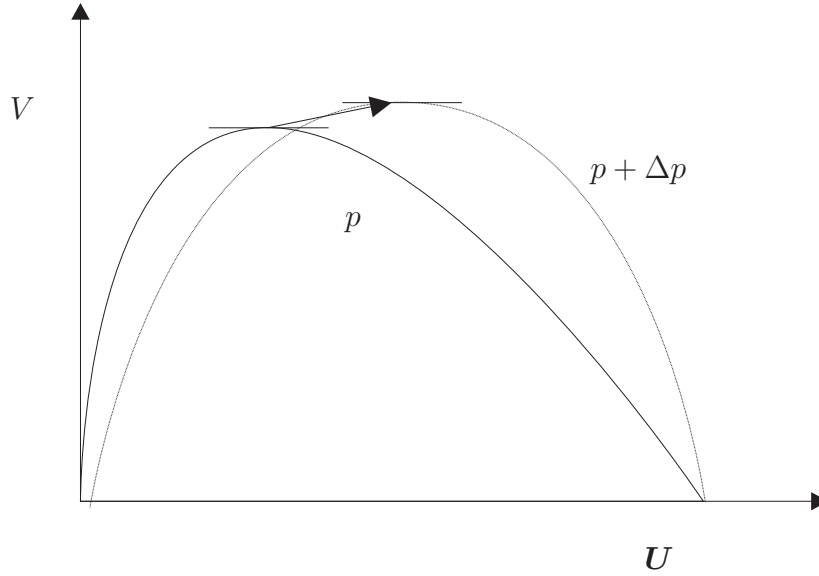


Figure 6.1: Pull curves for different elasticity-moduli.

energy. The goal is to see how the pull-in voltage changes when p changes (3.81):

$$W = W_{mech} + W_{elec} = W(\mathbf{U}, p, V), \quad (6.2)$$

the equilibrium equations are in that case defined as:

$$-\frac{\partial W}{\partial \mathbf{U}} = \mathbf{F}^{elec} - \mathbf{F}^{int} = 0. \quad (6.3)$$

Because equilibrium has to be satisfied for a model with a perturbed parameter of $p = p + \Delta p$ as well, it is imposed that the derivative of the equilibrium equations with respect to the Young's modulus has to be zero as well. So it will be assumed that $\mathbf{U}(p)$ and $V(p)$ are functions of p :

$$\frac{d}{dp} \left(\frac{\partial W(\mathbf{U}(p), V(p), p)}{\partial \mathbf{U}} \right) = \frac{\partial^2 W}{\partial \mathbf{U}^2} \frac{d\mathbf{U}}{dp} + \frac{\partial^2 W}{\partial \mathbf{U} \partial V} \frac{dV}{dp} + \frac{\partial^2 W}{\partial \mathbf{U} \partial p} = 0. \quad (6.4)$$

Because the tangent stiffness is defined as

$$\frac{\partial^2 W}{\partial \mathbf{U}^2} = \mathbf{K}, \quad (6.5)$$

and only the mechanical energy within the internal force depends on p :

$$\begin{aligned} \frac{\partial^2 W}{\partial \mathbf{U} \partial p} &= -\frac{\partial}{\partial p} (\mathbf{F}^{elec} - \mathbf{F}^{int}) = \frac{\partial}{\partial p} (\mathbf{F}^{int}) = \\ &= \frac{\partial}{\partial p} \begin{bmatrix} \mathbf{K}_{uu}^m \mathbf{u} \\ \mathbf{K}_{\phi\phi} \phi \end{bmatrix} = \begin{bmatrix} \frac{\partial \mathbf{K}_{uu}^m}{\partial p} & 0 \\ 0 & 0 \end{bmatrix} \mathbf{U} = \frac{\partial \mathbf{K}}{\partial p} \mathbf{U}, \end{aligned} \quad (6.6)$$

equation (6.4) can be simplified as:

$$\frac{d}{dp} \left(\frac{\partial W}{\partial \mathbf{U}} \right) = \mathbf{K} \frac{d\mathbf{U}}{dp} + \frac{\partial^2 W}{\partial \mathbf{U} \partial V} \frac{dV}{dp} + \frac{\partial \mathbf{K}}{\partial p} \mathbf{U} = 0. \quad (6.7)$$

6.2.1 Matrix sensitivity to mechanical parameters

For structural parameters the term $\frac{\partial \mathbf{K}}{\partial p}$ can be derived rather straightforward. If p is the Young's modulus it follows from equations (3.93-3.97) that the only entry of p is found in the Hooke's matrix \mathbf{C} in equation (3.93), therefore the derivative is:

$$\frac{\partial \mathbf{K}}{\partial p} = \begin{bmatrix} \frac{\partial \mathbf{K}_{uu}^m}{\partial p} & 0 \\ 0 & 0 \end{bmatrix}, \quad (6.8)$$

where:

$$\frac{\partial \mathbf{K}_{uu}^m}{\partial p} = \int_V \mathbf{B}_u^T \frac{\partial \mathbf{C}}{\partial E} \mathbf{B}_u dV. \quad (6.9)$$

In the case of linear plane strain, the derivative of the Hooke's matrix is:

$$\begin{aligned} \frac{\partial}{\partial E} \left(\frac{E}{(1+\nu)(1-2\nu)} \begin{bmatrix} 1-\nu & \nu & 0 \\ \nu & 1-\nu & 0 \\ 0 & 0 & \frac{1-2\nu}{2} \end{bmatrix} \right) = \\ \frac{1}{(1+\nu)(1-2\nu)} \begin{bmatrix} 1-\nu & \nu & 0 \\ \nu & 1-\nu & 0 \\ 0 & 0 & \frac{1-2\nu}{2} \end{bmatrix}. \end{aligned} \quad (6.10)$$

Also the other possible structural parameters enter the stiffness matrix through \mathbf{K}_{uu}^m , therefore the computations are very similar. These matrix derivatives can also be computed by finite differences, yielding semi-analytical approaches.

Energy derivative with the applied potential

The remaining terms in (6.7) are not trivially computed. Let's start with equation (3.82) to derive the term $\frac{\partial^2 W}{\partial \mathbf{U} \partial V}$:

$$\frac{\partial}{\partial V} \left(\frac{\partial W}{\partial \mathbf{U}} \right) = \frac{\partial}{\partial V} (\mathbf{F}^{elec} - \mathbf{F}^{int}) = 0. \quad (6.11)$$

Since:

$$\mathbf{F}^{int} = \begin{bmatrix} \mathbf{K}_{uu}^m \mathbf{u} \\ \mathbf{K}_{\phi\phi} \phi \end{bmatrix}, \quad (6.12)$$

which does not depend directly on V , the following holds:

$$\frac{\partial}{\partial V} \left(\frac{\partial W}{\partial \mathbf{U}} \right) = \frac{\partial \mathbf{F}^{elec}}{\partial V}. \quad (6.13)$$

In the derivation above only the DOFs that are not constrained were considered: \mathbf{U} was only filled with the unconstrained displacements and nodal potentials. Hence not with the boundary potentials that have a zero or V value. It is possible to include those DOFs ($\bar{\phi}$) in the derivation:

$$\mathbf{U}_{tot} = \begin{bmatrix} \mathbf{U} \\ \bar{\phi} \end{bmatrix} = \begin{bmatrix} \mathbf{U} \\ \hat{\mathbf{1}}V \end{bmatrix}, \quad (6.14)$$

where:

$$\hat{\mathbf{1}} = \begin{bmatrix} 1 \\ \vdots \\ 1 \end{bmatrix}. \quad (6.15)$$

This will result in the following tangent stiffness definition:

$$\mathbf{K}_{tot} = \begin{bmatrix} \mathbf{K}_{uu} & \mathbf{K}_{u\phi} & \mathbf{K}_{u\bar{\phi}} \\ \mathbf{K}_{\phi u} & \mathbf{K}_{\phi\phi} & \mathbf{K}_{\phi\bar{\phi}} \\ \mathbf{K}_{\bar{\phi}u} & \mathbf{K}_{\bar{\phi}\phi} & \mathbf{K}_{\bar{\phi}\bar{\phi}} \end{bmatrix}, \quad (6.16)$$

which allows for the definition of:

$$\mathbf{K}_{U\bar{\phi}} = \begin{bmatrix} \mathbf{K}_{\bar{\phi}u}^T & \mathbf{K}_{\bar{\phi}\phi}^T \end{bmatrix}^T. \quad (6.17)$$

In that case the total energy can be seen as:

$$W = W(\mathbf{U}, \bar{\phi}(V), p), \quad (6.18)$$

and the energy derivative with \mathbf{U} and V as:

$$\frac{\partial}{\partial V} \left(\frac{\partial W}{\partial \mathbf{U}} \right) = \frac{\partial^2 W}{\partial \mathbf{U} \partial \bar{\phi}} \frac{\partial \bar{\phi}}{\partial V} = \frac{\partial^2 W}{\partial \mathbf{U} \partial \bar{\phi}} \begin{bmatrix} 1 \\ \vdots \\ 1 \end{bmatrix}. \quad (6.19)$$

It is clear from equation (6.17) that:

$$\frac{\partial}{\partial \bar{\phi}} (\mathbf{F}^{elec}) = \frac{\partial^2 W}{\partial \mathbf{U} \partial \bar{\phi}} = -\mathbf{K}_{U\bar{\phi}} \quad (6.20)$$

therefore:

$$\frac{\partial}{\partial V} \left(\frac{\partial W}{\partial \mathbf{U}} \right) = -\mathbf{K}_{U\bar{\phi}} \hat{\mathbf{1}}. \quad (6.21)$$

Finding the pull-in sensitivity by removing the displacement sensitivity

Thus equation (6.4) can be written as:

$$\frac{d}{dp} \left(\frac{\partial W}{\partial \mathbf{U}} \right) = \mathbf{K} \frac{d\mathbf{U}}{dp} - \mathbf{K}_{U\bar{\phi}} \begin{bmatrix} 1 \\ \vdots \\ 1 \end{bmatrix} \frac{dV}{dp} + \frac{\partial \mathbf{K}}{\partial p} \mathbf{U} = 0, \quad (6.22)$$

in which all terms are known once the pull-in point has been computed except $\frac{dV}{dp}$ and $\frac{d\mathbf{U}}{dp}$. Since the main interested is $\frac{dV}{dp}$ the complete equation is premultiplied with the transpose of the first eigenvector $\boldsymbol{\mu}_1$. At pull in $\mathbf{K}\boldsymbol{\mu}_1 = 0$ and because \mathbf{K} is symmetric also $\boldsymbol{\mu}_1^T \mathbf{K} = 0$. If equation (6.22) is premultiplied with the pull-in mode the $\mathbf{K} \frac{\partial \mathbf{U}}{\partial p}$ term is removed. The resulting equation describes the relation for the voltage sensitivity such that the perturbed solution is still a pull-in point:

$$-\boldsymbol{\mu}_1^T \mathbf{K}_{U\bar{\phi}} \hat{\mathbf{1}} \frac{dV}{dp} \Big|_{PI} + \boldsymbol{\mu}_1^T \frac{\partial \mathbf{K}}{\partial p} \mathbf{U} \Big|_{PI} = 0, \quad (6.23)$$

which yields the sensitivity of the pull-in voltage to a variation of the parameter p :

$$\frac{dV}{dp} \Big|_{PI} = \frac{\boldsymbol{\mu}_1^T \frac{\partial \mathbf{K}}{\partial p} \mathbf{U} \Big|_{PI}}{\boldsymbol{\mu}_1^T \mathbf{K}_{U\bar{\phi}} \hat{\mathbf{1}}}. \quad (6.24)$$

Because the parameter p is a structural parameter only the mechanical part of \mathbf{K} depends on p , hence the derivative of \mathbf{K} times \mathbf{U} is simply the derivative of the internal force vector. Therefore it is possible to write the above equation as:

$$\left. \frac{dV}{dp} \right|_{PI} = \frac{-\boldsymbol{\mu}_1^T \frac{\partial \mathbf{F}^{int}}{\partial p}}{\boldsymbol{\mu}_1^T \frac{\partial \mathbf{F}^{elec}}{\partial V}}, \quad (6.25)$$

which is very similar to the traditional definition of sensitivity of the limit point buckling load [32, 95] and equal to the pull-in sensitivity computed in [78].

Computing the pull-in displacement sensitivity

If $\left. \frac{d\mathbf{U}}{dp} \right|_{PI}$ needs to be computed it can be computed with equation (6.22) in which all terms are known once $\left. \frac{dV}{dp} \right|_{PI}$ is known:

$$\left. \frac{d\mathbf{U}}{dp} \right|_{PI} = -\mathbf{K}^{-1} \left(-\mathbf{K}_{U\bar{\phi}} \hat{\mathbf{1}} \left. \frac{dV}{dp} \right|_{PI} + \frac{\partial \mathbf{K}}{\partial p} \mathbf{U} \Big|_{PI} \right). \quad (6.26)$$

Although \mathbf{K} is singular, the right-hand side of the equation above is forced to be orthogonal to $\boldsymbol{\mu}_1$ by equation (6.23), therefore a solution should exist.

The problem is that for any constant c the derivative $\left. \frac{d\mathbf{U}}{dp} \right|_{PI} = \left. \frac{d\mathbf{U}}{dp} \right|_{PI} + c\boldsymbol{\mu}_1$ will satisfy equation (6.22). A more robust approach in this case is to use a semi-analytical approach and compute $\left. \frac{d\mathbf{U}}{dp} \right|_{PI}$ by finite differences:

$$\left. \frac{d\mathbf{U}}{dp} \right|_{PI} \approx \frac{\Delta \mathbf{U}}{\Delta p} \Big|_{V=\text{constant}} + \frac{\Delta \mathbf{U}}{\Delta V} \Big|_{p=\text{constant}} \left. \frac{dV}{dp} \right|_{PI}. \quad (6.27)$$

This requires two more incremental steps to compute the two extra points required for the finite differences, causing extra computation time. However since no new pull-in point has to be computed a very expensive zero finding algorithm is not needed. When $\left. \frac{d\mathbf{U}}{dp} \right|_{PI}$ is approximated by finite differences directly, two actual pull-in points have to be computed hence it is more expensive.

6.3 Second order sensitivity of the pull-in voltage

The next step is to compute the second order sensitivity of the pull-in voltage to the parameter p :

$$\left. \frac{d^2 V}{dp^2} \right|_{PI}. \quad (6.28)$$

The simplest approach is to differentiate equation (6.24) with p :

$$\left. \frac{d^2 V}{dp^2} \right|_{PI} = \frac{\boldsymbol{\mu}_1^T \mathbf{K}_{U\bar{\phi}} \hat{\mathbf{1}} \cdot \frac{d}{dp} \left(\boldsymbol{\mu}_1^T \frac{\partial \mathbf{K}}{\partial p} \mathbf{U} \right)}{\left(\boldsymbol{\mu}_1^T \mathbf{K}_{U\bar{\phi}} \hat{\mathbf{1}} \right)^2} - \frac{\frac{d}{dp} \left(\mathbf{K}_{U\bar{\phi}} \hat{\mathbf{1}} \right) \boldsymbol{\mu}_1^T \frac{\partial \mathbf{K}}{\partial p} \mathbf{U}}{\left(\boldsymbol{\mu}_1^T \mathbf{K}_{U\bar{\phi}} \hat{\mathbf{1}} \right)^2}. \quad (6.29)$$

Basically there are two unknown terms in this equation:

$$A = \frac{d}{dp} \left(\boldsymbol{\mu}_1^T \frac{\partial \mathbf{K}}{\partial p} \mathbf{U} \right), \quad (6.30)$$

and:

$$B = \frac{d}{dp} (\boldsymbol{\mu}_1^T \mathbf{K}_{U\bar{\phi}} \hat{\mathbf{1}}). \quad (6.31)$$

Working out A

If the first term A is worked out, one finds (remember that $\mathbf{K} = \mathbf{K}(U, p, V)$):

$$A = \frac{d\boldsymbol{\mu}_1^T}{dp} \frac{\partial \mathbf{K}}{\partial p} \mathbf{U} + \boldsymbol{\mu}_1^T \left[\frac{\partial \mathbf{K}}{\partial p} + \frac{\partial^2 \mathbf{K}}{\partial p \partial \mathbf{U}} \mathbf{U} \right] \frac{d\mathbf{U}}{dp} + \boldsymbol{\mu}_1^T \frac{\partial^2 \mathbf{K}}{\partial p^2} \mathbf{U} + \boldsymbol{\mu}_1^T \frac{\partial^2 \mathbf{K}}{\partial V \partial p} \frac{dV}{dp} \mathbf{U} \Big|_{PI}. \quad (6.32)$$

Some of the terms in the equation above can be eliminated because they are zero:

$$\frac{\partial^2 \mathbf{K}}{\partial V \partial p} = 0, \quad (6.33)$$

because $\frac{\partial \mathbf{K}}{\partial p}$ only depends on \mathbf{K}_{uu}^m which does not depend on the applied voltage V , as was shown in section 6.2. The same section showed that for a linear elastic material model $\frac{\partial \mathbf{K}}{\partial p}$ does not depend on \mathbf{U} , hence:

$$\frac{\partial^2 \mathbf{K}}{\partial \mathbf{U} \partial p} = 0, \quad (6.34)$$

and if the parameter p is the Young's modulus also

$$\frac{\partial^2 \mathbf{K}}{\partial p^2} = 0, \quad (6.35)$$

however for other mechanical parameters, this is not the case. When for instance the sensitivity to variations of the beam thickness h is determined, the term $\frac{\partial \mathbf{K}}{\partial h}$ does depend on beam thickness h , though computation of $\frac{\partial^2 \mathbf{K}}{\partial h^2}$ is not too difficult in that case. Therefore equation (6.32) will be written as:

$$A = \frac{d\boldsymbol{\mu}_1^T}{dp} \frac{\partial \mathbf{K}}{\partial p} \mathbf{U} + \boldsymbol{\mu}_1^T \frac{\partial \mathbf{K}}{\partial p} \frac{d\mathbf{U}}{dp} + \boldsymbol{\mu}_1^T \frac{\partial^2 \mathbf{K}}{\partial p^2} \mathbf{U}. \quad (6.36)$$

where the computation of $\frac{d\boldsymbol{\mu}_1^T}{dp}$ will be discussed later.

Working out B

The second term B can be written as:

$$B = \frac{d\boldsymbol{\mu}_1^T}{dp} \mathbf{K}_{U\bar{\phi}} \hat{\mathbf{1}} + \boldsymbol{\mu}_1^T \frac{\partial \mathbf{K}_{U\bar{\phi}}}{\partial \mathbf{U}} \frac{d\mathbf{U}}{dp} \hat{\mathbf{1}} + \boldsymbol{\mu}_1^T \frac{\partial \mathbf{K}_{U\bar{\phi}}}{\partial V} \frac{\partial V}{\partial p} \hat{\mathbf{1}} \Big|_{PI} + \boldsymbol{\mu}_1^T \frac{\partial \mathbf{K}_{U\bar{\phi}}}{\partial p} \hat{\mathbf{1}}. \quad (6.37)$$

One term can be removed from this equation. Since there are no imposed non-zero displacements in the problem $\mathbf{K}_{U\bar{\phi}}$ does not contain any terms that are part of \mathbf{K}_{uu}^m , hence:

$$\frac{\partial \mathbf{K}_{U\bar{\phi}}}{\partial p} = 0, \quad (6.38)$$

which reduces equation (6.37) to:

$$B = \left(\frac{d\boldsymbol{\mu}_1^T}{dp} \mathbf{K}_{U\bar{\phi}} + \boldsymbol{\mu}_1^T \frac{\partial \mathbf{K}_{U\bar{\phi}}}{\partial \mathbf{U}} \frac{d\mathbf{U}}{dp} + \boldsymbol{\mu}_1^T \frac{\partial \mathbf{K}_{U\bar{\phi}}}{\partial V} \frac{\partial V}{\partial p} \right) \Big|_{PI} \hat{\mathbf{1}}. \quad (6.39)$$

Basically most terms in the equations above are known or already computed during the computation of $\frac{dV}{dp} \Big|_{PI}$. The only remaining unknowns are: $\frac{\partial \mathbf{K}_{U\bar{\phi}}}{\partial V}$, $\frac{\partial \mathbf{K}_{U\bar{\phi}}}{\partial \mathbf{U}}$ and $\frac{d\boldsymbol{\mu}_1^T}{dp}$.

6.3.1 Matrix sensitivity with the potential

The computation of $\frac{\partial \mathbf{K}_{U\bar{\phi}}}{\partial V}$ is not difficult, since the boundary potential is only explicitly present in \mathbf{K}_{uu}^e and $\mathbf{K}_{u\phi}$. Therefore the derivative of these matrices with respect to $\bar{\phi}$ can be found easily.

6.3.2 Matrix sensitivity with the total state vector

The computation of $\frac{\partial \mathbf{K}_{U\bar{\phi}}}{\partial \mathbf{U}}$ is more difficult, but this derivation can be split into a derivation with \mathbf{u} and a derivation with ϕ . Determining $\frac{\partial \mathbf{K}_{U\bar{\phi}}}{\partial \phi}$ is straightforward, because the constituent sub-matrices of $\mathbf{K}_{U\bar{\phi}}$ depend directly on ϕ .

Determining $\frac{\partial \mathbf{K}_{U\bar{\phi}}}{\partial \mathbf{u}}$ is slightly more difficult. Note that in the mechanically linear case \mathbf{K}_{uu}^m does not depend on \mathbf{u} , but the other matrices (\mathbf{K}_{uu}^e , $\mathbf{K}_{u\phi}$ and $\mathbf{K}_{\phi\phi}$) depend on \mathbf{u} through the shape functions that depend on the position of the electric nodes. However, only the structural displacements of the interface \mathbf{u}_i have an influence on the position of the electric nodes. Moreover a change in position of the internal nodes of the electric domain should have no influence on the electric solution, theoretically only the boundary nodes determine the solution. Therefore:

$$\frac{\partial \mathbf{K}_{U\bar{\phi}}}{\partial \mathbf{u}} = \frac{\partial \mathbf{K}_{U\bar{\phi}}}{\partial \mathbf{x}_i} \frac{\partial \mathbf{x}_i}{\partial \mathbf{u}_i}. \quad (6.40)$$

The interface positions are simply the initial interface positions plus the structural displacements:

$$\mathbf{x}_i = \mathbf{x}_i^0 + \mathbf{u}_i, \quad (6.41)$$

thus:

$$\frac{\partial \mathbf{x}_i}{\partial \mathbf{u}_i} = 1, \quad (6.42)$$

and:

$$\frac{\partial \mathbf{K}_{U\bar{\phi}}}{\partial \mathbf{u}} = \frac{\partial \mathbf{K}_{U\bar{\phi}}}{\partial \mathbf{x}_i}, \quad (6.43)$$

which can be differentiated analytically with relative ease.

6.3.3 Sensitivity of the pull-in mode

The last term required for B that has to be computed is $\frac{d\boldsymbol{\mu}_1}{dp}$. An important characteristic of an eigenvalue is that the following equation always holds: [45, 93]:

$$(\mathbf{K} - \lambda_i \mathbf{I}) \boldsymbol{\mu}_i = 0, \quad (6.44)$$

hence:

$$\frac{d}{dp} ((\mathbf{K} - \lambda_i \mathbf{I}) \boldsymbol{\mu}_i) = 0, \quad (6.45)$$

which gives:

$$(\mathbf{K} - \lambda_i \mathbf{I}) \frac{d\boldsymbol{\mu}_i}{dp} = - \left(\frac{d\mathbf{K}}{dp} - \frac{d\lambda_i}{dp} \mathbf{I} \right) \boldsymbol{\mu}_i. \quad (6.46)$$

It is known that \mathbf{K} is symmetric and real, therefore

$$\boldsymbol{\mu}_i^T ((\mathbf{K} - \lambda_i \mathbf{I}) = 0 \quad (6.47)$$

as well. In other words, there is no distinction between a left and a right eigenvector. Furthermore, since the sensitivity of $\boldsymbol{\mu}_i$ while remaining on pull-in is of interest, the eigenvalue λ_i must remain zero, hence the sensitivity $\frac{d\lambda_i}{dp}$ must be 0. Therefore (6.46) simplifies to:

$$(\mathbf{K} - \lambda_i \mathbf{I}) \frac{d\boldsymbol{\mu}_i}{dp} = - \left(\frac{d\mathbf{K}}{dp} \right) \boldsymbol{\mu}_i, \quad (6.48)$$

which is rank deficient, but the equations are consistent, since the right-hand side of the equation is orthogonal to the eigenvector. It is possible to write $\frac{d\boldsymbol{\mu}_i}{dp}$ as:

$$\frac{d\boldsymbol{\mu}_i}{dp} = \sum_{r=1}^n \gamma_r \boldsymbol{\mu}_r, \quad (6.49)$$

which after substitution into equation (6.48) gives:

$$\gamma_r = - \frac{\boldsymbol{\mu}_r^T \left(\left(\frac{d\mathbf{K}}{dp} \right) \boldsymbol{\mu}_i \right)}{(\lambda_r - \lambda_i)}. \quad (6.50)$$

It is obvious that this equation cannot be used to determine γ_i because the denominator is zero for $r = i$. The sum can therefore only be written as:

$$\frac{d\boldsymbol{\mu}_i}{dp} = \sum_{r \neq i} \gamma_r \boldsymbol{\mu}_r + \gamma_i \boldsymbol{\mu}_i = \mathbf{V}_i + \gamma_i \boldsymbol{\mu}_i. \quad (6.51)$$

The coefficient γ_i can be determined by explicitly stating that the eigenmode is normalized ($\boldsymbol{\mu}_i^T \boldsymbol{\mu}_i = 1$). Differentiating this normalization constraint gives:

$$\frac{d}{dp} (\boldsymbol{\mu}_i^T \boldsymbol{\mu}_i = 1). \quad (6.52)$$

$$2\boldsymbol{\mu}_i^T \frac{d\boldsymbol{\mu}_i}{dp} = 0. \quad (6.53)$$

If equation (6.51) is substituted into equation (6.53) the result can be used to determine γ_i :

$$\gamma_i = -\boldsymbol{\mu}_i^T \mathbf{V}_i. \quad (6.54)$$

This procedure is rather expensive because all eigenvectors have to be known, which is nearly impossible for large systems. In 1976 Nelson proposed an alternative method which does not require the computation of all eigenvectors [93]. He showed that by removing one DOF from the rank $n - 1$ system (6.48) it is possible to compute the

non-homogeneous part of the solution \mathbf{V}_i without the need to compute all eigenvectors. When starting with:

$$(\mathbf{K} - \lambda_i \mathbf{I}) \frac{d\boldsymbol{\mu}_I}{dp} = \mathbf{R}, \quad (6.55)$$

where \mathbf{R} denotes the right-hand side of equation (6.48), it is possible to remove the equation k :

$$\begin{bmatrix} (\mathbf{K} - \lambda_i \mathbf{I})_{11} & 0 & \mathbf{K}_{13} \\ 0 & 1 & 0 \\ \mathbf{K}_{31} & 0 & (\mathbf{K} - \lambda_i \mathbf{I})_{33} \end{bmatrix} = \begin{bmatrix} \mathbf{V}_1 \\ V_k \\ \mathbf{V}_3 \end{bmatrix} = \begin{bmatrix} \mathbf{R}_1 \\ 0 \\ \mathbf{R}_3 \end{bmatrix}. \quad (6.56)$$

This gives the proper vector \mathbf{V} for determination of the derivative of $\boldsymbol{\mu}_i$ only if the k^{th} value of $\boldsymbol{\mu}_i$ is not zero.

Total matrix derivative with a parameter

To be able to determine the derivative of the eigenmode the total derivative of the stiffness matrix \mathbf{K} with p has to be known. The derivative of the stiffness matrix with p can be written as:

$$\frac{d\mathbf{K}}{dp} = \left(\frac{\partial \mathbf{K}}{\partial p} + \frac{\partial \mathbf{K}}{\partial \mathbf{U}} \frac{d\mathbf{U}}{dp} + \frac{\partial \mathbf{K}}{\partial V} \frac{dV}{dp} \right) \Big|_{PI}, \quad (6.57)$$

in which the only unknowns are: $\frac{\partial \mathbf{K}}{\partial \mathbf{U}}$ and $\frac{\partial \mathbf{K}}{\partial V}$ which can be computed as has been explained above for the computation of the derivatives of $\mathbf{K}_{U\bar{\phi}}$. Therefore all unknowns to compute A and B , hence $\frac{d^2 V}{dp^2}$ can be computed. Because the derivative of the state vector with p : $\frac{d\mathbf{U}}{dp}$ was determined with a semi-analytical method, this derivation of $\frac{d^2 V}{dp^2}$ does not give an analytical, but a semi-analytical sensitivity.

Second order sensitivities with multiple parameters

When it is assumed that there are multiple parameters p_i , there is no longer a single sensitivity. In that case the second order sensitivity becomes a Hessian matrix:

$$\mathbf{H} = \left[\frac{d^2 V}{dp_i dp_j} \right]. \quad (6.58)$$

6.4 2D FEM test case

The sensitivities of a 2D FEM model will be discussed in this section. The computed analytical sensitivities will be compared with finite difference approximations. First the electric part of the simple model is described, thereafter the mechanical part and finally the results are discussed.

6.4.1 The electric domain

The initial domain shown in figure 6.2 is very simple.² The electric domain is the blue gap under the beam. Only the actuated electrode at the top can deform. The

²For more detail about this test case see chapter 4.

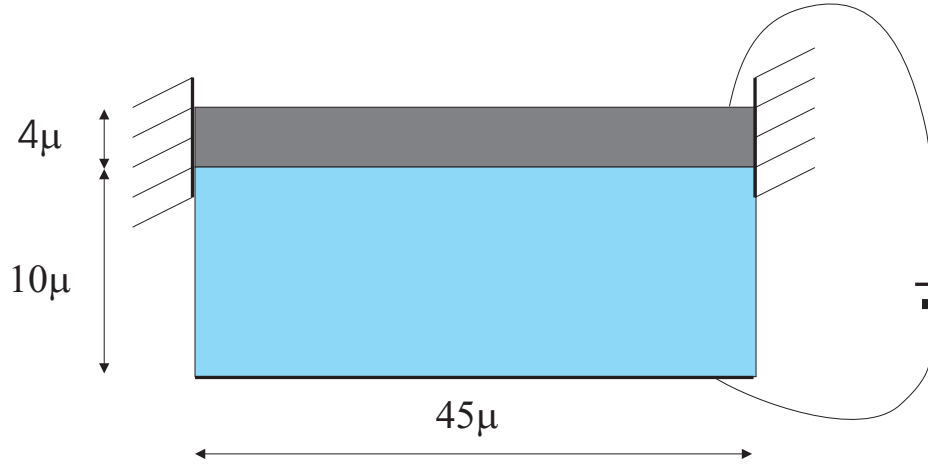


Figure 6.2: Simple beam.

permittivity of the structure is equal to the vacuum permittivity of: $\varepsilon_0 = 8.8541 \cdot 10^{-12}$. On the sides, where there are no electrodes, the symmetry boundary condition or *zero charge* condition is applied.

6.4.2 The mechanical domain

The mechanical domain is the gray beam shown in figure 6.2 is almost as simple as the electric domain. It is a beam clamped on both sides. The electrostatic pressure acts on the bottom side of the beam, which corresponds to the top electrode of the electric domain. The mechanical domain is modeled with beam elements.

Table 6.1: Summary of the material properties.

Air gap			
Property	Symbol	Value	Units
<i>Electric permittivity</i>	ε	$8.8541 \cdot 10^{-12}$	F/m
Structure			
Property	Symbol	Value	Units
<i>Elasticity modulus</i>	E	$1 \cdot 10^5$	Pa
<i>Beam thickness</i>	h_0	$4 \cdot 10^{-6}$	m

6.4.3 Results

In this section the sensitivities for parameter variations where all element parameters change together will be computed and validated first. Secondly the sensitivities for individual element changes will be computed and validated.

Constant beam properties

Once the pull-in voltage and the corresponding displacement have been determined, the value of the sensitivity of the pull-in voltage to perturbations of the thickness can be computed numerically with the approach presented in section 6.2:

$$\left. \frac{dV}{dh} \right|_{PI} = 1.6462 \cdot 10^7 V/m. \quad (6.59)$$

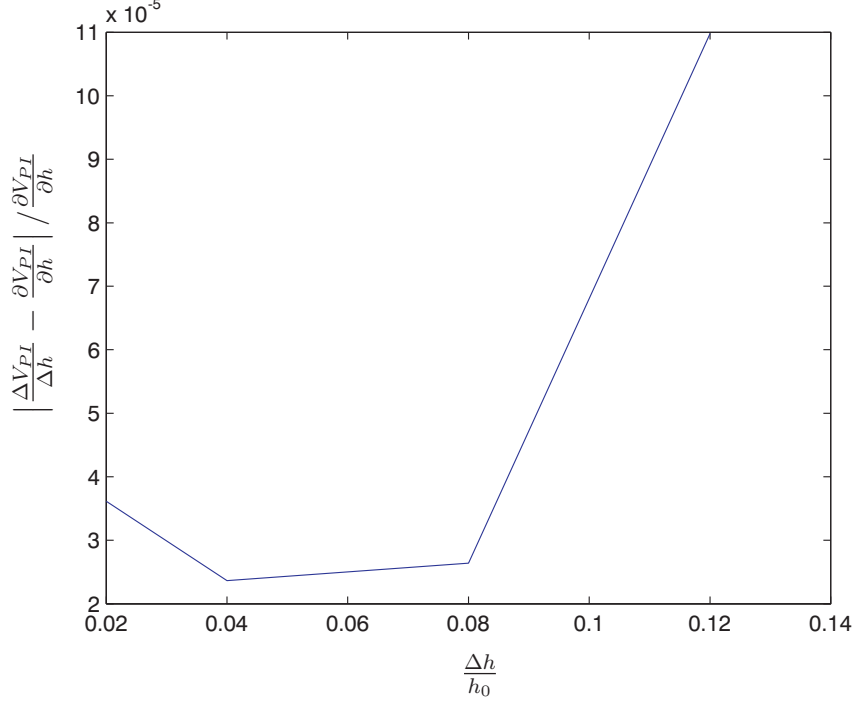


Figure 6.3: Convergence of the finite difference approximation to the analytical solution for the first order sensitivity.

Another way to compute the sensitivity is by a finite difference approximation. The pull-in voltage is computed for a model where $h = h_0 + \frac{1}{2}\Delta h$ and one where $h = h_0 - \frac{1}{2}\Delta h$, in that case the approximation of the sensitivity is:

$$\left. \frac{dV}{dh} \right|_{PI} \approx \frac{V_{PI}(h = h_0 + \frac{1}{2}\Delta h) - V_{PI}(h = h_0 - \frac{1}{2}\Delta h)}{\Delta h}. \quad (6.60)$$

The approximation with a perturbation of $\Delta h = 4 \cdot 10^{-8} m$ is:

$$\left. \frac{\Delta V}{\Delta h} \right|_{PI} = 1.6462 \cdot 10^7 V/m, \quad (6.61)$$

which is equal to the approach of section 6.2, indicating that this approach is a correct method to compute the sensitivity. This is confirmed by the result in figure 6.3 which shows that the finite difference result converges to the analytical solution when the thickness increment decreases. It converges from above until the increment is smaller than 4% of the original thickness. At that point errors due to the tolerances on the pull-in determination start dominating the accuracy. This tolerance cannot be set to tight due to time limitations.

Using the same approach an accuracy estimate of the second order sensitivity can be made. Once the pull-in voltage and the corresponding displacement have been determined, the value of the second order sensitivity of the pull-in voltage to perturbations of the thickness can be computed numerically with the approach presented in section 6.3:

$$\left. \frac{d^2V}{dh^2} \right|_{PI} = 2.0537 \cdot 10^{12} V/m^2. \quad (6.62)$$

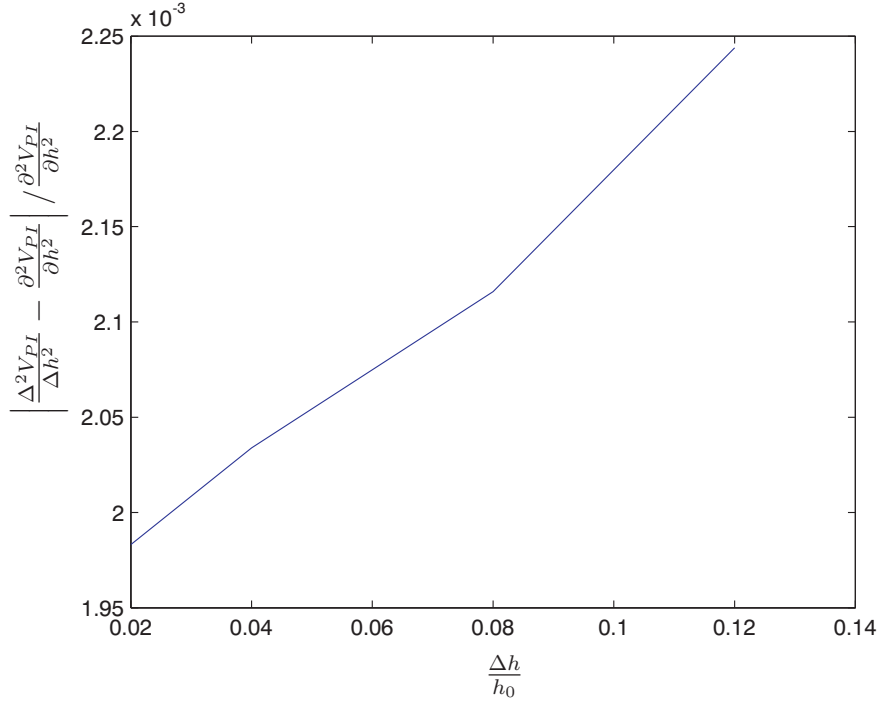


Figure 6.4: Convergence of the finite difference approximation to the semi-analytical solution for the second order sensitivity.

The approximation with finite difference is computed as follows: the pull-in voltage is computed for a model where $h = h_0 + \frac{1}{2}\Delta h$ one where $h = h_0 - \frac{1}{2}\Delta h$ and one where $h = h_0$, next the approximation of the second order sensitivity is derived with:

$$\left. \frac{d^2V}{dh^2} \right|_{PI} \approx \frac{V_{PI}(h = h_0 + \frac{1}{2}\Delta h) - 2V_{PI}(h = h_0) + V_{PI}(h = h_0 - \frac{1}{2}\Delta h)}{(\frac{1}{2}\Delta h)^2}. \quad (6.63)$$

The approximation with a perturbation of $0.02 \cdot 10^5 Pa$ is:

$$\left. \frac{\Delta^2V}{\Delta h^2} \right|_{PI} = 2.0577 \cdot 10^{12} V/m^2, \quad (6.64)$$

The match is slightly worse than the match for the first order sensitivity. But that can be explained by the fact that finite difference computation converges a bit slower, but also by the fact that $\frac{\partial^2V_{PI}}{\partial h^2}$ was computed *semi*-analytically. The convergence of the finite difference approximation to the semi-analytical solution is illustrated in figure 6.4.

The results above were computed with a 6 by 18 mesh, thus 18 beam elements and 108 electrostatic elements. Using a 4 by 12 mesh the results are:

$$\left. \frac{dV}{dh} \right|_{PI} = 1.6519 \cdot 10^7 V/m, \quad (6.65)$$

and

$$\left. \frac{d^2V}{dh^2} \right|_{PI} = 2.0618 \cdot 10^{12} V/m^2, \quad (6.66)$$

therefore the mesh was already converged. And from this point onwards a 4 by 12 mesh is used. Note that for this mesh pull-in is 44.05V.

For the same mesh also the sensitivities with respect to the elasticity modulus can be determined:

$$\left. \frac{dV}{dE} \right|_{PI} = 2.20 \cdot 10^{-4} V/Pa, \quad (6.67)$$

and:

$$\left. \frac{d^2V}{dE^2} \right|_{PI} = -1.10 \cdot 10^{-9} V/Pa^2, \quad (6.68)$$

These values are completely different and incomparable due the fact that the units are completely different. A better way of comparing both sensitivities is by looking at the logarithmic sensitivity:

$$\left. \frac{d \log(V)}{d \log(p)} \right|_{PI} = \frac{p}{V} \left. \frac{dV}{dp} \right|_{PI}, \quad (6.69)$$

If this value is bigger than 1 the response is sensitive to that parameter, if the value is smaller than one, the response is not sensitive. For the Young's modulus and the thickness these values are:

$$\left. \frac{d \log(V)}{d \log(h)} \right|_{PI} = 1.5, \quad (6.70)$$

and

$$\left. \frac{d \log(V)}{d \log(E)} \right|_{PI} = 0.5. \quad (6.71)$$

Therefore the pull-in voltage is more sensitive to thickness variations.

Distributed beam properties

If not only the sensitivity with respect to the global thickness is of interest, but also the sensitivities with respect to individual element thicknesses, these can be computed. In that case the gradient will be defined as:

$$\left. \frac{\partial V}{\partial h_i} \right|_{PI}, \quad (6.72)$$

and the Hessian as:

$$\left. \frac{\partial^2 V}{\partial h_i \partial h_j} \right|_{PI}. \quad (6.73)$$

These are computed with the 12 by 4 element mesh for the electrostatics and the 12 element mesh for the beam. Hence the Hessian (6.73) is a 12 by 12 matrix and the gradient (6.72) a vector with 12 elements.

The gradient can also be computed with finite differences, which is computationally expensive. Figure 6.5 gives the gradients with finite differences and the analytical method. They compare very well, actually no difference is seen. The black line giving the finite difference solution is behind the dashed red line that gives the analytical solution. What is clear from this figure is that the beam is very sensitive to thickness variations on those points where the beam undergoes a large bending strain, thus at the points with the highest bending stresses. This seems to comply with intuition.

Another test is to project the gradient and the Hessian on the following uniform perturbation mode:

$$\mathbf{T} = [t_i], \quad (6.74)$$

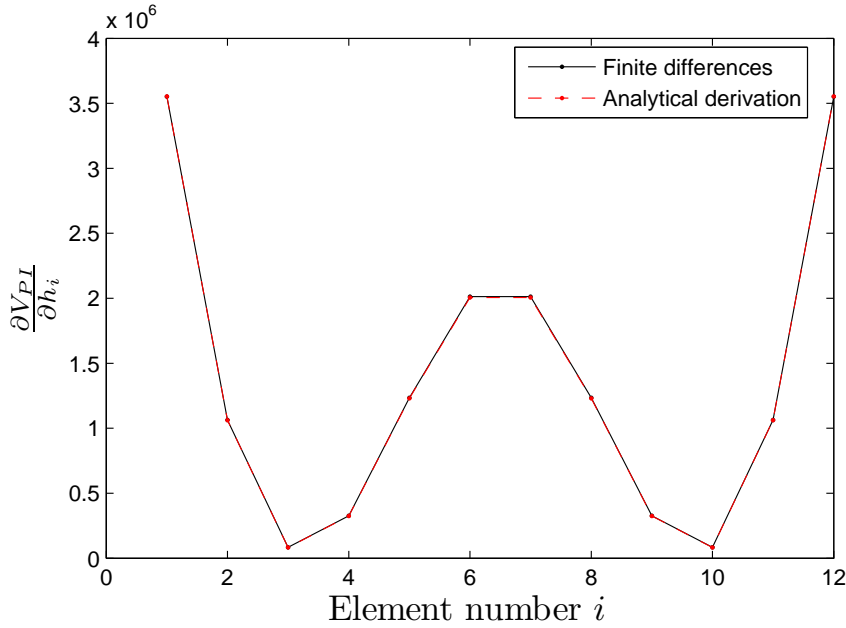


Figure 6.5: Gradient computed with the analytical method and with finite differences.

where:

$$t_i = 1. \quad (6.75)$$

So \mathbf{T} is a column of ones. In that case we know that if we project the gradient on this uniform perturbation mode we should find the derivative of the pull in voltage with respect to the uniform perturbation of the thickness:

$$\left. \frac{dV}{dh} \right|_{PI} = \mathbf{T}^T \left. \frac{\partial V}{\partial \mathbf{h}} \right|_{PI} = t_i \left. \frac{\partial V}{\partial h_i} \right|_{PI}. \quad (6.76)$$

Similarly:

$$\left. \frac{d^2 V_{PI}}{dh^2} \right|_{PI} = \mathbf{T}^T \left. \frac{\partial^2 V}{\partial \mathbf{h}^2} \mathbf{T} \right|_{PI} = t_i \left. \frac{\partial V}{\partial h_i \partial h_j} t_j \right|_{PI}. \quad (6.77)$$

In both cases the algorithm provides the correct values.

6.5 Conclusions

An analytical approach has been presented to compute the sensitivity of the pull-in voltage to variations of structural parameters for numerical models. With this approach it is possible to compute the sensitivity without having to compute the pull-in curve twice, such as with finite difference approximations. Also the sensitivity to variations of the electric permittivity can be determined using this approach.

A semi-analytical approach has been presented for second order sensitivities. With this approach it is possible to compute the second order sensitivity without having to compute the pull-in curve three times, as required with finite difference approximations. However it does need two extra incremental steps to find a proper approximation of the pull-in state vector sensitivity.

It was shown that the approach yields the same results as finite difference approximations for a simple FEM model.

Chapter 7

Stochastic analysis of pull-in

7.1 Introduction

So far all geometry and material parameters were known or at least assumed to be known. In MEMS design that is rarely the case. Thicknesses regularly depend on processing and can be different for each wafer or even for each individual device on the wafer or within a device. Similarly the Young's modulus is an uncertain value at these scales. These variations are rather random. Hence the response of the device is often random.¹

Suppose that one can estimate the statistical properties of the thickness variations due to processing. In that case it would be useful to predict the statistical distribution of the pull-in voltage. Of course one can just generate a lot of different random thicknesses with the correct statistical distribution, compute the pull-in voltage for each of them and analyze the data set. However this *Monte Carlo* simulation is extremely expensive.

A sensitivity analysis was performed in the previous chapter. With this sensitivity analysis more efficient methods are available for estimating the pull-in statistics: Stochastic Finite Element Methods [49, 116]. In this chapter these methods will be used to estimate the statistical properties of pull-in. First random variables and Stochastic FEM will be introduced, after which the techniques will be applied to the microbridge model.

7.2 Random numbers and Stochastic FEM

7.2.1 Random variables

Stochastic FEM starts with the assumption that some properties are random. In this work random numbers are indicated by a tilde, thus parameter \tilde{p} is random and p is a specific realization of that parameter.

Normally a random variable is characterized by its probability distribution function $F_p(p)$ that gives the probability that $\tilde{p} \leq p$. Similarly the probability density function $f_p(p)$ gives the probability that \tilde{p} is in the interval $[p, p + dp]$. Hence the distribution

¹This chapter is the result of a collaboration with C. Verhoosel.

and density are related by:

$$F_p(p) = \int_{-\infty}^p f_p(\tilde{p}) d\tilde{p}. \quad (7.1)$$

These functions fully describe the random variable but are often very difficult to obtain. Easier variables to work with are the mean, which is the expectation of a variable:

$$\mu_p = E[\tilde{p}] = \int_{-\infty}^{\infty} p f_p(p) dp, \quad (7.2)$$

and the variance, which is the expectation of the square of the deviation of \tilde{p} from the mean value:

$$\Sigma_{pp} = E[(\tilde{p} - \mu_p)^2] = Var[\tilde{p}] = \int_{-\infty}^{\infty} (p - \mu_p)^2 f_p(p) dp. \quad (7.3)$$

The variance has a different dimension from the mean, therefore it is sometimes convenient to use the standard deviation:

$$\sigma_p = \sqrt{\Sigma_{pp}}. \quad (7.4)$$

A non-dimensional measure of the deviation is the coefficient of variation:

$$V_p = \frac{\sigma_p}{\mu_p}. \quad (7.5)$$

Often there is more than one random variable within a model. In that case there is another important characterization required: the statistical dependency of one variable on the other, the covariance:

$$\Sigma_{p_i p_j} = \int_{-\infty}^{\infty} \int_{-\infty}^{\infty} (p_i - \mu_{p_i})(p_j - \mu_{p_j}) f_{p_i p_j}(p_i, p_j) dp_i dp_j. \quad (7.6)$$

Often the mean and (co)variances provide enough information to study the propagation of statistical properties through the FEM models. However if it is required to assume a specific distribution for \tilde{p} it is assumed that the input distribution is a normal (or Gaussian) distribution. In that case the probability density function is:

$$f_p(p) = \frac{1}{\sigma_p \sqrt{2\pi}} e^{-\frac{(p - \mu_p)^2}{2\sigma_p^2}}. \quad (7.7)$$

The probability density function of a normal distribution with $\mu_p = 0$ and $\sigma_p = 1$ is shown in figure 7.1. The normal distribution assumes that most realizations are centered around the mean, which has frequently been seen in nature.

When a random field is used it is assumed that the parameter of interest is a function of location: $\tilde{p} = \tilde{p}(x)$. Of course in a FEM setting this field has to be discretized. In this work the *Midpoint* method will be used for random field discretization. In that case it is assumed that within an element the parameter is uniform and equal to the value at the center of the element. This means that there are n different random parameters \tilde{p}_j , which can be written as a vector $\tilde{\mathbf{p}}$. It is assumed that all elements have the same $\mu_{p_j} = \mu_p$ and $\sigma_{p_j} = \sigma_p$. However, also the dependency of the elements on each other has to be decided. Of course this has to be in line with experience. But care has to be taken, because when it is assumed that all \tilde{p}_j are totally unrelated, the problem becomes mesh dependent. Therefore it is assumed that:

$$\Sigma_{p_i p_j} = \sigma_p^2 e^{-\frac{(x_i - x_j)^2}{l_e^2}}, \quad (7.8)$$

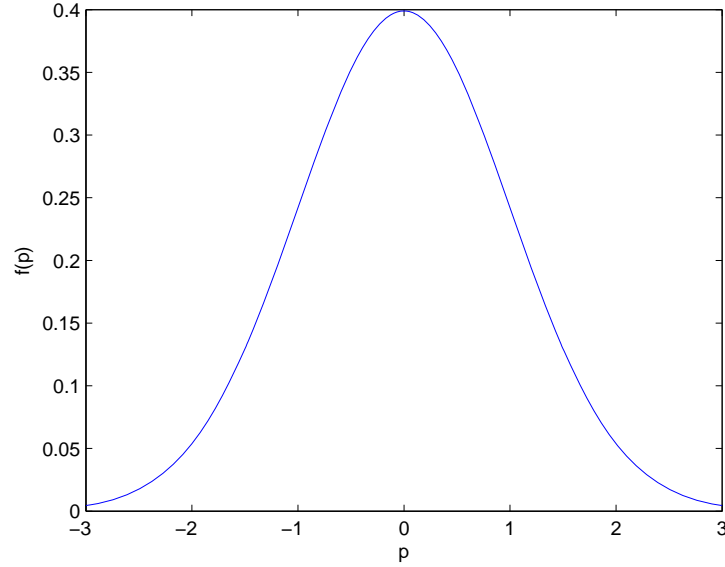


Figure 7.1: Normal distribution

where l_c is a correlation length, which can be determined from experiments or literature.

Basically a random field discretization is required when the device on the wafer is big compared to the wafer size. In that case properties tend to vary within the device.

7.2.2 Uncertainty analysis

To estimate the propagation of the uncertainty of a parameter $\tilde{\mathbf{p}}$ to a certain output property, the perturbation technique is used. Let's assume that this output variable of interest is $w(\mathbf{p})$. In that case the Taylor expansion of w with respect to the expectation of $\tilde{\mathbf{p}}$ is in matrix vector notation:

$$w(\mathbf{p}) = w(\boldsymbol{\mu}_p) + \frac{\partial w}{\partial \mathbf{p}}(\mathbf{p} - \boldsymbol{\mu}_p) + \frac{1}{2}(\mathbf{p} - \boldsymbol{\mu}_p)^T \frac{\partial^2 w}{\partial \mathbf{p}^2}(\mathbf{p} - \boldsymbol{\mu}_p) + \dots \quad (7.9)$$

However for the next step index notation will be more convenient:

$$w(\mathbf{p}) = w(\boldsymbol{\mu}_p) + \frac{\partial w}{\partial p_i}(p_i - \mu_{pi}) + \frac{1}{2}(p_i - \mu_{pi})(p_j - \mu_{pj}) \frac{\partial^2 w}{\partial p_i \partial p_j} + \dots, \quad (7.10)$$

When higher order terms are neglected the expectation of $w(\mathbf{p})$ or μ_w can be written as:

$$\begin{aligned} \mu_w = E \left[w(\boldsymbol{\mu}_p) + \frac{\partial w}{\partial p_i}(p_i - \mu_{pi}) + \frac{1}{2}(p_i - \mu_{pi})(p_j - \mu_{pj}) \frac{\partial^2 w}{\partial p_i \partial p_j} \right] = \\ w(\boldsymbol{\mu}_p) + \frac{1}{2} \sum_{p_i p_j} \frac{\partial^2 w}{\partial p_i \partial p_j}, \end{aligned} \quad (7.11)$$

due to the fact that the expectation of $(p_i - \mu_{pi})$ is zero and that of $(p_i - \mu_{pi})(p_j - \mu_{pj})$ is Σ_{ij} . Similarly the variance of \tilde{w} is:

$$\Sigma_{ww} = E[(w(\tilde{\mathbf{p}}) - \mu_w)^2] = \frac{\partial w}{\partial p_i} \Sigma_{p_i p_j} \frac{\partial w}{\partial p_j}. \quad (7.12)$$

The connection between logarithmic sensitivities and uncertainty analysis

The usefulness of logarithmic sensitivities to compare sensitivities for different parameters can be explained from a stochastic point of view. Consider the 1D version of equation (7.12):

$$\sigma_w^2 = \left(\frac{\partial w}{\partial p} \right)^2 \sigma_p^2, \quad (7.13)$$

and remember that the coefficient of variation was defined as:

$$V_w = \frac{\sigma_w}{\mu_w}. \quad (7.14)$$

This means that (7.13) can be written as:

$$V_w^2 \mu_w^2 = \left(\frac{\partial w}{\partial p} \right)^2 V_p^2 \mu_p^2, \quad (7.15)$$

which defines the coefficient of variation as:

$$V_w = \frac{\mu_p}{\mu_w} \frac{\partial w}{\partial p} V_p. \quad (7.16)$$

If the second order effect on the output mean is neglected this can be written as:

$$V_w = \frac{\mu_p}{\mu_w} \frac{\partial w}{\partial p} V_p = \frac{\partial \log(w)}{\partial \log(p)} V_p, \quad (7.17)$$

Hence the uncertainty analysis explains why the logarithmic sensitivity as defined in the previous chapter is such a good method to compare sensitivities to very different variables. Basically a logarithmic sensitivity gives the linearized relation between the non-dimensional input and output uncertainties.

7.2.3 Reliability analysis

The approach above can be used to compute the output uncertainty based on an input uncertainty. But it does not provide an accurate measure of the chance of failure. However, a perturbation based approach can be used to determine that measure as well.

Often design fails if \tilde{w} is bigger or smaller than a critical value w_c . In that case \tilde{w} should not exceed w_c . If a limit state function is defined:

$$\tilde{g} = w_c - \tilde{w}, \quad (7.18)$$

the chance on failure can be defined as:

$$Pr[\tilde{g} > 0]. \quad (7.19)$$

Only 1 random variable

It is assumed that \tilde{p} can be written as:

$$\tilde{p} = \mu_p + \sigma_p \tilde{z}, \quad (7.20)$$

where \tilde{z} is the standard normal distribution ($\mu_z = 0, \sigma_z = 1$). Further more z_c is defined as:

$$w_c = w(z_c). \quad (7.21)$$

In that case the chance on failure is:

$$Pr[\tilde{z} < z_c] = f_p(z_c) = \int_{-\infty}^{z_c} \frac{1}{\sqrt{2\pi}} e^{\left(\frac{-z^2}{2}\right)} dz \quad (7.22)$$

where equation (7.7) was used. Therefore only the value z_c has to be computed, also known as the design point.

A Newton algorithm seems to be best for that in 1D. Therefore an initial z_0 is chosen, which is used to compute the initial estimate of the output $w_0(z_0)$. This can be used to compute the update for the Newton procedure using:

$$\Delta z_k = (w_c - w_{k-1}) \left. \frac{\partial z}{\partial w} \right|_{z_{k-1}}, \quad (7.23)$$

where:

$$\left(\frac{\partial z}{\partial w} \right)^{-1} = \frac{\partial w}{\partial p} \frac{\partial p}{\partial z} = \frac{\partial w}{\partial p} \sigma_p. \quad (7.24)$$

Multiple random variables

When there are multiple variables present in the model, as is the case for a discretized random field, it is assumed that that:

$$\tilde{\mathbf{p}} = \boldsymbol{\mu}_p + \mathbf{G}\tilde{\mathbf{z}}, \quad (7.25)$$

where \mathbf{G} is a transformation matrix which is related to the covariance by:

$$\mathbf{G}\mathbf{G}^T = \boldsymbol{\Sigma}_{pp}. \quad (7.26)$$

When this equation is written in terms of the columns of \mathbf{G} , \mathbf{g}_i , it becomes:

$$\boldsymbol{\Sigma}_{pp} = \mathbf{G}\mathbf{G}^T = \mathbf{g}_i \mathbf{g}_i^T, \quad (7.27)$$

where it should be noted that Einstein's summation convention is used throughout the document. To compute the \mathbf{g}_i the problem is rewritten as the following eigenvalue problem, where the λ_i are the eigenvalues of $\boldsymbol{\Sigma}_{pp}$:

$$\boldsymbol{\Sigma}_{pp} \mathbf{g}_i = \lambda_i \mathbf{g}_i, \quad (7.28)$$

$$\mathbf{g}_i^T \mathbf{g}_i = \lambda_i. \quad (7.29)$$

In these two equations no summation over double indexes should be performed.

The Newton algorithm cannot be used for multiple random variables because $\tilde{g} = w_c - \tilde{w} = 0$ does not define enough equations to solve for the design point. However for multiple random variables it is still assumed that:

$$\tilde{g} = w_c - \tilde{w}, \quad (7.30)$$

but \tilde{g} linearized around the most critical point \mathbf{z}_c . This most critical point is that realization \mathbf{z} for which $g(\mathbf{z}) = 0$ and the norm $\|\mathbf{z}\|$ reaches a minimum. Therefore it the most likely realization of the many realizations that satisfy $g(\mathbf{z}) = 0$.

The used linearization is:

$$\bar{g} = \alpha_i z_i + \beta. \quad (7.31)$$

where $\|\alpha\| = 1$. Thus once z_c is computed, this provides $\beta = -\|z_c\|$ and:

$$Pr[\bar{g} < 0] = \int_{-\infty}^{\beta} \frac{1}{\sqrt{2\pi}} e^{\left(\frac{-x^2}{2}\right)} dx. \quad (7.32)$$

Therefore the only remaining problem is the computation of z_c . This is more difficult than in the 1D case, hence in the reference used throughout this chapter [49] it is recommended to use the Hasofer-Lind-Rackwitz-Fiessler algorithm. This is a standard algorithm for constrained optimization, which can be used because finding the most likely realization under certain conditions is essentially an optimization problem. The goal is to optimize:

$$\begin{cases} \text{minimize} & \|z\| \\ \text{with constraint} & \bar{g}(z) = 0 \end{cases} \quad (7.33)$$

This can be done by starting with a guess z_0 :

$$z_k^T = \frac{\frac{\partial g_{k-1}}{\partial z} z_{k-1} - g_{k-1} \frac{\partial g_{k-1}}{\partial z}}{\left\| \frac{\partial g_{k-1}}{\partial z} \right\|^2}, \quad (7.34)$$

where the derivative of g is defined as follows:

$$\frac{\partial g}{\partial z} = -\frac{\partial w}{\partial z} = -\frac{\partial w}{\partial \mathbf{p}} \frac{\partial \mathbf{p}}{\partial z}, \quad (7.35)$$

where:

$$\frac{\partial \mathbf{p}}{\partial z} = \mathbf{G}. \quad (7.36)$$

The shape of z_c provides some extra information. As mentioned it gives the most critical perturbation of \mathbf{p} , thus it gives the most likely failure mode. Therefore elements with a high z_c should be handled with care.

7.3 Uniform microbridge

This section will treat the uniform bridge as shown in figure 7.2. It is meshed with 4 by 12 elements (12 beam elements, 48 electrostatic elements). The material properties are those in table 7.1. It is assumed that \tilde{E} or \tilde{h} can be stochastic, but are uniform within the beam.

7.3.1 Uncertainty analysis

Young's modulus

The sensitivities of the pull-in voltage with respect to the elasticity modulus are:

$$\frac{\partial V_{PI}}{\partial E} = 2.20 \cdot 10^{-4} V/Pa, \quad (7.37)$$

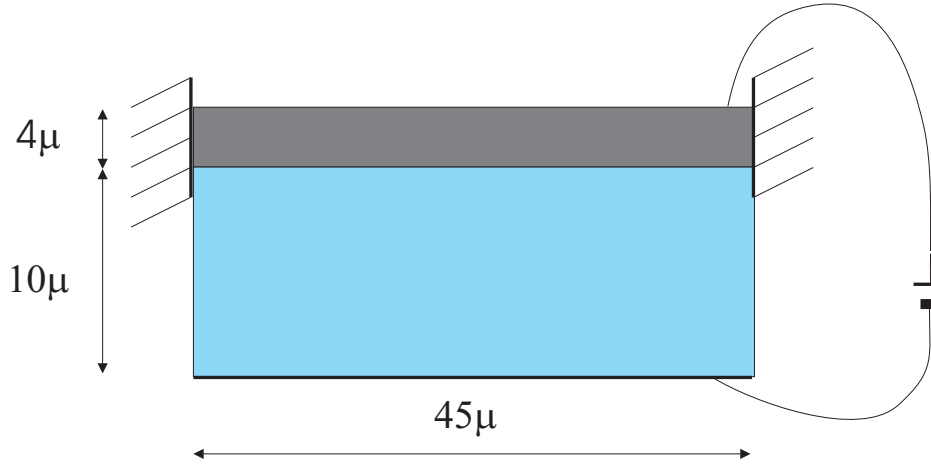


Figure 7.2: Simple beam.

Table 7.1: Summary of the material properties.

Air gap			
Property	Symbol	Value	Units
<i>Electric permittivity</i>	ε	$8.8541 \cdot 10^{-12}$	F/m
Structure			
Property	Symbol	Value	Units
<i>Elasticity modulus</i>	μ_E	$1 \cdot 10^5$	Pa
<i>Beam thickness</i>	μ_h	$4 \cdot 10^{-6}$	m

and:

$$\frac{\partial^2 V_{PI}}{\partial E^2} = -1.10 \cdot 10^{-9} V/Pa^2, \quad (7.38)$$

The elasticity modulus is assumed to have a mean value of $\mu_E = 1 \cdot 10^5 Pa$ and a coefficient of variation of $V_E = 0.1$, which gives a standard deviation of $\sigma_E = 1 \cdot 10^4 Pa$.

Using the second order perturbation method the mean of the pull-in voltage would be:

$$\mu_{V_{PI}} = V_{PI}(\mu_E) + \frac{1}{2} \sigma_E^2 \frac{\partial^2 V_{PI}}{\partial E^2}(\mu_E) = 44.05 - 0.05 = 44.0 V. \quad (7.39)$$

Notice the small influence of the second order term.

Using the first order perturbation method the standard deviations is computed:

$$\sigma_{V_{PI}} = \sqrt{\left(\frac{\partial V_{PI}}{\partial E}(\mu_E)\right)^2 \sigma_E^2} = 2.20 V. \quad (7.40)$$

Therefore the coefficient of variation is:

$$V_{V_{PI}} = \frac{\sigma_{V_{PI}}}{\mu_{V_{PI}}} = 0.05, \quad (7.41)$$

hence the device filters some of the statistical variation in the elasticity modulus.

The same values can also be estimated by a crude Monte Carlo simulation. The most expensive part of the perturbation technique is the pull-in point determination, which takes about 90% of the time. A Monte Carlo simulation starts with creating a sample of N different Young's moduli. This sample is constructed such that the mean

of this sample is equal to $1 \cdot 10^5$ and the standard deviation $1 \cdot 10^4$. Subsequently there are N different pull-in voltages computed. And the mean and standard deviation of this set are determined. Hence the computation time is in the order of N times longer than the perturbation based computation.

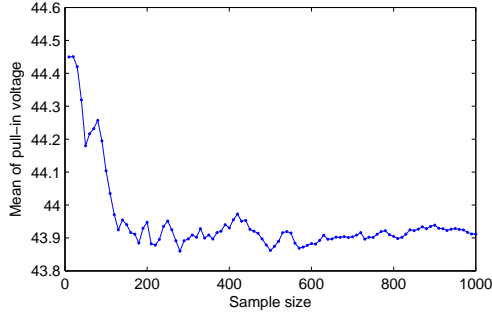


Figure 7.3: Convergence of the mean with sample size (random elasticity).

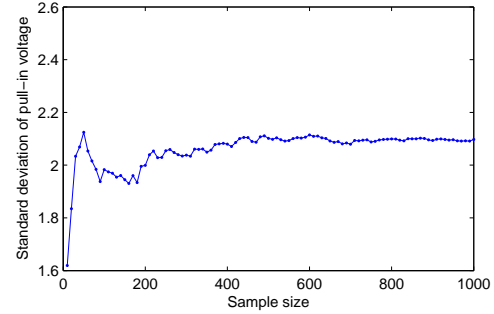


Figure 7.4: Convergence of the standard deviation with sample size (random elasticity).

The convergence rate of the mean value and standard deviation with respect to sample size is shown in figures 7.3 and 7.4. From this figure it is clear that the values have not converged for a sample of $N = 1000$. Consider the computation time! However it is possible to conclude that the first three significant digits of the values are:

$$\mu_{V_{PI}} = 43.9 V, \quad (7.42)$$

$$\sigma_{V_{PI}} = 2.10 V, \quad (7.43)$$

$$V_{V_{PI}} = 0.0478. \quad (7.44)$$

Hence the perturbation approach is very accurate. The second order approach improves the already accurate first order approach slightly.

Thickness

The sensitivities of the pull-in voltage with respect to the thickness are:

$$\frac{\partial V_{PI}}{\partial h} = 1.6519 \cdot 10^7 V/m, \quad (7.45)$$

and:

$$\frac{\partial^2 V_{PI}}{\partial h^2} = 2.0618 \cdot 10^{12} V/m^2, \quad (7.46)$$

The thickness is assumed to have a mean value of $\mu_h = 4 \cdot 10^{-6}$ and a coefficient of variation of $V_h = 0.1$, which gives a standard deviation of $\sigma_h = 4 \cdot 10^{-7}$.

Using the second order perturbation method the mean of the pull-in voltage will be:

$$\mu_{V_{PI}} = V_{PI}(\mu_h) + \frac{1}{2} \sigma_h^2 \frac{\partial^2 V_{PI}}{\partial h^2}(\mu_h) = 44.05 + 0.16 = 44.22 V. \quad (7.47)$$

Notice the influence of the second order term. It is still very small, but bigger than the influence of the second order term for the elasticity modulus computations. This is logical, because the stiffness matrix depends linearly on the elasticity modulus and cubically on the thickness.

Using the first order perturbation method the standard deviations is computed:

$$\sigma_{V_{PI}} = \sqrt{\left(\frac{\partial V_{PI}}{\partial h}(\mu_h)\right)^2} \sigma_h^2 = 6.61 V, \quad (7.48)$$

thus the coefficient of variation is:

$$V_{V_{PI}} = \frac{\sigma_{V_{PI}}}{\mu_{V_{PI}}} = 0.15, \quad (7.49)$$

hence the device amplifies some of the statistical variation in the thickness. Therefore the device amplifies thickness variations and decreases elasticity variation. This is consistent with the logarithmic sensitivity analysis in the previous chapter.

These numbers were validated with a Monte Carlo simulation as well. This time the sample size was much bigger $N = 18750$, providing the following statistical moments:

$$\mu_{V_{PI}} = 44.29 V, \quad (7.50)$$

$$\sigma_{V_{PI}} = 6.64 V, \quad (7.51)$$

$$V_{V_{PI}} = 0.15. \quad (7.52)$$

The results are very close to the perturbation approach. From figures 7.5 and 7.6 it can be seen that the mean and standard deviation have converged well.

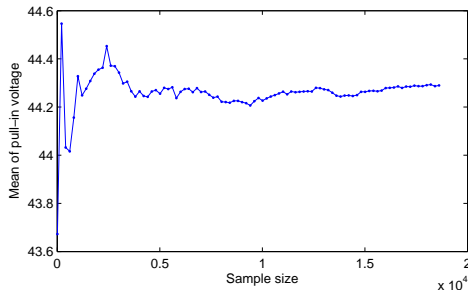


Figure 7.5: Convergence of the mean with sample size (random thickness).

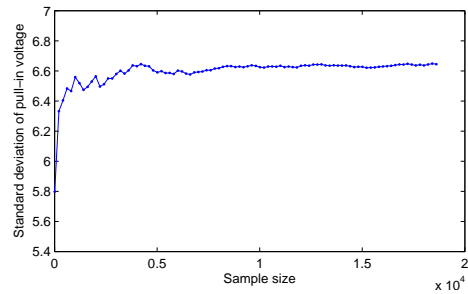


Figure 7.6: Convergence of the standard deviation with sample size (random thickness).

7.3.2 Reliability analysis

For such a electro-mechanically coupled device there are basically two operation options: (a) it is designed to operate within the stable region or (b) it is designed to switch at a certain potential. In case a the device fails if the pull-in voltage is to low, in case b the device fails if the pull-in voltage is to high. In this section the probability that pull-in voltage is lower than 41 (case a) and that it is higher than 46.5 (case b) will be investigated.

Young's modulus

For case a the 1000 realizations Monte Carlo approach gave a failure chance of:

$$Pr[V_{PI} < 41] = 0.088, \quad (7.53)$$

which was easily computed: divide the number of realizations that gave a voltage below the critical voltage by the total sample size. With the sensitivity based approach, which required 4 function and derivative evaluations only, the chance was:

$$Pr[V_{PI} < 41] = 0.091, \quad (7.54)$$

which is rather close. Note that with 1000 realizations, the Monte Carlo analysis is not very accurate as can be seen from figure 7.7.

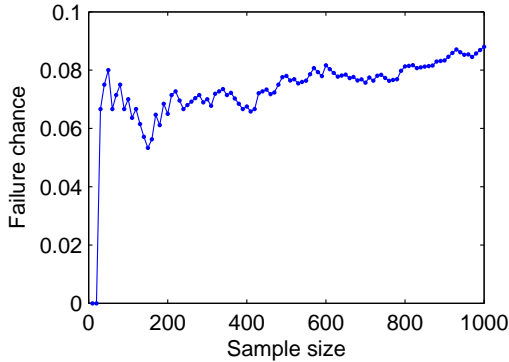


Figure 7.7: Convergence of the failure chance with sample size (case *a*, random elasticity).

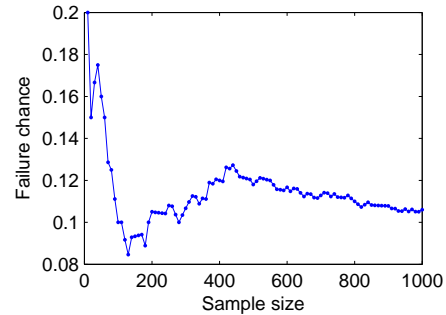


Figure 7.8: Convergence of the failure chance with sample size (case *b*, random elasticity).

For case *b* the 1000 realizations Monte Carlo approach gave a failure chance of:

$$Pr[V_{PI} > 46.5] = 0.1060. \quad (7.55)$$

The sensitivity based approach, which again required 4 function and derivative evaluations, the chance was:

$$Pr[V_{PI} > 46.5] = 0.1266, \quad (7.56)$$

which is less good. This is explained by the small number of Monte Carlo attempts.

Thickness

For case *a* the 18750 sample size Monte Carlo approach gave a failure chance of:

$$Pr[V_{PI} < 41] = 0.317. \quad (7.57)$$

With the sensitivity based approach which only required 4 function and derivative evaluations the chance was:

$$Pr[V_{PI} < 41] = 0.320, \quad (7.58)$$

which is rather close. Here with the 17500 sample size it is safe to assume that the Monte Carlo method has converged.

Similarly for case *b* Monte Carlo approach gave a failure chance of:

$$Pr[V_{PI} > 46.5] = 0.366. \quad (7.59)$$

The sensitivity based approach the chance was:

$$Pr[V_{PI} > 46.5] = 0.357, \quad (7.60)$$

which required 4 function evaluations. The match between the numbers is good. The quality of the Monte Carlo analyses can be estimated from the convergences in figures 7.9 and 7.10, which due to the large number of realizations shows a much better convergence than the elasticity computations. This also explains the better validation of the thickness failure chance compared with the elasticity computation.

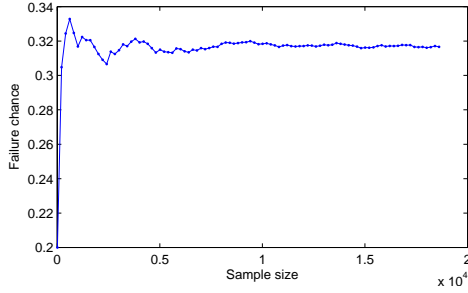


Figure 7.9: Convergence of the failure chance with sample size (case *a*, random thickness).

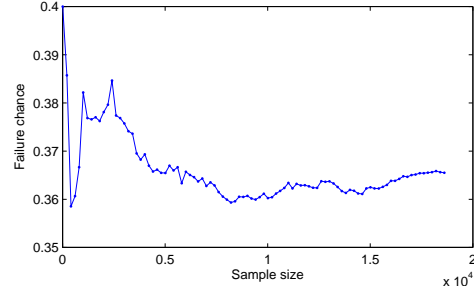


Figure 7.10: Convergence of the failure chance with sample size (case *b*, random thickness).

7.4 Random field discretization

For a lot of MEMS type applications the randomness cannot be assumed to be uniform within a device. Grain sizes can be in the order of the characteristic length of the device, hence young's modulus variations can be very big within the device. Therefore, often the properties have to be described by a random field. In that case the correlation length of the field depends on the grain sizes and their distribution.

7.4.1 Uncertainty analysis

Young's modulus

The random properties of \tilde{E} are: $\mu_E = 1 \cdot 10^5 m$, $\sigma_E = 1 \cdot 10^4 m$ and $V_E = 0.1$. The correlation length is one third of the beam length: $15 \cdot 10^{-6} m$.

Using the perturbation approach this yields:

$$\mu_{V_{PI}} = V_{PI}(\boldsymbol{\mu}_h) + \frac{1}{2} \sum_{E_i E_j} \frac{\partial^2 V_{PI}}{\partial E_i \partial E_j} = 44.05 - 0.056 = 44.00 V, \quad (7.61)$$

for the mean value and for the standard deviation the perturbation approach yields:

$$\sigma_{V_{PI}} = \sqrt{\frac{\partial V_{PI}}{\partial E_i} \Sigma_{h_i h_j} \frac{\partial V_{PI}}{\partial E_j}} = 1.44 V, \quad (7.62)$$

hence the coefficient of variation is:

$$V_{V_{PI}} = 0.033. \quad (7.63)$$

A Monte Carlo simulation with 4638 random evaluations gave the following statistical properties:

$$\mu_{V_{PI}} = 43.98 V, \quad (7.64)$$

$$\sigma_{V_{PI}} = 1.44 V, \quad (7.65)$$

$$V_{V_{PI}} = 0.033. \quad (7.66)$$

These numbers are really close. From figure 7.11 it can be seen that the mean value, as computed with the Monte Carlo simulation, has definitely converged to 44.0 if one is interested in 3 significant digits. The standard deviation that is presented in figure 7.12 is less well converged, but seems to be within the bandwidth 1.4 - 1.5.

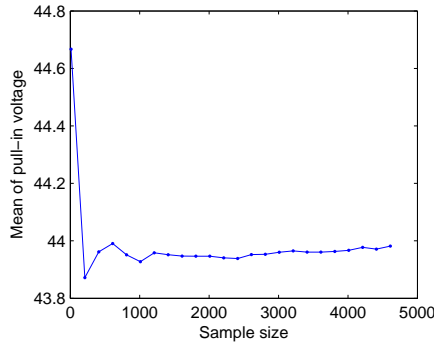


Figure 7.11: Convergence of the mean with sample size (random elasticity field).

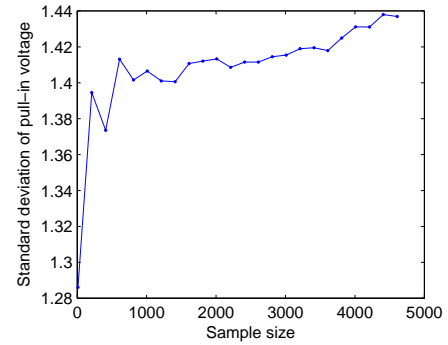


Figure 7.12: Convergence of the standard deviation with sample size (random elasticity field).

Thickness

The perturbation approach was also performed for variations in the thickness. The used random properties of \tilde{h} are: $\mu_h = 4 \cdot 10^{-6} m$, $\sigma_h = 4 \cdot 10^{-7} m$ and $V_h = 0.1$. The used correlation length is one third of the beam length as well: $15 \cdot 10^{-6} m$.

With the perturbation approach the mean pull-in voltage is computed to be:

$$\mu_{V_{PI}} = V_{PI}(\boldsymbol{\mu}_h) + \frac{1}{2} \sum_{h_i h_j} \frac{\partial^2 V_{PI}}{\partial h_i \partial h_j} = 44.05 + 0.16 = 44.21 V, \quad (7.67)$$

and the standard deviation:

$$\sigma_{V_{PI}} = \sqrt{\frac{\partial V_{PI}}{\partial h_i} \sum_{h_i h_j} \frac{\partial V_{PI}}{\partial h_j}} = 4.3 V, \quad (7.68)$$

hence the corresponding coefficient of variation is:

$$V_{V_{PI}} = 0.097. \quad (7.69)$$

A Monte Carlo simulation with 7500 random evaluations gave:

$$\mu_{V_{PI}} = 43.87 V, \quad (7.70)$$

$$\sigma_{V_{PI}} = 4.29 V, \quad (7.71)$$

$$V_{V_{PI}} = 0.098. \quad (7.72)$$

The convergence of this Monte Carlo simulation is shown in figures 7.13 and 7.14. The Monte Carlo approach seems to have converged. Standard deviation and coefficient of variation are accurate, however the second order mean is not that accurate.

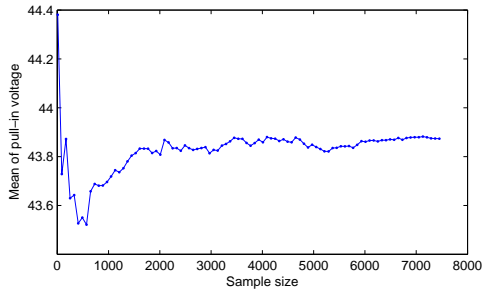


Figure 7.13: Convergence of the mean with sample size (random thickness field).

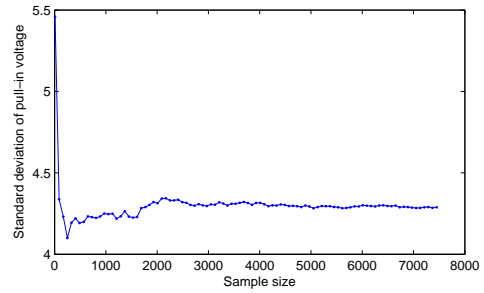


Figure 7.14: Convergence of the standard deviation with sample size (random thickness field).

7.4.2 Reliability analysis

Young's modulus

When the failure chance for the two cases is determined with the sensitivity based approach, this yields for case *a*:

$$Pr[V_{PI} < 41] = 0.0202, \quad (7.73)$$

which required only 5 function evaluations to obtain with the HL-RF algorithm. For case *b* the failure chance is:

$$Pr[V_{PI} > 46.5] = 0.0397, \quad (7.74)$$

also requiring 5 function evaluations.

The 4638 realizations Monte Carlo simulation of which the convergence is shown in figures 7.15 and 7.16, gave:

$$Pr[V_{PI} < 41] = 0.023, \quad (7.75)$$

and

$$Pr[V_{PI} > 46.5] = 0.040. \quad (7.76)$$

The numbers are really close, validating the

Thickness

Also a reliability analysis for thickness variations was done for case *a* as well as case *b*. Using the perturbation based approach the chance that the pull in voltage is lower than 41 (case *a*) i:

$$Pr[V_{PI} < 41] = 0.2367, \quad (7.77)$$

which required only 4 function evaluations to obtain with the HL-RF algorithm.

The distribution of the z_c gives the failure mode, which is that realization z that gives the minimum deviation from the mean values such that a device is created that fails. The thickness distribution for this failure mode is shown in figure 7.17.

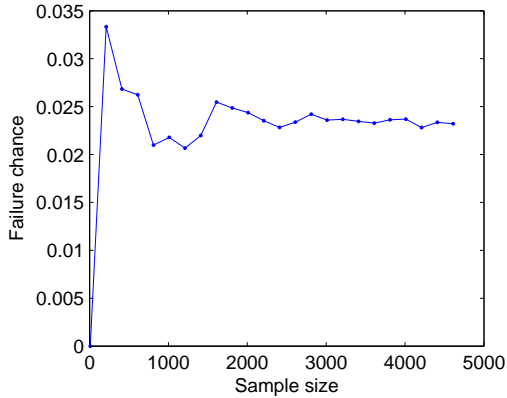


Figure 7.15: Convergence of the failure chance with sample size (case *a*, random elasticity field).

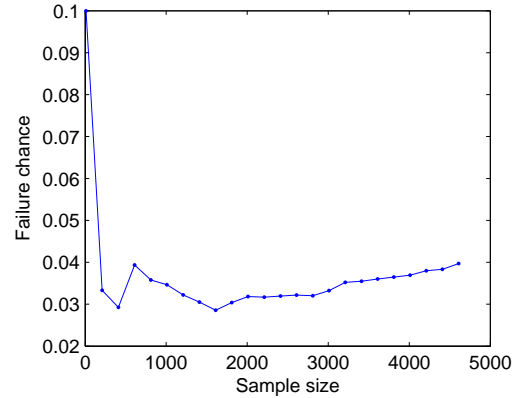


Figure 7.16: Convergence of the failure chance with sample size (case *b*, random elasticity field).

For case *b* the chance of failure computed with the sensitivity based reliability method was:

$$Pr[V_{PI} > 46.5] = 0.2865. \quad (7.78)$$

The corresponding failure mode is shown in figure 7.18. The mode is the inverse of the mode for case *a*. It would be expected that the failure mode is very similar to the sensitivity shape that was presented in figure 6.5, however from the simulation it is clear that the large correlation length makes the solution smoother.

A 7500 sample size Monte Carlo simulation gave the following numbers:

$$Pr[V_{PI} < 41] = 0.248, \quad (7.79)$$

and

$$Pr[V_{PI} > 46.5] = 0.270. \quad (7.80)$$

The difference between the Monte Carlo and the perturbation approach is really small. Figures 7.19 and 7.20 show clearly that the Monte Carlo simulation is converged.

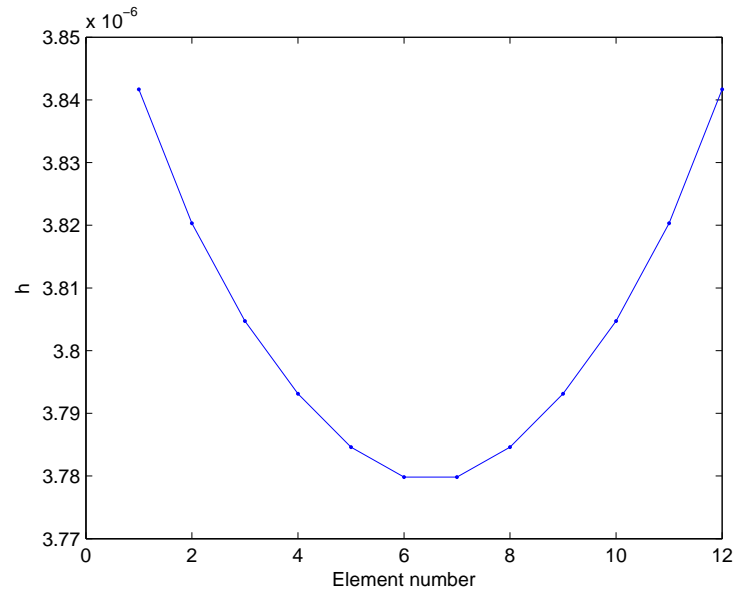
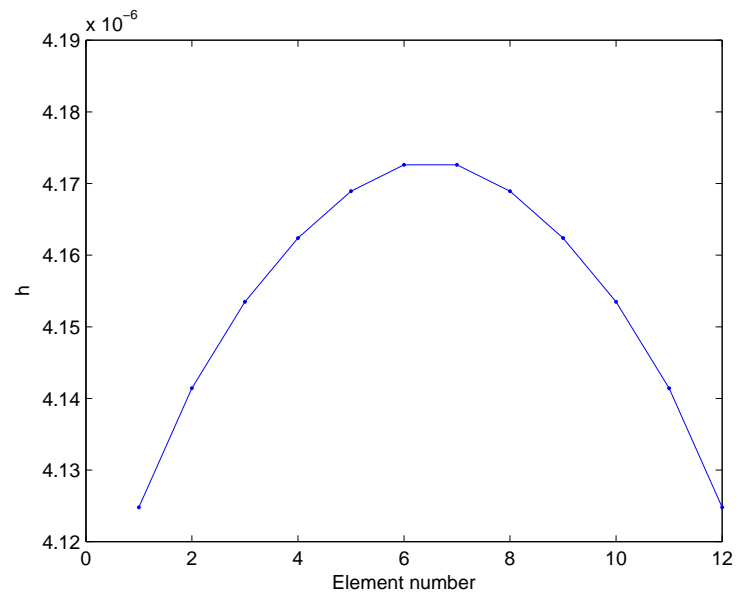
In figure 7.17 it was seen that the deviation from the mean thickness ($4 \cdot 10^{-6}$) was biggest in the middle of the beam. Sensitivity analysis suggested that near the clamp there should be a big influence as well, however the correlation length smoothes out this influence. Therefore the correlation length was decreased to one fifth of the beam length (9μ) and the sensitivity based reliability computation was performed again. This lowered the failure chance to:

$$Pr[V_{PI} < 41] = 0.1967, \quad (7.81)$$

and provided the failure mode of figure 7.21, which clearly shows that the influence near the clamps becomes more dominant.

7.5 A uniform beam with realistic numbers

So far the used material and geometry properties in this chapter were not really realistic. However an estimate of the mean and variance of the elasticity modulus of polysilicon for several fabrication procedures has been made [25]. For a specific polysilicon

Figure 7.17: Failure mode for case *a*.Figure 7.18: Failure mode for case *b*.

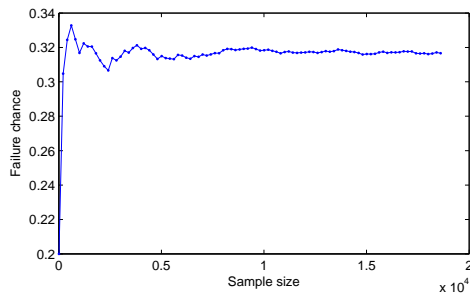


Figure 7.19: Convergence of the failure chance with sample size (case *a*, random thickness field).

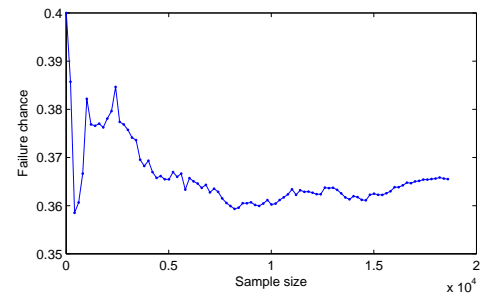


Figure 7.20: Convergence of the failure chance with sample size (case *b*, random thickness field).

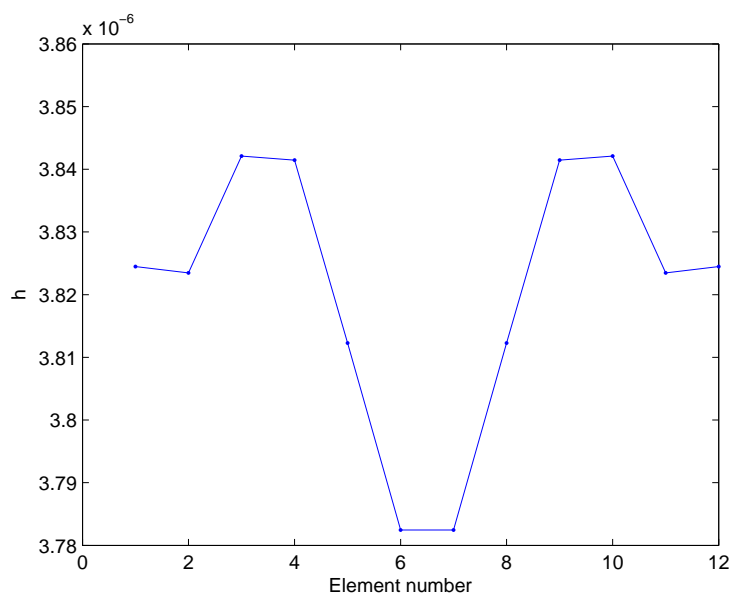


Figure 7.21: Failure mode for case *b*.

production method² an elasticity modulus of 164 *GPa* with a standard deviation of 7 *GPa* was reported. This can be used for modeling a device that is assumed to have a uniform but random elasticity modulus.

7.5.1 Model

The device under consideration is a plate clamped on both sides with a air gap between the plate and a conducting electrode. The characteristics of this plate model are introduced in section 4.3, but the material properties are different. The used properties in this chapter are realistic and listed in table 7.2. The plate was meshed with 25 by 10 mechanical elements. The electric gap was meshed with 25 by 10 by 8 elements.

²The Multi-user MEMS Processes or MUMPs

Table 7.2: Summary of the material properties.

Air gap			
Property	Symbol	Value	Units
<i>Gap size</i>	g	$2 \cdot 10^{-6}$	m
<i>Electric permittivity</i>	ε	$8.8541 \cdot 10^{-12}$	F/m
Structure			
Property	Symbol	Value	Units
<i>Length</i>	L	$250 \cdot 10^{-6}$	m
<i>Width</i>	w	$30 \cdot 10^{-6}$	m
<i>Beam thickness</i>	h_0	$1 \cdot 10^{-6}$	m
<i>Elasticity modulus</i>	E	$164 \cdot 10^9$	Pa
<i>Poisson's ratio</i>	ν	0.22	—
<i>Density</i>	ρ	2330	kg/m^3

7.5.2 Pull-in and its sensitivity

The load-displacement curve up to pull-in can be found in figure 7.22. The static pull-in voltage for this beam is 21.39 volts. The model can be used to compute the sensitivity as discussed in chapters 6 which is:

$$\left. \frac{\partial V}{\partial E} \right|_{PI} = 6.47 \cdot 10^{-11} V/Pa, \quad (7.82)$$

which was confirmed by a global finite difference computation ($\Delta E = 10GPa$):

$$\left. \frac{\Delta V}{\Delta E} \right|_{PI} = 6.40 \cdot 10^{-11} V/Pa. \quad (7.83)$$

The second order sensitivity is:

$$\left. \frac{\partial^2 V}{\partial E^2} \right|_{PI} = -1.98 \cdot 10^{-22} V/Pa^2, \quad (7.84)$$

which is validated by:

$$\left. \frac{\Delta V}{\Delta E^2} \right|_{PI} = -2.04 \cdot 10^{-22} V/Pa^2, \quad (7.85)$$

7.5.3 Uncertainty and reliability

Using the sensitivities the mean of the pull-in voltage can be computed:

$$\mu_{V_{PI}} = 21.39 - 4.9 \cdot 10^{-3} = 21.38 V, \quad (7.86)$$

hence the second order effect is very small for this elasticity with a low standard deviation. The standard deviation of pull-in is:

$$\sigma_{V_{PI}} = 0.45 V, \quad (7.87)$$

Let's assume that the device does not meet its specifications if the pull-in is below 19.13. This failure criterion is not 6 standard deviations away as the popular *Six Sigma* business management strategy prescribes, but it is 5 standard deviations from

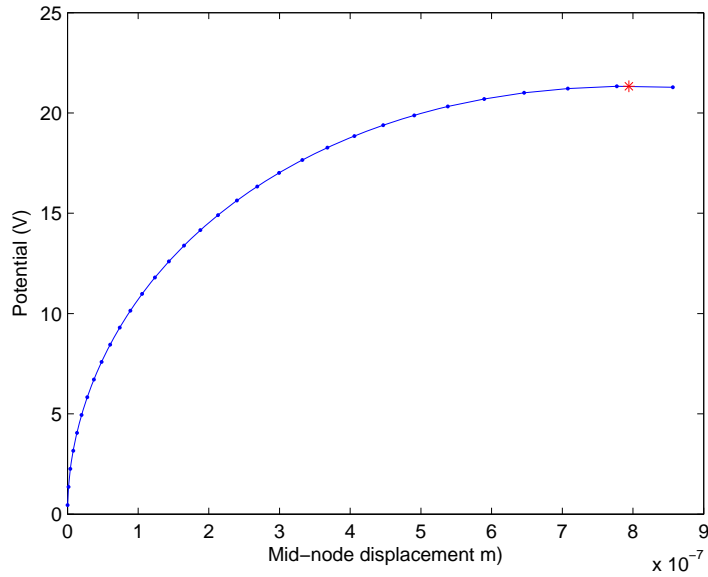


Figure 7.22: Potential vs. displacement.

the mean. Therefore the failure chance will still be really small [126]. If pull-in would be normally distributed as well, the failure chance would be $Pr[V_{PI} < 19.13] = 2.87 \cdot 10^{-7}$. However if the perturbation based algorithm is used the failure chance increases to $Pr[V_{PI} < 19.13] = 2.35 \cdot 10^{-6}$, showing that even if the elasticity is distributed normally, pull-in is not distributed normally³. It would still be a pretty safe design though.

7.6 Conclusions

This chapter provides a very short introduction to stochastic FEM. After this introduction stochastic FEM was applied on the pull-in problem for the propagation of thickness and elasticity randomness. Both the uncertainty as well as the reliability of the device was treated.

These methods were applied for two scenarios: when the device is small, thus giving uniform statistical properties and when the device is big, giving statistical properties that are random fields. For each scenario two cases were inspected: *a* the device is designed to operate below pull-in, hence it fails if the pull-in voltage is too low and *b* the device is designed to switch, thus it fails if the pull-in is too high.

For all situations it was shown that sensitivity based approaches could compare very well with crude Monte Carlo simulations. After the validation, the method was used to compute the uncertainty of pull-in for a realistic device. This showed that for realistic elasticity distributions the second order stochastic FEM approach is not really required.

³This failure chance would be extremely hard to validate with Monte Carlo sampling, because your sample would need more than 10^6 realizations.

Part III

Dynamic simulation



Chapter 8

Undamped modeling

8.1 Introduction

This chapter is first chapter within the dynamic simulation part. Before only static simulation issues were presented. The only exception was a short discussion of coupled eigenfrequencies in chapter 3. However a lot of models above were applicable for modeling micro switches and logically one of the major aspects of these switches is their switching behavior. This switching behavior is characterized by the trajectory and response time of switching motion.

Another dynamic aspect, resonance frequencies, is of vital importance to the operation of sensors and resonators, hence frequency modeling is of vital importance. This chapter first discusses frequency modeling and thereafter discusses transient simulations. Finally the methods are evaluated by solving an example.

Just to refresh memory, the discretized form of the coupled electromechanical system as derived in chapter 3 (eq:3.103) is repeated below:

$$\mathbf{M}_{uu}\ddot{\mathbf{u}} + \mathbf{K}_{uu}^m \mathbf{u} = \mathbf{f}^{elec}(\mathbf{u}, \phi, V), \quad (8.1)$$

$$\mathbf{K}_{\phi\phi}(\mathbf{u})\phi = \mathbf{q}(\mathbf{u}, V). \quad (8.2)$$

8.2 Undamped eigenfrequency modeling

As mentioned the eigenfrequencies were first presented in chapter 3. The frequencies ω_i around a equilibrium are found by solving the linearized eigenvalue problem (3.107):

$$[\mathbf{K} - \omega_i^2 \mathbf{M}] \mathbf{X}_i = 0, \quad (8.3)$$

which can be written as:

$$\omega_i^2 \begin{bmatrix} \mathbf{M}_{uu} & 0 \\ 0 & 0 \end{bmatrix} \begin{bmatrix} \mathbf{x}_i^u \\ \mathbf{x}_i^\phi \end{bmatrix} - \begin{bmatrix} \mathbf{K}_{uu} & \mathbf{K}_{u\phi} \\ \mathbf{K}_{u\phi}^T & \mathbf{K}_{\phi\phi} \end{bmatrix} \begin{bmatrix} \mathbf{x}_i^u \\ \mathbf{x}_i^\phi \end{bmatrix} = 0. \quad (8.4)$$

Because the electric field is static, it does not have terms proportional to accelerations, hence the electrostatic equation can be condensed out of the system to give:

$$\omega_i^2 \mathbf{M}_{uu} \mathbf{x}_i^u - (\mathbf{K}_{uu} - \mathbf{K}_{u\phi} \mathbf{K}_{\phi\phi}^{-1} \mathbf{K}_{u\phi}^T) \mathbf{x}_i^u = 0, \quad (8.5)$$

which essentially is the same as:

$$\omega_i^2 \mathbf{M}_{uu} \mathbf{x}_i^u - \left(\mathbf{K}_{uu}^m - \frac{\partial \mathbf{f}^{elec}}{\partial \mathbf{u}} \right) \mathbf{x}_i^u = 0, \quad (8.6)$$

8.2.1 Staggered method

If only a co-simulation model is available, the tangent matrices are not available. Therefore equation (8.4) or (8.5) cannot be fully obtained. However it is possible to make an accurate estimate of the frequencies.

This estimation starts with the purely mechanical problem:

$$\mathbf{M}_{uu}\ddot{\mathbf{u}} + \mathbf{K}_{uu}^m \mathbf{u} = \mathbf{f}^{ext}, \quad (8.7)$$

which is almost equal to the mechanical equation in the coupled set of equation (3.103). However the external force is not depending on other DOFs in this case. The linear eigenfrequencies are obtained by the assumption that the time derivative of the external force is zero, therefore the external force will only create a bias displacement and can be omitted from the equation. Therefore the eigenfrequencies ω_j and eigenmodes \mathbf{x}_j follow from the solution to homogeneous equation. Furthermore it is assumed that the non-constant part of the displacement is harmonic and can be written as:

$$\mathbf{u} = \mathbf{x}_j e^{i\omega_j t}, \quad (8.8)$$

$$\ddot{\mathbf{u}} = i^2 \omega_j^2 \mathbf{x}_j e^{i\omega_j t} = -\omega_j^2 \mathbf{x}_j e^{i\omega_j t}. \quad (8.9)$$

Substitution of this \mathbf{u} and $\ddot{\mathbf{u}}$ into the equation of motion plus the assumption of zero external force defines the eigenvalue problem:

$$-\omega_j^2 \mathbf{M}_{uu} \mathbf{x}_j + \mathbf{K}_{uu}^m \mathbf{x}_j = 0, \quad (8.10)$$

which can be used to compute the linear eigenfrequencies and modes. Of these eigenfrequencies only the lowest few are of practical interest. For instance a tunable microresonator normally operates near its lowest eigenfrequency.

However for an electromechanically coupled problem the external force \mathbf{f}^{elec} depends on \mathbf{u} :

$$\mathbf{M}_{uu}\ddot{\mathbf{u}} + \mathbf{K}_{uu}^m \mathbf{u} = \mathbf{f}^{elec}(\mathbf{u}, V). \quad (8.11)$$

In a staggered model, this effect is not incorporated in the mechanical stiffness matrix, therefore not in the eigenfrequencies. In literature there exists a method to compute the influence of this dependency on the eigenfrequency [75]. The idea starts with projection of the nonlinear equation on the lowest mechanical eigenmode \mathbf{x}_1 . In that case it is assumed that the displacement vector around an equilibrium can be approximated by $\mathbf{u} = \mathbf{u}_{eq} + \mathbf{x}_1 \Delta u$. When the non linear equation of motion is projected on the first eigenmode one finds

$$\mathbf{x}_1^T \mathbf{M}_{uu} \mathbf{x}_1 \Delta \ddot{u} + \mathbf{x}_1^T \mathbf{K}_{uu}^m \mathbf{x}_1 \Delta u + \mathbf{x}_1^T \mathbf{K}_{uu}^m \mathbf{u}_{eq} = \mathbf{x}_1^T \mathbf{f}^{elec}(\mathbf{u}_{eq} + \mathbf{x}_1 \Delta u, V). \quad (8.12)$$

Since at equilibrium

$$\mathbf{K}_{uu}^m \mathbf{u}_{eq} = \mathbf{f}^{elec}(\mathbf{u}_{eq}, V), \quad (8.13)$$

one can also write

$$\mathbf{x}_1^T \mathbf{M}_{uu} \mathbf{x}_1 \Delta \ddot{u} + \mathbf{x}_1^T \mathbf{K}_{uu}^m \mathbf{x}_1 \Delta u = \mathbf{x}_1^T (\mathbf{f}^{elec}(\mathbf{u}_{eq} + \mathbf{x}_1 \Delta u, V) - \mathbf{f}^{elec}(\mathbf{u}_{eq}, V)), \quad (8.14)$$

which reduces the set of equations to a single differential equation:

$$m_r \Delta \ddot{u} + k_r \Delta u = \Delta f_r(\mathbf{u}_{eq}, \mathbf{x}_1 \Delta u, V), \quad (8.15)$$

where m_r is the modal mass, k_r the modal stiffness and f_r the modal participation of the force.

Subsequently an estimate of the coupled eigenfrequency can be found by:

$$\omega = \sqrt{\frac{k_r}{m_r} - \frac{1}{m_r} \frac{\partial \Delta f_r}{\partial \Delta u}}. \quad (8.16)$$

where the term

$$\frac{\partial \Delta f_r}{\partial \Delta u}$$

can be obtained by a finite difference approximation. Of course this method only works properly if the electric forces do not change the modeshape too much.

Monolithic method

Monolithically the computation is straightforward. One just has to solve equation 8.4. Because the full electromechanical coupling is accounted for in this equation the correct eigenfrequencies and modeshapes will be found. The only problem is that the inertia matrix is singular, hence there are infinite eigenfrequencies. However, as stated above, the static DOFs can be condensed out, which yields equation (8.5), that defines an eigenvalue problem that can be solved exactly like the purely mechanic eigenvalue problem.

8.3 Transient modeling and dynamic pull-in

Not only frequencies are interesting, also the non linear response over time of a device for a certain applied potential can be very useful. Therefore the equations of motion have to be integrated over time. Using the results from such a time integration procedure, displacement as a function of time, the dynamic version of pull-in will be defined.

8.3.1 Time integration

When performing time integration, there is a choice between explicit and implicit integration. Explicit schemes use the displacement and velocity at the beginning of a time step to estimate the behavior during the time step. Classic examples are the forward Euler scheme and the Runge-Kutta schemes. Therefore the dynamic equilibrium equations will not be satisfied at the end of the time step. On the other hand, implicit schemes require the dynamic equilibrium to be satisfied at the end of the time step. Therefore they need to solve a system of (non-)linear equations for each time step, hence they are computationally more expensive. However they are more stable, therefore bigger time steps are allowed when implicit algorithms are used. Classic examples are the backward Euler and the Newmark schemes. For more information on this matter see for instance [45].

A non linear implicit time integration algorithm for the coupled equations can be derived based on the trapezoidal rule [12]. First the nonlinear dynamic equilibrium equations have to be written in a form that can be solved by an iterative procedure:

$$\mathbf{M}_{uu} \ddot{\mathbf{u}}_k^{t+\Delta t} + \hat{\mathbf{K}} \Delta \mathbf{u}_k = \mathbf{f}^{elec}(\mathbf{u}_{k-1}^{t+\Delta t}) - \mathbf{K}_{uu}^m \mathbf{u}_{k-1}^{t+\Delta t}, \quad (8.17)$$

$$\mathbf{u}_k^{t+\Delta t} = \mathbf{u}_{k-1}^{t+\Delta t} + \Delta \mathbf{u}_k. \quad (8.18)$$

where $\hat{\mathbf{K}}$ is the Schur complement of the $\mathbf{K}_{\phi\phi}$ block of \mathbf{K} :

$$\hat{\mathbf{K}} = \frac{\partial \mathbf{f}}{\partial \mathbf{u}} = \mathbf{K}_{uu} - \mathbf{K}_{uv} \mathbf{K}_{\phi\phi}^{-1} \mathbf{K}_{u\phi}^T. \quad (8.19)$$

The Schur complement is required, because during the time integration the electric equations are condensed out of the monolithic equations. Note that the time $t + \Delta t$ indicates that this equation has to be satisfied at the end of the time step

The trapezoidal rule assumption states that the displacements and velocities at the end of the time step are defined as:

$$\mathbf{u}^{t+\Delta t} = \mathbf{u} + \frac{\Delta t}{2} (\dot{\mathbf{u}}^t + \dot{\mathbf{u}}^{t+\Delta t}) \quad (8.20)$$

$$\dot{\mathbf{u}}^{t+\Delta t} = \dot{\mathbf{u}} + \frac{\Delta t}{2} (\ddot{\mathbf{u}}^t + \ddot{\mathbf{u}}^{t+\Delta t}). \quad (8.21)$$

Combining equations (8.18) to (8.21) yields:

$$\ddot{\mathbf{u}}_k^{t+\Delta t} = \frac{4}{\Delta t^2} (\mathbf{u}_{k-1}^{t+\Delta t} - \mathbf{u}^t + \Delta \mathbf{u}_k) - \frac{4}{\Delta t} \dot{\mathbf{u}}^t - \ddot{\mathbf{u}}^t, \quad (8.22)$$

which can be substituted in (8.17) to give:

$$\left[\hat{\mathbf{K}} + \frac{4}{\Delta t^2} \mathbf{M}_{uu} \right] \Delta \mathbf{u}_k = \mathbf{f}^{elec} (\mathbf{u}_{k-1}^{t+\Delta t}) - \mathbf{K}_{uu}^m \mathbf{u}_{k-1}^{t+\Delta t} - \mathbf{M}_{uu} \left(\frac{4}{\Delta t^2} (\mathbf{u}_{k-1}^{t+\Delta t} - \mathbf{u}^t) - \frac{4}{\Delta t} \dot{\mathbf{u}}^t - \ddot{\mathbf{u}}^t \right), \quad (8.23)$$

which provides the equation that can be used to compute $\Delta \mathbf{u}_k$. The algorithm is converged when this $\Delta \mathbf{u}_k$ is small enough. The time integration algorithm is summarized in figure 8.1. To keep the notation simple, in that scheme the right-hand side of equation (8.23) is denoted by:

$$\Delta \mathbf{f} (\mathbf{u}_{k-1}^{t+\Delta t}, \dot{\mathbf{u}}_{k-1}^{t+\Delta t}) = \mathbf{f}^{elec} (\mathbf{u}_{k-1}^{t+\Delta t}) - \mathbf{K}_{uu}^m \mathbf{u}_{k-1}^{t+\Delta t} - \mathbf{M}_{uu} \left(\frac{4}{\Delta t^2} (\mathbf{u}_{k-1}^{t+\Delta t} - \mathbf{u}^t) - \frac{4}{\Delta t} \dot{\mathbf{u}}^t - \ddot{\mathbf{u}}^t \right). \quad (8.24)$$

8.3.2 Dynamic pull-in

Pull-in is defined as the maximum point of the quasi-static load-displacement relation. However, dynamically the response can become unbounded at lower voltages, calling for the definition of a *dynamic pull-in*.

A way of defining *dynamic pull-in* could be: *The lowest voltage V_{DPI} for which, when it is applied as a step from zero to V_{DPI} , the displacement response is unbounded.* This means that if the device is pulled down after the voltage is applied as a step, the voltage step was above the dynamic pull-in. This is the definition that was used in [36, 107]. This dynamic pull-in voltage is in general lower than the static pull-in voltage (see also chapter 3).

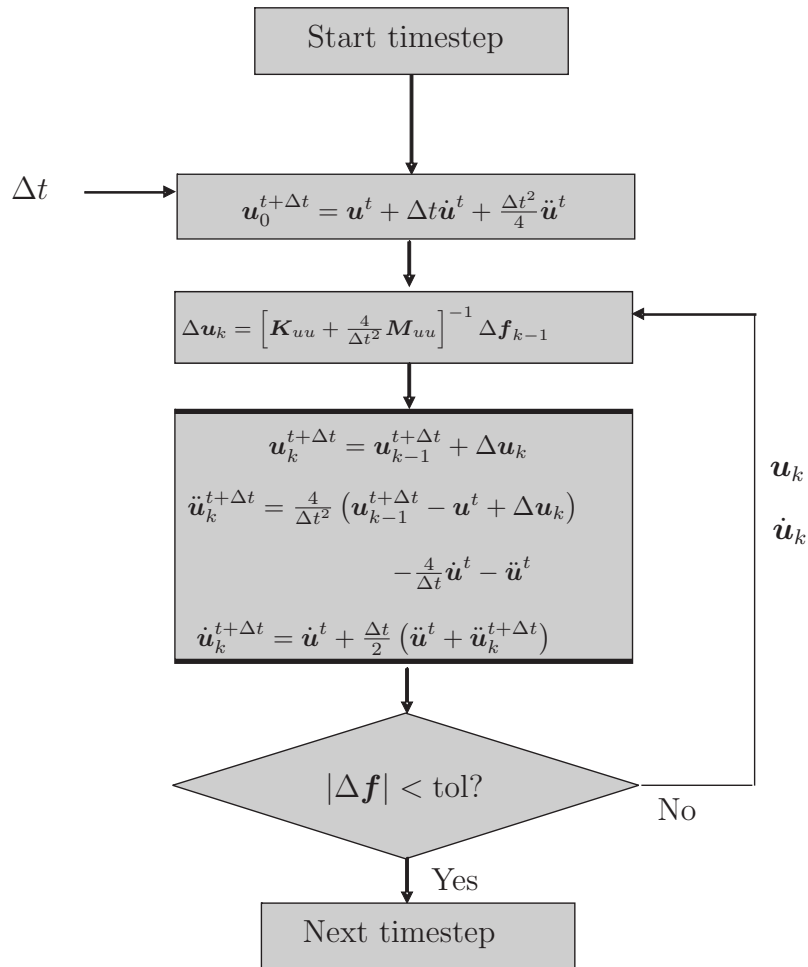


Figure 8.1: Nonlinear implicit time integration algorithm.

Another relevant and competing definition is: *that applied AC voltage in combination with a DC voltage: $V = V_{DC} + V_{AC} \cdot \sin(\Omega t)$ that gives an unstable response.* Here Ω is the frequency of the alternating part of the drive voltage. This definition is used in [62, 92]. This definition is especially relevant if the drive frequency Ω is near a mechanical resonance frequency of the device. Most devices avoid those frequencies or keep the alternating part V_{AC} really low. Furthermore each DC voltage has a corresponding AC pull-in voltage, hence this definition is rather ambiguous. Also, in a FEM setting these values are hard to compute, therefore in this work the first definition will be used.

Automated search

Dynamic pull-in can be computed automatically for finite element models. The first step to do is determine the static pull-in voltage. Then one has to start a bisection algorithm between 0 and static pull-in.

The way to detect if the current voltage estimate is below or above dynamic pull-in is by time integrating the equations of motion for about two oscillations.

Without damping the transition is pretty sharp, thus when the applied voltage is above dynamic pull-in the displacement will become bigger than the gap-size within two oscillations. In that case the search algorithm can stop because the applied voltage is determined to be above pull-in.

The algorithm can be stopped when the error is considered small enough. Note that bisection algorithms often converge slowly, hence this computation can become pretty expensive. However gradient information is not available, furthermore the answer to the question: *above pull in?* is either true or false, and cannot be written as a continuous function. Therefore one is limited to the bisection algorithm.

8.4 The two dimensional model

8.4.1 Eigenfrequencies

These algorithms were tested on the model of a simple beam that was also used in the previous chapters. The load displacement relation and deformed shape are recapitulated in figures 8.2 and 8.3.

The used density is $5 \times 10^3 \text{ kg/m}^3$. The first and third purely mechanical eigenmodes of the beam are shown in figures 8.4 and 8.5. After the computation of each static solution shown in figure 8.2 the first and second eigenfrequency and eigenmode around this static solution were determined. The first eigenmode is very similar to the shape of the static deflection shown in figure 8.3, thus the mode shape will not be changed very much by the electric field. Therefore it is expected that the staggered method will be accurate for the first eigenfrequency. The second mode shape is more complex. The electrostatic load might affect the mode shape, thus the eigenfrequency. This will affect the accuracy of the results obtained with the staggered method, but not with the monolithic method.

The curves for the first eigenfrequency, shown in figure 8.6, confirm that the staggered method computes the same curve as the monolithic method. It also shows that the frequency goes to zero at the pull-in point, similarly to what is found for limit point buckling. Both methods compute the same curve, however the curve obtained

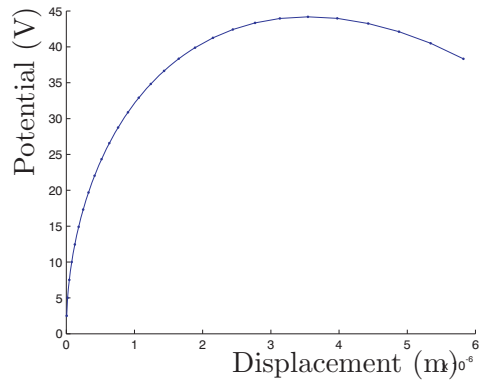


Figure 8.2: Voltage displacement curve

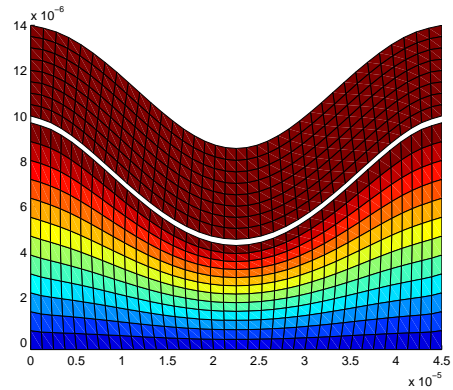


Figure 8.3: Deformed shape of the simple beam

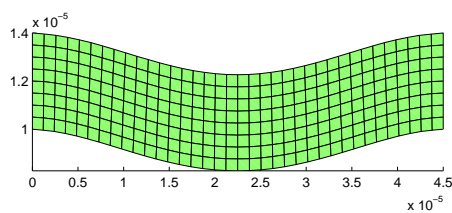


Figure 8.4: First mechanical eigenmode of the beam

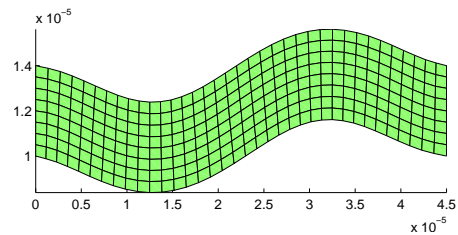


Figure 8.5: Second mechanical eigenmode of the beam

with the staggered method is less smooth. A disadvantage of the staggered method is that the accuracy depends heavily on the size of the generalized displacement step that is used for the finite difference approximation.

The curves for the second eigenfrequency are shown in figure 8.7. As expected the curves are very similar, but there is a small discrepancy due the very large displacements above static pull-in at which these frequencies are obtained. Therefore the mode induces more influence of the electrostatic forces on the mode shape. It is interesting to note that the second eigenvalue is not zero at pull-in, which is the case for all the higher modes.

8.4.2 Transient results and dynamic pull-in

If the transient solution due to a step of 10 volts is obtained, the result is that of figure 8.8. The solid black line gives the static solution and it is clear that it oscillates nicely around the static solution.

The automated dynamic pull-in algorithm gave a voltage of 40.62 volts when a relative error tolerance of $1 \cdot 10^{-3}$ is used. Figure 8.9 gives some step responses. It is clear that the frequency of the oscillation varies greatly for the curves, which is consistent with the linearized eigenfrequency curve. Above the pull-in the response is really unstable. Figure 8.10 shows how sensitive the undamped system is. A voltage of 40.6 gives a stable result and a voltage of 40.7 gives a result that within one oscillation snaps to the fixed electrode. Note that the maximum displacement that is reached during some of the stable transients is much bigger than the pull-in displacement of about $3.5 \mu\text{m}$. The static pull-in voltage was about 43.8V, thus the dynamic pull-in is

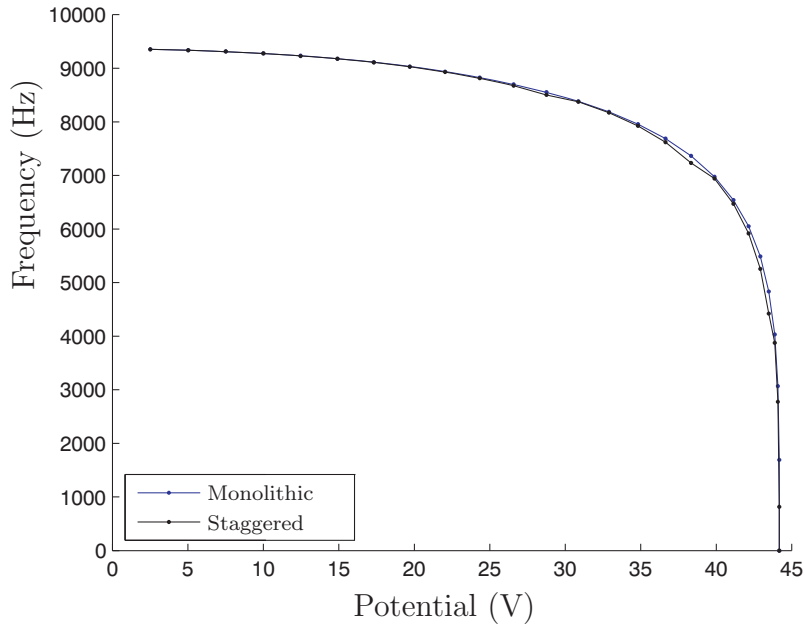


Figure 8.6: First eigenfrequency as a function of applied potential

approximately 7% lower than the static pull-in.

8.5 Experimental validation of the frequency computations

In chapter 5 a 1994 paper of Tilmans and Legtenberg that presents pull-in measurements was used for experimental validation [130]. That paper also presents electro-mechanical frequency measurements. For those measurements a very simple micro-bridge is used which is ideal for a computation with the plate type model that was introduced in chapter 4.

The thickness of the plate is 1.5μ , the gap between plate and ground plane is 1.2μ and the width is 100μ (distance from free to free edge). Amongst others a bridge of length 210μ was used (distance from clamped to clamped edge). For the material properties a value of $E = 160 \text{ GPa}$ for the elasticity modulus, $\rho = 2300 \text{ kg/m}$ for the density of silicon and $\nu = 0.22$ for Poisson's ratio is used. Since it was concluded in section 5.8 that the initial strain is important the initial strain of $\epsilon = 36.8 \cdot 10^{-6}$ is included here as well.

For the modeling of the mechanics of the plate a mesh of 22 elements in the length and 14 elements in the width of the plate is used. A convergence study like the one that was performed in chapter 4 for the pull-in voltage, shows that this mesh provides a relative accuracy better than $1 \cdot 10^{-3}$ for the first frequency. The electric mesh in the air gap contained 4 elements in the direction perpendicular to the plate. In the other 2 directions the number of elements was equal to the number of elements in the mechanical mesh.

In the reference paper a pull-in voltage of 27.95 was reported. When this voltage is computed with the FEM model a value of 28.3 is found, which is close enough to the measured one. The frequency as a function of the DC bias voltage is plotted in figure

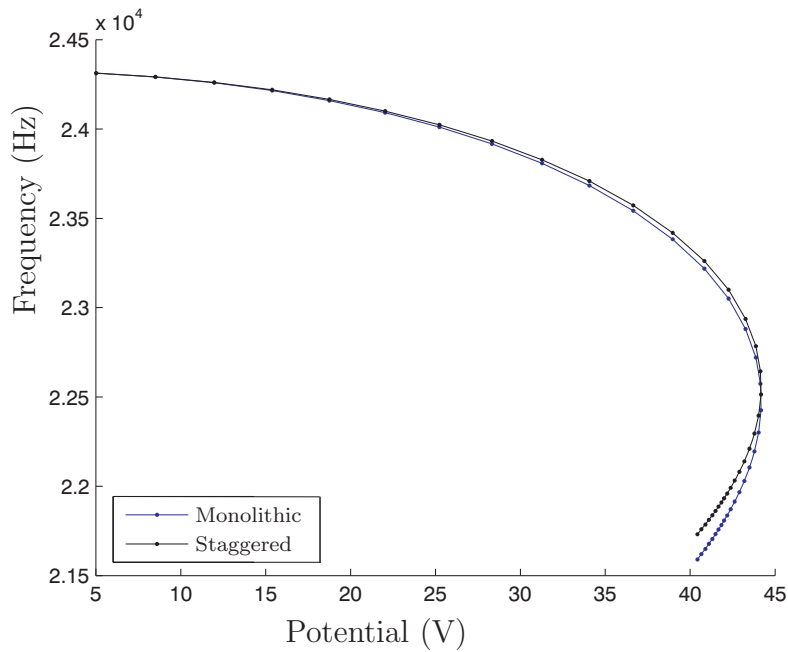


Figure 8.7: Second eigenfrequency as a function of applied potential

8.11, which shows that the model nicely captures the behavior. Therefore those results show that the coupled frequency computations are reasonably accurate.

8.6 Conclusions

The dynamic modeling of an undamped electro-mechanical problem was discussed. The modeling was split into eigenfrequency computations and transient simulations. Also the concept of dynamic pull-in was introduced

These algorithms were tested on a 2D model for which transient analysis were performed. Furthermore the first coupled electro-mechanical eigenfrequency was computed as a function of applied potential and the shape of this curve was found to be similar to the 1D analytical curve in chapter 3. The eigenfrequency computations can be done in a staggered and a monolithic way. The monolithic method is more robust.

The dynamic pull-in for the test beam was 7% lower than static pull-in.

Finally a measurement from literature allowed for an experimental validation of the frequency computations and their decrease with applied potential.

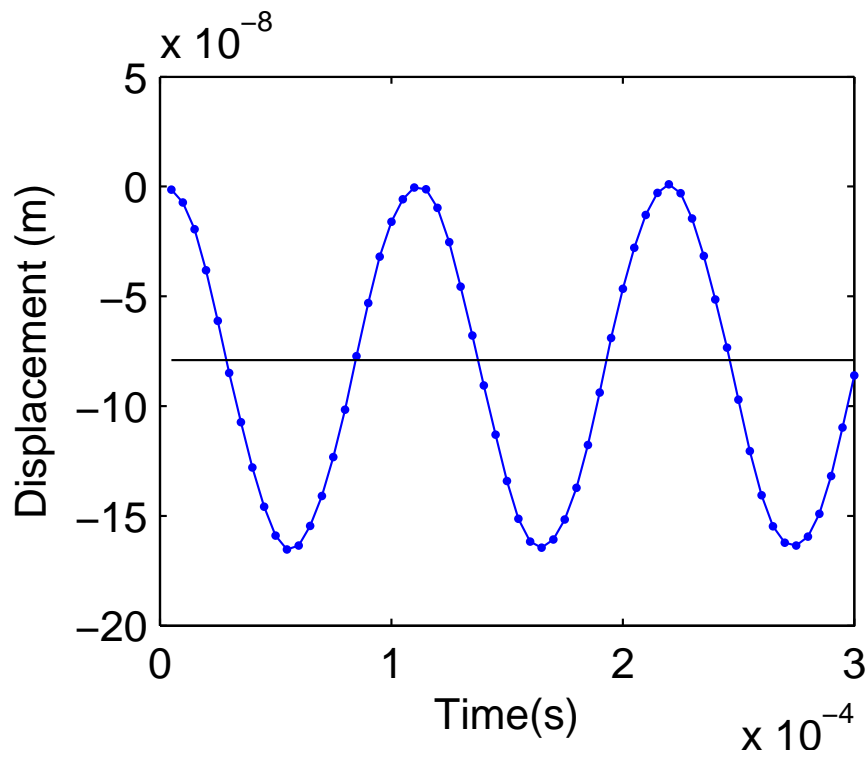


Figure 8.8: Step response at 10 volts.

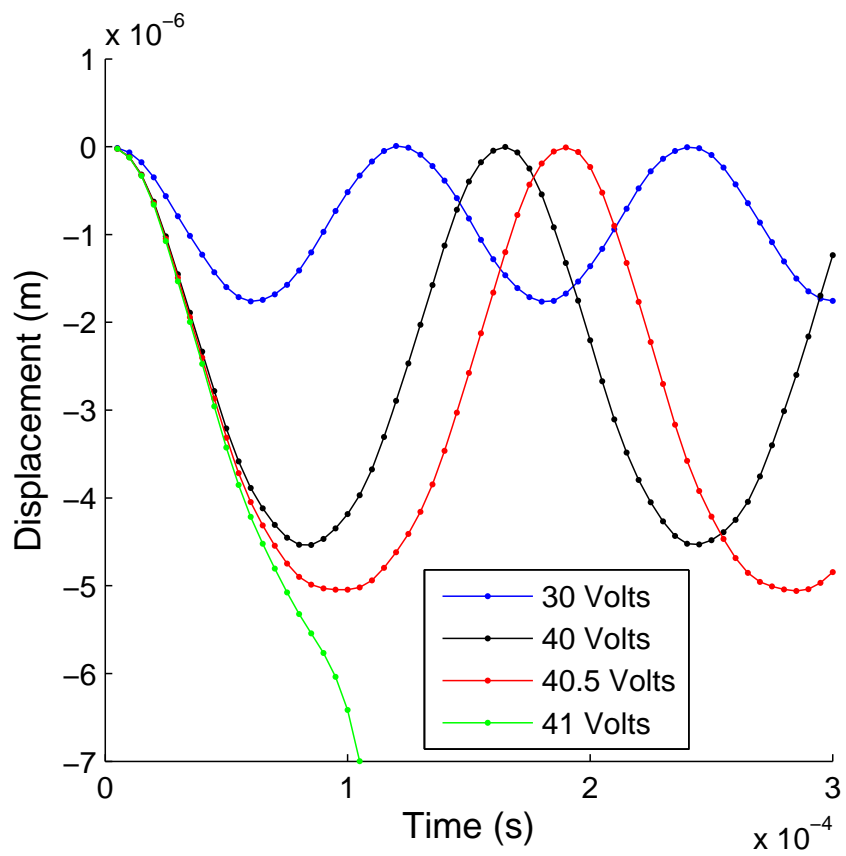


Figure 8.9: Step responses for different voltages.

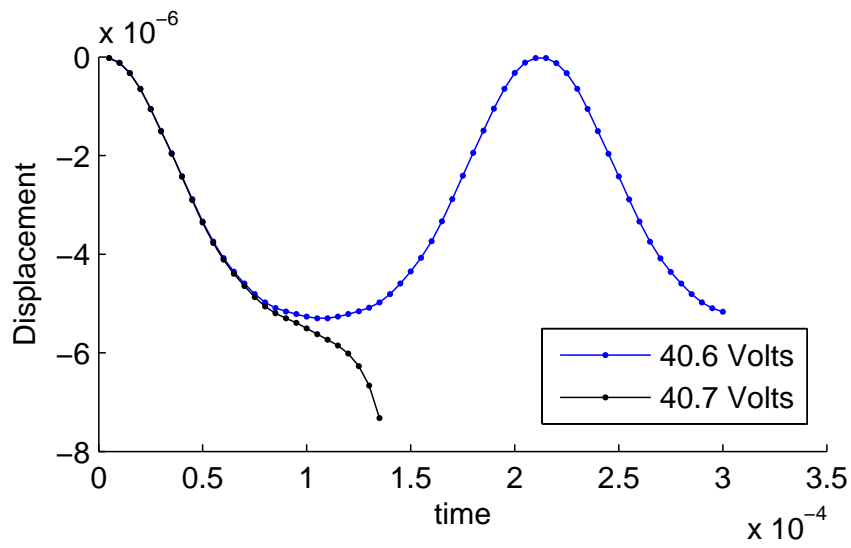


Figure 8.10: Step responses near the dynamic pull-in.

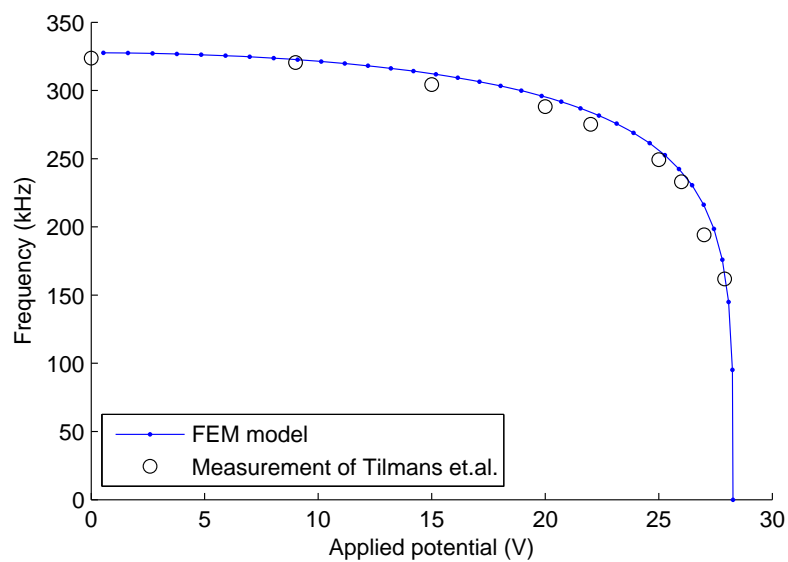


Figure 8.11: Frequency versus potential of the measured beam.

Chapter 9

Sensitivity based stochastic analysis of dynamic pull-in

9.1 Introduction

In chapter 8 the dynamic pull-in voltage was introduced. It was defined similar to [107] and [72] as: *The lowest voltage V_{DPI} for which, when it is applied with a step from zero to V_{DPI} , the displacement response is unbounded.* Furthermore that chapter presented a method to actually compute the dynamic pull-in value with a FEM model in a systematic way.

But in chapter 7 it was stated that material and shape parameters for MEMS are rarely deterministic. In general they have a stochastic nature. Therefore that chapter focused on finding how random material parameters influence the random static pull-in value. Of course if the material properties are random not only the static pull-in value is random, also the dynamic pull-in value will be random. Computing the random distribution of the dynamic pull-in value once the random distribution of the material properties are known will be the objective of this chapter.

The same perturbation based approaches as used in chapter 7 will be used, hence the sensitivity of the dynamic pull-in voltage with respect to parameter variations will be required. That is the focus of the first part of this chapter. Thereafter an uncertainty and reliability analysis will be performed.

9.2 Sensitivity of dynamic pull-in

The stated definition of dynamic pull-in is much vaguer than that of static pull-in. For static pull-in it was known that the tangent stiffness matrix is singular, providing a very strict definition. Because such a strict definition is not available for dynamic pull-in a work-around will be used.

In section 3.3 it was shown for a 1D example that the static pull-in displacement ($x_{PI} = \frac{2}{3}x_0$) only depended on the initial gap, not on the stiffness of the used spring. Is it possible to say that when a geometry is chosen, the dynamic pull-in displacement does not depend on mechanical properties as element stiffnesses or beam element thicknesses?

This statement is nearly impossible to prove mathematically, but with some heuristic reasoning it is possible to show that this claim is very likely to hold. Consider the

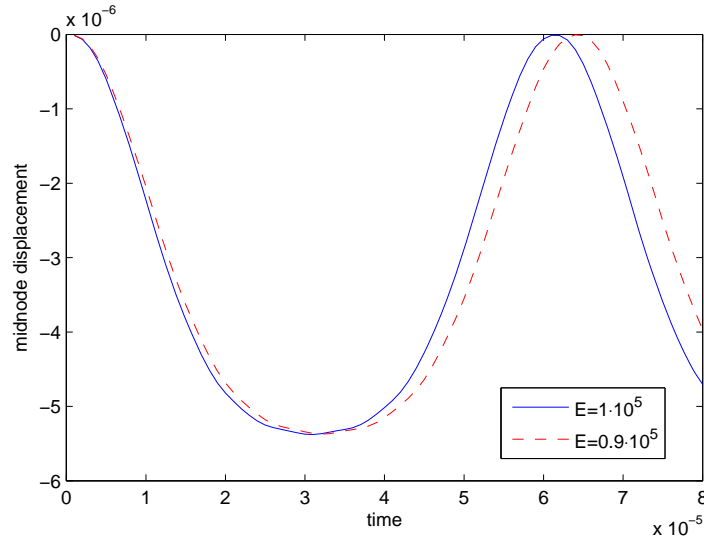


Figure 9.1: Transient results at the dynamic pull-in voltage

beam problem used as reference in chapter 7, using exactly the same discretization: 12 beam elements and a 4 by 12 mesh for the electrostatic domain. For this beam the dynamic pull-in voltage can be computed with the algorithm presented in section 8.3.2. With the standard Young's modulus of $E = 1 \cdot 10^5 Pa$ it was computed to be 40.42 V (8% lower than the static pull-in of 44.05). When the Young's modulus is lowered to $E = 0.9 \cdot 10^5$ dynamic pull-in decreases to 38.34V. When the transient response is computed for both moduli just below pull-in, the results for the middle node displacement are the curves in figure 9.1. The maximum displacement of both curves (different potential, different stiffness) is equal. Thus the statement that *the dynamic pull-in displacement does not depend on mechanical properties such as element stiffnesses* seems to be plausible.

Note that this statement only holds for mechanical properties like the elasticity modulus or the thickness of beam and plate elements. If the electric domain changes in shape the pull-in displacement will change, hence this derivation will not work. Also the addition of damping will make the pull-in displacement sensitive for parameters that influence this damping, thus limiting the approach presented below.

When that statement is accepted, the point at which dynamic pull-in occurs can be defined as the voltage for which:

$$f = \min(u(V, p, t)) - u_{DPI} = 0, \quad (9.1)$$

where u is the displacement of the middle node and u_{DPI} the stiffness invariant pull-in displacement. The displacement u is a function of the applied voltage step V , which at pull-in is assumed to be a function of the mechanical parameter p . The displacement is also directly a function of p .

This defines dynamic pull-in, but the purpose of this derivation is to find how the dynamic pull changes with a mechanical parameter p . Therefore f is differentiated with respect to p :

$$\frac{df}{dp} = \frac{\partial f}{\partial V} \frac{dV}{dp} + \frac{\partial f}{\partial p} + \frac{\partial f}{\partial t} \frac{dt_{min}}{dp}. \quad (9.2)$$

where the term $\frac{dt_{min}}{dp}$ gives the change of the time at which the minimum is reached due to a change of parameter p . Because variation of V while remaining at pull-in is of

interest, hence while f remains zero, this derivative is restricted to zero values:

$$\left. \frac{df}{dp} \right|_{DPI} = \frac{\partial f}{\partial V} \frac{dV}{dp} + \frac{\partial f}{\partial p} + \left. \frac{\partial f}{\partial t} \frac{dt_{max}}{dp} \right|_{DPI} = 0, \quad (9.3)$$

Furthermore when $f = 0$, the displacement reaches a minimum in time. Therefore f reaches a minimum in time, therefore the derivative with respect to time, the velocity of f , will be:

$$\frac{\partial f}{\partial t} = 0, \quad (9.4)$$

thus the value computed by:

$$\left. \frac{dV}{dp} \right|_{DPI} = - \left(\frac{\partial f}{\partial V} \right)^{-1} \left. \frac{\partial f}{\partial p} \right|_{f=0}, \quad (9.5)$$

will give the proper sensitivity.

However, this still requires the computation of the derivatives:

$$\frac{\partial f}{\partial p}, \quad (9.6)$$

$$\frac{\partial f}{\partial V}. \quad (9.7)$$

Because the assumption that $f = 0$ at dynamic pull-in does not have to hold to compute the derivative of f with a general parameter, both derivatives are essentially the same: the computation of the derivative of f with a parameter r , where $r = p$ or $r = V$. Therefore only the derivative of f with respect to a parameter r has to be derived. Using the chain rule this derivative simplifies to:

$$\frac{\partial f}{\partial r} = \frac{\partial f}{\partial u} \frac{\partial u}{\partial r} = \frac{\partial u}{\partial r} = \frac{\partial u(t)}{\partial r}. \quad (9.8)$$

In the following section will be shown how to compute this sensitivity of the displacement with respect to a parameter.

9.2.1 Computing the displacement sensitivity

Instead of computing the derivative of the mid node displacement, the derivative of the displacement vector will be derived. So the goal is computing:

$$\mathbf{s} = \frac{\partial \mathbf{u}(t)}{\partial r}. \quad (9.9)$$

An efficient method of computing these sensitivities was presented in [19], but they were derived for a state space formulation and applied on an Euler backward time integration scheme. That approach is very similar to the method discussed in [77]. In this work that approach is derived for the non-linear Newmark time integration algorithm.

The derivation starts with the dynamic equilibrium equation:

$$\mathbf{M}_{uu} \ddot{\mathbf{u}}(r, t) = \mathbf{f}^{elec}(\mathbf{u}(r, t), r) - \mathbf{K}_{uu}^m(r) \mathbf{u}(r, t), \quad (9.10)$$

where the mechanical stiffness matrix can be a function of r if r is a material property and the electric force can be a function of $r = V$. In short this can be written as:

$$\mathbf{M}_{uu}\ddot{\mathbf{u}}(r, t) = \mathbf{f}(\mathbf{u}(r, t), r). \quad (9.11)$$

In section 8.3 the implicit time integration scheme for this problem was derived. This required making an initial guess for the displacement:

$$\mathbf{u}_0^{t+\Delta t} = \mathbf{u}^t + \Delta t \dot{\mathbf{u}}^t + \frac{\Delta t^2}{4} \ddot{\mathbf{u}}^t, \quad (9.12)$$

and subsequently computing the correction for the displacement by:

$$\left[\hat{\mathbf{K}} + \frac{4}{\Delta t^2} \mathbf{M}_{uu} \right] \Delta \mathbf{u}_k = \mathbf{f}^{elec}(\mathbf{u}_{k-1}^{t+\Delta t}) - \mathbf{K}_{uu}^m \mathbf{u}_{k-1}^{t+\Delta t} - \mathbf{M}_{uu} \left(\frac{4}{\Delta t^2} (\mathbf{u}_{k-1}^{t+\Delta t} - \mathbf{u}^t) - \frac{4}{\Delta t} \dot{\mathbf{u}}^t - \ddot{\mathbf{u}}^t \right), \quad (9.13)$$

where:

$$\hat{\mathbf{K}} = \frac{\partial \mathbf{f}}{\partial \mathbf{u}} = \mathbf{K}_{uu} - \mathbf{K}_{u\phi} \mathbf{K}_{\phi\phi}^{-1} \mathbf{K}_{\phi u}^T, \quad (9.14)$$

where this Schur complement has to be used because the electrostatic equations are condensed out of the electro-mechanic equations. Once the $\Delta \mathbf{u}_k$ is known the update for the displacement, velocity and accelerations will be:

$$\mathbf{u}_k^{t+\Delta t} = \mathbf{u}_{k-1}^{t+\Delta t} + \Delta \mathbf{u}_k, \quad (9.15)$$

$$\ddot{\mathbf{u}}_k^{t+\Delta t} = \frac{4}{\Delta t^2} (\mathbf{u}_{k-1}^{t+\Delta t} - \mathbf{u}^t + \Delta \mathbf{u}_k) - \frac{4}{\Delta t} \dot{\mathbf{u}}^t - \ddot{\mathbf{u}}^t, \quad (9.16)$$

$$\dot{\mathbf{u}}_k^{t+\Delta t} = \dot{\mathbf{u}}^t + \frac{\Delta t}{2} (\ddot{\mathbf{u}}^t + \ddot{\mathbf{u}}_k^{t+\Delta t}). \quad (9.17)$$

After which a new $\Delta \mathbf{u}$ can be computed, which can be used to update displacement, velocities and accelerations again. This procedure will be repeated until convergence.

In this chapter the sensitivity of the solution is required, hence let's differentiate (9.11) with r :

$$\mathbf{M}_{uu} \frac{\partial \ddot{\mathbf{u}}}{\partial r} = \frac{\partial \mathbf{f}}{\partial r} + \frac{\partial \mathbf{f}}{\partial \mathbf{u}} \frac{\partial \mathbf{u}}{\partial r}, \quad (9.18)$$

$$\mathbf{M}_{uu} \dot{\mathbf{s}} = \frac{\partial \mathbf{f}}{\partial r} + \hat{\mathbf{K}} \mathbf{s}. \quad (9.19)$$

This is a linear second order differential equation of the sensitivity \mathbf{s} . The initial conditions are easily evaluated. If a step voltage is applied, the initial displacement is a zero vector, hence it does not depend on r . Therefore the initial sensitivity is zero as well. Similarly the initial time derivative of the sensitivity is zero. Thus when the Newmark scheme is applied, a guess for \mathbf{s}_0^t is made as:

$$\mathbf{s}_0^{t+\Delta t} = \mathbf{s}^t + \Delta t \dot{\mathbf{s}}^t + \frac{\Delta t^2}{4} \ddot{\mathbf{s}}^t, \quad (9.20)$$

and due to the linearity only one update is required:

$$\mathbf{s}^{t+\Delta t} = \mathbf{s}_0^{t+\Delta t} + \Delta \mathbf{s}, \quad (9.21)$$

where $\Delta \mathbf{s}$ is computed with:

$$\left[\hat{\mathbf{K}} + \frac{4}{\Delta t^2} \mathbf{M}_{uu} \right] \Delta \mathbf{s} = \frac{\partial \mathbf{f}}{\partial r} - \hat{\mathbf{K}} \mathbf{s}_0^{t+\Delta t} - \mathbf{M}_{uu} \left(\frac{4}{\Delta t^2} (\mathbf{s}_0^{t+\Delta t} - \mathbf{s}^t) - \frac{4}{\Delta t} \dot{\mathbf{s}}^t - \ddot{\mathbf{s}}^t \right), \quad (9.22)$$

which gives the following sensitivity velocity and acceleration:

$$\ddot{\mathbf{s}}^{t+\Delta t} = \frac{4}{\Delta t^2} (\mathbf{s}_0^{t+\Delta t} - \mathbf{s}^t + \Delta \mathbf{s}) - \frac{4}{\Delta t} \dot{\mathbf{s}}^t - \ddot{\mathbf{s}}^t, \quad (9.23)$$

$$\dot{\mathbf{s}}^{t+\Delta t} = \dot{\mathbf{s}}^t + \frac{\Delta t}{2} (\ddot{\mathbf{s}}^t + \ddot{\mathbf{s}}^{t+\Delta t}). \quad (9.24)$$

Note that the left hand-side of equation (9.22) contains the same matrix as equation (9.13), thus for solving equation (9.22) the same factorized matrix as for the final iteration of each displacement time step can be reused. Hence computing the sensitivity is not computationally expensive. Only one extra matrix multiplication per time step is required.

One unknown term remains is the derivative of the force \mathbf{f} with r . When r is a mechanical parameter p , such as the elasticity modulus this is not that difficult. As in chapter 6 linear mechanics is assumed:

$$\frac{\partial \mathbf{f}}{\partial p} = \frac{\partial}{\partial p} (-\mathbf{K}_{uu}(p)\mathbf{u}) = \frac{\partial \mathbf{K}_{uu}}{\partial p} \mathbf{u}. \quad (9.25)$$

The derivative of the stiffness matrix with a material parameter is fairly trivial and was discussed in that chapter.

If $r = V$, the derivative is a little more complicated. In chapter 6 only the derivative of \mathbf{F} with V where $\mathbf{F} = [\mathbf{f} \quad \mathbf{q}]^T$ was discussed. If one would only use the mechanical terms from that derivative, one would get the wrong result. One should start with the original equation (6.16) mentioned in that chapter:

$$\mathbf{K}_{tot} = \begin{bmatrix} \mathbf{K}_{uu} & \mathbf{K}_{u\phi} & \mathbf{K}_{u\bar{\phi}} \\ \mathbf{K}_{\phi u} & \mathbf{K}_{\phi\phi} & \mathbf{K}_{\phi\bar{\phi}} \\ \mathbf{K}_{\bar{\phi}u} & \mathbf{K}_{\bar{\phi}\phi} & \mathbf{K}_{\bar{\phi}\bar{\phi}} \end{bmatrix}, \quad (9.26)$$

and condense out the terms for ϕ :

$$\hat{\mathbf{K}}_{tot} = \begin{bmatrix} \mathbf{K}_{uu} & \mathbf{K}_{u\bar{\phi}} \\ \mathbf{K}_{\bar{\phi}u} & \mathbf{K}_{\bar{\phi}\bar{\phi}} \end{bmatrix} - \begin{bmatrix} \mathbf{K}_{u\phi} \mathbf{K}_{\phi\phi}^{-1} \mathbf{K}_{\phi u} & \mathbf{K}_{u\phi} \mathbf{K}_{\phi\phi}^{-1} \mathbf{K}_{\phi\bar{\phi}} \\ \mathbf{K}_{\bar{\phi}\phi} \mathbf{K}_{\phi\phi}^{-1} \mathbf{K}_{\phi u} & \mathbf{K}_{\bar{\phi}\phi} \mathbf{K}_{\phi\phi}^{-1} \mathbf{K}_{\phi\bar{\phi}} \end{bmatrix} \quad (9.27)$$

Therefore the derivative is:

$$\frac{\partial \mathbf{f}}{\partial V} = \hat{\mathbf{K}}_{u\bar{\phi}} \frac{\partial \bar{\phi}}{\partial V}, \quad (9.28)$$

$$\frac{\partial \mathbf{f}}{\partial V} = [\mathbf{K}_{u\bar{\phi}} - \mathbf{K}_{u\phi} \mathbf{K}_{\phi\phi}^{-1} \mathbf{K}_{\phi\bar{\phi}}] \begin{bmatrix} 1 \\ \vdots \\ 1 \end{bmatrix}. \quad (9.29)$$

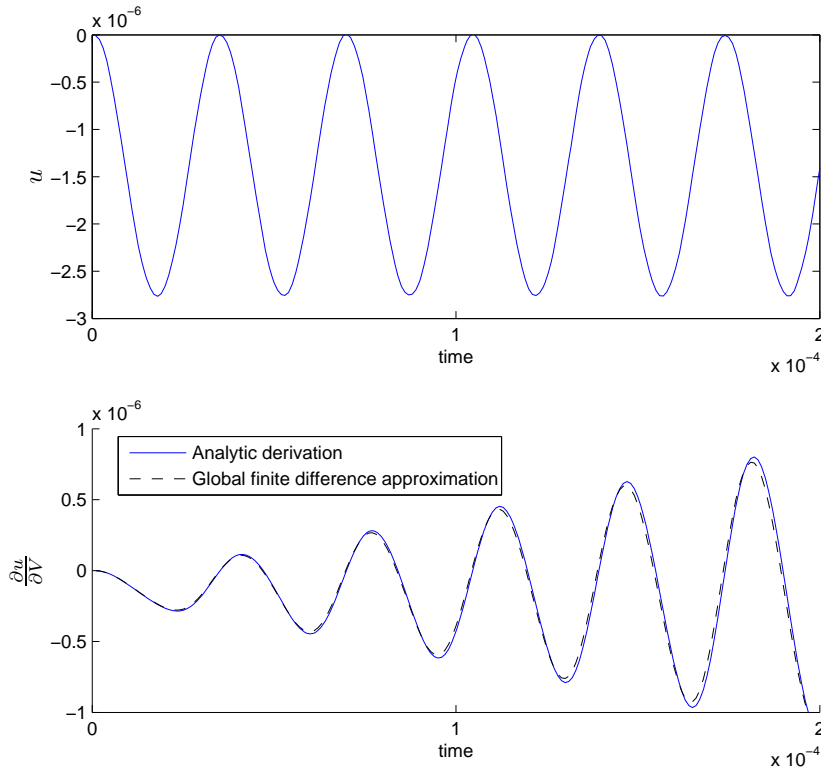


Figure 9.2: Transient results of the mid node displacement and the sensitivity ($V=35$).

9.2.2 Example: uniform beam

The methods discussed above are tested using the test beam of chapter 7. For more details the reader is referred back to section 7.3. To test if the method for computing the simple displacement sensitivities (\mathbf{s}) is correct a step response has been computed with a voltage step of 35, well below the static ($44.05V$) and dynamic ($40.72V$) pull-in values. For this voltage the sensitivity of u with V is determined using the analytical approach. The sensitivity is also determined with global finite differences. This is done by computing u for a step of 34.7 volts as well and defining the sensitivity as:

$$\frac{\Delta u(t)}{\Delta V} = \frac{u(t)|_{V=35} - u(t)|_{V=34.7}}{35 - 34.7}. \quad (9.30)$$

Figure 9.2 shows the transient result on top and below the sensitivity determined analytically as well as by finite differences. Clearly the analytic sensitivity computation is very accurate.

Figure 9.3 shows the analytic sensitivity with elasticity variation of a step response. Here a typical beating behavior can be seen, caused by the frequency modulation due to the parameter change. Note that only half an oscillation of this lower beating frequency is shown.

Because the displacement sensitivities are validated by finite differences, the pull-in sensitivity can be computed. Figure 9.4 shows the transient for V just below pull-in and the two required displacement sensitivities. The star indicates the point where

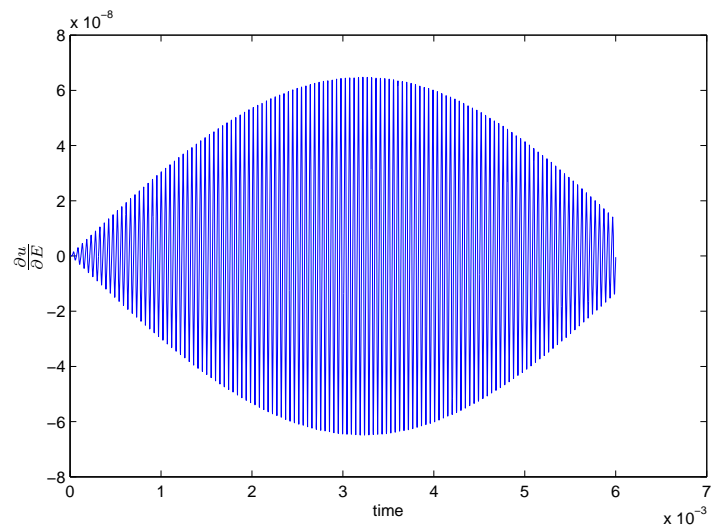


Figure 9.3: Transient results of the elasticity sensitivity ($V=40.2$).

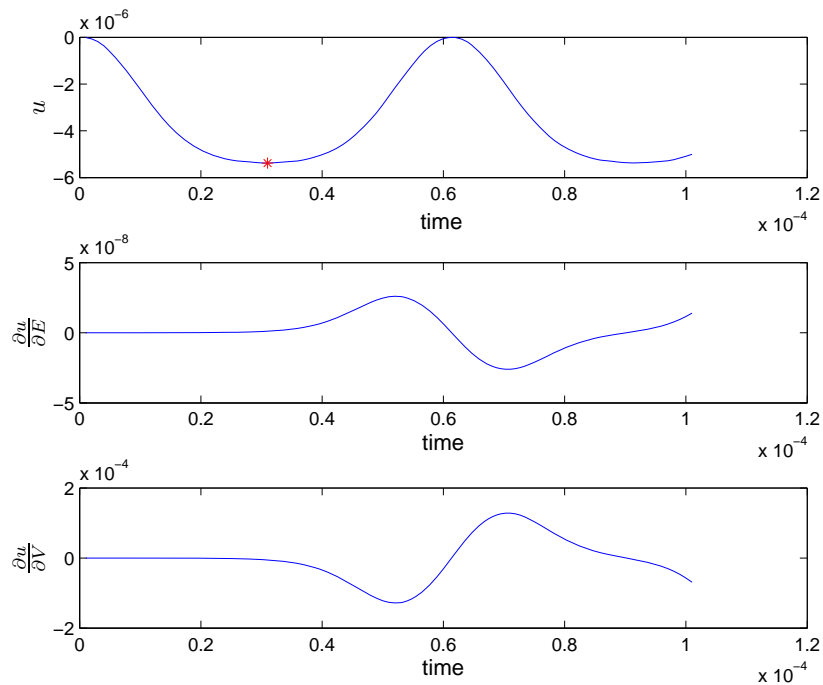


Figure 9.4: Transient results used for pull-in sensitivity computations ($V=40.41$).

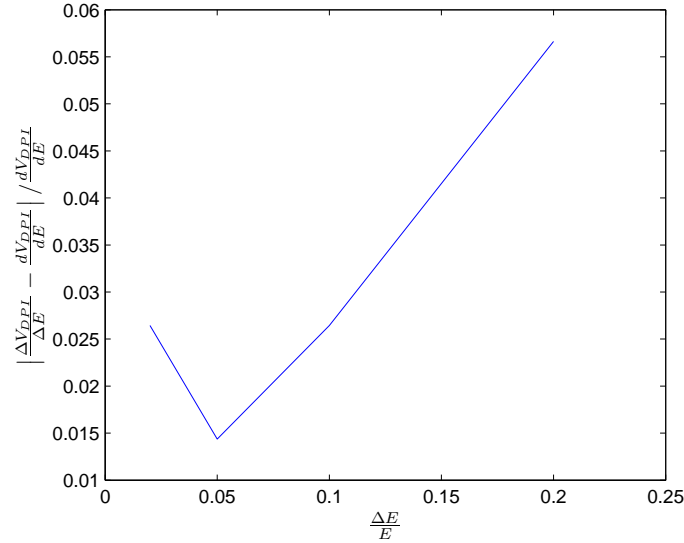


Figure 9.5: Convergence of the finite difference sensitivity to the analytic sensitivity.

$f = u - u_{cr} = 0$ and at that point the sensitivity was computed to be:

$$\left. \frac{dV}{dE} \right|_{DPI} = - \left(\frac{\partial f}{\partial V} \right)^{-1} \left. \frac{\partial f}{\partial E} \right|_{f=0} = 2.0217 \cdot 10^{-4}. \quad (9.31)$$

Also this sensitivity can be validated by global finite differences. If the dynamic pull-in is computed at $E = 1 \cdot 10^5$ and $E = 0.95 \cdot 10^5$ this gives respectively $V_{DPI} = 40.4175$ and $V_{DPI} = 39.3921$, yielding:

$$\left. \frac{\Delta V}{\Delta E} \right|_{DPI} = 2.0508 \cdot 10^{-4}. \quad (9.32)$$

which is reasonably accurate.

The convergence of the finite difference sensitivity to the analytical one is shown in figure 9.5. The reason that for very small ΔE values the error goes up is that the error tolerance of the dynamic pull-in computation is not sufficiently small for that small ΔE values.

It would be interesting to see how the dynamic pull-in sensitivity compares with the static one. In section 7.3 it was shown that for this mesh the static sensitivity was:

$$\left. \frac{dV}{dE} \right|_{PI} = 2.20 \cdot 10^{-4} V/Pa, \quad (9.33)$$

which is a little higher. However because the static pull-in voltage itself is higher it is very difficult to compare these numbers. It is better to look at the logarithmic sensitivity, which in the static case was:

$$\left. \frac{d \log(V)}{d \log(E)} \right|_{PI} = \frac{E}{V} \left. \frac{dV}{dE} \right|_{PI} = 0.50. \quad (9.34)$$

For the dynamic equation the logarithmic sensitivity is:

$$\left. \frac{d \log(V)}{d \log(E)} \right|_{DPI} = \frac{E}{V} \left. \frac{dV}{dE} \right|_{DPI} = 0.50. \quad (9.35)$$

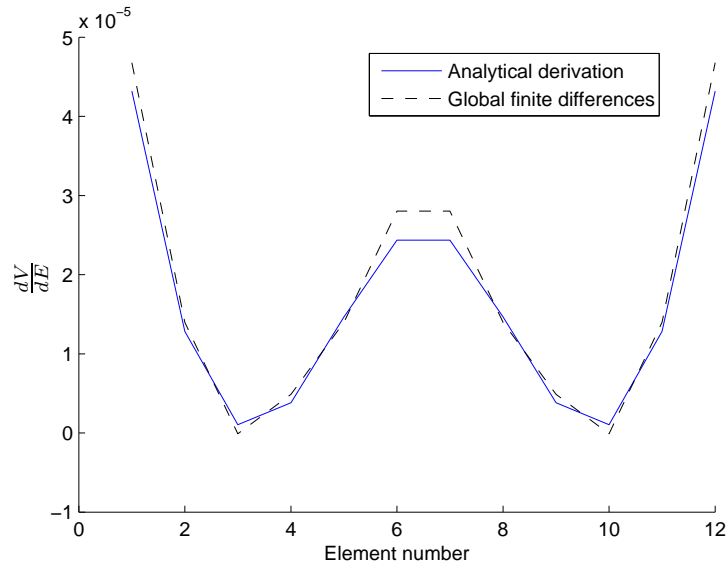


Figure 9.6: Analytical and finite difference sensitivities to individual element elasticity variations.

which is basically the same. It would be an interesting question if this is the case for any geometry.

9.2.3 Example: multiple parameters

As in chapter 6 the computation is also performed for sensitivities to single element elasticity variations. In that case the parameter of interest is:

$$\left. \frac{\partial V}{\partial E_i} \right|_{DPI}. \quad (9.36)$$

Of course the values are also computed by finite differences for comparison. The sensitivity curve is shown in figure 9.6. The finite difference sensitivities were computed by decreasing the Young's modulus of an element from $1 \cdot 10^5$ to $0.95 \cdot 10^5$. The curves show some differences, but overall the match is rather good. Thus it provides a validation of the analytic derivation.

9.2.4 Intermezzo: pull-in time sensitivity

The dynamic pull-in value sensitivity has some problems. It only holds for a limited number of parameter variations: those that do not influence the shape of the electric domain. Also damping is not allowed to be present. However if a fixed voltage is applied that is well above pull-in, there is a parameter which says something about pull-in and for which the sensitivities can be computed in any case: the dynamic pull-in time. This will be defined as: *The time it takes from applying the voltage step to reaching contact between the deformable and fixed electrode.* Contact is somewhat difficult to model, therefore the point where the maximum displacement reaches 95% of the gap will be used as *contact displacement*. Note that each applied voltage above pull-in will provide a different pull-in time. The pull-in time provides a measurement of the switching time for micro-switches.

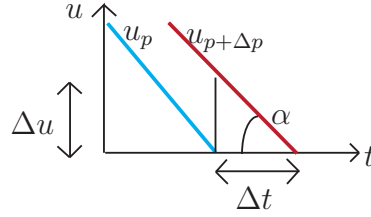


Figure 9.7: Infinitesimal part of the time displacement curve.

Computing the contact point is relatively easy. A dynamic step response until the contact displacement is reached has to be computed. This provides the time for which the contact displacement is reached, the velocity for which that happens as well as the displacement sensitivity.

Studying figure 9.7 will show that these three numbers are enough. Figure 9.7 depicts an infinitesimal region around the contact condition. The blue curve shows the displacement $u_p = u(t, p)$ as a function of time. If a curve would be computed for a new slightly changed parameter $p + \Delta p$ the red curve would be found: $u_{p+\Delta p} = u(t, p + \Delta p)$. This red curve reaches the contact displacement is small amount of time later: Δt . This is the change in pull-in time due to the parameter change which is the goal of this derivation.

Using a first order approximation the displacement change can written as $\Delta u = \frac{\partial u}{\partial p} \Delta p$. Similarly the time change can be written in terms of the actual sensitivity that is needed: $\Delta t = \frac{\partial t_c}{\partial p} \Delta p$. Trigonometry shows that $\tan(\alpha) = \frac{\Delta u}{\Delta t}$ or:

$$\frac{\partial t_c}{\partial p} \Delta p = \frac{\frac{\partial u}{\partial p} \Delta p}{\tan(\alpha)} \quad (9.37)$$

The term $-\tan(\alpha)$ is of course equal to the velocity $v_{p+\Delta p}$ of the perturbed curve at contact, which can be written in terms of the unperturbed curve as:

$$v_{p+\Delta p} = v_p + \frac{\partial v}{\partial p} \Delta p. \quad (9.38)$$

Substitution of the velocity into the tangent of equation (9.37) yields:

$$\frac{\partial t_c}{\partial p} \Delta p = \frac{\frac{\partial u}{\partial p} \Delta p}{-v_p - \frac{\partial v}{\partial p} \Delta p}, \quad (9.39)$$

which can be simplified to:

$$\frac{\partial t_c}{\partial p} = \frac{\frac{\partial u}{\partial p}}{-v_p - \frac{\partial v}{\partial p} \Delta p}. \quad (9.40)$$

Taking the limit of this equation for $\Delta p \rightarrow 0$ gives the final sensitivity:

$$\frac{\partial t_c}{\partial p} = \frac{\frac{\partial u}{\partial p}}{-v_p}, \quad (9.41)$$

where:

$$v_p = \frac{\partial u}{\partial t}. \quad (9.42)$$

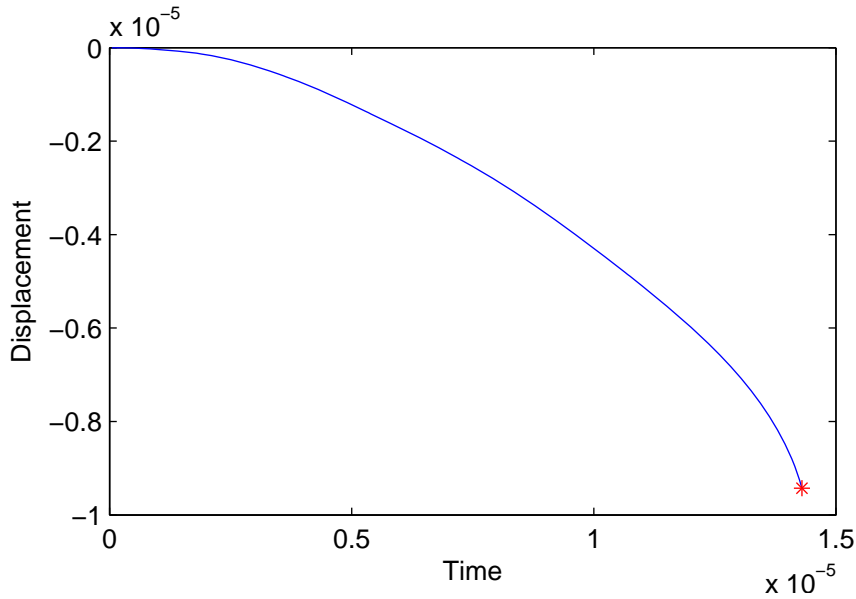


Figure 9.8: Displacement versus time for a voltage step of 50 volts, the star indicates the moment of contact.

The analytic derivation just presented is tested on the beam as used in the previous section. The applied load is 50 volts which gives a pull-in time of $1.430 \cdot 10^{-5}$ seconds. The displacement versus time is shown in figure 9.8. The analytic pull-in time sensitivity to the elasticity is:

$$\frac{\partial t_c}{\partial E} = 5.69 \cdot 10^{-11} \text{ s/Pa}, \quad (9.43)$$

which is validated by global finite differences:

$$\frac{\Delta t_c}{\Delta E} = 6.00 \cdot 10^{-11} \text{ s/Pa}, \quad (9.44)$$

hence the pull-in time sensitivity can be computed by the method presented above.

9.3 Uncertainty analysis

When the beam is considered homogeneous the uncertainty analysis is quite straightforward. Since second order sensitivities are a bit too complicated for dynamic pull-in, only a first order perturbation based uncertainty analysis is performed [49]. Perturbation based approaches have been used on dynamical problems before [77], the novelty of this chapter are the pull-in sensitivities and the pull-in application. It is assumed that the stochastic parameter of interest \tilde{p} is normally distributed and has a mean value μ_p and standard deviation σ_p .

Using the same reasoning as presented in section 7.2 this gives for the mean value:

$$\mu_{V_{DPI}} = V_{DPI}(\mu_E), \quad (9.45)$$

and for the standard deviation:

$$\sigma_{V_{DPI}} = \sqrt{\left(\frac{dV}{dE}\right)^2 \sigma_p^2}. \quad (9.46)$$

9.3.1 Example

These formulas will be used to find the stochastic properties of the reference problem, for which the elasticity is assumed to be a random property. The statistical distribution of \tilde{E} is the same as in section 7.3: the elasticity modulus is assumed to have a mean value of $\mu_E = 1 \cdot 10^5 Pa$ and a coefficient of variation of $V_E = 0.1$, which gives a standard deviation of $\sigma_E = 1 \cdot 10^4 Pa$.

The perturbation based uncertainty analysis gives for the mean value:

$$\mu_{V_{DPI}} = 40.42, \quad (9.47)$$

and for the standard deviation:

$$\sigma_{V_{DPI}} = 2.02, \quad (9.48)$$

giving a coefficient of variation.

$$V_{V_{DPI}} = 0.05. \quad (9.49)$$

The non dimensional coefficient of variation is exactly the same as the static one (just as the logarithmic sensitivity).

Of course also this dynamic analyses requires *Monte Carlo* validation. Hence a sample of 13352 realizations was used for this validation and gave a mean value of:

$$\mu_{V_{DPI}} = 40.38, \quad (9.50)$$

and a standard deviation of:

$$\sigma_{V_{DPI}} = 2.03, \quad (9.51)$$

which is pretty close to the perturbation SFEM approach. Therefore it seems that the unavailable second order reliability analysis is not necessary. The convergence of the Monte Carlo approach is shown in figures 9.9 and 9.10, respectively for the mean value and the standard deviation.

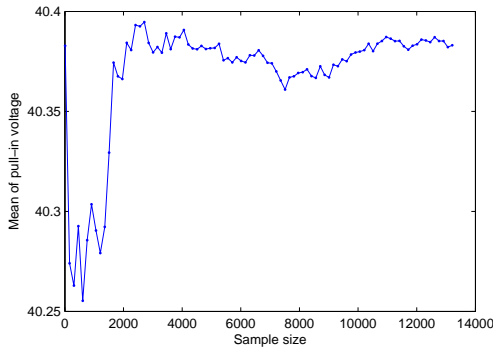


Figure 9.9: Convergence of the mean with sample size.

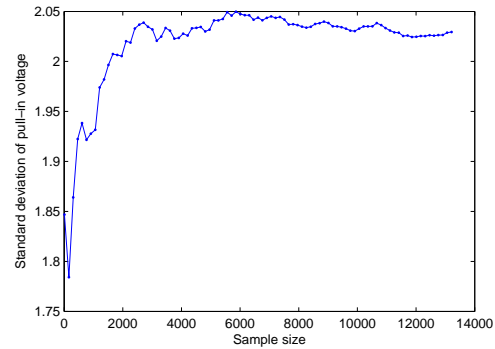


Figure 9.10: Convergence of the standard deviation with sample size.

9.4 Reliability analysis

A 1D reliability analysis is not difficult. The failure criteria from chapter 7 will be used: a device fails if the pull-in voltage is lower or higher than some critical value V_c .

This leads to the definition of the design point: the most likely value of \tilde{p} that will result in a device that has a pull-in voltage equal to the critical value:

$$V_c = V_{DPI}(p_c). \quad (9.52)$$

When it is subsequently assumed that the stochastic parameter \tilde{p} is normally distributed:

$$\tilde{p} = \mu_p + \sigma_p \tilde{z}, \quad (9.53)$$

the design point can be written as a critical deviation z_c from the average parameter value μ_p .

In that case the failure chance is the chance that $\tilde{z} < z_c$:

$$Pr[\tilde{z} < z_c] = f_p(z_c) = \int_{-\infty}^{z_c} \frac{1}{\sqrt{2\pi}} e^{\left(\frac{-z^2}{2}\right)} dz \quad (9.54)$$

The design point can be computed with a Newton iteration. Choose z_0 , compute $V_{DPI,0}(z_0)$ and start the following iteration procedure:

$$\Delta z_k = (V_c - V_{DPI,k-1}) \left. \frac{\partial z}{\partial V} \right|_{z_{k-1}}, \quad (9.55)$$

where:

$$\left(\frac{\partial z}{\partial V} \right)^{-1} = \frac{\partial V}{\partial p} \frac{\partial p}{\partial z} = \frac{\partial V}{\partial p} \sigma_p. \quad (9.56)$$

9.4.1 Example

This reliability approach was tested using the reference beam. For the static problem it was decided that the failure criterion would be: $V_{PI} < 41$. However the mean of the dynamic pull-in is already below that value and the failure chance would be really big. Therefore the dynamic failure criterion is set to be $V_{DPI} < 38$, hence $V_c = 38$. This gives the following failure chance:

$$Pr[V_{DPI} < 38] = 0.123. \quad (9.57)$$

This result can also be validated by crude Monte Carlo, which gives:

$$Pr[V_{DPI} < 38] = 0.119. \quad (9.58)$$

The number is really close to the perturbation result, therefore validating the perturbation approach. Figure 9.11 shows that the Monte Carlo simulation has converged to a band between 0.115 and 0.125.

9.5 A uniform beam with realistic numbers

The model is the same one as used for static pull-in in section 7.5. Therefore all mechanical parameters are the same and most importantly, the stochastic parameter is the elasticity modulus of silicon which has the following random properties: mean

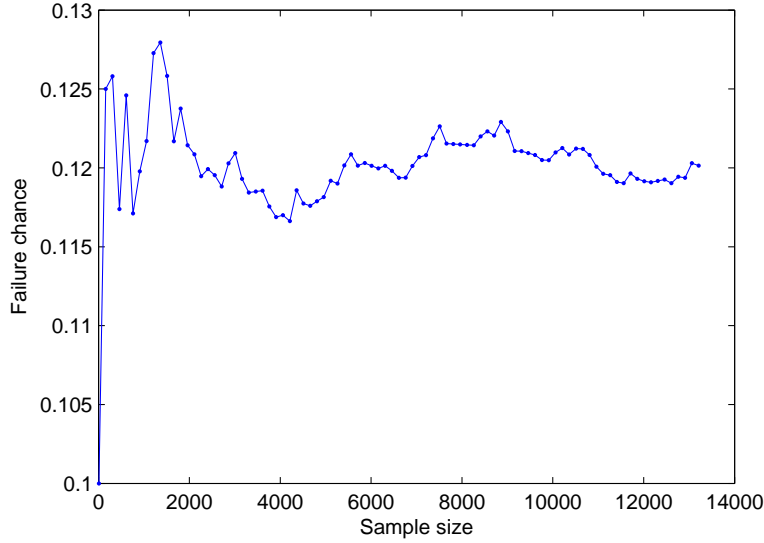


Figure 9.11: Convergence of the failure chance with sample size.

164 *GPa* and standard deviation 7 *GPa*. This gave a deterministic dynamic pull-in voltage of 19.47. The analytic first order sensitivity is:

$$\left. \frac{\partial V}{\partial E} \right|_{DPI} = 5.94 \cdot 10^{-11} V \cdot m^2/N. \quad (9.59)$$

which is validated with the following finite difference sensitivity:

$$\left. \frac{\partial V}{\partial E} \right|_{DPI} = 5.86 \cdot 10^{-11} V \cdot m^2/N. \quad (9.60)$$

Since second order sensitivities are very difficult to compute for dynamic pull-in the uncertainty analysis is limited to a first order one. Hence the mean of the expected pull-in will be the deterministic one:

$$\mu_{V_{DPI}} = 19.47 V, \quad (9.61)$$

and the standard deviation will be:

$$\sigma_{V_{DPI}} = 0.42 V. \quad (9.62)$$

The same failure criterion is used as for the static computations: the device fails if the pull-in is below 19.13 volts. To reach a 19.13 dynamic pull-in the elasticity must be 158 *GPa*, therefore the failure chance is $Pr[V_{PI} < 19.13] = 0.209$. This is a really big failure chance, hence if the resonator is likely to experience step loads, dynamic pull-in can be critical.

9.6 Conclusions and recommendations

In this chapter a method for the analytic estimation of dynamic pull-in sensitivities was derived. This method was validated by global finite difference computations. Those

sensitivities were used for a perturbation based stochastic FEM analysis of dynamic pull-in. The numerical experiments showed that the perturbation based method could be validated by expensive Monte Carlo simulations.

The sensitivity computation also showed that for a simple mechanically linear beam the logarithmic sensitivities of static and dynamic pull-in were equal, thus those sensitivities could be derived from each other. However this does not seem likely to hold for non-linear mechanics, because dynamic pull-in occurs at a much higher displacement.

Furthermore the uncertainty analysis showed that due to the equal logarithmic sensitivities, the coefficients of variation of dynamic and static pull-in were equal. This makes the statistical moments of dynamic and static pull-in related. However the same caution to generalize this statement for any geometry or mechanical model should be used as with the sensitivity computation. Results from the reliability analysis of dynamic pull-in cannot be computed directly from the static computation.

The computation can be generalized to a random field discretization of the element elasticity moduli.

However there is a big limit. The pull-in displacement is not allowed to change due to the parameter variations, hence only parameters, which do not really change the shape of the domain, can be analyzed. The exact limitations of this assumption should be investigated within future work as well as the options to circumvent the used pull-in criterion. Due to this limitation it will be more useful for some problems to investigate the pull-in time. Therefore the pull-in time sensitivity was computed and validated as well.

Chapter 10

Damped modeling

10.1 Introduction

Micro switches operate in general not in a vacuum. Hence their motion is heavily influenced by air damping. For proper prediction this air damping has to be included in the modeling strategy.

The motion of the switch (figure 10.1) is mainly in the direction perpendicular to the plate, therefore if the ratio between gap-height and gap-width is relatively small (< 3) the damping is dominated by squeeze film damping and not by traditional air drag forces [11]. Squeeze film damping can be modeled with the Reynolds equation very effectively [136]. This squeeze film damping dominates the damping of all MEMS that move mainly in the out-of-plane direction.

The Reynolds equation is a 2D equation that is based on the assumption that the air-pressure does not vary in the direction perpendicular to the plate and that the inertia effects in the gas are negligible compared to the viscous effects. To model the squeeze film behavior of a micro bridge, a 2D model similar to a plate FEM model is required to describe the damping. Therefore if a coupled electro-mechanical-fluidic model is needed, this will be combined with a 3D electrostatic model to give a 3D model as in figure 10.1.

In this chapter the inclusion of damping based on the Reynolds equation is discussed as well as the development of a numerical solution strategy. The linearization around an equilibrium equation is derived to be able to compute damped eigenfrequencies. Thereafter the validity of the Reynolds equation for MEMS modeling is investigated.

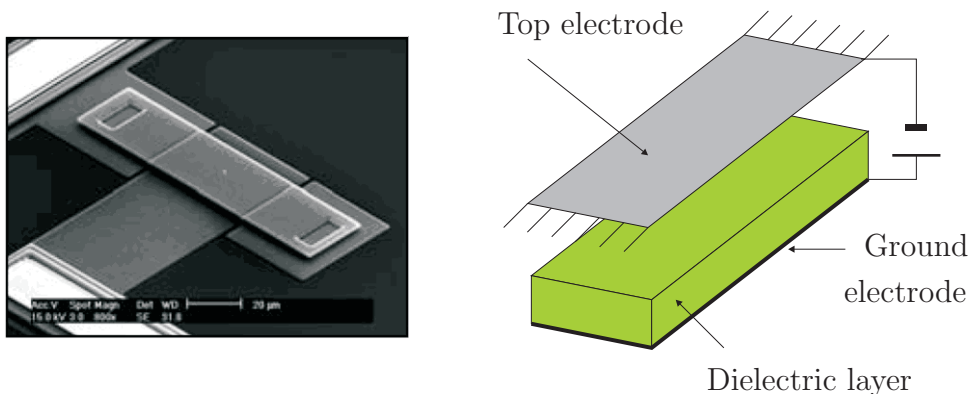


Figure 10.1: A microswitch and a model of a microswitch.

Finally the equations are tested using examples and experiments from literature.

10.2 Damping model

10.2.1 Reynolds equation

Squeeze film damping can be simulated with Reynolds equation [11]. When the motion is purely in the out-of-plane direction, as with the model under investigation the form of the Reynolds equation can be derived quite easily. The derivation is based on [134]. A cross section of the gap is shown in figure 10.2. When laminar flow is assumed, the equilibrium of force on the infinitesimal region in x -direction can be written as:

$$(p + \Delta p) dydz + \tau dx dy = p dydz + (\tau + \Delta\tau) dx dy, \quad (10.1)$$

where dy is the size of the infinitesimal element in the third dimension, τ represents the viscous shear stress and p represents the pressure. It is clear that inertia effects are neglected in this equation, because it is assumed that that inertia forces are negligible compared to viscous forces! Normally this can be done when the Reynolds number is relatively small ($R \ll 1$)[11]:

$$R = \frac{\omega \rho h^2}{\mu}. \quad (10.2)$$

For air, the density is about 1.2 kg/m^3 and the viscosity is about $18 \cdot 10^{-6} \text{ Pa} \cdot \text{s}$. Thus with a gap of about $1 \mu\text{m}$ the Reynolds number is:

$$R \approx \omega 5 \cdot 10^{-8}, \quad (10.3)$$

therefore in that case the equation would be valid for oscillations up to several MHz .

For an infinitesimal element Δp and $\Delta\tau$ can be written as:

$$\Delta p = \frac{\partial p}{\partial x} dx. \quad (10.4)$$

$$\Delta\tau = \frac{\partial \tau}{\partial z} dz. \quad (10.5)$$

Hence equation (10.1) can be written as:

$$\left(p + \frac{\partial p}{\partial x} dx \right) dydz + \tau dx dy = p dydz + \left(\tau + \frac{\partial \tau}{\partial z} dz \right) dx dy, \quad (10.6)$$

which reduces to:

$$\frac{\partial p}{\partial x} = \frac{\partial \tau}{\partial z}. \quad (10.7)$$

When it is assumed that the fluid is Newtonian, the relation between the shear stress and the strain rate is linear:

$$\tau = \mu \frac{\partial u}{\partial z}. \quad (10.8)$$

this relation can be substituted into (10.7). If the viscosity μ is assumed to be constant in the z direction this yields:

$$\frac{\partial p}{\partial x} = \mu \frac{\partial^2 u}{\partial z^2}, \quad (10.9)$$

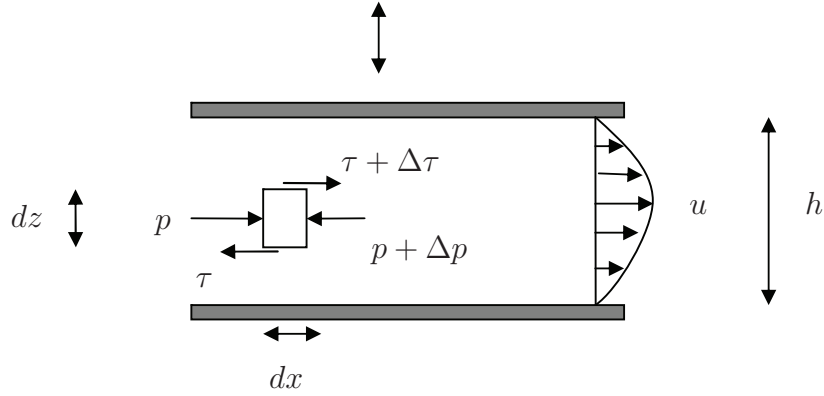


Figure 10.2: Infinitesimal fluid region in the air gap.

which can be integrated with respect to z :

$$\frac{\partial p}{\partial x} z = \mu \frac{\partial u}{\partial z} + C_1, \quad (10.10)$$

and once more:

$$\frac{\partial p}{\partial x} \frac{z^2}{2} = \mu u + C_1 z + C_2. \quad (10.11)$$

Using the no-slip boundary conditions:

$$u(z = 0) = 0, \quad (10.12)$$

$$u(z = h) = 0, \quad (10.13)$$

this gives the following velocity profile in x -direction:

$$u = \frac{1}{2\mu} \frac{\partial p}{\partial x} (z^2 - hz). \quad (10.14)$$

This describes the so called Poisseuille flow velocity profile, which is illustrated in figure 10.2 as well.

When it is assumed that the density is constant in the z -direction, the mass flow parallel to the plates in x -direction can be written as:

$$\dot{m}_x = \rho \int_0^h u(z) dz = -\frac{h^3}{12\mu} \frac{\partial p}{\partial x}. \quad (10.15)$$

Similarly the mass flow in y -direction is:

$$\dot{m}_y = \rho \int_0^h v(z) dz = -\frac{h^3}{12\mu} \frac{\partial p}{\partial y}. \quad (10.16)$$

The continuity equation states that:

$$\frac{\partial \dot{m}_x}{\partial x} + \frac{\partial \dot{m}_y}{\partial y} + \frac{\partial(\rho h)}{\partial t} = 0, \quad (10.17)$$

which basically states that the increase in the amount of mass within an infinitesimal element of the cross-section must equal to the outflow minus the inflow of mass.

Substitution of \dot{m}_x and \dot{m}_y into the continuity equation gives the Reynolds equation that can be used to simulate the fluid domain (remember the Einstein summation convention) [140]:

$$\frac{\partial(h\rho)}{\partial t} = \frac{\partial}{\partial x_i} \left(\rho \frac{h^3}{12\mu} \frac{\partial p}{\partial x_i} \right), \quad (10.18)$$

where h is the gap-height, ρ is the density, p the total pressure and μ the viscosity of the fluid.

When it is assumed that, at the small dimensions MEMS operate at, temperature variations are negligible, the density is proportional to the pressure, hence equation (10.18) can be written as [14]:

$$h \frac{\partial p}{\partial t} + p \frac{\partial h}{\partial t} = \frac{\partial}{\partial x_i} \left(p \frac{h^3}{12\mu} \frac{\partial p}{\partial x_i} \right). \quad (10.19)$$

10.2.2 Rarefied gas effects

At very low pressures or at very small length scales the fluid does not behave as a proper continuum anymore, this is called the rarefied gas effect.

The Knudsen number is a measure for the rarefaction of a gas and defined as:

$$Kn = \frac{\lambda}{L}, \quad (10.20)$$

where λ is the mean free path of the molecules in the gas and L is the characteristic length of the system under consideration. The characteristic length L is chosen to be equal to the gap height h . The mean free path is the average distance which a molecule travels before it collides with another molecule. When the Knudsen number is close to zero, the characteristic dimension is much bigger than the mean free path, therefore the gas behaves as a continuum, however when it is near one, the continuum assumption does not hold anymore and the gas behaves as a discrete set of molecules or particles. If that effect is to be modeled rigorously one should rely on modeling techniques from statistical mechanics such as ‘Direct Monte Carlo’ simulations [98], which is outside the scope of this thesis,

However it is also possible to estimate the effect by measurements and incorporate it into continuum models such as the Reynolds equation [136, 137]. The advantage is that continuum methods are in general computationally much cheaper than the particle based modeling techniques. Of course they are inaccurate outside their validity range, which is smaller than that of discrete methods.

The method proposed in [136] to model the rarefied gas effect is to make the viscosity μ a function of the local Knudsen number. This Knudsen number dependent viscosity relation was determined experimentally.

However the Knudsen number, as stated above, depends on variables that are not constant: the mean free path and the local gap height. The mean free path depends on the local pressure. Therefore, to compute the Knudsen number, following [14], the

assumption is made that the mean free path can be defined by¹:

$$\lambda = \frac{\lambda_0 p_0}{p}, \quad (10.21)$$

where λ_0 is the mean free path at pressure p_0 . The function that can then be used to define the effective viscosity is:

$$\mu = \frac{\mu_0}{1 + 9.638 Kn^{1.159}}, \quad (10.22)$$

where μ_0 is the *normal* viscosity at p_0 .

Note that for high pressures such as atmospheric pressure ($\approx 10^5 Pa$) and relatively large gaps (10μ) the Knudsen number is smaller than $\frac{1}{100}$, hence the viscosity has to be multiplied by a number between 0.96 and 1 to correct for rarefaction. This is a pretty small change.

10.2.3 Boundary conditions

The final definitions that are required to define the problem are the boundary conditions. There are two types of boundary conditions in a simple fluid problem. On the part of the boundary where the fluid is in direct contact with the environment the pressure equals the ambient pressure p_A :

$$p(x, y) = p_A. \quad (10.23)$$

On the part of boundary where the boundary is a wall of solid material the flow of gas through the wall must be zero, in other words the pressure gradient in the direction perpendicular to the wall is zero:

$$\frac{\partial p}{\partial x} n_x + \frac{\partial p}{\partial y} n_y = 0, \quad (10.24)$$

where n_x and n_y are the respectively the x and y components of the normal vector to the boundary.

One problem with Reynolds equation is that it cannot handle zero gaps. if $h = 0$ the equation becomes singular. Therefore it is assumed that the surface of the dielectric is that rough that there is always some gas between the electrodes.

10.2.4 Incompressibility and the squeeze number

To estimate the effect of certain terms in equation (10.19), the equation will be linearized around h_0 and p_A to:

$$p_A \left(\frac{\partial}{\partial x_i} \frac{\partial p}{\partial x_i} \right) - \frac{12\mu}{h_0^2} \frac{\partial p}{\partial t} = \frac{12\mu p_A}{h_0^3} \frac{\partial h}{\partial t}, \quad (10.25)$$

¹From kinetic theory it follows that the mean free path is inversely proportional to the pressure. Furthermore when the temperature is constant, it does not depend on other variables, but only on the difficult to estimate diameter of the gas particle and the Boltzmann constant. Therefore an effective method to estimate the pressure dependent mean free path is to use a measured mean free path at a certain pressure and using the inverse proportionality of the mean free path on pressure.

where it was assumed that μ was constant as well. Thereafter it is assumed that the oscillation frequency of the plate is ω and the characteristic length is L . Subsequent normalization with $\tilde{p} = \frac{p}{p_A}$, $\tilde{x}_i = \frac{x_i}{l}$, $\tilde{h} = \frac{h}{h_0}$ and $\tau = \omega t$ gives:

$$\frac{\partial}{\partial \tilde{x}_i} \frac{\partial \tilde{p}}{\partial \tilde{x}_i} - \sigma \left(\frac{\partial \tilde{p}}{\partial \tau} + \frac{\partial \tilde{h}}{\partial \tau} \right) = 0, \quad (10.26)$$

which leads to the definition of the squeeze number σ :

$$\sigma = \frac{12\mu\omega L^2}{p_A h_0^2}. \quad (10.27)$$

When this squeeze number is large, from (10.25) it follows that $p_A \Delta h + h_0 \Delta p = 0$, or that as Boyle's law states it: $p \cdot V$ will be constant, therefore the gas is fully compressible.

However for very low squeeze numbers this relation does not hold and the gas behaves somewhat incompressible [11]. Hence, the gas has enough time to flow out of the film and is not fully compressed. Therefore this means that $\frac{\Delta p}{p_A} \ll \frac{\Delta h}{h_0}$. In that case it can be seen in equation (10.25) that the factor in front of the $\frac{\partial p}{\partial t}$ term will be very small and can be neglected:

$$\frac{h_0^3}{12\mu} \left(\frac{\partial}{\partial x_i} \frac{\partial p}{\partial x_i} \right) = \frac{\partial h}{\partial t}, \quad (10.28)$$

where the direct pressure dependency drops from the equation.

For this derivation the dependency on h was linearized as well, which does not have to be the case. If the actual incompressibility condition, density $\rho = \text{constant}$, is substituted directly into equation (10.18), all occurrences of this density drop from that equation and the full non-linear incompressible Reynolds equation is found directly:

$$\frac{\partial h}{\partial t} = \frac{\partial}{\partial x_i} \left(\frac{h^3}{12\mu} \frac{\partial p}{\partial x_i} \right). \quad (10.29)$$

In this case the μ was not assumed to be constant either, therefore it can be made a function of the Knudsen number. Hence this equation is also depending non-linearly on p for rarefied gases.

If the gas behaves incompressible it will yield forces that are proportional to the velocity of the plate, causing a decrease of the damped frequency. However if the gas behaves compressible there is also a big elastic component to the forces which is proportional to displacement. These increase the damped eigenfrequency. Sometimes this increase is that big that the damped frequency is higher than the undamped one.

There is a critical squeeze number for which the forces proportional to displacement are equal to those proportional to the velocity. Sadly the critical squeeze number is shape dependent. If the electrode is a rectangular plate with the length L the width b the critical squeeze numbers is [11]:

$$\sigma_c = \pi^2 \left(1 + \frac{b^2}{L^2} \right). \quad (10.30)$$

This critical squeeze number can be used to determine whether the compressibility is important.

10.2.5 Weak form and FEM discretization

The equations are fully defined, therefore the FEM discretization can be discussed. Equation (10.19) will be written as:

$$h \frac{\partial p}{\partial t} + p \frac{\partial h}{\partial t} - \frac{\partial}{\partial x_i} \left(p \frac{h^3}{12\mu} \frac{\partial p}{\partial x_i} \right) = 0. \quad (10.31)$$

This relation must also hold when pre-multiplied by a test function v and integrated over the fluid domain:

$$\int v \left[h \frac{\partial p}{\partial t} + p \frac{\partial h}{\partial t} - \frac{\partial}{\partial x_i} \left(p \frac{h^3}{12\mu} \frac{\partial p}{\partial x_i} \right) \right] dV = 0, \quad (10.32)$$

which is the so called weak form of the equation. Split into parts this becomes:

$$\int v h \frac{\partial p}{\partial t} dV + \int v p \frac{\partial h}{\partial t} dV - \int v \frac{\partial}{\partial x_i} \left(p \frac{h^3}{12\mu} \frac{\partial p}{\partial x_i} \right) dV = 0, \quad (10.33)$$

The last term of this equation can be integrated by parts to give:

$$\int v \frac{\partial}{\partial x_i} \left(p \frac{h^3}{12\mu} \frac{\partial p}{\partial x_i} \right) dV = \int v p \frac{h^3}{12\mu} \frac{\partial p}{\partial x_i} n_i dS - \int \frac{\partial v}{\partial x_i} p \frac{h^3}{12\mu} \frac{\partial p}{\partial x_i} dV. \quad (10.34)$$

Substitution of the Neumann boundary condition (10.24) gives:

$$\int v \frac{\partial}{\partial x_i} \left(p \frac{h^3}{12\mu} \frac{\partial p}{\partial x_i} \right) dV = - \int \frac{\partial v}{\partial x_i} p \frac{h^3}{12\mu} \frac{\partial p}{\partial x_i} dV, \quad (10.35)$$

hence the weak form of the Reynolds equation can be written as:

$$\int v h \frac{\partial p}{\partial t} dV + \int v p \frac{\partial h}{\partial t} dV = - \int \frac{\partial v}{\partial x_i} p \frac{h^3}{12\mu} \frac{\partial p}{\partial x_i} dV. \quad (10.36)$$

To derive the final FEM discretized form the traditional assumption is made that both h and p can be approximated by piecewise linear functions using the FEM shape functions:

$$p = N_j p_j, \quad (10.37)$$

$$h = N_j h_j, \quad (10.38)$$

The same FEM shape functions can be used as test functions:

$$v = N_i. \quad (10.39)$$

Substitution of p , h and v into equation (10.36) results in:

$$\int N_i h N_j \frac{\partial p_j}{\partial t} dV + \int N_j p \frac{\partial h_j}{\partial t} dV = - \int \frac{\partial N_i}{\partial x_k} p \frac{h^3}{12\mu} \frac{\partial N_j}{\partial x_k} p_j dV, \quad (10.40)$$

which after some rearrangements can be written as:

$$\int N_i h N_j dV \frac{\partial p_j}{\partial t} + \int N_i p N_j \frac{\partial h_j}{\partial t} dV = - \int \frac{\partial N_i}{\partial x_k} p \frac{h^3}{12\mu} \frac{\partial N_j}{\partial x_k} dV p_j. \quad (10.41)$$

In matrix vector notation equation (10.41) becomes:

$$\mathbf{L}(\mathbf{h})\dot{\mathbf{p}} + \mathbf{R}(\mathbf{p})\dot{\mathbf{h}} = -\mathbf{D}(\mathbf{p}, \mathbf{h})\mathbf{p}, \quad (10.42)$$

where:

$$L_{ij} = \int N_i h N_j dV, \quad (10.43)$$

$$R_{ij} = \int N_i p N_j dV, \quad (10.44)$$

$$D_{ij} = \int \frac{\partial N_i}{\partial x_k} \frac{p h^3}{12\mu} \frac{\partial N_j}{\partial x_k} dV. \quad (10.45)$$

There is one simplification of the formulation that can, but does not have to be made. The idea starts with replacing some manifestations of p with $p_A + p^R$, where p_A is the ambient (thus constant) pressure and p^R is the difference between local pressure and ambient pressure. In that case the pressure distribution becomes:

$$p = p_A + N_j p_j^R. \quad (10.46)$$

Substitution of this pressure into equation (10.41) yields:

$$\int N_i h N_j dV \frac{\partial p_j^R}{\partial t} + \int N_i N_j p \frac{\partial h_j}{\partial t} dV = - \int \frac{\partial N_i}{\partial x_k} \frac{p h^3}{12\mu} \frac{\partial N_j}{\partial x_k} dV p_j^R, \quad (10.47)$$

which does not change the matrices \mathbf{L} , \mathbf{R} or \mathbf{D} but greatly simplifies the implementation of the Dirichlet boundary condition (10.23).

If the squeeze number is fairly low, the gas can be modeled as incompressible. In that case the term $\frac{h \partial p}{p \partial t}$ is neglected, greatly simplifying the fluid equation:

$$\mathbf{R}\dot{\mathbf{h}} = -\mathbf{D}(\mathbf{p}, \mathbf{h})\mathbf{p}, \quad (10.48)$$

where also the \mathbf{p} dependency of \mathbf{R} drops due to the incompressibility assumption. If the h follows from some external applied displacement this equation is quasi-static, because it only depends on \dot{h} , h and p of which p is the only true fluid DOF type. However it may be *static*, it still is non-linear in both \mathbf{p} and \mathbf{h} , due to the dependency of \mathbf{D} on p and h .

10.2.6 Coupling with the electro-mechanical equations

Coupling with the structural model is relatively simple. The following relations can be used to couple the model:

$$h_k = h_0 + u_k, \quad (10.49)$$

$$\dot{h}_k = \dot{u}_k, \quad (10.50)$$

where h_0 is the initial gap height and u_k is the structural displacement at node k that results from the mechanical solution. The fluid force on node k of the mechanical domain is simply defined by:

$$f_k^{fluid} = \int N_k p^R dV, \quad (10.51)$$

where it was assumed that that only a relative pressure causes forces, because the ambient pressure caused forces on both sides of the plate that cancel each other. The fluid force is integrated over the complete volume of the fluid domain, because all fluid nodes exert forces on plate nodes.

The three equations above are enough to completely define the coupling. However, if one wants to use monolithic solvers, also the linearized coupling matrices have to be evaluated.

For the mass matrix this is a very simple problem: there is no coupling because there are no second derivatives in the fluid equations. Also there is no coupling between the fluid and the electrostatic domain. Therefore the following coupling terms remain:

$$\begin{aligned} \begin{bmatrix} \mathbf{M}_{uu} & 0 & 0 \\ 0 & 0 & 0 \\ 0 & 0 & 0 \end{bmatrix} \begin{bmatrix} \Delta \ddot{\mathbf{u}} \\ \Delta \ddot{\phi} \\ \Delta \ddot{\mathbf{p}} \end{bmatrix} + \begin{bmatrix} -\frac{\partial \mathbf{f}^{fluid}}{\partial \dot{\mathbf{u}}} & 0 & -\frac{\partial \mathbf{f}^{fluid}}{\partial \dot{\mathbf{p}}} \\ 0 & 0 & 0 \\ -\frac{\partial \mathbf{r}}{\partial \dot{\mathbf{u}}} & 0 & -\frac{\partial \mathbf{r}}{\partial \dot{\mathbf{p}}} \end{bmatrix} \begin{bmatrix} \Delta \dot{\mathbf{u}} \\ \Delta \dot{\phi} \\ \Delta \dot{\mathbf{p}} \end{bmatrix} \\ + \begin{bmatrix} \mathbf{K}_{uu} - \frac{\partial \mathbf{f}^{fluid}}{\partial \mathbf{u}} & \mathbf{K}_{u\phi} & -\frac{\partial \mathbf{f}^{fluid}}{\partial \mathbf{p}} \\ \mathbf{K}_{\phi u} & \mathbf{K}_{\phi\phi} & 0 \\ -\frac{\partial \mathbf{r}}{\partial \mathbf{u}} & 0 & -\frac{\partial \mathbf{r}}{\partial \mathbf{p}} \end{bmatrix} \begin{bmatrix} \Delta \mathbf{u} \\ \Delta \phi \\ \Delta \mathbf{p} \end{bmatrix} = \begin{bmatrix} \Delta \mathbf{f} \\ \Delta \mathbf{q} \\ \Delta \mathbf{r} \end{bmatrix}, \quad (10.52) \end{aligned}$$

where the following definitions were used:

$$\mathbf{f} = \mathbf{f}^{elec} + \mathbf{f}^{fluid} - \mathbf{K}_{uu} \mathbf{u}, \quad (10.53)$$

$$\mathbf{q} = \mathbf{q}^{elec}(V) - \mathbf{K}_{\phi\phi}, \quad (10.54)$$

$$\mathbf{r} = \mathbf{L}\dot{\mathbf{p}} + \mathbf{R}\dot{\mathbf{h}} + \mathbf{D}\mathbf{p}. \quad (10.55)$$

The computation of \mathbf{K}_{uu} , $\mathbf{K}_{u\phi}$, $\mathbf{K}_{\phi u}$, $\mathbf{K}_{\phi\phi}$ and \mathbf{M}_{uu} has been discussed in chapter 3. From equation (10.51) it is clear that the fluid force only depends directly on the pressure, therefore all partial derivatives of \mathbf{f}^{fluid} with other variables are zero. The derivative with the pressure is rather simple:

$$[\mathbf{K}_{uf}]_{ij} = \left[-\frac{\partial \mathbf{f}^{fluid}}{\partial \mathbf{p}} \right]_{ij} = - \int N_i N_j dV. \quad (10.56)$$

Also the derivatives of \mathbf{r} with $\dot{\mathbf{u}}$ and $\dot{\mathbf{p}}$ are relatively simple:

$$-\frac{\partial \mathbf{r}}{\partial \dot{\mathbf{u}}} = -\frac{\partial \mathbf{r}}{\partial \dot{\mathbf{h}}} = -\mathbf{R}, \quad (10.57)$$

$$-\frac{\partial \mathbf{r}}{\partial \dot{\mathbf{p}}} = -\mathbf{L}. \quad (10.58)$$

The final two derivatives are the derivatives of \mathbf{r} with \mathbf{p} and \mathbf{h} . Let's first treat the derivative with \mathbf{p}

$$\mathbf{K}_{ff} = -\frac{\partial \mathbf{r}}{\partial \mathbf{p}} = -\mathbf{D} - \frac{\partial \mathbf{D}}{\partial \mathbf{p}} \mathbf{p} - \frac{\partial \mathbf{R}}{\partial \mathbf{p}} \dot{\mathbf{h}}, \quad (10.59)$$

which can be worked out in index notation as:

$$[\mathbf{K}_{ff}]_{ij} = -D_{ij} - \int -\frac{\partial N_i}{\partial x_k} \frac{ph^3}{12\mu^2} \frac{\partial \mu}{\partial p} \frac{\partial p}{\partial p_j} \frac{\partial N_m}{\partial x_k} p_m^R - \int \frac{\partial N_i}{\partial x_k} \frac{h^3}{12\mu^2} \frac{\partial p}{\partial p_j} \frac{\partial N_m}{\partial x_k} p_m^R dV, \quad (10.60)$$

where $\frac{\partial p}{\partial p_j}$ follows from equation (10.37). The derivative of \mathbf{r} with \mathbf{h} is:

$$\mathbf{K}_{fu} = -\frac{\partial \mathbf{r}}{\partial \mathbf{h}} = -\frac{\partial \mathbf{D}}{\partial \mathbf{h}} \mathbf{p} - \frac{\partial \mathbf{L}}{\partial \mathbf{h}} \dot{\mathbf{p}}, \quad (10.61)$$

which can be worked out in index notation as:

$$[\mathbf{K}_{fu}]_{ij} = - \int -\frac{\partial N_i}{\partial x_k} \frac{ph^3}{12\mu^2} \frac{\partial \mu}{\partial h_j} \frac{\partial N_m}{\partial x_k} p_m^R + \frac{\partial N_i}{\partial x_k} \frac{3ph^2}{12\mu} \frac{\partial h}{\partial h_j} \frac{\partial N_m}{\partial x_k} p_m^R + N_i \frac{\partial h}{\partial h_j} N_m \dot{p}_m^R dV. \quad (10.62)$$

where $\frac{\partial h}{\partial h_j}$ follows from equation (10.38).

These last two terms \mathbf{K}_{ff} and \mathbf{K}_{fu} look very complicated. However, when one is interested in the linearized behavior (e.g. eigenfrequencies) around a static equilibrium only p^R and \dot{p}^R are zero. Therefore in that case the following coupling matrices can be used:

$$\mathbf{K}_{ff} = -\mathbf{D}, \quad (10.63)$$

$$\mathbf{K}_{fu} = \mathbf{0}. \quad (10.64)$$

In any case the equations that can be used are given below:

$$\begin{aligned} \begin{bmatrix} \mathbf{M}_{uu} & 0 & 0 \\ 0 & 0 & 0 \\ 0 & 0 & 0 \end{bmatrix} \begin{bmatrix} \Delta \ddot{\mathbf{u}} \\ \Delta \ddot{\phi} \\ \Delta \ddot{\mathbf{p}} \end{bmatrix} + \begin{bmatrix} 0 & 0 & 0 \\ 0 & 0 & 0 \\ -\mathbf{R} & 0 & -\mathbf{L} \end{bmatrix} \begin{bmatrix} \Delta \dot{\mathbf{u}} \\ \Delta \dot{\phi} \\ \Delta \dot{\mathbf{p}} \end{bmatrix} \\ + \begin{bmatrix} \mathbf{K}_{uu} & \mathbf{K}_{u\phi} & \mathbf{K}_{uf} \\ \mathbf{K}_{\phi u} & \mathbf{K}_{\phi\phi} & 0 \\ \mathbf{K}_{fu} & 0 & \mathbf{K}_{ff} \end{bmatrix} \begin{bmatrix} \Delta \mathbf{u} \\ \Delta \phi \\ \Delta \mathbf{p} \end{bmatrix} = \begin{bmatrix} \Delta \mathbf{f} \\ \Delta \mathbf{q} \\ \Delta \mathbf{r} \end{bmatrix}, \quad (10.65) \end{aligned}$$

or:

$$\mathbf{M} \Delta \ddot{\mathbf{U}} + \mathbf{C} \Delta \dot{\mathbf{U}} + \mathbf{K} \Delta \mathbf{U} = \Delta \mathbf{F}. \quad (10.66)$$

10.2.7 Inertia effects

When the Reynolds equation was derived, this started with the equilibrium of forces (10.7):

$$\frac{\partial p}{\partial x} = \frac{\partial \tau}{\partial z}, \quad (10.67)$$

in which the inertia terms were neglected. The criterion that was used to decide if these terms can be neglected was derived by comparing inertia values for the fluid compared to the viscosity and is called the Reynolds number. However it is dangerous to use the Reynolds number when it is defined as:

$$R = \frac{\omega \rho h^2}{\mu}, \quad (10.68)$$

because in that case the inertia direction is the squeeze direction. But with squeeze film damping, the highest flow directions will be in the direction tangential to the

plate. The plate is pushing out or pumping in air at velocities that are higher than the squeeze velocity. Therefore more investigation into the inertia terms is needed.

The additional mass flow that these inertia terms generate can be estimated by a method presented in [123]. The derivation of that method starts with adding the inertia terms the original equilibrium of forces:

$$\rho \frac{Du}{Dt} + \frac{\partial p}{\partial x} = \frac{\partial \tau}{\partial z}. \quad (10.69)$$

where $\frac{Du}{Dt}$ is the material derivative of the velocity u with respect to time. Due to fact that the film thickness is small, the inertia term in equation (10.69) can be averaged:

$$\rho \frac{Du}{dt} \approx \rho \left(\frac{1}{h} \int_0^h \frac{Du}{dt} dz \right), \quad (10.70)$$

which can be substituted into (10.69)

$$\left(\frac{1}{h} \int_0^h \frac{Du}{dt} dz \right) + \frac{\partial p}{\partial x} = \frac{\partial \tau}{\partial z}. \quad (10.71)$$

Substitution of the Newtonian fluid (10.8) constitutive relation:

$$\tau = \mu \frac{\partial u}{\partial z}. \quad (10.72)$$

gives:

$$\left(\frac{1}{h} \int_0^h \frac{Du}{dt} dz \right) + \frac{\partial p}{\partial x} = \mu \frac{\partial^2 u}{\partial z^2}. \quad (10.73)$$

Integrating the complete equation from 0 to h and applying the no slip boundary conditions gives:

$$u = \frac{z^2 - zh}{2\mu} \left(\frac{\rho}{h} \int_0^h \frac{Du}{Dt} dz + \frac{\partial p}{\partial x} \right), \quad (10.74)$$

Thus the mass flow becomes:

$$\dot{m}_x = \left(-\frac{h^3 \rho}{12\mu} \frac{\partial p}{\partial x} \right) + \left(-\frac{h^2 \rho^2}{12\mu} \int_0^h \frac{Du}{Dt} dz \right). \quad (10.75)$$

The extra term is rather complex. If this term is introduced into the continuity equation (10.17) this would give a difficult non-linear equation. It can be solved as shown by the original reference, however here it will be used differently. The equation will not be solved, but it will be used to derive an estimator of the error introduced by neglecting inertia terms.

This requires the computation of the pressure field over time with the original Reynolds equation, giving the mass flow as:

$$\dot{m}_x^n = -\frac{h^3 \rho}{12\mu} \frac{\partial p}{\partial x}. \quad (10.76)$$

When it is assumed that the velocity profile does not change, this gives

$$\frac{Du}{dt} = \frac{1}{2\mu} (z^2 - hz) \frac{\partial}{\partial x} \left(\frac{Dp}{dt} \right), \quad (10.77)$$

which is substituted into the inertia term of the mass flow, yielding (remember the summation convention):

$$\dot{m}_x^i = \frac{h^5 \rho^2}{144\mu} \frac{\partial}{\partial x} \left(\frac{\partial p}{\partial t} + \frac{\partial p}{\partial x_i} \frac{\partial p}{\partial x_i} \right). \quad (10.78)$$

Within a finite element context, where $p = p_j N_j$ and $\frac{\partial p}{\partial t} = \dot{p}_j N_j$ the convective terms in this equation can be written as:

$$\frac{\partial p}{\partial x_i} \frac{\partial p}{\partial x_i} = \left(\frac{\partial N_j}{\partial x_i} p_j \right) \left(\frac{\partial N_k}{\partial x_k} p_j \right), \quad (10.79)$$

which due to the linearity of the shape functions N_j , will be piecewise constant in the spatial directions, hence:

$$\frac{\partial}{\partial x} \left(\frac{\partial p}{\partial x_i} \frac{\partial p}{\partial x_i} \right) = 0 \quad (10.80)$$

within each element. This greatly simplifies the material derivative at an integration point to:

$$\dot{m}_x^i = \frac{h^5 \rho^2}{144\mu} \left(\frac{\partial N_j}{\partial x} \dot{p}_j \right). \quad (10.81)$$

Subsequently a measure of the error made by neglecting the inertia effects is:

$$\epsilon = \frac{|\dot{m}^i|}{|\dot{m}^n|}. \quad (10.82)$$

10.3 Time integration

To actually solve the transient behavior of the Reynolds equation coupled with the electro-mechanical model time integration is required. For 3D models the total number of unknowns rapidly increases and for this type of moderately non-linear equations implicit time-integration techniques are ideal. A characteristic of implicit time integration is that for each time step a system of equations has to be solved (see chapter 8).

In the previous section it was seen that the monolithically coupled equations are asymmetric. Therefore, when a monolithic implementation is used the total system that has to be solved each time step will be asymmetric and solving a symmetric system is computationally expensive. Thus it is better to split the two problems and use a staggered approach. This will also prevent scaling problems.

In that case the mechanical equation of motion can be written as:

$$\mathbf{M}_{uu} \ddot{\mathbf{u}} + \mathbf{K}_{uu}^m \mathbf{u} = \mathbf{f}^{elec}(V, \mathbf{u}) + \mathbf{f}^{fluid}(\mathbf{p}). \quad (10.83)$$

When the term corresponding to the mechanical stiffness is written as $\mathbf{f}^m = \mathbf{K}_{uu}^m \mathbf{u}$ and the right-hand side term of the equation as \mathbf{f}^{elec} , this equation equals:

$$\mathbf{M}_{uu} \ddot{\mathbf{u}} = \mathbf{f}^{elec} - \mathbf{f}^m. \quad (10.84)$$

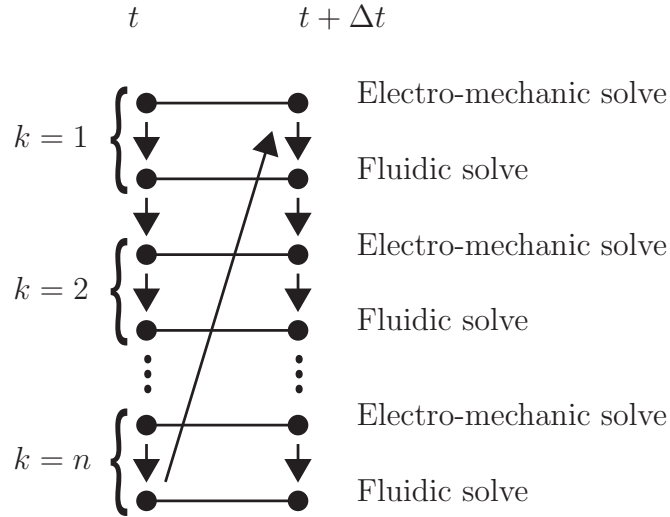


Figure 10.3: Some iterations for the incompressible fluid algorithm.

10.3.1 Time integration for an incompressible fluid

A time-integration algorithm for the *incompressible* case will be developed first, based on the trapezoidal rule. In that case it is known that:

$$\mathbf{f}^{fluid} = \mathbf{f}^{fluid}(\mathbf{u}, \dot{\mathbf{u}}), \quad (10.85)$$

because:

$$\mathbf{p} = \mathbf{p}(\mathbf{u}, \dot{\mathbf{u}}), \quad (10.86)$$

as can be seen in equation (10.48).

Because for the pressure this is a quasi-static relation, it is very easy to recompute the fluid force after each electromechanical iteration step. Hence the fluid problem will be condensed onto the mechanical problem as was done for the electrostatic problem in chapter 8. Therefore the iteration procedure will be the one visualized in figure 10.3.

To write down the actual implementation the nonlinear dynamic equilibrium equations have to be written in a form that is solvable by an iterative procedure:

$$\mathbf{M}_{uu} \ddot{\mathbf{u}}_k^{t+\Delta t} + \mathbf{K}_{uu}^m \Delta \mathbf{u}_k = \mathbf{f}^{elec}(\mathbf{u}_{k-1}^{t+\Delta t}) + \mathbf{f}^{fluid}(\mathbf{u}_{k-1}^{t+\Delta t}, \dot{\mathbf{u}}_{k-1}^{t+\Delta t}) - \mathbf{K}_{uu}^m \mathbf{u}_{k-1}^{t+\Delta t}, \quad (10.87)$$

which used the following iteration assumption:

$$\mathbf{u}_k^{t+\Delta t} = \mathbf{u}_{k-1}^{t+\Delta t} + \Delta \mathbf{u}_k. \quad (10.88)$$

The trapezoidal rule assumption states that the displacements and velocities at the end of the time step are defined as follows [12]:

$$\mathbf{u}^{t+\Delta t} = \mathbf{u} + \frac{\Delta t}{2} (\dot{\mathbf{u}}^t + \dot{\mathbf{u}}^{t+\Delta t}) \quad (10.89)$$

$$\dot{\mathbf{u}}^{t+\Delta t} = \dot{\mathbf{u}} + \frac{\Delta t}{2} (\ddot{\mathbf{u}}^t + \ddot{\mathbf{u}}^{t+\Delta t}). \quad (10.90)$$

Combining equations (10.88) to (10.90) yields:

$$\ddot{\mathbf{u}}_k^{t+\Delta t} = \frac{4}{\Delta t^2} (\mathbf{u}_{k-1}^{t+\Delta t} - \mathbf{u}^t + \Delta \mathbf{u}_k) - \frac{4}{\Delta t} \dot{\mathbf{u}}^t - \ddot{\mathbf{u}}^t, \quad (10.91)$$

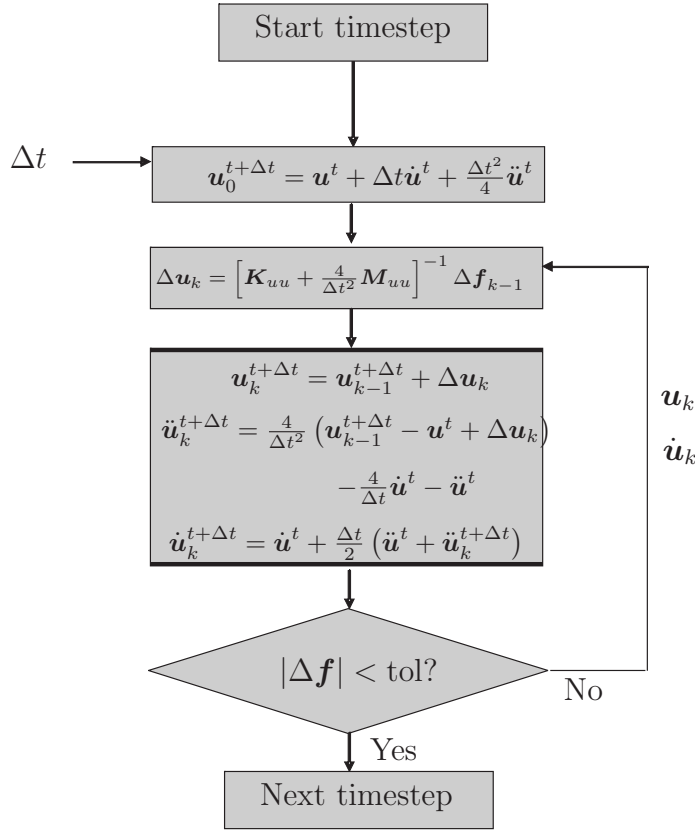


Figure 10.4: Integration algorithm for an incompressible fluid.

which can be substituted in (10.87) to give:

$$\left[\mathbf{K}_{uu}^m + \frac{4}{\Delta t^2} \mathbf{M}_{uu} \right] \Delta \mathbf{u}_k = \mathbf{f}^{elec}(\mathbf{u}_{k-1}^{t+\Delta t}) + \mathbf{f}^{fluid}(\mathbf{u}_{k-1}^{t+\Delta t}, \dot{\mathbf{u}}_{k-1}^{t+\Delta t}) - \mathbf{K}_{uu}^m \mathbf{u}_{k-1}^{t+\Delta t} - \mathbf{M}_{uu} \left(\frac{4}{\Delta t^2} (\mathbf{u}_{k-1}^{t+\Delta t} - \mathbf{u}^t) - \frac{4}{\Delta t} \dot{\mathbf{u}}^t - \ddot{\mathbf{u}}^t \right), \quad (10.92)$$

which is the equation that can be used to compute $\Delta \mathbf{u}_k$. The time integration algorithm is summarized in figure 10.4. To keep the notation simple, the right-hand side of equation (10.92) is written as:

$$\Delta \mathbf{f}(\mathbf{u}_{k-1}^{t+\Delta t}, \dot{\mathbf{u}}_{k-1}^{t+\Delta t}) = \mathbf{f}^{elec}(\mathbf{u}_{k-1}^{t+\Delta t}) + \mathbf{f}^{fluid}(\mathbf{u}_{k-1}^{t+\Delta t}, \dot{\mathbf{u}}_{k-1}^{t+\Delta t}) - \mathbf{K}_{uu}^m \mathbf{u}_{k-1}^{t+\Delta t} - \mathbf{M}_{uu} \left(\frac{4}{\Delta t^2} (\mathbf{u}_{k-1}^{t+\Delta t} - \mathbf{u}^t) - \frac{4}{\Delta t} \dot{\mathbf{u}}^t - \ddot{\mathbf{u}}^t \right). \quad (10.93)$$

10.3.2 Time integration for an compressible fluid

When it is not possible to assume that the gas behaves almost as an incompressible fluid it is necessary use equation (10.42). This equation is a first order differential equation, which has to be time integrated to provide \mathbf{p} as a function of time. The pressure as function of time can subsequently be used to compute the forces on the structure.

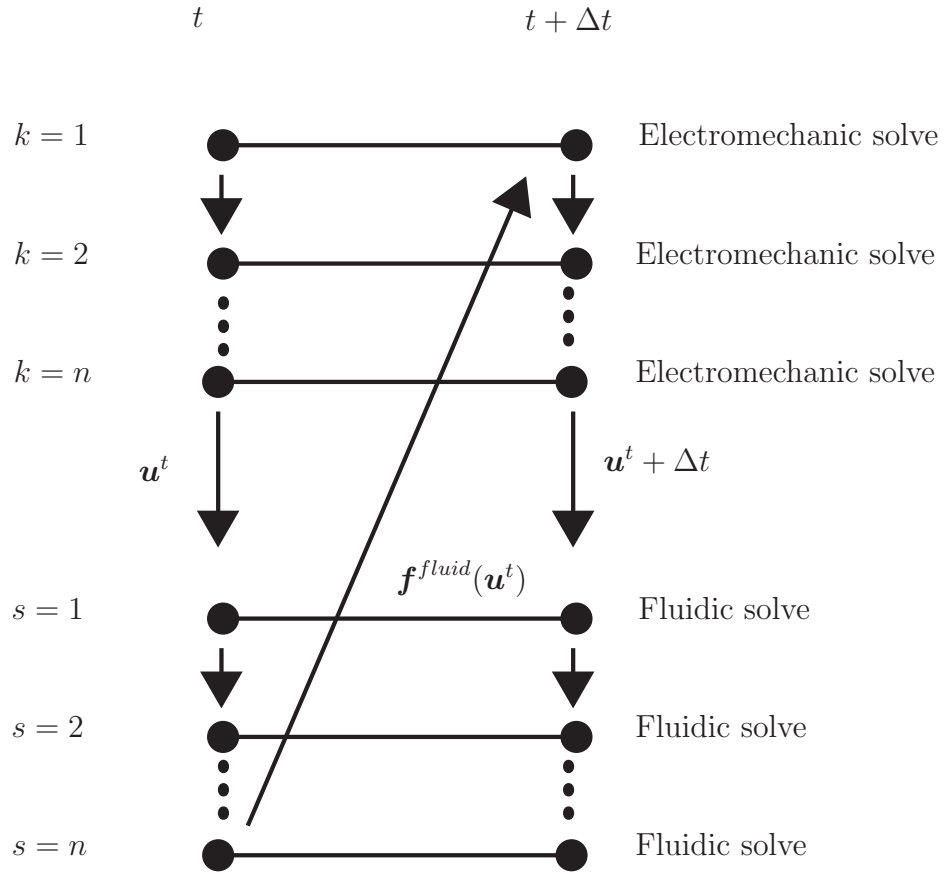


Figure 10.5: Some iterations for the compressible fluid algorithm.

As mentioned before, the monolithic system is asymmetric and poorly scaled. Therefore the electromechanical and fluidic equation are integrated separately with a staggered algorithm.

Two assumptions are made when implementing this coupling: (a), during a structural time step the fluid pressure is kept constant and (b), during a fluidic time step the structural displacement and velocity are kept constant. These assumptions are visualized in figure 10.5, where it can be seen that the fluidic iterations follow the mechanic iterations.

Assumption (a) reduces the structural equation that has to be integrated to:

$$\mathbf{M}_{uu} \ddot{\mathbf{u}}_k^{t+\Delta t} + \mathbf{K}_{uu}^m \Delta \mathbf{u}_k = \mathbf{f}^{elec}(\mathbf{u}_{k-1}^{t+\Delta t}) + \mathbf{f}^{fluid}(\mathbf{u}^t) - \mathbf{K}_{uu}^m \mathbf{u}_{k-1}^{t+\Delta t}, \quad (10.94)$$

and therefore the update of the displacement to:

$$\left[\mathbf{K}_{uu}^m + \frac{4}{\Delta t^2} \mathbf{M}_{uu} \right] \Delta \mathbf{u}_k = \mathbf{f}^{elec}(\mathbf{u}_{k-1}^{t+\Delta t}) + \mathbf{f}^{fluid}(\mathbf{u}^t) - \mathbf{K}_{uu}^m \mathbf{u}_{k-1}^{t+\Delta t} - \mathbf{M}_{uu} \left(\frac{4}{\Delta t^2} (\mathbf{u}_{k-1}^{t+\Delta t} - \mathbf{u}^t) - \frac{4}{\Delta t} \dot{\mathbf{u}}^t - \ddot{\mathbf{u}}^t \right), \quad (10.95)$$

hence the right-hand side of the structural equation is:

$$\Delta \mathbf{f}(\mathbf{u}_{k-1}^{t+\Delta t}) = \mathbf{f}^{elec}(\mathbf{u}_{k-1}^{t+\Delta t}) + \mathbf{f}^{fluid}(\mathbf{u}^t) - \mathbf{K}_{uu} \mathbf{u}_{k-1}^{t+\Delta t} - \mathbf{M}_{uu} \left(\frac{4}{\Delta t^2} (\mathbf{u}_{k-1}^{t+\Delta t} - \mathbf{u}^t) - \frac{4}{\Delta t} \dot{\mathbf{u}}^t - \ddot{\mathbf{u}}^t \right). \quad (10.96)$$

Assumption (b) results in a constant h and $\frac{\partial h}{\partial t}$ during the fluidic time step. The non linear equation that has to be integrated (10.42) can be written in the form:

$$\mathbf{L} \dot{\mathbf{p}}^{t+\Delta t} + \mathbf{D} \mathbf{p}^{t+\Delta t} + \mathbf{R} \dot{\mathbf{h}} = 0, \quad (10.97)$$

which is non linear because both \mathbf{R} and \mathbf{D} depend on p . However when at iteration s the equation is not satisfied yet, this equation can be used to define an error:

$$\Delta \mathbf{r}_s = \mathbf{L} \dot{\mathbf{p}}_{s-1}^{t+\Delta t} + \mathbf{D} \mathbf{p}_{s-1}^{t+\Delta t} + \mathbf{R} \dot{\mathbf{h}}. \quad (10.98)$$

To derive the iteration and integration algorithm that integrates the non linear equation (10.97), the trapezoidal rule will be used:

$$\mathbf{p}^{t+\Delta t} = \mathbf{p}^t + \frac{\Delta t}{2} (\dot{\mathbf{p}}^t + \dot{\mathbf{p}}^{t+\Delta t}), \quad (10.99)$$

which can be substituted into (10.97) to give:

$$\left[\mathbf{L} + \frac{\Delta t}{2} \mathbf{D} \right] \dot{\mathbf{p}}^{t+\Delta t} = -\mathbf{D} \left(\mathbf{p}^t + \frac{\Delta t}{2} \dot{\mathbf{p}}^t \right) - \mathbf{R} \dot{\mathbf{h}}. \quad (10.100)$$

To derive the proper $\dot{\mathbf{p}}^{t+\Delta t}$ a Newton-Raphson iteration will be used, hence the following assumption is made:

$$\dot{\mathbf{p}}_s^{t+\Delta t} = \dot{\mathbf{p}}_{s-1}^{t+\Delta t} + \Delta \dot{\mathbf{p}}_s, \quad (10.101)$$

which after substitution into (10.100) provides:

$$\left[\mathbf{L} + \frac{\Delta t}{2} \mathbf{D} \right] \Delta \dot{\mathbf{p}}_s = -\mathbf{D} \left(\mathbf{p}^t + \frac{\Delta t}{2} \dot{\mathbf{p}}^t \right) - \mathbf{R} \dot{\mathbf{h}} - \left[\mathbf{L} + \frac{\Delta t}{2} \mathbf{D} \right] \dot{\mathbf{p}}_{s-1}^{t+\Delta t}, \quad (10.102)$$

which can be written as:

$$\left[\mathbf{L} + \frac{\Delta t}{2} \mathbf{D} \right] \Delta \dot{\mathbf{p}}_s = -\mathbf{D} \left(\mathbf{p}^t + \frac{\Delta t}{2} (\dot{\mathbf{p}}^t + \dot{\mathbf{p}}_{s-1}^{t+\Delta t}) \right) - \mathbf{R} \dot{\mathbf{h}} - \mathbf{L} \dot{\mathbf{p}}_{s-1}^{t+\Delta t}. \quad (10.103)$$

By using the trapezoidal rule at iteration $s-1$ (10.99) it is easy to show that the right hand side of this equation is equal to $\Delta \mathbf{r}_s$. Thus equation (10.103) can be used in a Newton Raphson scheme to compute the update for $\dot{\mathbf{p}}^{t+\Delta t}$: $\Delta \dot{\mathbf{p}}$.

Both the structural and the fluidic time integration scheme are combined to form the flowchart in figure 10.6.

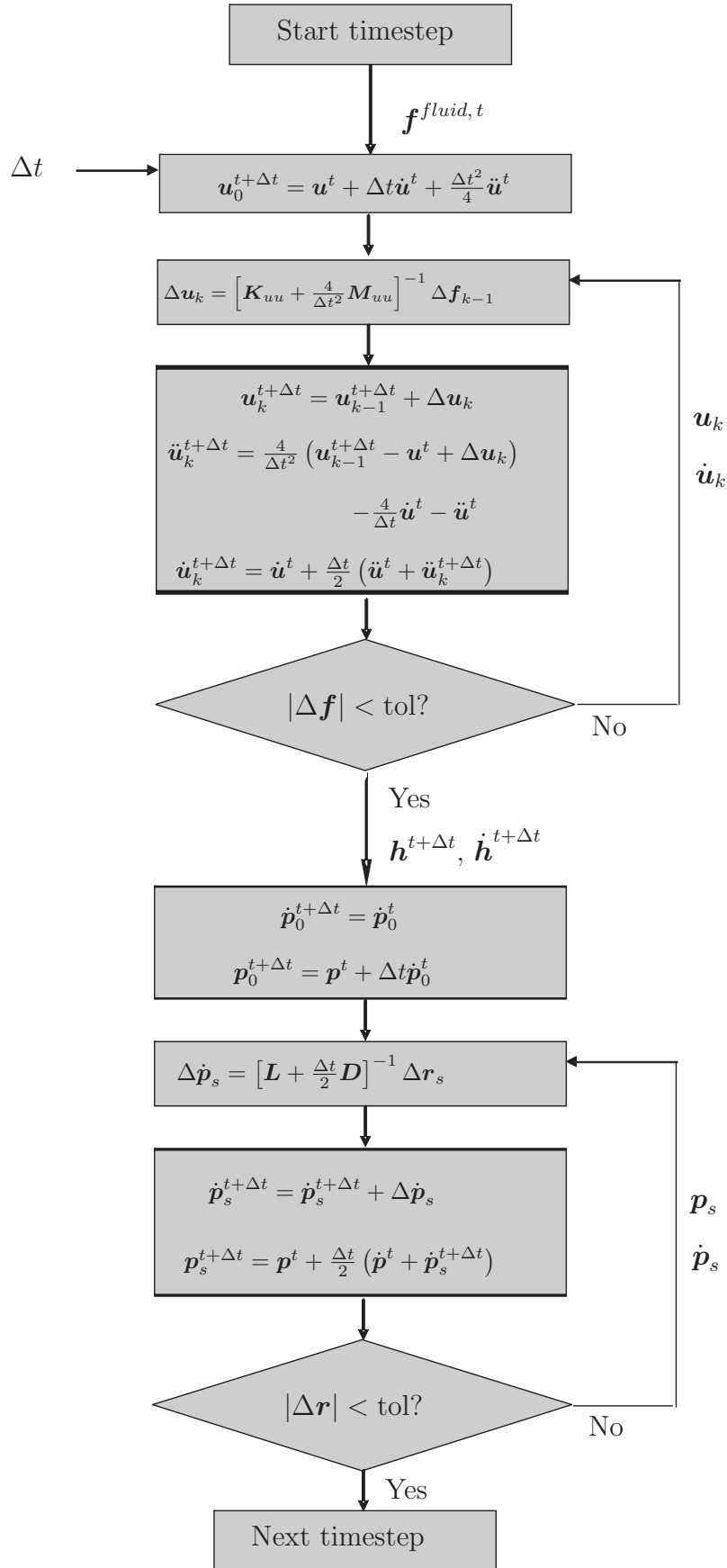


Figure 10.6: Compressible time integration algorithm.

10.4 Eigenfrequencies with damping

When the eigenfrequency is determined, the homogeneous solution of the linearized equation of motion (10.65) is searched. The homogeneous equation is:

$$\begin{bmatrix} \mathbf{M}_{uu} & 0 & 0 \\ 0 & 0 & 0 \\ 0 & 0 & 0 \end{bmatrix} \begin{bmatrix} \Delta \ddot{\mathbf{u}} \\ \Delta \ddot{\boldsymbol{\phi}} \\ \Delta \ddot{\mathbf{p}} \end{bmatrix} + \begin{bmatrix} 0 & 0 & 0 \\ 0 & 0 & 0 \\ -\mathbf{R} & 0 & -\mathbf{L} \end{bmatrix} \begin{bmatrix} \Delta \dot{\mathbf{u}} \\ \Delta \dot{\boldsymbol{\phi}} \\ \Delta \dot{\mathbf{p}} \end{bmatrix} + \begin{bmatrix} \mathbf{K}_{uu} & \mathbf{K}_{u\phi} & \mathbf{K}_{uf} \\ \mathbf{K}_{\phi u} & \mathbf{K}_{\phi\phi} & 0 \\ 0 & 0 & -\mathbf{D} \end{bmatrix} \begin{bmatrix} \Delta \mathbf{u} \\ \Delta \boldsymbol{\phi} \\ \Delta \mathbf{p} \end{bmatrix} = \begin{bmatrix} 0 \\ 0 \\ 0 \end{bmatrix}. \quad (10.104)$$

In chapter 3 it was shown that for the homogeneous equation of an electro-mechanical system the electric part could be condensed out. Also for a damped electro-mechanical system this can be done. The middle line of equation (10.104) gives a direct relation between $\Delta \boldsymbol{\phi}$ and $\Delta \mathbf{u}$:

$$\Delta \boldsymbol{\phi} = -\mathbf{K}_{\phi\phi}^{-1} \mathbf{K}_{\phi u} \Delta \mathbf{u}, \quad (10.105)$$

which can be substituted in the top line of (10.104) to give:

$$\begin{bmatrix} \mathbf{M}_{uu} & 0 \\ 0 & 0 \end{bmatrix} \begin{bmatrix} \Delta \ddot{\mathbf{u}} \\ \Delta \ddot{\mathbf{p}} \end{bmatrix} + \begin{bmatrix} 0 & 0 \\ -\mathbf{R} & -\mathbf{L} \end{bmatrix} \begin{bmatrix} \Delta \dot{\mathbf{u}} \\ \Delta \dot{\mathbf{p}} \end{bmatrix} + \begin{bmatrix} (\mathbf{K}_{uu} - \mathbf{K}_{u\phi} \mathbf{K}_{\phi\phi}^{-1} \mathbf{K}_{\phi u}) & \mathbf{K}_{uf} \\ 0 & -\mathbf{D} \end{bmatrix} \begin{bmatrix} \Delta \mathbf{u} \\ \Delta \mathbf{p} \end{bmatrix} = \begin{bmatrix} 0 \\ 0 \end{bmatrix}. \quad (10.106)$$

This condensed equation will be written from this point on as:

$$\mathbf{M}_c \Delta \ddot{\mathbf{U}}_c + \mathbf{C}_c \Delta \dot{\mathbf{U}}_c + \mathbf{K}_c \Delta \mathbf{U}_c = 0. \quad (10.107)$$

To compute the eigenfrequencies the solution is restricted to harmonic solutions:

$$\mathbf{U}_c = \boldsymbol{\mu}_j e^{\lambda_j t}, \quad (10.108)$$

$$\dot{\mathbf{U}}_c = \boldsymbol{\mu}_j \lambda_j e^{\lambda_j t}, \quad (10.109)$$

$$\ddot{\mathbf{U}}_c = \boldsymbol{\mu}_j \lambda_j^2 e^{\lambda_j t}, \quad (10.110)$$

where $\boldsymbol{\mu}_j$ and λ_j are complex, therefore the second order eigenvalue problem that can be defined is:

$$\mathbf{M}_c \lambda_j^2 \boldsymbol{\mu}_j + \mathbf{C}_c \lambda_j \boldsymbol{\mu}_j + \mathbf{K}_c \boldsymbol{\mu}_j = 0, \quad (10.111)$$

which is, without further assumptions, not a standard eigenvalue problem.

However it is possible to circumvent this problem: the following trivial equation is added to the linearized equation (10.107):

$$\mathbf{I} \Delta \dot{\mathbf{U}}_c - \mathbf{I} \Delta \dot{\mathbf{U}}_c = 0. \quad (10.112)$$

In literature the mass matrix is used frequently to write down this extra constraint, however in this case the mass matrix is singular due to the fact that the Reynolds equation neglects inertia terms, therefore the identity matrix is used. This defines the state space form of the monolithic equation:

$$\begin{bmatrix} \mathbf{C}_c & \mathbf{M}_c \\ \mathbf{I} & 0 \end{bmatrix} \begin{bmatrix} \Delta \dot{\mathbf{U}}_c \\ \Delta \ddot{\mathbf{U}}_c \end{bmatrix} + \begin{bmatrix} \mathbf{K}_c & 0 \\ 0 & -\mathbf{I} \end{bmatrix} \begin{bmatrix} \Delta \mathbf{U}_c \\ \Delta \dot{\mathbf{U}}_c \end{bmatrix} = \begin{bmatrix} 0 \\ 0 \end{bmatrix}. \quad (10.113)$$

In state space form it is possible to define the solvable eigenvalue problem:

$$\begin{bmatrix} \mathbf{C}_c & \mathbf{M}_c \\ \mathbf{I} & 0 \end{bmatrix} \lambda_j \begin{bmatrix} \boldsymbol{\mu}_j \\ \lambda_j \boldsymbol{\mu}_j \end{bmatrix} + \begin{bmatrix} \mathbf{K}_c & 0 \\ 0 & -\mathbf{I} \end{bmatrix} \begin{bmatrix} \boldsymbol{\mu}_j \\ \lambda_j \boldsymbol{\mu}_j \end{bmatrix} = \begin{bmatrix} 0 \\ 0 \end{bmatrix}, \quad (10.114)$$

or:

$$\mathbf{A} \lambda_j \mathbf{m}_j + \mathbf{B} \mathbf{m}_j = 0. \quad (10.115)$$

In general the eigenvalue λ_j that will be found is complex, having a real part and an imaginary part: $\lambda_j = \zeta_j + i\omega_j$. In the beginning it was assumed that the motion could be described by:

$$\mathbf{U}_c = \boldsymbol{\mu}_j e^{(\zeta_j + i\omega_j)t}, \quad (10.116)$$

which can be written as:

$$\mathbf{U}_c = \boldsymbol{\mu}_j e^{\zeta_j t} e^{i\omega_j t}. \quad (10.117)$$

The term $e^{i\omega_j t}$ describes a sinusoidal motion with frequency ω_j . The part $e^{\zeta_j t}$ describes how the sinusoidal motion damps out ($\zeta_j < 0$) or explodes ($\zeta_j > 0$) and $\boldsymbol{\mu}_j$ gives the shape of the mode. Of course the amplitude of the mode does not have a physical meaning, because when c is a constant scalar, $\boldsymbol{\mu}_j \cdot c$ will also be a solution to equation (10.113).

10.5 Numerical results

The theoretical aspects of squeeze film damping were treated above. First a damping model based on the Reynolds equation was presented including the implementation of this model into a finite element model. The use of the incompressible gas assumption was discussed as well as the influence of neglecting the inertia terms. Thereafter the time integration of the electro-mechanical-fluidic model was treated before the computation of coupled eigenfrequencies were discussed. The next step will be to investigate the models by looking at some numerical test cases.

Therefore a microbridge plate model as shown in section 4.3 is enhanced by a squeeze film mesh. The used geometry and material properties are realistic. The geometry is expressed by the following numbers: length of the plate = $250\mu\text{m}$, plate width = $30\mu\text{m}$, plate thickness = $1.4\mu\text{m}$ and the gap between the electrodes is $3\mu\text{m}$. The material properties were approximately those of polysilicon: a Young's modulus of 160GPa , a density of 2330kg/m^3 and a Poisson's ratio of 0.28. These numbers give a static pull-in voltage of $V_{PI} = 64.7$ and the pull-in curve shown in figure 10.7.

The gas is assumed to be air at an atmospheric pressure of $p_A = 1 \cdot 10^5\text{Pa}$ unless stated otherwise. Air has a viscosity of $18.27 \cdot 10^{-6}\text{Pa} \cdot \text{s}$ and a mean free path of 64nm . Because 1 micron of the dielectric gap is filled with a solid dielectric that has the same electric permittivity as air, the squeeze film gap is only 2 microns wide.

10.5.1 Transient simulation

Step response

The first test of the formulation is a simple step response with a voltage well below pull-in: $V_D = 30$. As expected the transient response of the middle node, shown in figure 10.8, shows a nice damped oscillation. Figure 10.9 shows the deformed shape during an instant of the first downward part of the motion. The color indicates the pressure at that time.

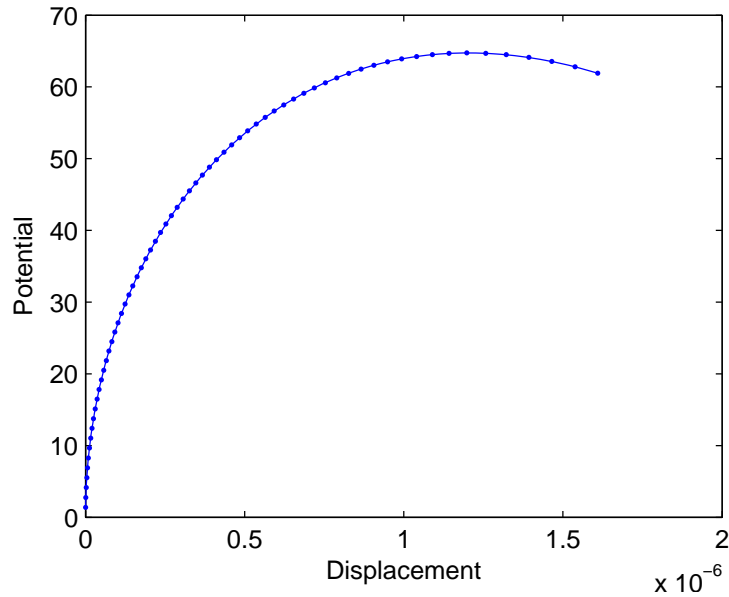


Figure 10.7: Pull-in curve.

Pull-in transient

For a pull-in transient some contact assumptions have to be made. Non linear springs are used to model the mechanical contact between the fixed plate and the dielectric. It is assumed that, due to roughness of the plate, there is still a little bit of air left between the plates when they are in contact. This is used to prevent the equations from braking down if $h = 0$.

The following load procedure is applied to the beam:

$$V_D = \begin{cases} 80 & t < 1.5 \cdot 10^{-5}, \\ 0 & t \geq 1 \cdot 10^{-5}. \end{cases} \quad (10.118)$$

Figure 10.10 shows the resulting transient. It is closed for a short period of time after which the switch is released. Therefore this model shows that it is possible to simulate the switching transient.

Compressibility assumption

Figure 10.11 shows the results of both compressible and incompressible simulations for a step response of 20 Volts. From the results it is clear that for the used properties it is not necessary to include compressibility.

Inertia effects

With the same mechanical parameters and for a 20V load step the relative inertia error for each element was determined:

$$\epsilon = \frac{|\dot{m}^i|}{|\dot{m}^n|}. \quad (10.119)$$

For each time step the maximum value of the error was determined. The highest maximum value during the time integration was $8.4 \cdot 10^{-4}$ while the average error was $3.9 \cdot 10^{-5}$. Hence the effects are really small for beams in the scale of actual MEMS.

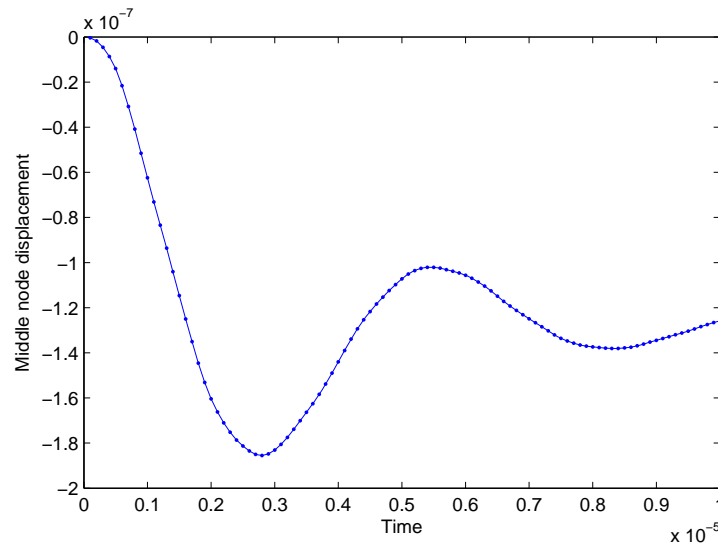


Figure 10.8: Midnode displacement as function of time for a load step of 30V.

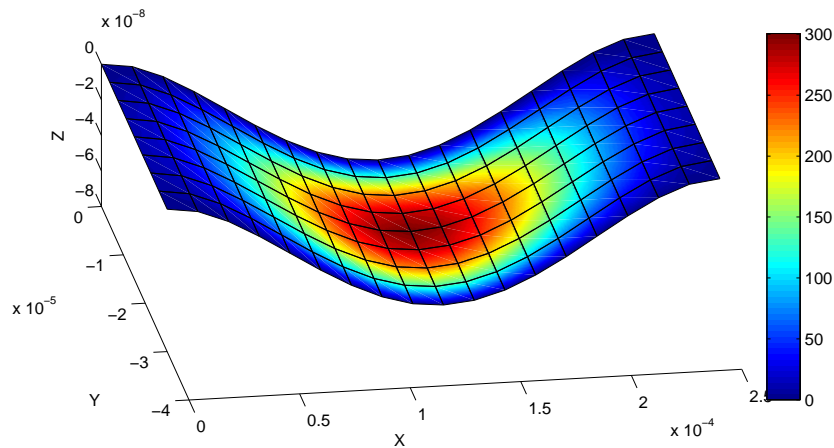


Figure 10.9: Deformed shape at $t = 1 \cdot 10^{-6}$ (color = pressure, load = 30V).

10.5.2 Eigenfrequency computations

Atmospheric pressure

Figure 10.7 showed the pull-in curve for the beam. As discussed in previous chapters the frequency depends on the applied voltage, but also the damping influences the frequency. Therefore this pull-in curve is traced and the linearized damped and undamped frequencies around the equilibria are computed.

The top graph of figure 10.12 shows this coupled eigenfrequencies of the damped plate as a function of the equilibrium displacement together with the eigenfrequencies of the undamped plate. What happens is that the air damping slows down the oscillation, which decreases the frequency. Therefore the zero frequency is reached at a lower potential, but does that also mean that pull-in is reached at a lower potential?

This is examined by looking at the bottom half of figure 10.12. It shows the real part of the eigenvalue (which is ζ_j). If the real part is negative the system is stable. It is clear that the real part is negative until the original pull-in point. It does show a clear change in the slope of the curve at the point where the plate reaches a zero

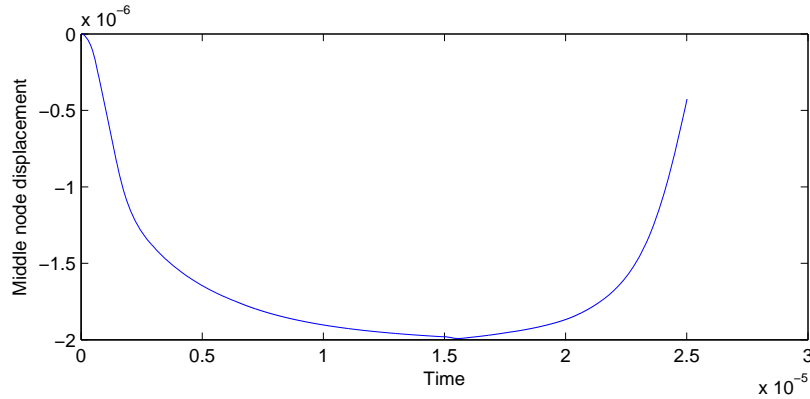


Figure 10.10: Transient result during switching.

frequency. Beyond that point the mode is not an oscillatory mode, but it is a stable mode until it reaches the point where the real part of the electro-mechanical eigenvalue becomes zero.

Hence gas damping does not influence first order stability. However it does lower the eigenfrequency, which causes the rule of thumb *a zero eigenfrequency coincides with the pull-in point* to be invalid when damping is present.

Influence of pressure and squeeze number variations

The previous computations were done at atmospheric pressure ($p_A = 1 \cdot 10^5 Pa$). It is known that the unloaded eigenfrequency is $\omega = 1.25 \cdot 10^6 rad/s$. With the 30μ width of the beam this gives a squeeze factor of $\sigma = 0.61$. The same geometric properties give a critical squeeze number of $\sigma_c = 10$ for a plate that is rigid. This plate is not rigid hence the actual critical squeeze number will be different, however this critical value gives an indication of the order of magnitude. When the pressure is lowered to $p_A = 1 \cdot 10^4 Pa$, the squeeze factor increases to $\sigma = 6.1$ which is in the order of magnitude of σ_c .

To see what happens for higher squeeze numbers the eigenvalue curves were also computed for $p_A = 1 \cdot 10^4 Pa$ and $p_A = 1 \cdot 10^3 Pa$, which are presented together with the atmospheric one in figure 10.13.

For higher applied potentials thus higher equilibrium displacements and lower frequencies the squeeze number is really low again, thus incompressible behavior dominates for all curves. The red $p_A = 1 \cdot 10^4 Pa$ curve for instance starts with an increased frequency due to compressible behavior, but at about 75% of the pull-in displacement it crosses the undamped line and shows more incompressible behavior.

The damping at $p_A = 1 \cdot 10^3 Pa$ (the magenta line) is so low that it is not easy to see a difference from the undamped one. But due to the higher squeeze number of $\sigma = 61$ that line is almost up until pull-in higher than the undamped line. Only at about 95% of pull-in, it crosses the undamped line to show more incompressible behavior.

As has been mentioned at a zero potential or displacement only the $p_A = 1 \cdot 10^5 Pa$ line shows incompressible behavior as it is the only line below the undamped one, which is clearly shown in close up shown in figure 10.14.

The bottom part of that graph shows the close up of the real part of the eigenvalues, which are all below zero. Indicating that although for high squeeze numbers the terms proportional to displacement might dominate the terms proportional to velocities, those velocity related terms will always have some influence, therefore giving a negative real

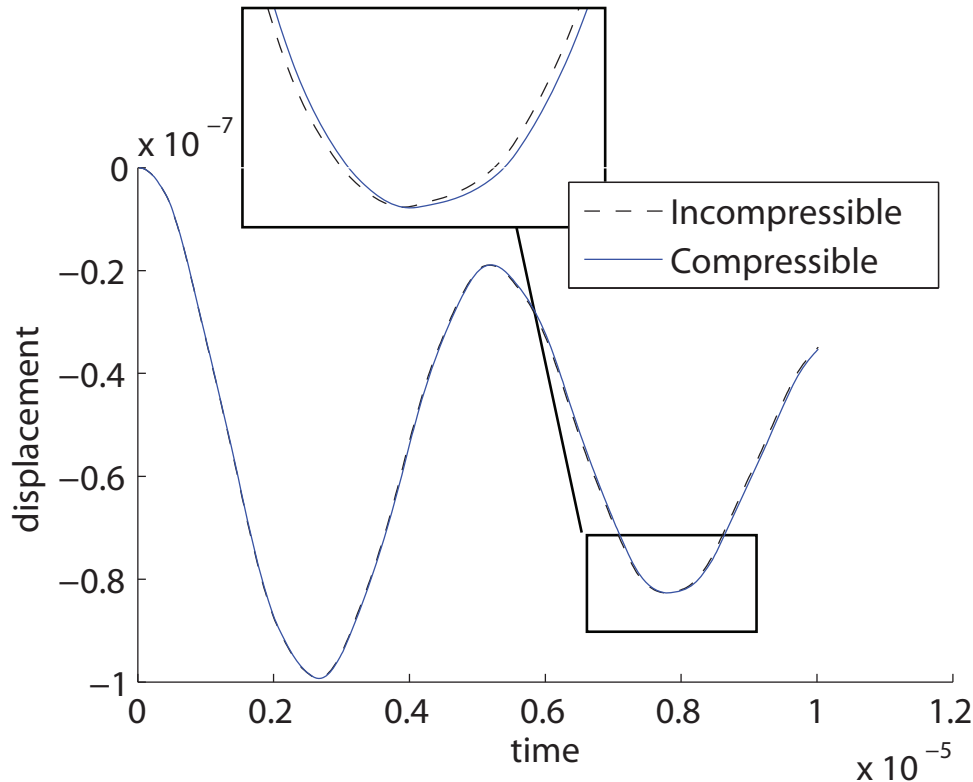


Figure 10.11: Midnode displacement as function of time.

part of the eigenvalue and damping.

10.6 Experimental validation

The coupled electromechanical frequency modeling was already validated in sections 5.8 and 8.5, hence this section will focus on the mechanical-fluidic interaction. The Reynolds equation as modeling strategy has been validated in literature frequently (e.g. [90]) but this specific FEM implementation needs validation. A nice paper in literature that measures the response of a micro bridge resonator at different pressures is a paper by Legtenberg and Tilmans [76]. Those measurements will be used for experimental validation. Note that this is the same device as was used by the same authors in [130], which describes the measurements used for validation in sections 5.8 and 8.5.

For the measurements a simple micro bridge was used. The thickness of the plate is 1.5μ , the gap between plate and ground plane is 1.2μ and the width is 100μ (distance from free to free edge). Two bridges of different lengths were used: 210μ and 310μ (distance from clamped to clamped edge).

For the modeling of the mechanics of the plate a mesh of 22 elements in the length and 14 elements in width of the plate were used. The electric mesh in the air gap contained 4 elements in the direction perpendicular to the plate. In the other 2 directions the number of elements was equal to the number elements in the mechanical mesh.

For the material properties a value of $E = 160 \text{ GPa}$ for the elasticity modulus, $\rho = 2300 \text{ kg/m}$ for the density of silicon and $\nu = 0.22$ for Poisson's ratio was used. An initial strain of $\epsilon = 36.8 \cdot 10^{-6}$ in the direction of the longest edge was used. Since it appears in the paper that the experiments were done in Nitrogen, the viscosity was

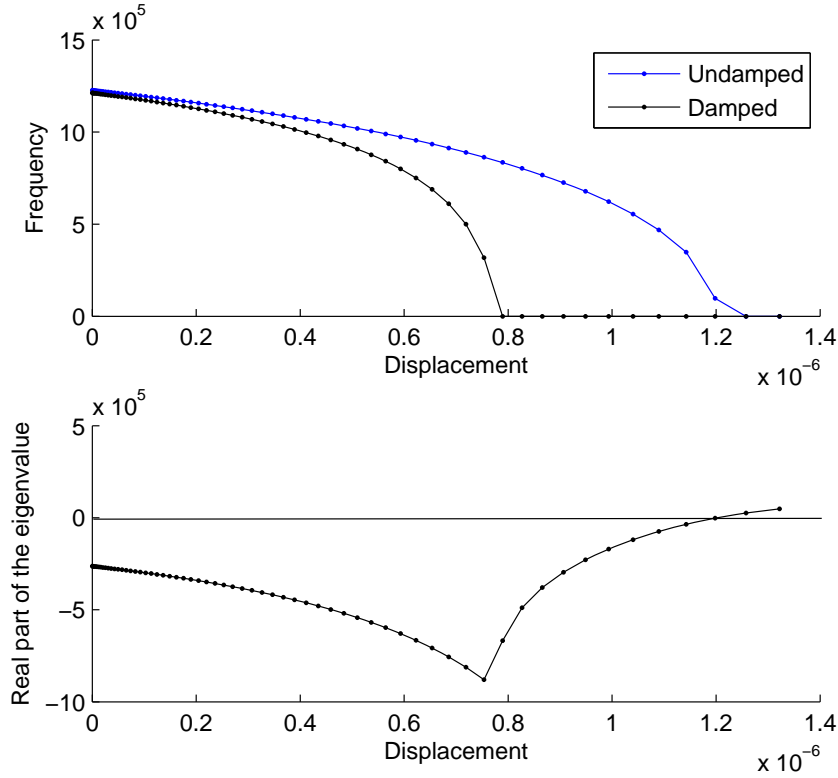


Figure 10.12: Eigenvalue vs. displacement ($p_A = 1 \cdot 10^5$ for the damped one).

chosen to be $\mu = 17.8 \cdot 10^{-6} Pa \cdot s^2$. The rarefaction effects were modeled with Veijola's *effective viscosity* relation (eq. 10.22) [136]:

$$\mu = \frac{\mu_0}{1 + 9.638 Kn^{1.159}}, \quad (10.120)$$

where for the Knudsen number the following relation was used

$$Kn = \frac{6.9 \cdot 10^{-3}}{p \cdot h}, \quad (10.121)$$

When the eigenfrequency of the 210μ long beam is computed it gives a value of $\omega = 321 kHz$, which is very close the value of $324 kHz$ measured and reported by Legtenberg.

It is very difficult to validate the damping model by the frequency alone. Definitely for low pressures the damping will hardly cause any frequency shift. However transient measurements are very difficult. Furthermore it is nearly impossible to excite the resonator with a known force, thus a proper frequency response function is also impossible. However one value is relatively easy to determine from the measured frequency response, even if the input force is almost unknown: the quality factor.

The Quality factor or Q-factor gives a measure of the damping and is defined as:

$$Q = \text{OscillationFrequency} \times \frac{\text{StoredEnergy}}{\text{PowerLoss}}. \quad (10.122)$$

²From the paper it is not really clear whether the measurements were done in air or nitrogen. However the viscosity and mean free path for nitrogen and air are that close together that changing those parameters does not change the Q-factor values.

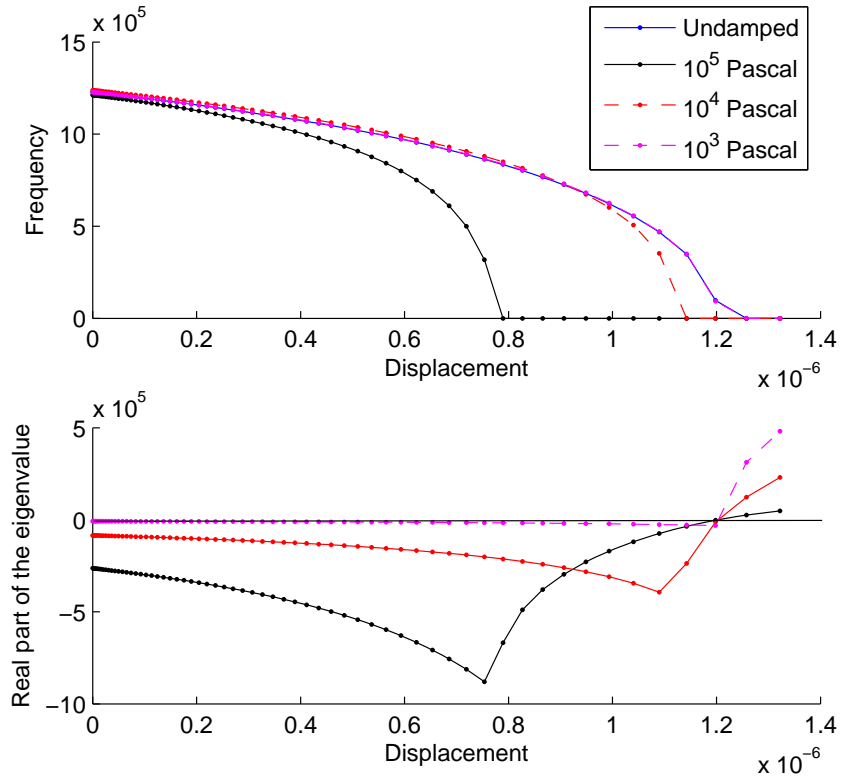


Figure 10.13: Eigenvalue vs. displacement (different pressures).

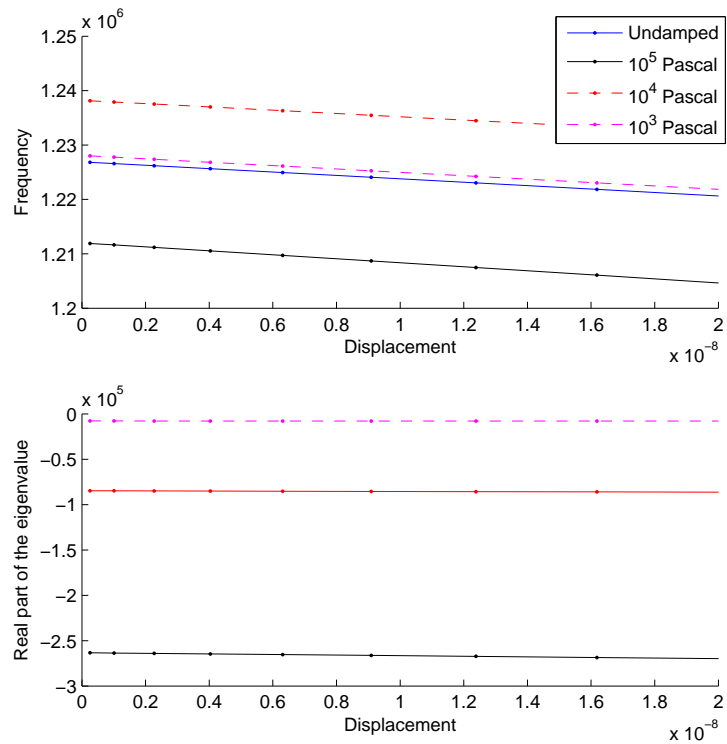


Figure 10.14: Close up of figure 10.13: the eigenvalues near a zero displacement (different pressures).

Experimentally this can be determined from the frequency response using for instance the *half power bandwidth* method [102]. In simulation the computation is equally simple. If the damped eigenvalue is known the Q-factor of the accompanying mode can be computed with the following relation [102]:

$$Q_i = \left| \frac{\text{Im}(\lambda_i)}{2\text{Re}(\lambda_i)} \right| = \left| \frac{\omega_i}{2\zeta_i} \right|. \quad (10.123)$$

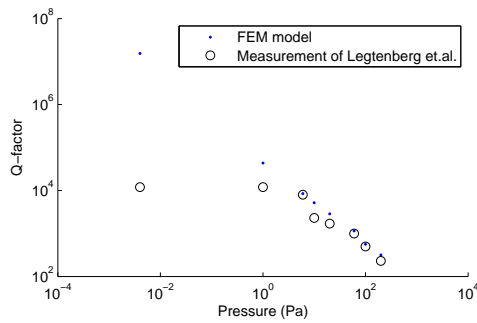


Figure 10.15: Q-factor of the 210 μ beams a function of pressure.

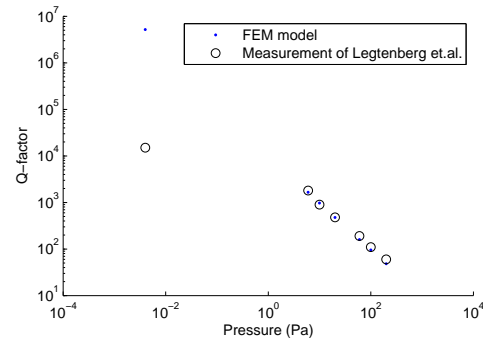


Figure 10.16: Q-factor of the 310 μ beams a function of pressure.

The measured and simulated Q-factors for the two beam lengths are presented in figures 10.15 and 10.16 as a function of the ambient pressure. From the figures it is clear that for higher pressures, although lower than atmospheric pressure, the model works very well. This can even better be seen in the zoom-in presented in figures 10.17 and 10.18. However from these result there seems to be a point somewhere around a pressure of 1 Pa where the equations do not hold anymore. This can be explained by the assumption that at these low pressures particle based theories are required or that thermo-mechanical damping becomes crucial at this point.

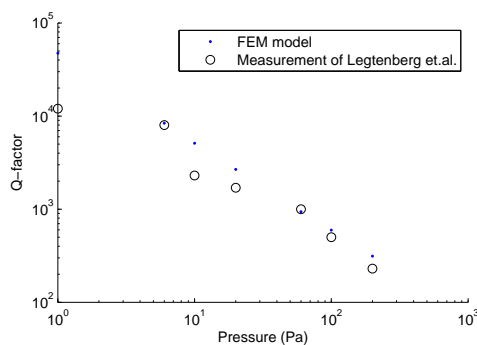


Figure 10.17: High pressure Q-factors of the 210 μ beams a function of pressure.

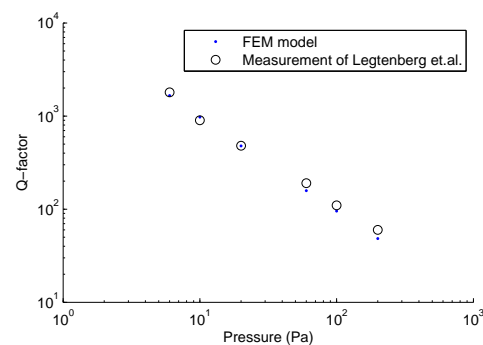


Figure 10.18: High pressure Q-factors of the 310 μ beam as a function of pressure.

To be able to pinpoint the end of the validity range of the squeeze film equation the same results were plotted as a function of the Knudsen number in figures 10.19 and 10.20. From those figures follows that Reynold's equation with rarefaction correction fails near a Knudsen number of about 600.

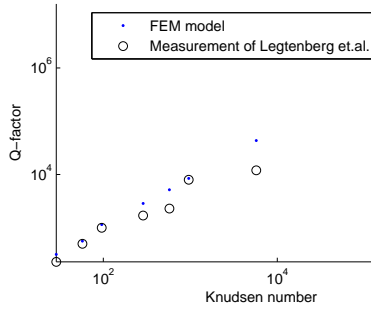


Figure 10.19: Q-factors of the 210 μ beam as a function of Kn .

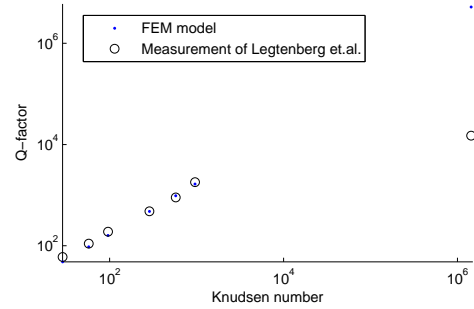


Figure 10.20: Q-factors of the 310 μ beam as a function of Kn .

10.6.1 Intermezzo: thermoelastic damping

There is a very simple method to estimate the Q factor of a vibrating plate or beam due to thermoelastic damping. Thermoelastic damping is the loss of energy due to the irreversible heating of a vibrating structure. The simplest model is Zener's model, which provides the following relation for the thermoelastic Q-factor [79]:

$$Q^{-1} = \frac{E\alpha^2 T_0}{C_p} \frac{\omega\tau}{1 + \omega^2\tau^2}, \quad (10.124)$$

where $\alpha = 2.5 \cdot 10^{-6} 1/K$ is the thermoelastic expansion coefficient of silicon, $T_0 = 300 K$ the temperature, $C_p = 711 J/kg/K$ the specific heat capacity of silicon and τ the relaxation time:

$$\tau = \frac{h^2 C_p}{\kappa \pi^2}, \quad (10.125)$$

where $\kappa = 170 W/m \cdot K$ the thermal conductivity. For the 210 beam this equation gives $Q = 1.2 \cdot 10^6$ and for the 310 beam this gives $Q = 2.4 \cdot 10^6$. Comparing these Q-factors with the figures 10.19 and 10.20 shows that this would mean that above a Knudsen number of 10^5 , one does not need to include gas damping since it would be dominated by thermoelastic damping.

Furthermore there are anchor losses that need to be included in the modeling if one would like to go to Knudsen numbers above 600 [99]. Therefore the range of Knudsen numbers that are not covered by this squeeze film model is even smaller. Hence the range where particle based methods have something to add for predictive modeling is very small, while their computational cost is immense.

10.7 Conclusions

First the squeeze film damping model was introduced. It is based on Reynolds equation, which assumes that the fluid is viscous, hence the inertia effects in the fluid were neglected. To test this assumption an error measure was developed. Rarefied gas effects are included through an effective viscosity that is a function of the Knudsen number. This function is experimentally approximated in literature [136]. The weak form of the non-linear Reynolds equation was derived and the coupling terms with the electro-mechanical equations were determined.

Thereafter numerical solution algorithms were discussed. A non-linear implicit time integration algorithm based on the trapezoidal rule was developed for *incompressible*

gas and one for *compressible* gas. Also the most efficient way to write the linearized equations for the computation of the damped eigenmodes was derived.

Finally the results were presented. The transient results showed that for the material properties in this chapter the incompressible gas assumption is valid. Furthermore the frequency analysis showed that the squeeze number for the undeformed configuration provides an accurate estimator of the validity of the incompressibility assumption. An deformed equilibrium displacement however, can cause the validity range to be different compared to the estimate for the undeformed squeeze number. Because the critical squeeze number is only defined for simple geometries it does require extra research to find out what the exact limitations for this assumption are and when the compressible gas assumption has to be used.

The transient results also showed that this method can be used to determine switching behavior. Though, one important limitation of the method is that it was assumed that when the plate is in contact with the dielectric layer there is still some air in the gap (this is not completely unrealistic because in reality there is surface roughness, preventing full contact).

The coupled electro-mechanical-fluidic eigenfrequency computations showed that for high pressures the gas damping does lower the coupled eigenfrequency, therefore the zero eigenfrequency is reached at lower potential. But the real part of the eigenmode is still negative in the part between zero imaginary part and electro-mechanical pull-in, thus electro-mechanical-fluidic pull-in is not reached at a zero frequency, but at a zero real part of the eigenvalue. This point coincides with electro-mechanical pull-in.

Finally the model was compared with measurements from literature to estimate the quality of the modeling strategy. The model showed to be accurate up to a Knudsen number of around 600.

Chapter 11

Sensitivity and stochastic analysis of damped frequencies

11.1 Introduction

Eigenfrequencies and Q-factors are important properties for MEMS that use resonance during their operation [73, 69]. Therefore the sensitivity and uncertainty of these values are crucial for the designer.

Most of these devices operate in near vacuum. Hence damping might be neglected, in which case eigenvalue sensitivities will be quite trivial. Moreover if the damping in vacuum has to be determined accurately, one finds that the damping is mainly caused by thermoelastic damping [34, 91], which is not within the scope of this thesis.

But there are also quite some resonators operating under higher pressure, for instance mass sensors that use the frequency shift due to added mass for measuring. Those sensors use a chemical reaction to attach a material to the resonator. This changes the mass of the resonator, therefore the frequency. It is clear that in this case the damped frequency sensitivity is of vital importance. The Q-factor is also a measure of the amount of damping, hence it can be very useful to know its sensitivity for non-resonator applications as well.

The sensitivity computation for damped frequencies and Q-factors is less trivial and will be partly based on the derivation for thermoelastic Q-factor sensitivities presented in [111]. Although for most purposes, such as optimization and first order stochastic analysis first order sensitivities are sufficient, also second order sensitivities are discussed. After the derivation of the sensitivities they are used for a stochastic analysis.

11.2 Undamped frequency sensitivity

The equation under consideration is equation (8.5), which can be written as¹:

$$\omega^2 \mathbf{M}_{uu} \mathbf{x} - \hat{\mathbf{K}} \mathbf{x} = 0, \quad (11.1)$$

where $\hat{\mathbf{K}}$ is the mechanical stiffness including the Schur complement that results from condensing the electrostatic terms out of the coupled equation.

¹Note that for simplicity indices that indicate the number of the eigenvalue have been dropped.

The sensitivity can be derived by differentiating the complete eigensolution equation with respect to a parameter p [45]:

$$\left(\omega^2 \frac{\partial \mathbf{M}_{uu}}{\partial p} - \frac{\partial \hat{\mathbf{K}}}{\partial p} \right) \mathbf{x} + \frac{\partial \omega^2}{\partial p} \mathbf{M}_{uu} \mathbf{x} + \left(\omega^2 \mathbf{M}_{uu} - \hat{\mathbf{K}} \right) \frac{\partial \mathbf{x}}{\partial p} = 0. \quad (11.2)$$

This equation is pre-multiplied with the transpose of \mathbf{x} . Due to fact that left and right eigenvectors are equal for this problem, one can use (11.1) to drop the term related to the derivative of the eigenvector from the equation². Subsequent rearrangement gives:

$$\frac{\partial \omega^2}{\partial p} = - \frac{\mathbf{x}^T \left(\omega^2 \frac{\partial \mathbf{M}_{uu}}{\partial p} - \frac{\partial \hat{\mathbf{K}}}{\partial p} \right) \mathbf{x}}{\mathbf{x}^T \mathbf{M}_{uu} \mathbf{x}}, \quad (11.3)$$

which provides the sensitivity of the square of the eigenfrequency. The eigenvalue sensitivity follows from the chain rule:

$$\frac{\partial \omega}{\partial p} = \frac{1}{2\omega} \frac{\partial \omega^2}{\partial p}. \quad (11.4)$$

The computation of the undamped eigenfrequency sensitivity is really cheap. Once the eigenvalue and mode have been computed, no more matrix factorizations are required. Only the matrix derivatives have to be computed to find the eigenvalue sensitivity.

11.3 Damped eigenvalue sensitivities

11.3.1 First order sensitivity

For the damped situation it is a little bit more difficult, therefore the approach as presented in [111] is followed. The equation that defines the eigenvalue is (10.111):

$$\mathbf{M}_c \lambda^2 \boldsymbol{\mu} + \mathbf{C}_c \lambda \boldsymbol{\mu} + \mathbf{K}_c \boldsymbol{\mu} = 0, \quad (11.5)$$

where $\boldsymbol{\mu}$ contains the mechanical and pressure DOF's. Electric DOFs are condensed out of the equation as indicated by the c subscript, for clarity this subscript will be dropped from now on. To solve this equation it is written in state space form:

$$\begin{bmatrix} \mathbf{C} & \mathbf{M} \\ \mathbf{I} & \mathbf{0} \end{bmatrix} \lambda \begin{bmatrix} \boldsymbol{\mu} \\ \lambda \boldsymbol{\mu} \end{bmatrix} + \begin{bmatrix} \mathbf{K} & \mathbf{0} \\ \mathbf{0} & -\mathbf{I} \end{bmatrix} \begin{bmatrix} \boldsymbol{\mu} \\ \lambda \boldsymbol{\mu} \end{bmatrix} = \begin{bmatrix} \mathbf{0} \\ \mathbf{0} \end{bmatrix}, \quad (11.6)$$

or:

$$\mathbf{A} \lambda \mathbf{m} + \mathbf{B} \mathbf{m} = 0, \quad (11.7)$$

Where \mathbf{C} , \mathbf{K} , \mathbf{A} and \mathbf{B} are non-symmetric.

The non-symmetric forms will cause the left and right eigenvalue problem to have different eigenvector solutions. In other words the solution to:

$$\mathbf{n}^T \mathbf{A} \lambda + \mathbf{n}^T \mathbf{B} = 0, \quad (11.8)$$

²This trick was also used in the derivation of the pull-in sensitivity in section 6.2.

will give the same eigenvalue set as equation (11.7) but a different eigenvector set when $\mathbf{A}^T \neq \mathbf{A}$ and/or $\mathbf{B}^T \neq \mathbf{B}$.

If one computes the left eigenvector \mathbf{n} one could use the approach as used in the previous section for undamped problems, however that is somewhat expensive. A cheaper option is using equation (11.5). First compute \mathbf{m} and λ using the normal method. If the left eigenvector $\boldsymbol{\nu}$ is defined by:

$$\mathbf{n} = \begin{bmatrix} \boldsymbol{\nu} \\ \lambda \boldsymbol{\nu} \end{bmatrix}, \quad (11.9)$$

it can be computed by:

$$\boldsymbol{\nu}^T (\mathbf{M}\lambda^2 + \mathbf{C}\lambda + \mathbf{K}) = 0, \quad (11.10)$$

in which when the already computed λ is entered to form a new eigenvalue problem for which a zero eigenvalue is found that has as corresponding eigenvector the wanted one.

Once $\boldsymbol{\nu}$ is computed the sensitivity follows from deriving (11.5) with p :

$$(\mathbf{M}\lambda^2 + \mathbf{C}\lambda + \mathbf{K}) \frac{\partial \boldsymbol{\mu}}{\partial p} = - (2\lambda \mathbf{M} + \mathbf{C}) \boldsymbol{\mu} \frac{\partial \lambda}{\partial p} - \left(\frac{\partial \mathbf{M}}{\partial p} \lambda^2 + \frac{\partial \mathbf{C}}{\partial p} \lambda + \frac{\partial \mathbf{K}}{\partial p} \right) \boldsymbol{\mu}, \quad (11.11)$$

which basically is one equation for two unknowns. But it can be pre-multiplied with $\boldsymbol{\nu}$ to remove the left-hand side of the equation above to give:

$$\frac{\partial \lambda}{\partial p} = - \frac{\boldsymbol{\nu}^T \left(\frac{\partial \mathbf{M}}{\partial p} \lambda^2 + \frac{\partial \mathbf{C}}{\partial p} \lambda + \frac{\partial \mathbf{K}}{\partial p} \right) \boldsymbol{\mu}}{\boldsymbol{\nu}^T (2\lambda \mathbf{M} + \mathbf{C}) \boldsymbol{\mu}}. \quad (11.12)$$

However, a more efficient option is available, because this computation still requires the computation of two different eigenvectors. Following [111] and [26] the right eigenvector is normalized as follows:

$$\boldsymbol{\mu}^T (2\lambda \mathbf{M} \mathbf{C}) \boldsymbol{\mu} = 1, \quad (11.13)$$

This normalization can be differentiated with respect to p :

$$\begin{aligned} \frac{\partial \boldsymbol{\mu}}{\partial p} (2\lambda \mathbf{M} + \mathbf{C}) \boldsymbol{\mu} + \boldsymbol{\mu}^T (2\lambda \mathbf{M} + \mathbf{C}) \frac{\partial \boldsymbol{\mu}}{\partial p} + 2\boldsymbol{\mu}^T \mathbf{M} \boldsymbol{\mu} \frac{\partial \lambda}{\partial p} = \\ - \boldsymbol{\mu}^T \left(2\lambda \frac{\partial \mathbf{M}}{\partial p} + \frac{\partial \mathbf{C}}{\partial p} \right) \boldsymbol{\mu}, \end{aligned} \quad (11.14)$$

which can slightly be rewritten to yield:

$$\begin{aligned} \boldsymbol{\mu}^T (2\lambda \mathbf{M} + \mathbf{C} + 2\lambda \mathbf{M}^T + \mathbf{C}^T) \frac{\partial \boldsymbol{\mu}}{\partial p} + 2\boldsymbol{\mu}^T \mathbf{M} \boldsymbol{\mu} \frac{\partial \lambda}{\partial p} = \\ - \boldsymbol{\mu}^T \left(2\lambda \frac{\partial \mathbf{M}}{\partial p} + \frac{\partial \mathbf{C}}{\partial p} \right) \boldsymbol{\mu}. \end{aligned} \quad (11.15)$$

This defines one extra equation for the two unknowns of equation (11.11), hence both equations can be combined to give:

$$\begin{aligned} \begin{bmatrix} \mathbf{M}\lambda^2 + \mathbf{C}\lambda + \mathbf{K} & (2\lambda \mathbf{M} + \mathbf{C}) \boldsymbol{\mu} \\ \boldsymbol{\mu}^T (2\lambda \mathbf{M} + \mathbf{C} + 2\lambda \mathbf{M}^T + \mathbf{C}^T) & 2\boldsymbol{\mu}^T \mathbf{M} \boldsymbol{\mu} \end{bmatrix} \begin{bmatrix} \frac{\partial \boldsymbol{\mu}}{\partial p} \\ \frac{\partial \lambda}{\partial p} \end{bmatrix} = \\ - \begin{bmatrix} \left(\frac{\partial \mathbf{M}}{\partial p} \lambda^2 + \frac{\partial \mathbf{C}}{\partial p} \lambda + \frac{\partial \mathbf{K}}{\partial p} \right) \boldsymbol{\mu} \\ \boldsymbol{\mu}^T \left(2\lambda \frac{\partial \mathbf{M}}{\partial p} + \frac{\partial \mathbf{C}}{\partial p} \right) \boldsymbol{\mu} \end{bmatrix}, \end{aligned} \quad (11.16)$$

which gives with only one extra unknown the proper eigenvalue and eigenvector derivative.

The eigenvalue λ is known to be complex and is found in complex conjugate pairs: $\lambda = \zeta \pm i\omega$. When numerical algorithms are used it is not known if $\lambda = \zeta + i\omega$ or $\lambda = \zeta - i\omega$ is found. The derivation above gives the correct eigenvalue sensitivity, however if one is interested in the frequency one should note that the frequency is defined as:

$$\omega = |\text{Im}(\lambda)|, \quad (11.17)$$

which will have the following frequency derivative:

$$\frac{\partial\omega}{\partial p} = \frac{\text{Im}(\lambda)}{|\text{Im}(\lambda)|} \text{Im} \left(\frac{\partial\lambda}{\partial p} \right). \quad (11.18)$$

11.3.2 Second order sensitivities

As previously discussed, often first order sensitivities provide enough sensitivity information. However for second order perturbation approaches this is not the case and second order sensitivities are required. Therefore second order sensitivities of the eigenvalue and Q-factor will be derived below. The second order sensitivity of the undamped frequency is not derived separately, because it can be seen as limit case for $\mathbf{C} = 0$. Again the method is valid for any system that can be written in second order form.

The most elegant method to compute first order sensitivities was the method that resulted in equation (11.16). The same idea can also be used to derive second order sensitivities. When equations (11.11) and (11.13) are differentiated twice first with p_s and subsequently with p_t , the result can be rearranged to give the following matrix vector equation, which can be used to compute the components of the Hessian [111]:

$$\begin{bmatrix} M\lambda^2 + \mathbf{C}\lambda + \mathbf{K} & (2\lambda\mathbf{M} + \mathbf{C})\boldsymbol{\mu} \\ \boldsymbol{\mu}^T (2\lambda\mathbf{M} + \mathbf{C} + 2\lambda\mathbf{M}^T + \mathbf{C}^T) & 2\boldsymbol{\mu}^T \mathbf{M}\boldsymbol{\mu} \end{bmatrix} \begin{bmatrix} \frac{\partial^2 \boldsymbol{\mu}}{\partial p_s \partial p_t} \\ \frac{\partial^2 \lambda}{\partial p_s \partial p_t} \end{bmatrix} = - \begin{bmatrix} \mathbf{R}_\mu \\ R_\lambda \end{bmatrix}, \quad (11.19)$$

where:

$$\begin{aligned} \mathbf{R}_\mu = & \left(\frac{\partial \mathbf{M}}{\partial p_s} \lambda^2 + \frac{\partial \mathbf{C}}{\partial p_s} \lambda + \frac{\partial \mathbf{K}}{\partial p_s} \right) \frac{\partial \boldsymbol{\mu}}{\partial p_t} + \left(\frac{\partial \mathbf{M}}{\partial p_t} \lambda^2 + \frac{\partial \mathbf{C}}{\partial p_t} \lambda + \frac{\partial \mathbf{K}}{\partial p_t} \right) \frac{\partial \boldsymbol{\mu}}{\partial p_s} + \\ & (2\lambda\mathbf{M} + \mathbf{C}) \frac{\partial \boldsymbol{\mu}}{\partial p_s} \frac{\partial \lambda}{\partial p_t} + (2\lambda\mathbf{M} + \mathbf{C}) \frac{\partial \boldsymbol{\mu}}{\partial p_t} \frac{\partial \lambda}{\partial p_s} + \left(2\lambda \frac{\partial \mathbf{M}}{\partial p_s} + \frac{\partial \mathbf{C}}{\partial p_s} \right) \boldsymbol{\mu} \frac{\partial \lambda}{\partial p_t} + \\ & \left(2\lambda \frac{\partial \mathbf{M}}{\partial p_t} + \frac{\partial \mathbf{C}}{\partial p_t} \right) \boldsymbol{\mu} \frac{\partial \lambda}{\partial p_s} + 2\mathbf{M}\boldsymbol{\mu} \frac{\partial \lambda}{\partial p_s} \frac{\partial \lambda}{\partial p_t} + \\ & \left(\frac{\partial^2 \mathbf{M}}{\partial p_s \partial p_t} \lambda^2 + \frac{\partial^2 \mathbf{C}}{\partial p_s \partial p_t} \lambda + \frac{\partial^2 \mathbf{K}}{\partial p_s \partial p_t} \right) \boldsymbol{\mu}, \quad (11.20) \end{aligned}$$

and:

$$\begin{aligned}
R_\lambda = & \frac{\partial \boldsymbol{\mu}^T}{\partial p_s} (2\lambda \mathbf{M} + \mathbf{C} + 2\lambda \mathbf{M}^T + \mathbf{C}^T) \frac{\partial \boldsymbol{\mu}^T}{\partial p_t} + \\
& \boldsymbol{\mu}^T \left(2\lambda \frac{\partial \mathbf{M}}{\partial p_s} + \frac{\partial \mathbf{C}}{\partial p_s} + 2\lambda \frac{\partial \mathbf{M}^T}{\partial p_s} + \frac{\partial \mathbf{C}^T}{\partial p_s} \right) \frac{\partial \boldsymbol{\mu}}{\partial p_t} + \\
& 2 \frac{\partial \boldsymbol{\mu}}{\partial p_s} (\mathbf{M} + \mathbf{M}^T) \boldsymbol{\mu} \frac{\partial \lambda}{\partial p_t} + 2 \frac{\partial \boldsymbol{\mu}}{\partial p_t} (\mathbf{M} + \mathbf{M}^T) \boldsymbol{\mu} \frac{\partial \lambda}{\partial p_s} + 2 \boldsymbol{\mu}^T \frac{\partial \mathbf{M}}{\partial p_s} \boldsymbol{\mu} \frac{\partial \lambda}{\partial p_t} + \\
& 2 \boldsymbol{\mu}^T \frac{\partial \mathbf{M}}{\partial p_t} \boldsymbol{\mu} \frac{\partial \lambda}{\partial p_s} + \boldsymbol{\mu}^T \left(2\lambda \frac{\partial^2 \mathbf{M}}{\partial p_s \partial p_t} + \frac{\partial^2 \mathbf{C}}{\partial p_s \partial p_t} \right) \boldsymbol{\mu}. \quad (11.21)
\end{aligned}$$

11.4 Q-factor sensitivities

The Quality-factor or Q-factor is the frequency times the power stored in a oscillation divided by the power loss during the oscillation. In section 10.6 this Q-factor was presented and shown to be defined as:

$$Q = \left| \frac{\text{Im}(\lambda)}{2\text{Re}(\lambda)} \right| = \frac{\omega}{2\zeta}. \quad (11.22)$$

The Q-factor is a frequently used measure of resonator performance. The higher the value, the lower the damping, thus a high Q-factor means a sharp resonance peak. This is desired for resonators in electronic circuits.

11.4.1 First order sensitivity

The derivative of Q with a parameter follows from the chain rule and is:

$$\frac{\partial Q}{\partial p} = \frac{\text{Im}(\lambda)}{\text{Re}(\lambda)} \left| \frac{\text{Re}(\lambda)}{\text{Im}(\lambda)} \right| \frac{1}{2} \frac{\text{Im}(\frac{\partial \lambda}{\partial p}) \text{Im}(\lambda) - \text{Im}(\lambda) \text{Re}(\frac{\partial \lambda}{\partial p})}{\text{Im}(\lambda)^2}. \quad (11.23)$$

For which all variables are known once the eigenvalue sensitivities have been determined. Note that the first two fractions follow from the definition of the derivative of an absolute function:

$$\frac{\partial |y|}{\partial x} = \frac{y}{|y|} \frac{\partial y}{\partial x}. \quad (11.24)$$

11.4.2 Second order sensitivity

The second order sensitivity is computed by differentiating equation (11.23) one more time.

$$\begin{aligned}
\frac{\partial^2 Q}{\partial p_s \partial p_t} = & \frac{\text{Im}(\lambda)}{\text{Re}(\lambda)} \left| \frac{\text{Re}(\lambda)}{\text{Im}(\lambda)} \right| \frac{1}{2\text{Re}(\lambda)^3} \left(\text{Im} \left(\frac{\partial^2 \lambda}{\partial p_s \partial p_t} \right) \text{Re}(\lambda)^2 - \right. \\
& \text{Im} \left(\frac{\partial \lambda}{\partial p_s} \right) \text{Re} \left(\frac{\partial \lambda}{\partial p_t} \right) \text{Re}(\lambda) - \text{Im} \left(\frac{\partial \lambda}{\partial p_t} \right) \text{Re} \left(\frac{\partial \lambda}{\partial p_s} \right) \text{Re}(\lambda) - \\
& \left. \text{Re}(\lambda) \text{Re} \left(\frac{\partial^2 \lambda}{\partial p_s \partial p_t} \right) \text{Im}(\lambda) + 2\text{Re} \left(\frac{\partial \lambda}{\partial p_t} \right) \text{Re} \left(\frac{\partial \lambda}{\partial p_s} \right) \text{Im}(\lambda) \right). \quad (11.25)
\end{aligned}$$

Note again that all procedures discussed here work for any symmetric or non-symmetric problem that is written in second order formulation. The only things that are problem specific are the matrix sensitivities, which will be discussed in the next section.

11.5 Matrix sensitivities

The first thing that has to be made clear is that the two of the three matrices (mass, damping and stiffness) depend on the linearization point. Therefore they depend on the equilibrium solution, hence on the current displacement and potential. In other words for material parameters that influence the equilibrium point this has to be considered. For parameters such as the Young's modulus or plate thickness the equilibrium point depends on those parameters, hence the stiffness matrix derivative can be written as:

$$\frac{d\mathbf{K}}{dp} = \frac{\partial\mathbf{K}}{\partial p} + \left. \frac{\partial\mathbf{K}}{\partial\mathbf{U}} \frac{d\mathbf{U}}{dp} \right|_{eq}. \quad (11.26)$$

The second term is pretty difficult to compute for non-zero voltages and will be discussed below.

11.5.1 Remaining on equilibrium

The computation of the last term of equation (11.26) is simplified by the fact that the linearization pressure is always zero, because the pressure DOFs are the pressures relative to the ambient pressure. This relative pressure is zero because at equilibrium the velocity of the structural part is zero. Thus for the computation of the derivative of \mathbf{U} only the electromechanical terms are relevant $\mathbf{U} = [\mathbf{u} \ \phi]$. Hence in the two equations below only the electromechanical part of the stiffness matrix (\mathbf{K}_{em}) is considered.

For the nonlinear static problem, the static state derivative can be written as [32]:

$$\frac{d\mathbf{F}}{dp} = \frac{\partial\mathbf{F}}{\partial p} + \frac{\partial\mathbf{F}}{\partial\mathbf{U}} \frac{d\mathbf{U}}{dp}, \quad (11.27)$$

substitution of the definition of the stiffness matrix ($\mathbf{K}_{em} = -\frac{\partial\mathbf{F}}{\partial\mathbf{U}}$) yields:

$$\frac{d\mathbf{U}}{dp} = \mathbf{K}_{em}^{-1} \left. \frac{\partial\mathbf{F}}{\partial p} \right|_{eq}, \quad (11.28)$$

If the parameter p equals the elasticity modulus E , the derivative on the right-hand side is:

$$\frac{\partial\mathbf{F}}{\partial p} = \frac{\partial\mathbf{F}}{\partial E} = - \begin{bmatrix} \frac{\partial\mathbf{K}_{uu}}{\partial E} & 0 \\ 0 & 0 \end{bmatrix} \mathbf{U}, \quad (11.29)$$

which was discussed in chapter 6.

Note that for an applied voltage of zero, the equilibrium solution is zero and therefore does not depend on any parameters. Thus if $V = 0$:

$$\frac{\partial\mathbf{U}}{\partial p} = 0. \quad (11.30)$$

11.5.2 Matrix derivative with the static state vector

The computation of $\frac{\partial \mathbf{K}}{\partial \mathbf{U}}$ is rather tedious, however has been discussed in chapter 6 as well. Basically this derivation can be split into a derivation with \mathbf{u} and a derivation with ϕ . Determining $\frac{\partial \mathbf{K}}{\partial \phi}$ is straightforward, determining $\frac{\partial \mathbf{K}}{\partial \mathbf{u}}$ is slightly more difficult. Note that in the mechanically linear case \mathbf{K}_{uu}^m does not depend on \mathbf{u} , but the other matrices (\mathbf{K}_{uu}^e , $\mathbf{K}_{u\phi}$ and $\mathbf{K}_{\phi\phi}$) depend on \mathbf{u} through the shape functions that depend on the position of the electric nodes. The precise implementation of those derivatives with the nodal positions has been presented in section 6.3.2.

Although the fluid does not influence the equilibrium position, the equilibrium position does influence the Reynolds equation. Therefore the fluidic matrices \mathbf{K}_{ff} and \mathbf{C}_{ff} do depend on \mathbf{U} . Because they depend on \mathbf{U} through the gap size term in their matrix definition, the derivatives of those matrices are similar to derivatives of the structural stiffness matrix with the plate element thicknesses. Hence these derivatives are relatively straightforward. The mass matrix \mathbf{M} never depends on \mathbf{U} .

11.5.3 Second order matrix derivative

The second order sensitivity of matrices requires the second order derivative of the equilibrium force vector \mathbf{F} :

$$\frac{d\mathbf{F}}{dp} = \frac{\partial^2 \mathbf{F}}{\partial \mathbf{U}^2} \frac{d\mathbf{U}}{dp} \frac{d\mathbf{U}}{dp} + 2 \frac{\partial^2 \mathbf{F}}{\partial \mathbf{U} \partial p} \frac{d\mathbf{U}}{dp} + \frac{\partial \mathbf{F}}{\partial \mathbf{U}} \frac{d^2 \mathbf{U}}{dp^2} + \frac{\partial^2 \mathbf{F}}{\partial p^2}, \quad (11.31)$$

which gives using the same reasoning as used for equation (11.28):

$$\frac{d^2 \mathbf{U}}{dp^2} = -\mathbf{K}_{em} \left(\frac{\partial^2 \mathbf{F}}{\partial p^2} - 2 \frac{\partial \mathbf{K}_{em}}{\partial p} \frac{d\mathbf{U}}{dp} - \frac{\partial \mathbf{K}_{em}}{\partial \mathbf{U}} \frac{d\mathbf{U}}{dp} \frac{d\mathbf{U}}{dp} \right). \quad (11.32)$$

For a derivative with E it is known that the second order partial derivative of the equilibrium force \mathbf{F} with E is zero because the first order derivative is not depending on E , however if the sensitivity with thickness variations would be computed this term would be important.

The second order derivative of the equilibrium displacement \mathbf{U} can be used to compute:

$$\frac{d^2 \mathbf{K}}{dp^2} = \frac{\partial^2 \mathbf{K}}{\partial p^2} + \frac{\partial^2 \mathbf{K}}{\partial p \partial \mathbf{U}} \frac{d\mathbf{U}}{dp} + \frac{\partial \mathbf{K}}{\partial \mathbf{U}} \frac{d^2 \mathbf{U}}{dp^2} + \frac{\partial^2 \mathbf{K}}{\partial \mathbf{U}^2} \frac{d\mathbf{U}}{dp} \frac{d\mathbf{U}}{dp}. \quad (11.33)$$

The second order derivative of \mathbf{K} with state vector is zero due to the linear relation between shape function and state variables. The cross derivative with \mathbf{U} and p is zero due to the fact that the mechanical stiffness does not depend on the displacement (linear mechanics). The second order derivative of \mathbf{K} with p is zero only for the Young's modulus, if the thickness would be the parameter of interest this would not be the case. Therefore equation (11.33) for elasticity sensitivities reduces to:

$$\frac{d^2 \mathbf{K}}{dE^2} = \frac{\partial \mathbf{K}}{\partial \mathbf{U}} \frac{d^2 \mathbf{U}}{dE^2}. \quad (11.34)$$

11.5.4 Individual matrix sensitivities

The matrix sensitivities for parameters related to the structural domain have already been discussed in chapter 6, except for mass matrix sensitivities. However those are

quite trivial if the so called consistent mass matrix is used:

$$\mathbf{M} = \int \rho \mathbf{N} \mathbf{N}^T dV, \quad (11.35)$$

where \mathbf{N} is a matrix containing the shape functions. In that case:

$$\frac{\partial \mathbf{M}}{\partial \rho} = \int \mathbf{N} \mathbf{N}^T dV, \quad (11.36)$$

and

$$\frac{\partial^2 \mathbf{M}}{\partial \rho^2} = \mathbf{0}. \quad (11.37)$$

Also sensitivities to perturbations of the fluid properties are very important but it is often possible to derive the matrices in a similar fashion as shown above for the mass matrix.

11.6 Stochastic FEM

Once the sensitivities are known a stochastic analysis follows nearly the same procedure as described in section 7.2, hence this will not be repeated here. The only difference is that in this case the failure criteria are different, which need careful consideration as will be elaborated in the example below.

11.7 Example

The reference problem on which the methods are tested is the plate with realistic numbers as used in sections 7.5 and 9.5 for static and dynamic pull-in stochastics. All material and geometry properties are the same as in those two sections. Since those two sections did not include damping the properties of the squeeze film in between the plate are shown in table 11.1.

Table 11.1: Squeeze film properties.

Property	Symbol	Value	Units
<i>Gap size</i>	g	$2 \cdot 10^{-6}$	m
<i>Ambient pressure</i>	P_A	$1 \cdot 10^5$	Pa/m^2
<i>Viscosity</i>	μ	$18.27 \cdot 10^{-6}$	$Pa \cdot s$
<i>Mean free path</i>	λ_0	$94 \cdot 10^{-9}$	m

The deterministic results around the static equilibrium solution are obtained with techniques discussed in previous chapters. The results: the damped and undamped frequency and eigenvalues, are presented in figure 11.1.

11.7.1 Sensitivities around the non-actuated equilibrium

The first sensitivities that are computed are those at the initial position, hence at $\mathbf{U} = \mathbf{0}$. The undamped frequency ω_u , damped eigenfrequency $\omega_d = |\text{Im}(\lambda)|$ and

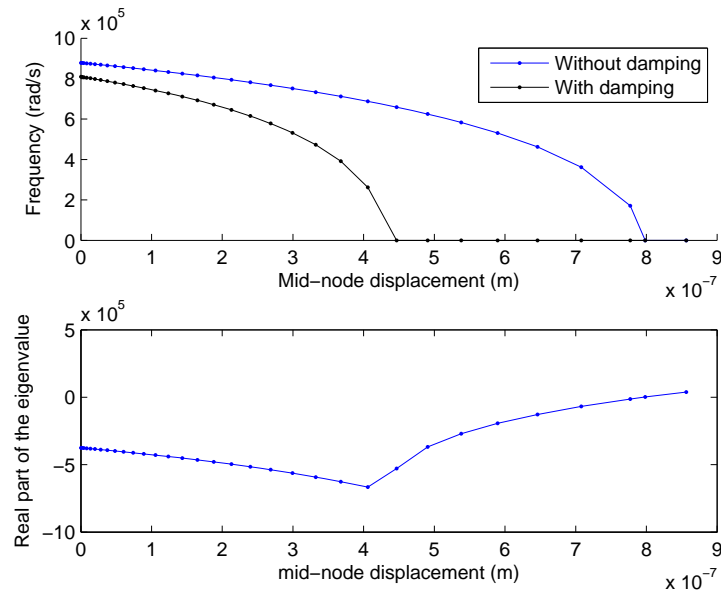


Figure 11.1: Eigenvalue vs. displacement.

quality factor Q are:

$$\omega_u = 8.7838 \cdot 10^5 \text{ rad/s}, \quad (11.38)$$

$$\omega_d = 8.0958 \cdot 10^5 \text{ rad/s}, \quad (11.39)$$

$$Q = 1.0797. \quad (11.40)$$

It is clear from the small Q -factor that damping must be high. The frequency is lowered by adding damping. Hence the added damping effect dominates the added stiffness for the used material and geometry properties. In other words: for these properties incompressible effects dominate compressible effects.

The sensitivities to elasticity modulus and density variations have been computed and are shown in table 11.2. The results show that adding damping increases the sensitivity to both stiffness and mass variations a little bit.

The sensitivities were also computed with global finite differences. Those results show that the analytical method, which is computationally much cheaper, gives almost the same results as the finite difference computations. Therefore the finite difference computations validate analytical sensitivity computations.

The sensitivity of the frequencies not only indicates the vulnerability of the resonant frequency to fabrication uncertainties, but also the sensitivity to intentional mass and stiffness variations. Therefore frequency sensitivities can for instance be used to measure the amount of vapor in a gas flow [128]. For a proper design of such a sensor both the sensitivities to mass variations and stiffness variations are important [124, 112]. In that case the second order sensitivities can be used to do a first order uncertainty analysis of the sensor sensitivity.

11.7.2 Sensitivity around actuated equilibriums

Table 11.3 shows analytical and finite difference sensitivities for a nonzero potential. For an actuated potential mass sensitivities should be no problem at all, because only

Table 11.2: Sensitivities for a linearization with an applied potential $V = 0$.

Sensitivity	Analytical	Finite Difference ($\Delta E = 10 \cdot 10^9$)	Units
$\frac{\partial \omega_u}{\partial E}$	$2.6780 \cdot 10^{-6}$	$2.6384 \cdot 10^{-6}$	$m^2/N \cdot s$
$\frac{\partial \omega_d}{\partial E}$	$2.9989 \cdot 10^{-6}$	$2.9453 \cdot 10^{-6}$	$m^2/N \cdot s$
$\frac{\partial Q}{\partial E}$	$4.0090 \cdot 10^{-12}$	$3.9379 \cdot 10^{-12}$	m^2/N
$\frac{\partial^2 \omega_d}{\partial E^2}$	$-1.1111 \cdot 10^{-17}$	$-1.1130 \cdot 10^{-17}$	$m^4/N^2 \cdot s^2$
$\frac{\partial^2 Q}{\partial E^2}$	$-1.4749 \cdot 10^{-23}$	$-1.4774 \cdot 10^{-23}$	m^4/N^2
Sensitivity	Analytical	Finite Difference ($\Delta \rho = 10$)	Units
$\frac{\partial \omega_u}{\partial \rho}$	-188.5	-187.3	$m^3/kg \cdot s$
$\frac{\partial \omega_d}{\partial \rho}$	-141.0	-140.4	$m^3/kg \cdot s$
$\frac{\partial Q}{\partial \rho}$	$2.89744 \cdot 10^{-4}$	$2.8896 \cdot 10^{-4}$	m^3/kg
$\frac{\partial^2 \omega_d}{\partial \rho^2}$	0.0667	0.0667	$m^6/kg^2 \cdot s^2$
$\frac{\partial^2 Q}{\partial \rho^2}$	$-7.7986 \cdot 10^{-8}$	$-7.7990 \cdot 10^{-8}$	m^6/kg^2
Sensitivity	Analytical	Finite Difference ($\Delta p = 1 \cdot 10^3$)	Units
$\frac{\partial \omega_d}{\partial p}$	-0.3760	-0.3730	$1/Pa \cdot s$
$\frac{\partial Q}{\partial p}$	$-2.1932 \cdot 10^{-6}$	$-2.1697 \cdot 10^{-6}$	$1/Pa$
$\frac{\partial^2 \omega_d}{\partial p^2}$	$5.5025 \cdot 10^{-6}$	$5.9278 \cdot 10^{-6}$	$1/Pa^2 \cdot s^2$
$\frac{\partial^2 Q}{\partial p^2}$	$4.3897 \cdot 10^{-11}$	$4.7670 \cdot 10^{-11}$	$1/Pa^2$

the mass matrix depends on the density, but the mass matrix does not depend on any other variables.

The stiffness sensitivities are more complicated for nonzero potential situations because both damping and stiffness matrices do depend on the displacement. This equilibrium displacement depends on the stiffness, therefore extra terms have to be included within the sensitivity computation as is discussed in section 11.5.1. If these terms are not included the first and second order sensitivity of the damped frequency with E would respectively be: $3.85 \cdot 10^{-6}$ and $-2.32 \cdot 10^{-17}$. The finite difference computations in table 11.3 clearly show that those are wrong and the extra terms are really required. The second order sensitivities are less accurate, though better than without extra terms. This could be due to the convergence of the finite difference computation.

11.7.3 Stochastic analysis

Damped frequency variations caused by elasticity variations

The uncertainty of the damped eigenfrequency due to Young's modulus variations is estimated. The mean value for the Young's modulus is the previously used $164GPa$ and the standard deviation is the previously used $7GPa$. The sensitivity based stochastic FEM gives an average value of:

$$\mu_{\omega_d} = 8.0958 \cdot 10^5 - \frac{1}{2} 1.1111 \cdot 10^{-17} \cdot (7 \cdot 10^9)^2 = 8.0931 \cdot 10^5 \text{ rad/s}, \quad (11.41)$$

and gives a standard deviation of:

$$\sigma_{\omega_d} = \sqrt{(2.9989 \cdot 10^{-6})^2 \cdot (7 \cdot 10^9)^2} = 2.0992 \cdot 10^4 \text{ rad/s}. \quad (11.42)$$

Table 11.3: Sensitivities for a linearization with an applied potential $V = 15$.

Sensitivity	Analytical	Finite Difference ($\Delta E = 1 \cdot 10^9$)	Units
$\frac{\partial \omega_u}{\partial E}$	$3.1714 \cdot 10^{-6}$	$3.1633 \cdot 10^{-6}$	$m^2/N \cdot s$
$\frac{\partial \omega_d}{\partial E}$	$4.9664 \cdot 10^{-6}$	$4.8827 \cdot 10^{-6}$	$m^2/N \cdot s$
$\frac{\partial Q}{\partial E}$	$6.5653 \cdot 10^{-12}$	$6.3787 \cdot 10^{-12}$	m^2/N
$\frac{\partial^2 \omega_d}{\partial E^2}$	$-4.6818 \cdot 10^{-17}$	$-6.1063 \cdot 10^{-17}$	$m^4/N^2 \cdot s^2$
$\frac{\partial^2 Q}{\partial E^2}$	$-2.3132 \cdot 10^{-23}$	$-5.9576 \cdot 10^{-23}$	m^4/N^2
Sensitivity	Analytical	Finite Difference ($\Delta \rho = 10$)	Units
$\frac{\partial \omega_u}{\partial \rho}$	-169.1	-170.2	$m^3/kg \cdot s$
$\frac{\partial \omega_d}{\partial \rho}$	-57.90	-58.20	$m^3/kg \cdot s$
$\frac{\partial Q}{\partial \rho}$	$2.3256 \cdot 10^{-4}$	$2.3172 \cdot 10^{-4}$	m^3/kg
$\frac{\partial^2 \omega_d}{\partial \rho^2}$	-0.0314	-0.0314	$m^6/kg^2 \cdot s^2$
$\frac{\partial^2 Q}{\partial \rho^2}$	$-8.4542 \cdot 10^{-8}$	$-8.4547 \cdot 10^{-8}$	m^6/kg^2

Both values can be confirmed with a 10000 sample size Monte Carlo analysis that gives:

$$\mu_{\omega_d} = 8.0933 \cdot 10^5 \text{ rad/s}, \quad (11.43)$$

and:

$$\sigma_{\omega_d} = 2.0104 \cdot 10^4 \text{ rad/s}. \quad (11.44)$$

Both values are really close and the second order term used in the computation of the SFEM mean value improves the result, though the improvement is very limited, due to the accuracy of the first order result. Hence for a stochastic analysis the second order sensitivity is not very useful.

Frequencies are often very important characteristics for resonators and accelerometers. In the case of accelerometers air damping is often present, therefore investigating the damped eigenfrequency is important. If the frequency is deviating too far from the specifications the device cannot function properly. This provides a usable failure criterion. Especially if the frequency is too low this is problematic. If it is too high one can tune it by pre-loading the sensor using electrostatic actuation. Therefore it is assumed that the device fails if:

$$\omega_d < 7.7 \cdot 10^5 \text{ rad/s}. \quad (11.45)$$

When the failure chance is computed with the stochastic FEM method this gives a design point of $E = 151 \text{ GPa}$ and failure chance of:

$$Pr[\omega_d < 7.7 \cdot 10^5] = 0.0329, \quad (11.46)$$

or about 3%. The Monte Carlo simulation gives:

$$Pr[\omega_d < 7.7 \cdot 10^5] = 0.0331, \quad (11.47)$$

therefore the reliability analysis is confirmed by the Monte Carlo simulation.

Q-factor variations caused by pressure variations

The last example to test the method is focused on the uncertainty caused by variations of the ambient pressure. For instance [76] mentioned that the sealing pressure of a

MEMS resonator package is very difficult to control. Therefore it is assumed that the operating pressure for the resonator above has a mean value of $p = 1 \cdot 10^5 Pa$ with a standard deviation of $p = 1 \cdot 10^4 Pa$. The relationship between the viscosity and the pressure dependent Knudsen number was included in this analysis. The perturbation based FEM gives the following uncertainty for the Q-factor:

$$\mu_Q = 1.0797 + 0.0022 = 1.0819, \quad (11.48)$$

and the stochastic FEM yields a standard deviation of:

$$\sigma_Q = 0.0219. \quad (11.49)$$

These values are validated by a very expensive 20000 sample size Monte Carlo analysis that provides a mean value of:

$$\mu_Q = 1.0821, \quad (11.50)$$

and a standard deviation of:

$$\sigma_Q = 0.0231. \quad (11.51)$$

The standard deviation is really low. Hence the pressure variation does not seem to have a big influence. This seems strange because in section 10.6 a simulation, confirmed by experiments, showed a high sensitivity of the Q-factor to pressure variations. However it can be explained: the simulation for this example uses a pressure of $1 \cdot 10^5 Pa$, which in combination with the gap-size will give a Knudsen number of 0.03. Since this number is well below one, the gas is not rarefied, hence the effective viscosity is locally not a function of the pressure, therefore overall the sensitivity to pressure variations is low. This is in contrast to the simulations of section 10.6 which were done in the rarefied regime. That the transition from rarefied to continuum flow shows a change from pressure dependent to pressure independent results has also been confirmed by experiments in literature [17].

The Q-factor is a measure for damping. For microsichtes the damping determines the switching time. When it is assumed that the device is slower than its specifications when the Q-factor is above 1.15, this defines a failure criterion. The FEM model predicts that the design point will in that case be a pressure of $7.616 \cdot 10^4 Pa$ which will give a failure chance of:

$$Pr[Q > 1.15] = 0.0086, \quad (11.52)$$

which was validated by the Monte Carlo simulation:

$$Pr[Q > 1.15] = 0.0095. \quad (11.53)$$

11.8 Conclusions

This chapter first showed the computation of eigenvalue and Q-factor sensitivities. Thereafter the matrix sensitivities, while remaining on electromechanical equilibrium, were derived. Those sensitivities were used to perform a perturbation based stochastic analysis consisting of uncertainty and reliability computations using a reference bridge.

An attempt was made to validate all results by either finite difference or Monte Carlo simulations. This showed that if a parameter does not change the equilibrium

position all sensitivities can be validated by finite differences. Such parameters are fluid and mass properties, but also all properties at a zero volt actuation voltage. Also all stochastic properties were validated for this type of parameters by the Monte Carlo simulation.

If the parameter does change the equilibrium position, such as the Young's modulus, the first order sensitivity could be validated by finite differences, but not the second order sensitivity. This second order sensitivity was in the right order of magnitude though.

Chapter 12

Model reduction for electro mechanically actuated systems

12.1 Introduction

Time integrating the non-linear electro mechanical equations is a very time consuming business. However due to the fact that MEMS are often used in combination with a large electrical circuit their interaction with this electric circuit is essential and this interaction should be simulated. The time dependent behavior of circuits is often analyzed with low DOF non linear differential equation solvers such as Spice or Simulink. If a computationally expensive FEM model is included in such a loop this destroys the analytical capability of the circuit designer who is using the simulation tool to design a circuit in which the MEMS is only a small building block. Therefore it is important to create low DOF models from these big physical level models [118].

Note that for circuit analysis normally only a input/output model is enough. However, another purposes of model reduction is a detailed transient analysis of the model, while would be to expensive with the full model. In that case the reduced model should be large enough to capture mechanical stresses and similar results with a sufficient accuracy.

The art of generating models with a low number of DOFs from larger FEM models that still behave almost in the same manner as the larger models is called *model reduction* (e.g. [45]). Due to the nonlinear and multi-physical nature of the problem, model reduction for MEMS is not trivial. This chapter will start with the linear modal projection method, the starting point for the derivation of non linear reduced models based on a larger coupled FEM model addressed later in the chapter.

The first section introduces the very basics of modal truncation methods and there it is explained why they are used for model reduction in this chapter. It also explains the challenges for simulating electro-mechanically coupled microsystems as well as a possible simplification, which removes one challenge. The second section is concerned with step responses (the actuation voltage is applied with a step). The time dependency of the electric field is rather simple after application of a step; a characteristic that will be abused. In section 12.4 the reduction of the electric field itself is extended to enable time dependent applied voltages. Finally a reduction approach for the squeeze film damping model is developed in section 12.6.

12.2 Modal truncation and the remaining challenges

12.2.1 Modal truncation of the coupled equations

Once more the full non-linear equations under consideration are:

$$M_{uu}\ddot{\mathbf{u}} + \mathbf{K}_{uu}^m \mathbf{u} = \mathbf{f}^{elec}(\mathbf{u}, \phi, V) \quad (12.1)$$

$$\mathbf{K}_{\phi\phi}(\mathbf{u})\phi = \mathbf{q}(\mathbf{u}, V). \quad (12.2)$$

The electric problem is static and at each instant in time depends directly on the mechanical domain. Furthermore the shape of the coupled modes in in general only really altered by the electrics close to pull-in. Therefore it seems logical to start with reducing the mechanics and project the electrics on the mechanical behavior.

Modal reduction of the mechanics starts with assuming that the displacement \mathbf{u} can be described by a number of generalized DOFs $\boldsymbol{\eta}$ and there associated shapes $\boldsymbol{\Psi}$:

$$\mathbf{u} = \boldsymbol{\Psi}\boldsymbol{\eta}, \quad (12.3)$$

where the dimension of $\boldsymbol{\eta}$ is much smaller than \mathbf{u} and $\boldsymbol{\Psi}$ is a matrix with a length equal to the length of \mathbf{u} and a width equal to the length of $\boldsymbol{\eta}$. The columns of $\boldsymbol{\Psi}$ must be linearly independent, therefore a good choice seems to be the first n_r eigenvectors of the following eigenvalue problem:

$$-\omega^2 M_{uu}\boldsymbol{\mu} + \mathbf{K}_{uu}^m \boldsymbol{\mu} = 0. \quad (12.4)$$

Substituting equation (12.3) into equation (12.1) gives:

$$M_{uu}\boldsymbol{\Psi}\ddot{\boldsymbol{\eta}} + \mathbf{K}_{uu}^m \boldsymbol{\Psi}\boldsymbol{\eta} = \mathbf{f}^{elec}(\boldsymbol{\Psi}\boldsymbol{\eta}, \phi, V) + \mathbf{r}, \quad (12.5)$$

a set of n_u equations for only n_r DOFs. The vector \mathbf{r} is the residual caused by the fact that part of the feasible solution space is not reachable when the reduced basis is used. Because it is not reachable by the basis this residual must be orthogonal to the basis: $\boldsymbol{\Psi}^T \mathbf{r} = 0$. Therefore this set of equations is projected onto the basis, $\boldsymbol{\Psi}$:

$$\boldsymbol{\Psi}^T M_{uu}\boldsymbol{\Psi}\ddot{\boldsymbol{\eta}} + \boldsymbol{\Psi}^T \mathbf{K}_{uu}^m \boldsymbol{\Psi}\boldsymbol{\eta} = \boldsymbol{\Psi}^T \mathbf{f}^{elec}(\boldsymbol{\Psi}\boldsymbol{\eta}, \phi, V), \quad (12.6)$$

which gives exactly n_r equations of n_r DOFs:

$$M_r\ddot{\boldsymbol{\eta}} + \mathbf{K}_r\boldsymbol{\eta} = \boldsymbol{\Psi}^T \mathbf{f}^{elec}(\boldsymbol{\Psi}\boldsymbol{\eta}, \phi, V). \quad (12.7)$$

Hence modal truncation provides a reduction solution for the linear part of the problem. However the non-linear part is not reduced. Still an electric solution has to be obtained and the forces have to be computed at each time step, which is the key problem. Therefore this chapter is essentially concerned with the reduction of the non-linear part: the right-hand side of equation (12.7).

12.2.2 Laplacian mesh deformation assumption

To simplify the reduction of that right-hand side, the right hand side can be simplified. Therefore, let's return to section 3.6.3. There it was stated that when the mesh

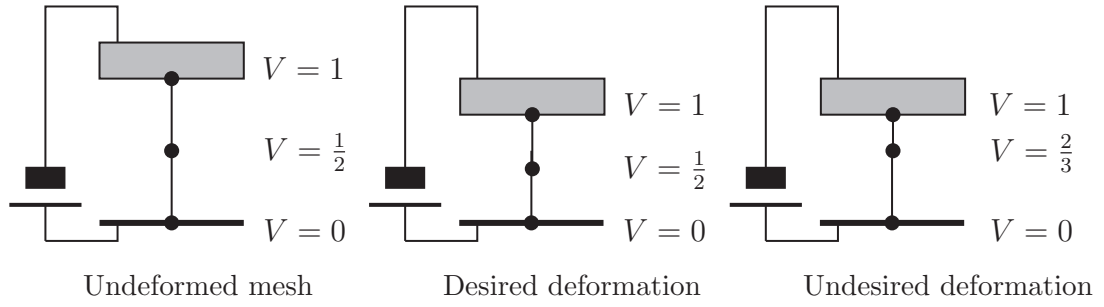


Figure 12.1: Mesh deformation of a one dimensional mesh.

deformation is included within the formulation the problem can be written as (eq: 3.68)

$$\mathbf{K}_{uu}^m \mathbf{u}_m = \mathbf{f}^{elec}(\mathbf{u}_e, \phi, V), \quad (12.8)$$

$$\mathbf{K}_{u_e u_e} \mathbf{u}_e = -\mathbf{K}_{u_e \bar{u}_e} \mathbf{u}_m, \quad (12.9)$$

$$\mathbf{K}_{\phi\phi}(\mathbf{u}_e) \phi = \mathbf{q}^{elec}(\mathbf{u}_e, V). \quad (12.10)$$

where \mathbf{u}_e is the mesh displacement and \mathbf{u}_m the mechanical displacement that is denoted above by \mathbf{u} . After condensing out the mesh deformation the system of equations can be written as:

$$\mathbf{K}_{uu}^m \mathbf{u}_m = \mathbf{f}^{elec}(\mathbf{u}_e(\mathbf{u}_m), \phi, V), \quad (12.11)$$

$$\phi = [\mathbf{K}_{\phi\phi}(\mathbf{u}_e(\mathbf{u}_m))]^{-1} \mathbf{q}^{elec}(\mathbf{u}_e(\mathbf{u}_m), V), \quad (12.12)$$

where the mesh deformation is a function of the mechanical deformation.

The reduction problem would be greatly reduced if that function $\mathbf{u}_e(\mathbf{u}_m)$ would be such that once it is substituted into equation (12.12) the effect would be that:

$$\begin{aligned} \phi &= [\mathbf{K}_{\phi\phi}(\mathbf{u}_e(\mathbf{u}_m))]^{-1} \mathbf{q}^{elec}(\mathbf{u}_e(\mathbf{u}_m), V) = [\mathbf{K}_{\phi\phi}(\mathbf{u}_e(\mathbf{u}_m))]^{-1} \mathbf{K}_{\phi, \bar{\phi}}(\mathbf{u}_e(\mathbf{u}_m)) \hat{\mathbf{1}} V = \\ &= [\mathbf{K}_{\phi\phi}(\mathbf{u}_e(\mathbf{u}_m^0))]^{-1} \mathbf{K}_{\phi, \bar{\phi}}(\mathbf{u}_e(\mathbf{u}_m^0)) \hat{\mathbf{1}} V = \mathbf{K}_{\phi\phi}^{-1} \mathbf{K}_{\phi, \bar{\phi}} \hat{\mathbf{1}} V = \phi_0 V, \end{aligned} \quad (12.13)$$

where:

$$\phi_0 = \mathbf{K}_{\phi\phi}^{-1} \mathbf{K}_{\phi, \bar{\phi}} \hat{\mathbf{1}} \quad (12.14)$$

and $\hat{\mathbf{1}} = [1 \ 1 \ \dots \ 1]^T$ and \mathbf{u}_m^0 is the displacement in the initial configuration. Or in other words, it would simplify the implementation if the mesh deformation equation is chosen such that the nodal potentials do not change if the applied external voltage does not change. In that case the mesh deforms in such a manner that, if the shape of the electrode changes while the voltage remains constant, the nodes relocate such that their potentials remain constant.

The 1D form of such an deformation is shown in figure 12.1, where three configurations are shown, each with an applied potential of 1 volt on the top electrode and 0 volt on the bottom electrode. The problem is discretized with only two elements and therefore three nodes. The left hand configuration shows the original undeformed problem and the middle configuration shows how after deformation the mesh is nicely distributed and the in-between node still has a $\frac{1}{2}$ potential. The right hand side shows a deformation that does not result in the desired potential distribution, because in that case the in-between node has a $\frac{2}{3}$ potential.

The basic simplification assumption is the following: *Using the Laplacian mesh deformation approach, results in a mesh displacement that satisfies the criteria mentioned above.* The Laplacian mesh deformation approach was presented in section 4.2.4 and is repeated below:

$$\nabla^2 \mathbf{u}_m^i = 0, \quad (12.15)$$

where \mathbf{u}_m^i is the mesh deformation in i -direction ($i = x, y, z$). The boundary conditions to this Laplacian problem follow from the structural displacement. Once this mesh deformation is used, this mesh deformation has to be considered during all derivative computations.

Using this mesh deformation assumption the term ϕ_0 can be written as:

$$\phi_0 = \mathbf{K}_{\phi\phi}^{-1}(\mathbf{u}_0)\mathbf{q}(\mathbf{u}_0, V = 1), \quad (12.16)$$

where \mathbf{u}_0 is initial configuration. Remember that the potential distribution is simply: $\phi = \phi_0 V$, therefore the coupled equation can be written as:

$$\mathbf{M}_r \ddot{\boldsymbol{\eta}} + \mathbf{K}_r \boldsymbol{\eta} = \boldsymbol{\Psi}^T \mathbf{f}^{elec}(\boldsymbol{\Psi}\boldsymbol{\eta}, \phi(V), V). \quad (12.17)$$

12.3 Step response reduction

In this section the problem is simplified even more by looking at step responses only. In that case the applied voltage V is zero before time $t = 0$ and constant but non zero for $t > 0$. Since nothing happens when $t < 0$, it is only required to simulate for $t > 0$ with initial conditions equal to the equilibrium displacement for $V = 0$. Because V does not change equation (12.17) for $t > 0$, it can be simplified to:

$$\mathbf{M}_r \ddot{\boldsymbol{\eta}} + \mathbf{K}_r \boldsymbol{\eta} = \boldsymbol{\Psi}^T \mathbf{f}^{elec}(\boldsymbol{\Psi}\boldsymbol{\eta}). \quad (12.18)$$

In that case three options will be developed. When the first option is used the right-hand side is not reduced at all. For a mechanical FEM model combined with simple parallel plate capacitor elements this approach was followed by [132]. The second approach is using a Taylor expansion of the right-hand side with respect to the modal displacement. The used Taylor expansions are either first or second order. For a simple non linear beam model (non-FEM) a similar approach was presented in [23]. The last method is a combination of a second order Taylor with a variable centering point and a first order Taylor method to estimate the error.

The methods will be tested on the FEM example also used in sections 7.5 and 9.5: a deformable plate suspended above an air gap. The plate is $250\mu m$ long by $30\mu m$ wide, $1\mu m$ thick and the air gap is 2 microns. The plate is meshed with a 25 by 10 mesh of plate elements giving 792 DOFs. The electric domain is meshed with 25 by 10 by 8 elements giving 2002 DOFs. The static pull-in value of this beam is about 21.4 V. More info on such a plate above air gap model can be found in chapter 4.

The reduction basis $\boldsymbol{\Psi}$ is formed from the first 6 eigenmodes of the uncoupled mechanical problem. This means that only the first 3 symmetric modes actually contribute to the motion due to the fact that this clamped-clamped beam will not show asymmetric behavior.

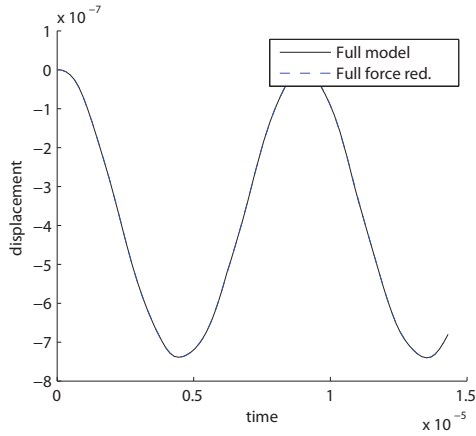


Figure 12.2: Step response of 18V for the full force reduction

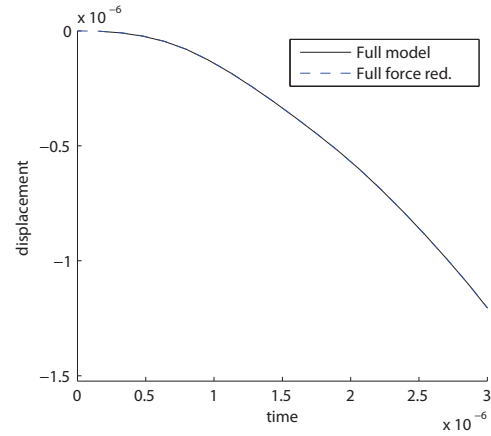


Figure 12.3: Step response of 24V for the full force reduction

12.3.1 Full force vector

The first option is to actually compute $\mathbf{f}^{elec}(\boldsymbol{\eta})$ and not reduce it. Due to the linear relation between mesh displacement and structural displacement the electric displacement is described by:

$$\mathbf{u}_e(\boldsymbol{\eta}) = \mathbf{K}_{u_e u_e}^{-1} \mathbf{K}_{u_e \bar{u}_e} \boldsymbol{\Psi} \boldsymbol{\eta} = \mathbf{K}_{u_e r} \boldsymbol{\eta}, \quad (12.19)$$

where $\mathbf{K}_{u_e r}$ is n_e by n_r sized matrix, hence not too large. When a computation of the electric force is required during the time integration $\mathbf{u}_e(\boldsymbol{\eta})$ is computed using the relation above. The nodal voltage vector $\boldsymbol{\phi}(V)$ is constant and can be computed before the time integration procedure is started. Hence it is possible at a certain displacement to loop over the interface elements to compute the electric force:

$$\mathbf{f}^{elec}(\mathbf{u}_e, \boldsymbol{\phi}). \quad (12.20)$$

This removes the need to solve both the full electric and mechanic matrix equation, but still the expensive loop over all interface electric elements to compute the full force vector has to be performed every time step. Hence the expected speed-up of the computation is limited. This reduction was applied on the reference FEM problem with the 6 mode basis, of which the results with 2 different step voltages are presented in figures 12.2 and 12.3. The figures show that this method is highly accurate, however the time gain is indeed limited. Remember that the full model required 2600 seconds, this method requires about 35 seconds to generate all the matrices and about 620 seconds to compute the solution.

12.3.2 A first order Taylor expansion of the force

The force is linearized with respect to the displacement terms:

$$\boldsymbol{\Psi}^T \mathbf{f}^{elec} \approx \boldsymbol{\Psi}^T \mathbf{f}^{elec}(\mathbf{u}_0, \boldsymbol{\phi}_0) + \boldsymbol{\Psi}^T \frac{\partial \mathbf{f}^{elec}}{\partial \boldsymbol{\eta}} \boldsymbol{\eta}. \quad (12.21)$$

which can be written as:

$$\frac{\partial \mathbf{f}^{elec}}{\partial \boldsymbol{\eta}} \approx \frac{\partial \mathbf{f}^{elec}}{\partial \mathbf{u}} \boldsymbol{\Psi} = \mathbf{K}_{uu}^e \boldsymbol{\Psi}, \quad (12.22)$$

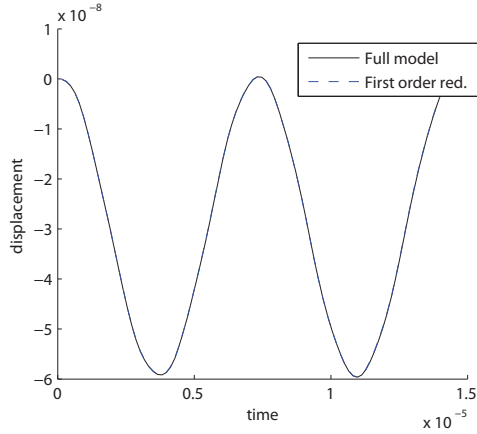


Figure 12.4: Step response of 6V for the first order reduction

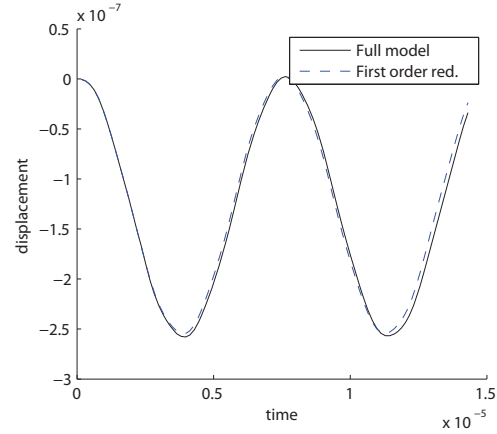


Figure 12.5: Step response of 12V for the first order reduction

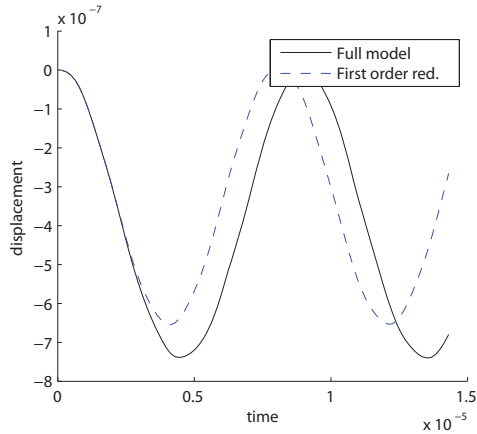


Figure 12.6: Step response of 18V for the first order reduction

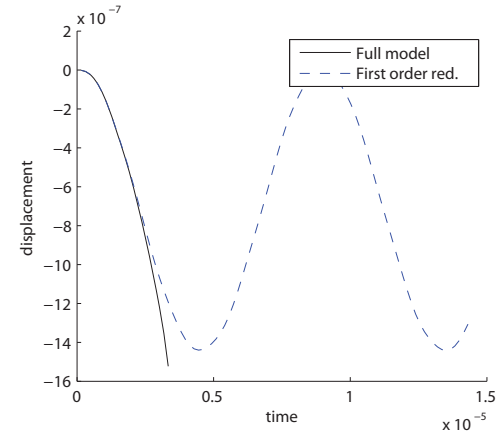


Figure 12.7: Step response of 24V for the first order reduction

where the \mathbf{K}_{uu}^e has been defined in chapter 3 ¹.

The step responses of the reduced model are compared with the full model for several different voltages: $V = 6, 12, 18, 24V$. The results are presented in figures 12.4 to 12.7.

From these figures it is clear that the response for low voltage steps is really accurate, but for a 12 volt excitation (30% of pull-in) some inaccuracies appear and near and above pull-in it really fails, not pulling in well above the pull-in voltage. Because the forcing term $f^{elec}(\phi)$ still depends nonlinearly on the applied voltage, hence in the end this first order approach will show a kind of pull-in behavior, but for a much higher potential than the actual pull-in voltage. The time benefit is incredible though. For the 6 volts excitation the full model (implemented in Matlab) took about 2600 seconds on a 2GHz, 2GB desktop computer to compute the plotted 90 time steps. The reduced model needed 31 seconds to generate the reduced matrices, after which

¹This right hand side is simple due the fact that the displacement of internal nodes due to mesh deformation was included in the derivation. Whether or not these have been included it can be shown that $\frac{\partial f^{elec}}{\partial \eta} = (\mathbf{K}_{uu}^e - \mathbf{K}_{u\phi} \mathbf{K}_{\phi\phi}^{-1} \mathbf{K}_{\phi u}) \Psi$. If the displacement of internal nodes is included and the Laplacian mesh deformation algorithm is used, the Schur complement $-\mathbf{K}_{u\phi} \mathbf{K}_{\phi\phi}^{-1} \mathbf{K}_{\phi u}$ will be very close to zero.

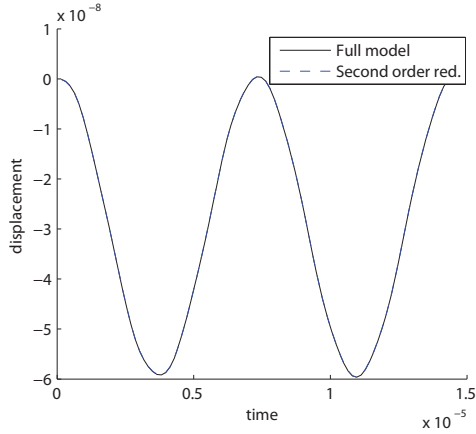


Figure 12.8: Step response of 6V for the second order reduction

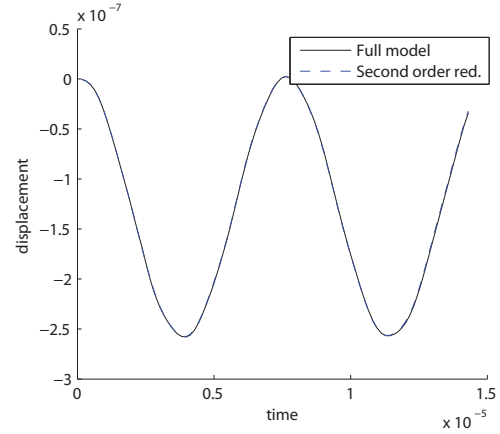


Figure 12.9: Step response of 12V for the second order reduction

the time integration was performed in less than 0.3 seconds.

12.3.3 A second order Taylor expansion of the force

To have some accuracy approaching pull-in, but without the computational cost, the right-hand side is approximated with a second order Taylor polynomial:

$$\Psi^T \mathbf{f}^{elec} = \Psi^T \mathbf{f}^{elec}(\phi_0) + \Psi^T \frac{\partial \mathbf{f}^{elec}}{\partial \boldsymbol{\eta}} \boldsymbol{\eta} + \frac{1}{2} \Psi^T \frac{\partial^2 \mathbf{f}^{elec}}{\partial \boldsymbol{\eta}^2} \boldsymbol{\eta}^2, \quad (12.23)$$

where the ‘third order matrix’:

$$\frac{\partial^2 \mathbf{f}^{elec}}{\partial \boldsymbol{\eta}^2}, \quad (12.24)$$

is essentially a reduction of:

$$\frac{\partial^2 \mathbf{f}^{elec}}{\partial \mathbf{u}^2} = \frac{\partial \mathbf{K}_{uu}^e}{\partial \mathbf{u}}, \quad (12.25)$$

which has been evaluated in section 6.3 for the computation of the second order sensitivity of the static pull-in voltage.

After evaluation the term $\Psi^T \frac{\partial^2 \mathbf{f}^{elec}}{\partial \boldsymbol{\eta}^2}$ will be a three dimensional array with dimensions n_r by n_r by n_r , which will not give a storage problem if $n_r \ll n_u$.

This approach was tested again for the reference FEM problem, for which the results are presented in figure 12.8 to 12.11. The 6 and 12 volt simulations are fully accurate. This contrasts with the 12 volt response of the first order approach, which was already somewhat inaccurate. The 18 volt is not accurate anymore, but the 24 volt simulation shows that the pull-in voltage computed with this method is smaller than 24 volts (the actual value is 21.4) .

The impact on the computation time is really positive. It took about 60 seconds to generate all matrices but the time integration lasted less than 0.4 second.

12.3.4 A piecewise quadratic Taylor approach

Above it was seen that the first order Taylor approximation works until 6 volts and the second order until 12 volts. However both methods had problems with the 18 volt

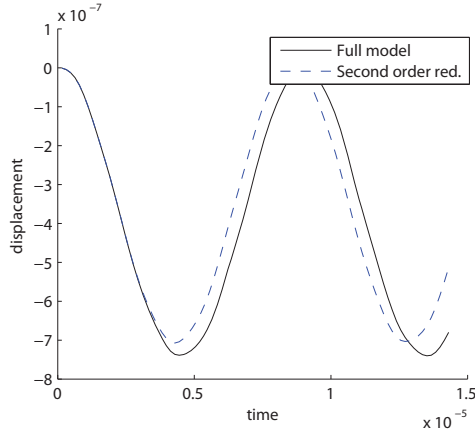


Figure 12.10: Step response of 18V for the second order reduction

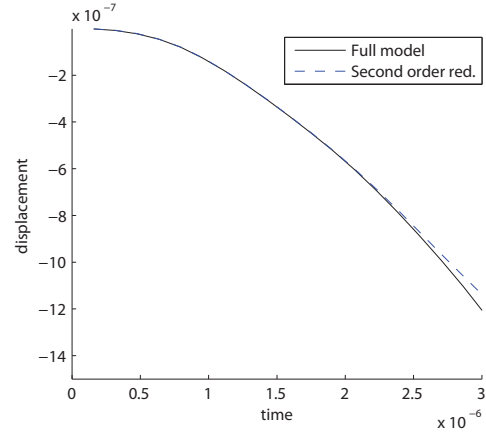


Figure 12.11: Step response of 24V for the second order reduction

load and could not provide an accurate estimation of dynamic pull-in. The problem is the limited region in which the Taylor approximation is accurate.

However, there is no rule that says that the same center point for the Taylor approach has to be used for the complete simulation. If the error could be measured a point at which the accuracy of the second order Taylor approximation is no longer sufficient called η_c could be computed. Subsequently the new derivatives $\frac{\partial f}{\partial \eta}$ and $\frac{\partial^2 f}{\partial \eta^2}$ could be evaluated at η_c and from that point on the force would be computed with:

$$f^{elec} = f(u_0 + \Psi \eta_c, \phi_0)|_{\eta_c} + \frac{\partial f}{\partial \eta} \Big|_{\eta_c} (\eta - \eta_c) + \frac{1}{2} \frac{\partial^2 f}{\partial \eta^2} \Big|_{\eta_c} (\eta - \eta_c)^2, \quad (12.26)$$

until the error becomes too big again. This procedure could be repeated several times.

The remaining problem is the determination of the error ϵ . An easy method is to compare a solution obtained with the first order method η_1 with one obtained with the second order method η_2 :

$$\epsilon = \frac{|\eta_2| - |\eta_1|}{|\eta_2|}. \quad (12.27)$$

This is an accurate estimate of the error made by the first order approach and it is assumed that its indication of the error made by the second order approach is good enough.

The combination of this error estimator with updating of the Taylor center point provides the algorithm as presented in figure 12.12. This method was used to compute the curves in figures 12.13 and 12.14. The points where the error became too big and a re-computation of the Taylor terms was performed are indicated. The error tolerance for re-computation of the Taylor expansion was $1 \cdot 10^{-2}$. It is clear that the method is more accurate than the Taylor approaches, however there is a price to pay.

The first initialization of this model costs about 60 seconds. The reinitialization of the Taylor terms costs about 40 seconds for the used model. This computation times caused the total time to compute the curve of figure 12.13 to be $320 + 60 = 380$ seconds. The 320 seconds were mainly caused by the 8 reinitialization procedures. However this 380 second computation time is still considerably shorter than the 700 seconds required by the full force reduction algorithm. Furthermore the full-force computation time is almost independent from the applied voltage step, where this method needs less reinitialization for lower voltage step.

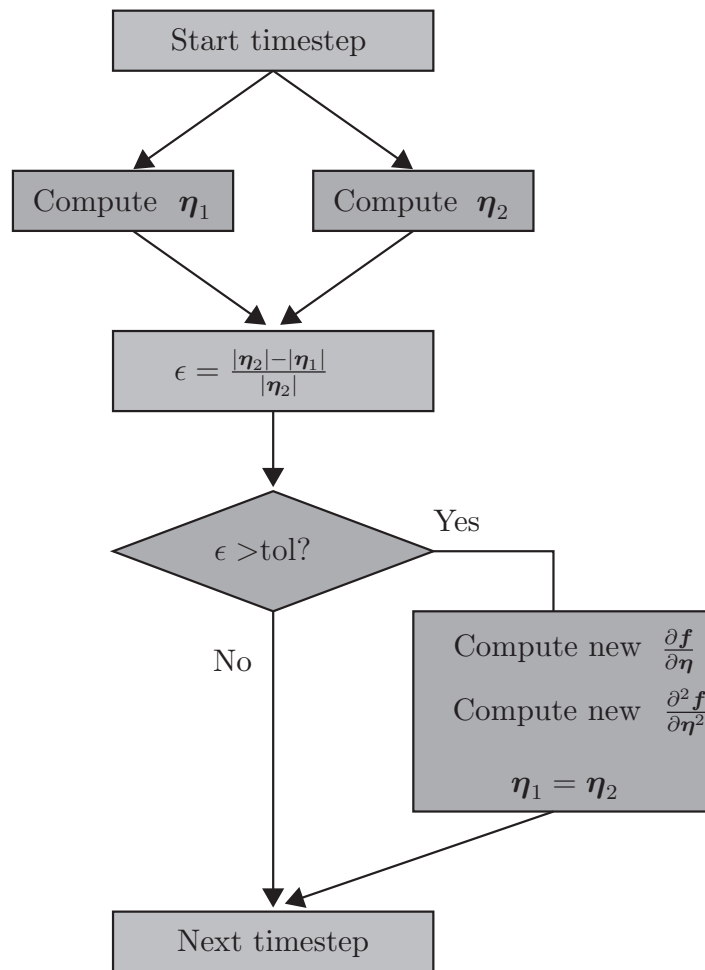


Figure 12.12: The piecewise quadratic Taylor reduction approach

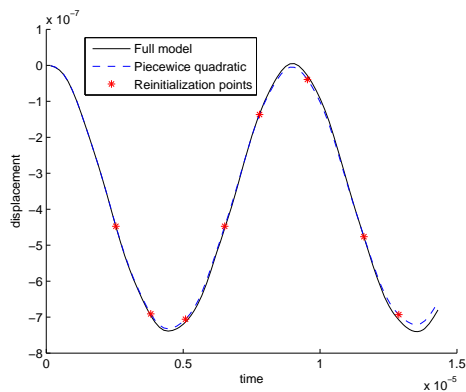


Figure 12.13: Step response of 18V for the piecewise quadratic reduction (error tolerance $1 \cdot 10^{-2}$)

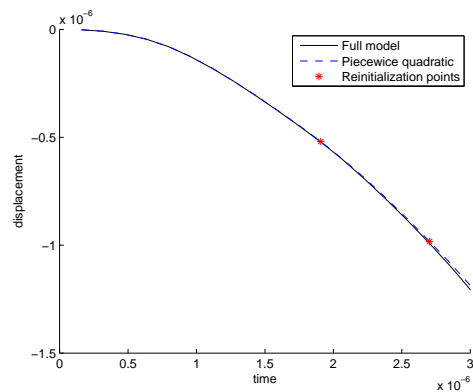


Figure 12.14: Step response of 24V for the piecewise quadratic reduction (error tolerance $1 \cdot 10^{-2}$)

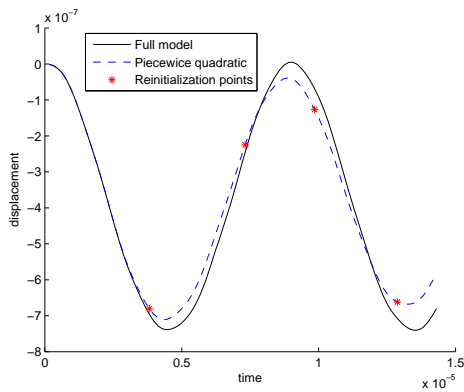


Figure 12.15: Step response of 18V for the piecewise quadratic reduction (error tolerance $5 \cdot 10^{-2}$)

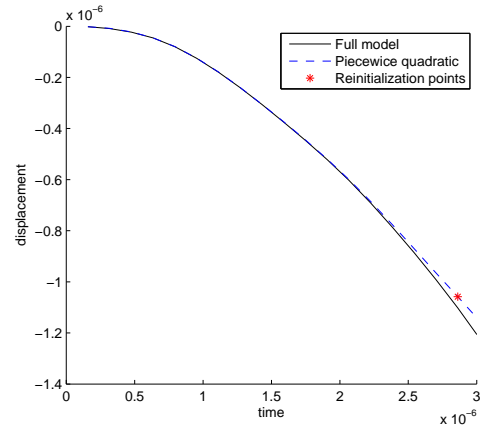


Figure 12.16: Step response of 24V for the piecewise quadratic reduction (error tolerance $5 \cdot 10^{-2}$)

An approach to reduce time is to change the error tolerance. This is investigated in figures 12.15 and 12.16, which were computed with an error of $5 \cdot 10^{-2}$. Clearly the accuracy is less, but the 18 volt step costs only 210 seconds. The frequency of the response is better than the normal second order Taylor method, however the amplitude is less good.

Artificial frequencies could be created in the response due to the fact that at a reinitialization point the force as a function of time will show a discontinuity. However, due to the reduction only a limited number of modes and frequencies will present in the response, therefore this does not seem to be problematic.

From figure 12.13 can also be seen that the accuracy decreases over simulation time. Hence the first dip is accurate but the second one is less accurate. Because the first dip is accurate and dynamic pull-in occurs when the first dip is too low, this method is very effective for dynamic pull-in computations.

A disadvantage of this accuracy loss over time is that it creates artificial damping. Furthermore this method is ill suited for long term simulations due to this accuracy loss. It is also ill suited for harmonic analyses, because as can be seen in figure 12.13 the Taylor terms are computed at approximately the same displacement three times, hence the same information is generated three times. If a harmonic analysis is done, a sinusoidal solution is expected and this should be used to avoid recomputing the basis at the same point. An approach to tackle that problem could be to combine this method with the trust region approach as presented in [104].

If static modes are used in stead of dynamic modes, the static problem can be reduced as well using the Taylor series based approaches. However, they cannot predict pull-in accurately, because the force is inaccurate for large displacement. Therefore they are not very useful for static analyses. But the piecewise quadratic Taylor approach was accurate for dynamic pull-in. On the other hand: it was computationally expensive. It would be interesting to see if the method is efficient for static problems as well.

12.4 Time varying applied potential

So far only step responses were studied, however a lot of the circuit type of simulations for which model reduction is required are interested in the response as a function of a time varying potential $V = V(t)$. The voltage distribution $\phi(t)$ depends linearly on $V(t)$, therefore one way of including a time varying load is by using:

$$\phi(t) = \mathbf{K}_{\phi\phi}^{-1} \mathbf{q} = -\mathbf{K}_{\phi\phi}^{-1} \mathbf{K}_{\phi\bar{\phi}} \begin{bmatrix} 1 \\ \vdots \\ 1 \end{bmatrix} V(t) = \phi_0 V(t). \quad (12.28)$$

Basically this defines ϕ and can be directly used in the full force reduction algorithm. This means that the equations under consideration can be written as:

$$\mathbf{M}_r \ddot{\boldsymbol{\eta}} + \mathbf{K}_r \boldsymbol{\eta} = \boldsymbol{\Psi}^T \mathbf{f}^{elec}(\boldsymbol{\eta}, V(t)). \quad (12.29)$$

The full force approach will not change considerably when this equation is used in stead of (12.18).

The Taylor based approach does change, as can be seen below where the full expansion of the right hand side is given:

$$\begin{aligned} \mathbf{f}^{elec}(\boldsymbol{\eta}, V(t)) &\approx \mathbf{f}^{elec}(\mathbf{u}_0, V_0) + \left. \frac{\partial \mathbf{f}}{\partial \boldsymbol{\eta}} \right|_{\mathbf{u}_0, V_0} \tilde{\boldsymbol{\eta}} + \left. \frac{\partial \mathbf{f}}{\partial V} \right|_{\mathbf{u}_0, V_0} \tilde{V}(t) \\ &\quad + \frac{1}{2} \left. \frac{\partial^2 \mathbf{f}}{\partial \boldsymbol{\eta}^2} \right|_{\mathbf{u}_0, V_0} \tilde{\boldsymbol{\eta}}^2 + \left. \frac{\partial^2 \mathbf{f}}{\partial \boldsymbol{\eta} \partial V} \right|_{\mathbf{u}_0, V_0} \tilde{\boldsymbol{\eta}} \tilde{V}(t) + \frac{1}{2} \left. \frac{\partial^2 \mathbf{f}}{\partial V^2} \right|_{\mathbf{u}_0, V_0} \tilde{V}^2(t) \\ &\quad + \frac{1}{6} \left. \frac{\partial^3 \mathbf{f}}{\partial \boldsymbol{\eta}^3} \right|_{\mathbf{u}_0, V_0} \tilde{\boldsymbol{\eta}}^3 + \frac{1}{6} \left. \frac{\partial^3 \mathbf{f}}{\partial \boldsymbol{\eta}^2 \partial V} \right|_{\mathbf{u}_0, V_0} \tilde{\boldsymbol{\eta}}^2 \tilde{V}(t) + \frac{1}{6} \left. \frac{\partial^3 \mathbf{f}}{\partial \boldsymbol{\eta} \partial V^2} \right|_{\mathbf{u}_0, V_0} \tilde{\boldsymbol{\eta}} \tilde{V}^2(t) \\ &\quad + \frac{1}{6} \left. \frac{\partial^3 \mathbf{f}}{\partial V^3} \right|_{\mathbf{u}_0, V_0} \tilde{V}^3(t) + \frac{1}{24} \left. \frac{\partial^4 \mathbf{f}}{\partial \boldsymbol{\eta}^4} \right|_{\mathbf{u}_0, V_0} \tilde{\boldsymbol{\eta}}^4 + \frac{1}{24} \left. \frac{\partial^4 \mathbf{f}}{\partial \boldsymbol{\eta}^3 \partial V} \right|_{\mathbf{u}_0, V_0} \tilde{\boldsymbol{\eta}}^3 \tilde{V}(t) \\ &\quad + \frac{1}{12} \left. \frac{\partial^4 \mathbf{f}}{\partial \boldsymbol{\eta}^2 \partial V^2} \right|_{\mathbf{u}_0, V_0} \tilde{\boldsymbol{\eta}}^2 \tilde{V}^2(t) + \frac{1}{24} \left. \frac{\partial^4 \mathbf{f}}{\partial \boldsymbol{\eta} \partial V^3} \right|_{\mathbf{u}_0, V_0} \tilde{\boldsymbol{\eta}} \tilde{V}^3(t) + \frac{1}{24} \left. \frac{\partial^4 \mathbf{f}}{\partial V^4} \right|_{\mathbf{u}_0, V_0} \tilde{V}^4(t), \quad (12.30) \end{aligned}$$

where:

$$\tilde{V}(t) = V(t) - V_0, \quad (12.31)$$

$$\tilde{\boldsymbol{\eta}} = \boldsymbol{\eta} - \boldsymbol{\eta}_0, \quad (12.32)$$

where $\boldsymbol{\eta}_0$ is defined by:

$$\mathbf{u}_0 \approx \boldsymbol{\Psi} \boldsymbol{\eta}_0. \quad (12.33)$$

The starting point of this Taylor expansion can be any combination of \mathbf{u}_0 and V_0 . Two terms in this expansion were seen before: $\left. \frac{\partial \mathbf{f}}{\partial \boldsymbol{\eta}} \right|_{\mathbf{u}_0, V_0}$, which is the linear electric stiffness and $\left. \frac{\partial^2 \mathbf{f}}{\partial \boldsymbol{\eta}^2} \right|_{\mathbf{u}_0, V_0}$, the second order derivative of the force.

The trivial full force algorithm will first be tested below. Thereafter several variants of the Taylor based approach will be developed and tested. The difference between the Taylor variants will be the number of included terms and the combination of \mathbf{u}_0 and V_0 .

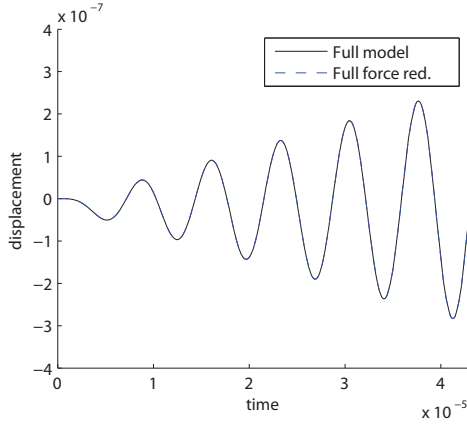


Figure 12.17: Sinusoidal response of 6V for the full force reduction

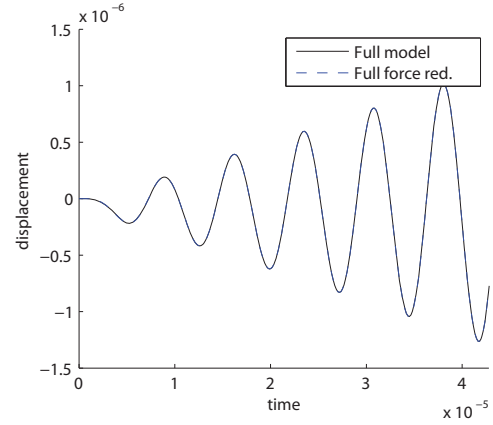


Figure 12.18: Sinusoidal response of 12V for the full force reduction

12.4.1 Full force algorithm

The full force algorithm (12.20) for time varying loads is not more complicated than the one for step responses, because instead of a constant $\phi(V)$ a time varying $\phi(V(t)) = \phi_0 V(t)$ can be used in the algorithm. Of course the time benefits will be limited. The method is tested with the FEM model used before. The applied load is:

$$V(t) = V_0 \cdot \sin(\Omega t), \quad (12.34)$$

where a V_0 of 6 and 12 is used and Ω is chosen to be half the lowest mechanical resonance frequency. For a better understanding of the graphs: this means that $\Omega = 4.4 \cdot 10^5 \text{ rad/s}$ and the period of the excitation $T = 1.43 \cdot 10^{-5}$ seconds. The resulting curves are shown in figures 12.17 and 12.18. Clearly this method is extremely accurate, and also extremely versatile, any signal $V(t)$ can be inserted into the model without problems. The full model simulations took each about 5 and a quarter hours to compute where the reduced models took only 30 minutes to compute. A big reduction, though it still takes a rather long time.

12.4.2 Force reduction

Because the full force reduction still requires a considerable amount of time another way of finding $\mathbf{f}^{elec}(\mathbf{u}_0, V)$ is necessary, because computing $\mathbf{f}^{elec}(\mathbf{u}_0)$ every time that $V(t)$ changes can become expensive for complicated loading voltages. Therefore the following relation will be used, which uses the first two voltage derivatives of the Taylor expansion (12.30):

$$\mathbf{f}^{elec}(\mathbf{u}_0, \phi(V(t)), V(t)) = \left. \frac{\partial \mathbf{f}}{\partial V} \right|_{V=0} V(t) + \frac{1}{2} \left. \frac{\partial^2 \mathbf{f}}{\partial V^2} \right|_{V=0} V^2(t), \quad (12.35)$$

Chapter 9 showed that the first derivative can be computed with:

$$\frac{\partial \mathbf{f}}{\partial V} = [\mathbf{K}_{u\bar{\phi}} - \mathbf{K}_{u\phi} \mathbf{K}_{\phi\phi}^{-1} \mathbf{K}_{\phi\bar{\phi}}] \begin{bmatrix} 1 \\ \vdots \\ 1 \end{bmatrix}. \quad (12.36)$$

The second derivative can be computed by using² :

$$\frac{\hat{\partial}^2 \mathbf{f}(\boldsymbol{\eta}, \phi(V), V)}{\partial V^2} = \frac{\partial^2 \mathbf{f}}{\partial V^2} \Big|_{\phi=\text{const}} + \frac{\partial^2 \mathbf{f}}{\partial \phi \partial V} \Big|_{V=\text{const}} \frac{\partial \phi}{\partial V}, \quad (12.37)$$

which requires derivatives of the matrices used in (12.36) with ϕ and $\bar{\phi}$ which have been discussed in section 6.3.

It can be shown that around $V = 0$ the first derivative is zero, simplifying equation (12.35) to³:

$$\mathbf{f}^{elec}(t, \mathbf{u}_0) = \frac{1}{2} \frac{\partial^2 \mathbf{f}}{\partial V^2} \Big|_{V=0} V^2(t), \quad (12.38)$$

After projection onto the reduction basis, this only requires an n_r long vector to store.

This provides the exact relation for computing the zero displacement force as a function of the applied voltage⁴. However reducing the electrostatic forcing term is not as simple as stating:

$$\boldsymbol{\Psi}^T \mathbf{f}^{elec}(V, \boldsymbol{\eta}) = \boldsymbol{\Psi}^T \mathbf{f}^{elec}(\phi, V) + \boldsymbol{\Psi}^T \frac{\partial \mathbf{f}^{elec}}{\partial \boldsymbol{\eta}} \boldsymbol{\eta} \Big|_{V=0} + \text{h.o.t.}, \quad (12.39)$$

because the term $\frac{\partial \mathbf{f}^{elec}}{\partial \boldsymbol{\eta}}$ is highly dependent on V and even more problematic: it is zero when $V = 0$. Evaluating this term at each time step is of course impossible, therefore another approach is needed. The next two subsections will investigate two such approaches: finding the behavior around an equilibrium in section 12.4.3 and derivative based nonlinear behavior in section 12.4.4.

12.4.3 Approach for biased sinusoidal loads

Often electromechanical systems such as resonators have a specific mode of operation: the load is a constant bias load around which a relatively small oscillating driving voltage is used:

$$V(t) = V_{DC} + V_{AC}(t), \quad (12.40)$$

where:

$$V_{AC} \ll V_{DC}. \quad (12.41)$$

In that case it is assumed that the motion can be described as a small motion around the equilibrium displacement \mathbf{u}_{eq} , which is the static displacement that results from the V_{DC} load defined as:

$$\mathbf{f}^{elec}(V_{DC}, \mathbf{u}_{eq}) - \mathbf{K}_{uu}^m \mathbf{u}_{eq} = 0. \quad (12.42)$$

This allows the displacement to be written as:

$$\mathbf{u} = \mathbf{u}_{eq} + \boldsymbol{\Psi} \tilde{\boldsymbol{\eta}}, \quad (12.43)$$

²The hat notation was defined in section 3.6.3. It defines the derivative of \mathbf{f} with a parameter, which is present as one of the three arguments of the equation as well as indirectly through one of the other arguments.

³This can be shown for a 1D problem very easy. In that case $f^{elec} = \frac{1}{2} \varepsilon \frac{V^2}{x_0^2}$, for which $\frac{\partial f^{elec}}{\partial V} = \varepsilon \frac{V}{x_0^2}$ which is zero for $V = 0$. The second derivative is: $\frac{\partial^2 f^{elec}}{\partial V^2} = \varepsilon \frac{1}{x_0^2}$, which is not zero if $V = 0$.

⁴Again easily shown for a 1D problem: $\frac{1}{2} \cdot \frac{\partial^2 f^{elec}}{\partial V^2} \cdot V^2 = \frac{1}{2} \varepsilon \frac{V^2}{x_0^2}$, which is the exact force.

and the acceleration as:

$$\ddot{\mathbf{u}} = \Psi \ddot{\tilde{\boldsymbol{\eta}}}. \quad (12.44)$$

The modal basis Ψ is constructed used the uncoupled modes.

The next step is to assume that if $V_{AC} \ll V_{DC}$, the derivative of forces with displacement only depends on the static part of the voltage:

$$\frac{\partial \mathbf{f}^{elec}(V)}{\partial \tilde{\boldsymbol{\eta}}} \approx \frac{\partial \mathbf{f}^{elec}(V_{DC})}{\partial \tilde{\boldsymbol{\eta}}}, \quad (12.45)$$

which has to be evaluated at the equilibrium displacement for maximum accuracy. If only this first order displacement sensitivity is used for determining the right-hand side and the equilibrium condition (12.42) is used, one finds the following relation (linear in $\tilde{\boldsymbol{\eta}}$, but non linear in $V_{AC}(t)$):

$$\mathbf{M}_r \ddot{\tilde{\boldsymbol{\eta}}} + \mathbf{K}_r \tilde{\boldsymbol{\eta}} = \Psi^T \left(\frac{1}{2} \frac{\partial^2 \mathbf{f}}{\partial V^2} \Big|_{\mathbf{u}_{eq}} V_{AC}^2 + \frac{\partial \mathbf{f}^{elec}}{\partial \tilde{\boldsymbol{\eta}}} \Big|_{V_{DC}, \mathbf{u}_{eq}} \tilde{\boldsymbol{\eta}} \right), \quad (12.46)$$

This first order displacement approach has already been used before (e.g. [131]) and has been implemented in commercial FEM codes.

However, because this equation already requires a non linear time integration algorithm, it can be expanded with the second order displacement term without significantly increasing the integration time. This increases the applicability to a large extend. The following relation gives the reduced model including this second order term:

$$\mathbf{M}_r \ddot{\tilde{\boldsymbol{\eta}}} + \mathbf{K}_r \tilde{\boldsymbol{\eta}} = \Psi^T \left(\frac{1}{2} \frac{\partial^2 \mathbf{f}}{\partial V^2} \Big|_{V=0, \mathbf{u}_{eq}} (V^2 - V_{DC}^2) + \frac{\partial \mathbf{f}^{elec}}{\partial \boldsymbol{\eta}} \Big|_{V_{DC}, \mathbf{u}_{eq}} \tilde{\boldsymbol{\eta}} + \frac{1}{2} \frac{\partial^2 \mathbf{f}^{elec}}{\partial \boldsymbol{\eta}^2} \Big|_{V_{DC}, \mathbf{u}_{eq}} \tilde{\boldsymbol{\eta}}^2 \right), \quad (12.47)$$

where the term $(V^2 - V_{DC}^2)$ follows from the fact that the mechanical force should be $\mathbf{K}_r(\boldsymbol{\eta}_{eq} + \tilde{\boldsymbol{\eta}})$, however the constant term $\mathbf{K}_r \boldsymbol{\eta}_{eq}$ has been removed from the left-hand side of the equation. Therefore, through the the bias equilibrium condition:

$$\frac{1}{2} \frac{\partial^2 \mathbf{f}}{\partial V^2} \Big|_{V=0, \mathbf{u}_{eq}} V_{DC}^2 = \Psi^T \mathbf{f}^{elec}(\mathbf{u}_{eq}, V_{DC}) = \mathbf{K}_r \boldsymbol{\eta}_{eq}, \quad (12.48)$$

the term:

$$\frac{1}{2} \frac{\partial^2 \mathbf{f}}{\partial V^2} \Big|_{V=0, \mathbf{u}_{eq}} V_{DC}^2,$$

has to be removed on the right-hand side.

These two approaches are tested with the FEM model and the following load:

$$V(t) = 15 + V_{AC} \cdot \sin(\Omega t), \quad (12.49)$$

where Ω is half the lowest mechanical resonance frequency (thus an excitation period of $1.43 \cdot 10^{-5}$ s). The results are shown in figure 12.19 and 12.20 for $V_{AC} = 1$ and $V_{AC} = 2$ respectively. These alternating actuation voltages are not much smaller than the bias component, but definitely smaller. The term linear (first order) or non linear (second

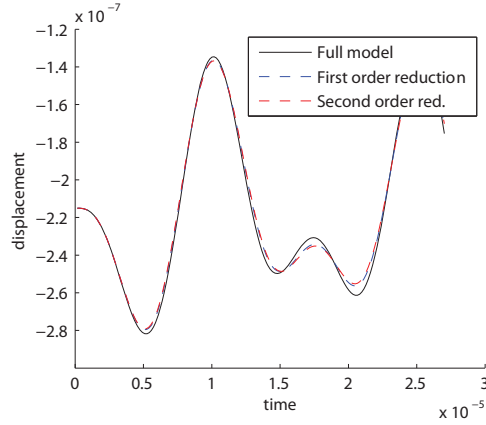


Figure 12.19: Response of $V = 15 + 1 \cdot \sin(\Omega t)$ for the two reduction methods

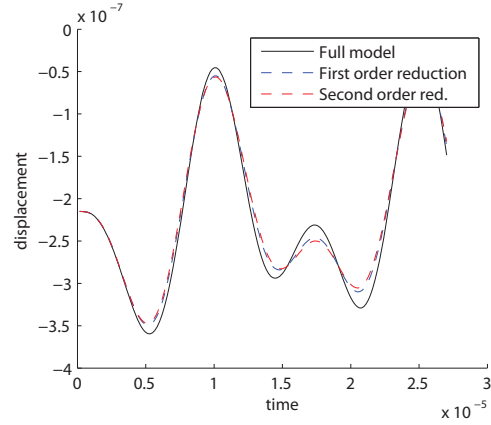


Figure 12.20: Response of $V = 15 + 2 \cdot \sin(\Omega t)$ for the two reduction methods

order) in the figures indicates the linearity of the force with respect to displacement. They are both non-linear with respect to the applied potential.

The results show that both methods are pretty accurate for the 1 Volt AC load, though the quadratic one is a little more accurate. For the 2 volt AC part both methods are clearly more off, although the non linear one is a little less wrong. The computation time required to solve the full non linear static problem to find equilibrium and determine the reduced matrices is about 140 seconds for the linear one and 165 seconds for the quadratic one. Time integration requires about 0.5 seconds for both approaches. The full model required 3.5 hours for the total time integration. From the figure it is clear that the error made by the reduction hardly reduced by the addition of a second order term. It will be shown later that this error is mainly due to the dependency of the derivatives $(\frac{\partial \mathbf{f}}{\partial \mathbf{u}}, \frac{\partial^2 \mathbf{f}}{\partial \mathbf{u}^2})$ on the applied potential V .

12.4.4 Approach for random loads

When the DC plus AC assumption cannot be made another approach should be used. Let's assume that the applied voltage is $V(t)$. In that case the right-hand side can be written as:

$$\mathbf{f}^{elec}(\mathbf{u}, V) = \frac{1}{2} \frac{\partial^2 \mathbf{f}^{elec}(\mathbf{u})}{\partial V^2} \Big|_{V=0} V^2. \quad (12.50)$$

If the initial displacement is substituted into this equation and the resulting term used to approximate the force, one finds a force reduction which is constant with respect to displacement:

$$\mathbf{f}^{elec}(\mathbf{u}, V) = \frac{1}{2} \frac{\partial^2 \mathbf{f}^{elec}(\mathbf{u})}{\partial V^2} \Big|_{V=0, \mathbf{u}=0} V^2. \quad (12.51)$$

which assumes that the non-linearity can be described by the quadratic relation between applied voltage and zero displacement force only. Adding Taylor terms leads to the first order force approximation:

$$\mathbf{f}^{elec}(\mathbf{u}, V) = \frac{1}{2} \frac{\partial^2 \mathbf{f}^{elec}}{\partial V^2} \Big|_{V=0, \mathbf{u}=0} V^2 + \frac{1}{2} \frac{\partial^3 \mathbf{f}^{elec}}{\partial V^2 \partial \mathbf{u}} \Big|_{V=0, \mathbf{u}=0} V^2 \mathbf{u}, \quad (12.52)$$

and one could go one step further and make the force second order in \mathbf{u} :

$$\mathbf{f}^{elec}(\mathbf{u}, V) \approx \frac{1}{2} \left. \frac{\partial^2 \mathbf{f}^{elec}}{\partial V^2} \right|_{V=0, \mathbf{u}=0} V^2 + \frac{1}{2} \left. \frac{\partial^3 \mathbf{f}^{elec}}{\partial V^2 \partial \mathbf{u}} \right|_{V=0, \mathbf{u}=0} V^2 \mathbf{u} + \frac{1}{4} \left. \frac{\partial^4 \mathbf{f}^{elec}}{\partial V^2 \partial \mathbf{u}^2} \right|_{V=0, \mathbf{u}=0} V^2 \mathbf{u}^2. \quad (12.53)$$

The last equation includes all the terms of the Taylor expansion (12.30) as presented before that are non-zero when it is expanded around a zero voltage.

These three force equations define three Taylor approach based reduction strategies. The standard one, which is sometimes implemented in commercial FEM codes, is defined by (12.51). It provides a constant relation between force and displacement. However, this thesis proposes to use the linear displacement correction (12.52) or the non linear correction (12.53) for more accuracy when the applied voltage is high.

The derivatives are determined by starting with the elemental definitions of $\frac{\partial \mathbf{f}^{elec}}{\partial \mathbf{u}}$ and $\frac{\partial^2 \mathbf{f}^{elec}}{\partial \mathbf{u}^2}$ that have been discussed before and differentiating them⁵. If a is one of those two matrices its derivative with V should be computed with the hat-derivative as defined before:

$$\frac{\hat{\partial} a}{\partial V} = \frac{\partial a}{\partial V} + \frac{\partial a}{\partial \phi} \frac{\partial \phi}{\partial V}. \quad (12.54)$$

This hat-definition is required due to the dependency of $a(\mathbf{u}, \phi(V), V)$ on $\phi(V)$, V and \mathbf{u} . The second hat-derivative is defined as:

$$\frac{\hat{\partial}^2 a}{\partial V^2} = \frac{\partial^2 a}{\partial V^2} + 2 \frac{\partial^2 a}{\partial \phi \partial V} \frac{\partial \phi}{\partial V} + \frac{\partial a}{\partial \phi} \frac{\partial^2 \phi}{\partial V^2}, \quad (12.55)$$

which due to the linear dependency of ϕ on V reduces to:

$$\frac{\hat{\partial}^2 a}{\partial V^2} = \frac{\partial^2 a}{\partial V^2} + 2 \frac{\partial^2 a}{\partial \phi \partial V} \frac{\partial \phi}{\partial V}. \quad (12.56)$$

The three approaches are tested on the FEM example using the following applied voltage:

$$V(t) = 12 \cdot \sin(\Omega t), \quad (12.57)$$

with Ω half the mechanical eigenfrequency. The results are shown in figures 12.21 and 12.22. The load amplitude of $12V$ is about 60% of pull-in. Clearly the constant approach result is really wrong, but the first order one (linear in \mathbf{u}) is not far off and the second order one (non-linear in \mathbf{u}) is really accurate.

The first order approach required 61 seconds to generate matrices and about 0.4 seconds to compute the solution. The second order method required 110 seconds to generate the matrices and 1.2 seconds to solve. Remember that the full model required more than 5 hours.

⁵If it impossible to use this approach due to the unavailability of matrix derivatives or laziness in programming, which is not a bad habit, the following principle can be used. It is known that for the electrostatic force and its derivatives with displacement, here generally called a : $\frac{1}{2} \frac{\partial^2 a}{\partial V^2} V^2 = a(V)$ and $\frac{\partial^2 a}{\partial V^2}$, is not a function of V , hence $\frac{\partial^2 a}{\partial V^2} V^2 = 2a(1)$. This can be used to compute all second order derivatives with the applied voltage as well.

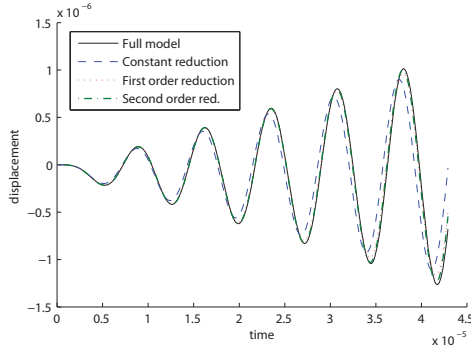


Figure 12.21: Response of $V = 12 \cdot \sin(\Omega t)$ for the two reduction methods

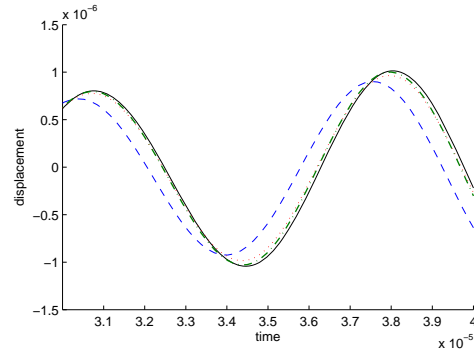


Figure 12.22: Close up of figure 12.21

An important note to make is that the step voltage algorithms (12.21) and (12.23) are limit cases of the general approaches (12.52) and (12.53) due to the exact relations:

$$\frac{\partial \mathbf{f}^{elec}(V)}{\partial \mathbf{u}} = \frac{1}{2} \frac{\partial^3 \mathbf{f}^{elec}}{\partial V^2 \partial \mathbf{u}} V^2, \quad (12.58)$$

$$\frac{\partial^2 \mathbf{f}^{elec}(V)}{\partial \mathbf{u}^2} = \frac{1}{2} \frac{\partial^4 \mathbf{f}^{elec}}{\partial V^2 \partial \mathbf{u}^2} V^2. \quad (12.59)$$

Therefore if a general approach has been programmed no need for a special step voltage algorithm is required.

Small oscillations around a bias voltage

As mentioned before, small oscillations around a bias form an important benchmark for reduction methods. Therefore the general approach is compared with the specialized approach of section 12.4.3. The applied load is the most difficult one of those that were used to test the biased approaches:

$$V(t) = 15 + 3 \cdot \sin(\Omega t), \quad (12.60)$$

where Ω is half the mechanical eigenfrequency.

The only thing required for the general approach is computing the static equilibrium \mathbf{u}_{eq} and use the following definition:

$$\mathbf{u}_{eq} \approx \Psi \boldsymbol{\eta}_{eq}, \quad (12.61)$$

to compute the equilibrium $\boldsymbol{\eta}_{eq}$, which is the required initial condition for the time integration.

For both methods (biased and general) the version that is second order with respect to the displacement is used. Thus (12.47) for the biased version and (12.53) for the general version. Figure 12.23 shows the results. The general approach is even better than the biased version, proving the versatility of the approach. Note that the bias voltage $V_{DC} = 15$ is about 75% of the pull-in voltage.

However if one is *really* interested in accurate simulations around a bias, nothing prevents the usage of the equilibrium displacement as center point of the Taylor expansion:

$$\mathbf{u} = \mathbf{u}_{eq} + \Psi \tilde{\boldsymbol{\eta}}, \quad (12.62)$$

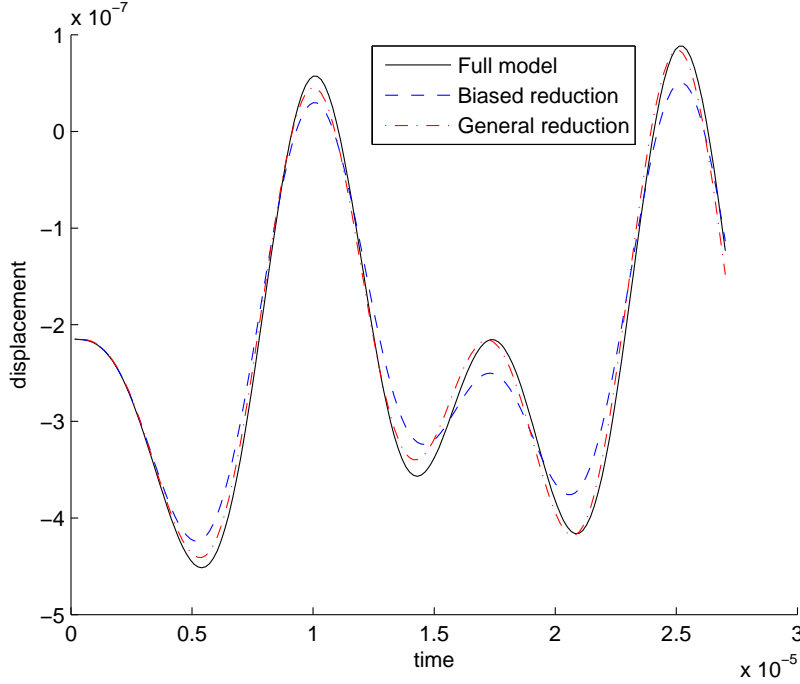


Figure 12.23: Response of $V = 15 + 3 \cdot \sin(\Omega t)$ for the biased reduction approach of section 12.4.3 and the general reduction approach of section 12.4.4

which leads to the definition of the reduced system as:

$$\mathbf{M}_r \ddot{\tilde{\boldsymbol{\eta}}} + \mathbf{K}_r \tilde{\boldsymbol{\eta}} = \boldsymbol{\Psi}^T \left(\frac{1}{2} \frac{\partial^2 \mathbf{f}}{\partial V^2} \Big|_{V=0, \mathbf{u}_{eq}} (V^2 - V_{DC}^2) + \frac{1}{2} \frac{\partial^3 \mathbf{f}^{elec}}{\partial V^2 \partial \boldsymbol{\eta}} \Big|_{V=0, \mathbf{u}_{eq}} V^2 \tilde{\boldsymbol{\eta}} + \frac{1}{4} \frac{\partial^4 \mathbf{f}^{elec}}{\partial V^2 \partial \boldsymbol{\eta}^2} \Big|_{V=0, \mathbf{u}_{eq}} V^2 \tilde{\boldsymbol{\eta}}^2 \right), \quad (12.63)$$

which gives all the non-zero terms of the Taylor expansion around $\mathbf{u}_0 = \mathbf{u}_{eq}$ and $V_0 = 0$. The term $(V^2 - V_{DC}^2)$ has been explained in section 12.4.3.

When this method is applied on the bias problem $V = 15 + 3 \cdot \sin(\Omega t)$ the result of figure 12.24 is obtained. It clearly has a spot on accuracy. Because there was a very large eccentricity from the bias of 3 volt, or 20% of the bias voltage, it can be said that this approach works even if V_{AC} is approaching the order of magnitude of V_{DC} .

12.5 Which modes to use?

So far only purely mechanical modes were used to fill the reduction basis $\boldsymbol{\Psi}$. However in chapter 8 it was shown that electrostatics can change the coupled mode shape. So would it be better to use the coupled modes?

$$\omega_i^2 \mathbf{M}_{uu} \mathbf{x}_i - (\mathbf{K}_{uu} - \mathbf{K}_{uv} \mathbf{K}_{\phi\phi}^{-1} \mathbf{K}_{u\phi}^T) \mathbf{x}_i = 0, \quad (12.64)$$

evaluated around the zero geometry.

This idea is tested on the slightly modified plate geometry of which the side view is shown in figure 12.25. This electric geometry will cause an asymmetric electric force,

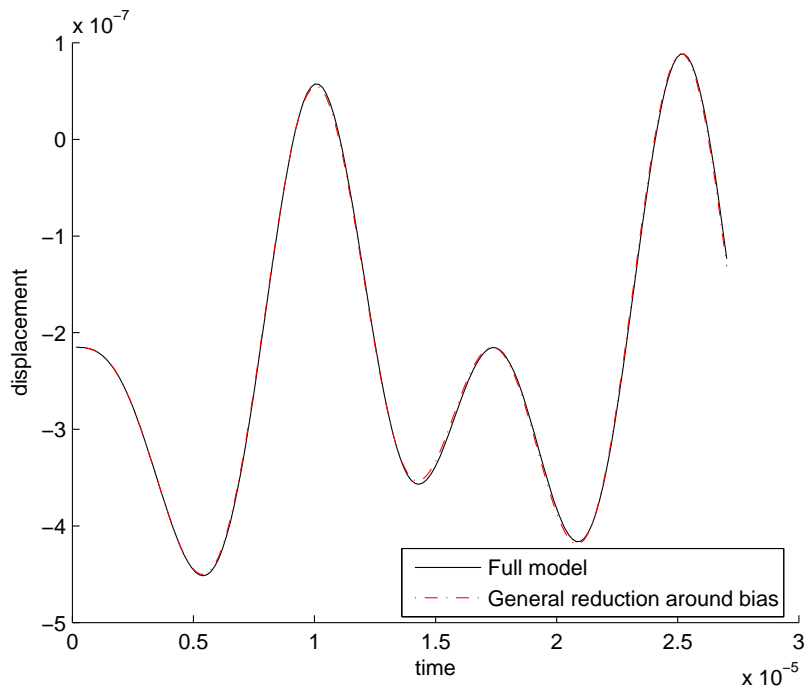


Figure 12.24: Response of $V = 15 + 3 \cdot \sin(\Omega t)$ the general reduction approach of section 12.4.4 determined around the biased displacement \mathbf{u}_{eq}

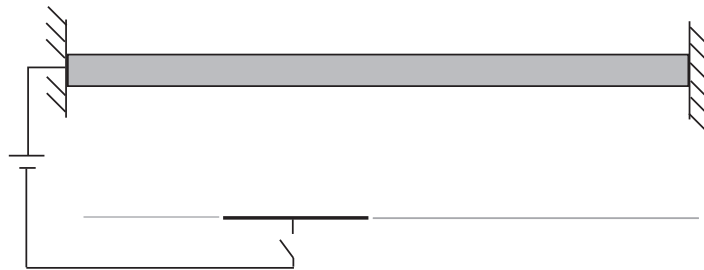


Figure 12.25: Side view of an asymmetrically actuated plate

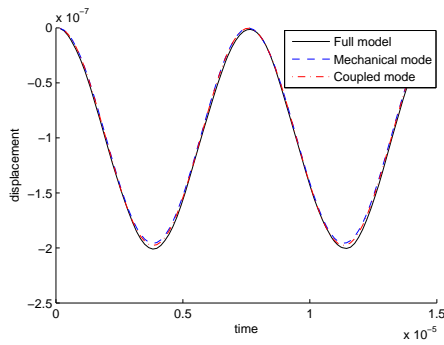


Figure 12.26: Step response of the asymmetric plate at 17.5 volt

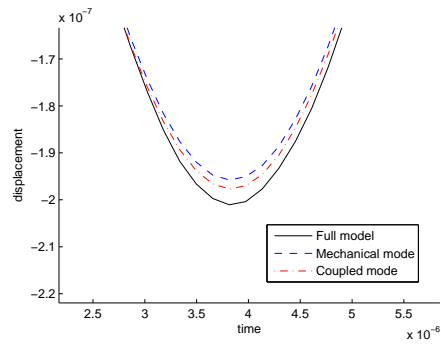


Figure 12.27: Close up of figure 12.26

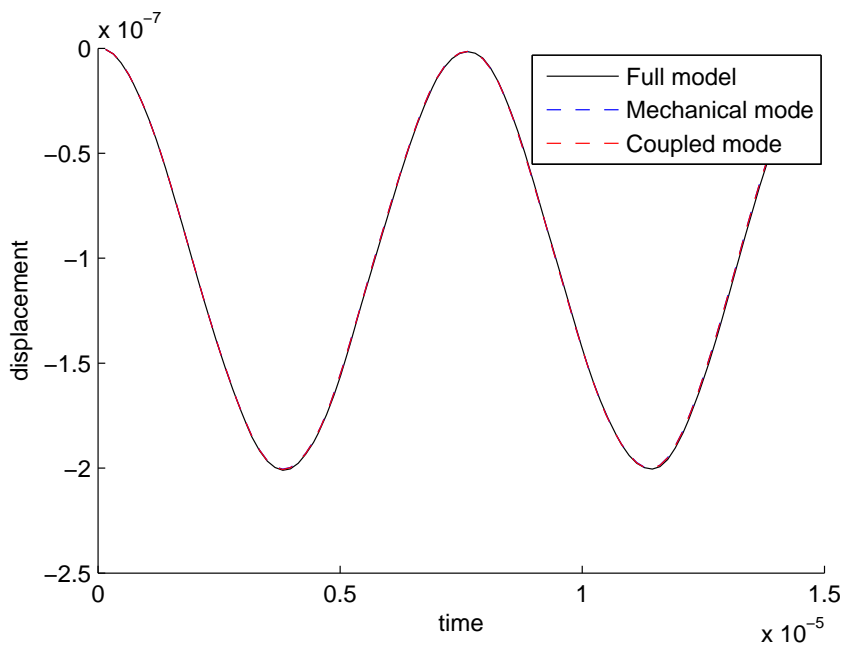


Figure 12.28: Response with 4 modes to a 17.5 volt step

therefore a change of the mode shape. The step response is computed for 17.5 Volts which is about 60% of the 32.6V pull-in voltage. The full model response is shown as well as the reduced curves computed with only one mode in the basis. The used reduction algorithm was the second order in η force reduction approach (12.23).

The coupled mode does better than the uncoupled one. Therefore for more complicated geometries this might be a better alternative than uncoupled modes. However for this simple geometry using only 4 either mechanical or coupled modes in the basis gives a fully accurate result as shown in figure 12.28.

12.6 Including squeeze film damping

Squeeze film damping is very important for a large range of MEMS devices. Therefore its modeling has received ample attention in this work so far and will continue to receive that attention in the remainder of this chapter.

In chapter 10 it was stated that the Reynolds equation describing the fluid can be

written as:

$$\mathbf{L}(\mathbf{u})\dot{\mathbf{p}} + \mathbf{D}(\mathbf{p}, \mathbf{u})\mathbf{p} = -\mathbf{R}(\mathbf{p})\dot{\mathbf{u}}, \quad (12.65)$$

where \mathbf{p} is the pressure in the fluid and the matrices \mathbf{R} , \mathbf{L} and \mathbf{D} are non constant matrices following from the discretization of the partial differential equation. The force on the structure was defined as:

$$\mathbf{f}^p = \mathbf{K}_{up}\mathbf{p}. \quad (12.66)$$

Equation (12.65) can be linearized, which is often done for MEMS that experience a displacement that is relatively small compared to the gap. Hence this assumption is dubious for large step responses. But it will hold very well for oscillations around a DC bias and small step responses. This linearized version is simply:

$$\mathbf{L}(\mathbf{u}_0)\dot{\mathbf{p}} + \mathbf{D}(\mathbf{p}_0, \mathbf{u}_0)\mathbf{p} = -\mathbf{R}(\mathbf{p}_0)\dot{\mathbf{u}}, \quad (12.67)$$

where a zero subscript indicates an initial or equilibrium state of a variable.

In chapter 10 it was mentioned that the equation describing damping can be simplified to neglect compressibility if the squeeze number is small. Therefore this section will first discuss the relatively simple reduction of incompressible damping before moving on towards compressible damping. Finally a reduced model including the non linear effects is derived for incompressible flow.

12.6.1 Incompressible fluid flow

The linearized incompressible fluid equation is:

$$\mathbf{R}\dot{\mathbf{u}} + \mathbf{D}(\mathbf{p}_0, \mathbf{u}_0)\mathbf{p} = 0. \quad (12.68)$$

where \mathbf{D} depends on \mathbf{p}_0 through the Knudsen number dependent viscosity. From this equation follows that:

$$\mathbf{p} = -\mathbf{D}^{-1}\mathbf{R}\dot{\mathbf{u}}, \quad (12.69)$$

hence the fluid force is:

$$\mathbf{f}^p = -\mathbf{K}_{up}\mathbf{D}^{-1}\mathbf{R}\dot{\mathbf{u}} = -\mathbf{C}_{uu}^p\dot{\mathbf{u}}, \quad (12.70)$$

which is essentially a linear damping force as characterized by a linear damping matrix.

Using this linear damping matrix the equations of motion become:

$$\mathbf{M}_{uu}\ddot{\mathbf{u}} + \mathbf{C}_{uu}^p\dot{\mathbf{u}} + \mathbf{K}_{uu}^m\mathbf{u} = \mathbf{f}^{elec}(\mathbf{u}, \phi), \quad (12.71)$$

which are reduced as follows:

$$\Psi^T \mathbf{M}_{uu} \Psi \ddot{\boldsymbol{\eta}} + \Psi^T \mathbf{C}_{uu}^p \Psi \dot{\boldsymbol{\eta}} + \Psi^T \mathbf{K}_{uu}^m \Psi \boldsymbol{\eta} = \Psi^T \mathbf{f}^{elec}(\Psi \boldsymbol{\eta}, \phi). \quad (12.72)$$

The approach is tested for the 6 and 12 volt step responses. For these two responses the ‘electric forces that are quadratic in \mathbf{u} ’ approach is still really accurate for the electrostatics, hence only the damping part of the reduction is tested, not the already discussed electrostatics. For larger voltages the linearization assumption for the fluid equation does not hold, hence it is not really relevant to test the capability of this damping approach for those voltages. The test model is again the symmetric plate used before. The gas in the gap is air at approximately atmospheric pressure. Thus

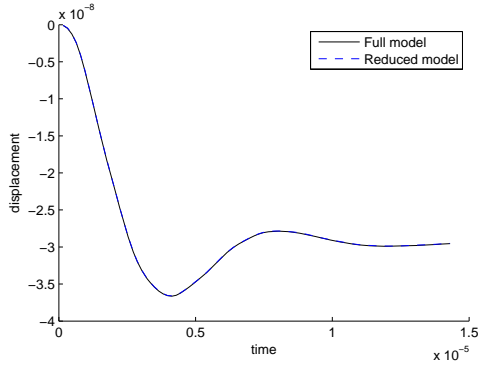


Figure 12.29: Damped step response of 6 volts

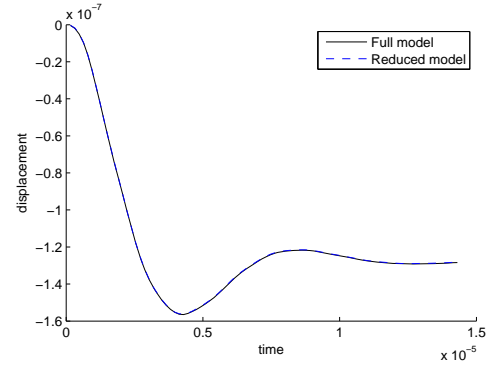


Figure 12.30: Damped step response of 12 volts

the ambient pressure is $P_A = 1 \cdot 10^5 Pa$, the viscosity is $\mu = 18.27 \cdot 10^{-6} Pa \cdot s$ and the mean free path is $64 nm$.

The results for these two steps are the subjects of figures 12.29 and 12.30 that show a very good reduced model accuracy when capturing damping. Again the time integration time was in the order of 0.3 seconds for the reduced model, compared to about 1 and a half hours for the full model.

12.6.2 Compressible fluid flow

When the incompressibility assumption can not be made, the fluid effects cannot be modeled using a simple damping matrix. The full fluid equations (12.65) have to be reduced. This discussion on compressible model reduction will be limited to the linearized fluid equations (12.67). Again modal truncation will be chosen as the basic principle, thus the pressure will be reduced by assuming that:

$$\mathbf{p} = \mathbf{\Gamma}\boldsymbol{\xi}, \quad (12.73)$$

where $\boldsymbol{\xi}$ are the reduced pressures and $\mathbf{\Gamma}$ is the modal basis. A simple approach would be to use the first n_r modes of the eigenvalue problem:

$$\mathbf{L}\boldsymbol{\nu}\lambda = -\mathbf{D}\boldsymbol{\nu}, \quad (12.74)$$

where λ is the eigenvalue and $\boldsymbol{\nu}$ the eigenvector.

With this definition and the original reduction for the mechanics, the reduced system of equations becomes:

$$\boldsymbol{\Psi}^T \mathbf{M}_{uu} \boldsymbol{\Psi} \ddot{\boldsymbol{\eta}} + \boldsymbol{\Psi}^T \mathbf{K}_{uu}^m \boldsymbol{\Psi} \dot{\boldsymbol{\eta}} = \boldsymbol{\Psi}^T \mathbf{K}_{up} \boldsymbol{\Gamma} \boldsymbol{\xi} + \boldsymbol{\Psi}^T \mathbf{f}^{elec}(\boldsymbol{\Psi} \boldsymbol{\eta}, \boldsymbol{\phi}), \quad (12.75)$$

$$\boldsymbol{\Gamma}^T \mathbf{L} \boldsymbol{\Gamma} \dot{\boldsymbol{\xi}} + \boldsymbol{\Gamma}^T \mathbf{D} \boldsymbol{\Gamma} \boldsymbol{\xi} = -\boldsymbol{\Gamma} \mathbf{R} \boldsymbol{\Psi} \dot{\boldsymbol{\eta}}, \quad (12.76)$$

which can be written as:

$$\mathbf{M}_r \ddot{\boldsymbol{\eta}} + \mathbf{K}_r \dot{\boldsymbol{\eta}} = \mathbf{K}_r^p \boldsymbol{\xi} + \boldsymbol{\Psi}^T \mathbf{f}^{elec}(\boldsymbol{\Psi} \boldsymbol{\eta}, \boldsymbol{\phi}), \quad (12.77)$$

$$\mathbf{L}_r \dot{\boldsymbol{\xi}} + \mathbf{D}_r \boldsymbol{\xi} = -\mathbf{R}_r \dot{\boldsymbol{\eta}}, \quad (12.78)$$

and integrated by a time integration algorithm of choice. This can be done either staggered or monolithically.

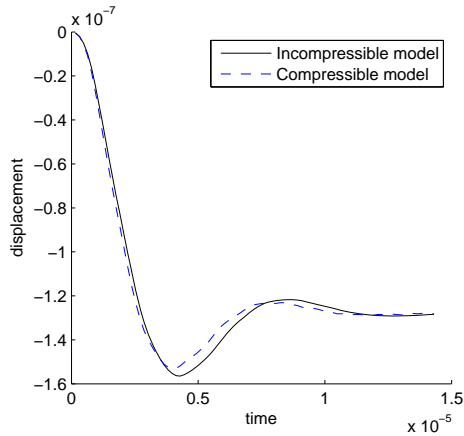


Figure 12.31: Incompressible and compressible full model solution for a 12 volt step

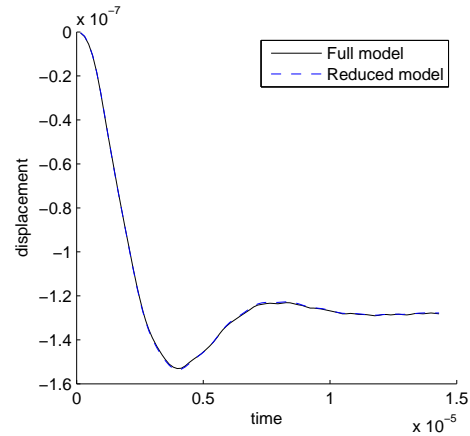


Figure 12.32: Incompressible damped step response of 12 volts

The method is tested using the same reference problem as the incompressible one. First the full model solution for the full model with a 12 volt step is obtained. This result is compared with the incompressible solution in figure 12.31. It shows that the compressible equations have some added stiffness effect, which is not present in the incompressible model. This results in a slightly higher frequency of the compressible response compared to the incompressible response as seen in the figure 12.31. It is important check if there is a difference between the compressible and incompressible results, as small as it is, otherwise this test case cannot be used to properly test an incompressible algorithm.

Figure 12.32 shows the reduced result obtained using 6 mechanical modes in Ψ and 6 fluid modes in Γ compared with the full model result. Clearly the reduced model is capable of capturing the incompressible response. Due to the linearity of the fluid equations, the time for the integration did not really increase compared to reduction without fluid (below 0.4 seconds). However the generation time increased because the fluid modes have to be computed.

The modal basis

So far only solutions to the eigenvalue problem (12.74) were used as fluid basis. However if one zooms in on part of picture 12.32 one sees the red curve of figure 12.33, which is somewhat off the proper solution.

However the reduction basis is not restricted to solutions to that eigenvalue problem (12.74). For the fluid problem one knows what the right hand side of (12.67) can be:

$$R\dot{u} = R\Psi\eta, \quad (12.79)$$

hence if μ is one of the (electro)-mechanical modes used to fill Ψ it seems logical to fill part of Γ with projections of these mechanical modes:

$$\nu^p = D^{-1}R\mu. \quad (12.80)$$

If the total number of vectors in the basis Γ is kept constant and equal to 6, but only 4 of those vectors are purely fluid modes and the other 2 are the projections of the

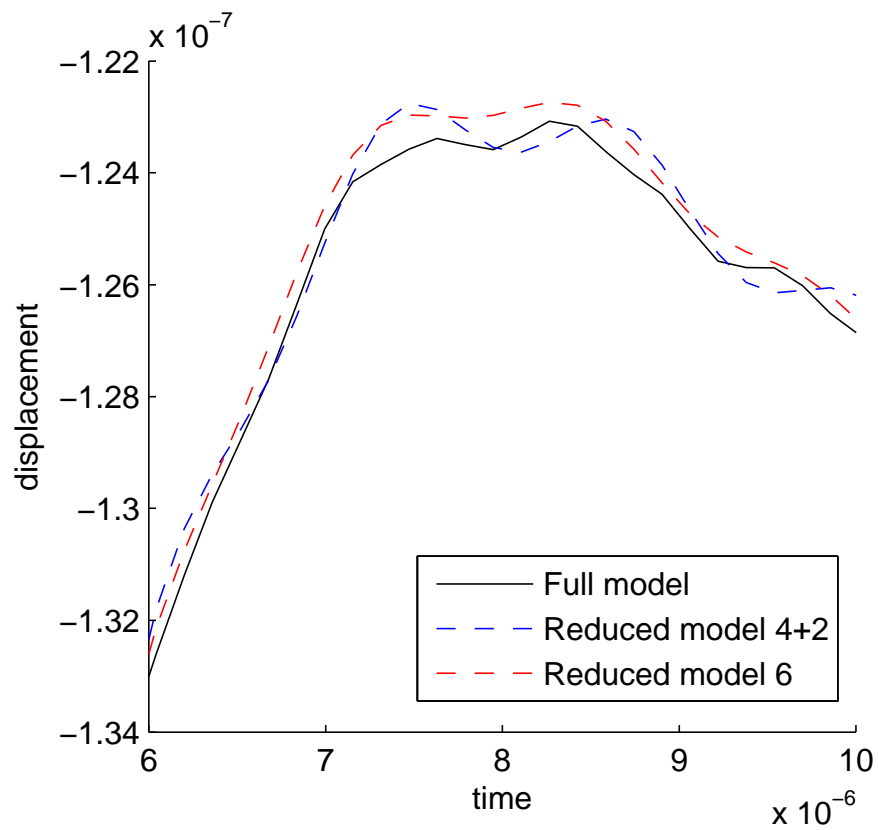


Figure 12.33: Close up of the curve in figure 12.32 including the curve with projected fluid modes. The term 4 + 2 means four pure fluid modes plus two projected modes and the term 6 means six fluid modes only.

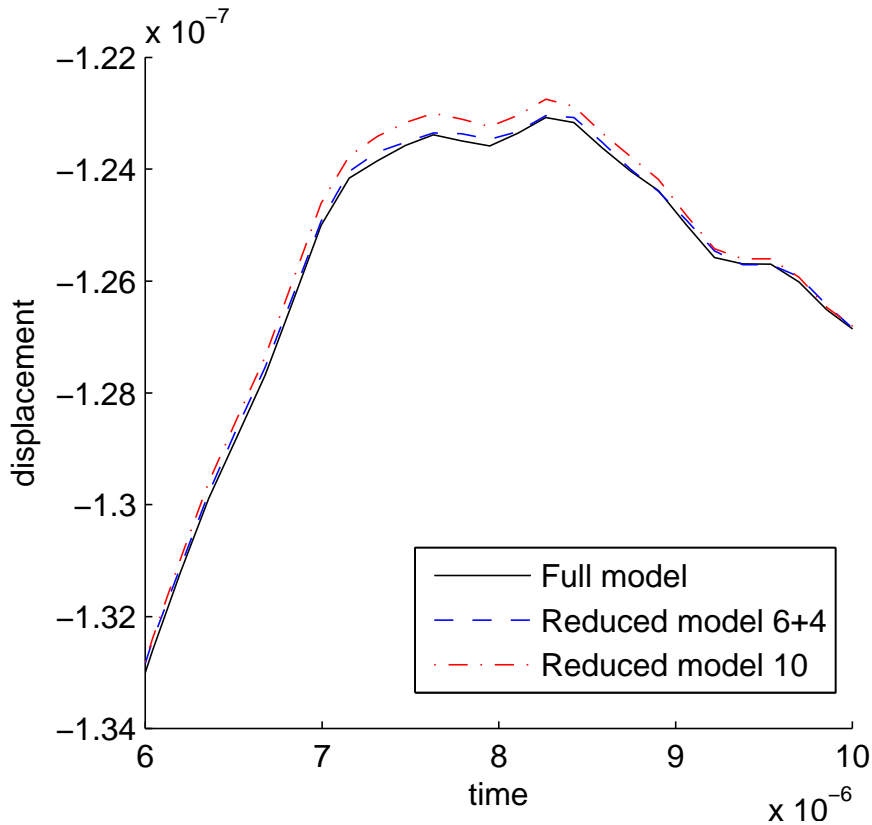


Figure 12.34: Response with 10 mechanical modes and either 10 purely fluid modes or 6 purely fluid modes and 4 projected fluid modes (close up)

2 mechanical modes that correspond to the 2 lowest eigenfrequencies the blue curve in figure 12.33 is obtained. It seems to be slightly better than the red curve, but it is not a decisive victory.

However if the total number of mechanical modes is increased from 6 to 10 and the total number of modes in the fluid basis to 10 as well; then there is a clear difference between using 10 pure fluid modes and 6 fluid modes combined with 4 projected modes. This can be seen in figure 12.34 where the blue curve of the ‘6+4’ reduction is clearly more accurate than the red curve created using fluid modes only.

12.6.3 Adding nonlinearity to the fluid equations

So far the damping was assumed to be linear, thus for the incompressible model it was assumed that:

$$\mathbf{p} = -\mathbf{D}^{-1}(\mathbf{p}_0, \mathbf{u}_0)\mathbf{R}\dot{\mathbf{u}}, \quad (12.81)$$

however, the actual incompressible relation is:

$$\mathbf{p} = -\mathbf{D}^{-1}(\mathbf{p}, \mathbf{u})\mathbf{R}\dot{\mathbf{u}}, \quad (12.82)$$

which has to be solved iteratively, because \mathbf{D} depends on \mathbf{p} . The matrix \mathbf{D} depends only on \mathbf{p} through the Knudsen number dependent viscosity. If the pressure is high enough, that dependency drops, and the equation is only non-linear in \mathbf{u} . Therefore the equation is linearized with respect to p :

$$\mathbf{p} = -\mathbf{D}^{-1}(\mathbf{p}_0, \mathbf{u})\mathbf{R}\dot{\mathbf{u}}, \quad (12.83)$$

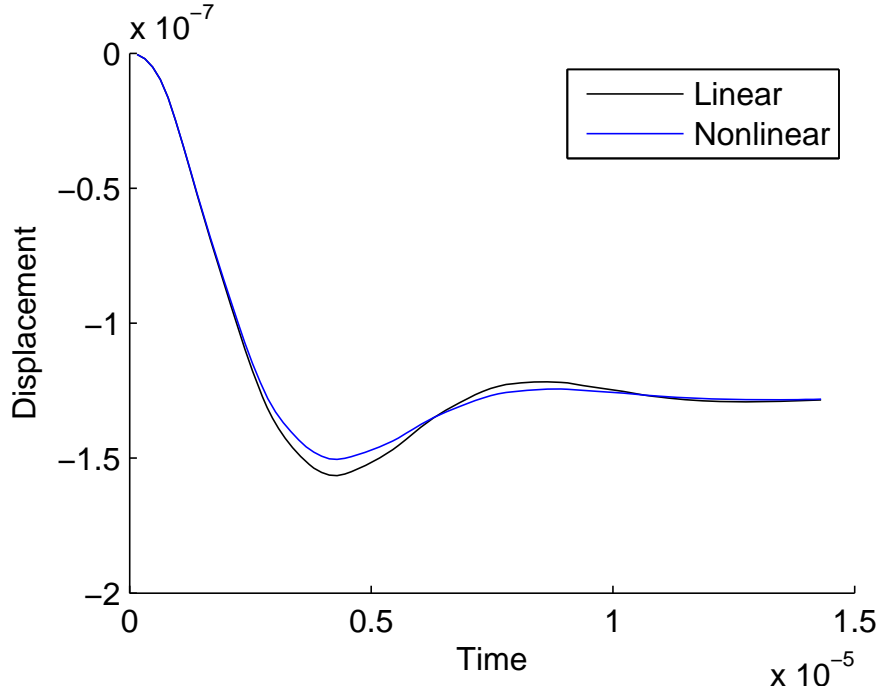


Figure 12.35: Linearized and non linear damped step responses computed with full incompressible models

Hence for each instant in time at which the pressure force needs to be calculated during the time integration this equation is linear in p and depends on the actual displacement at that time. Thus one could write this as:

$$\mathbf{f}^p = -\mathbf{K}_{up}\mathbf{D}^{-1}(\mathbf{u})\mathbf{R}\dot{\mathbf{u}} = -\mathbf{C}_{uu}^p(\mathbf{u})\dot{\mathbf{u}}, \quad (12.84)$$

The definition of \mathbf{D} was given by equation (10.45) as:

$$D_{ij} = \int \frac{\partial N_i}{\partial x_k} \frac{ph^3}{12\mu} \frac{\partial N_j}{\partial x_k} dV, \quad (12.85)$$

where h was defined as:

$$h = N_k(h_0 + u)_k, \quad (12.86)$$

where Einstein's summation convention was used. Hence the matrix \mathbf{C}_{uu}^p depends on h as on $1/h^3$.

The 12 Volts step response used before is solved including the nonlinear effects and compared with the linearized solution in figure 12.35. Clearly the non-linearity increases the damping. This is because a large displacement means that the damping matrix is computed at a smaller gap size, since the damping matrix is inversely proportional to the gap size cubed, a smaller gap gives a larger damping. Therefore damping increases for big displacements. This effect is not present in the linear model, hence the linear model experiences less damping.

Taylor expansion of the damping matrix

Two methods will be developed to reduce this non linearity. The first one is the computationally cheapest one based on a Taylor expansion of \mathbf{C}_{uu}^p . For a simple finite

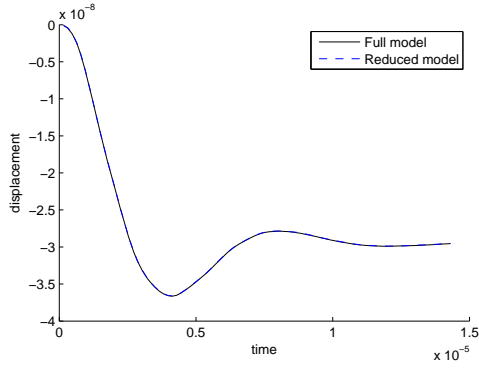


Figure 12.36: Non-linearly damped step response of 6 volts

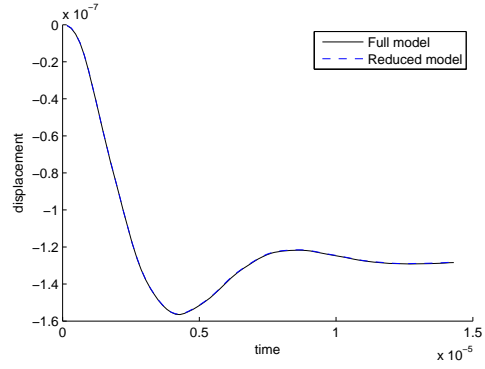


Figure 12.37: Non-linearly damped step response of 12 volts

difference based beam model this was done before in [23]. The dependency of this damping matrix on the gap will be linearized as:

$$\mathbf{C}_{uu}^p = \mathbf{C}_{uu}^p(h_0) + \left. \frac{\partial \mathbf{C}_{uu}^p}{\partial \mathbf{u}} \right|_{\mathbf{u}=0} \mathbf{u}. \quad (12.87)$$

From the definition of the damping matrix (12.70) follows:

$$\frac{\partial \mathbf{C}_{uu}^p}{\partial u_i} = -\mathbf{K}_{up} \mathbf{D}^{-1} \frac{\partial \mathbf{D}}{\partial u_i} \mathbf{D}^{-1} \mathbf{R}. \quad (12.88)$$

which after projection on the basis results in a n_r by n_r by n_r array.

The derivative of \mathbf{D} follows from (12.85):

$$\frac{\partial D_{ij}}{\partial u_s} = \int \frac{\partial N_i}{\partial x_k} \frac{3ph^2}{12\mu} \frac{\partial N_j}{\partial x_k} N_s dV, \quad (12.89)$$

where:

$$\frac{\partial h}{\partial u_s} = \frac{\partial N_l(h_0 + u)_l}{\partial u_k} = N_s, \quad (12.90)$$

was used.

The responses obtained using this damping matrix that depends linearly on the displacement are shown in figures 12.36 and 12.37, which shows that for the 6 and 12 volts steps, this method is really accurate. So in principle up to the point where the voltage reduction using quadratic displacement dependency of the electric force is accurate, this method is accurate as well. Time integration of this reduced responses only required 0.3 seconds after a 64 second matrix generation time, where the full model required more than an hour.

Fully non-linear damping matrix

More accuracy can be required. For instance when the full force reduction is used, hence the electric force computation is really accurate, therefore the reduced modal is used for large displacements⁶. In that case a different approach can be used.

⁶Or if a non FEM based electric model is used which allows really fast computation of the electric force for simple geometries

The reduced non-linear damping matrix can be written as:

$$\mathbf{C}_r = \mathbf{\Psi}^T \mathbf{K}_{up} \mathbf{D}^{-1}(\mathbf{u}) \mathbf{R} \mathbf{\Psi}. \quad (12.91)$$

Furthermore it is assumed that the fluid can be reduced with a modal basis as well:

$$\mathbf{p} = \mathbf{\Gamma} \boldsymbol{\xi}, \quad (12.92)$$

which can be used to reduce the squeeze film equation (12.65). When this reduced squeeze film equation is used to obtain the reduced damping matrix it gives:

$$\mathbf{C}_r = (\mathbf{\Psi}^T \mathbf{K}_{up} \mathbf{\Gamma}) (\mathbf{\Gamma}^T \mathbf{D}(\mathbf{u}) \mathbf{\Gamma})^{-1} \mathbf{\Gamma}^T \mathbf{R} \mathbf{\Psi}, \quad (12.93)$$

or:

$$\mathbf{C}_r = \mathbf{K}_{rup} \mathbf{D}_r^{-1}(\mathbf{u}) \mathbf{R}_r. \quad (12.94)$$

Note that there is no term related to $\dot{\mathbf{p}}$ within this incompressible model, therefore there is no reason to use fluid modes in the basis $\mathbf{\Gamma}$ only the projected modes as described by equation (12.80) are used to fill $\mathbf{\Gamma}$.

Using the definition of \mathbf{D} :

$$\begin{aligned} \mathbf{D}_{ij} = \int \frac{\partial N_i}{\partial x_k} \frac{p(N_i h_i)^3}{12\mu} \frac{\partial N_j}{\partial x_k} dV &= \int \frac{\partial N_i}{\partial x_k} \frac{p(h_0)^3}{12\mu} \frac{\partial N_j}{\partial x_k} dV + \\ &\int \frac{\partial N_i}{\partial x_k} \frac{p^3(h_0)^2}{12\mu} \frac{\partial N_j}{\partial x_k} N_l dV u_l + \int \frac{\partial N_i}{\partial x_k} \frac{p^3(h_0)}{12\mu} \frac{\partial N_j}{\partial x_k} N_l^2 dV u_l^2 + \\ &\int \frac{\partial N_i}{\partial x_k} \frac{p}{12\mu} \frac{\partial N_j}{\partial x_k} N_l^3 dV u_l^3, \end{aligned} \quad (12.95)$$

which can be written as⁷:

$$\mathbf{D}_r = \mathbf{D}_3 + \mathbf{D}_2 \mathbf{\Psi} \boldsymbol{\eta} + \mathbf{D}_1 (\mathbf{\Psi} \boldsymbol{\eta})^2 + \mathbf{D}_0 (\mathbf{\Psi} \boldsymbol{\eta})^3, \quad (12.96)$$

where \mathbf{D}_3 is a n_f by n_f matrix, if n_f is number of modes in $\mathbf{\Gamma}$. The other three ($\mathbf{D}_2 \mathbf{\Psi}$, $\mathbf{D}_1 \mathbf{\Psi}^2$ and $\mathbf{D}_0 \mathbf{\Psi}^3$) are n_f by n_f by n_r arrays.

When using this approach 3 such $n_f^2 n_r$ big arrays need to be stored, after which a n_f by n_f matrix equation has to be solved to compute the damping force. Since only projected modes are used the number of n_f should be chosen equal to n_r .

In principle this approach can capture the full non-linearity of the Reynolds equation with respect to \mathbf{u} , hence it can be used until that equation is no longer valid when $\mathbf{h} \rightarrow 0$.

These fully non-linear responses for the 6 and 12 voltage steps are shown in figures 12.38 and 12.39. The computation time was only 67 seconds for the generation and less than 0.4 seconds for the time integration.

Figure 12.40 shows the step responses of this fully non linear reduction method and the Taylor based one discussed just before. For the 6 and 12 volt responses both reductions gave the same response. For the 18 volt step the maximum displacement is that big that there is a difference. The maximum displacement is about 20% of the gap for this 18 volts step. The 12 volt step only gave a maximum displacement of about 8% of the gap. Therefore it is crucial to use the full non-linear version if one expects, or finds, a maximum displacement bigger than 10%.

⁷Superscripts in this equation indicate element wise powers of the matrix and vector elements.

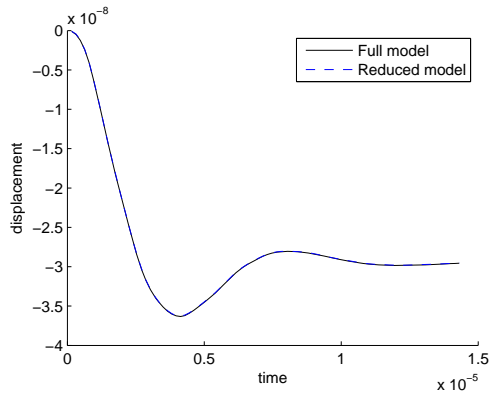


Figure 12.38: Fully non linearly damped step response of 6 volts

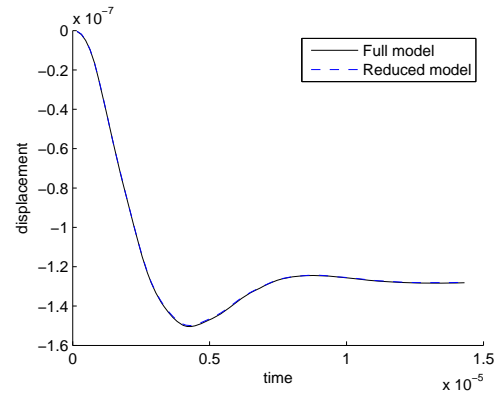


Figure 12.39: Fully non linear damped step response of 12 volts

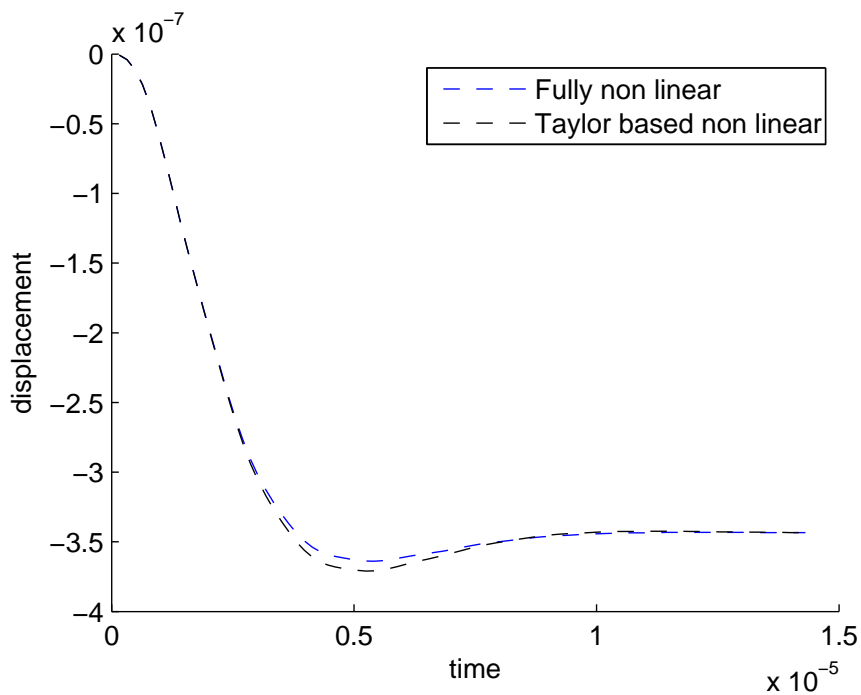


Figure 12.40: Fully non-linear and Taylor based non-linear damping for a 18 volt step response.

This approach can easily be expanded to the incompressible integration. One can just use the dependency of the reduced matrix on the mechanical modal amplitudes. Similarly the \mathbf{L} matrix can be expanded. These can then be used for computing the time derivatives of the pressure.

12.7 Conclusions

This chapter was concerned with modal truncation based reduction algorithms for electro-mechanical finite element models. The reduction of electro-mechanics was split into step response reduction, for which the electric force is only depending on the displacement and time varying reduction for which the electric force is also depending on a time varying applied potential. It was required that the electrostatic force reduction is applicable for any electrostatic problem, not for simple parallel plate geometries only.

For the step response problem in total four methods were discussed:

1. Full force reduction, which was adapted to coupled FEM from a non coupled FEM method described in literature,
2. A first order Taylor approach, which has been described in literature before.
3. A second order Taylor approach, which has been described in literature for a non FEM model.
4. A piecewise quadratic Taylor approach, newly derived in this work.

The numerical experiments showed that for finding the actual dynamic pull-in value the piecewise quadratic approach is most efficient with respect to computation time. However up to about 70% of the pull-in value the second order Taylor approach displacement is very accurate.

For time varying potentials the distinction between the discussed methods blurs, therefore the total list is longer:

1. Full force reduction, adapted from the same work as the full force step response reduction approach.
2. An approach without a dependency of the force on displacement but with a quadratic dependency of the force on the applied voltage. This method can be found in literature and commercial FEM packages.
3. A first order Taylor approach for the displacement dependency combined with a quadratic applied voltage relation, specially adapted for oscillations around biases, which can be found in literature and commercial FEM as well.
4. A second order Taylor approach for displacement dependency combined with a quadratic relation with respect to the applied voltage, adapted for biased oscillation, which has not yet been found in literature.
5. A third order Taylor approach in which essentially the force depends linearly on the displacement and newly developed in this work.
6. A fourth order Taylor approach, where the force depends quadratically on the displacement, newly developed as well.

For the last two methods the Taylor expansion can be centered around any displacement, hence also a bias displacement.

Of these methods, the most effective method is the last one, the fourth order Taylor approach. It is computationally very cheap and accurate up to about 70% of pull-in. As mentioned this approach can be expanded around a bias displacement as well. In that case the 70% of pull-in limit only restricts the AC part of the applied voltage. Also the last method was more effective than the two specially tailored bias methods for bias problems (methods: 3 and 4). Only if one is interested in higher applied voltages than the 70% limits, the full force reduction is best.

Finally the fluid equations were reduced for incompressible and compressible flows. For the compressible equations this required the application of modal truncation for the fluid DOFs as well. Here the concept of *projected modes* proved to be really beneficial for accuracy. It was also shown that the extension to fully non linear fluid equations can be made without great computational costs. This simplicity was partly due to limitation of the squeeze film model. It is only applicable for parallel plate geometries, which is in contrast to the presented electrostatic force reduction.

One open question that remains is if the trust region approach as presented in [104] can be used in combination with the second order Taylor approaches and if this has an advantage over the presented methods.

Part IV

Combining and concluding



Chapter 13

A general modeling framework

13.1 The basic framework

In chapter 1, the introduction, it was stated that the main goal of this thesis is the development of an integrated framework of electromechanical physical level modeling strategies. The FEM method is such a physical level modeling method. This requires a definition of what is considered by the term *framework*: a modeling framework is an annotated diagram that shows the characteristics of the different modeling approaches and the relationships between them. It should allow a designer to choose the required modeling capabilities based upon the purpose of the model. For example if the designer is interested in the pull-in voltage, this framework should provide the possible modeling options, including advice for selecting one of those options.

In sections 3.4 and 3.5 the building of a model and the solution of the equations were placed in a general structure. In each of the chapters that constitute parts II and III of this thesis, an attempt was made to cast discussed algorithms into that structure. When those attempts are combined this provides the basic framework that is presented schematically in figure 13.1.

Once the modeler has decided that a physical level model is required, he or she should decide what results are needed from the model and look for those results in the bottom part of figure 13.1. The number of times that the desired result can be found provides the number of ways to obtain that result.

The lines from the top box *decide to make an electro-mechanical model* to the desired result go through numbered rhombi. Each rhombus signifies a necessary choice that has to be made during the modeling:

1. Is a coupled simulation or co-simulation preferred?
2. Will the solution be obtained in a staggered, hybrid or monolithic manner?
3. Is the problem static or dynamic?

Below, section 13.2 will elaborate on the first choice between the simulation approaches. Subsequently section 13.3 will elaborate on the second choice between the solution strategies. Finally section 13.4 will discuss the division between part II and part III of this thesis: the division between statics and dynamics. Of course that division corresponds to the third required choice, however the flexibility to choose is limited. Essentially the desired result determines if a static computation is sufficient or if dynamics should be included.

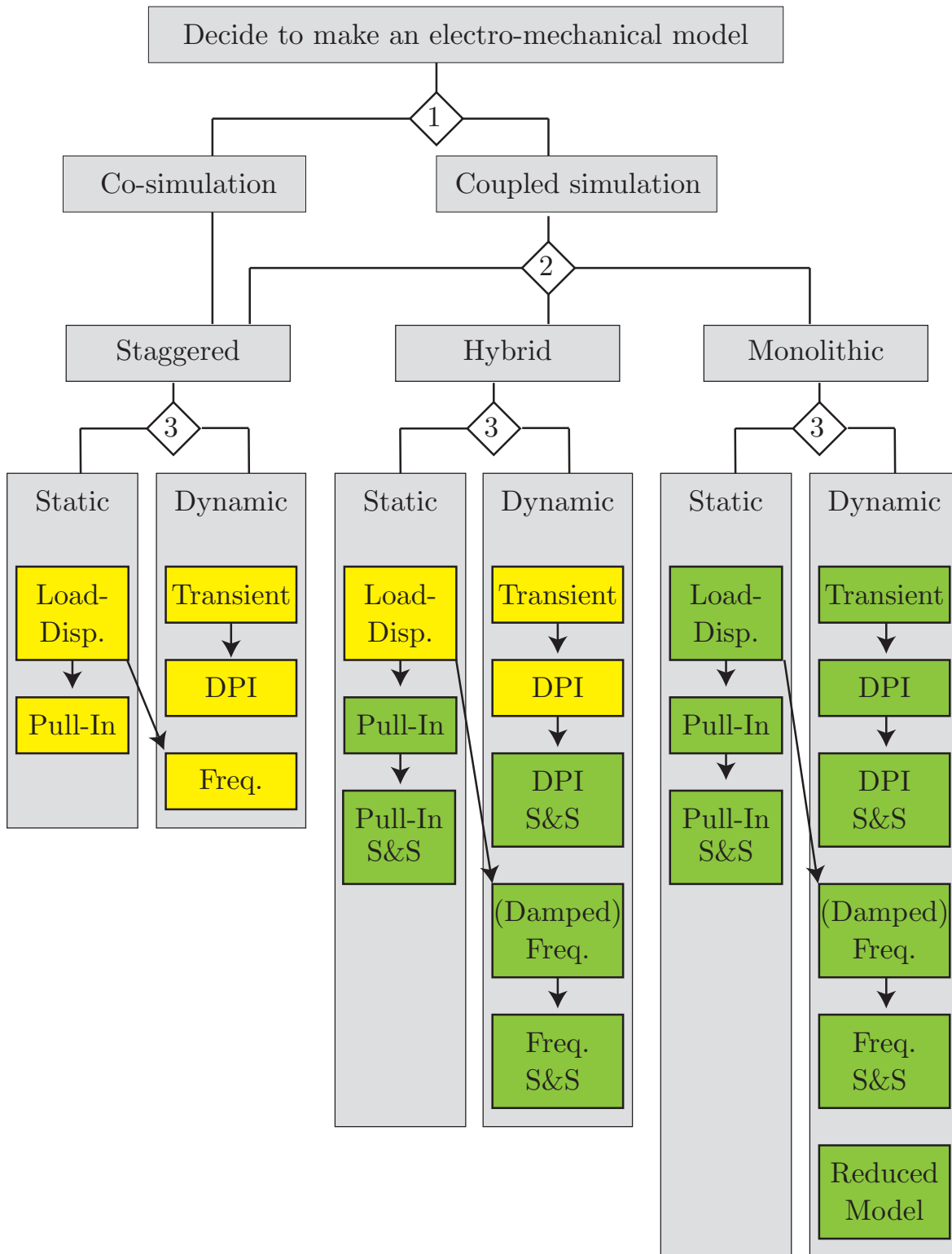


Figure 13.1: Schematic representation of the relation between the methods derived and discussed in this thesis. Yellow boxes indicate staggered solution procedures and green boxes indicate monolithic solution procedures. The used abbreviations are: Freq. for Frequency, Disp. for Displacement, DPI for Dynamic Pull-In and S&S for Sensitivity and Stochastic analysis.

One remark has to be made: the quality of the results derived in the context of this framework stands or falls with the quality of the constituent numerical models of the electrostatic and mechanic domains.

13.2 Selecting a simulation approach

Co-simulation was defined as the combination of two different discretization approaches, often from different codes, to build a coupled model. Such a simulation needs the transfer of data from one code to the other. This limits the ability to compute derivatives, such as tangent matrices and design sensitivities. Therefore monolithic methods as well as sensitivity and stochastic analyses are highly impractical for co-simulation. Theoretically finite difference approaches could be used to derive the matrices and sensitivities, however, due to the lack of robustness and efficiency, those are omitted from figure 13.1. The only exception is the frequency as computed by the staggered approach. They were not omitted because of their frequent appearance in literature and commercial codes.

An advantage of co-simulation is that highly dedicated solvers for each physical domain can be used, providing high accuracy. Especially if the needed mesh density differs greatly on specific locations such as corners or if the problem is really large a co-simulation can be the best option. However this requires the methods to transfer data between non-matching meshes, an issue that has generated large body of literature (e.g. [40, 67, 6]).

Coupled simulation was defined as the discretization of all fields within one code, preferably using matching meshes. This simplifies the coupling and enables analytic tangent matrix and sensitivity computations. Therefore the flexibility of the models is greatly increased. A disadvantage is that the code has to be able to discretize all physical fields.

This flexibility allows for the efficient computation of analytical design sensitivities as derived in this work. The sensitivities enabled the efficient stochastic analyses that were derived. With a co-simulation approach only Monte Carlo type approaches are feasible for uncertainty quantification.

For more detail on the difference between both simulation approaches see section 3.4.

13.3 Selecting a solution strategy

The second rhombus defines the choice between the two available solution strategies: staggered or monolithic, a distinction made in section 3.5. When a staggered procedure is used, one solves the physical domains separately. For instance first the electric equations are solved, which provide electrostatic forces. Subsequently the mechanical equations are solved, providing displacements, after which the electric domain is deformed and the process starts all over again. The advantage is that relatively small systems have to be solved, the disadvantage is slow convergence.

The alternative is a monolithic approach: combining the electric and mechanical equations into one big system of equations, which can be solved directly. This solution starts with the computation of the tangent matrix of the system, which can be used to iterate the non-linear equations at once. The advantage is a fast convergence, but the

costs are large matrices which have to be solved and scaling issues. Those scaling issues can become especially prominent for the three field problem of squeeze film damped electro-mechanics.

If, at rhombus number one, the choice was made to use a co-simulation model, only the staggered solution procedure can be used. Therefore in that case the choice is not a real choice. However for coupled simulation models, the choice is a real one. If one has a coupled simulation model, one can choose to do everything monolithic or staggered, however there is a third option.

Experience in chapter 5 showed that for a mechanically linear problem a staggered procedure is often optimal for the computation of one of the basic results: the quasi-static load-displacement computation. For a transient analysis the time step limits accuracy, therefore the time step should be relatively small. Thus the number of non-linear iterations needed at each time step is limited, hence also for transient analyses, staggered procedures are often optimal. However it is well conceivable that one is interested in more than those basic computations: accurate frequencies around static equilibria and sensitivities. In that case a hybrid method can be used. In figure 13.1 a hybrid method is characterized by a yellow box containing the basic solution combined with an arrow pointing to a green box which contains the monolithic method used to compute a result based on the staggered solution.

13.4 Statics and dynamics

As was mentioned the last choice is not a real choice. Also for some dynamic results a static computation is required, which blurs the separation. Furthermore assuming that something is static, means in essence that it is assumed that the inertia terms can be neglected from the dynamic equation, making statics a limit case of dynamics. However, literature and this work have made the clear distinction between statics and dynamics due to the fact that the equations are different. Therefore this third choice is included within the framework, essentially to help find the methods within this thesis. Static methods and results are in part II of this thesis, dynamic methods and results in part III.

The dynamic methods can be categorized even more as is shown in figure 13.2. The first separation is between transient and frequency analysis. When a transient analysis is performed the goal is to find the actual displacement as a function of time by solving (integrating) the non-linear dynamic equations. When a frequency analysis is done, it is assumed that the device moves with a displacement relative to an equilibrium position. Furthermore it is assumed that the displacements over time remain small. Therefore it is allowed to assume that the device will vibrate as an oscillatory system. In that case the equations are linearized around the equilibrium system and the goal is to find the eigenfrequencies and modes by doing an eigenvalue analysis on that system. Such an eigenfrequency analysis is in general much cheaper than a transient analysis. Because transient analyses are so expensive, they are often performed using a reduced model.

The goal of a reduced model is doing transient analyses, which explains the position of model reduction within figure 13.2. However, the reduced models discussed in this thesis need a frequency analysis to be created. Once again a division gets blurred somewhat.

	Undamped analysis	Damped analysis (squeeze film)
	Chapter 8	Chapter 10
Transient	Dynamic pull-in (Sens. and Stoch) Chapters 8 & (9)	Dynamic pull-in Not explicitly discussed
	Reduced model Chapter 12	Reduced model Chapter 12
Frequency	Frequencies (sens. and stoch) Chapters 8 & (11)	Frequencies (sens. and stoch) Chapters 10 & (11)

Figure 13.2: Categorization of the dynamic results.

The second separation is between damped and undamped models. In the undamped case it is assumed that no energy is lost within the system, hence there is no friction. When this assumption is not made, damping is allowed. In this work the only kind of damping that is considered is squeeze film damping: damping due to the compression of air between two parallel plates. Basically the addition of damping will generate forces that are proportional to the velocity of the device, hence energy will be removed. Of course the necessity to include damping in the model depends on the purpose and design of the device.

13.5 Where to find the methods?

The last section of this chapter will give an overview of the location within this thesis of the methods presented in figure 13.1.

If one is interested in the purely static load displacement relationships one has to look for chapter 5. To estimate a pull-in value, one needs such a load-displacement relationship, thus one is referred to chapter 5 as well. When the pull-in value is not enough but also its sensitivity to parameter variations or the stochastic properties of the pull-in value are needed, respectively chapters 6 and 7 should be consulted.

If also the eigenfrequencies of an electro-mechanical device are desired, it is needed to progress to chapter 8 for undamped problems and chapter 10 for damped problems. Both chapters are in part III. However for frequencies a static analysis from chapter 5 might be required. The sensitivity and stochastic analysis of those frequencies is treated in chapter 11.

How to determine a transient is discussed in chapters 8 and 10 as well. If dynamic pull-in needs to be found, one needs transient results, therefore one can find the methods to compute dynamic pull-in in chapter 8 as well. If the value is not enough, the

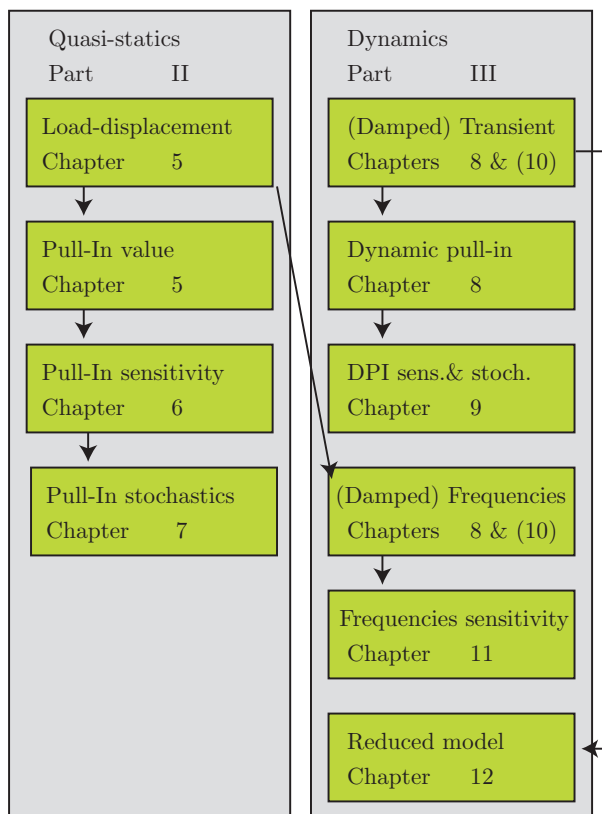


Figure 13.3: Distribution of the desired results categorized in the framework (figure 13.1) over the thesis.

methods to compute the sensitivity, uncertainty and reliability properties of dynamic pull-in can be found in chapter 9.

It is also possible that the desired number of transient analyses is really large. Or one could be interested in creating a model that can be used in a circuit simulator. In those cases a reduced order model is probably required and chapter 12 could be of interest.

This distribution of the desired goals and methods to obtain those results is summarized in figure 13.3. In the chapters mentioned in figure 13.3 both the monolithic method and the staggered (if available) can be found. The conclusions about the optimal methods for each desired result will be summarized in the next chapter as well. The modeling of an application using the approaches of this framework is presented in appendix C.

Chapter 14

Conclusions and recommendations

Waarheid is net een toverbal die om
de drie seconden van kleur verandert

De mensheid zij geprezen

Arnon Grunberg

14.1 Conclusions

This thesis had one primary goal: presenting a framework for the numerical solution of electro-mechanical problems based on physical level modeling. The developed framework presents a logical oldening of the available methods for electro-mechanical modeling. The creation of the framework has been split into three parts: electro-mechanical modeling, quasi-static simulation and dynamic simulation. The conclusions from those three parts are presented below.

14.1.1 Electro-mechanical modeling

When an electrostatic model is used for electro-mechanical simulation the quality of the model has to be assessed by the quality of the electrostatic forces it generates. Because forces are computed using the electric field, the gradient of the electric potential, it is not enough to have a converged electric potential solution. Especially corner singularities can cause convergence problems. Several options exist for computing the electric forces once an electric field has been computed. After numerical experiment and discussion, it turned out that the most efficient approach to compute the electric force is the variational approach. All approaches using special corner elements performed less or equal to the variational approach and require expensive corner detection algorithms. The combination of special corner elements with the variational approach does perform better than the variational approach, but the difference is that small that it is not worth the extra effort.

Once such an electrostatic model is coupled with a mechanical model, an electro-mechanical model is created. There are two methods to couple them: co-simulation where two models are coupled on an ad hoc basis and fully coupled simulation where both domains are modeled simultaneously in the same code. Co-simulation gives the possibility to use advanced electrostatic and mechanical solvers for each domain, coupled simulation gives more options to the analyst.

If a fully coupled model is created one has the choice to solve everything in one go, or to iterate between the electric and mechanical problem. In other words: to solve the problem in a monolithic or a staggered manner. For co-simulation only the staggered option is available.

14.1.2 Quasi-static modeling

Quasi-static load-displacement curves can explain much of the behavior of an electro-mechanic device. One of the most important characteristics that can be derived from such a load displacement relation is the *pull-in voltage*.

To find this load-displacement curve using a numerical algorithm an extra constraint has to be added to the system of equations, for which there are 5 options:

1. Prescribe the applied voltage,
2. Prescribe a relation between applied voltage and displacement,
3. Prescribe the applied charge,
4. Prescribe a relation between applied charge and displacement,
5. Prescribe an applied displacement.

The second choice that can be made is if the problem is solved in a staggered or a monolithic manner. Simulations of a reference problem showed that for linear elastic structural problems the staggered approach with constraint number 4 worked best, while for non-linear elastic problems the monolithic approach with constraint number 4 worked best. Some of the constraint types had not yet been published in literature before.

It was also shown that these methods can be easily enhanced to cope with bifurcations. Furthermore it was shown that pull-in as computed with this method could be matched with experiments.

The pull-in sensitivity analysis that was performed provides analytical first order sensitivities and newly derived semi-analytical second order sensitivities that could be validated by finite differences. The analytical sensitivities require fewer function evaluations and are therefore computationally cheaper. It was shown that a stochastic analysis could be performed with these sensitivities that gives reliable results when compared with crude Monte Carlo simulations

14.1.3 Dynamic modeling

Undamped modeling

Dynamic modeling can be split into undamped modeling and damped modeling. Subsequently each of those problems can be split into transient and frequency analysis. In this work the undamped frequency analysis was briefly discussed, staggered and monolithic approaches were compared. The monolithic method is favored due to its robustness. The typical decrease of the linearized frequency with applied potential was validated by experiments.

The newly developed analytic dynamic pull-in sensitivities could be used for a stochastic analysis. The validation with crude Monte Carlo sampling showed that for the reference problem a second order uncertainty analysis was not required.

Damped modeling

A non-linear FEM model of the Reynolds equation was developed. When the Reynolds equation is used to model squeeze film damping, there exist the possibility to neglect to compressible terms in that equation. This can greatly simplify the implementation of the time integration algorithms needed for transient analysis. When computing damped eigenfrequencies the amount of extra work needed when compressibility is included is less dramatic. The validity of the incompressible Reynolds equation was tested and it was shown that the critical squeeze number for the undeformed configuration gives a good indication of the validity, but a deformation of the plate changes the validity range slightly.

Also the effect of rarefaction was introduced: when the critical dimension of the air film becomes very small compared to the mean free path of a gas molecule the gas cannot be modeled as a continuum anymore. Rarefaction can be measured by considering the Knudsen number. An approach from literature was used to model the rarefaction. This approach allowed the favorable comparison of the derived squeeze film model to experiments from literature. Those experiments also showed that the viscosity correction for rarefaction works up to a Knudsen number of 600.

Another conclusion of the damped modeling approach was that damping makes one rule of thumb invalid: the eigenfrequency is zero at static pull-in. It should be corrected to: the real part of the damped eigenvalue changes sign at static pull-in.

The coupled electro-mechanical(-fluidic) eigenfrequency is an important parameter therefore the eigenfrequency and Q-factor sensitivities were discussed. This required the derivation of matrix sensitivities, while remaining on electro-mechanic equilibrium. These sensitivities were successfully used to perform a stochastic analysis, which was validated using crude Monte Carlo sampling.

Reduced modeling

Finally the transient equations were reduced by applying modal truncation. The key problem proved to be the reduction of the non-linear electrostatic forces, which depend non-linearly on both the applied potential and the displacement. Because the dependency on the applied potential is quadratic this could be easily reduced by applying a second order Taylor approximation.

The dependency on the displacement is that complicated that there exist no optimal method. However a newly developed second order Taylor approximation proved to be very effective in reducing the computation time and is reasonably accurate up to 70% of pull-in. If the voltage is applied with a step and one is interested in pull-in one is advised to use the developed piecewise quadratic Taylor approach to cope with the displacement sensitivity.

It was shown that linear and non-linear damping can be included into the reduced model without much computational cost.

14.2 Recommendations

14.2.1 Quasi-static modeling

It was shown that the approach with a constraint on charge and displacement was the best option to find the load-displacement curve. However there are several options to

define a constraint on charge and displacement (e.g. circular or normal flow [101, 27, 105]). It is an open question that can be solved with relative ease by future work.

Normally the Taylor based reduction approaches are not useful for quasi-static analyses because they cannot predict pull-in accurately. However the computationally expensive piecewise quadratic Taylor approach was accurate for dynamic pull-in. It would be interesting to test if it is an efficient option to compute static pull-in as well.

14.2.2 Dynamic modeling

The dynamic pull-in sensitivity could only be computed for a limited number of parameter variations, due to the assumption that the pull-in displacement does not change due to the parameter change. Research is still required to pinpoint the exact limitations that are induced by this assumption and whether there exists an alternative dynamic pull-in criterion.

Furthermore it was shown that the logarithmic sensitivities of dynamic and static pull-in were equal for the reference problem. An interesting open question is if this is always the case.

For the damped model it was shown that the squeeze number gives a good indication of the validity of the incompressibility assumption. However this requires knowledge of the critical squeeze number, which is only defined for simple geometries. It does require extra research to find out what the exact limitations of this assumption are and when the compressible gas equation has to be used.

For the reduced model, the remaining problem is to find a reduction approach for very large displacement that is computationally cheap. It is recommended to consider the *Trust region approach*, possibly in combination with the piecewise quadratic Taylor approach [104].

Appendix A

Summary of the classical Finite Element equations

To be able to understand the differences between the different modeling approaches, it is essential to understand the general finite element modeling of mechanics and electrostatics. Therefore the modeling of electrostatics and mechanics using FEM will be discussed briefly in this appendix. This will also provide the experienced FEM user with a feeling for the notations used in this thesis.

A.1 Finite Element formulation of electrostatics

A.1.1 In two dimensions

The electrostatic equation, a partial differential equation (PDE) valid on an electrostatic domain (e.g. domain Ω in figure A.1), can be written in 2D as [48]:

$$\frac{\partial}{\partial x} \left(\varepsilon \frac{\partial \phi}{\partial x} \right) + \frac{\partial}{\partial y} \left(\varepsilon \frac{\partial \phi}{\partial y} \right) = -\rho, \quad (\text{A.1})$$

where ϕ is the electric potential and ρ the charge density. In air or a vacuum this charge density is zero, therefore the equation reduces to Laplace's equation:

$$\frac{\partial}{\partial x} \left(\varepsilon \frac{\partial \phi}{\partial x} \right) + \frac{\partial}{\partial y} \left(\varepsilon \frac{\partial \phi}{\partial y} \right) = 0. \quad (\text{A.2})$$

The boundary conditions are the potential values on the boundary and the boundary charges. Thus on the part of the boundary where the potentials are applied the boundary condition is:

$$\phi(x, y) = \bar{\phi}, \quad (\text{A.3})$$

which is also known as a Dirichlet boundary condition. On the boundary where the boundary charges are applied the boundary condition is:

$$\varepsilon \frac{\partial \phi}{\partial x} n_x + \varepsilon \frac{\partial \phi}{\partial y} n_y - Q = 0, \quad (\text{A.4})$$

with n_x and n_y the direction cosines of the outward normal vector. This type of boundary condition is also known as a Neumann or natural boundary condition.

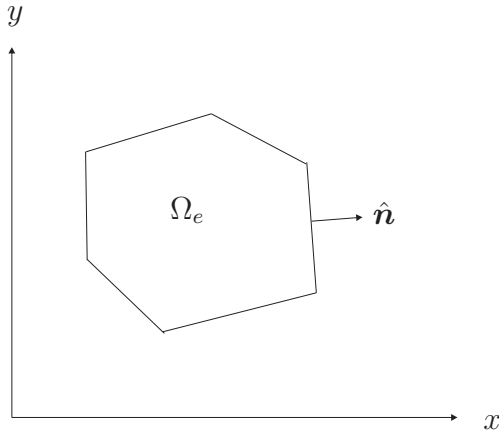


Figure A.1: Electrostatic domain

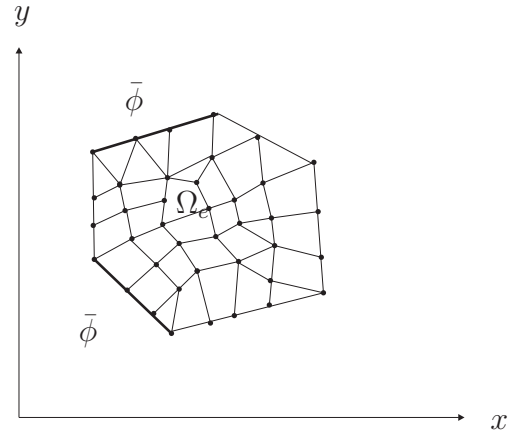


Figure A.2: Mesh consisting of triangles and quadrilaterals.

The standard approach in Finite Element theory is to divide the domain in different elements as in figure A.2. Each element is connected to the other elements at a finite number of points (called nodes, normally the corner points of the element), subsequently it is assumed that within an element, the value ϕ can be written as a linear function of the nodal values of the potential and the shape functions that only depend on the geometry of the element:

$$\phi = N_i \phi_i, \quad (\text{A.5})$$

where the N_i are the shape functions and ϕ_i the nodal potentials.

The next step is to multiply equation (A.2) with a test function v . If this product is integrated over the domain it should still be zero.

$$\int_{\Omega} v \left[\frac{\partial}{\partial x} \left(\varepsilon \frac{\partial \phi}{\partial x} \right) + \frac{\partial}{\partial y} \left(\varepsilon \frac{\partial \phi}{\partial y} \right) \right] d\Omega = 0. \quad (\text{A.6})$$

When Galerkin's method is used one uses the shape functions as n test functions v to define as a set of n integral equations [61]:

$$\int_{\Omega} N_i \left[\frac{\partial}{\partial x} \left(\varepsilon \frac{\partial \phi}{\partial x} \right) + \frac{\partial}{\partial y} \left(\varepsilon \frac{\partial \phi}{\partial y} \right) \right] d\Omega = 0, \quad (\text{A.7})$$

which can be integrated by parts as follows:

$$\int \int_{\Omega_e} \nabla a \cdot \mathbf{b} d\Omega = \int_{S_2} a \mathbf{b} \cdot \hat{\mathbf{n}} dS - \int \int_{\Omega_e} a \nabla \cdot \mathbf{b} d\Omega \quad (\text{A.8})$$

where $a = N_i$ and

$$\mathbf{b} = \varepsilon \begin{bmatrix} \frac{\partial \phi}{\partial x} \\ \frac{\partial \phi}{\partial y} \end{bmatrix},$$

where $\hat{\mathbf{n}}$ is the outward normal vector of the domain of integration and S_2 is that part of the boundary where a Neumann boundary condition is applied. When this method is applied one finds:

$$\int_{S_2} N_i \left(\varepsilon \frac{\partial \phi}{\partial x} n_x + \varepsilon \frac{\partial \phi}{\partial y} n_y \right) dS - \int \int_{\Omega_e} \left(\varepsilon \frac{\partial N_i}{\partial x} \frac{\partial \phi}{\partial x} + \varepsilon \frac{\partial N_i}{\partial y} \frac{\partial \phi}{\partial y} \right) dx dy, \quad (\text{A.9})$$

where the surface integral can be simplified by substituting the boundary condition (A.4)¹:

$$\int_{S_2} N_i Q dS - \int \int_{\Omega_e} \left(\varepsilon \frac{\partial N_i}{\partial x} \frac{\partial \phi}{\partial x} + \varepsilon \frac{\partial N_i}{\partial y} \frac{\partial \phi}{\partial y} \right) dxdy. \quad (\text{A.10})$$

Substituting equation (A.5) yields:

$$\left[\int \int_{\Omega_e} \left(\varepsilon \frac{\partial N_i}{\partial x} \frac{\partial N_j}{\partial x} + \varepsilon \frac{\partial N_i}{\partial y} \frac{\partial N_j}{\partial y} \right) \phi_j dxdy \right] - \int_{S_2} Q N_i dS = 0, \quad i = 1, 2, \dots, n, \quad (\text{A.11})$$

where Ω_e is the domain spanned by the element and S_2 that part boundary of the element where a natural boundary condition is applied. Thus in matrix vector notation, with ϕ a vector containing the nodal voltages, this equation can be written as:

$$\mathbf{K} \phi = \mathbf{Q}, \quad (\text{A.12})$$

where the forcing term \mathbf{Q} is defined as:

$$Q_i = \int_{S_2} Q(x, y) N_i dS, \quad (\text{A.13})$$

and the matrix \mathbf{K} is defined as:

$$K_{ij} = \int \int_{\Omega_e} \left(\varepsilon \frac{\partial N_i}{\partial x} \frac{\partial N_j}{\partial x} + \varepsilon \frac{\partial N_i}{\partial y} \frac{\partial N_j}{\partial y} \right) dxdy. \quad (\text{A.14})$$

Another way of writing the stiffness matrix often seen in literature is:

$$\mathbf{K} = \int \int_{\Omega_e} \varepsilon \nabla \mathbf{N}^T \cdot \nabla \mathbf{N} d\Omega, \quad (\text{A.15})$$

with \mathbf{N} a vector containing the shape functions.

Within air or a vacuum there are no space charges and the boundary values are all specified potentials or zero charges. Therefore all degrees of freedom have either a specified potential value or a free potential value. Hence the stiffness matrix \mathbf{K} can be split in several sub matrices, for free (ϕ) and prescribed ($\bar{\phi}$) degrees of freedom:

$$\begin{bmatrix} \mathbf{K}_{\phi\phi} & \mathbf{K}_{\phi\bar{\phi}} \\ \mathbf{K}_{\bar{\phi}\phi} & \mathbf{K}_{\bar{\phi}\bar{\phi}} \end{bmatrix} \begin{bmatrix} \phi \\ \bar{\phi} \end{bmatrix} = \begin{bmatrix} 0 \\ \bar{q} \end{bmatrix}. \quad (\text{A.16})$$

If the potential is imposed on a boundary, \bar{q} are the reaction charges on the surface of the conductor. Thus if the electric potential within the domain has to be calculated, the top line of the above equation can be used:

$$\mathbf{K}_{\phi\phi} \phi = -\mathbf{K}_{\phi\bar{\phi}} \bar{\phi}. \quad (\text{A.17})$$

When the free DOFs have been calculated the bottom line can be used to calculate the reaction charge on the boundary:

$$\bar{q} = \mathbf{K}_{\bar{\phi}\phi} \phi + \mathbf{K}_{\bar{\phi}\bar{\phi}} \bar{\phi}. \quad (\text{A.18})$$

¹This is the so called weak form of Laplace's equation, that can be used to find the solution : $\int_{\Omega} \nabla v \cdot \nabla \phi d\Omega = 0$, where ϕ is the potential solved for and v is a test function that can be anything. Galerkin's technique uses the shape functions that approximate the potential also as test functions.

A.1.2 In three dimensions

In 3D the electrostatic equation can be written as.

$$\frac{\partial}{\partial x} \left(\varepsilon \frac{\partial \phi}{\partial x} \right) + \frac{\partial}{\partial y} \left(\varepsilon \frac{\partial \phi}{\partial y} \right) + \frac{\partial}{\partial z} \left(\varepsilon \frac{\partial \phi}{\partial z} \right) = \rho. \quad (\text{A.19})$$

Using the same reasoning as in 2D, the stiffness matrix can be found to be the same expression as in 2D:

$$\mathbf{K} = \int \int_{\Omega} \varepsilon \nabla \mathbf{N}^T \cdot \nabla \mathbf{N} d\Omega \quad (\text{A.20})$$

with \mathbf{N} a vector containing the shape functions.

A 3D hexahedral element can be seen in figure A.3. Just like in the 2D case, shape functions can be defined as separable functions of the natural coordinates:

$$N_i(\xi, \eta, \zeta) = L_i(\xi)L_i(\eta)L_i(\zeta). \quad (\text{A.21})$$

For the hexahedral element, with nodes at $(\xi, \eta, \zeta) = (\pm 1, \pm 1, \pm 1)$, the linear shape functions are:

$$N_i = \frac{1}{8}(1 + \xi\xi_i)(1 + \eta\eta_i)(1 + \zeta\zeta_i). \quad (\text{A.22})$$

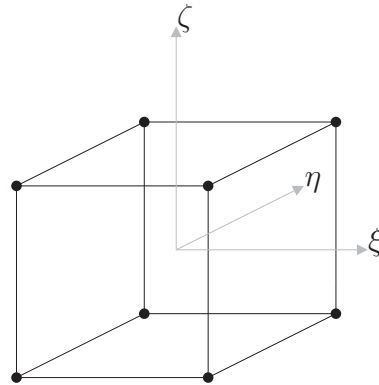


Figure A.3: A 3D hexahedral element in natural coordinates.

A.2 Finite Element formulation of structural mechanics

A.2.1 General 2D formulation

A short derivation of the linear version of 2D structural FEM will be provided here.² The mechanical equilibrium equations were discussed in section 3.2 and repeated below:

$$-\rho \ddot{u}_j + \frac{\partial}{\partial x_i} \sigma_{ji} + F_j = 0, \quad (\text{A.23})$$

²This complete section is based on the Rayleigh-Ritz method as presented in [45]

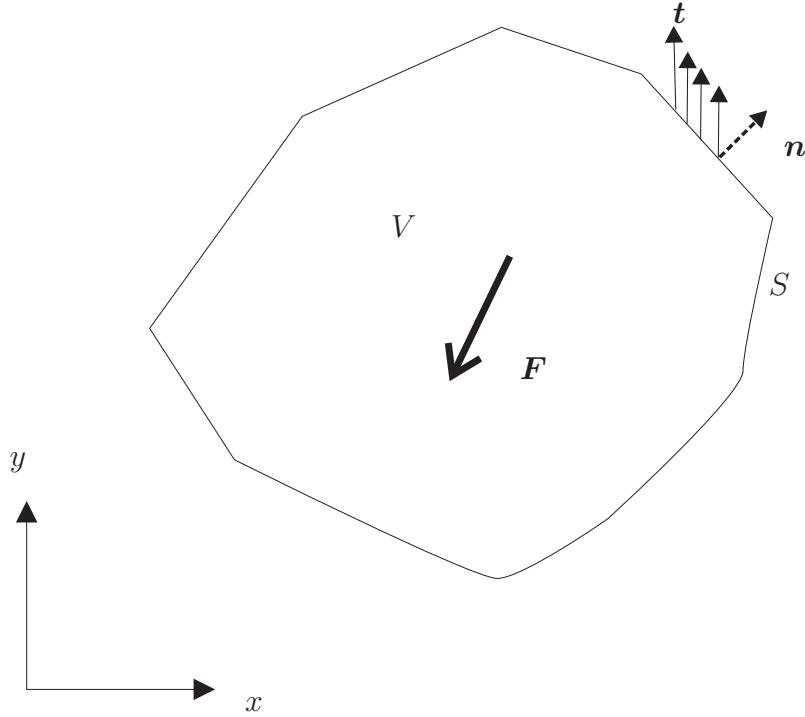


Figure A.4: Continuum mechanical domain.

For the FEM derivation also the surface traction on the domain is important is important. If the outward unit normal vector \mathbf{n} has components n_i the equilibrium between external traction and the stress tensor $\boldsymbol{\sigma}$ can be written as:

$$t_j = n_i \sigma_{ij}, \quad (\text{A.24})$$

where t_j is the surface traction in direction j .

If the derivation is restricted to the linear case the strain as function of the displacement field can be written as:

$$\begin{bmatrix} \epsilon_{xx} \\ \epsilon_{yy} \\ \gamma_{xy} \end{bmatrix} = \begin{bmatrix} \frac{\partial}{\partial x} & 0 \\ 0 & \frac{\partial}{\partial y} \\ \frac{\partial}{\partial y} & \frac{\partial}{\partial x} \end{bmatrix} \begin{bmatrix} u \\ v \end{bmatrix} = \mathbf{L} \begin{bmatrix} u \\ v \end{bmatrix}, \quad (\text{A.25})$$

where u and v are respectively the displacements in x and y direction and $\gamma_{xy} = 2\epsilon_{xy}$. The displacement field is discretized using shape functions:

$$\begin{bmatrix} u \\ v \end{bmatrix} = \begin{cases} N_i u_i \\ N_i v_i \end{cases} = \mathbf{N} \mathbf{u}. \quad (\text{A.26})$$

Thus a derivative matrix can be defined as: $\mathbf{B} = \mathbf{L} \mathbf{N}$.

In the case of linear elasticity the stresses are related to the strains by:

$$\sigma_{ij} = C_{ijkl} \epsilon_{kl}, \quad (\text{A.27})$$

which, due to the symmetry in C_{ijkl} , can be written as:

$$\begin{bmatrix} \sigma_{xx} \\ \sigma_{yy} \\ \tau_{xy} \end{bmatrix} = \mathbf{C}(E, \nu) \begin{bmatrix} \epsilon_{xx} \\ \epsilon_{yy} \\ \gamma_{xy} \end{bmatrix}, \quad (\text{A.28})$$

Using these assumptions equation (A.23) can be written as:

$$\mathbf{L}^T \mathbf{C} \mathbf{B} \mathbf{u} + \mathbf{F} - \rho \mathbf{N} \ddot{\mathbf{u}} = 0. \quad \text{in } V \quad (\text{A.29})$$

These equations basically say that the forces on all nodes must be zero. Equation (A.24) becomes:

$$\mathbf{D}^T \mathbf{C} \mathbf{B} \mathbf{u} = \mathbf{t} \quad \text{on } S, \quad (\text{A.30})$$

where:

$$\mathbf{D}^T = \begin{bmatrix} n_x & 0 & n_y \\ 0 & n_y & n_x \end{bmatrix}. \quad (\text{A.31})$$

In general it is impossible to exactly satisfy these equations, because the approximation (A.26) does not allow all possible continuum solutions. Therefore these equations can only be satisfied as:

$$\mathbf{L}^T \mathbf{C} \mathbf{B} \mathbf{u} + \mathbf{F} - \rho \mathbf{N} \ddot{\mathbf{u}} = \mathbf{r}_V. \quad \text{in } V \quad (\text{A.32})$$

$$\mathbf{t} - \mathbf{D}^T \mathbf{C} \mathbf{B} \mathbf{u} = \mathbf{r}_S \quad \text{on } S, \quad (\text{A.33})$$

However it possible to look at the problem from a different perspective: the goal is to find a solution to equations (3.4) and (3.4) under a constraint put on the solution (A.26). From this perspective the residual forces \mathbf{r}_V and \mathbf{r}_S are the reaction forces due to the constraint.

Now it is possible to find the values of the nodal displacements \mathbf{u} with the virtual work principle. The principle of virtual work says that the work produced by the forces due to any kinematically admissible virtual displacement should be zero. The residual forces \mathbf{r}_V and \mathbf{r}_S cancel each other out for kinematically admissible displacements. Therefore if the equations are pre-multiplied with the kinematically admissible virtual displacement:

$$\begin{bmatrix} \delta u \\ \delta v \end{bmatrix} = \mathbf{N} \delta \mathbf{u}, \quad (\text{A.34})$$

summed and integrated over the mechanical domain, the principle of virtual work gives:

$$\int_V \delta \mathbf{u}^T \mathbf{N}^T \mathbf{L}^T \mathbf{C} \mathbf{B} \mathbf{u} + \delta \mathbf{u}^T \mathbf{N}^T \mathbf{F} - \rho \delta \mathbf{u}^T \mathbf{N}^T \mathbf{N} \ddot{\mathbf{u}} dV + \int_S \delta \mathbf{u}^T \mathbf{N}^T (\mathbf{t} - \mathbf{D}^T \mathbf{C} \mathbf{B} \mathbf{u}) dS = 0, \quad (\text{A.35})$$

removing the arbitrary but non-zero variations $\delta \mathbf{u}$ gives:

$$\int_V \mathbf{N}^T \mathbf{L}^T \mathbf{C} \mathbf{B} \mathbf{u} + \mathbf{N}^T \mathbf{F} - \rho \mathbf{N}^T \mathbf{N} \ddot{\mathbf{u}} dV + \int_S \mathbf{N}^T (\mathbf{t} - \mathbf{D}^T \mathbf{C} \mathbf{B} \mathbf{u}) dS = 0. \quad (\text{A.36})$$

Integration by parts of the first term gives:

$$\int_V \mathbf{N}^T \mathbf{L}^T \mathbf{C} \mathbf{B} \mathbf{u} dV = \int_S \mathbf{N}^T \mathbf{D}^T \mathbf{C} \mathbf{B} \mathbf{u} dS - \int_V (\mathbf{L} \mathbf{N})^T \mathbf{C} \mathbf{B} \mathbf{u} dV. \quad (\text{A.37})$$

Substitution of this result into equation (A.36) yields:

$$\int_V \mathbf{B}^T \mathbf{C} \mathbf{B} dV \mathbf{u} + \int_V \rho \mathbf{u}^T \mathbf{N}^T \mathbf{N} dV \ddot{\mathbf{u}} = \int_V \mathbf{N}^T \mathbf{F} dV + \int_S \mathbf{N}^T \mathbf{t} dS, \quad (\text{A.38})$$

which can be written as:

$$\mathbf{M}_{uu} \ddot{\mathbf{u}} + \mathbf{K}_{uu}^m \mathbf{u} = \mathbf{f}. \quad (\text{A.39})$$

The 2D implementation of one element

There are two options to model linear mechanics in the 2D case: plane strain and plane stress. For the implementation in FEM this does not really matter, because both formulations can be written as (A.28):

$$\begin{bmatrix} \sigma_{xx} \\ \sigma_{yy} \\ \tau_{xy} \end{bmatrix} = \mathbf{C}(E, \nu) \begin{bmatrix} \epsilon_{xx} \\ \epsilon_{yy} \\ \gamma_{xy} \end{bmatrix}, \quad (\text{A.40})$$

where σ denotes stress, τ shear stress, ϵ strain and γ shear strain. The only difference is in the exact formulation of the 3 by 3 matrix \mathbf{C} as a function of Young's modulus and Poisson's ration. The constitutive relation for linear plane strain is defined by:

$$\mathbf{C} = \frac{E}{(1 + \nu)(1 - 2\nu)} \begin{bmatrix} 1 - \nu & \nu & 0 \\ \nu & 1 - \nu & 0 \\ 0 & 0 & \frac{1-2\nu}{2} \end{bmatrix}, \quad (\text{A.41})$$

and for linear plane stress it is defined by:

$$\mathbf{C} = \frac{E}{1 - \nu^2} \begin{bmatrix} 1 & \nu & 0 \\ \nu & 1 & 0 \\ 0 & 0 & 1 - \nu \end{bmatrix}. \quad (\text{A.42})$$

If quadrilateral volume elements are used one such an element will be the one shown in figure A.5. Node 1 has coordinates: $(\xi, \eta) = (-1, -1)$, node 2: $(\xi, \eta) = (1, -1)$, etc. The linear shape functions for this element are the same as the electrostatic shape functions:

$$\begin{aligned} N_1(\xi, \eta) &= \frac{1}{4}(\xi - 1)(\eta - 1), \\ N_2(\xi, \eta) &= -\frac{1}{4}(\xi + 1)(\eta - 1), \\ N_3(\xi, \eta) &= \frac{1}{4}(\xi + 1)(\eta + 1), \\ N_4(\xi, \eta) &= -\frac{1}{4}(\xi - 1)(\eta + 1), \end{aligned} \quad (\text{A.43})$$

but the matrix \mathbf{N} is defined by:

$$\begin{bmatrix} u \\ v \end{bmatrix} = \begin{bmatrix} N_1 \cdots N_4 & 0 \\ 0 & N_1 \cdots N_4 \end{bmatrix} \mathbf{u}, \quad (\text{A.44})$$

where:

$$\mathbf{u} = \begin{bmatrix} u_1 \\ \vdots \\ u_4 \\ v_1 \\ \vdots \\ v_4 \end{bmatrix}. \quad (\text{A.45})$$

The stiffness matrix can be computed as follows:

$$\mathbf{K} = \int_{\Omega} \mathbf{B}^T \mathbf{C} \mathbf{B} d\Omega, \quad (\text{A.46})$$

which can be used in the relation:

$$\mathbf{K} \mathbf{u} = \mathbf{F}, \quad (\text{A.47})$$

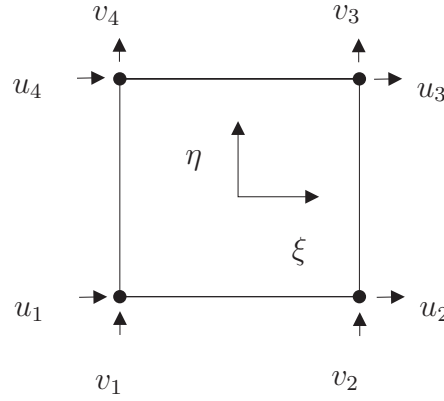


Figure A.5: One 2D volume element.

where \mathbf{F} is the vector containing the nodal forces.

Surface traction or body forces must be assembled using the following relations:

$$\mathbf{F}_b = \int_{\Omega} \mathbf{N}^T \mathbf{f}_b d\Omega \quad (\text{A.48})$$

$$\mathbf{F}_t = \int_S \mathbf{N}^T \mathbf{t} dS, \quad (\text{A.49})$$

where t is the surface traction and \mathbf{f}_b the body force. Initial strains can be added using:

$$\mathbf{F}_0 = \int_{\Omega} \mathbf{B}^T \mathbf{C} \epsilon_0 d\Omega. \quad (\text{A.50})$$

With the proper choice of \mathbf{L} and \mathbf{N} all these equations also hold in 3D. With a more complicated \mathbf{L} operator also geometric non-linearity can be included, without changing the equations above.

A.2.2 Beam elements

Another possibility to model the beam is not with volume elements, but with beam elements. Linear volume elements, such as the linear plane strain element need at least 3 to 4 elements through the thickness of the beam to capture the stress profile in the beam. Beam elements are specially designed to include the correct stress distribution. Basically a different equation is discretized:

$$EI \frac{d^4 u}{dx^4} = f, \quad (\text{A.51})$$

where I is the bending moment of the beam, u the vertical displacement of the beam perpendicular to the beam itself and f the pressure applied in the direction perpendicular to beam. The bending moment I is for a beam with a rectangular cross-section defined as:

$$I = \frac{wh^3}{12}, \quad (\text{A.52})$$

where h is the thickness of the beam and w the width. In the plane strain formulation an out of plane width of $w = 1$ was assumed and the thickness is $h = 4 \cdot 10^{-6}$, both will be used for the beam model as well.

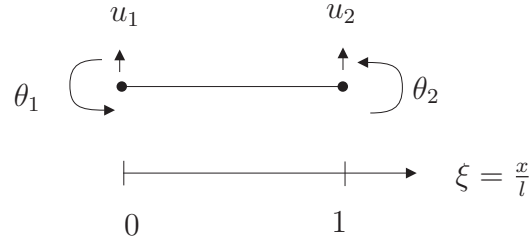


Figure A.6: One beam element.

The weak form of (A.51) is:

$$\int vEI \frac{d^4u}{dx^4} dx - \int v f dx = 0, \quad (\text{A.53})$$

where $v(x)$ is a non zero test-function that can be anything. Twice integrating the first term by parts yields:

$$\int EI \frac{d^2v}{dx^2} \frac{d^2u}{dx^2} dx = \int v f dx, \quad (\text{A.54})$$

One beam element is shown in figure A.6. The displacement u is discretized as:

$$u = \mathbf{N} \mathbf{u}, \quad (\text{A.55})$$

with:

$$\mathbf{N}^T = \begin{bmatrix} 1 - 3\xi^2 + 2\xi^3 \\ l\xi(1 - \xi)^2 \\ \xi^2(3 - 2\xi) \\ l\xi^2(\xi - 1) \end{bmatrix}, \quad (\text{A.56})$$

and:

$$\mathbf{u} = \begin{bmatrix} u_1 \\ \theta_1 \\ u_2 \\ \theta_2 \end{bmatrix}, \quad (\text{A.57})$$

where l is the length of the beam.

If the shape functions N_i are used as test-functions and substituted in stead of v , this yields for the beam element:

$$\mathbf{K} = \int EI \frac{d^2 \mathbf{N}^T}{d\xi^2} \frac{d^2 \mathbf{N}}{d\xi^2} \frac{d\xi}{l^3}, \quad (\text{A.58})$$

and the applied force is:

$$\mathbf{f} = \int \mathbf{N} f(x) dx, \quad (\text{A.59})$$

where \mathbf{f} is vector containing nodal forces and nodal torques. Together this gives a linear set of equations:

$$\mathbf{K} \mathbf{u} = \mathbf{f}. \quad (\text{A.60})$$

A.3 Shape functions and natural coordinates

A.3.1 Shape functions in natural coordinates

In the previous sections all equations were derived using unspecified shape functions. One of a few statements about these shape function was equation (A.5) that states that the shape functions help define the potential as a function of the nodal potentials. Similarly they helped define the displacements for the mechanical equations. It was assumed that these shape functions are only depending on the geometry of the element.

For each nodal DOF a shape function is defined, describing the influence of the nodal DOF on the element distribution. The shape functions approximate potential within an element when each shape function is multiplied with a corresponding nodal potential. The summation of these nodal potential distributions will then approximate the potential distribution within an element. The individual shape functions therefore have to be 1 at their corresponding nodes, but 0 on all the other nodes.

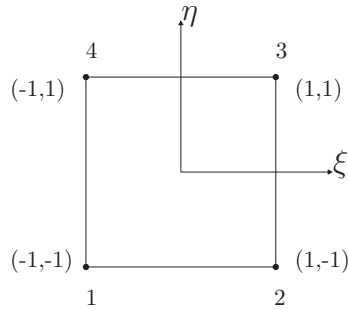


Figure A.7: Bilinear square element.

In this text we will only discuss quadrilateral elements, thus only elements with 4 corners. The simplest quadrilateral element is the square bilinear Lagrange element shown in figure A.7. The bilinear shape functions for this element are [61]:

$$\begin{aligned}
 N_1(\xi, \eta) &= \frac{1}{4}(\xi - 1)(\eta - 1), \\
 N_2(\xi, \eta) &= -\frac{1}{4}(\xi + 1)(\eta - 1), \\
 N_3(\xi, \eta) &= \frac{1}{4}(\xi + 1)(\eta + 1), \\
 N_4(\xi, \eta) &= -\frac{1}{4}(\xi - 1)(\eta + 1).
 \end{aligned}
 \tag{A.61}$$

To illustrate their behavior, one the shape functions of one of the nodes is shown in figure A.8:

A.3.2 Isoparametric mapping

For rectangular elements is quite easy to write the local or natural coordinates ξ and η as functions of the global coordinates x and y needed to perform the element integration, but when arbitrary quadrilaterals are used, this can become a tedious job, therefore normally some kind of mapping is used, e.g. a isoparametric mapping.

When using an isoparametric mapping, one assumes that the coordinates can be mapped using the same shape functions as the variable of interest. Thus the coordinate within the element is a function of the corner coordinates:

$$\begin{aligned}
 x &= N_i(\xi, \eta)x_i, \\
 y &= N_i(\xi, \eta)y_i,
 \end{aligned}
 \tag{A.62}$$

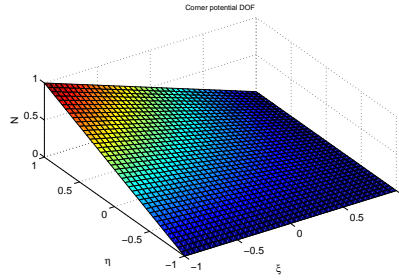


Figure A.8: Bilinear shape functions.

which has as Jacobian of transformation:

$$\begin{bmatrix} \frac{\partial}{\partial \xi} \\ \frac{\partial}{\partial \eta} \end{bmatrix} = \begin{bmatrix} \frac{\partial x}{\partial \xi} & \frac{\partial x}{\partial \eta} \\ \frac{\partial y}{\partial \xi} & \frac{\partial y}{\partial \eta} \end{bmatrix} \begin{bmatrix} \frac{\partial}{\partial x} \\ \frac{\partial}{\partial y} \end{bmatrix} = J \begin{bmatrix} \frac{\partial}{\partial x} \\ \frac{\partial}{\partial y} \end{bmatrix}, \quad (\text{A.63})$$

therefore:

$$\begin{bmatrix} \frac{\partial N_i}{\partial x} \\ \frac{\partial N_i}{\partial y} \end{bmatrix} = J^{-1} \begin{bmatrix} \frac{\partial N_i}{\partial \xi} \\ \frac{\partial N_i}{\partial \eta} \end{bmatrix}, \quad (\text{A.64})$$

which is an easy method to define the integrands in the matrix (A.14). But to calculate the integrals correctly the following relation has to be used:

$$\int \int f(x, y) dx dy = \int \int f(x(\xi, \eta), y(\xi, \eta)) \det(J) d\xi d\eta. \quad (\text{A.65})$$

Appendix B

Rounding corners

B.1 Introduction

In chapter 2 it was shown that the solution of the electric field becomes infinite near a corner. It was shown that these singularities cause convergence problems for standard FEM models. Solutions to overcome these issues were presented, however all these solutions required special FEM elements or variational force computation, both currently unavailable in most commercial FEM codes [65, 1].

A standard method to overcome these convergence problems consists in rounding off the corners, which removes the geometric singularity [143]. Because just a geometry is changed this can be done in any FEM code (although it can be a tedious procedure).

This approach seems very close to real life, because in reality sharp corners do not exist. All corners are rounded off a little bit. Therefore rounding the corners might actually be smarter than sharp corner modeling.

However it is obvious that rounded corners require dense meshes. Therefore it might be better to model rounded corners as sharp corners with the most optimal FEM elements if the influence of round off on the total corner force is small. This will be investigated numerically in section B.2 and analytically in section B.3.

B.2 Finite Element Modeling

Rounding the corners works because in that case the singularity is removed, thus the value of the charge at the corner becomes bounded, which will result in a finite force distribution at the corner. This will ensure that the force calculation with the local force method converges with considerable ease. This effect is illustrated in figures B.1 and B.2 where can be seen that with a rounded corner, the change for the electric field is smoother.

However one big disadvantage of a rounded corner is related to the mesh near a corner. To accurately mesh the curved geometry, a much higher number of elements is required compared to the sharp corner, as shown for triangular elements in figure B.3.

Another difficulty is that the magnitude of the radius has to be chosen. In reality sharp corners hardly ever exist, there is always some degree of a round off. However it is nearly impossible to predict this real radius beforehand or to measure each individual edge on a fabricated MEMS.

Thus it would be interesting to see the influence of the rounding radius on the

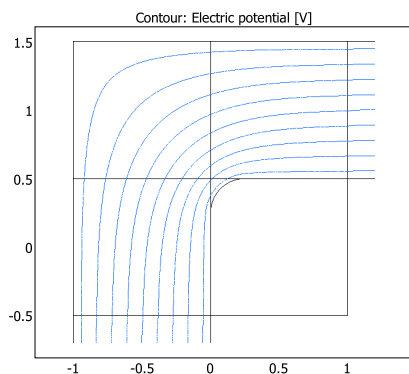


Figure B.1: Electric potential around a rounded corner.

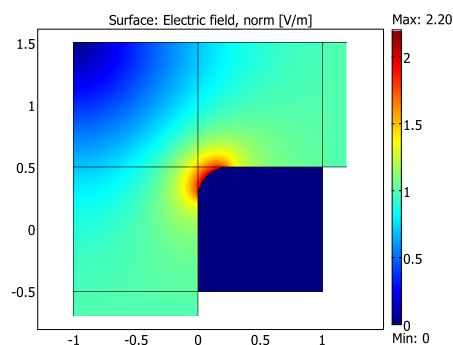


Figure B.2: Electric field around a rounded corner.

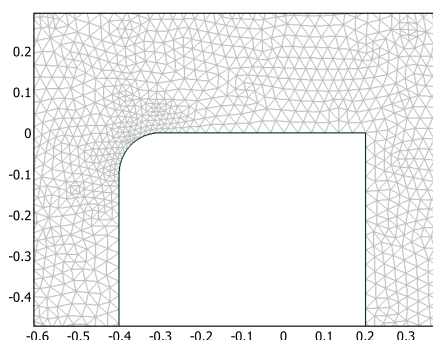


Figure B.3: Mesh near a sharp and a rounded corner.

computed electrostatic force and if the solution converges to the same value as the sharp corner when the radius is decreased. When the corner is rounded, the problem converges to a final solution for both the variational method as the local force approach. The corner is rounded with decreasing radii and the results are summarized in figure B.4. The x-axis signifies the inverse radius $1/r$ and the y-axis the electrostatic force in the x-direction.

In the figure it can be seen that the force converges to the same value as the solution for the sharp corner obtained with the variational method (2.113) in figure 2.18. Furthermore it converges rather fast, at $\frac{1}{5}$ (the corner side having a unit length) it is within 1 percent of the analytical sharp corner solution.

B.3 Analytical modeling

The rounding effects can also be studied with the help of conformal transformations. But transforming rounded corners is not a trivial case, therefore the geometry that is being investigated in the section is not the reference unit corner. For a slightly different problem however it is easier to perform the transformations, therefore a different reference will be used in this section.

The transformations are shown in figure B.5. First the sharp transformation will be shown, thereafter the rounded transformation will be discussed and finally their results will be compared.

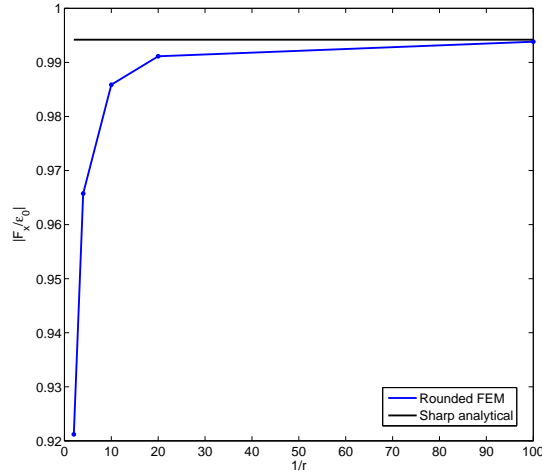


Figure B.4: Electrostatic forces for different rounding radii.

Sharp corner

The objectives of the transformation are summarized in table B.1.

z plane	t plane
$z = ig$	$t = -1$
$z = -\infty$	$t = 0$
$z = \infty$	$t = \infty$
$z = i\infty$	$t = -\infty$

Table B.1: Objectives for the transformation.

In the transformation library of [16] the following transformation can be found:

$$z = -\frac{g}{\pi} \left(2\sqrt{t+1} - 2\log(\sqrt{t+1} + 1) + \log(t) \right), \quad (\text{B.1})$$

the Jacobian of this transformation is:

$$\frac{\partial z}{\partial t} = \frac{g}{\pi t} \sqrt{t+1}. \quad (\text{B.2})$$

Since the origin of the t plane is at $z = -\infty$ and one of the boundaries is given a unit potential the electric field will be equal to:

$$w = \frac{1}{\pi} \log(t). \quad (\text{B.3})$$

thus the electric field in the z plane will be:

$$E = -\frac{\partial w}{\partial z} = -\frac{\partial w}{\partial t} \frac{\partial t}{\partial z} = -\frac{1}{g\sqrt{t+1}}. \quad (\text{B.4})$$

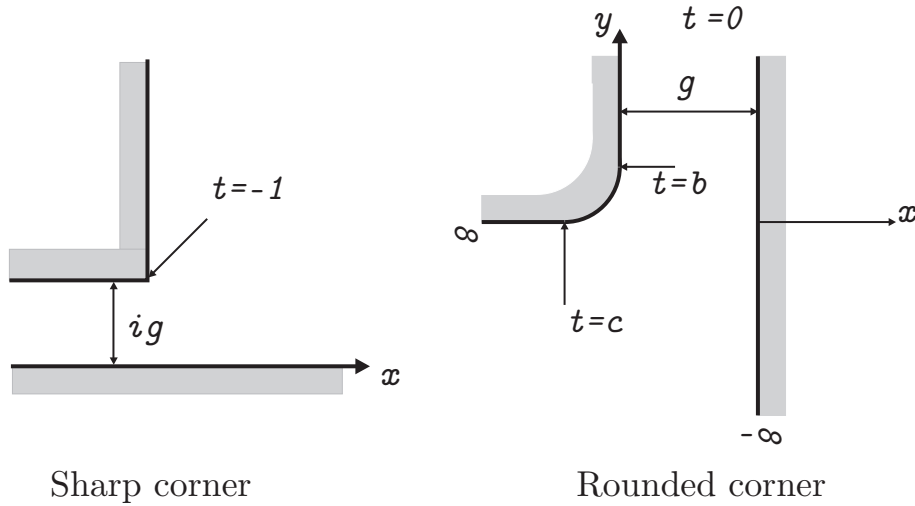


Figure B.5: Transformations for a sharp and a rounded corner near an infinitely long conductor.

Because the electric field has only an horizontal (imaginary) or a vertical (real) component on the boundary equation (2.79) can be used instead of equation (2.78), thus the electric pressure in the z plane will be:

$$f_{es} = \frac{\epsilon_0}{2g^2(t+1)}. \tag{B.5}$$

Again it is clear that at $t = -1$ there is a singular point, which can also be seen in figure B.6 that shows to distributed forces on the two boundaries. However when integrated over the boundary the Jacobian has to be considered, therefore the force in z coordinates becomes:

$$F_{es} = \int \frac{\epsilon_0}{2\pi g^2 \sqrt{t+1}t} dt, \tag{B.6}$$

which will remain bounded when integrated over the singular point.

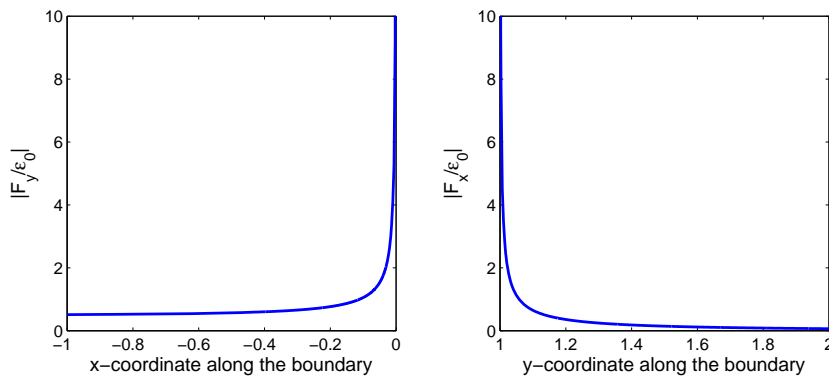


Figure B.6: Electric Force on sharp corner boundaries.

When a specific gap width of $g = 1$ is entered and the force is calculated from $z = -1 + i$ to $z = i$ this yields the following force:

$$F_{es} = iF_x + F_y = 0.3908\epsilon_0 i - 0.8145\epsilon_0. \tag{B.7}$$

Rounded corner

Using the transformation library in [16], the transformation for the rounded corner can be written as:

$$z = -\frac{2g}{\pi(\sqrt{b} + \lambda\sqrt{c})} \left[\sqrt{t-b} - \sqrt{b} \arctan\left(\sqrt{\frac{t-b}{b}}\right) + \lambda \left(\sqrt{t-c} - \sqrt{c} \arctan\left(\sqrt{\frac{t-c}{c}}\right) \right) \right], \quad (\text{B.8})$$

where b and c the t are plane coordinates as shown in figure B.5, g is the gap width and λ is a parameter used to determine the curvature of the round off which has to be determined by trial and error. The objectives of the transformation are summed up in table B.2. In this table is r the rounding radius.

z plane	t plane
$z = ir$	$t = b$
$z = -r$	$t = c$
$z = -\infty$	$t = \infty$
$z = -i\infty$	$t = -\infty$
$z = i\infty$	$t = 0$

Table B.2: Objectives for the transformation.

The Jacobian of the transformation becomes a lengthy expression but can be calculated:

$$\frac{\partial z}{\partial t} = \frac{1}{\pi(\sqrt{b} + \lambda\sqrt{c})} \left[\frac{1}{\sqrt{t-b} \left(1 + \frac{t-b}{b}\right)} - \frac{1}{\sqrt{t-b}} - 2\lambda \left(\frac{1}{2\sqrt{t-c}} - \frac{1}{2\sqrt{t-c} \left(1 + \frac{t-c}{c}\right)} \right) \right]. \quad (\text{B.9})$$

The values for constants b , c , g and λ will substituted at this moment for the sake of simplicity. By trial and error, the values $b = 0.7$, $c = 3$ and $\lambda = 0.75$ were found, which give an almost circular rounding with an approximately 0.2 value of the rounding radius.

The electric field in the t plane will be the logarithmic field, due to the position of the origin:

$$w = \frac{1}{\pi} \log(t). \quad (\text{B.10})$$

In this case the electric field at the boundary is not always parallel to one of the coordinate axes. Therefore the more complex equation (2.78) has to be used. The distributed force is shown in figure B.7. It is easy to see that the rounding of the corner has removed the singularity, there are still two peaks at the beginning and the end of round off, but these are finite peaks. At point $b = (x, y) = (0, 0.19)$ the distributed force is equal to $F = 1.7628\varepsilon_0 i$ and at point $c = (x, y) = (-0.19, 0)$ to $F = -0.9916\varepsilon_0$.

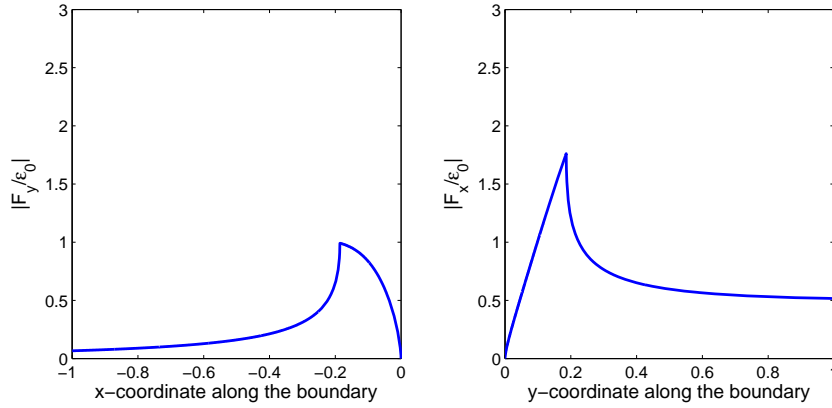


Figure B.7: Electric Force on round corner boundaries.

The total electric force in the z plane will be, when integrated from $t = 0.0403$ to $t = 12.92$, to get the force on the corner from $z = -1$ to $z = i$:

$$F_{es} = F_x i + F_y = -0.7858\epsilon_0 i - 0.3894\epsilon_0. \quad (\text{B.11})$$

It can be seen that this force is nearly the same as for the sharp problem. Therefore one can conclude that it has only a marginal influence on the corner force when that corner is rounded. When the radius is 20% of the characteristic length (the unit distance used as integration domain), the influence on the force is less than 3%.

For the sake of completeness, a contour plot of the potential field near the sharp corner is shown in figure B.8 and the plot of the field near a rounded corner in figure B.9. Care has to be taken when interpreting the results, because the transformations result in a two mirrored geometries, thus in mirrored solutions. It can be seen that on a large scale the potential fields are very similar, explaining the low change in integrated force. Only on close distance to the singularity the fields are very different.

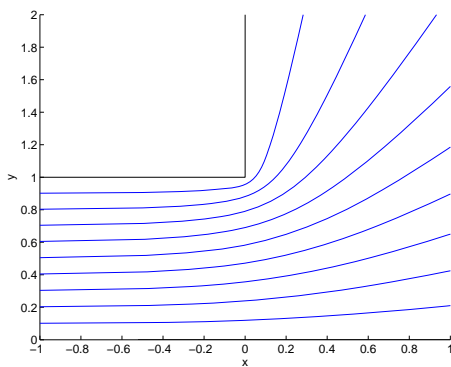


Figure B.8: Potential near a sharp corner.

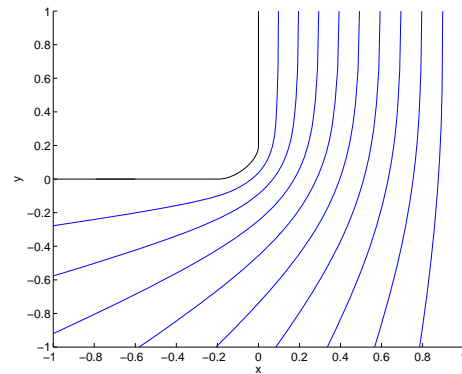


Figure B.9: Potential near a rounded corner.

Decreasing radii

Of course it is also possible to calculate the corner forces for different corner radii. To get a rounded corner with a certain radius, parameters a , b and λ in equation (B.9)

can be varied. The y-direction force at different radii is shown in figure B.10. The shown results sustain the conclusion that the force on a rounded corner converges to the sharp corner solution when the radius is decreased.

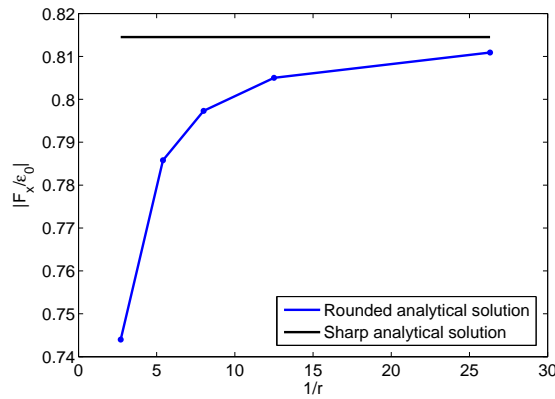


Figure B.10: Corner forces for different round off radii.

B.4 Conclusions

Chapter 2 showed that the variational approach is much more suited to model sharp corners than the local force approach. In this chapter it is shown that when the corners are rounded the local force approach can solve the problem as well, although at the expense of the extra elements to mesh the curve.

However the computed force does not really vary with the radius, therefore if the corners can be modeled with sharp elements it is much more efficient to use them in combination with the variational approach even if in reality there is a round off radius. Therefore it is not necessary to predict or measure the real radius, saving time.

Appendix C

A stiffness and mass sensing cantilever

C.1 Introduction

Within the Delft University a set of micro cantilevers ha been developed [113]. A scanning electron microscope (SEM) image of the cantilevers is presented in figure C.1. Their main goal is to: *a* sense stiffness variations due to size effects of exterior influences by pull-in measurements and *b* measuring mass variations due to exterior influences by frequency measurements. However other uses could be developed as well. Several measurements have been performed with these cantilevers, thus experimental data is available.

Because all purposes of the cantilever benefit from a good model and there are measurements available, this cantilever is an ideal test case for the finite element strategies as presented in this thesis. More specifically the chosen modeling steps will be presented within the framework of chapter 13. Furthermore the strategies could provide more applications or improvements to the cantilever design.

The cantilevers are created using a Silicon on Insulator (SOI) wafer. A SOI wafer consists of a thick single crystal SI substrate with on top of it two small layers: a layer of insulating SiO_2 and a layer of single crystal Si . The cantilevers are produced by patterning the top layer as follows: depositing a layer of photo resist on the silicon, illuminating that layer through a mask and developing it. Subsequently a directional etch is used to remove the silicon on the location were no cantilevers or their suspension are required. This insures that the thickness of the cantilever is equal to the thickness of the original layer in the SOI wafer. Thereafter an isotropic etch is used to remove the SiO_2 below the cantilevers. This makes sure that the gap below is equal to the original thickness of the SiO_2 , however due to the fact that the etch rate is equal in all directions the SiO_2 near the clamp will have a special shape as shown by figures C.3 and C.4.

The first section of this chapter describes the FEM model of the cantilevers. Next the basic stiffness and mass sensing properties of these cantilevers are described using FEM sensitivities in section C.3. The problem with the basic cantilever is that is very hard to measure the position of a mass attached to the cantilever. Therefore the possibility of slightly changing the design to improve that capability is investigated in section C.4. Of course such a sensor could also be used to sense the pressure of the fluid around the cantilever (see chapter 10), but is it also possible to measure different

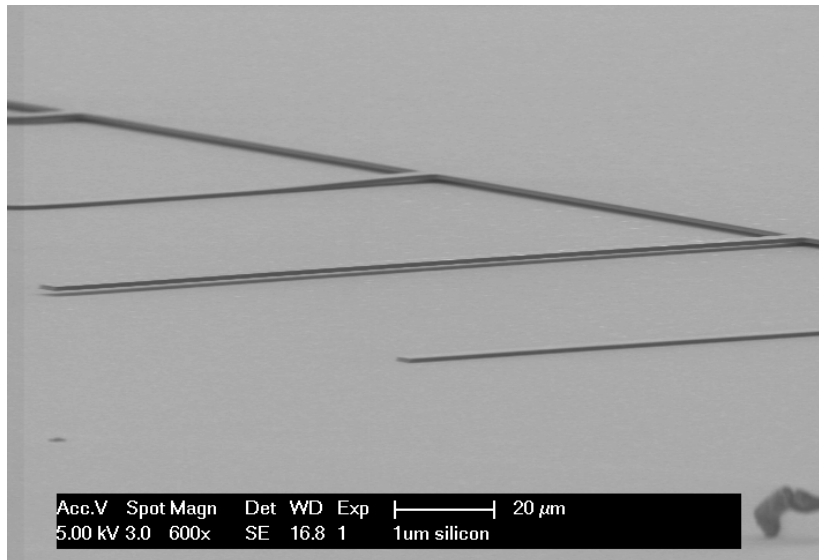


Figure C.1: SEM image of several cantilevers.

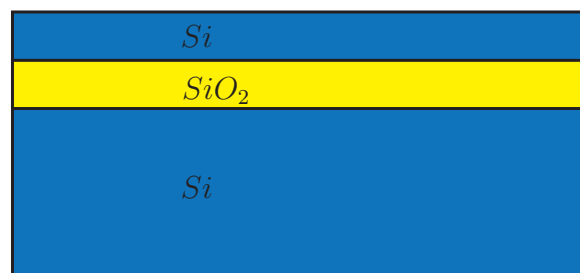


Figure C.2: Cross section of a SOI wafer.

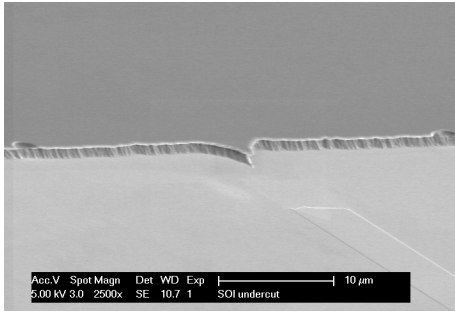


Figure C.3: Remainder of SiO_2 after forcefully removing the Si cantilever.

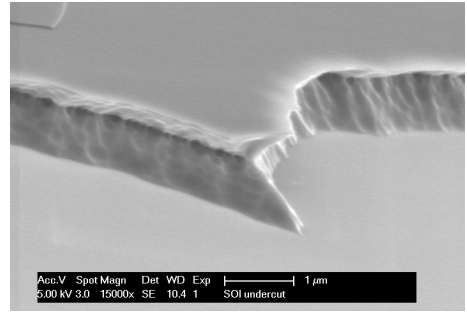


Figure C.4: Close up of fig. C.3.

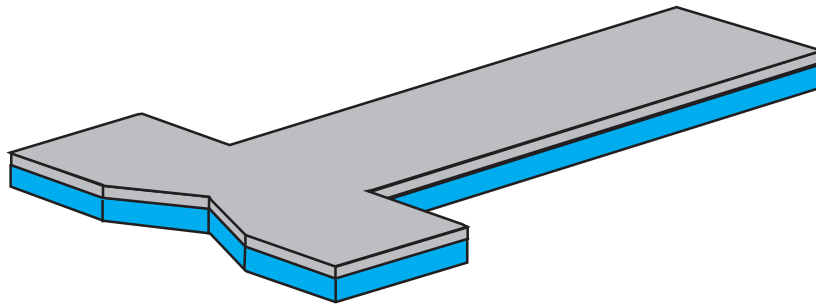


Figure C.5: Simplified 3D geometry of the cantilever.

properties? This question is investigated in section C.5.

C.2 Model

Basically the beam can be modeled using the shape shown in figure C.5. The gray part is the silicon cantilever which is clamped at the indented edge. The indentation is a model of the SiO_2 left by the isotropic etch used to release the cantilever as mentioned in the previous paragraph.

As mentioned a lot of different cantilevers were produced so the model should be parametric. Most of the parameters are defined in the top view as shown in figure C.6. Only the gap and plate thickness cannot be defined in the top view, but those are not difficult to define. Since the beams are used to measure stiffness and mass variations the elasticity modulus and the density are non-constant parameters as well. All constant and non-constant parameters are summarized in table C.1.

C.2.1 A 1D model

Of course a very simple model would be a simple 1D mass spring gap system. Figure 3.2 in chapter 3 showed such a 1D model and showed that the pull-in voltage was defined as:

$$V_{PI} = \sqrt{\frac{8 k x_0^3}{27 \epsilon}}, \quad (C.1)$$

where the difficulty is determining the stiffness k for a cantilever problem. However in literature a method for doing that can be found [97]. According to that paper for a

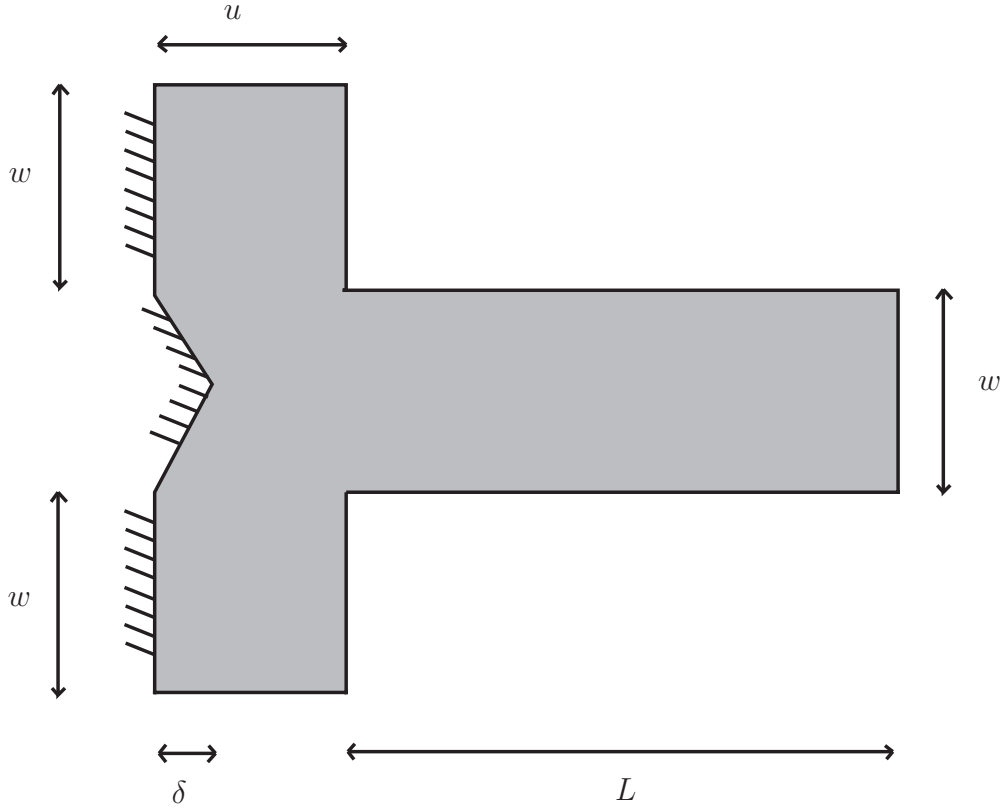


Figure C.6: Top view with parameter definition.

cantilever with distributed electrostatic load, width w , initial gap x_0 , thickness h and length $\ell = L + u$ the effective stiffness is:

$$k = \frac{2\hat{E}wh^3}{3\ell^3}, \quad (\text{C.2})$$

where the effective Young's modulus is:

$$\hat{E} = E, \quad (\text{C.3})$$

if $w \approx h$ and

$$\hat{E} = \frac{1}{1 - \nu^2}, \quad (\text{C.4})$$

if $w > 5h$.

C.2.2 FEM model

It is clear that such a 1D model is limited, it cannot cope with the SiO_2 left by the isotropic etch and it cannot handle malfunctions during production, therefore a FEM model is created. The cantilever is modeled with plate elements and the electrostatic gap with brick elements. The electrostatic mesh can deform to capture non-linearity. The plate mesh for which the results are converged is shown in figure C.7, the dimensions or the non-constant parameters are chosen arbitrarily. The electrostatic mesh is very similar to the plate mesh because it is an extrusion of the plate mesh in the third

Table C.1: Parameters of the cantilevers.

Constant parameters			
Property	Symbol	Value	Units
<i>Gap size</i>	g	$1.019 \cdot 10^{-6}$	m
<i>Electric permittivity</i>	ε	$8.8541 \cdot 10^{-12}$	F/m
<i>Poisson's ratio</i>	ν	0.22	–
<i>Ambient pressure</i>	P_A	$1 \cdot 10^5$	Pa/m^2
<i>Viscosity</i>	μ	$18.27 \cdot 10^{-6}$	$kg/(m \cdot s)$
<i>Mean free path</i>	λ_0	$94 \cdot 10^{-9}$	m
Non-constant parameters			
Property	Symbol	Value	Units
<i>Length</i>	L	–	m
<i>Width</i>	w	–	m
<i>Beam thickness</i>	h	–	m
<i>Undercut</i>	u	–	m
<i>Indentation depth</i>	δ	–	m
<i>Elasticity modulus</i>	E	–	Pa
<i>Density</i>	ρ	–	kg/m^3

dimension. The number of electrostatic elements in this third dimension is 4, which is low due to the fact that the electric problem is relatively simple.

It was modeled as a coupled-simulation model in Matlab, hence all tangent sensitivity information can be computed. Therefore the three solution strategies from the framework: staggered, hybrid and monolithic can be used.

C.2.3 Experimental validation

Two parameters are easily measured, pull-in and frequency. From the available simulation options provided within the framework a staggered approach is used to solve for pull-in. The staggered approach is used because the mechanic problem is linear. For the frequency computations a monolithic approach will be used because of its robustness.

Pull-in

For the experimental validation a measurement is used obtained with a beam that has thickness of 1019 nm. At that thickness size effects do not play a role so the Young's modulus is known to be 169GPa. The other properties for this beam are summarized in table C.2.

The analytical model gave a pull-in value of:

$$V_{PI}^{1D} = 12.16V, \quad (C.5)$$

Where the FEM model gave:

$$V_{PI}^{FEM} = 15.36V. \quad (C.6)$$

This is a pretty big difference, which cannot be explained by the indentation δ only. Because if the indentation is removed the FEM pull-in becomes:

$$V_{PI}^{FEM} = 14.63V. \quad (C.7)$$

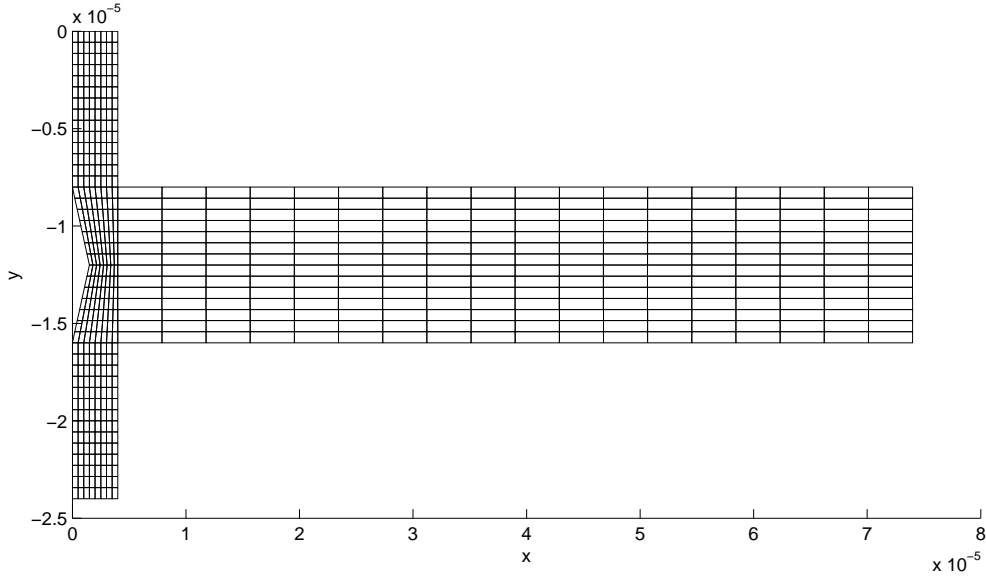


Figure C.7: Top view of the plate mesh.

Table C.2: Parameters of the cantilever used for validation.

Non-constant parameters			
Property	Symbol	Value	Units
<i>Length</i>	L	$70 \cdot 10^{-6}$	m
<i>Width</i>	w	$8 \cdot 10^{-6}$	m
<i>Beam thickness</i>	h	$1.019 \cdot 10^{-6}$	m
<i>Undercut</i>	u	$4 \cdot 10^{-6}$	m
<i>Indentation depth</i>	δ	$3 \cdot 10^{-6}$	m
<i>Elasticity modulus</i>	E	169	GPa
<i>Density</i>	ρ	2330	kg/m^3

The FEM model has an actual distributed load and simulates the redistribution of charge during loading, thus it has a different solution as the analytical one. The measured value for pull-in is:

$$V_{PI}^{meas} = 15.30 \pm 0.01V, \quad (C.8)$$

which is really close to the 15.36 of the FEM model.

Eigenfrequency

For the eigenfrequency validation a slightly different beam is used: one with a length of 84μ in stead of 70μ . All other properties are equal to the ones in table C.2. For this beam the frequency was measured in a high vacuum, but pull-in was not measured. The measured first eigenfrequency was:

$$\omega^{meas} = 1.201 \cdot 10^6 \text{ rad/s} = 191.2 \text{ kHz}. \quad (C.9)$$

The finite element model gives a first frequency of

$$\omega^{meas} = 1.221 \cdot 10^6 \text{ rad/s} = 194.3 \text{ kHz}, \quad (C.10)$$

which is really close to the measured one. Hence the FEM model predicts the correct values when size effects do not influence the behavior.

C.3 Simple stiffness and mass measurement

C.3.1 Stiffness measurement

One application of these cantilevers is for measuring the size dependency of the Young's modulus [113]. Another is the measurement of Young's modulus changes due to adsorption of material into the cantilever [114, 112]. In both cases the pull-in voltage is the value used for determining the elasticity. Hence the sensitivity of the pull-in voltage is crucial during operation¹.

For the beam that was used for experimental validation ($L = 70\mu$, $w = 8\mu$, $h = 1.019\mu$) this sensitivity is computed with the FEM model²:

$$\left. \frac{\partial V}{\partial E} \right|_{PI} = 45.5 \cdot 10^{-3} V/GPa, \quad (C.11)$$

which means that if the pull-in measurement was done with a resolution of 0.01 Volts, the resolution of the Elasticity measurement is $0.22 GPa$. This does not seem to be a very bad resolution.

The pull-in value was computed with a staggered scheme, after which the sensitivity computation required tangent information. Therefore the total approach is a hybrid one.

C.3.2 Frequency for mass measurement

Another goal is measuring the frequency change due to mass addition onto or adsorption into the cantilever [112]. This basically means that the effective density of the plate changes. For the ($L = 70\mu$, $w = 8\mu$, $h = 1.019\mu$) beam the first resonance frequency is:

$$\omega_1 = 278 kHz, \quad (C.12)$$

and the sensitivity for density variations is:

$$\frac{\partial \omega}{\partial \rho} = -59.7 Hz \cdot m^3/kg. \quad (C.13)$$

When the resolution of the frequency measurement is about $0.1 kHz$, this means that the resolution of the mass measurement is about $1.7 kg/m^3$.

In essence this was a pure mechanic problem, hence the framework as presented was not used.

C.3.3 Combining both measurements for accuracy

In general adsorption will cause both mass and stiffness changes [124]. Therefore both sensitivities should be considered. For instance if due to adsorption the frequency lowers by $\Delta\omega = 3 kHz$ and the pull-in voltage increases by $\Delta V_{PI} = 0.2 V$ this would mean that the adsorption had the following effect:

$$\Delta E = \left(\frac{\partial V}{\partial E} \right)^{-1} \Delta\omega = (45.5 \cdot 10^{-3})^{-1} 0.2 = 4.4 GPa, \quad (C.14)$$

¹Conveniently pull-in sensitivities have been discussed in chapter 6.

²All the FEM sensitivities presented in this chapter are computed using analytic derivations, none have been calculated by finite differences.

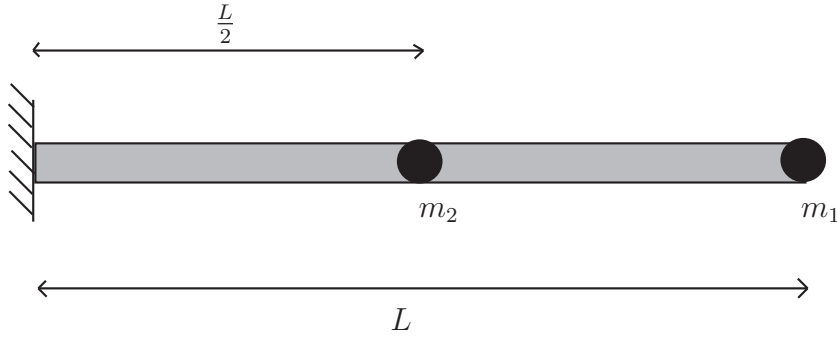


Figure C.8: Beam with two mass attachment points.

and from:

$$\Delta\omega = \frac{\partial\omega}{\partial E}\Delta E + \frac{\partial\omega}{\partial\rho}\Delta\rho, \quad (\text{C.15})$$

follows:

$$\Delta\rho = \left(\frac{\partial\omega}{\partial\rho}\right)^{-1} \left(\Delta\omega - \frac{\partial\omega}{\partial E}\Delta E\right) = (-59.7)^{-1}(-3000 - 824 \cdot 4.4) = 111 \text{ kg/m}^3, \quad (\text{C.16})$$

where the FEM result:

$$\frac{\partial\omega}{\partial E} = 824 \text{ Hz/GPa}, \quad (\text{C.17})$$

was used. In other words for an accurate mass measurement the frequency relationship alone could be not enough. If adsorption decreases stiffness and increases the density, they could even cancel out and destroy the measurement principle completely.

C.4 Multiple frequency mass sensing

So far, all analyses assumed basically a 1 dimensional mode of operation. The mass and stiffness variation were assumed to be uniform along the beam. This is perfectly valid if the reaction targets the complete beam³. However, if one wants to use the cantilever as a *single molecule* detector the point of bonding is not always known a priori.

For a simplified analysis a 2 dimensional mode of operation is investigated. Consider the beam in figure C.8 which has two possible attachment points for mass particles. Let's assume that at point 1 a mass of Δm_1 has been attached after exposure and at point 2 a mass of Δm_2 . How to distinguish between these mass additions?

One can measure of course not only the first but also the second eigenfrequency before and after the attachment of mass. This gives measured eigenfrequency shifts $\Delta\omega_1$ and $\Delta\omega_2$. Assuming a linear relation between eigenfrequencies and mass additions:

$$\begin{bmatrix} \Delta\omega_1 \\ \Delta\omega_2 \end{bmatrix} = \begin{bmatrix} \frac{\partial\omega_1}{\partial m_1} & \frac{\partial\omega_1}{\partial m_2} \\ \frac{\partial\omega_2}{\partial m_1} & \frac{\partial\omega_2}{\partial m_2} \end{bmatrix} \begin{bmatrix} \Delta m_1 \\ \Delta m_2 \end{bmatrix}, \quad (\text{C.18})$$

³If only 1 isolated point is treated with bonding material, such that adsorption or bonding only occurs at for instance the tip, the 1D assumption is kept valid as well.

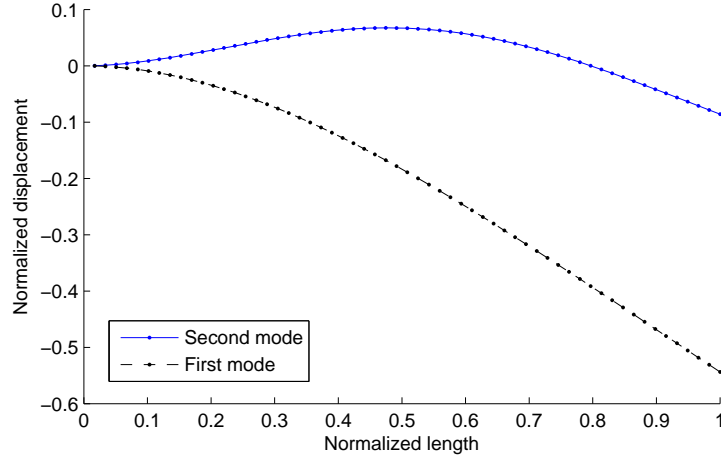


Figure C.9: Mode shapes of the uniform beam.

gives:

$$\begin{bmatrix} \Delta m_1 \\ \Delta m_2 \end{bmatrix} = \begin{bmatrix} \frac{\partial \omega_1}{\partial m_1} & \frac{\partial \omega_1}{\partial m_2} \\ \frac{\partial \omega_2}{\partial m_1} & \frac{\partial \omega_2}{\partial m_2} \end{bmatrix}^{-1} \begin{bmatrix} \Delta \omega_1 \\ \Delta \omega_2 \end{bmatrix}. \quad (\text{C.19})$$

This is of course not limited to two frequencies but one could use as many frequencies as one can measure. However relative frequency shifts of higher modes become very difficult to measure at some point, hence one would like to have relatively low higher frequencies or a high sensitivity of one mode to mass additions at a specific point.

The easiest method to change the frequency behavior of the sensor is by changing the shape of the cantilever. Changing thickness in out of plane direction will be difficult but it is possible. Hence this will be the approach of subsection C.4.1. Another approach is using multiple electrodes. This is much more difficult to fabricate because a SOI wafer as was used for the original cantilevers cannot be used anymore. However, the potential of mass differentiation is much bigger, hence this approach will be evaluated in subsection C.4.2.

C.4.1 Changing the cantilever shape

Equation (C.19) gives the formula to compute masses from frequency shifts. The method is most robust if one frequency is very sensitive to one mass variation, but very insensitive to the other mass variations. If the sensitivities for the uniform beam, as shown in figure C.8, are computed and normalized with the first eigenfrequency of this uniform beam (ω_1^o) one finds:

$$\frac{1}{\omega_1^o} \begin{bmatrix} \frac{\partial \omega_1}{\partial m_1} & \frac{\partial \omega_1}{\partial m_2} \\ \frac{\partial \omega_2}{\partial m_1} & \frac{\partial \omega_2}{\partial m_2} \end{bmatrix} = \begin{bmatrix} -6.6 \cdot 10^{-5} & -7.4 \cdot 10^{-6} \\ -3.2 \cdot 10^{-4} & -2.4 \cdot 10^{-4} \end{bmatrix}, \quad (\text{C.20})$$

which is what one expects when the mode shapes are considered (see figure C.9). The tip mass m_1 has a very big influence on both frequencies thus the power to dominate the results. Hence it destroys the robustness of the mass measurement. The second frequency is 6.3 times the first frequency.

The goal is finding a shape where the sensitivities per row of (C.20) are well separated. This goal seems a candidate for shape optimization [51].

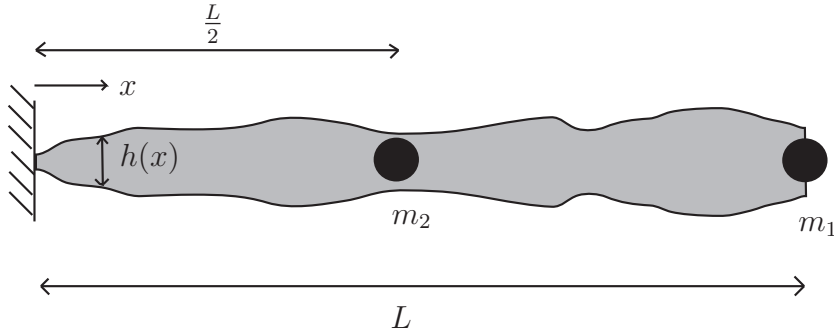


Figure C.10: Beam with two mass attachment points and varying shape.

Mechanical optimization

The optimization is limited to the mechanical domain, and reduced to optimizing a beam like structure. The thickness of the beam elements will be optimized. The shape distribution before optimization is shown in figure C.10. A minimum thickness is chosen, which is combined with a volume constraint that limits to total volume of the beam to be equal to that of the uniform beam. The optimization is summarized as the minimization of an objective function f with respect to the shape \mathbf{h} :

$$\begin{cases} \text{minimize} & f(\mathbf{h}) = \left| \frac{\partial m_2}{\partial \omega_2} \frac{\partial \omega_2}{\partial m_1} \right| \\ \text{with constraints} & \mathbf{h}^T \mathbf{L} = 0 \\ & \mathbf{h} > \mathbf{h}_{min} \end{cases}, \quad (\text{C.21})$$

where \mathbf{h} is the vector with element thicknesses, \mathbf{L} the vector with element lengths and \mathbf{h}_{min} the vector with required minimum widths. For the solution of this problem there are a wide variety of algorithms. Here the standard *matlab* routine *fmincon* will be used⁴.

The purely mechanical optimization gave the shape distribution shown in figure C.11. The optimized beam has a lower first eigenfrequency $\omega_1^n = 0.63\omega_1^o$. Also the second eigenfrequency is lower: $\omega_2^n = 4.8\omega_1^o$. But the most important criteria are the sensitivities:

$$\frac{1}{\omega_1^o} \begin{bmatrix} \frac{\partial \omega_1}{\partial \omega_1} & \frac{\partial \omega_1}{\partial \omega_2} \\ \frac{\partial \omega_2}{\partial \omega_1} & \frac{\partial \omega_2}{\partial \omega_2} \end{bmatrix} = \begin{bmatrix} -3.8 \cdot 10^{-5} & -1.0 \cdot 10^{-6} \\ -1.0 \cdot 10^{-4} & -3.9 \cdot 10^{-4} \end{bmatrix}, \quad (\text{C.22})$$

which have better separated sensitivities. The second frequency is more sensitive to the second mass. Also on the first row of (C.22) the values are better separated, even though the optimization was only performed on the second row of (C.22). Therefore this shape should be able to better sense the mass distribution between m_1 and m_2 .

Figure C.12 shows the mode shapes of the optimized beam. Compared to the unoptimized modeshapes (figure C.12) the first mode has relatively more displacement near the tip mass and less near the $L/2$ mass. For mode two the displacement near the $L/2$ mass is increased while the displacement near the tip mass is slightly decreased.

This was a purely mechanical problem, hence no need for the framework of chapter 13.

⁴Optimization algorithms are faster if the sensitivities of the objective function are known, in this case they contain the second order sensitivities of the eigenfrequency. Another use of the sensitivities discussed in chapter 11.

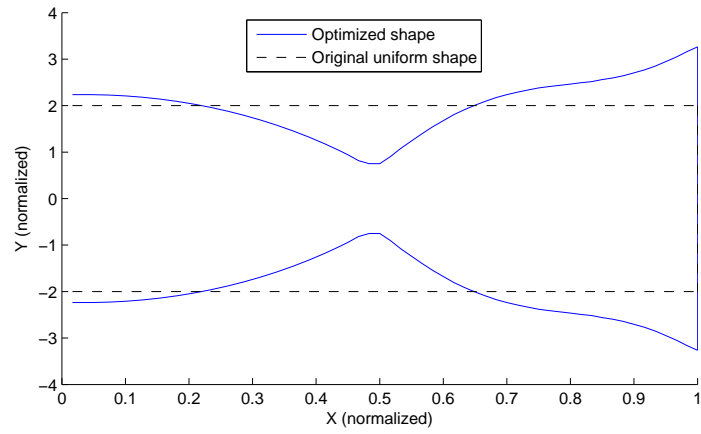


Figure C.11: Optimized cantilever shape and original shape (clamped on the left side, unsupported at the right side).

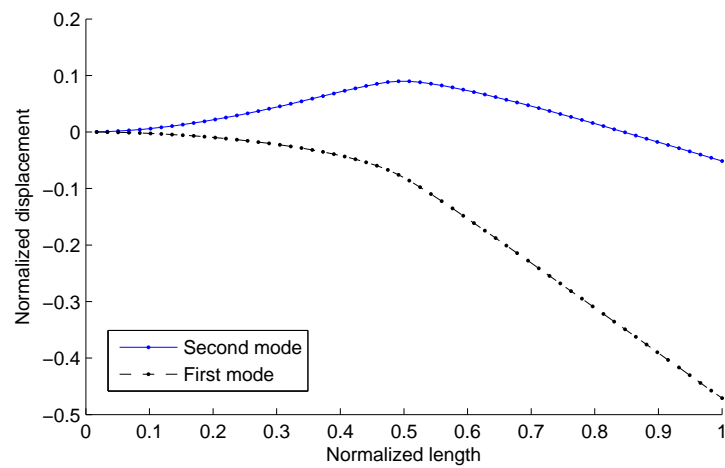


Figure C.12: Mode shapes of the optimized beam.

Application to the coupled model

Of course this thickness distribution is very difficult to produce, if not impossible. Therefore the idea is to deposit some extra polysilicon on the beam from 0 to 25% of the beam length and from 60 to 100% of the beam. The effects of this addition are simulated with the 3D FEM coupled model as used before. The 1019 *nm* thick beam with a length of 70 μm was used as reference. First the thickness was decreased to 500 *nm*. Next at the mentioned positions the thickness was increased to about 1.5 times the original thickness. The total volume remained more or less constant. Mass receptors were placed at the middle of the beam (m_2) and at the end of the beam (m_1). The sensitivity matrix for the original 1019 *nm* beam is:

$$\begin{bmatrix} \frac{\partial\omega_1}{\partial\omega_1} & \frac{\partial\omega_1}{\partial\omega_2} \\ \frac{\partial\omega_2}{\partial\omega_1} & \frac{\partial\omega_2}{\partial\omega_2} \end{bmatrix} = \begin{bmatrix} -2.6 \cdot 10^{18} & -2.1 \cdot 10^{17} \\ -1.7 \cdot 10^{19} & -8.4 \cdot 10^{18} \end{bmatrix} \text{rad/kg} \cdot \text{s}, \quad (\text{C.23})$$

where the tip mass can dominate the result (first column of the matrix). The first frequency for the original beam is $1.74 \cdot 10^6 \text{ rad/s}$ and the second frequency is $1.14 \cdot 10^7 \text{ rad/s}$.

The improved beam gave saw a reduced first frequency of $8.6 \cdot 10^5 \text{ rad/s}$ and an increased second frequency of $1.1 \cdot 10^6 \text{ rad/s}$. The pull-in voltage was reduced to 9.8 volts. The most relevant result, the new sensitivity matrix is:

$$\begin{bmatrix} \frac{\partial\omega_1}{\partial\omega_1} & \frac{\partial\omega_1}{\partial\omega_2} \\ \frac{\partial\omega_2}{\partial\omega_1} & \frac{\partial\omega_2}{\partial\omega_2} \end{bmatrix} = \begin{bmatrix} -1.1 \cdot 10^{18} & -2.4 \cdot 10^{16} \\ -8.1 \cdot 10^{18} & -6.9 \cdot 10^{18} \end{bmatrix} \text{rad/kg} \cdot \text{s}, \quad (\text{C.24})$$

which shows a significant improvement for the tip mass sensitivity ratio: the ratio of sensitivities of the for the first frequency increased from 12 to 46, which is a significant improvement. Also the ratio of the second frequency improved, it decreased from 2.5 to 1.2.

It would be interesting to see what a full optimization of the coupled problem would yield, even though the computation cost would be immense.

C.4.2 Using multiple electrodes

Two cases are studied to test if it is possible to improve the frequency sensitivity characteristics of a micro beam measurement device by using multiple electrodes, or in other words: whether it is feasible to improve the sensitivity of one mode to one specific mass. The two cases are a bridge clamped on both sides and a cantilever clamped on one side. Realistic geometry and material properties were chosen, for both cases this was a length of $L = 70\mu$, thickness $h = 300\text{nm}$, elasticity $E = 169 \text{ GPa}$ and a gap of $g = 1\mu$. The static equilibrium positions will be computed with a staggered scheme, because the problem is mechanically linear. The frequencies will be computed monolithically, because with this asymmetric actuation cases, the robustness of monolithic frequency computation is desired. Therefore the total solution scheme will be hybrid.

Clamped-clamped beam

The geometry of the clamped beam is shown in figure C.13. The non-actuated first and second frequency are $[\omega_i] = [5.0 \ 13.8]10^6 \text{ rad/s}$. Furthermore the first mode is most sensitive to mass m_2 and less but equally sensitive to both mass m_1 and m_3 . The

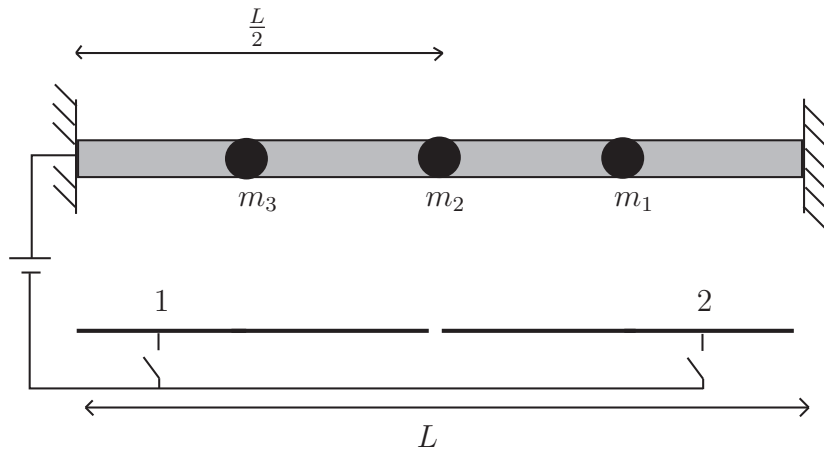


Figure C.13: Microbridge with three mass attachment points and two different actuation electrodes.

second frequency is not sensitive to mass m_2 at all, but equally sensitive to m_1 and m_3 .

Switching on both electrodes at once at about 90% of pull-in will not affect the second frequency very much (a slight decrease) but will dramatically lower the first frequency to $\omega_1 = 3.3 \cdot 10^6 \text{ rad/s}$. Also the ratio between the $\frac{\partial \omega_1}{\partial m_2}$ and $\frac{\partial \omega_1}{\partial m_{1,3}}$ will slightly improve from 2.8 to 2.9, so it will not be really useful.

Switching on only electrode 1 also lowers only the first frequency significantly. But the good thing is that both frequency 1 and 2 will become differently sensitive for mass m_3 and m_1 . Frequency 1 becomes 1.5 times more sensitive for m_3 than for m_1 , while surprisingly frequency 2 will become 1.14 times more sensitive for mass m_1 than for m_3 .

In general this will provide a method to distinguish between the 3 masses, which is impossible for a non-actuated micro bridge.

Cantilever beam

The configuration for the cantilever beam is shown in figure C.14. There are 16 different configuration for the switches connected to the electrodes. The one where all electrodes are disconnected will be called 0000, the one were electrode one is switched on and all others off will be called 1000, etcetera. Table C.3 lists all configurations and their pull-in voltages. Some configurations (e.g. 1000) do not have a pull-in voltage. In those cases the tip touches the non actuated ground electrode before pull-in is reached. In those cases the contact voltage is listed. In the cases were the cantilever does pull-in the contact voltage is equal to the pull-in voltage therefore it is not listed.

In the rest or 0000 position the first 6 eigenfrequencies of the cantilever are:

$$[\omega_i] = [0.78 \quad 4.9 \quad 14 \quad 27 \quad 45 \quad 67]^T \cdot 10^6 \text{ rad/s}, \quad (\text{C.25})$$

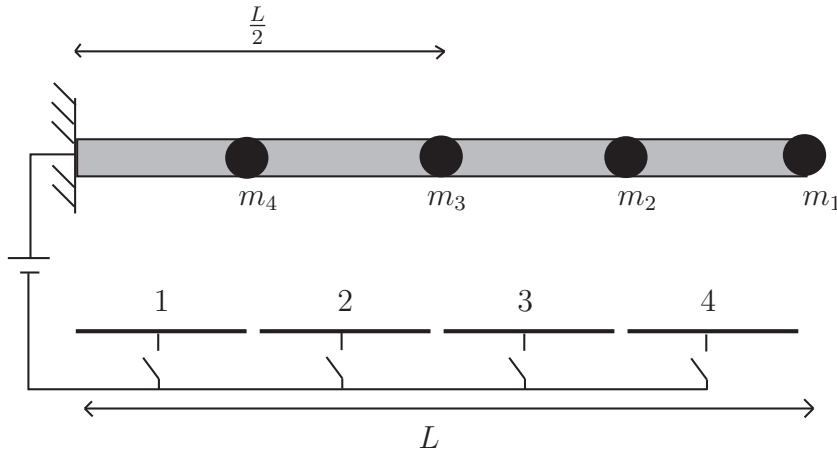


Figure C.14: Cantilever beam with four mass attachment points and four different actuation electrodes.

and the sensitivity matrix is:

$$\left[\frac{\partial \omega_i}{\partial m_j} \right] = - \begin{bmatrix} 0.075 & 0.035 & 0.009 & 0.003 \\ 0.47 & 0.002 & 0.24 & 0.15 \\ 1.3 & 0.37 & 0.00 & 0.02 \\ 2.6 & 1.1 & 1.3 & 1.1 \\ 4.2 & 0.67 & 0.00 & 0.00 \\ 6.4 & 0.04 & 3.2 & -2.0 \end{bmatrix}^T \cdot 10^{15} \text{ rad/s}. \quad (\text{C.26})$$

When looking at the sensitivity matrix there are a few things that are noticeable: the second and sixth frequency seem to be insensible to mass m_2 , hence this might be abused to very accurately sense one of the other masses by stimulating these modes. The third frequency is insensible to both mass m_3 and m_4 as is the fifth frequency. For sensing mass 3 and 4 the 2nd, 4th and 6th frequencies seem to be required.

It is uninteresting to report here the sensitivity matrices for all configurations. Therefore just the noteworthy results will be reported below.

- Switching on electrode 2 (config. 0100) only reduces the first frequency significantly. It will make the third frequency almost insensible to mass 3 and 4, but slightly more sensible to mass 1 and 2. Also the first frequency becomes more sensitive to the second mass. The ratio between second and first mass sensitivity goes up from 0.46 to 0.52. Small improvements though.
- Switching on electrode 4 (config. 0001) slightly improves the sensitivity ratio between mass 1 sensitivity and all other sensitivities for the first frequency.
- Configuration 1010 slightly improves the sensitivity of the fourth frequency to mass 2, but this is hardly measurable.
- Configuration 1001 gives the best sensitivity for mass 3 compared to the tip mass sensitivity. The ratio improves from 0.509 to 0.516.

The overall conclusion: if it is possible to measure up to the 6th frequency a cantilever can distinguish between the 4 masses. However electrostatic actuation does not really improve the sensing capabilities for a cantilever.

Table C.3: Pull-in voltages for different switching configurations of the beam actuated with multiple electrodes.

Configuration	Pull-in (V)	Contact (V)
0000	-	-
1000	-	40
1100	-	10
1110	5.2	-
1111	2.8	-
1101	3.7	-
1010	6.2	-
1011	3.0	-
1001	4.1	-
0100	-	11
0110	5.3	-
0111	2.9	0
0101	3.8	-
0010	6.3	-
0011	3.1	-
0001	4.1	-

C.5 Measuring surrounding fluid and gas properties

An application of this type of cantilever sensors could be for measuring the properties of the surrounding medium. The surrounding medium, gas or fluid, will heavily influence the behavior at atmospheric pressure due to the squeeze film effect⁵. This section tries to see if there are methods that can be used for measuring other fluid properties.

C.5.1 Using the eigenvalue characteristics

The first properties that come to mind are two of the eigenvalue characteristics of the lowest eigenvalue: the damped eigenfrequency and the Q-factor. Chapter 10 already showed that these values are highly pressure dependent, but are they also sensitive for other properties? This section will first discuss that question.

Computing frequency and Q-factor sensitivities has been discussed in chapter 11, hence it will not be repeated here. Below it is assumed that there is no electric load. Damped frequencies are always computed monolithically.

measuring gas properties

First the measurement of a gas is discussed. It is assumed that gases more or less have the same mean free path. Therefore for all gases the same Knudsen number correction is used:

$$\mu = \frac{\mu_0}{1 + 9.638 Kn^{1.159}}, \quad (\text{C.27})$$

⁵For more information on squeeze film damping and squeeze film modeling see chapter 10

where for the Knudsen number the following relation was used

$$Kn = \frac{6.9 \cdot 10^{-3}}{p \cdot g}. \quad (\text{C.28})$$

For a gas at room temperature in general the viscosity is in the order of $1 \cdot 10^{-5} Pa \cdot s$. For air it is $\mu_A = 18.27 \cdot 10^{-6} Pa \cdot s$ and for nitrogen it is $\mu_N = 17.80 \cdot 10^{-6} Pa \cdot s$. If the sensor has to be used to distinguish between air and nitrogen, the resolution has to be better than $1 \cdot 10^{-7} Pa \cdot s$.

The first cantilever that was tried is the test beam as used for the validation of the electromechanical model (length $L = 70 \mu$, thickness $h = 1019 nm$ and width $w = 8 \mu$). For this beam the lowest damped eigenfrequency is $\omega_d = 1.7418 \cdot 10^6 rad/s$ and the Q-factor is $Q = 6.2$. The damped eigenfrequency is slightly lower than the undamped one: $1.7497 \cdot 10^6 rad/s$. The eigenfrequency sensitivity for this beam is:

$$\frac{\partial \omega}{\partial \mu} = 1.00 \cdot 10^2 rad/Pa \cdot s^2, \quad (\text{C.29})$$

and the Q-factor sensitivity is:

$$\frac{\partial Q}{\partial \mu} = -0.039 1/Pa \cdot s. \quad (\text{C.30})$$

Both values are too low to distinguish between air and nitrogen, because for a $1 \cdot 10^{-7} Pa \cdot s$ resolution the frequency resolution should be $1 \cdot 11^{-4}$ or ten orders of magnitude lower than the measured frequency and the Q-factor resolution should be $4 \cdot 10^{-9}$, which is 10 orders of magnitude lower than the measured Q-factor. Thus the principle cannot be used for this beam in practice.

Therefore a thinner beam with more or less the same length is modeled (length $L = 77 \mu$, thickness $h = 57 nm$ and width $w = 8 \mu$). This beam was actually produced. A Young's modulus of $100 GPa$ was used to accommodate size effects. This gave a lowest damped eigenfrequency of $\omega_d = 1.08 \cdot 10^6 rad/s$, which is 2 orders of magnitude higher than the lowest undamped one of $\omega_u = 5.99 \cdot 10^4 rad/s$. Hence for this really thin beam the added stiffness effect dominates the viscous drag effect. This also resulted in the phenomenon that the lowest damped eigenmode is not the same as the lowest undamped one. Since the lowest lowly damped mode squeezes the air more, while the mode that is lowest in the highly damped case transports the fluid more from one side of the beam to other side and back. The lowest damped mode is shown in figure C.15. For the thick $h = 1019 nm$ beam the lowest damped mode is shown in figure C.16. Hence here the added stiffness does not dominate over the viscous drag yet.

The Q-factor for the thin beam is $Q = 1.0$, and the frequency and Q-factor sensitivities are respectively:

$$\frac{\partial \omega}{\partial \mu} = -1.1 \cdot 10^5 rad/Pa \cdot s^2, \quad (\text{C.31})$$

and:

$$\frac{\partial Q}{\partial \mu} = -0.045 1/Pa \cdot s. \quad (\text{C.32})$$

Therefore also for the thin beam using the damped eigenvalue for measuring would not work.

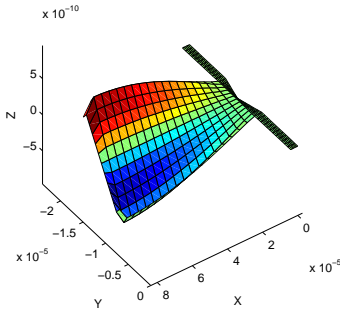


Figure C.15: Damped mode of the $h = 57 \text{ nm}$ beam.

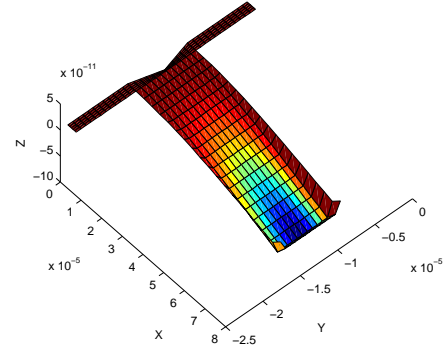


Figure C.16: Damped mode of the $h = 1019 \text{ nm}$ beam.

The last idea would be to measure at very low pressure, e.g. 0.1 mbar of 10 Pa . For this pressure the frequency is more or less equal to the undamped one. The Q-factor is $7.45 \cdot 10^4$. The frequency sensitivity goes down to about:

$$\frac{\partial \omega}{\partial \mu} = 0.023 \text{ rad/Pa} \cdot \text{s}^2, \quad (\text{C.33})$$

which is still too low.

measuring fluid properties

For all fluids it is assumed that the mean free path is that short that no Knudsen number correction has to be used. To see if the frequency data can be used for fluid properties is tested by the properties of water $\mu_W = 8.94 \cdot 10^{-4} \text{ Pa} \cdot \text{s}$. The thick beam was used for testing the behavior.

In this case the mode is highly damped $Q = 4.2$, but the sensitivity is still way too low:

$$\frac{\partial Q}{\partial \mu} = 3.2 \cdot 10^5 \text{ 1/Pa} \cdot \text{s}. \quad (\text{C.34})$$

Note that the sensitivity is inverted for the fluid. However using the Q-factor sensitivity will not help measuring fluid properties.

C.5.2 Using static pull-in

Most fluids have a different electric permittivity. Water for instance has at room temperature (20°C) a relative permittivity of $\varepsilon_{rW} = 80$. Formamide has at the same temperature a relative permittivity of $\varepsilon_{rF} = 84$. The pull-in voltage is highly sensitive to the permittivity, thus this could be used for measurements. For gases this will not work because their permittivities do not really differ.

If the pull-in voltage for water is computed it gives $V_{PI} = 1.718$ and the sensitivity of that value to the relative permittivity is:

$$\left. \frac{\partial V}{\partial \varepsilon_r} \right|_{PI} = -0.0537 \text{ V}. \quad (\text{C.35})$$

This means that if the pull-in voltage is measured with a $0.01 V$ resolution, the relative permittivity is measured with a 0.19 resolution; enough to measure the difference between water and formamide.

Similarly one could be interested in the difference between ethanol ($\varepsilon_{rE} = 24.3$) and methanol ($\varepsilon_{rM} = 32.7$), or drinkable and toxic alcohol. The pull-in voltage for methanol is $V_{PI} = 2.688$ and the sensitivity of that value is:

$$\left. \frac{\partial V}{\partial \varepsilon_r} \right|_{PI} = -0.205 V, \quad (\text{C.36})$$

which gives as 0.05 resolution if the voltage resolution is $0.01 V$, ergo the method could be used to distinguish between ethanol and methanol.

C.5.3 Using pull-in time

The problem with finding static pull-in and water is that static voltage can be problematic. It requires relatively long actuation times and the water could get self-ionized, therefore conductive. Therefore an actuation principle that requires shorter actuation times would be better. Dynamic pull-in springs to mind. Finding the actual dynamic pull-in value has the same problems as the static one. Moreover, fluids cause critical damping, hence no overshoot, therefore the dynamic pull-in will be equal to the static pull-in. Therefore the proposed measurement technique is applying a voltage higher than pull-in and measuring the pull-in time. This is a measurement that would last short enough to prevent self-ionization problems. Determining the analytic sensitivity of the pull-in time has been discussed in section 9.2.4.

The properties of methanol ($\varepsilon_r = 32.7$, $\mu = 5.9 \cdot 10^{-4}$ at $\pm 20^\circ C$) are used for computing the sensitivity of the pull-in time with the dielectric permittivity. Although it was shown above that the sensitivity for the viscosity is very small, that sensitivity is computed as well.

To shorten the computation time, especially due to convergence issues at small gaps, the pull-in displacement is set on 0.5 times the gap. It is assumed that this indicative for the full pull-in time. The pull-in time curves are shown in figure C.17. A voltage step of 3 volts was applied. This is higher than the static pull-in voltage for both fluids.

The computed pull-in time for methanol was $t_c^M = 2.29 \cdot 10^{-5} s$. The sensitivities are:

$$\frac{\partial t_c}{\partial \varepsilon_r} = 1.19 \cdot 10^{-5} s, \quad (\text{C.37})$$

and

$$\frac{\partial t_c}{\partial \mu} = 0.09571 / Pa. \quad (\text{C.38})$$

If the difference between ethanol ($\varepsilon_r = 24.3$, $\mu = 11.4 \cdot 10^{-4}$ at $\pm 20^\circ C$) and methanol is the goal of the measurement, this would result in a time difference of

$$\Delta t = \frac{\partial t_c}{\partial \varepsilon_r} (24.3 - 32.7) + \frac{\partial t_c}{\partial \mu} (11.4 - 5.9) \cdot 10^{-4} = 1.11 \cdot 10^{-4} + 0.52 \cdot 10^{-4} = 1.63 \cdot 10^{-4} s, \quad (\text{C.39})$$

which seems to be measurable when it is compared to the pull-in time itself. The difference is about 5 times the methanol pull-in time.

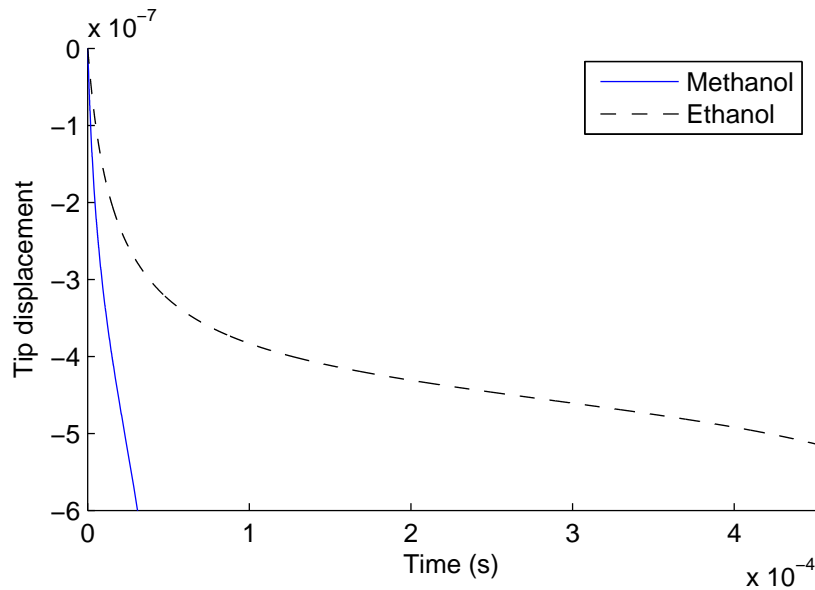


Figure C.17: Time-displacement curve for the cantilever submerged in different fluids, the actuation voltage is $3V$.

However due to the big difference in permittivity and viscosity that there is between ethanol and methanol, the *linear* sensitivities might not be a very good indicator. So when the actual pull-in time of ethanol is computed it turns out to be $t_c^E = 4.21 \cdot 10^{-4} s$, hence a difference of $\Delta t = 3.98 \cdot 10^{-4}$. This is in the same order of magnitude as the sensitivity based computations, showing that the measurement principle seems usable.

This last result was computed with time integration algorithm that is monolithic for electromechanical problem, because the electric equations were condensed onto the mechanic equations, while including the Schur complement. It was also monolithic in total because the fluid was assumed incompressible, therefore the fluidics were condensed onto the mechanics as well. Analytic sensitivities always require a monolithic implementation.

Bibliography

- [1] Comsol A.B., *Comsol Multiphysics 3.2 Users Guide*, 2006.
- [2] S.G. Adams, F.M. Bertsch, K.A. Shaw, P.G. Hartwell, F.C. Moon, and N.C. MacDonald, *Capacitance based tunable resonators*, Journal of Micromechanics and Microengineering **8** (1998), 15–23.
- [3] J.E. Akin, *The generation of elements with singularities*, International Journal for Numerical Methods in Engineering **10** (1976), no. 6, 1249–1259.
- [4] N.R. Aluru and J. White, *An efficient numerical technique for electrochemical simulation of complicated microelectromechanical structures*, Sensors & Actuators: A. Physical **58** (1997), no. 1, 1–11.
- [5] J. Andersen and V. Solodukhov, *Field behavior near a dielectric wedge*, Antennas and Propagation, IEEE Transactions on **26** (1978), no. 4, 598–602.
- [6] A. Andreykiv and D.J. Rixen, *Numerical modelling of electromechanical coupling using fictitious domain and level set methods*, International Journal for Numerical Methods in Engineering **80** (2009), no. 4.
- [7] I. Babuska and A. Miller, *The post-processing approach in the finite element method-Part 1: Calculation of displacements, stresses and other higher derivatives of the displacements*, International Journal for numerical methods in engineering **20** (1984), no. 6, 1085–1109.
- [8] ———, *The post-processing approach in the finite element method-part 2: The calculation of stress intensity factors*, International Journal for Numerical Methods in Engineering **20** (1984), no. 6, 1111–1129.
- [9] I. Babuška and M.B. Rosenzweig, *A finite element scheme for domains with corners*, Numerische Mathematik **20** (1972), no. 1, 1–21.
- [10] C. Bailey, G.A. Taylor, M. Cross, and P. Chow, *Discretisation procedures for multi-physics phenomena*, Journal of Computational and Applied Mathematics **103** (1999), no. 1, 3–17.
- [11] M. Bao and H. Yang, *Squeeze film air damping in MEMS*, Sensors & Actuators: A. Physical **136** (2007), no. 1, 3–27.
- [12] K.J. Bathe, *Finite element procedures*, Prentice Hall, Englewood Cliffs, NJ, 1996.
- [13] J.L. Batoz and M.B. Tahar, *Evaluation of a new quadrilateral thin plate bending element*, International Journal for Numerical Methods in Engineering **18** (1982), no. 11, 1.

- [14] J. Bielen, J. Stulemeijer, D. Ganjoo, D. Ostergaard, and S. Noijen, *Fluid-electrostatic-mechanical modeling of the dynamic response of RF-MEMS capacitive switches*, Thermal, Mechanical and Multi-Physics Simulation and Experiments in Microelectronics and Micro-Systems, 2008. EuroSimE 2008. International Conference on (2008), 1–8.
- [15] D. Bindel and J. DEmmel, *Reduced order models in microsystems and rf mems*, PARA'04 'state-of-the-Art in Scientific Computing (Lyngby, Denmark), IMM/DTU, June 2004.
- [16] K.J. Binns and P.J. Lawrenson, *Analysis and computation of electric and magnetic field problems*, Pergamon Press, 1973.
- [17] FR Blom, S. Bouwstra, M. Elwenspoek, and JHJ Fluitman, *Dependence of the quality factor of micromachined silicon beam resonators on pressure and geometry*, Journal of Vacuum Science & Technology B: Microelectronics and Nanometer Structures **10** (1992), 19.
- [18] O. Bochobza-Degani, D. Elata, and Y. Nemirovsky, *An efficient DIPIE algorithm for CAD of electrostatically actuated MEMS devices*, Microelectromechanical Systems, Journal of **11** (2002), no. 5, 612–620.
- [19] O. Bröls and P. Eberhard, *Sensitivity analysis for dynamic mechanical systems with finite rotations*, Int. Journal for Numerical Methods in Engineering **74** (2008), no. 13.
- [20] P. Bruschi, A. Nannini, F. Pieri, G. Raffaa, B. Vigna, and S. Zerbini, *Electrostatic analysis of a comb-finger actuator with Schwarz–Christoffel conformal mapping*, Sensors and Actuators A **113** (2004), 106–117.
- [21] B. Budianski, *Theory of buckling and post-buckling behavior of elastic structures*, Advances in applied mechanics 14 (C.S. Yih, ed.), Academic Press, 1974, pp. 1–65.
- [22] M. Cervera, R. Codina, and M. Galindo, *On the computational efficiency and implementation of block-iterative algorithms for nonlinear coupled problems*, Engineering Computations **13** (1996), no. 6, 4–30.
- [23] J. Chen and S.M. Kang, *An algorithm for automatic model-order reduction of nonlinear MEMS devices*, Circuits and Systems, 2000. Proceedings. ISCAS 2000 Geneva. The 2000 IEEE International Symposium on, vol. 2, 2000.
- [24] J. Cheng, J. Zhe, and X. Wu, *Analytical and finite element model pull-in study of rigid and deformable electrostatic microactuators*, Journal of Micromechanics and Microengineering **14** (2004), no. 1, 57–68.
- [25] S.W. Cho and I. Chasiotis, *Elastic properties and representative volume element of polycrystalline silicon for MEMS*, Experimental Mechanics **47** (2007), no. 1, 37–49.
- [26] K.M. Choi, H.K. Jo, W.H. Kim, and I.W. Lee, *Sensitivity analysis of non-conservative eigensystems*, Journal of Sound and Vibration **274** (2004), no. 3-5, 997–1011.

- [27] M.A. Crisfield, *A fast incremental/iterative solution procedure that handles snap-through*, Computers and Structures **13** (1981), no. 1-3, 55–62.
- [28] ———, *Non-Linear Finite Element Analysis of Solids and Structures, Volume 1: Essentials*, John Wiley & Sons, New York, 1991.
- [29] ———, *Non-Linear Finite Element Analysis of Solids and Structures, Volume 2: Advanced Topics*, John Wiley & Sons, New York, 1996.
- [30] C.L. Dai and W.C. Yu, *A micromachined tunable resonator fabricated by the CMOS post-process of etching silicon dioxide*, Microsystem Technologies **12** (2006), no. 8, 766–772.
- [31] A. De Boer, MS Van der Schoot, and H. Bijl, *Mesh deformation based on radial basis function interpolation*, Computers & Structures **85** (2007), no. 11-14, 784–795.
- [32] H. de Boer and F. van Keulen, *Refined semi-analytical design sensitivities*, Int. Journal for Numerical Methods in Engineering **37** (2000), no. 46-47, 6961–6980.
- [33] O. Degani, E. Socher, A. Lipson, T. Lejtner, DJ Setter, S. Kaldor, and Y. Nemirovsky, *Pull-in study of an electrostatic torsion microactuator*, Microelectromechanical Systems, Journal of **7** (1998), no. 4, 373–379.
- [34] A. Duwel, J. Gorman, M. Weinstein, J. Borenstein, and P. Ward, *Experimental study of thermoelastic damping in MEMS gyros*, Sensors & Actuators: A. Physical **103** (2003), no. 1-2, 70–75.
- [35] WP Eaton and JH Smith, *Micromachined pressure sensors: review and recent developments*, Smart Materials and Structures **6** (1997), 530–539.
- [36] D. Elata and H. Bamberger, *On the dynamic pull-in of electrostatic actuators with multiple degrees of freedom and multiple voltage sources*, Microelectromechanical Systems, Journal of **15** (2006), no. 1, 131–140.
- [37] News EDN Electronics Design, Strategy, *Mems plays in nintendos wii*, 2006, [Online; accessed 20-June-2008].
- [38] H.D. Espinosa, Y. Zhu, M. Fischer, and J. Hutchinson, *An experimental/computational approach to identify moduli and residual stress in MEMS radio-frequency switches*, Experimental Mechanics **43** (2003), no. 3, 309–316.
- [39] online european electronics Evertiq, *Stm's mems business to increase thanks to iphone*, 2007, [Online; accessed 20-June-2008].
- [40] C. Farhat, M. Lesoinne, and P. Le Tallec, *Load and motion transfer algorithms for fluid/structure interaction problems with non-matching discrete interfaces: momentum and energy conservation, optimal discretization and application to aeroelasticity*, Computer methods in applied mechanics and engineering **157** (1998), no. 1-2, 95–114.

- [41] C. Farhat, M. Lesoinne, and N. Maman, *Mixed explicit/implicit time integration of coupled aeroelastic problems: three-field formulation, geometric conservation and distributed solution*, International journal for numerical methods in fluids **21** (1995), no. 10, 807–835.
- [42] G.K. Fedder, *Simulation of Microelectromechanical Systems*, Ph.D. thesis, University of California at Berkeley, 1994.
- [43] J.H. Ferziger and M. Perić, *Computational methods for fluid dynamics*, Springer, 2002.
- [44] Y.C. Fung, *Foundation of solid mechanics*, Prentice-Hall, Englewood Cliffs, NJ, 1968.
- [45] M. Gerardin and D. Rixen, *Mechanical Vibrations*, John Wiley & Sons, New York, 1997.
- [46] O. Ghattas, X. Li, Engineering Design Research Center, and Carnegie-Mellon University, *A variational finite element method for stationary nonlinear fluid-solid interaction*, Journal of Computational Physics **121** (1995), no. 2, 347–356.
- [47] J.R. Gilbert, R. Legtenberg, and S.D. Senturia, *3D coupled electro-mechanics for MEMS: applications of CoSolve-EM*, Micro Electro Mechanical Systems, 1995, MEMS'95, Proceedings. IEEE.
- [48] D.J. Griffiths, *Introduction to Electrodynamics*, Prentice-Hall, Englewood Cliffs, NJ, 1999.
- [49] MA Gutierrez and S. Krenk, *Stochastic Finite Element Methods*, Encyclopedia of Computational Mechanics, volume 2: Solids and Structures (R. de Borst, E. Stein, and T.J.R. Hughes, eds.), Wiley, 2004, pp. 657–681.
- [50] M. Gyimesi, I. Avdeev, and D. Ostergaard, *Finite-element simulation of micro-electromechanical systems (MEMS) by strongly coupled electromechanical transducers*, Magnetics, IEEE Transactions on **40** (2004), no. 2, 557–560.
- [51] R.T. Haftka and Z. Gürdal, *Elements of structural optimization*, Springer, 1992.
- [52] S.D.A. Hannot and D.J. Rixen, *Determining pull-in curves with electromechanical FEM models*, Proceedings of the 9th International Conference on Thermal, Mechanical and Multiphysics Simulation and Experiments in Micro-Electronics and Micro-Systems, Freiburg, Germany, 2008, pp. 528–535.
- [53] SDA Hannot and DJ Rixen, *A fully coupled FEM model of Electromechanically acutated MEMS with squeeze film Damping*, Proceedings of the ASME 3rd International Conference on Micro- and Nanosystems, San Diego, USA, 2009, pp. 1–10.
- [54] ———, *Numerical Modeling of the Electromechanical Interaction in MEMS*, Advanced Computational Methods in Science and Engineering (B. Koren and K. Vuik, eds.), Springer, 2009, pp. 315–342.

- [55] S.D.A. Hannot and D.J. Rixen, *Pull-in curves determined with monolithic FEM models*, Proceedings of the 10th International Conference on Thermal, Mechanical and Multiphysics Simulation and Experiments in Micro-Electronics and Micro-Systems, Delft, Netherlands, 2009, pp. 528–535.
- [56] SDA Hannot and DJ Rixen, *Rounding the corners in an electromechanical FEM model*, Proceedings of the Third International Conference on Computational Methods for Coupled Problems in Science and Engineering, Ischia, Italy, 2009, pp. 1–4.
- [57] SDA Hannot, DJ Rixen, and V. Rochus, *Rounding the corners in an electromechanical FEM model*, Proceedings of the Second International Conference on Computational Methods for Coupled Problems in Science and Engineering, Ibiza, Spain, 2007, pp. 149–156.
- [58] Stephan D A Hannot, Clemens V Verhoosel, and Daniel J Rixen, *Stochastic finite element method for analyzing static and dynamic pull-in of microsystems*, IOP Conference Series: Materials Science and Engineering **10** (2010), no. 1, 012202.
- [59] V.A. Henneken, M. Tichem, and P.M. Sarro, *In-package MEMS-based thermal actuators for micro-assembly*, Journal of Micromechanics and Microengineering **16** (2006), no. 6, S107–S115.
- [60] ———, *Improved thermal U-beam actuators for micro-assembly*, Sensors & Actuators: A. Physical **142** (2008), no. 1, 298–305.
- [61] K.H. Heubner, E.A. Thornton, and T.G. Byrom, *The Finite Element Method for Engineers*, John Wiley & Sons, New York, 1995.
- [62] YC Hu, CM Chang, and SC Huang, *Some design considerations on the electrostatically actuated microstructures*, Sensors & Actuators: A. Physical **112** (2004), no. 1, 155–161.
- [63] E.S. Hung and S.D. Senturia, *Generating efficient dynamical models for micro-electromechanical systems from a few finite-element simulation runs*, Microelectromechanical Systems, Journal of **8** (1999), no. 3, 280–289.
- [64] T. Imamura, M. Katayama, Y. Ikegawa, T. Ohwe, R. Koishi, and T. Koshikawa, *MEMS-based integrated head/actuator/slider for hard disk drives*, IEEE/ASME transactions on mechatronics **3** (1998), no. 3, 166–174.
- [65] Ansys Inc., *Ansys Release 8.1 Documentation*, 2004.
- [66] J.D. Jackson, *Classical Electrodynamics*, John Wiley & Sons, 1975.
- [67] X. Jiao and M.T. Heath, *Common-refinement-based data transfer between non-matching meshes in multiphysics simulations*, Int. J. Numer. Meth. Engng **61** (2004), 2402–2427.
- [68] J.T. Katsikadelis, *Boundary Elements: Theory and Applications*, Elsevier, 2002.

- [69] B. Kim, R.N. Candler, M.A. Hopcroft, M. Agarwal, W.T. Park, and T.W. Kenny, *Frequency stability of wafer-scale film encapsulated silicon based MEMS resonators*, *Sensors & Actuators: A. Physical* **136** (2007), no. 1, 125–131.
- [70] E.S. Kolesar, P.B. Allen, J.T. Howard, J.M. Wilken, and N. Boydston, *Thermally-actuated cantilever beam for achieving large in-plane mechanical deflections*, *Thin Solid Films* **355** (1999), 295–302.
- [71] R. Kouhia and M. Mikkola, *Some aspects on efficient path-following*, *Computers and Structures* **72** (1999), no. 4-5, 509–524.
- [72] S. Krylov and R. Maimon, *Pull-in dynamics of an elastic beam actuated by continuously distributed electrostatic force*, *Journal of vibration and acoustics* **126** (2004), 332.
- [73] K.M. Lakin, *A review of thin-film resonator technology*, *IEEE microwave magazine* **4** (2003), no. 4, 61–67.
- [74] K.B. Lee and Y.H. Cho, *A triangular electrostatic comb array for micromechanical resonant frequency tuning*, *Sensors & Actuators: A. Physical* **70** (1998), no. 1-2, 112–117.
- [75] W.S. Lee, K.C. Kwon, B.K. Kim, J.H. Cho, and S.K. Youn, *Frequency-shifting analysis of electrostatically tunable micro-mechanical actuator*, *Journal of Modeling and Simulation of Microsystems* **2** (2001), no. 1, 83–88.
- [76] R. Legtenberg and H.A.C. Tilmans, *Electrostatically driven vacuum-encapsulated polysilicon resonators. I: Design and fabrication*, *Sensors and actuators. A, Physical* **45** (1994), no. 1, 57–66.
- [77] Z. Lei and C. Qiu, *Neumann dynamic stochastic finite element method of vibration for structures with stochastic parameters to random excitation*, *Computers and structures* **77** (2000), no. 6, 651–657.
- [78] E. Lemaire, V. Rochus, J.C. Golinval, and P. Duysinx, *Microbeam pull-in voltage topology optimization including material deposition constraint*, *Computer Methods in Applied Mechanics and Engineering* **197** (2008), no. 45-48, 4040–4050.
- [79] R. Lifshitz and ML Roukes, *Thermoelastic damping in micro-and nanomechanical systems*, *Physical Review B* **61** (2000), no. 8, 5600–5609.
- [80] RM Lin and WJ Wang, *Structural dynamics of microsystems current state of research and future directions*, *Mechanical systems and signal processing* **20** (2006), no. 5, 1015–1043.
- [81] Z. Liu, *Some Methods to Solve Singularity in Electrostatics with FEM*, IMTEK Albert-Ludwigs University Freiburg, Postdoc report, Freiburg, 2002.
- [82] Z. Liu, J.G. Korvink, and M. Reed, *Solving singularities in electrostatics with high-order FEM*, *Proceedings of IEEE Sensors, 2003.*, vol. 2, IEEE, October 2003, pp. 872–876.
- [83] N. Lobontiu, *Mechanics of Microelectromechanical Systems*, Springer, 2004.

- [84] S. Majumder, N.E. McGruer, G.G. Adams, P.M. Zavracky, R.H. Morrison, and J. Krim, *Study of contacts in an electrostatically actuated microswitch*, Sensors & Actuators: A. Physical **93** (2001), no. 1, 19–26.
- [85] R. Mestrom, *Multiphysics modelling and experimental validation of microelectromechanical resonator dynamics*, Eindhoven University of Technology, PhD Thesis, Netherlands, 2009.
- [86] A. Michael and C.Y. Kwok, *Design criteria for bi-stable behavior in a buckled multi-layered MEMS bridge*, Journal of Micromechanics and Microengineering **16** (2006), no. 10, 2034–2043.
- [87] S. Mukherjee, Z. Bao, M. Roman, and N. Aubry, *Nonlinear mechanics of mems plates with a total lagrangian approach*, Computers & Structures **83** (2005), 758–768.
- [88] R. Nadal-Guardia, A. Dehe, R. Aigner, and L.M. Castaner, *Current drive methods to extend the range of travel of electrostatic microactuators beyond the voltage pull-in point*, Microelectromechanical Systems, Journal of **11** (2002), no. 3, 255–263.
- [89] H.C. Nathanson, W.E. Newell, R.A. Wickstrom, and J.R. Davis Jr, *The resonant gate transistor*, Electron Devices, IEEE Transactions on **14** (1967), no. 3, 117–133.
- [90] A.H. Nayfeh and M.I. Younis, *A new approach to the modeling and simulation of flexible microstructures under the effect of squeeze-film damping*, Journal of Micromechanics and Microengineering **14** (2004), no. 2, 170–181.
- [91] ———, *Modeling and simulations of thermoelastic damping in microplates*, Journal of Micromechanics and Microengineering **14** (2004), no. 12, 1711–1717.
- [92] A.H. Nayfeh, M.I. Younis, and E.M. Abdel-Rahman, *Dynamic pull-in phenomenon in MEMS resonators*, Nonlinear Dynamics **48** (2007), no. 1, 153–163.
- [93] R.B. Nelson, *Simplified calculation of eigenvector derivatives*, AIAA Journal **14** (1976), no. 9, 1201–1205.
- [94] J. Nocedal and S.J. Wright, *Numerical optimization*, Springer Verlag, 1999.
- [95] M. Ohsaki and K. Ikeda, *Stability and optimization of structures: generalized sensitivity analysis*, Springer, 2007.
- [96] E.T. Ong and K.M. Lim, *Three-dimensional singular boundary elements for corner and edge singularities in potential problems*, Engineering Analysis with Boundary Elements **29** (2005), no. 2, 175–189.
- [97] S. Pamidighantam, R. Puers, K. Baert, and H.A.C. Tilmans, *Pull-in voltage analysis of electrostatically actuated beam structures with fixed-fixed and fixed-free end conditions*, Journal of Micromechanics and Microengineering **12** (2002), no. 4, 458–464.

- [98] L.S. Pan, G.R. Liu, and K.Y. Lam, *Determination of slip coefficient for rarefied gas flows using direct simulation Monte Carlo*, Journal of Micromechanics and Microengineering **9** (1999), no. 1, 89–96.
- [99] Y.H. Park and KC Park, *High-fidelity modeling of MEMS resonators. part I. anchor loss mechanisms through substrate*, Microelectromechanical Systems, Journal of **13** (2004), no. 2, 238–247.
- [100] JS Przemieniecki, *Theory of matrix structural analysis*, Dover Pubns, 1985.
- [101] SA Ragon, Z. G ”urdal, and LT Watson, *A comparison of three algorithms for tracing nonlinear equilibrium paths of structural systems*, International Journal of Solids and Structures **39** (2002), no. 3, 689–698.
- [102] SS Rao, *Mechanical vibrations*, Addison Wesley Publishing Company, 1995.
- [103] G.M. Rebeiz, *RF MEMS: theory, design, and technology*, John Wiley and Sons, 2003.
- [104] M.J. Rewienski, *A trajectory piecewise-linear approach to model order reduction of nonlinear dynamical systems*, Ph.D. thesis, Massachusetts Institute of Technology, USA, 2003.
- [105] E. Riks, *An incremental approach to the solution of snapping and buckling problems*, International Journal of Solids and Structures **15** (1979), no. 7, 529–551.
- [106] V. Rochus, *Finite element modeling of strong electro-mechanical coupling in MEMS*, Universite de Liege, PhD Thesis, Belgium, 2006.
- [107] V. Rochus, DJ Rixen, and J.C. Golinval, *Electrostatic coupling of MEMS structures: transient simulations and dynamic pull-in*, Nonlinear Analysis **63** (2005), no. 5-7, 1619–1633.
- [108] V. Rochus, D.J. Rixen, and J.C. Golinval, *Monolithic modelling of electro-mechanical coupling in micro-structures*, Int. Journal for Numerical Methods in Engineering **65** (2006), no. 4, 461–493.
- [109] V. Rochus, L. Van Miegroet, P. Duysinx, J.C. Golinval, and D. Rixen, *Modelling the electromechanical coupling of RF switch using Extended Finite Element*, Thermal, Mechanical and Multi-Physics Simulation and Experiments in Microelectronics and Micro-Systems, 2008. EuroSimE 2008. International Conference on (2008), 655–659.
- [110] X. Rottenberg, H. Jansen, P. Fiorini, W. De Raedt, and H.A.C. Tilmans, *Novel RF-MEMS capacitive switching structures*, European Microwave Conference, 2002. 32nd (2002), 1–4.
- [111] Lepage S., *Stochastic finite element method for the modeling of thermoelastic damping in micro-resonators*, Universite de Liege, PhD Thesis, Belgium, 2007.

- [112] H. Sadeghian, JFL Goosen, A. Bossche, and F. van Keulen, *A mechanistic model for adsorption-induced change in resonance response of submicron cantilevers*, Proceedings of SPIE, vol. 6885, 2008, p. 68850E.
- [113] H. Sadeghian, CK Yang, JFL Goosen, E. van der Drift, A. Bossche, PJ French, and F. van Keulen, *Characterizing size-dependent effective elastic modulus of silicon nanocantilevers using electrostatic pull-in instability*, Applied Physics Letters **94** (2009), 221903.
- [114] Hamed Sadeghian, Hans Goosen, Andre Bossche, and Fred van Keulen, *Application of electrostatic pull-in instability on sensing adsorbate stiffness in nanomechanical resonators*, Thin Solid Films **518** (2010), no. 17, 5018 – 5021.
- [115] J.B. Sampsel, *Digital micromirror device and its application to projection displays*, Journal of Vacuum Science & Technology B: Microelectronics and Nanometer Structures **12** (1994), 3242.
- [116] G.I. Schuëller, *Developments in stochastic structural mechanics*, Archive of Applied Mechanics **75** (2006), no. 10, 755–773.
- [117] J.I. Seeger and B.E. Boser, *Charge control of parallel-plate, electrostatic actuators and the tip-in instability*, Microelectromechanical Systems, Journal of **12** (2003), no. 5, 656–671.
- [118] S.D. Senturia, *Simulation and design of microsystems: a 10-year perspective*, Sensors & Actuators: A. Physical **67** (1998), no. 1-3, 1–7.
- [119] SD Senturia, N. Aluru, and J. White, *Simulating the behavior of MEMS device: Computational method and needs*, IEEE Computational Science and Engineering **4** (1997), no. 1.
- [120] K. Silverbrook, *Inkjet device encapsulated at the wafer scale*, July 10 2003, US Patent App. 10/250,967.
- [121] P.P. Silvester and R.L. Ferrari, *Finite Elements for Electrical Engineers*, Cambridge University Press, 1996.
- [122] A.K. Slone, K. Pericleous, C. Bailey, and M. Cross, *Dynamic fluid–structure interaction using finite volume unstructured mesh procedures*, Computers and Structures **80** (2002), no. 5-6, 371–390.
- [123] TA Stolarski and W. Chai, *Inertia effect in squeeze film air contact*, Tribology International **41** (2008), no. 8, 716–723.
- [124] J. Tamayo, D. Ramos, J. Mertens, and M. Calleja, *Effect of the adsorbate stiffness on the resonance response of microcantilever sensors*, APPLIED PHYSICS LETTERS **89** (2006), 224104.
- [125] W.C. Tang, T.C.H. Nguyen, and R.T. Howe, *Laterally driven polysilicon resonant microstructures*, Sensors & Actuators: A. Physical **20** (1989), no. 1-2, 25–32.
- [126] G. Tennant, *Six Sigma: SPC and TQM in manufacturing and services*, Gower Pub Co, 2001.

- [127] J.M.T. Thompson and G.W. Hunt, *Elastic instability phenomena*, John Wiley & Sons, 1984.
- [128] T. Thundat, GY Chen, RJ Warmack, DP Allison, and EA Wachter, *Vapor detection using resonating microcantilevers*, *Analytical Chemistry* **67** (1995), no. 3, 519–521.
- [129] M.M. Tilleman, *Analysis of electrostatic comb-driven actuators in linear and non-linear regions*, *International Journal of Solids and Structures* **41** (2004), no. 18-19, 4889–4898.
- [130] H.A.C. Tilmans and R. Legtenberg, *Electrostatically driven vacuum-encapsulated polysilicon resonators. II: Theory and performance*, *Sensors and actuators. A, Physical* **45** (1994), no. 1, 67–84.
- [131] L.D. Tin, A. Greiner, and JG Korvink, *Model Order Reduction for Circuit Level Simulation of RF MEMS Frequency Selective Devices*, *Sensor Letters* **6** (2008), no. 1, 1–8.
- [132] P. Tiso and E. Jansen, *A Finite Element Based Reduction Method for Nonlinear Dynamics of Structures*, 46 th AIAA/ASME/ASCE/AHS/ASC Structures, Structural Dynamics, and Materials Conference; Austin, TX; USA; 18-21 Apr. 2005. pp. 1-12. 2005, American Institute of Aeronautics and Astronautics, The Aerospace Center, 370 L'Enfant Promenade, SW, Washington, DC, 20024, USA, 2005, pp. 1–12.
- [133] P. Tiso and D.J. Rixen, *Reduction methods for mems nonlinear dynamic analysis*, IMAC XXVIII A Conference and Exposition on Structural Dynamics, Jacksonville, FL (Bethel, CT), Society for Experimental Mechanics, February 2010.
- [134] A. van Beek, *Advanced Engineering Design*, Engineering-abc. com, Delft, The Netherlands, 2006.
- [135] F. Van Keulen and J. Booij, *Refined consistent formulation of a curved triangular finite rotation shell element*, *International Journal for Numerical Methods in Engineering* **39** (1996), 2803–2820.
- [136] T. Veijola, H. Kuisma, J. Lahdenperä, and T. Ryhänen, *Equivalent-circuit model of the squeezed gas film in a silicon accelerometer*, *Sensors & Actuators: A. Physical* **48** (1995), no. 3, 239–248.
- [137] T. Veijola and P. Raback, *Methods for Solving Gas Damping Problems in Perforated Microstructures Using a 2D Finite-Element Solver*, *Sensors* **7** (2007), 1069–1090.
- [138] H.K. Versteeg and W. Malalasekera, *An Introduction to Computational Fluid Dynamics: The Finite Volume Method*, Longman Scientific & Technical, Harlow, Essex, 1995.
- [139] M. Wautelet, *Scaling laws in the macro-, micro-and nanoworlds*, *European Journal of Physics* **22** (2001), no. 6, 601–611.

- [140] M.I. Younis, *Modeling and Simulation of Microelectromechanical Systems in Multi-Physics Fields*, Ph.D. thesis, Virginia Polytechnic Institute and State University, 2004.
- [141] C. Zenger and H. Gietl, *Improved difference schemes for the Dirichlet problem of Poisson's equation in the neighbourhood of corners*, *Numerische Mathematik* **30** (1978), no. 3, 315–332.
- [142] L.X. Zhang and Y.P. Zhao, *Electromechanical model of RF MEMS switches*, *Microsystem Technologies* **9** (2003), no. 6, 420–426.
- [143] Y. Zhao and T. Cui, *Fabrication of high-aspect-ratio polymer-based electrostatic comb drives using the hot embossing technique*, *Journal of Micromechanics and Microengineering* **13** (2003), no. 3, 430–435.
- [144] V.I. Zhulin, S.J. Owen, and D.F. Ostergaard, *Finite Element Based Electrostatic-Structural Coupled Analysis with Automated Mesh Morphing*, *Proceedings of the International Conference on Modeling and Simulation of Microsystems MSM* (2000), 501–504.
- [145] O.C. Zienkiewicz, C. Emson, and P. Bettess, *A novel boundary infinite element*, *International Journal for Numerical Methods in Engineering* **19** (1983), no. 3, 393–404.
- [146] O.C. Zienkiewicz and D. Lefebvre, *A robust triangular plate bending element of the Reissner-Mindlin type*, *International Journal for Numerical Methods in Engineering* **26** (1988), 1169–1184.

Illustration credits

- The picture of Eiffel tower on the cover, which is repeated at the beginning of part I, was made in 1902 and was first published by Camille Flammarion (1842-1924). Currently the copyright on this picture has expired.
- The copyright on the miniature on page 2 by Niccolò da Bologna has expired.
- The picture at the beginning of part II shows a typical *hunebed* as can be found in the Netherlands. It is over 5000 years old. This picture was been made by Gouwenaar and has been released by the photographer without copyright restriction.
- The picture of the car at the beginning of part III was taken in 1903 and shows Marcel Renault. Currently the copyright on this picture has expired.
- The sunset with flying red-winged blackbirds at the beginning of part IV was photographed by J. Segraves, who has released the picture without copyright restrictions.
- For all other illustrations the copyright holder is either acknowledged in the caption or the copyright is owned by the author.

Curriculum vitae

Stephan Hannnot was born in Rotterdam on the 26th of July 1983. His secondary education was followed at the *Develstein college* in Zwijndrecht. After finishing his secondary education in 2001, he started studying mechanical engineering at the *Delft University of Technology*. In 2006 he obtained his M.Sc. degree after performing a graduation project on the modeling of electro-mechanical microsystems. This graduation project started his interest in numerical modeling and microsystems. Therefore he continued his investigations into the numerical modeling of microsystems as a Ph.D. candidate within the faculty of Mechanical, Maritime and Materials Engineering of the *Delft University of Technology* in November 2006.